Lanthanide Metal-Organic Frameworks for Advanced Energy Systems

A thesis submitted to the University of Dublin for the degree of

Doctor of Philosophy

Gearóid Manning, M. Sc.

School of Chemistry

University of Dublin

2026

Declaration

I declare that this thesis has not been submitted as an exercise for a degree at this or any other university and that it is entirely my own work, except where otherwise citied, referenced, acknowledged or accredited.

I agree to deposit this thesis in the University's open access institutional repository or allow the library to do so on my behalf, subject to Irish Copyright Legislation and Trinity College Library conditions of use and acknowledgement.

Gearóid Manning

Summary

This thesis, entitled *Lanthanide Metal-Organic Frameworks for Advanced Energy Systems*, focuses on use of novel lanthanide metal-organic frameworks (Ln-MOFs) and their derivatives as electrocatalysts and photocatalysts for solar-to-fuel applications. Particular emphasis is placed demonstrating the efficacy of redox active Ln-MOFs catalyst (utilising Ce^{3+}/Ce^{4+} and Eu^{3+}/Eu^{2+} redox couples) and examining how the choice of MOF linker influences performance.

Chapter 1 contextualises this work by introducing the key topics addressed in this thesis. It begins with a broad overview of anthropogenic climate change and the associated challenges, before discussing the concept of artificial photosynthesis and solar-to-fuel applications such as the generation of H_2 from water and the production of synthetic carbon fuels derived from captured CO_2. The chapter then turns to metal–organic frameworks (MOFs), reviewing current literature from synthesis to their electrocatalytic and photocatalytic applications. Finally, the focus narrows to lanthanide-based MOFs—which, to date, have received far less attention than their extensively studied transition-metal counterparts—and their potential catalytic applications, thereby laying the groundwork for the aims of this thesis.

Chapter 2 details the synthesis and characterisation of an isoreticular series of Ce(III) MOFs followed by a systematic study of their electrocatalytic water oxidation activity in acidic conditions. This work provides the first investigation of Ln-MOFs as sole electrocatalysts for the oxygen evolution reaction (OER). It was found that the Ce(III) MOFs acted as pre-catalysts to generate OER-active cerium(IV) oxide phases, with the choice of MOF linker appearing to influence catalytic performance.

Chapter 3 explores the use of the Ce(III) MOF isoreticular series from the previous chapter, introduced in Chapter 2, as sacrificial templates to produce cerium oxide–carbon composites via pyrolysis. The resulting materials were characterised by Raman spectroscopy, PXRD, SEM, and TEM. Electrochemical studies revealed that pyrolysis markedly enhanced electrocatalytic water oxidation activity and kinetics. The composites displayed good performance and stability at 1 mA cm^{-2} in 0.5 M H_2SO_4.

The second part of this work explores the incorporation of an acetylene-extended Ru(II)

polypyridyl metalloligand, $\mathbf{[H_4L_{Ru}]^{2+}}$, as a photosensitising linker for lanthanide-based MOFs. Chapter 4 describes the synthesis and characterisation of a novel series of two-dimensional lanthanide-based MOFs (**LnRu-MOFs**) incorporating $\mathbf{L_{Ru}^{2-}}$ as the linker. These MOFs comprise dinuclear Ln(III) secondary building units (SBUs) and are isostructural from Ce to Er—a rare example of a lanthanide coordination series structurally unaffected by the *gadolinium break* in Lewis acidity. The Ru(II) polypyridyl metalloligands retain their photosensitising properties, with photoluminescence emission bands shifted relative to the free metalloligand. The direction and magnitude of these shifts (blue or red) correlate with the Lewis acidity of the coordinating Ln(III) ion, with the influence of the *gadolinium break* is clearly evident in this case.

Chapter 5 builds on the work of chapter 4 by investigating the photocatalytic activity of **CeRu-MOF** and **EuRu-MOF** for the OER and HER, as well as the CO_2RR in the case of **EuRu-MOF**. Both MOFs were shown to be viable platforms for redox photocatalysis, with performance compared against reported MOF photocatalysts. In addition, the feasibility of integrating LnRu-MOFs into photoelectrochemical (PEC) systems was assessed. Thin films of **CeRu-MOF** and **EuRu-MOF** were electrochemically grown on conductive substrates and preliminarily tested as photoelectrodes.

Chapter 6 details the experimental procedures undertaken in this work, with additional supporting information provided in the Appendix.

Chapter 7 provides the overall conclusions of this thesis and outlines potential directions for future research based on the findings.

Acknowledgements

Firstly, I would like to express my sincere gratitude to my supervisor, Prof. Wolfgang Schmitt for his support and encouragement throughout my PhD studies, as well as his invaluable guidance throughout the course of this work and the writing of this thesis. I would also like to gratefully acknowledge the Irish Research Council (now Research Ireland) for their financial support.

The work presented in this thesis is the result of a collaborative effort. I would like to thank all the School of Chemistry staff for their tireless work, in particular: Dr. Brendan Twamley for SCXRD measurements, his extensive crystallography knowledge and many enlightening conversations; Dr. John O'Brien for NMR measurements and advice; Dr. Manuel Ruether for training on many analytic instruments, as well as somehow keeping them all running; Dr. Gary Hessman for mass spectrometry measurements; Ben Power and Anne Maire Farrell for their administrative work; Peter O'Brien and Mark Keegan without whom the whole place would probably fall apart; and also to the staff on the Cocker Laboratory, Margaret 'Peggy' Brehon, Marina Kilduff and Geraldine Dunne, for their friendliness and always ensuring that demonstrating for the undergraduate labs went by seamlessly.

I am very grateful to my collaborators both near and far: Prof. Louise Bradley and Kseniia Mamaeva (School of Physics) for photophysical measurements; Dr. Igor Chunin (CRANN) for XPS measurements; Dr. Clive Downing (AML) for SEM-EDX training and HR-TEM imaging; Prof. Chris Batchelor-McAuley and Andrea Scutti; Prof. Dominic Ryan (McGill University, Canada) for ^{151}Eu Mössbauer spectroscopic studies; Dr Cora O'Donnell and Alexandru Paiu (TU Dublin) for Ion Chromatography measurements.

I would like to thank all members of the Schmitt group, past and present, for their support and camaraderie. A special mention to Dr. Muhamhed Mulahmetović for his guidance and advice at the beginning of my PhD studies, as well as his work on ruthenium metalloligands which—along with Dr. Éadaoin Whelan's work on lanthanide MOFs—laid the foundation for my own research. Dr. Sebastien Vaesen and Dr. Navaneetha Tokala for their encouragement and advice. Dr. Athira Ravi for generously sharing her electrochemistry knowledge. Dr. Shrabana Sarkar for BET measurements and Dr. Karl Ackland for TEM

imaging. My talented project students Bhattacharjee Dwaipayan, James Evans, Liam Power, Claire Bradley, Elisa Mathieu and Róisin Maguire, all of whom it was a pleasure and privilege to collaborate with.

Lastly, I would like to thank my family and friends. To my parents, Ursula and Patrick, for their love, support, and everything they have given me throughout my life. To my brother (and fellow PhD chemist) Patrick, for his encouragement, support and possibly just a touch of competition. To my partner, Dearbháil, for her love, support, patience and ability to always make me smile, I would be lost without you. And finally, I would be remiss to leave out my cats, Pangur Bán and Nóinín, for their (mostly) peaceful company during the long hours of writing this thesis.

Table of Contents

Abbreviations

1D	One-Dimensional
^{1}H-NMR	Proton Nuclear Magnetic Resonance
2D	Two-Dimensional
3D	Three-Dimensional
^{13}C-NMR	Carbon-13 Nuclear Magnetic Resonance
ATR	Attenuated Total Reflectance
BET	Brunauer–Emmett–Teller (surface area analysis)
BID	Barrier Ionization Detector
bpy	2,2'-bipyridine
BTB	4,4',4''-(benzene-1,3,5-triyl)tris(benzoate)
CB	Conduction Band
CCD	Charge-Coupled Device
CO_2RR	Carbon Dioxide Reduction Reaction
CP	Carbon Paste
CV	Cyclic Voltammetry
DCM	Dichloromethane
DFT	Density Functional Theory
DMA	N,N-dimethylaniline
DMF	N,N-dimethylformamide
DMSO	Dimethyl sulfoxide
DPA	Diisopropylamine
EDX	Energy-Dispersive X-ray Spectroscopy
e.g.	*Exempli gratia* (for example)
ESI	Electrospray Ionisation
ESI-MS	Electrospray Ionisation Mass Spectrometry
et al.	*Et alii* (and others)
EtOH	Ethanol
FE	Faradaic Efficiency
Fc	Ferrocene
FFT	Fast Fourier Transform
FTIR	Fourier Transform Infrared Spectroscopy
FTO	Fluorine-Doped Tin Oxide
GC	Gas Chromatography

GC-BID	Gas Chromatography with Barrier Ionization Detector
GooF	Goodness of Fit
HER	Hydrogen Evolution Reaction
HPLC	High-Performance Liquid Chromatography
HOCO	Highest Occupied Crystal Orbital
HOMO	Highest Occupied Molecular Orbital
HRMS	High-Resolution Mass Spectrometry
HR-TEM	High-Resolution Transmission Electron Microscopy
i.e.	*Id est* (that is)
IPA	Isopropanol
IR	Infrared Spectroscopy
IRF	Instrument Response Function
J	Coupling Constant
j	Current Density
LED	Light Emitting Diode
LLCT	Ligand-to-Ligand Charge Transfer
LMCT	Ligand-to-Metal Charge Transfer
Ln	Lanthanide
Ln-MOF	Lanthanide Metal-Organic Framework
LnRu-MOF	Lanthanide–Ruthenium Metal-Organic Framework
LSV	Linear Sweep Voltammetry
LUCO	Lowest Unoccupied Crystal Orbital
LUMO	Lowest Unoccupied Molecular Orbital
m	Multiplet
MeOH	Methanol
MLCT	Metal-to-Ligand Charge Transfer
MMCT	Metal-to-Metal Charge Transfer
MOF	Metal-Organic Framework
m/z	Mass-to-Charge Ratio
NMR	Nuclear Magnetic Resonance
OEP	Oxygen Evolution Photocatalyst
OER	Oxygen Evolution Reaction
PEC	Photoelectrochemical
PL	Photoluminescence
ppm	Parts per Million

ppb	Parts per Billion
PXRD	Powder X-ray Diffraction
RDE	Rotating Disk Electrode
s	Singlet
SBU	Secondary Building Unit
SCXRD	Single-Crystal X-ray Diffraction
SEA	Sacrificial Electron Acceptor
SED	Sacrificial Electron Donor
SEM	Scanning Electron Microscopy
SHE	Standard Hydrogen Electrode
t	Triplet
$TBAPF_6$	Tetrabutylammonium hexafluorophosphate
TEM	Transmission Electron Microscopy
TGA	Thermogravimetric Analysis
THF	Tetrahydrofuran
TOF	Turnover Frequency
TRPL	Time-Resolved Photoluminescence
TTB	4,4′,4″-(1,3,5-triazine-2,4,6-triyl)tris(benzoate)
TTT	5,5′,5″-(1,3,5-triazine-2,4,6-triyl)tris(thiophene-2-carboxylate)
UiO	University of Oslo (MOF family)
VB	Valence Band
WOR	Water Oxidation Reaction
XRD	X-ray Diffraction

Chapter 1: Introduction

1.1 Motivation and Global Context

Exponential growth of the global economy since the Industrial Revolution, driven primarily by the combustion of fossil fuels, has caused an unprecedented rise in atmospheric greenhouse gas concentrations.[1] In 2024, the global average atmospheric CO_2 concentration reached 423 ppm—the highest value on record, and part of a continuous year-on-year increase since direct atmospheric measurements began in 1959.[2] Ice-core records, which capture air bubbles from previous millennia, clearly show that this post-industrial increase breaks with the natural trend of the past 800,000 years (Figure 1.1) and coincides directly with humanity's industrialisation through fossil fuel combustion (Figure 1.2).[1]

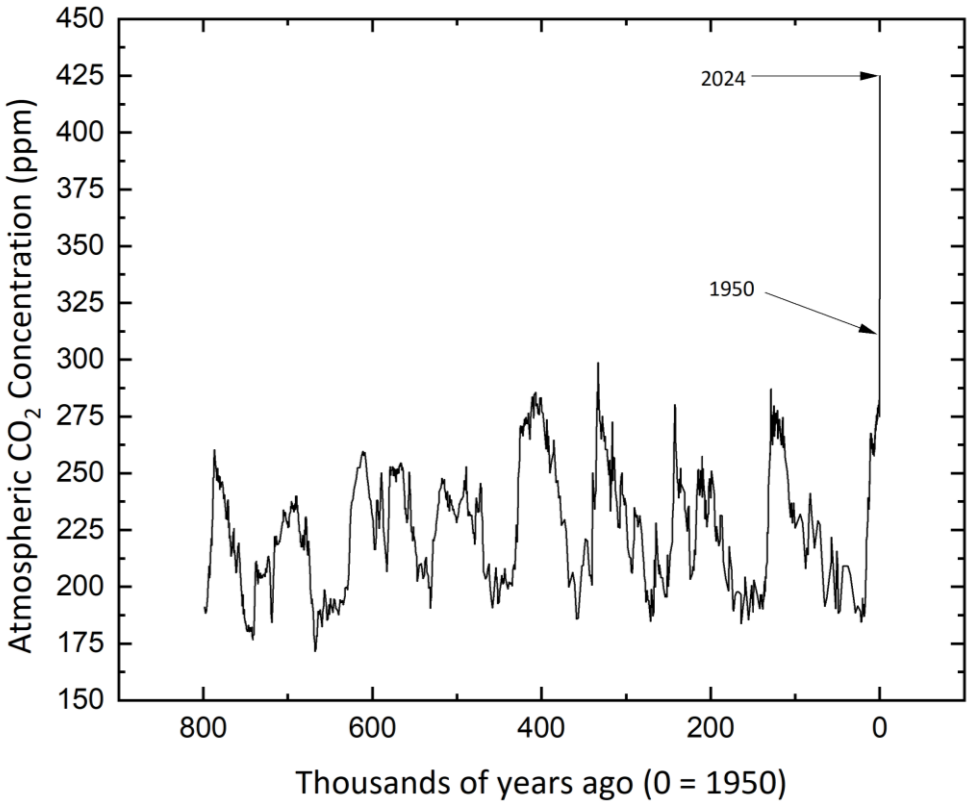

Figure 1.1: Atmospheric carbon dioxide in parts per million (ppm) over the past 800,000 years. Based on ice-core data from Lüthi et al.[3] up to 1958. Direct atmospheric measurement data used from 1959 to 2024, from Keeling et al.[4]

Further evidence from paleo-CO_2 data suggests that current atmospheric concentrations are higher than at any point in the last two million years.[2] As a consequence, global surface temperatures during 2011–2020 were, on average, 1.1 °C warmer than in the 1861–1890

baseline period, with this trend set to continue (Figure 1.2). Moreover, warming between 1970 and 2020 occurred faster than in any other 50-year window for at least the past two millennia.[2] The effect of this rapid warming is already evident in rising sea levels and increased frequency of extreme weather events worldwide, with an estimated 3.3–3.6 billion people considered highly vulnerable to cascading impacts of climate change, such as food and water insecurity.[2]

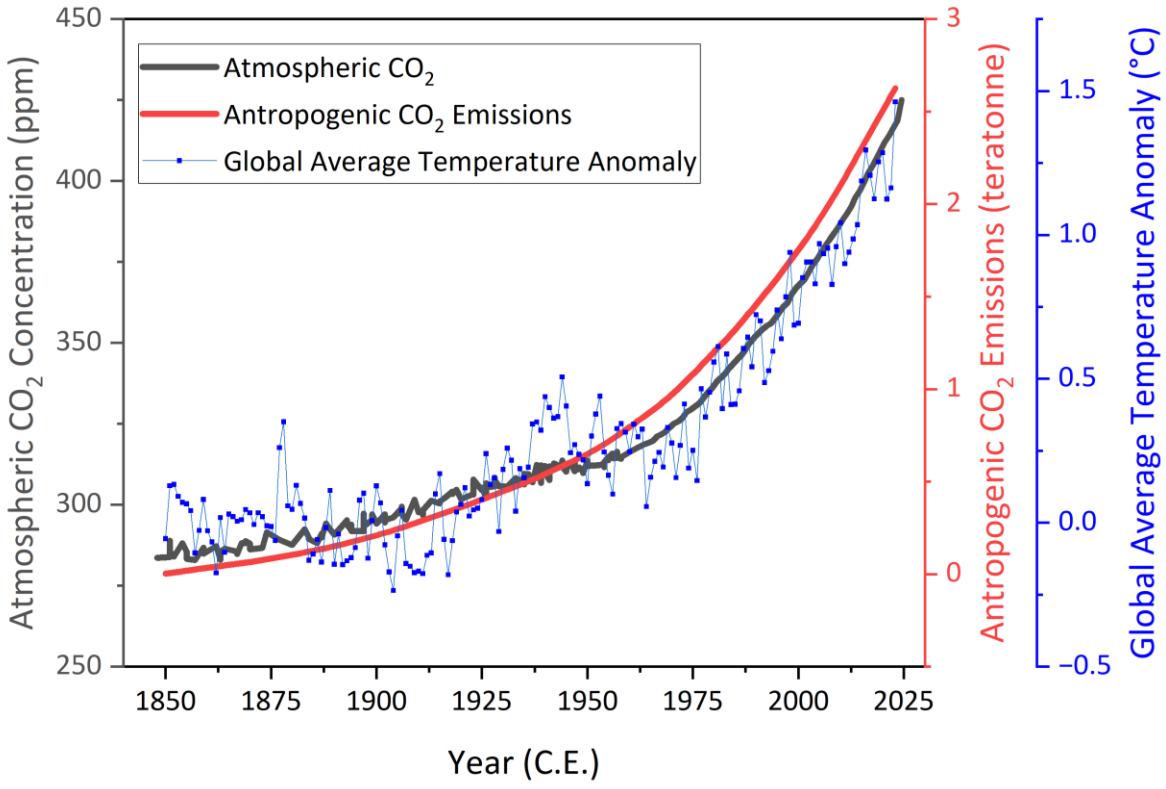

Figure 1.2: Atmospheric carbon dioxide concentrations (black line; parts per million) have increased in parallel with cumulative anthropogenic CO_2 emissions (red line; 1 teratonne = 1 × 10^{12} kg), coinciding with a rise in global average surface temperature (blue line and squares; relative to the 1861–1890 baseline). Atmospheric CO_2 data are from Lüthi et al.[3] (pre-1958) and Keeling et al.[4] (1959–2024). Cumulative anthropogenic CO_2 emissions (from fossil fuel combustion and land-use change) and global temperature anomaly data are taken from the Global Carbon Project (Global Carbon Budget, 2024) and the Met Office Hadley Centre (HadCRUT5, 2025), with data processing by Our World in Data.[5]

Avoiding the most severe outcomes of climate change and upholding the commitments of the Paris Agreement—to limit global temperature rise to well below 2 °C, and ideally to 1.5 °C above pre-industrial levels—requires a rapid and timely transition to a carbon-neutral global economy.[6]

1.2 Challenges in Decarbonising Global Energy Systems

Electricity generation from renewable energy technologies—such as solar, wind, and hydro—as well as nuclear power, will play a central role in the decarbonisation of the global energy sector.[7] However, fossil-fuel-based electricity generation retains a practical advantage in its flexibility and the speed with which output can be ramped up or down in response to fluctuations in consumer demand.[7,8] Solar photovoltaics, for example, depend on sunlight availability, while wind turbines require sufficient wind to operate; therefore, peak generation from these sources is intermittent and cannot be easily controlled to match demand. Hydroelectric reservoirs can provide rapid load-following capabilities but are geographically constrained.[7,9] Nuclear and geothermal technologies are valuable for baseload electricity generation, as they provide a stable, continuous output, but they lack the ability to respond dynamically to demand fluctuations.[7-9]

This operational flexibility of fossil fuels arises from their role as energy carriers: they represent solar energy captured via photosynthesis over geological timescales and stored in the form of C–C and C–H chemical bonds. This intrinsic chemical energy storage enables stable, storable, and dispatchable energy supply.[8]

To decarbonise power generation, the ability to store renewable energy in a stable form is therefore crucial. Several energy storage technologies are currently available or under development, including mechanical storage (e.g., pumped hydroelectric), thermal storage, and electrochemical storage (batteries). For chemical energy storage, the most established pathway is the production of hydrogen via water electrolysis.[7,8] Hydrogen can subsequently be used to regenerate electricity on demand through proton-exchange membrane (PEM) fuel cells or by combustion in gas turbines.[7] As illustrated in Figure 1.3, hydrogen possesses an exceptionally high gravimetric energy density but suffers from a relatively low volumetric energy density, even when compressed to 700 bar. This limitation presents challenges in applications where space and storage constraints are critical, particularly in the transport sector.

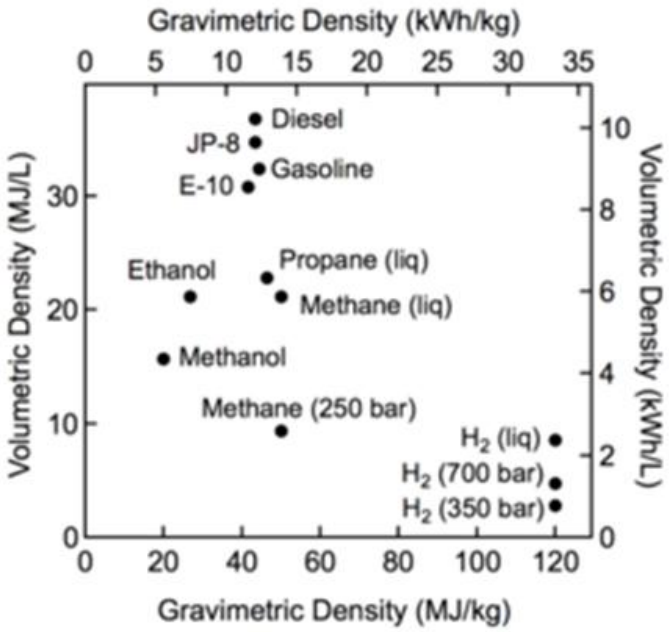

Figure 1.3: Gravimetric energy density and volumetric density of fuels. JP-8: jet propellant 8; E-10: ethanol blended fuel. Credit: US Department of Energy, Fuel Cell Technologies Office.[10]

Alternative chemical energy storage strategies are therefore being explored, most notably the production of synthetic carbon-based fuels, which possess volumetric energy densities comparable to conventional fossil fuels. Although combustion of these synthetic fuels inevitably releases CO_2, their use can still achieve carbon neutrality if the CO_2 feedstock is captured directly from the atmosphere or from industrial emissions. In this case, no additional net carbon is introduced into the atmosphere, unlike fossil-fuel-derived hydrocarbons. While this approach may not represent the ideal long-term solution, it offers a pragmatic route for decarbonising difficult-to-electrify sectors such as aviation and shipping in the near to medium term.[7-9]

1.3 Inspiration from Photosynthesis in Nature

In natural photosynthesis, solar energy is captured and stored within the chemical bonds of organic molecules, which serve as the fundamental building blocks of living organisms and, over geological timescales, the precursors of fossil fuels. Central to this process is the photocatalytic splitting of water into molecular oxygen and hydrogen equivalents (protons and electrons).[11,12] The oxygen is released into the atmosphere, where it becomes available for respiration and other oxidation reactions. The hydrogen equivalents, in the form of reducing equivalents (ATP and NADPH), are subsequently used

to reduce carbon dioxide to simple carbohydrates in the Calvin cycle.[11,12] These carbohydrates function as both energy reserves and precursors for more complex organic molecules.

Photosynthesis: $xH_2O + xCO_2 + h\nu \rightarrow C_xH_{2x}O_x$ Eq. 1.1

Respiration: $C_xH_{2x}O_x \rightarrow xH_2O + xCO_2 + \text{energy}$ Eq. 1.2

When carbohydrates are metabolised by organisms, the reverse process—respiration—occurs. In this reaction, oxygen and reducing equivalents are recombined via controlled metabolic pathways, releasing stored energy to power cellular processes and producing H_2O and CO_2 as by-products, thereby completing the cycle. From an energetic perspective, photosynthesis represents a strategy for storing hydrogen (derived from water splitting) and, by extension, solar energy in the form of chemical bonds. Unlike other organisms, humanity has harnessed this reverse process not only metabolically but also artificially, through the combustion of fossil fuels and biomass to power technological advancement.

Plants, algae, and cyanobacteria accomplish photosynthesis through the coordination of several subsystems. Antenna complexes, such as chlorophyll molecules in photosystem II, are finely tuned to absorb visible light (~1.8 eV).[11] The absorbed excitation energy is transferred to reaction centres, where electron transfer occurs from donor to acceptor species. This electron–hole separation enables the generation of oxidising and reducing equivalents, which subsequently migrate to catalytic sites for water oxidation and CO_2 reduction.[11,12] Drawing inspiration from this natural process, artificial photosynthetic systems aim to mimic these functions—using light-harvesting antennae to capture solar energy and drive catalytic water oxidation, as well as the reduction of either protons to H_2 or CO_2 to value-added organic molecules.

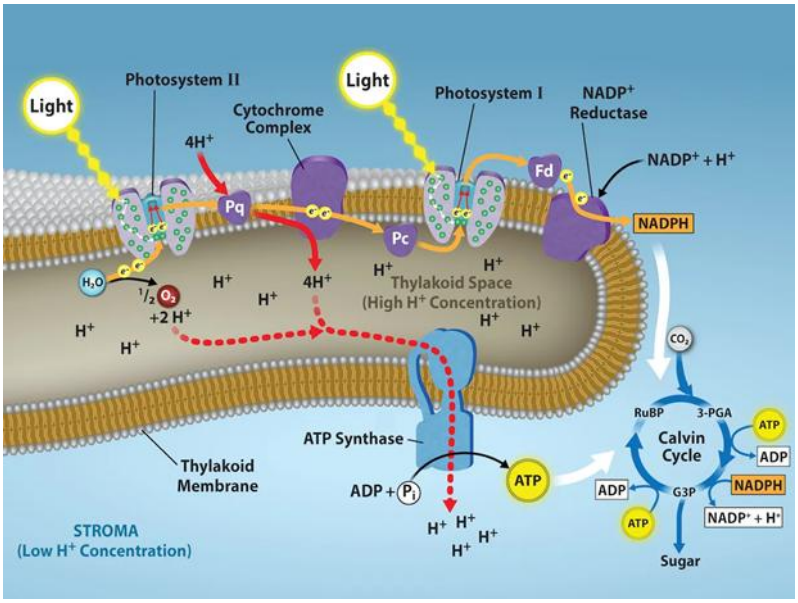

Figure 1.4: Simplified schematic representation of photosynthesis. The light-dependent reactions occur in the thylakoid membranes of the chloroplast, beginning with the absorption of visible light (680 nm) by chlorophyll in photosystem II. This excites an electron, which is transferred to the acceptor pheophytin and subsequently shuttled along an electron transport chain to photosystem I, generating a proton gradient that drives adenosine triphosphate (ATP) synthesis. At photosystem I, the electron is re-excited by absorption of a second photon (700 nm) and then passed along another transport chain before being used in the reduction of nicotinamide adenine dinucleotide phosphate (NADPH). The electron deficit in photosystem II is replenished via the oxidation of H_2O by the Mn–Ca oxygen-evolving complex. In the light-independent Calvin cycle, CO_2 is captured by the enzyme RuBisCo and, through a series of steps, converted into short-chain sugars, with ATP and NADPH providing the reducing power. Reproduced with permission from A. Rao et al.[13]

1.4 Artificial Photosynthesis

Artificial photosynthesis, in its broadest sense, refers to systems that convert solar energy into chemical energy stored in the form of a fuel—commonly termed a "solar fuel."[14,15] Hydrogen, generated by water splitting through photocatalysis, photoelectrocatalysis, or even electrocatalysis powered by solar cells or wind turbines, qualifies as a solar fuel. Similarly, synthetic carbon-based fuels produced via solar-driven CO_2 reduction are also categorised as solar fuels. [14,16]

1.4.1. Key Reactions in Artificial Photosynthesis

Fundamental to artificial photosynthesis is the oxidation and reduction half-reactions. The water oxidation half-reaction providing protons and electrons needed for the reduction half-reaction with produces the solar fuel. The ubiquity of water on earth makes in an ideal source of protons and electrons, as exploited in natural photosynthesis.

1.4.1.1 Water Oxidation Reaction

Due to its central role in both photosynthetic and artificial photosynthetic systems, the

water oxidation reaction—commonly referred to as the oxygen evolution reaction (OER)—is the subject of intensive research and discussion.[17-20] The inherent stability of water makes OER energetically challenging, as indicated by the thermodynamically determined onset potential of 1.23 V vs. SHE (Eq. 1.4):

$$2H_2O \rightarrow 4H^+ + 4e^- + O_2 \qquad \Delta G° = 237.13\ kJ\ mol^{-1} \qquad \text{(Eq. 1.3)}$$

$$E° = \frac{\Delta G°}{nF} = \frac{237.13\ kJ\ mol^{-1}}{2\ (96\ 485\ C\ mol^{-1})} = 1.23\ V \qquad \text{(Eq. 1.4)}$$

Because liquid water is converted to gaseous oxygen, an additional enthalpic requirement of 48.7 kJ mol^{-1} must be considered.[17,21] Incorporating this (Eq. 1.5), the thermoneutral potential under standard conditions (25 °C, 1 atm) is 1.48 V vs. SHE:

$$E = \frac{\Delta H}{nF} = \frac{\Delta G + T\Delta S}{nF} = \frac{237.13\ kJ\ mol^{-1} + 48.7\ kJ\ mol^{-1}}{2\ (96\ 485\ C\ mol^{-1})} = 1.48\ V \quad \text{(Eq. 1.5)}$$

In the electrocatalysis community, it is generally accepted that this additional heat need not be supplied by applied potential, and instead can be provided by the surroundings.[17]As a result, reported OER onset potentials are often below 1.48 V vs. SHE.[17] However, this remains contentious, with some arguing that under steady-state conditions the majority of this additional heat requirement must be supplied by applied potential on the working electrode.[21] Trivedi *et al.* recently contended that when both thermodynamic and kinetic factors are considered, it is highly improbable that an OER onset overpotential below 100 mV or a steady-state overpotential below 200 mV (at 10 mA cm^{-2}) can be realistically achieved—casting doubt on many literature claims.[21]

When an applied overpotential produces a constant Faradaic current, a steady-state reaction rate is established.[17] As shown in Eq. 1.6, the rate (*v*) is proportional to the Faradaic current (*i*) divided by the number of electrons transferred of per reactant (*n*) and the Faraday constant (*F*):

$$v = \frac{i}{nF} \qquad \text{(Eq. 1.6)}$$

The OER is a complex multi-step, four-electron process involving the cleavage of four O–H bonds, formation of an O–O bond, and generation of four protons. This complexity results in the OER having sluggish kinetics at low overpotentials.[17-20] Like all

electrochemical electron transfer reactions, each electron transfer reaction of the mulit-step OER process has an associated activation barrier. These activation barriers can be overcome by increasing applied overpotential, temperature, and/or pressure. Under standard conditions, additional overpotential is therefore required to drive OER at rates relevant for solar fuel production. [17-20]

The charge transfer coefficient (α) in the Butler-Volmer equation (Eq. 1.7) indicates the proportion of the applied overpotential that goes towards overcoming the activation barrier.[17,21]

$$j = j_0 \left(e^{\frac{\alpha n F \eta}{RT}} - e^{\frac{(1-\alpha) n F \eta}{RT}} \right) \qquad \text{(Eq. 1.7)}$$

where j is current density, j_o the exchange current density, α the charge transfer coefficient, n the number of electrons transferred per reactant, F the Faraday constant, η the overpotential, R the universal gas constant, and T the absolute temperature. At low overpotentials, α tends to be low due to the thermoneutrality constraint described above.

1.4.1.2 Hydrogen Evolution Reaction

In acidic solution the thermodynamic potential of the HER, the proton reduction half-reaction, is 0 V vs. SHE, making it appear trivial when relative to the water oxidation half-reaction discussed above. However kinetic constraints mean that overpotential is generally required to drive the reaction.[22,23] This arises from the fact that for reduction to take place, a proton must first be adsorbed to a catalytic site, this is known as the Volmer reaction (Eq. 1.9), which is then followed by the electrochemical Heyrovsky reaction (Eq. 1.10) and/or the chemical Tafel reaction (Eq. 1.11). In both cases H_2 is formed and desorbed.[22] At some noble metal surfaces (Rh, Ru,Pt, Pd and Ir) H^+ is strongly adsorbed which is known as underpotentially deposited hydrogen, UPD. Another form of adsorbed hydrogen is overpotentially deposited hydrogen, OPD. Both can exist on noble metals but only OPD hydrogens are involved in HER.[22]

$$2H^+ + 2e^- \rightarrow H_2 \qquad E° = 0\ V\ vs.\ SHE \qquad \text{(Eq. 1.8)}$$

$$\mathrm{H^+ + M + e^-} \underset{k_{-1}}{\overset{k_1}{\rightleftharpoons}} \mathrm{MH_{ads}} \qquad \text{Volmer} \qquad \text{(Eq. 1.9)}$$

$$MH + H^+ + e^- \underset{k_{-2}}{\overset{k_2}{\rightleftharpoons}} M + H_2 \qquad \text{Heyrovsky} \qquad \text{(Eq. 1.10)}$$

$$2MH \underset{k_{-3}}{\overset{k_3}{\rightleftharpoons}} 2M + H_2 \qquad \text{Tafel} \qquad \text{(Eq. 1.11)}$$

In neutral or alkaline HER is achieved by the water reduction half-reaction (Eq. 1.12) which has a thermodynamic potential of – 0.83 V vs. SHE.[23] As with the proton reduction half-reaction, kinetic constraints, in the form so a similar Volmer-Heyrovsky-Tafel mechanism (Eq. 1.13-1.15) result in an overpotential being required to drive the reaction.

$$2H_2O + 2e^- \rightarrow H_2 + 2OH^- \qquad E° = -0.83\,V\ vs.\ SHE \qquad \text{(Eq. 1.12)}$$

$$H_2O + M + e^- \underset{k_{-1}}{\overset{k_1}{\rightleftharpoons}} MH_{ads} + OH^- \qquad \text{Volmer} \qquad \text{(Eq. 1.13)}$$

$$MH + H_2O + e^- \underset{k_{-2}}{\overset{k_2}{\rightleftharpoons}} M + H_2 + OH^- \qquad \text{Heyrovsky} \qquad \text{(Eq. 1.14)}$$

$$2MH \underset{k_{-3}}{\overset{k_3}{\rightleftharpoons}} 2M + H_2 \qquad \text{Tafel} \qquad \text{(Eq. 1.15)}$$

1.4.1.3 Carbon Dioxide Reduction Reaction

Carbon dioxide (CO_2) represents the highest oxidation state of carbon and is a highly stable molecule, with a standard enthalpy of formation of –393.5 kJ mol^{-1}.[24,25] Humanity has long exploited this large energy release through the combustion of fossil fuels. It logically follows that the carbon dioxide reduction reaction (CO_2RR) is an endergonic reaction. One that can yield a wide variety of products, depending on the number of protons and electrons involved, as well as the energy of the electrons driving the reaction. The most common products are C_1 species such as CO, HCOOH, HCHO, CH_3OH, and CH_4, though C_2 products (e.g. CH_3CH_2OH, C_2H_4, C_2H_6) and even C_3 products (e.g. C_3H_7OH) can also be generated, particularly with copper-based electrocatalysts.[25-27] Table 1.1 summarises the standard reduction potentials (25 °C, 1 atm, pH = 7) for several representative CO_2RR half-reactions. Thermodynamically, these CO_2RR pathways are within ±0.2 V of the hydrogen evolution reaction (HER). However, the high activation

barrier of CO_2 and the complexity of multi-electron, multi-proton transfer mechanisms result in sluggish kinetics, poor product selectivity, and large overpotentials.[28] A key challenge for CO_2RR, not typically encountered in the OER or HER, is product selectivity: low selectivity leads to mixtures of products that require energy-intensive separation, undermining the practicality of large-scale processes. Furthermore, the generation of undesired by-products consumes electrons that could otherwise contribute to the formation of the target product, reducing overall efficiency.[25]

Table 1.1: Standard potentials for selected CO_2RR products in a pH 7 aqueous solution, under standard temperature and pressure (25°, 1 atm). Taken from Zhao et al.[26]

Reactions	***E*⁰ (V) *vs.* SHE, STP, pH = 7**
$CO_2 + e^- \rightarrow CO_2^{\cdot-}$	−1.90
$2H^+ + 2e^- \rightarrow H_2(g)$	−0.42
$CO_2 + 2H^+ + 2e^- \rightarrow HCOOH(l)$	−0.55
$CO_2 + 2H^+ + 2e^- \rightarrow CO(g) + H_2O$	−0.52
$CO_2 + 4H^+ + 4e^- \rightarrow HCHO(l) + H_2O$	−0.48
$CO_2 + 6H^+ + 6e^- \rightarrow CH_3OH(l) + H_2O$	−0.39
$CO_2 + 8H^+ + 8e^- \rightarrow CH_4(g) + 2H_2O$	−0.25
$2CO_2 + 12H^+ + 12e^- \rightarrow C_2H_4(g) + 4H_2O$	−0.38
$2CO_2 + 12H^+ + 12e^- \rightarrow C_2H_5OH(l) + 3H_2O$	−0.35
$2CO_2 + 14H^+ + 14e^- \rightarrow C_2H_6(g) + 4H_2O$	−0.28
$3CO_2 + 18H^+ + 18e^- \rightarrow C_3H_7OH(l) + 5H_2O$	−0.30

In photocatalytic CO_2 reduction, the reaction begins with light absorption by the photocatalyst. If the absorbed photons are of sufficient energy, electron–hole pairs are generated. The photogenerated electrons are promoted to the conduction band (or to the LUMO in molecular photocatalysts) and subsequently transferred to catalytic sites where CO_2 reduction occurs. Product selectivity is influenced by several factors, including the conduction band potential, which determines the reducing power of the electrons,

and light intensity, which governs the rate of electron–hole pair generation and thereby affects reaction kinetics. Efficient charge separation increases the density of available electrons, favouring multi-electron reduction pathways. The nature and density of catalytic active sites, the presence of cocatalysts, and the adsorption–desorption behaviour of reactants, intermediates, and products further dictate the reaction pathway and overall selectivity.[25]

Product selectivity in electrocatalytic CO_2RR is influenced by many of the same factors as in photocatalysis, with the key difference being the source of electrons. In this case, electrons are supplied by applying an external voltage across the anode and cathode of the electrochemical cell, with their reduction potential directly controlled by the applied voltage. This precise control of potential can be advantageous for tuning product selectivity.[26,28] Additional factors such as CO_2 adsorption and activation, the choice of electrolyte, the nature of the catalytic sites, and the adsorption–desorption behaviour of intermediates also play critical roles in determining both selectivity and overall yield.[25,26,28]

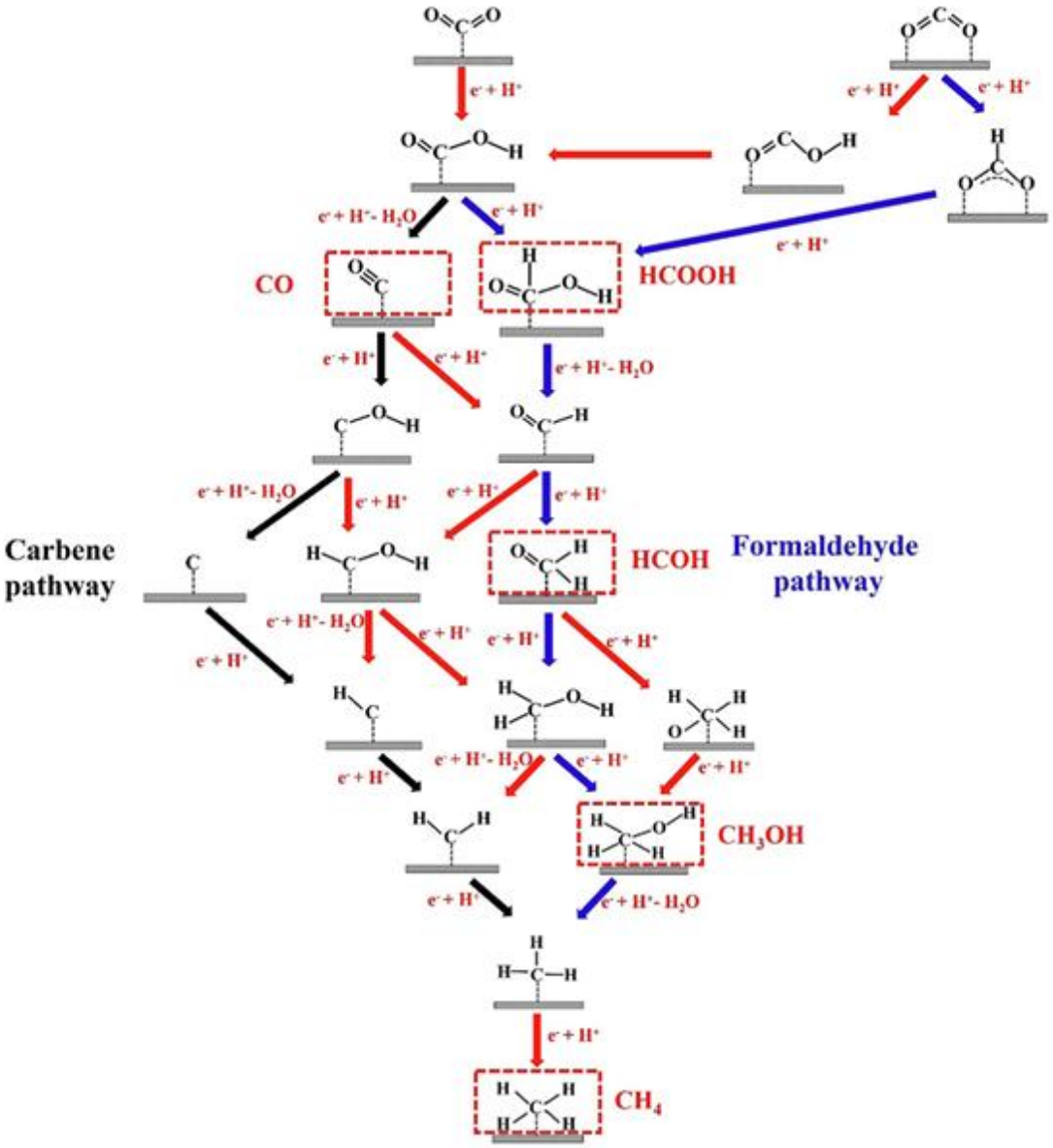

Figure 1.5: Possible pathways of CO_2 reduction to various C_1 products. Reproduced with permission from Fu et al.[25]

Figure 1.5 illustrates the possible CO_2RR pathways leading to various C_1 products, with particular focus on the most hydrogenated product, CH_4. The reaction begins with adsorption of CO_2 at the catalyst active site, either through carbon or oxygen coordination, producing a partially charged $CO_2^{\delta-}$species.[25,29] The coordination mode of $CO_2^{\delta-}$ plays a decisive role in dictating the subsequent reaction pathway and the intermediates formed. Two well-established pathways to CH_4 are the *formaldehyde pathway* and the *carbene pathway*. [25,29]

In the *formaldehyde pathway* (blue arrows, Figure 1.5), the 8-electron reduction proceeds via CO_2 → HCOOH → H_2CO → CH_3OH → CH_4, with formic acid, formaldehyde, and

methanol serving as the 2-, 4-, and 6-electron intermediates/side-products, respectively. [25,29] The binding strength of these intermediates to the active site determines whether they desorb as products or remain bound for further hydrogenation/deoxygenation. The pathway begins with the reduction of adsorbed $CO_2^{\delta-}$ to either a carboxyl radical or formate anion, which is further reduced to HCOOH. Successive reductions generate HCO*, then H_2CO, which undergoes further hydrogenation to yield CH_3OH. Finally, CH_3OH is reduced to CH_3*, which is subsequently hydrogenated to CH_4. [25,29,30]

In the *carbene pathway* (black arrows, Figure 1.5), the reduction progresses as $CO_2 \rightarrow CO \rightarrow C^* \rightarrow CH_3^* \rightarrow CH_4$. Adsorbed $CO_2^{\delta-}$ first reduces to a carboxyl radical (monodentate binding), which undergoes further reduction to CO. [25,29,30] Depending on its binding strength, CO may either desorb as a product or remain coordinated for further reduction to COH*. COH* then undergoes dehydration to yield C*, which is hydrogenated stepwise to CH_3*. This intermediate can either reduce further to CH_4 or, in a competing reaction, undergo nucleophilic attack by a hydroxyl radical to form CH_3OH as a side-product. [25,29,30]

1.4.2 Electrocatalytic Systems

Solar energy harvested by photovoltaic devices, or indirectly via wind turbines (as wind arises from solar-driven atmospheric convection), can be converted to electricity to power electrocatalytic water splitting or CO_2 reduction systems, thereby achieving an indirect form of artificial photosynthesis.

The first experiments on water electrolysis were reported in 1789 by Jan Rudolph Deiman and Adriaan Paets van Troostwijk, who used an electrostatic generator to discharge an electrical current across two gold electrodes immersed in water, producing hydrogen at the cathode and oxygen at the anode. [31-33] In 1800, Nicholson and Carlisle, using Volta's newly invented voltaic pile, demonstrated water splitting with copper electrodes, followed shortly after by Ritter, who was the first to separately collect hydrogen and oxygen gases. [31-33] Despite these early advances, industrial application of water electrolysis only began at the end of the nineteenth century with the advent of reliable direct current (DC) power sources and the development of effective diaphragms to

separate anodic and cathodic chambers, preventing the formation of explosive H_2/O_2 mixtures. By 1902, more than 400 alkaline electrolysers were in use.[31,33]

The twentieth century brought major advancements in water electrolysis, including the development of pressurised alkaline electrolysers in the 1940s, proton exchange membrane (PEM) electrolysers in the 1960s, and solid oxide electrolysers in the 1980s. [31-33] In the twenty-first century, research has focused on developing cost-effective electrocatalysts to enable large-scale coupling of water electrolysis with renewable energy sources. To date, however, deployment remains limited due to the reliance on platinum-group metals.[31-36]

PEM electrolysis was first developed in the 1960s by General Electric, building on the work of W. T. Grubb, who demonstrated the use of sulfonated polystyrene membranes as solid polymer electrolytes.[31,34] This concept replaced the liquid alkaline electrolyte with a thin polymer membrane (e.g., Nafion, fumapem etc.), providing high proton conductivity, low gas crossover, compact system design, and the ability to operate under differential pressure. Early PEM units were used in spacecraft and submarines for oxygen generation before being adapted for terrestrial hydrogen production.[31,33-35]

The PEM electrolyser cell (Figure 1.6) comprises a proton-exchange membrane (PEM) sandwiched between anode and cathode catalyst layers, typically based on platinum-group metals. These catalyst layers are coated of porous diffusion layers, typically carbon or titanium felt, which provide electrical contact to the catalyst layer and facilitate the transport of water and gaseous products, while titanium distribution (bipolar) plates separate individual cells and water flow.[37] A key advantage over alkaline systems is their ability to operate at high current densities (>2 A cm^{-2}) with rapid dynamic response, making them well suited to intermittent renewable energy inputs such as wind and solar. Their low hydrogen crossover also allows safe operation, while the ability to operate under differential pressure enables in situ compression of hydrogen to up to 350 bar, reducing downstream compression costs.[34,35]

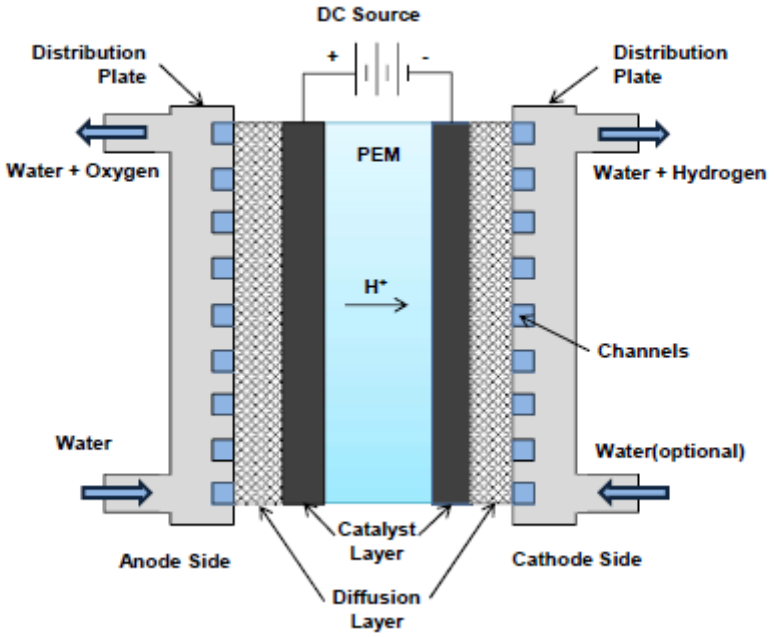

Figure 1.6: Simplified schematic of PEM electrolyser. Reproduced with permission from Sood et al.[37]

Despite these advantages, PEM electrolysers face challenges. The acidic environment (pH ≈ 2) and high overpotentials necessitate the use of corrosion-resistant materials: IrO_2 for the oxygen evolution reaction (OER) and Pt for the hydrogen evolution reaction (HER), supported on titanium-based current collectors and separator plates.[31,33-35] The scarcity and high cost of iridium, in particular, is a significant barrier to scale-up. Considerable research efforts have therefore focused on reducing Ir loadings, alloying with other metals (Ru, Sn, Co), and engineering nanostructured morphologies to improve activity and durability.X Recent studies have demonstrated Ir loadings as low as ~0.8 mg cm^{-2} with excellent stability, and thermal efficiencies exceeding 90% under industrially relevant conditions.[38,39] Siemens Energy, a leading PEM electrolyser manufacturer, estimates that Ir loading must be reduced to ≤ 0.1 mg cm^{-2} for the technology to scale to projected global demand.[40]

PEM electrolysis is now advancing towards MW-scale systems, such as the 54 MW plant operated by BASF in Ludwigshafen, Germany.[41] With rapid start-up, wide operating range, and compatibility with intermittent renewable electricity, PEM technology offers a highly attractive route for converting excess renewable energy into hydrogen as a storable energy vector. While precious-metal dependence remain an obstacle, ongoing advances in electrocatalysts, membranes, and stack engineering continue to reduce costs and

improve durability, positioning PEM electrolysis as a cornerstone technology for a future hydrogen economy.[31,33-41]

1.4.3 Photoelectrocatalytic Systems

One of the first examples of direct artificial photosynthesis was reported by Fujishima and Honda in 1972.[42] In their pioneering study, they demonstrated a photoelectrochemical

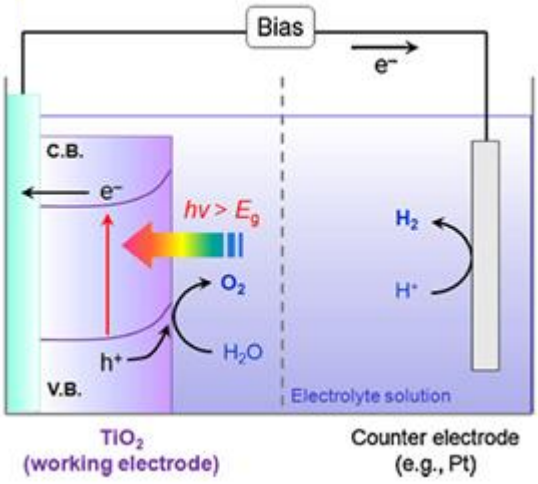

Figure 1.7: Simplified schematic of PEC water splitting. Reproduced with permission from K. Maeda.[43]

cell (PEC) in which TiO_2 was employed as an n-type semiconductor photoanode for the water oxidation half-reaction, coupled with a Pt cathode for proton reduction under an applied external bias. As illustrated in Figure 1.7, upon irradiation of the TiO_2 photoanode with UV light of energy greater than its band gap, electron–hole pairs were generated, with electrons promoted to the conduction band (CB) and holes left in the valence band (VB). Under anodic bias, the photogenerated electrons migrated through the external circuit to the Pt cathode, where they reduced protons to H_2. Simultaneously, the holes in the valence band of TiO_2 oxidised water to O_2, generating additional protons and electrons to sustain the cycle.[42,43]

PEC systems for water splitting have further refined since this initial work, particularly the development of photoanode materials can effectively harness more of the solar spectrum i.e. visible light. However, despite many advances, achieving solar-to-hydrogen (STH) efficiency of more than 10% while maintaining long term stability has proved challenging, limiting industrial application.[44-47] Zhou et al. achieved a STH of 10.5% and stability for 40 hours in 1 M KOH (aq.) using a GaAs/InGaP/TiO_2 photoanode coated on a Ni electrode and

NiMo coated cathode.[44] PEC systems for CO_2RR have also gained much interest in recent years, for example Andrei et al. used a perovskite-$BiVO_4$ PEC device coupled with a molecular Co catalyst to demonstrate solar-to-fuel efficiencies of 0.58% and 0.053% for H_2 and CO, respectively.[49] As exemplified by this study, the HER strongly competes with the CO_2RR as is typically the case in aqueous electrolyte. To suppress the competing HER and aprotic organic solvent electrolytes are typically used, however a small concentration of a proton source, e.g. water, must be added must be present for CO_2RR to take place.[45] While this can effectively supress HER is generally limits CO_2RR products to CO and HCOOH.[45,50-52]

1.4.4 Photocatalytic Systems

There are two types of photocatalytic water splitting: one-step and two-step photoexcitation processes. In the one-step process (Figure 1.8), a single-component photocatalyst is employed, with the bandgap and band edge potential of the material exceeding 1.23 eV to enable proton reduction to H_2 by photogenerated electrons in the conduction band (CB) and water oxidation to O_2 and protons by photogenerated holes in the valence band (VB).[53] Only a few single-component photocatalysts meet these criteria—for example, β-Ge_3N_4 and $BaTaO_2$—but their solar-to-hydrogen (STH) efficiencies remain low (typically <1%) due to rapid electron–hole recombination.[53,54] A further challenge arises because H_2 and O_2 are generated in the same chamber, requiring downstream separation of the oxyhydrogen mixture, careful engineering to mitigate safety risks such as spontaneous combustion, and inevitably some product loss. [53,54] Despite these challenges, Nishiyama et al. demonstrated this approach at pilot scale with a 100 m² photocatalytic solar hydrogen production system (Figure 1.9).[55] The system comprised 1,600 reactor units, each designed as an individual panel that could be assembled into 3 m² modules. Each panel contained a photocatalyst layer of aluminium-doped strontium titanate ($SrTiO_3$:Al), through which water was flowed at the base while the resulting oxyhydrogen mixture was collected from the top via narrow polyurethane tubing. The pilot plant operated safely and largely autonomously for several months, achieving a maximum STH efficiency of 0.76%.[55]

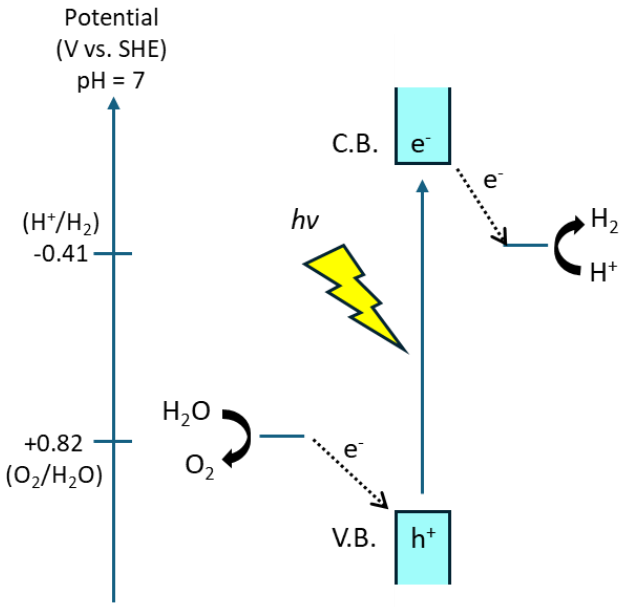

Figure 1.8: Simplified schematic representing the one-step excitation process for the photocatalytic splitting of water.

Figure 1.9: An aerial photograph of the 100 m^2 scale photocatalytic solar hydrogen production system consisting of 1,600 reactor panel units and a gas separation unit (indicated by the yellow box). Reproduced with permission from Nishiyama et al.[55]

In a two-step photoexcitation system (Figure 1.10), also known as a Z-scheme, the two half-reactions of water splitting are carried out by separate photocatalysts: a hydrogen evolution photocatalyst (HEP) for the HER and an oxygen evolution photocatalyst (OEP) for the OER.[53,54] Charge transfer between the two is mediated by either a solution-based redox couple mediator (e.g., Fe^{3+}/Fe^{2+} or IO_3^-/I^-) or a solid-state mediator such as gold or carbon.[53-56] These mediators shuttle electrons between the OEP and HEP, effectively suppressing rapid electron–hole recombination by spatially separating the charge carriers. The Z-scheme also broadens the variety of potential photocatalyst, as each photocatalyst only needs to perform one half-reaction, thereby relaxing band gap requirements and therefore extending the usable wavelength range. Furthermore, this potentially allows for the OER and HER to be physically isolated by use of a membrane, with a redox mediator shuttling electrons across it, enabling product separation at source, lowering downstream separation costs, and improving safety. [54]

The selection of OEP, HEP, and mediator for an overall water splitting system is non-trivial and requires careful optimisation. Owing to this complexity, photocatalysts are often first studied for each half-reaction independently using sacrificial reagents.[57,58] For OER studies, a sacrificial electron acceptor (SEA), such as sodium persulfate, captures the photogenerated electron in the OEP conduction band, preventing recombination and allowing the valence band hole to oxidise water. Conversely, for HER studies, a sacrificial electron donor (SED), such as methanol or ascorbic acid, donates an electron to fill the valence band hole of the HEP, enabling the conduction band electron to reduce protons to H_2. This approach allows OEPs and HEPs to be optimised separately before integration into a complete photocatalytic water splitting system. [57,58] This same principle applies for CO_2RR photocatalyst which would replace the hydrogen evolution photocatalyst in the above strategy.

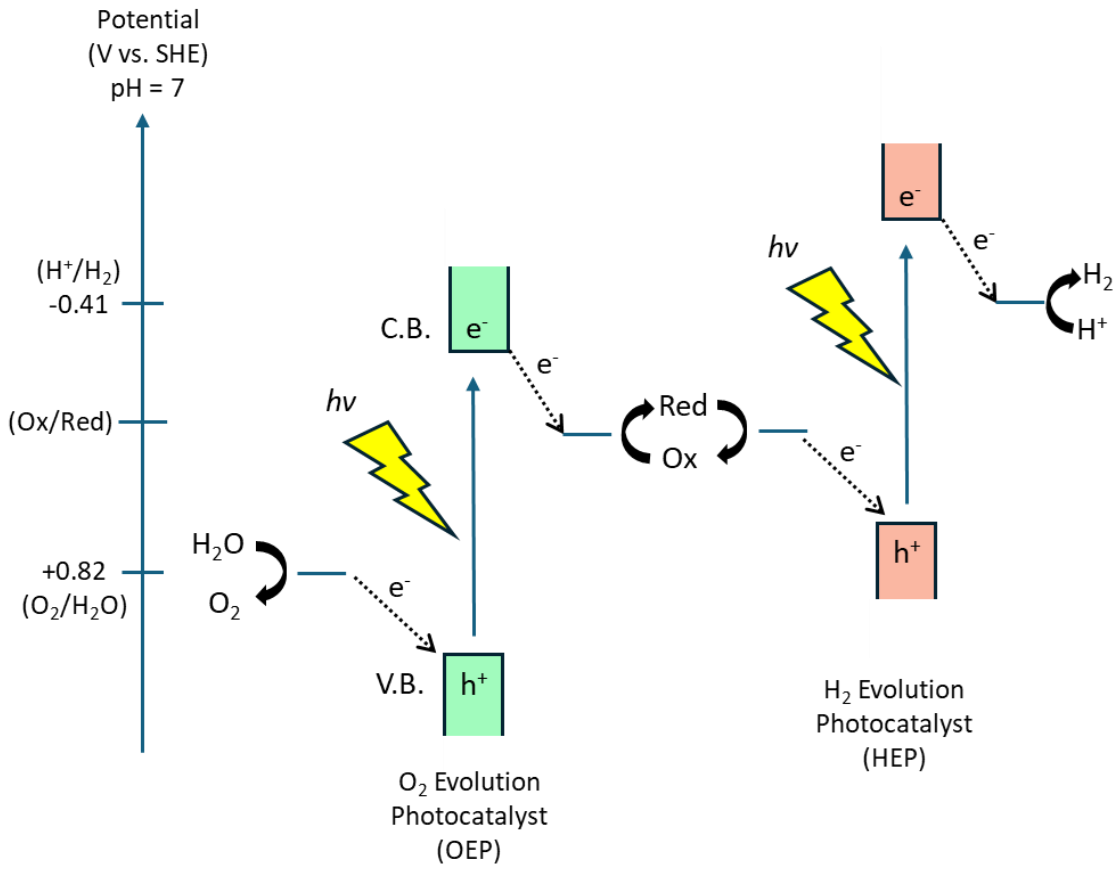

Figure 1.10: Simplified schematic representing the two-step excitation process for the photocatalytic splitting of water, using a redox couple electron shuttle.

1.5 Ceria as a Catalyst

Cerium dioxide (CeO_2, ceria) is a versatile catalytic material with established applications in three-way catalytic converters, fuel cells, and growing roles in photocatalytic and electrocatalytic energy conversion.[59-61] Its catalytic properties arise primarily from the reversible Ce^{3+}/Ce^{4+} redox couple, which facilitates rapid oxygen storage and release via surface oxygen vacancy formation. CeO_2 crystallises in a fluorite-type face-centred cubic structure, where Ce^{4+} cations are eightfold coordinated by O^{2-} anions which occupy tetrahedral lattice sites. At the surface, ceria can expose three stable surfaces—(100), (110), and (111)—with the (111) surface being the most thermodynamically stable.[59,62,63] However, the (100) and (110) surface exhibit lower oxygen vacancy formation energies and are therefore more catalytically active.[64] For example, nanorods and nanowires that preferentially expose these facets display superior oxygen storage capacity and CO

oxidation activity compared to polyhedral nanoparticles dominated by the (111) surface.[65] At the nanoscale, morphology plays a decisive role in tuning activity, stability, and selectivity.[59,65] Nanostructured ceria not only promotes oxygen transfer but also strongly influences the behaviour of supported metal particles, stabilising them against sintering and even enabling single-atom dispersion.[60] Facet engineering has been directly correlated with reactivity in reactions such as CO oxidation, consistent with both experimental observations and DFT studies.[60,66,67] Beyond morphology, defect engineering (e.g., annealing, plasma treatment) and heteroatom doping can further enhance catalytic performance by increasing oxygen vacancy density and electronic conductivity.[68,69] For instance, N- and S-doped ceria exhibits significantly improved oxygen evolution reaction (OER) activity in alkaline media by raising surface Ce^{3+} concentrations.[69]

In electrocatalysis, CeO_2 serves multiple functions: (i) Ce^{3+} sites and oxygen vacancies promote water dissociation, providing active centres for the hydrogen and oxygen evolution reactions (HER and OER); (ii) CeO_2–metal interfaces generate additional catalytic sites; (iii) CeO_2 modifies the coordination and electronic environment of transition-metal components, enhancing their activity.[59-61] Moreover, CeO_2 is highly stable in alkaline electrolytes and can act as a protective scaffold that prevents dissolution of less stable transition-metal components. These properties have enabled Ce-based hybrid catalysts (e.g., CeO_2 combined with Ni, Co, or Fe oxides/phosphides) that achieve low overpotentials and excellent durability in water-splitting applications.[68]

By contrast, few studies have examined ceria-based materials as electrocatalysts for acidic water splitting, and those that exist primarily use hybrid systems with platinum group metals.[70,71] A systematic investigation of ceria-based catalysts in acidic conditions—without additional metal components—is needed to clarify how preparation methods and morphology influence intrinsic electrocatalytic performance before integration into hybrid systems.

1.6 Metal-Organic Frameworks (MOFs)

Metal–organic frameworks (MOFs) are a class of metallo-supramolecular polymeric materials that self-assemble from organic linkers and inorganic nodes, coordinating in a

regular, repeating fashion to generate two- or three-dimensional networks with long-range order (i.e. high crystallinity).[72,73] The inorganic nodes may be single metal ions or coordination clusters, while the organic linkers are multidentate ligands, most commonly bearing carboxylate or pyridyl coordinating groups. Owing to the virtually unlimited combinations of organic linkers and inorganic nodes, an immense variety of MOF structures can be realised. Systematic study of the design, control, and predictability of these MOF architectures has led to the emergence of reticular chemistry and associated topological concepts.[74]

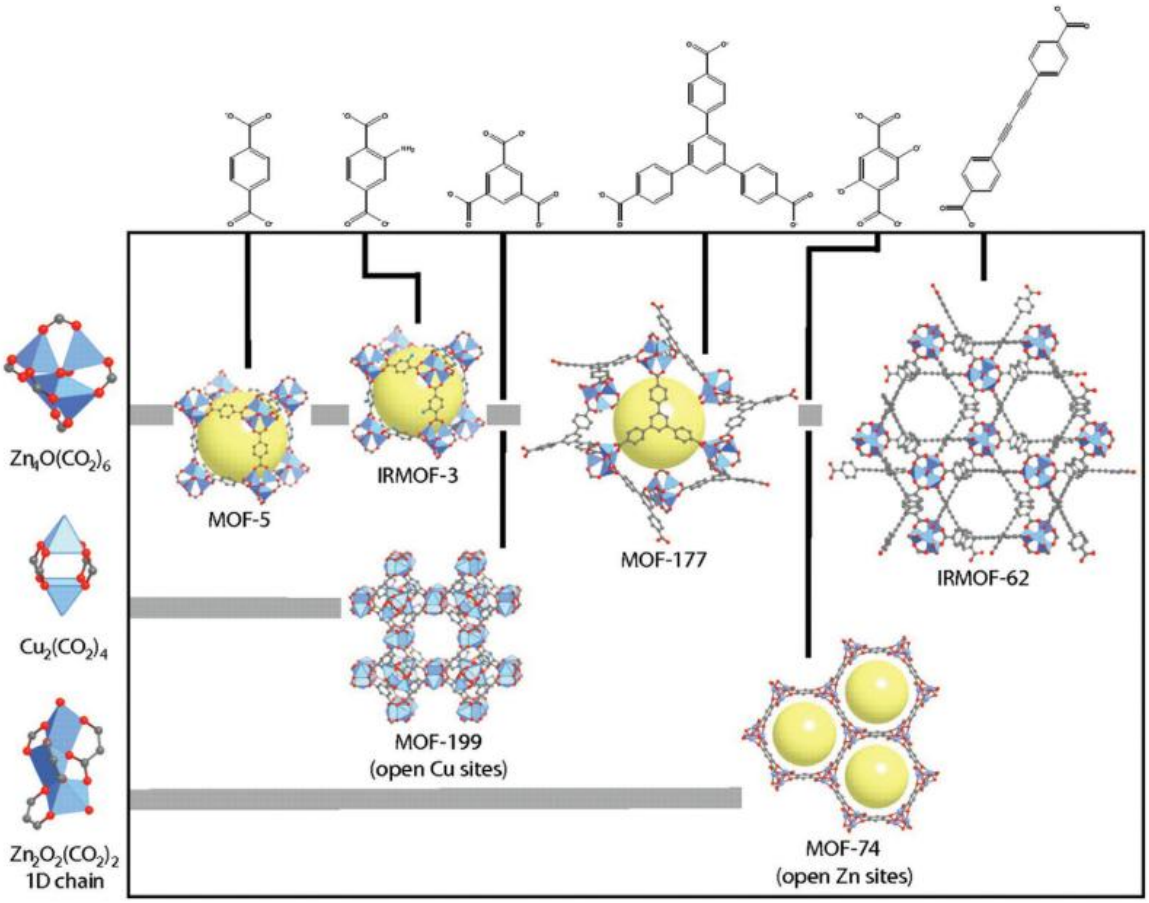

Figure 1.11: The structural versatility of MOFs arises from the diverse array of available inorganic and organic secondary building units (SBUs). Centre, examples of MOF crystal structures, MOF-5, IRMOF-3, MOF-177, IRMOF-62, and MOF-199. Left, inorganic SBUs belonging to MOFs centred. Top, organic linkers belonging to MOFs centred. Reproduced with permission from D. Britt et al.[76]

Reticular chemistry is based on the principle that MOFs can be reduced to the geometrical features of their constituent subcomponents and categorised accordingly.[75] Both the organic linkers and inorganic nodes are referred to as secondary building units (SBUs). The

structure of the inorganic SBU dictates the relative orientation in which the organic linkers assemble, while the organic linkers act as geometrically defined connectors between inorganic SBUs. If one knows the coordination geometry of the most likely inorganic SBUs to self-assemble under certain synthetic conditions and the geometry of the multidentate organic linker is also known, it becomes is possible to predict the resultant MOF structure.[72,74] Moreover, MOFs whose component SBUs share the same geometrical characteristics will form isoreticular structures with analogous topologies.[77] Advances in the understanding of these reticular chemistry concepts, and the development of synthetic strategies based on them, have led to the discovery of a vast number of new MOF structures.[78]

MOF-5 ($[Zn^{II}_4O(BDC)_3]$, BDC = 1,4-benzenedicarboxylate) and its many isoreticular analogues (IRMOFs) represent a classic example of the reticular synthesis concept. MOF-5 is a three-dimensional porous framework constructed from octahedral $\{Zn^{II}_4O\}$ inorganic SBUs connected by linear ditopic BDC ligands, giving rise to a primitive cubic (**pcu**) topology.[77] By substituting BDC with other linear ditopic carboxylate-based ligands, a family of IRMOF analogues can be obtained that retain the **pcu** topology of MOF-5, thereby forming an isoreticular series.[77] Such ligand substitution enables systematic tuning of MOF properties, including porosity and photoactivity.[78] The predictability and tunability of MOF structures afforded by reticular chemistry has driven immense research interest, with over 100,000 MOFs now reported in the Cambridge Structural Database (CSD).[79] The chemical and structural adaptability of MOFs has seen their application in areas such as catalysis[80], chemical sensing,[81] water purification,[82] gas storage and separation,[83] electroluminescence,[84] as well as other applications.[85]

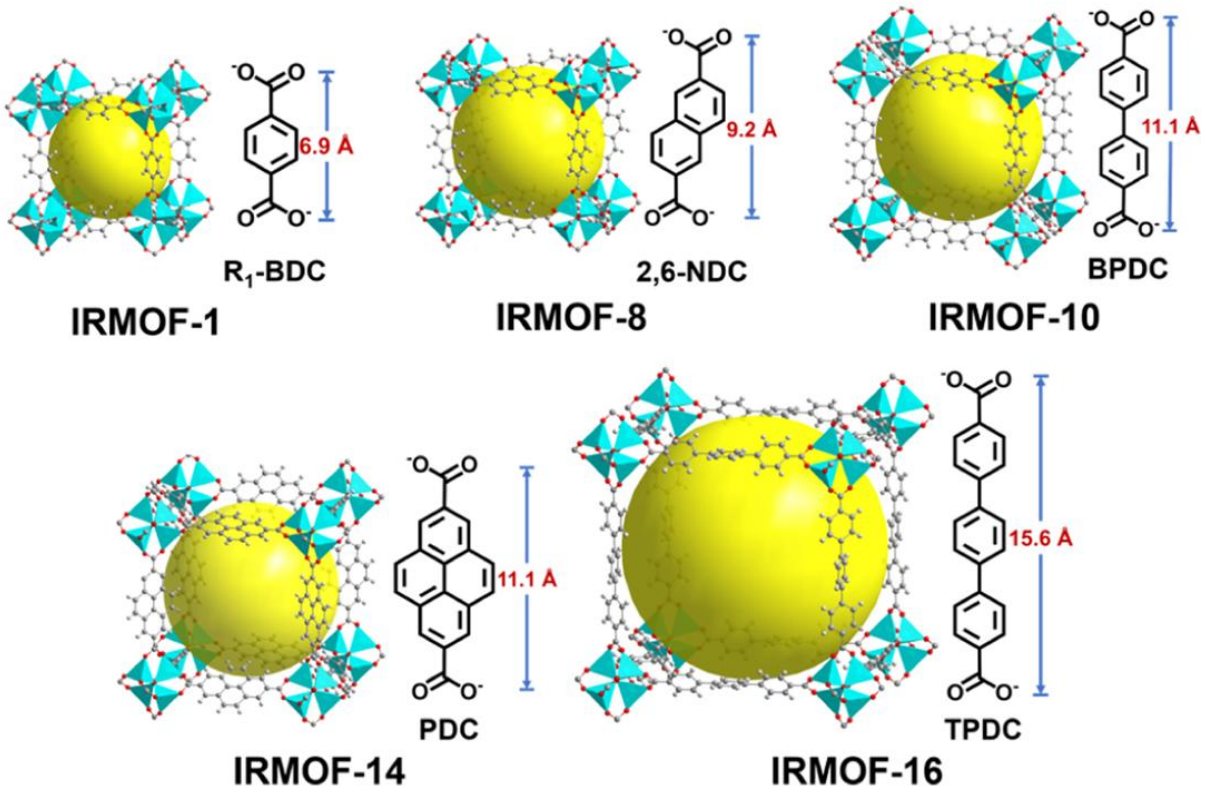

Figure 1.12: The isoreticular expansion of MOF-5. Reproduced with permission from Chen et al. [86]

1.6.1 Synthesis of MOFs

The synthesis of MOFs typically involves combining a metal salt with a multidentate organic ligand in a suitable solvent system, where, under appropriate conditions, the components undergo self-assembly to yield crystalline frameworks. Two principal approaches are commonly employed: the classical method, in which the reaction is maintained below the solvent's boiling point, and the solvothermal method, in which the sealed reaction mixture is heated above the solvent's boiling point, usually in a Teflon-lined autoclave.[87] The latter is generally preferred, as elevated temperatures improve reactant solubility and provide the thermodynamic driving force for self-assembly.[88] Colón et al. showed that MOF self-assembly proceeds through multiple metastable intermediates, and that nucleation requires at least four unit cells to achieve thermodynamic stability.[89] Furthermore, they found that the formation of ordered MOF crystals is entropically favoured due to solvent contributions during the assembly

process.[89] Crystallinity and crystal morphology are strongly influenced by temperature, pH, solvent properties, metal-to-ligand molar ratio, and the presence of counter-ions or auxiliary templating ligands.[90] Dialkylformamide-type solvents, such as dimethylformamide (DMF), are commonly employed in MOF synthesis because their slow decomposition (when heated) generates dialkylamines, which can deprotonate carboxylic acid-based ligands and thereby facilitate MOF formation.[91]

Despite the rational design principles offered by reticular chemistry, in practice the synthesis of new MOFs remains highly empirical. Identifying optimal conditions for each metal–ligand combination is often a matter of trial and error, with undesired phases frequently competing with the target MOF. Obtaining single crystals of sufficient quality for X-ray diffraction (needed for structure elucidation), or phase-pure MOF powders, often requires numerous failed attempts before optimum conditions are identified. To address this, high-throughput approaches are commonly adopted, in which multiple small-scale (~1 mL) reactions are carried out in parallel under systematically varied conditions, conserving time and reagents prior to scaling up under optimised parameters.[92] Alongside these conventional routes, several alternative synthesis methods have been developed, including electrochemical, microwave-assisted, mechanochemical, sonochemical, and atomic-layer deposition approaches.[87]

MOF thin films can be synthesised in situ on conductive substrates via electrochemical deposition, an attractive alternative to solvothermal synthesis as it enables rapid film growth under ambient temperature and pressure, making it both time-efficient and cost-effective.[91,93] Two principal approaches are employed: anodic electrodeposition (AED) and cathodic electrodeposition (CED). In AED, metal ions are supplied by anodic dissolution (oxidation) of the metal substrate into an electrolyte solution containing the organic linker, with MOF nucleation and growth occurring at the electrode–diffusion layer interface.[93] As the MOF layer forms, metal ions from the substrate can diffuse through it and coordinate with additional linker molecules, allowing growth to proceed at the solution interface. Parameters such as current density, deposition time, and electrolyte composition strongly influence the process, with current density being inversely proportional to MOF particle size and deposition time controlling film thickness.[93] In contrast, CED relies on the generation of hydroxide anions at the cathode surface, either by electrolysis of water or through the reduction of oxoanions such as nitrate. These

hydroxide anions deprotonate the organic linkers, which then coordinate with solvated metal ions (supplied by the electrolyte) to form a MOF layer at the electrode surface. Applied potential, deposition time, and electrolyte composition are key factors in determining film quality.[91,94,95] CED was first demonstrated by Li and Dincă for the deposition of MOF-5 on fluorine-doped tin oxide (FTO) coated glass, and it has since proven to be a versatile approach for fabricating MOF electrodes for photo- and electrocatalytic applications. [91,94,95]

1.6.2 Electrocatalytic MOFs

Electrocatalysis is central to many clean energy technologies such as water splitting and CO_2 reduction, yet conventional electrocatalysts (e.g., noble metals or transition-metal oxides on planar supports) are constrained by low atom utilisation, limited tunability, and poor conductivity.[96] MOFs have gained much interest as an alternative class of electrocatalytic materials owing to their crystalline, porous architectures, where metal nodes (single ions or clusters) and organic linkers can be accessed and tuned at the atomic level.[96-99] Their well-defined structures, high surface areas, and chemical flexibility enable systematic design of active sites and modulation of the surrounding microenvironment, reminiscent of enzymatic catalytic pockets.[97] Functionalisation strategies including ligand modification, mixed-metal incorporation, post-synthetic functionalisation, and the introduction of guest molecules, all provide the opportunity for optimisation of catalytic activity and selectivity. [96-99]

Despite these advantages, application of pristine MOFs can be often hindered by poor electronic conductivity and limited stability under harsh electrochemical conditions (due to breaking of coordination bonds between the metal atoms and organic linkers) particularly during demanding reactions such as the OER.[97,98,100,101] To overcome these limitations, MOFs are frequently converted into MOF-derived materials through pyrolysis or chemical transformation. These derivatives, which are typically metal nanoparticles or oxide/sulfides/carbides/phosphides dispersed in a porous carbon matrix, can inherit the high surface area, morphology, and porosity of the parent MOF, while exhibiting improved electronic conductivity and chemical stability. [97,98,100,101]

Together, these features make MOFs and their derivatives a versatile platform for probing

structure–activity relationships and developing next-generation electrocatalysts. While pristine MOFs provide model systems with atomic precision for mechanistic understanding, their derivatives bridge the gap to practical applications by combining inherited structural features with enhanced stability and conductivity. [97,98,100,101]

Previously in the Schmitt Group, K. D. Byrne synthesised a highly porous Co MOF and studied its electrocatalytic OER activity under neutral pH conditions.[102] Building this work, M. O'Doherty used the same highly porous Co MOF as a sacrificial template to generate spherical Co_3O_4 nanoparticles embedded in a microporous carbon matrix. As an electrocatalyst this Co_3O_4@C composite exhibited excellent OER activity and stability in alkaline conditions.[103]

1.6.3 Photoactive MOFs

In the photocatalysis literature, MOFs are often described as semiconductors, reflecting the dominance of inorganic semiconductor concepts in heterogeneous photocatalysis. [104,105] This analogy is partly justified as like inorganic semiconductors, photoactive MOFs can undergo light-induced charge separation into electron–hole pairs, as demonstrated by photocurrent experiments where illumination of a MOF-based photoelectrode generates an external current. [104,105] However, in contrast to inorganic semiconductors, charge-carrier mobility in most MOFs is considerably slower.[104] For this reason, some have proposed that MOF photocatalysts are more accurately viewed as ordered assemblies of metal complexes fixed in a rigid lattice, usually undergoing photoinduced ligand-to-metal electron transfer with limited electron mobility. Metal-to-ligand, metal-to-metal and metal-to-metal cluster electron transfer are also possible and depending on individual MOF structure.[106] To reconcile these models, it has been proposed to refer to the highest occupied crystal orbital (HOCO) and the lowest unoccupied crystal orbital (LUCO) as the maximum and minimum occupied and unoccupied electronic levels, respectively, bridging the gap between the traditional solid state model of valence band (VB) and conduction band (CB), and the molecular model of high occupied molecular orbital (HOMO) and lowest unoccupied molecular orbital (LUMO). [104,107]

The development of photoactive MOFs requires the incorporation of light-harvesting units, typically through photosensitive organic linkers or, less commonly, by direct

excitation of metal nodes or clusters (e.g., $\{Fe^{III}_3(\mu_3\text{-}O)\}^{7+}$).[108-110] Commonly, MOFs utilise aromatic organic ligands which absorb light is the UV or visible region, giving rise to π–π* or n–π* transitions. Extending the conjugation of the aromatic system or introducing functional groups to the backbone of the organic linker, enables tuning of the wavelength range absorbed.[108,111] Alternatively, photoactive guests can be encapsulated into the MOF pores, or metalloligands, such as those based on metalloporhyrins and polypyridyl complexes, can be introduced to impart photosensitising properties.[108]

Polypyridyl ligands can undergo ligand-centred, ligand-to-metal and metal-to-ligand transitions which can be harnessed to photosensitise MOFs. Ruthenium(II) polypyridyl complexes are among the most extensively studied photosensitisers, due to their strong visible absorption, long-lived excited states, and robust redox properties.[108,112] The archetypal $[Ru(bpy)_3]^{2+}$ (bpy = 2,2′-bipyridine) exemplifies these features, although its integration into MOF structures remains limited to only a few examples. Kent et al. incorporated $\{Ru^{II}(4,4'\text{-}(HO_2C)_2\text{-}bpy)_2bpy\}^{2+}$ into a Zn(II)-based MOF via carboxylate-functionalised bipyridyl ligands, while Wang et al. doped the Zr(IV) MOF UiO-67 with $\{Ru^{II}(5,5'\text{-}(HO_2C)_2\text{-}bpy)(bpy)_2\}^{2+}$. A Eu-based MOF containing Ru(II) polypyridyl linkers has also been reported as a robust photocatalyst for CO_2 reduction.[113-115]

Previously in the Schmitt group, L. Martins (Co- and Mn-based MOFs) and M. Mulahmetović (Ni-, Co-, and Zn-based MOFs) have further demonstrated highly porous, photoactive MOFs using Ru(II) polypyridyl linkers with extended aromatic backbones.[112,116,117]

1.6.4 Lanthanide MOFs

The lanthanide series (atomic numbers 57–71) possess distinctive electronic and magnetic properties arising from their 4f electron configurations, strong spin–orbit coupling, and pronounced magnetic anisotropy.[118,119] The *4f* orbitals, which progressively fill with atomic number across the series, contribute little to bonding, meaning that only a small amount of vibronic coupling takes place to enable Laporte-forbidden *f–f* transitions, giving rise to very weak and distinctly sharp emission bands.[118] In MOFs, lanthanides typically adopt the +3 oxidation state, though alternative states such as Ce^{4+} and Eu^{2+} are accessible.[118] Their typically high coordination numbers and flexible coordination

environments allow for novel topologies not achievable with transition-metal MOFs. Additionally, the ability of lanthanide ions to form coordinatively unsaturated sites allows them to behave as Lewis acid catalysts.[118]

While much less explored than transition-metal MOFs, lanthanide-based MOFs (Ln-MOFs) have demonstrated excellent stability, including high thermal resistance and tolerance to water and a wide pH range.[120-125] Their photoluminescent properties, arising from *f–f* transitions, can be enhanced by the antenna effect, in which electron-rich chromophores transfer energy to Ln^{3+} centres.[108,119] Europium- and terbium-based Ln-MOFs are especially attractive as chemical sensors owing to their strong visible fluorescence.[108] Ln-MOFs have also shown promise in magnetism, gas storage and separation, and heterogeneous catalysis.[118]

Focusing on heterogeneous catalysis, Ln-MOFs and their derivatives have been investigated for a wide variety of organic and photocatalytic reactions.[118] A few examples are given as follows. D'Vries et al. synthesised an isostructural Ln-MOF series, $[Ln_2(C_2H_4C_2O_4)_2(SO_4)(H_2O)_2]_n$ (Ln = La, Pr, Nd, Sm), and utilised their abundant Lewis acid sites for the hydrogenation of 4-nitrophenol to 4-aminophenol.[126] The Lewis acid sites decomposed H_2 to form Ln–hydride intermediates, which subsequently hydrogenated 4-nitrophenol. Sen et al. synthesised two 3D Ln-MOFs, $[Ln(HCOO)_3]_n$ (Ln = Nd, Pr), and found that they catalysed the epoxidation of various cycloalkenes and linear alkenes with higher activity and selectivity than the corresponding Ln(III) oxides, particularly for the epoxidation of cyclopentene, which showed excellent conversion and 100% selectivity.[127] Other examples of organic catalysis include the cycloaddition of CO_2, Friedel–Crafts alkylation reactions, cyanosilylation, and the polymerisation of isoprene.[118] These reactions predominantly exploit the Lewis acidity of Ln(III) centres, whereas the redox accessibility of Ce^{3+}/Ce^{4+} and Eu^{3+}/Eu^{2+} couples have been comparatively underexploited in Ln-MOF catalysis.

For photocatalysis, Dai et al. reported the successful use of Ce-UiO-66-NH_2 for photocatalytic hydrogen evolution, while Yan et al. synthesised a Eu-based MOF containing Ru(II) polypyridyl linkers that functioned as a robust photocatalyst for CO_2 reduction.[115,128] Beyond these isolated examples, systematic studies across the lanthanide series and the use of photosensitising metalloligands in Ln-MOFs remain limited.

In terms of electrocatalysis, very little work has been reported on Ln-MOFs to date. While there are a few reports of transition-metal MOF electrocatalysts doped with lanthanides, no studies have yet focused on pristine Ln-MOFs as electrocatalysts. [118,129]

1.7 Aims & Objectives

The combination of accessible Ce^{3+}/Ce^{4+} and Eu^{3+}/Eu^{2+} redox couples, the established aqueous and pH stability of Ln-MOFs, and the tunability afforded by reticular chemistry makes lanthanide-based MOFs a promising but underexploited platform for redox catalysis in artificial photosynthesis. The overarching goal of this thesis is to investigate the use of novel lanthanide MOFs and their derivatives as electrocatalysts and photocatalysts for solar-to-fuel applications, with a particular focus on demonstrating the efficacy of redox-active Ln-MOF catalysts (utilising the Ce^{3+}/Ce^{4+} and Eu^{3+}/Eu^{2+} redox couples) and on how the choice of MOF linker can influence performance.

As highlighted in the previous section, there are no reports of pristine Ln-MOFs being used as the sole electrocatalyst to drive a reaction, and there have been few reports of CeO_2 as an electrocatalyst for acidic OER other than as a support or co-catalyst. Reducing reliance on iridium for the anodes of PEM electrolysers, where it is used for acidic OER catalysis, is a significant research priority given the scarcity of iridium (Section 1.4.2), and motivates the focus on acidic conditions in the first part of this thesis. Isoreticular synthesis provides a means to systematically vary the organic linker while preserving topology, and is exploited in this thesis as a tool to investigate how linker chemistry influences the catalytic performance of Ce(III)-MOFs and their derivatives. Therefore, Chapter 2 begins with a systematic study of the electrocatalytic OER activity of an isoreticular series of pristine Ce(III)-MOFs constructed from tritopic aromatic linkers with differing heterocyclic substitution (Figure 1.13). The main aim was to establish whether Ce(III)-MOFs exhibit electrocatalytic OER activity and what influence, if any, Oheteroatom substitution of the organic linker has on performance. To mimic the acidic conditions of a PEM electrolyser, aqueous 0.5 M H_2SO_4 was chosen as the electrolyte. A further aim was to benchmark the OER performance of the MOFs against that of commercial CeO_2 nanoparticles.

In Chapter 3, this isoreticular series of Ce(III)-MOFs is derivatised via pyrolysis. The resulting CeO_2-carbon composite materials are fully characterised, and their

electrocatalytic OER activity is investigated. The objective of this study was to demonstrate whether Ce(III)-MOFs are suitable sacrificial templates to generate composite nanomaterials with enhanced catalytic properties when compared to the precursor MOFs.

Given the established photosensitising properties of Ru(II) polypyridyl complexes (Section 1.6.3) and the accessible redox chemistry of Ln centres (Section 1.6.4), their combination within a MOF framework represents a promising route to redox-active photosensitised catalysts. However, as highlighted earlier in the introduction, only one report (Yan et al.[118]) describes a Ln-MOF photosensitised by a Ru(II) polypyridyl metalloligand linker. Consequently, the second part of this work (starting in Chapter 4) focuses on the synthesis of a series of photosensitised Ln-MOFs using an acetylene-extended Ru(II) polypyridyl metalloligand, $\mathbf{[H_4L_{Ru}]^{2+}}$, (Figure 1.13). This novel **LnRu-MOF** series is fully characterised, and their photophysical properties are examined. The main aim of this study was to investigate how the structural and photophysical properties of the **LnRu-MOF** series vary across the lanthanides. The well-known *lanthanide contraction* in ionic radii, and accompanying increase in Lewis acidity, are anticipated to influence these properties.

Following the successful synthesis and characterisation of the **LnRu-MOF** series, Chapter 5 explores the photocatalytic activity of **CeRu-MOF** and **EuRu-MOF**, which were selected from the series for their accessible Ce^{3+}/Ce^{4+} and Eu^{3+}/Eu^{2+} redox couples. Their activity was investigated for the OER and HER, as well as the CO_2RR in the case of **EuRu-MOF**, with the aim of establishing whether these MOFs are viable platforms for redox photocatalysis and of benchmarking their performance against reported MOF photocatalysts. Building on the MOF thin film electrosynthesis described in Section 1.6.1, a further aim was to assess the feasibility of integrating **LnRu-MOFs** as photoactive materials in PEC systems, for which thin films of **CeRu-MOF** and **EuRu-MOF** were electrochemically grown on fluorine-doped tin oxide (FTO) substrates and preliminarily tested as photoelectrodes.

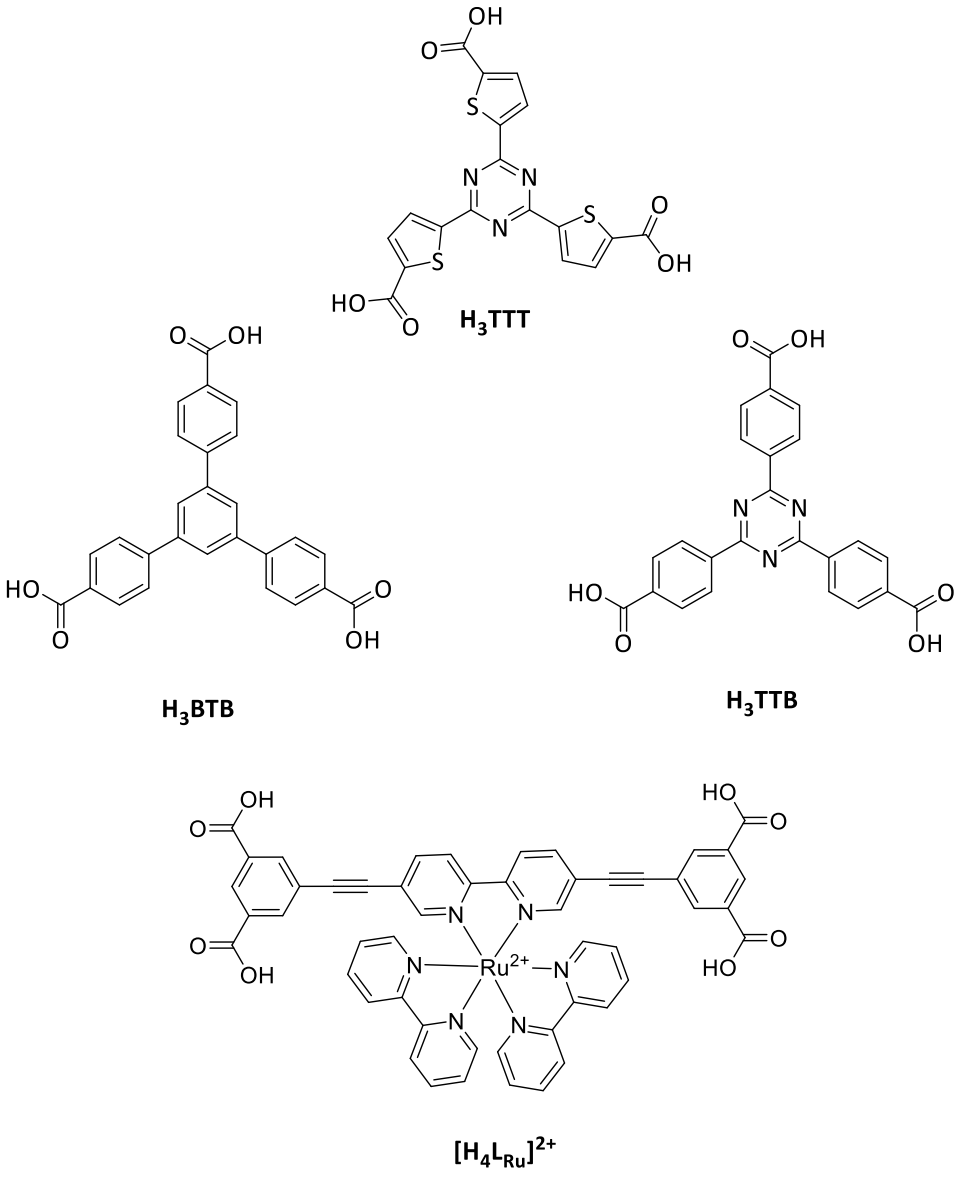

Figure 1.13: Organic ligands and metalloligand exploited as linkers for the Ln-MOFs studied in this work.

1.8 References

1. IPCC, Summary for Policymakers, in *Climate Change 2023: Synthesis Report. Contribution of Working Groups I, II and III to the Sixth Assessment Report of the Intergovernmental Panel on Climate Change*, ed. H. Lee and J. Romero, IPCC, Geneva, Switzerland, 2023, pp. 1–34, DOI: 10.59327/IPCC/AR6-9789291691647.001.
2. X. Lan, P. Tans and K. W. Thoning, *Trends in globally-averaged CO_2*, National Oceanic and Atmospheric Administration, Version 05-Aug-2025 15:05:29 MDT, https://doi.org/10.15138/9N0H-ZH07
3. D. Lüthi, M. Le Floch, B. Bereiter, T. Blunier, J.-M. Barnola, U. Siegenthaler, D. Raynaud, J. Jouzel, H. Fischer, K. Kawamura and T. F. Stocker, *Nature*, 2008, **453**, 379–382.

4. R. F. Keeling, E. J. Morgan, C. D. Keeling, *Atmospheric Monthly In-Situ CO_2 Data - Mauna Loa Observatory, Hawaii*, Scripps CO_2 Program Data, UC San Diego Library Digital Collections, Archive 2024-11-13, https://doi.org/10.6075/J08W3BHW (accessed August 2025).
5. H. Ritchie, P. Rosado, and M. Roser, *CO_2 and Greenhouse Gas Emissions*, OurWorldinData.org, 2023, https://ourworldindata.org/co2-and-greenhouse-gas-emissions (accessed August 2025).
6. R. Eisenberg, H. B. Gray and G. W. Crabtree, *Proc. Natl. Acad. Sci. U. S. A*., 2020, **117**, 12543–12549.
7. International Energy Agency report. *Net Zero by 2050 A Roadmap for the Global Energy Sector.* 4th Revision, October 2021.
8. P. Styring, E. A. Quadrelli, and K. Armstrong. *Carbon Dioxide Utilisation: Closing the Carbon Cycle.* Elsevier, 2015.
9. D. McKay, *Sustainable Energy - Without the Hot Air.* UIT Cambridge, 2008.
10. US Department of Energy, Fuel Cell Technologies Office, Hydrogen Storage, https://www.energy.gov/eere/fuelcells/hydrogen-storage (accessed August 2025).
11. J. Barber and P.D. Tran, *Journal of the Royal Society Interface*, 2013, **10**, 20120984.
12. D. Gust, T. A. Moore, and A. L. Moore, *Accounts of Chemical Research*, 2009, **42**, 12, 1890-1890.
13. A. Rao, K. Ryan, A. Tag, S. Fletcher, and A. Hawkins, Department of Biology, Texas A&M University.
14. A. F. Collings and C. Critchley. *Artificial photosynthesis: From basic biology to industrial application.* Wiley, 2015.
15. D. Gust, T. A. Moore, and A. L. Moore. *Acc. Chem. Res.* 2009, **42**, 12, 1890–1898.
16. S. Xu, Q. Shen, J. Zheng, Z. Wang, X. Pan, N. Yang, and G. Zhao. *Adv. Sci.*2022, **9**, 2203941.
17. T. E. Jones, D. Teschner, and S. Piccinin, Chem. Rev. 2024, 124, 9136−9223.
18. Y. Zhao, D. P. Adiyeri Saseendran, C. Huang, C. A. Triana, W.R. Marks, H. Chen, H. Zhao, G. R. Patzke, Chem. Rev., 2023, 123, 6257−6358.

19. J. Song, C. Wei, Z.-F. Huang, C. Liu, L. Zeng, X. Wang, Z. J. Xu, Chem. Soc. Rev., 2020, 49, 2196−2214.
20. X. Wang, H. Zhong, S. Xi, W. S. V. Lee, J. Xue, Adv. Mater., 2022, 34, 2107956.
21. P. Trivedi, N. C. Minj, S. Mittal, B. Kamaraj, S. Yadav and A. Sengeni, *J. Mater. Chem. A*, 2025, **13**, 21436-21452.
22. A. Lasia, *International Journal of Hydrogen Energy*, 2019, **44**, 36, 19484-19518.
23. B. You and Y. Sun, *Acc.Chem.Res.*, 2018, **51**, 1571−1580.
24. S. R. Kass, *J. Org. Chem.*, 2024, **89**, 11353−11356.
25. J. Fu, K. Jiang, X. Qiu, J. Yu, and M. Liu, *Materials Today*, 2020, **32**, 222-242.
26. J. Zhao, S. Xue, J. Barber, Y. Zhou, J. Menga and X. Ke, *J. Mater. Chem. A*, 2020, **8**, 4700.
27. N, Sakamoto, K. Sekizawa, S. Shirai, T. Nonaka, T. Arai, S. Sato and T. Morikawa, *Nat. Catal, 2024,* **7**, 574–584.
28. M. Li, H. Wang, Wei Luo, P. C. Sherrell, J. Chen, and J. Yang, *Adv. Mater.,* 2020, ***32***, 2001848.
29. X. Chang, T. Wanga and J. Gong, *Energy Environ. Sci.*, 2016, **9**, 2177-2196.
30. Y. Wang, E. Chen and J. Tang, *ACS Catal.,* 2022, **12**, 12, 7300–7316.
31. S.A. Grigoriev, V.N. Fateev, D.G. Bessarabov, and P. Millet, *International Journal of Hydrogen Energy*, 2020, **45**, 49, 26036-26058.
32. S. Trasatti, *Journal of Electroanalytical Chemistry*,1999, **476**, 1, 90-91.
33. X.-W. Lv, W.-W. Tian, and Z.-Y. Yuan, *Electrochem. Energy Rev.*, 2023, **6**, 23.
34. M. Carmoa, D. L. Fritza, J. Mergela, D. Stolten, *International Journal of Hydrogen Energy*, 2013, **38**, 4901-4934.
35. K. Ayers, N. Danilovic, K. Harrison, and H. Xu, E*lectrochem. Soc. Interface*, 2021, **30**, 67.
36. C. Locci, M. Mertens, S. Höyng, G. Schmid, T. Bagus, and P. Lettenmeier, *Chem. Ing. Tech. 2024, **96,** 1–2, 22–29.*
37. S. Sood, O. Prakash, M. Boukerdja, J.-Y. Dieulot, B. Ould-Bouamama, M. Bressel, A.-L. Gehin, *Energies*, 2020, **13**, 6556.
38. J. Chi and H. Yu, *Chinese Journal of Catalysis*, 2018, **39**, 390-364.
39. G. F. Li, H. M. Yu, W. Song, X. Y. Wang, Y. K. Li, Z. G. Shao, B. L. Yi, *J. Power Sources*, 2014, **249**, 175−184.

40. C. Locci, M. Mertens, S. Höyng, G. Schmid, T. Bagus, and P. Lettenmeier, *Chem. Ing. Tech. 2024, **96,** 1–2, 22–29.*
41. BASF.com, https://www.basf.com/global/en/media/news-releases/2025/03/p-25-046 (accessed August 2025).
42. A. Fujishima and K. Honda, Nature, 1972, **238**, 37–38.
43. *K. Maeda, J. Photochem. Photobiol. C.*, 2011, **12**, 4, 237-268.
44. Z. Xi, M. Liu, *npj Mater. Sustain.*, 2025, **3**, 18.
45. V. Kumaravel, J. Bartlett, and S. C. Pillai, *ACS Energy Lett.*, 2020, **5**, 486−519.
46. U. Ulmer, T. Dingle, P.N. Duchesne, R.H. Morris, A. Tavasoli, T. Wood, G.A. Ozin, *Nat. Commun.*, 2019, **10**, 1, 1−12.
47. C. Jiang, S. J. A. Moniz, A. Wang, T. Zhang and J. Tang, *Chem. Soc. Rev.*, 2017, **46**, 4645.
48. X. Zhou, R. Liu, K. Sun, Y. Chen, E. Verlage, S. A. Francis, N. S. Lewis, and C. Xiang, *ACS Energy Lett.,* 2016, **1**, 764−770.
49. V. Andrei, G. M. Ucoski, C. Pornrungroj, C. Uswachoke, Q. Wang, D. S. Achilleos, H. Kasap, K. P. Sokol, R. A. Jagt, H. Lu,T. Lawson, A. Wagner, S. D. Pike, D. S. Wright, R. L. Z. Hoye, J. L. MacManus-Driscoll, H. J. Joyce, R. H. Friend and Erwin Reisner, *Nature*, 2022, **608**, 518-522.
50. T. Mairegger, H.Li, C. Grießer, D. Winkler, J. Filser, N. G. Hörmann, K. Reuter, and J. Kunze-Liebhäuser, *ACS Catal*., 2023, **13**, 5780−5786.
51. M. C. Figueiredo, I. Ledezma-Yanez, M.T. Koper, *ACS Catal.*, 2016, **6**, 4, 2382−2392.
52. A. V. Rudnev, U. E. Zhumaev, A. Kuzume, S. Vesztergom, J. Furrer, P. Broekmann, T. Wandlowski, *Electrochim. Acta*, 2016, **189**, 38−44.
53. H. Y. Chung, R. J. Wong, H. Wu, D. Gunawan, R. Amal and Y. H. Ng, *Adv. Energy Mater.,* 2025, ***15***, 2404956.
54. T. Hisatomi, Q. Wang, F. Zhang, S. Ardo, E. Reisner, H. Nishiyama, A. Kudo, T. Yamada and K. Domen, *Front. Sci.*, 2024, **2**, 1411644.
55. H. Nishiyama, T. Yamada, M. Nakabayashi, Y. Maehara, M. Yamaguchi, Y. Kuromiya, Y. Nagatsuma, H. Tokudome,S. Akiyama, T. Watanabe, R. Narushima, S. Okunaka, N. Shibata, T. Takata, T. Hisatomi and K. Domen, *Nature*, 2021, **598**, 304-307.

56. Y. Wei, Z. Zhang, W. Wang, Z. Song, M. Cai, and S. Sun, *ChemPhysChem,* 2023, **24**, e2023002.
57. J. Schneider and D. W. Bahnemann, *J. Phys. Chem. Lett.* 2013, **4**, 20, 3479–3483.
58. M. Wang, S. Shen, L. Li, Z. Tang and J. Yang, *J. Mater. Sci.*, 2017, **52**, 5155–5164.
59. X. Wang, J. Wang, Y. Sun, K. Li, T. Shang and Y. Wan. *Front. Chem.*,2022, **10**, 89708.
60. Alessandro Trovarelli, and Jordi Llorca, *ACS Catal.,* 2017, **7**, 4716−4735.
61. J. Yu, X. Du, H. Liu, C. Qiu, R. Yu,S. Li, J. Ren and S. Yang, *Energy Fuels*, 2021, **35**, 19000−19011.
62. S.Y. Zhong and X.Q. Gong, *Applied Surface Science*, 2019, **496**, 143712.
63. G. Spezzatia, A. D. Benavidezb, A. T. DeLaRivab, Y. Sua, J. P. Hofmanna, S. Asahinac, E. J. Olivierd, J. H. Neethlingd, J. T. Millere, A. K. Datyeb, E. J.M. Hensen, *Applied Catalysis B: Environmental*, 2019, **243**, 36.
64. M. Nolan, S. C. Parker, G. W. Watson, *Surface Science*, 2005, **595**, 223–232.
65. Tana, M. Zhang, J. Li, H. Li, Y. Li, W. Shen, *Catalysis Today*, 2009, **148**, 179–183.
66. M. Huang and S, Fabris, *J. Phys. Chem. C,* 2008, **112**, 8643−8648.
67. F. Chen, D. Liu, J. Zhang, P. Hu, X. Q. Gong and G. Lu, *Phys. Chem. Chem. Phys.* 2012, **14**, 16573−16580.
68. J. Yu, Z. Wang, J. Wang, W. Zhong, M. Ju, R. Cai, C. Qiu, X. Long and S. Yang, *ChemSusChem,* 2020, **13**, 5.
69. A. Rajapriya, S. Keerthana, A. Rebekah, C. Viswanathan, N. Ponpandian, *International Journal of Hydrogen Energy,* 2021, **46**, 75, 37281-37293.
70. T. Audichon, S. Morisset, T. W. Napporn, K. B. Kokoh, C. Comminges, and C. Morais, *ChemElectroChem,* 2015, **2**, 1128 – 1137.
71. H. Song, X. Yong, G. I.N. Waterhouse, J. Yu, H. Wang, J. Cai, Z. Tang, B. Yang, J. Chang, and S. Lu, *ACS Catalysis,* 2024, **14**, 3298-3307.
72. O. M. Yaghi and H. Li, *J. Am. Chem. Soc.*, 1995, **117**, 10401–10402.
73. H. Furukawa, K. E. Cordova, M. O'Keeffe and O. M. Yaghi, *Science*, 2013, **341**, 1230444-1230444.
74. M. Eddaoudi, D. B. Moler, H. Li, B. Chen, T. M. Reineke, M. O'Keeffe and O. M. Yaghi, *Acc. Chem. Res*., 2001, **34**, 319–330.

75. O. M. Yaghi, M. O'Keeffe, N. W. Ockwig, H. K. Chae, M. Eddaoudi and J. Kim, *Nature*, 2003, **423**, 705–714.
76. D. Britt, D. Tranchemontagne, O. M. Yaghi, *Proc. Natl. Acad. Sci. USA*, 2008, **105**, 11623.
77. M. Eddaoudi, J. Kim, N. Rosi, D. Vodak, J. Wachter, M. O'Keeffe and O. M. Yaghi, *Science*, 2002, **295**, 469–472.
78. H. Jiang, D. Alezi, & M. Eddaoudi, M. *Nat. Rev. Mater*., 2021, **6**, 466–487.
79. L. T. Glasby, K. Gubsch, R. Bence, R. Oktavian, K. Isoko, S. M. Moosavi, J. L. Cordiner, J. C. Cole, and P. Z. Moghadam, *Chem. Mater.,* 2023, **35**, 4510−4524.
80. D. Yang and B. C. Gates, *ACS Catal.,* 2019, **9**, 3, 1779–1798.
81. L. E. Kreno, K. Leong, O. K. Farha, M. Allendorf, R. P. Van Duyne and J. T. Hupp, *Chem. Rev*., 2012, **112**, 2, 1105–1125.
82. M. Kadhom and B. Deng, *Applied Materials Today,* 2018, **11**, 219-230.
83. H. Li, K. Wang, Y. Sun, C. T. Lollar, J. Li, and H.-C. Zhou, *Materials Today*, 2018, **21**, 108-121.
84. G. Haider, M. Usman, T.-P. Chen, P. Perumal, K.-L. Lu, and Y.-F. Chen, *ACS Nano*, 2016, **10**, 8366−8375.
85. R. Freund, O. Zaremba, G. Arnauts, R. Ameloot, G. Skorupskii, M. Dincă, A. Bavykina, J. Gascon, A. Ejsmont, J. Goscianska, M. Kalmutzki, U. Lächelt, E. Ploetz, C. S. Diercks, S. Wuttke, *Angew. Chem. Int. Ed.* **2021**, *60*, 23975.
86. Y. Chen, Y. You, C. Xin, X Dong. H. Gong, *Journal of Environmental Chemical Engineering*, 2024**, 12**, 114163.
87. M. Rubio-Martinez, C. Avci-Camur, A. W. Thornton, I. Imaz, D. Maspochbc and M. R. Hill. *Chem. Soc. Rev.*, 2017, **46**, 3453-3480.
88. T. R. Cook, Y.-R. Zheng and P. J. Stang, *Chem. Rev.*, 2013, **113**, 734–777.
89. Y. J. Colón, A. Z. Guo, L. W. Antony, K. Q. Hoffmann, and J. J. de Pablo, *J. Chem. Phys*., 2019, **150**, 104502.
90. C. McKinstry, E. J. Cussen, A. J. Fletcher, S. V. Patwardhan, J. Sefcik. *Cryst. Growth Des.* 2013, **13**, 12, 5481–5486.
91. M. Li and M. Dincă, *J. Am. Chem. Soc.*, 2011, **133**, 12926–12929.
92. N. Stock and S. Biswas, *Chem. Rev*., 2012, **112**, 933–969.

93. X. Zhang, K Wan, P. Subramanian, M. Xu, J. Luo, J. Fransaer, *J. Mater. Chem. A*, 2020, **8**, 7569-7587.

94. M. Li and M. Dincă, *Chemical Science*, 2014, **5**, 107-111.

95. M. Li and M. Dincă, *Chemistry of Materials*, 2015, **27**, 3203-3206.

96. Y. Yang, Y. Yang, Y. Liu, S. Zhao, and Z. Tang. *Small Sci.,* 2021, **1**, 2100015.

97. N. Sun, S. S. A. Shah, Z. Lin, Y.-Z. Zheng, L. Jiao, and H.-L. Jiang, *Chem.Rev*., 2025, **125**, 2703−2792.

98. C. Li, H. Zhang, M. Liu, F.-F. Lang, J. Pang and X.-H. Bu, *Ind. Chem. Mater*., 2023, **1**, 9–38.

99. Y. Peng, S. Sanati, A. Morsali, and H. García, *Angew. Chem. Int. Ed.*, 2023, ***62,*** e202214707.

100. B. Zhang, Y. J. Zheng, T. Ma, C. D. Yang, Y. F. Peng, Z. H. Zhou, M. Zhou, S. Li, Y. H. Wang, C. Cheng, *Adv. Mater.,* 2021, **33**, 2006042.

101. M. Zhang, Q. Dai, H. Zheng, M. Chen and l. Dai, *Adv. Mater.*, 2018, **30**, 1705431.

102. K. D. Byrne, PhD Thesis, University of Dublin, 2020.

103. M. O'Doherty, PhD Thesis, University of Dublin, 2022.

104. S. Navalón, A. Dhakshinamoorthy, M. Alvaro, B. Ferrer, and H. García, *Chem.Rev.,* 2023, **123**, 445−490.

105. Q. Wang, Q. Gao, A. M. Al-Enizi, A, Nafady and Shengqian Ma, *Inorg. Chem. Front*., 2020, **7**, 300–339.

106. M. Fumanal, A. Ortega-Guerrero, K. Maik Jablonka, B. Smit, and I. Tavernelli, *Adv. Funct. Mater.,* 2020, ***30***, 2003792.

107. A. Wagner, C.D. Sahm, & E. Reisner, *Nat Catal., 2020,* **3**, 775–786.

108. É. Whelan, F.W. Steuber, T. Gunnlaugsson and W. Schmitt, *Coordination Chemistry Reviews*, 2021, **437**, 213757.

109. K.G.M. Laurier, F. Vermoortele, R. Ameloot, D.E. De Vos, J. Hofkens, M.B.J. Roeffaers, *J. Am. Chem. Soc.*, 2013, **135**, 14488–14491.

110. C.-K. Lin, D. Zhao, W.-Y. Gao, Z. Yang, J. Ye, T. Xu, Q. Ge, S. Ma, D.-J. Liu, I*norg. Chem.*, 2012**, 51**, 9039–9044.

111. E. Flage Larsen, A. Røyset, J.H. Cavka, K. Thorshaug, *J. Phys. Chem. C*, 2013, **117** 20610-20616.

112. L. Martins, L. K. Macreadie, D. Sensharma, S. Vaesen, X. Zhang, J. J. Gough, M. O'Doherty, N.-Y. Zhu,a M. Rüther, J. E. O'Brien, A. L. Bradley and W. Schmitt, *Chem. Commun.*, 2019, **55**, 5013-5016.

113. C. A. Kent, B. P. Mehl, L. Ma, J. M. Papanikolas, T. J. Meyer and W. Lin, *J. Am. Chem. Soc.*, 2010, **132**, 12767.

114. C. Wang, Z. Xie, K. E. deKrafft and W. Lin, *J. Am. Chem. Soc.*, 2011, **133,** 13445.

115. Z.-H. Yan, M.-H. Du, J. Liu, S. Jin, C. Wang, G.-L. Zhuang, X.-J. Kong, L.-S. Long and L.-S. Zheng, *Nat. Commun.*, 2018, **9**, 3353.

116. L. Martins, PhD Thesis, University of Dublin, 2021.

117. M. Mulahmetović, PhD Thesis, University of Dublin, 2023.

118. Y. Zhang, S. Liu, Z.-S. Zhao, Z. Wang, R. Zhang, L. Liu and Z.-B. Han, *Inorg. Chem. Front.*, 2021, **8**, 590–619.

119. Y. Cui, B. Chen, G Qian, *Coordination Chemistry Reviews*, 2014, **273–274**, 76-86.

120. L. Xu, Y. Li, Q. Pan, D. Wang, S. Li, G. Wang, Y. Chen, P. Zhu and W. Qin, *ACS Appl. Mater. Interfaces*, 2020, **12**, 18934–18943.

121. Q.-R. Liu, B. Liu, M.-M. Qiu, W.-N. Miao and L. Xu, *J. Solid State Chem.*, 2022, 123138.

122. H. Li, Y. Han, Z. Shao, N. Li, C. Huang and H. Hou, *Dalt. Trans.*, 2017, **46**, 12201–12208.

123. X. Han, J. Liu, K. Yu, Y. Lu, W. Xiang, D. Zhao and Y. He, *Inorg. Chem.*, 2022, **61**, 5067–5075.

124. Y. Yang, L. Chen, F. Jiang, M. Wu, J. Pang, X. Wan and M. Hong, *CrystEngComm*, 2019, **21**, 321–328.

125. H. Yu, Q. Liu, J. Li, Z. M. Su, X. Li, X. Wang, J. Sun, C. Zhou and X. Hu, *J. Mater. Chem. C*, 2021, **9**, 562–568.

126. R. F. D'Vries, M. Iglesias, N. Snejko, S. Alvarez-Garcia, E. Gutierrez-Puebla and M. A. Monge, *J. Mater. Chem*., 2012, **22**, 1191.

127. R. Sen, D. Saha and S. Koner, *Catal. Lett.*, 2011, **142**, 124–130.

128. S. Dai, E. Montero-Lanzuela, A. Tissot, H. G. Baldoví, H. García, S. Navalón and C. Serre*, Chem. Sci.*, 2023, **14**, 3451.

129. S. Meng, G. Li, P. Wang, M. He, X Sun and Z. Li, *Mater. Chem. Front.*, 2023, **7**, 806.

Chapter 2: Investigation of One-Dimensional Ce(III) SBU based MOFs for Electrocatalytic OER in Acidic Media

2.1 Introduction

Key to climate change mitigation and upholding the Paris Agreement commitment (stopping global temperatures increasing by more than 1.5°C, or at least less than 2°C compared to preindustrial levels), is the timely transition to a carbon neutral global economy.[2] The electrochemical splitting of water to generate hydrogen, using renewable energy sources, represents an ideal way of storing energy in chemical bonds of a non-carbon fuel with high gravimetric energy density.[3] So far, deployment of such technology has been limited by reliance on expensive platinum-group based materials as robust and efficient catalysts.[4] The water oxidation half-reaction, also known as the oxygen evolution reaction (OER), is a highly endergonic 4-electron reaction that requires large overpotentials (η) to achieve satisfactory oxygen evolution rates. As a result, OER is considered the limiting step in the overall water splitting reaction.[5] Significant t progress has been made developing earth-abundant materials as OER electrocatalysts in alkaline media. However, alkaline water splitting technologies have a number of disadvantages such as relatively low current densities, hindered by OH^- transport through the anion-exchange membrane.[5] Greater current densities can be reached under acidic conditions due to fast proton transport through a proton exchange membrane (PEM) and high proton concentration for hydrogen generation (HER).[5,6] However, only iridium or ruthenium-based materials are regarded to act as robust and efficient electrocatalysts under these conditions.[5-7]

Metal-organic frameworks (MOFs) are a class of porous coordination polymers, consisting of metal ions or clusters linked together by multitopic ligands into a two or three dimensional network with long range ordering.[8,9] Due to their chemical and structural versatility, as well as their high surface areas, MOFs have found application as catalysts,[10-12] materials for gas storage[13] and separation[14,15] and as sensors.[16,17] MOFs advantage over other porous materials such as zeolites, is that their properties can be tuned for an application by varying the linkers and/or the metal ions in the structure.[18]

MOFs can however suffer from some drawbacks such as stability issues and low electronic conductivity. This may be mitigated via controlled pyrolysis of the MOF to achieve the synthesis composite of carbonous material and metal nanoparticles, while maintaining some of the MOF's structure and porosity.[19]

Cerium is the most abundant of the lanthanides, and the 25th most abundant element in the earth's crust, with an abundance on par with copper and zinc, and nearly 6.7x10^4 times more abundant than iridium or ruthenium.[20] Cerium dioxide (CeO_2, ceria) is well known for its catalytic properties, with established uses such as in three-way catalytic converters, as well as being used as a catalyst/cocatalyst in energy conversion systems (both photocatalytic and electrocatalytic).[21] Ceria's catalytic properties derive form the reversible Ce^{3+}/Ce^{4+} redox couple and consequent reversible surface oxygen anion exchange.[21,22]

In recent years there has been growing interest in cerium-based metal-organic frameworks (Ce-MOFs) owing to the combination of tuneable microporosity, Ce^{3+}/Ce^{4+} redox properties and the presence of low energy 4f orbitals.[23] Potential application in fluorescence sensing, colorimetric sensing, catalysis and as templates for CeO_2 nanostructures are described in the literature.[23,24] Ce(III)-MOFs based on tritopic ligands with trigonal geometry, commonly possess 1D Ce(III) SBUs linked in a way that creates 1D channels running parallel to the propagation direction of the SBU. This structure type is advantageous for gas adsorption, catalysis or as template for CeO_2 nanostructures or composite materials.[23] To this end Cheng et al. explored the use of Ce-BTC MOF, [Ce(1,3,5-BTC)(H_2O)$_6$] , as an electrocatalyst for the urea oxidation reaction (UOR). They found that controlled partial pyrolysis of Ce-BTC MOF in a nitrogen atmosphere resulted in "quasi-MOF" material that maintained the porous structure of the precursor while increasing the number of active sites and greatly improving the catalytic activity toward UOR.[25]

While CeO_2 is well known for its catalytic properties and has often been employed as a cocatalyst for electrochemical water oxidation,[26-31] there has been little exploration of cerium-based materials as primary electrocatalysts for the OER.[32] In particular, no examples of pristine Ce-based MOFs—or, more broadly, any lanthanide-based MOFs—have been reported as electrocatalysts for this reaction. This chapter seeks to explore this gap in the field.

2.1.1 Aims & Objectives

This chapter investigates the use of isoreticular Ce(III)-based metal–organic frameworks (MOFs), constructed from tritopic ligands and featuring one-dimensional (1D) Ce(III) secondary building units (SBUs), as electrocatalytic or pre-electrocatalytic materials for the oxygen evolution reaction (OER) in acidic media. The effect of heteroatom substitution in the tritopic linker is explored through a comparative study of three Ce(III)-MOFs synthesised from structurally related ligands with varying degrees of heteroatomic substitution. These ligands include 5,5′,5″-(1,3,5-triazine-2,4,6-triyl)tris(thiophene-2-carboxylic acid) **(H_3TTT**); 4,4′,4″-(1,3,5-triazine-2,4,6-triyl)tris(benzoic acid) (**H_3TTB**); and 4,4′,4″-(benzene-1,3,5-triyl)tris(benzoic acid) (**H_3BTB**). The corresponding Ce-MOFs synthesised from these ligands are referred to as **Ce-TTT**, **Ce-TTB**, and **Ce-BTB**, respectively.

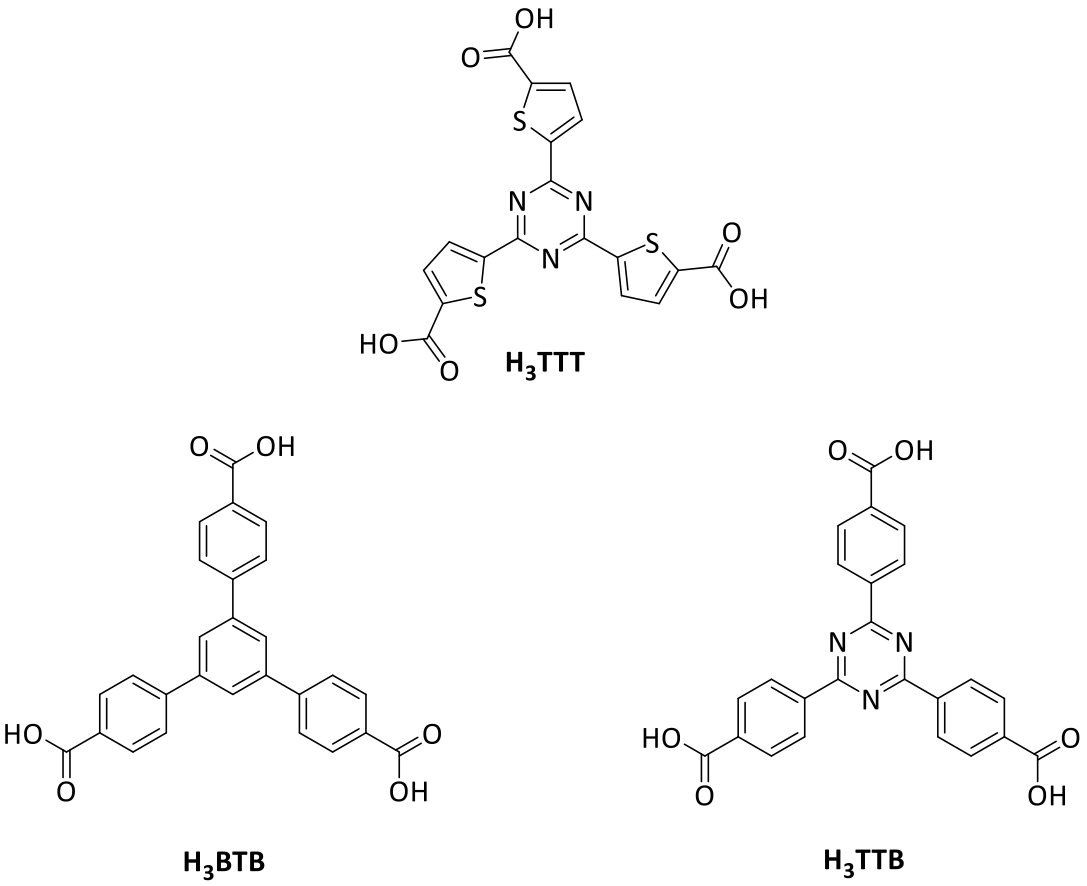

*Figure 2.1: Schematic representation of tritopic organic ligands; **H_3TTT** (5,5′,5″-(1,3,5-triazine-2,4,6-triyl)tris(thiophene-2-carboxylic acid)); **H_3BTB** (4,4′,4″-(benzene-1,3,5-triyl)tris(benzoic acid)); **H_3TTB** (4,4′,4″-(1,3,5-triazine-2,4,6-triyl)tris(benzoic acid)).*

2.2 Synthesis and Structure of [Ce(TTT)(DMF)], Ce-TTT

The self-assembly of [Ce(**TTT**)(DMF)] (**Ce-TTT**), was achieved under solvothermal conditions. This synthesis involved dissolving equimolar amounts of **H_3TTT** and $CeCl_3 \cdot 7H_2O$ in DMF and heating the solution at 100 °C for 24 hours. This resulted in the formation of pale-yellow clusters composed of densely packed, needle-shaped **Ce-TTT** crystals, seen in Figure 2.2. Powder X-ray diffraction (P-XRD) was used to confirm that the structure and phase purity of the as-synthesised **Ce-TTT** crystals were consistent with the reported crystal structure.[33] Figure 2.3 shows that the measured P-XRD pattern and the simulated pattern (calculated from single-crystal XRD data[33]) are in excellent agreement.

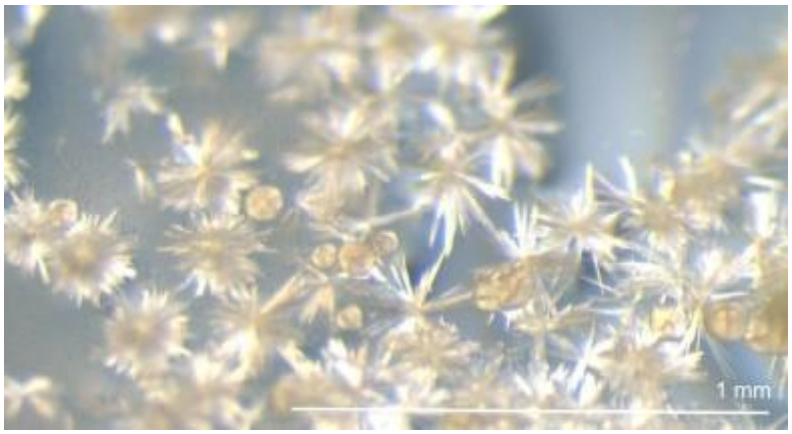

*Figure 2.2: Optical microscope image of **Ce-TTT** crystals.*

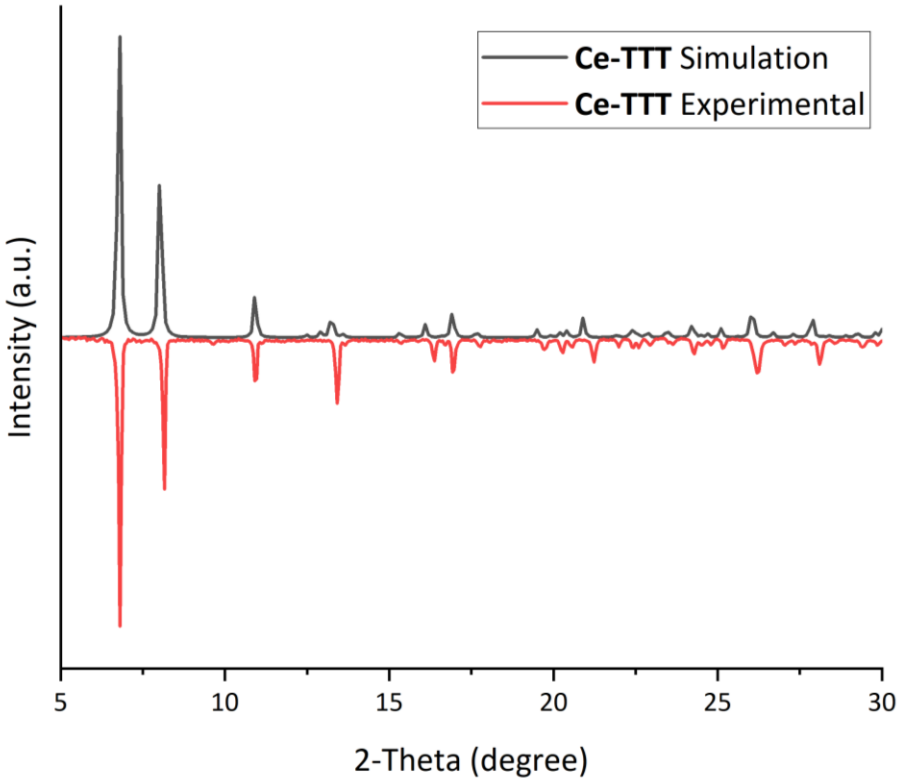

*Figure 2.3: PXRD plot showing the experimental **Ce-TTT** pattern (red) matching the simulated pattern of **Ce-TTT** (black).*

The structure of **Ce-TTT** has been reported to crystallise in the monoclinic space group *Cc* and having the structural formula [Ce(**TTT**)(DMF)]. The asymmetric unit of **Ce-TTT** contains one Ce^{III} ion, one $\mathbf{TTT^{3-}}$ ligand, and one coordinated DMF molecule. The Ce^{III} ions form an infinite rod-shaped secondary building unit (SBU), in which the one-dimensional chain of Ce^{III} ions extends parallel to the crystallographic *c*-axis (Figure 2.4). Each Ce^{III} ion is ten-coordinate, with one bond to the oxygen atom of a coordinated DMF molecule and nine bonds to the carboxylate oxygen atoms of the $\mathbf{TTT^{3-}}$ ligand. Each carboxylate group of the $\mathbf{TTT^{3-}}$ ligand adopts a chelating bridging μ_2-η^2:η^1 coordination mode.

These infinite rod-shaped SBUs of Ce^{III} ions, previously described, are linked by bridging carboxylate groups of the $\mathbf{TTT^{3-}}$ ligands. An interesting feature of **Ce-TTT** is that the coordinated DMF molecules on successive Ce^{III} centres are oriented in the same direction, giving rise to a chain of DMF molecules projecting into the channels that run along the *c*-axis of **Ce-TTT**. This arrangement suggests the presence of an accessible site on each cerium centre, which may be exploited in applications such as electrocatalysis.

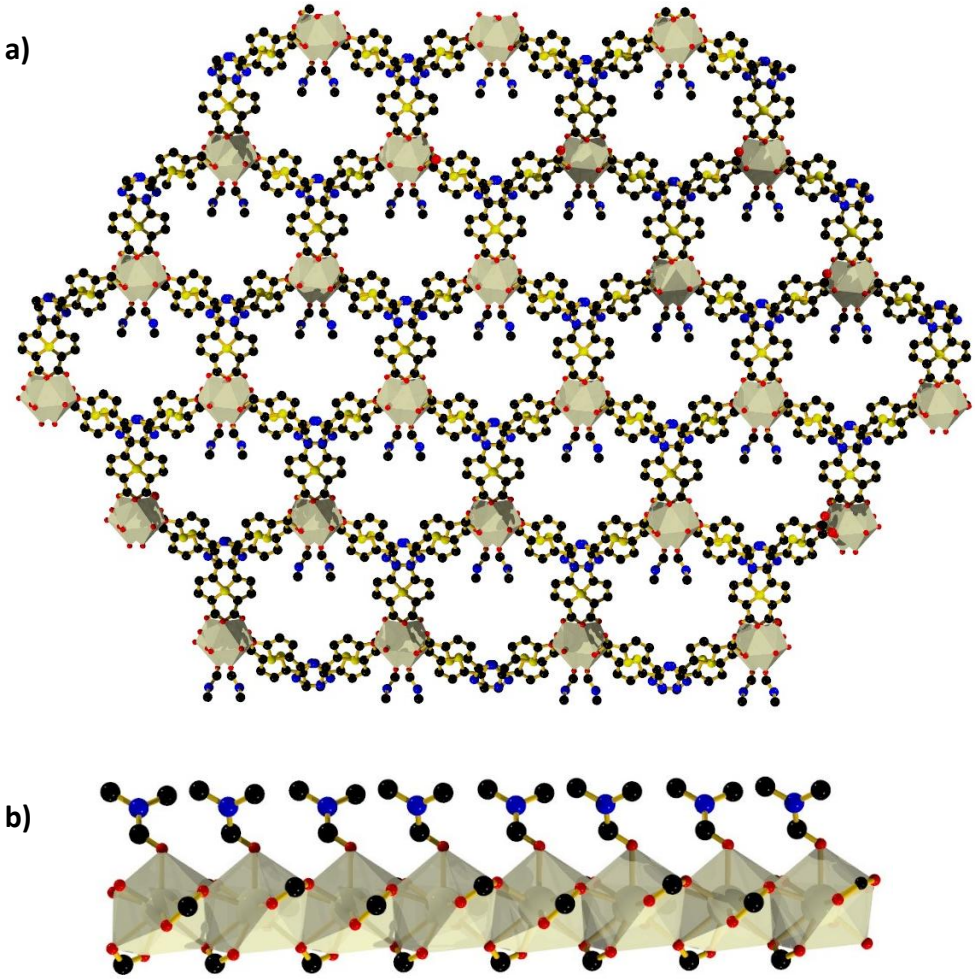

*Figure 2.4: Crystal structure of **Ce-TTT**. a) Extended structure of **Ce-TTT** viewed along the crystallographic c-axis. b) The coordination environment of the Ce^{III} ions in the rod SBU, as viewed from the crystallographic b-axis. Atom colour scheme: black (carbon), red (oxygen), blue (nitrogen), yellow (sulfur), beige polyhedral (cerium), hydrogens omitted for clarity.*

2.3.1 Further Physicochemical Characterisation of Ce-TTT

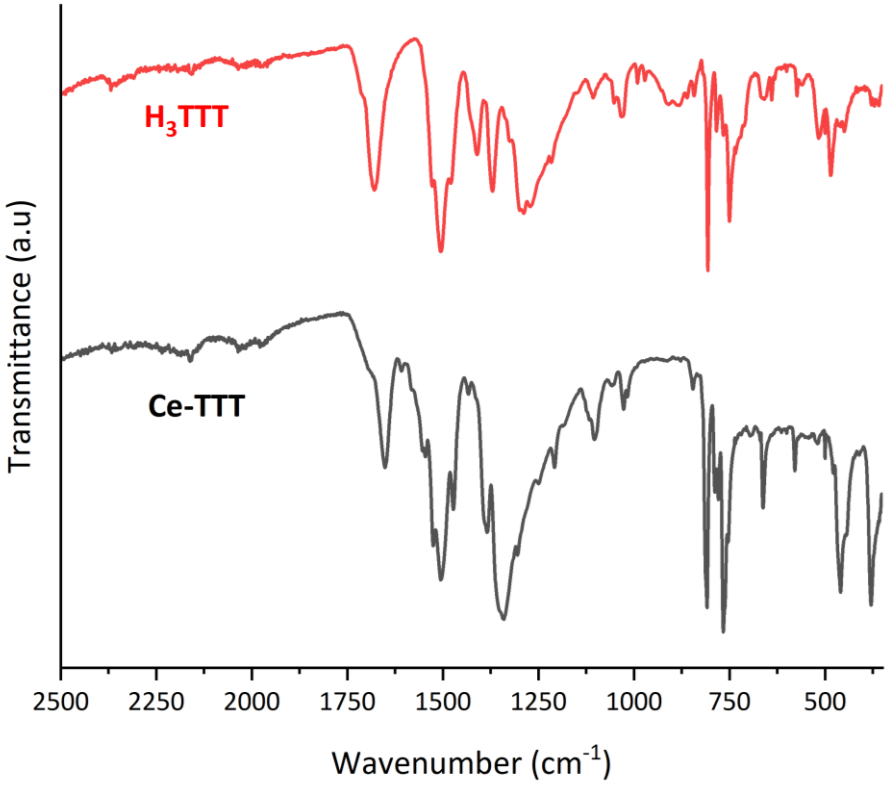

*Figure 2.5: FTIR spectra of **Ce-TTT** (black) and **H_3TTT** (red).*

The Fourier-transform infrared (FTIR) spectrum of **Ce-TTT** is presented in Figure 2.5. In-plane vibrations of the triazine ring appear as strong bands at 1342 cm^{-1} and 1504 cm^{-1}.[34] The coordinating carboxylate groups exhibit asymmetric stretching vibrations (ν_{as}(COO)) at approximately 1651 cm^{-1}, and symmetric stretching vibrations (ν_s(COO)) at approximately 1473 cm^{-1}. The difference between the asymmetric and symmetric carboxylate stretching frequencies ($\Delta\nu = \nu_{as} - \nu_s$) was found to be 178 cm^{-1}. This $\Delta\nu$ value is within range that would be expected for the μ_2-η^2:η^1 chelating-bridging coordination mode adopted by the carboxylates of **TTT^{3-}**.[35] Two medium-intensity bands at 380 and 460 cm^{-1}, absent in the spectra of **H_3TTT,** can be assigned to Ce-O stretching vibrations.[36-39]

The thermal stability of **Ce-TTT** was assessed using thermogravimetric analysis (TGA), performed under a nitrogen atmosphere (20 mL min^{-1}) at a heating rate of 3 °C min^{-1}. The TGA curve of **Ce-TTT** (Figure 2.6) reveals three major mass-loss events. The first mass loss, accounting for 13% of the initial mass, occurs below approximately 110 °C and corresponds to the release of guest solvent molecules and atmospheric moisture (H_2O) from the MOF pores. Above 120 °C, a second mass loss of 5% occurs, attributable to the removal of coordinated DMF molecules from the Ce^{III} centres. A two-step decomposition of the organic ligand (**TTT^{3-}**) occurs between 400 and 900 °C, resulting in the loss of approximately 56% of the initial mass. The remaining 26% of the initial mass corresponds to the inorganic SBU. **Ce-TTT** is therefore thermally stable up to 400 °C under a nitrogen atmosphere.

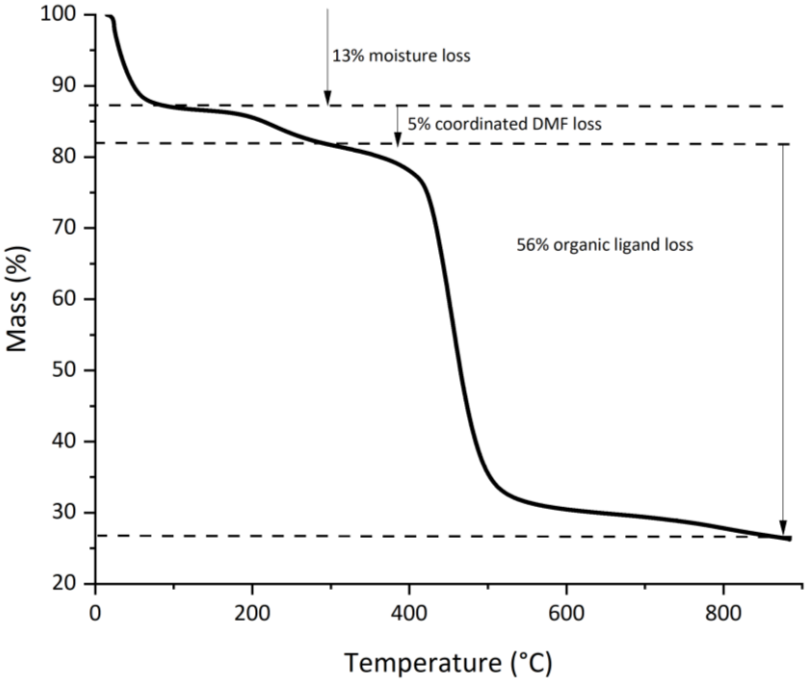

*Figure 2.6: TGA profile of **Ce-TTT** under a nitrogen atmosphere at a flow rate of 20 ml min^{-1} and a heating rate of 3 °C min^{-1}.*

Ce-TTT crystals were imaged using scanning electron microscopy (SEM). The as-synthesised crystals were briefly sonicated in deionised water and drop-cast onto a silicon substrate. The crystals exhibit a rod-like morphology, as shown in Figure 2.7, with lengths ranging from 1–4 µm, widths from 200–400 nm, and aspect ratios between 5 and 16.

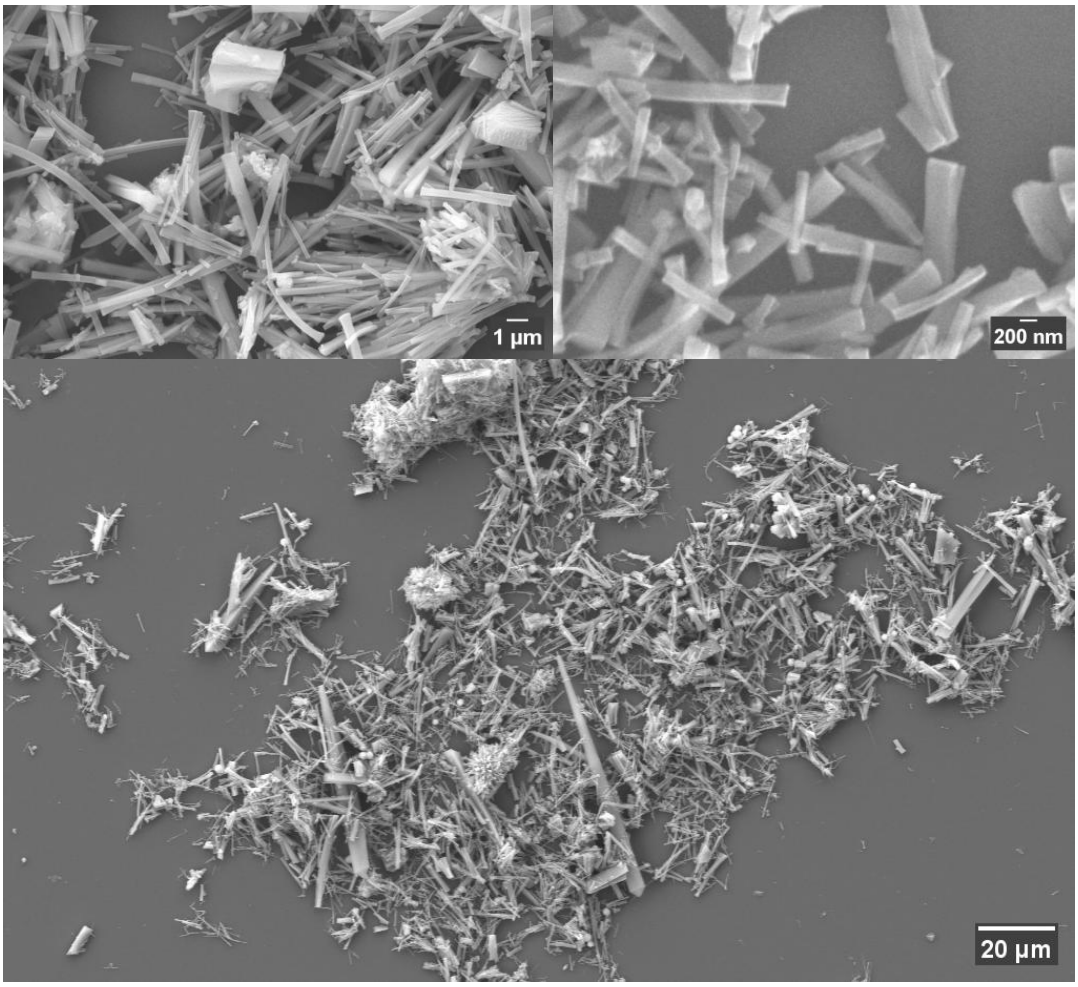

*Figure 2.7: SEM images of **Ce-TTT** crystals. Taken at an accelerating voltage of 15 kV using a secondary electron detector.*

Energy-dispersive X-ray (EDX) spectroscopy was performed on **Ce-TTT** crystals dispersed on a silicon substrate to confirm the elemental composition. EDX analysis verified the presence of cerium and sulfur in the expected 1:3 ratio (Table 2.1). The observed oxygen and nitrogen contents were slightly higher than the theoretical values, which is likely due to the presence of adsorbed DMF molecules within the pores of the **Ce-TTT** crystals.

*Table 2.1: Experimentally observed atomic ratios in **Ce-TTT**.*

Compound	Expected Ce:S:O:N ratio	Observed Ce:S:O:N ratio
Ce-TTT	1:3:7:4	1:3:8.5:5.5

2.3 Synthesis and Structure of [Ce(BTB)(DMF)], Ce-BTB

2.3.1 Synthesis [Ce(BTB)(DMF)]

The procedure reported by Lin *et al.*[40] was followed to synthesise the [Ce(**BTB**)(DMF)] MOF (**Ce-BTB**). Equimolar amounts of cerium(III) nitrate hexahydrate and 1,3,5-benzenetrisbenzoic acid (**H_3BTB**) were dissolved in DMF, and one drop of triethylamine was added as a base. The reaction was carried out in a Teflon autoclave at 120 °C for 72 hours. Off-white, needle-like crystals were obtained in 80% yield.

The P-XRD pattern obtained for these crystals was compared to a simulated pattern generated from single-crystal data reported by Lin *et al.*[40], as illustrated in Figure 2.8. The peaks observed in the experimental pattern match well with those in the simulated pattern, indicating good agreement. However, not all predicted peaks are observed in the experimental pattern, likely due to preferential orientation of the crystals. To verify this conclusion, the software package Expo2014 was used to fit the experimental pattern to the single-crystal data using the Le Bail method.[41,42]

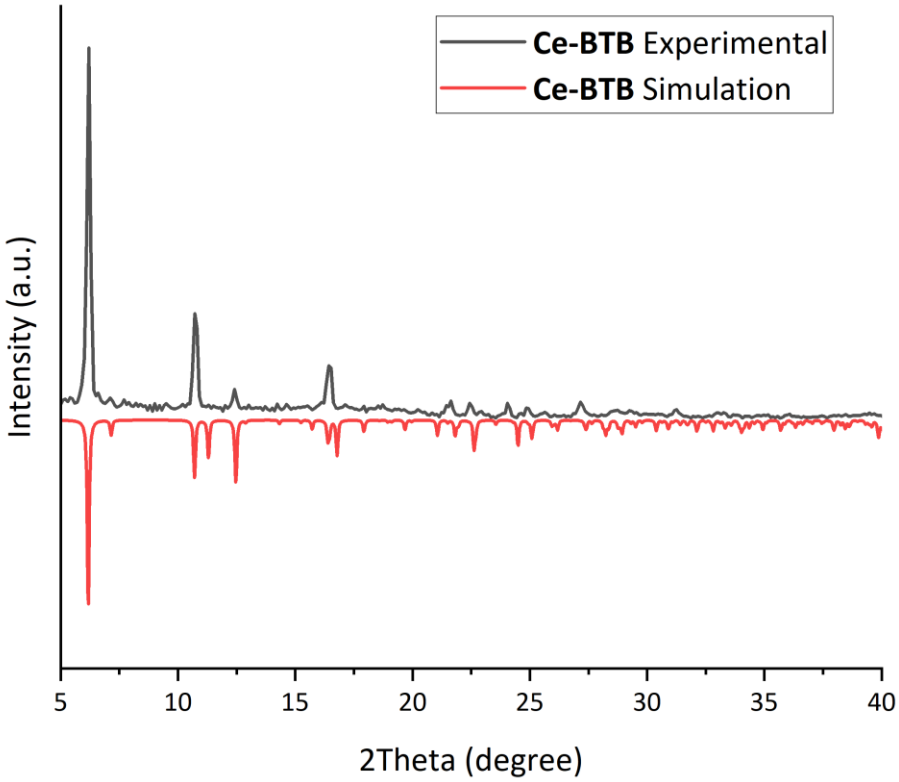

*Figure 2.8: PXRD plot showing the experimental **Ce-BTB** pattern (black) matching the simulated pattern of **Ce-BTB** (red).*

The resulting Le Bail fit (Appendix A: Figure A.1) shows good agreement between the experimental and simulated patterns, as indicated by final R-values of R_p = 2.157 and R_{wp} = 3.083. These results confirm that the synthesised **Ce-BTB** crystals were phase pure.

2.4.2 Structure of Ce-BTB

Like **Ce-TTT**, the Ce^{III} ions of **Ce-BTB** form an infinite rod-shaped secondary building unit (SBU), in which the one-dimensional chain of Ce^{III} ions extends parallel to the crystallographic *c*-axis (Figure 2.9). Each Ce^{III} ion is nine-coordinate, with one bond to the oxygen atom of a coordinated solvent molecule and eight bonds to the carboxylate oxygen atoms of the **BTB^{3-}** ligand. Each carboxylate group of the **BTB^{3-}** ligand adopts either syn-syn bridging or chelating bridging μ_2-η^2:η^1 coordination modes.[40]

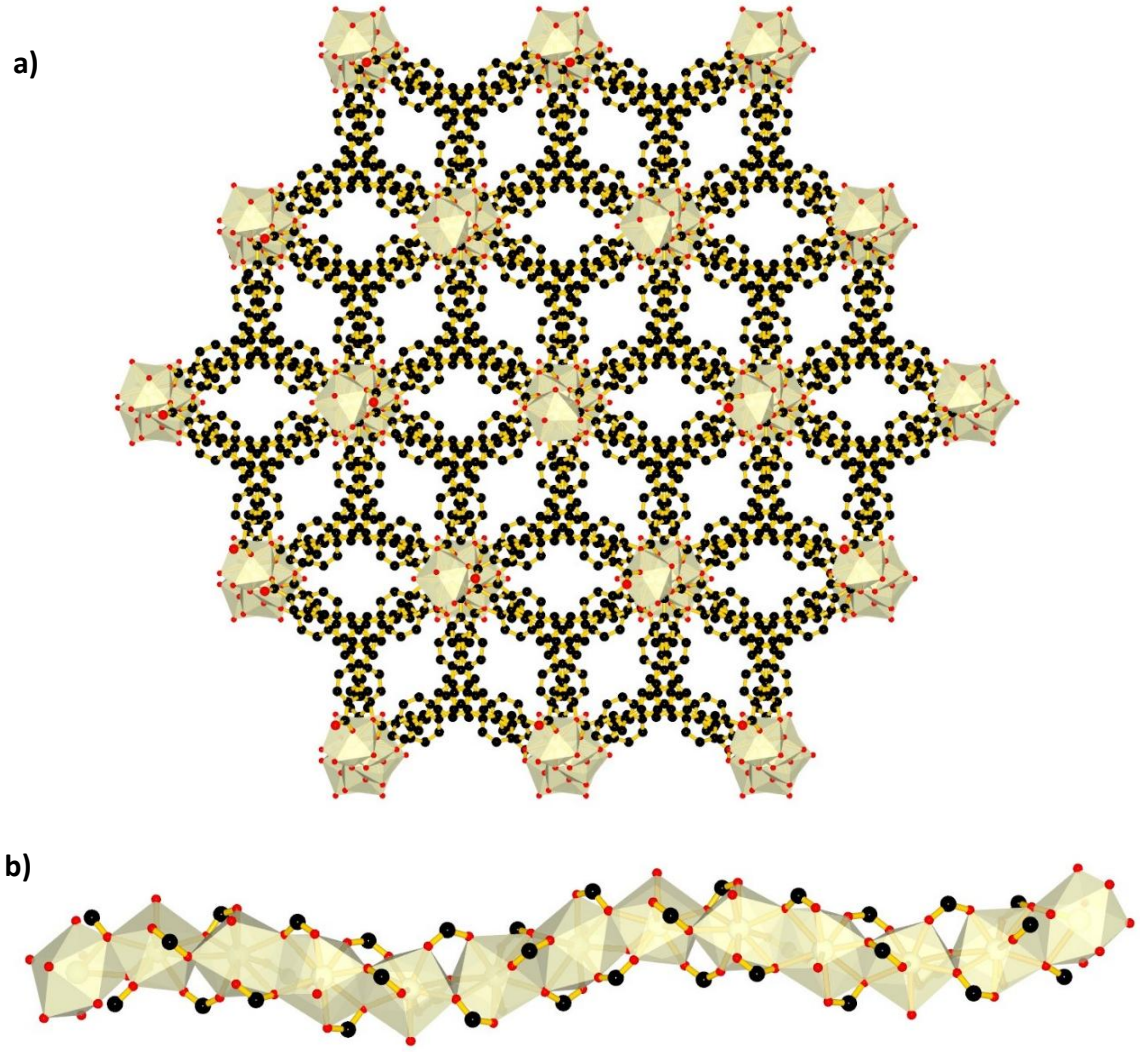

Figure 2.9:Crystal structure of Ce-BTB. a) Extended structure of Ce-BTB viewed along the crystallographic c-axis. b) The coordination environment of the CeIII ions in the rod SBU, as viewed from the crystallographic b-axis. Atom colour scheme: black (carbon), red (oxygen), blue (nitrogen), yellow (sulfur), beige polyhedral (cerium), hydrogens omitted for clarity.

2.4.2 Other Physicochemical Characterisation of Ce-BTB

The Fourier-transform infrared (FTIR) spectrum of **Ce-BTB** is presented in Figure 2.10. The coordinating carboxylate groups exhibit asymmetric stretching vibrations (ν_{as}(COO)) at approximately 1682 and 1651 cm^{-1}, and symmetric stretching vibrations (ν_{s}(COO)) at approximately 1507 and 1474 cm^{-1}. The difference between the asymmetric and symmetric carboxylate stretching frequencies ($\Delta\nu = \nu_{as} - \nu_{s}$) was found to be 175 and 176 cm^{-1}, respectively. The presence of two distinct two distinct carboxylate coordination modes aligns with SCXRD data reported by Lin et al. whereby the carboxylate group of the $\mathbf{BTB^{3-}}$ ligand adopt either syn-syn bridging or chelating bridging μ_2-η^2:η^1 coordination modes.[40]

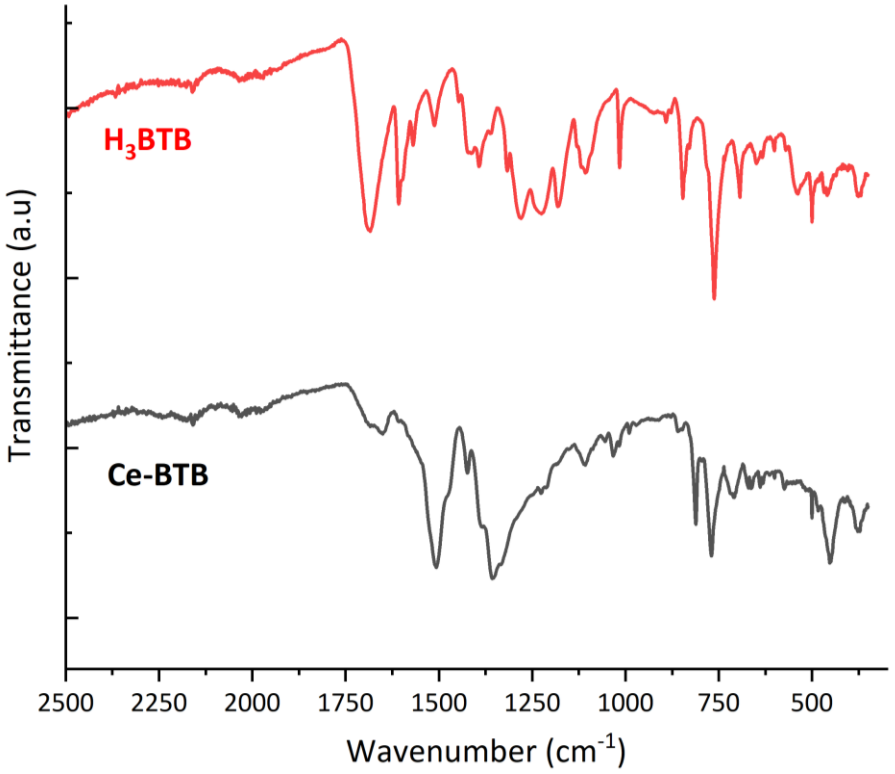

*Figure 2.10: FTIR spectra of **Ce-BTB** (black) and **H_3BTB** (red).*

The thermal stability of **Ce-BTB** was evaluated via thermogravimetric analysis (TGA), conducted under a nitrogen atmosphere (20 mL min^{-1}) at a heating rate of 3 °C min^{-1}. The TGA profile of **Ce-BTB** (Figure 2.11) exhibits three major mass-loss events. The first event, corresponding to a 7% reduction in mass below ~120 °C, is attributed to the removal of

constitutional solvent and atmospheric moisture (H_2O) from within the MOF pores. A second mass-loss event accounting for approximately 8% occurs above 120 °C, consistent with the removal of coordinated solvent molecules from Ce^{III} centres. As for the organic linker (**BTB^{3-}**) decomposes in a two-step process between 400 and 1000 °C, accounting for a cumulative 68% mass loss. The remaining 17% of the initial mass is ascribed to the residual inorganic SBU. This TGA data indicates that **Ce-BTB** is thermally stable up to 400 °C under a nitrogen atmosphere.

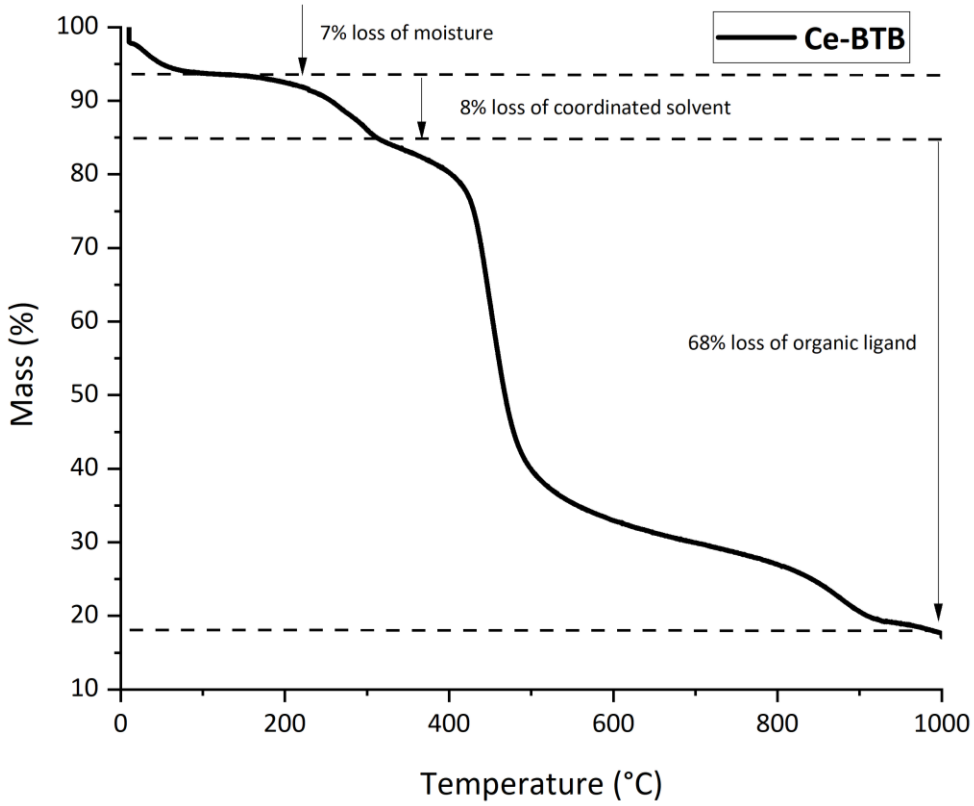

*Figure 2.11: TGA profile of **Ce-BTB** under a nitrogen atmosphere at a flow rate of 20 ml min^{-1} and a heating rate of 3 °C min^{-1}.*

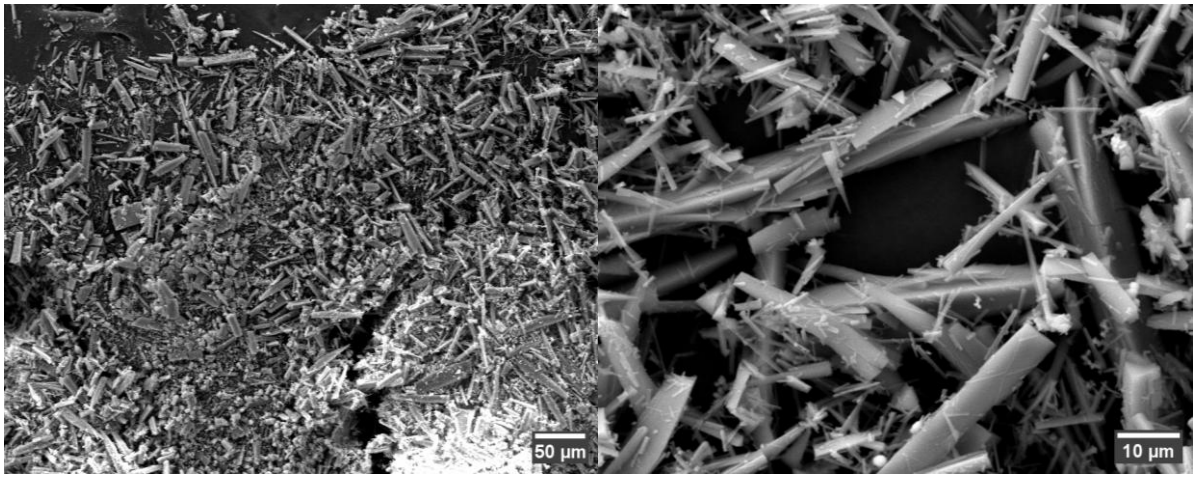

*Figure 2.12: SEM images of **Ce-TTB** crystals. Taken at an accelerating voltage of 15 kV using a secondary electron detector.*

2.4 Synthesis and Characterisation of Ce-TTB

To better assess the influence—if any—of heteroatomic ligand substitution on the oxygen evolution reaction (OER) activity of Ce-based MOFs, the synthesis of a third MOF was undertaken. For consistency, 4,4′,4″-(1,3,5-triazine-2,4,6-triyl)tris(benzoic acid) (**H_3TTB**), was selected as the organic linker. This ligand contains a triazine moiety, as found in **H_3TTT**, but lacks thiophene substituents, instead incorporating benzoate groups akin to those in H_3**BTB**.

A MOF based on Ce(III) dinuclear secondary building units (SBUs) and **TTB^{3-}** linkers has been previously reported in the literature.[43] The authors synthesised this MOF using a double-layer diffusion method involving methanol, DMF, and 4,4′-bipyridine as a modulating agent. However, as both **Ce-TTT** and **Ce-BTB** crystallise with one-dimensional infinite chain Ce(III) SBUs, the previously reported dinuclear SBU structure was deemed unsuitable for direct comparison.

Therefore, a new MOF structure was targeted using synthetic conditions previously established to promote the formation of Ce-based MOFs comprising one-dimensional infinite chain SBUs coordinated to tritopic carboxylate ligands.[23]

2.4.1 Synthesis and Analysis of Ce-TTB

Following the synthetic method employed for **Ce-TTB**, equimolar amounts of **H_3TTB** and $CeCl_3 \cdot 7H_2O$ were dissolved in DMF and heated at 100 °C for 24 hours. This resulted in the formation of an off-white crystalline powder. Examination under a polarised light microscope revealed that the powder was entirely polycrystalline, with no crystals suitable for single-crystal X-ray diffraction (SCXRD) analysis. Attempts to vary reaction conditions—such as varying temperature, reaction time, including the addition of base (mirroring **Ce-BTB** synthesis conditions)—did not yield single crystals of suitable size for SCXRD.

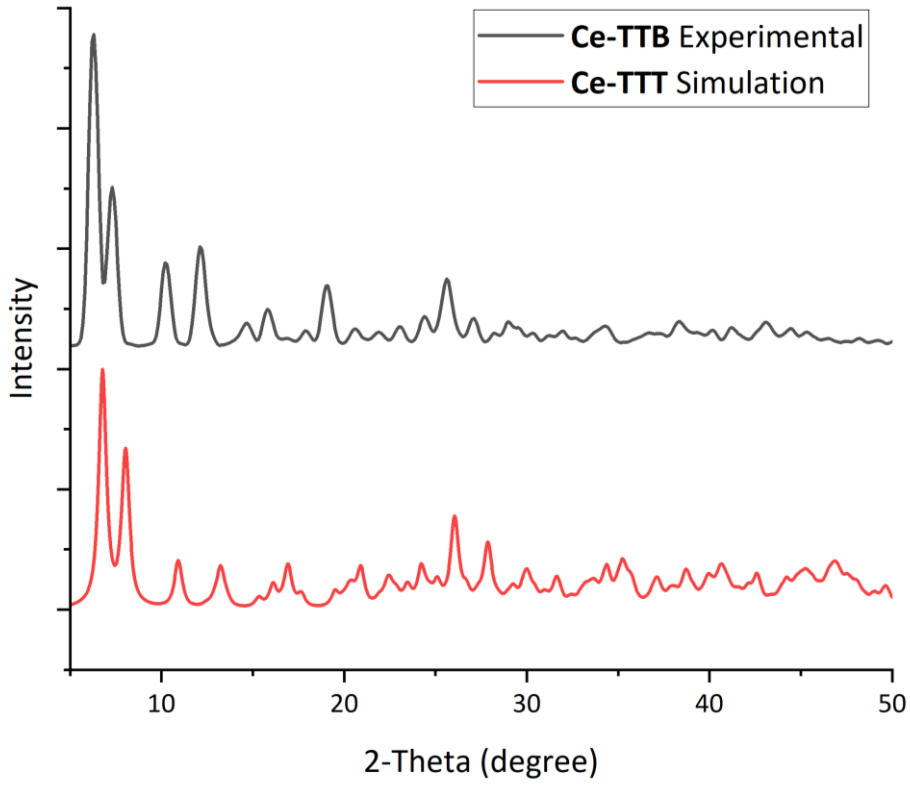

*Figure 2.13: PXRD plot showing the experimental **Ce-TTB** pattern (black) matching the simulated pattern of **Ce-TTT** (red).*

However, the P-XRD pattern of this off-white product (**Ce-TTB**) closely matches that of **Ce-TTT**, as illustrated in Figure 2.13. The software package Expo2014 was used to fit the **Ce-TTB** experimental pattern to the **Ce-TTT** pattern, derived from single-crystal data, using the Le Bail method.[41,42] The resulting Le Bail fit (Appendix A: Figure A.2) shows close agreement, as indicated by final R-values of R_p = 4.640 and R_{wp} = 6.468. These results suggest that **Ce-TTB** shares close structural similarities with **Ce-TTT**. Combined with the literature precedent for these synthetic conditions, it is highly likely that **Ce-TTB** consists of 1D infinite chain Ce^{III} SBUs linked by tritopic $\mathbf{TTB^{3-}}$ ligands.

2.4.2 Further Physicochemical Characterisation of Ce-TTB

The Fourier-Transform Infrared (FTIR) spectrum of **Ce-TTB** is presented in Figure 2.14. In-plane vibrations of the triazine ring appear as strong bands at 1353 cm^{-1} and 1512 cm^{-1}.[34] The coordinating carboxylate groups exhibit asymmetric stretching vibrations (ν_{as}(COO)) at approximately 1593 cm^{-1}, and symmetric stretching vibrations (ν_{s}(COO)) at approximately 1419 cm^{-1}. The difference between the asymmetric and symmetric carboxylate stretching frequencies ($\Delta\nu = \nu_{as} - \nu_{s}$) was found to be 174 cm^{-1}. While SCXRD data is unavailable to confirm the carboxylate coordination modes in **Ce-TTB**, the fact that this Δν value is very close to Δν values for **Ce-TTT** (178 cm^{-1}) and **Ce-BTB** (175 and 176 cm^{-1}), indicates a similar coordination environment.[35] A strong band at 495 cm^{-1} and a medium-intensity bands at 394 cm^{-1}, can be assigned to Ce-O stretching vibrations.[36-39]

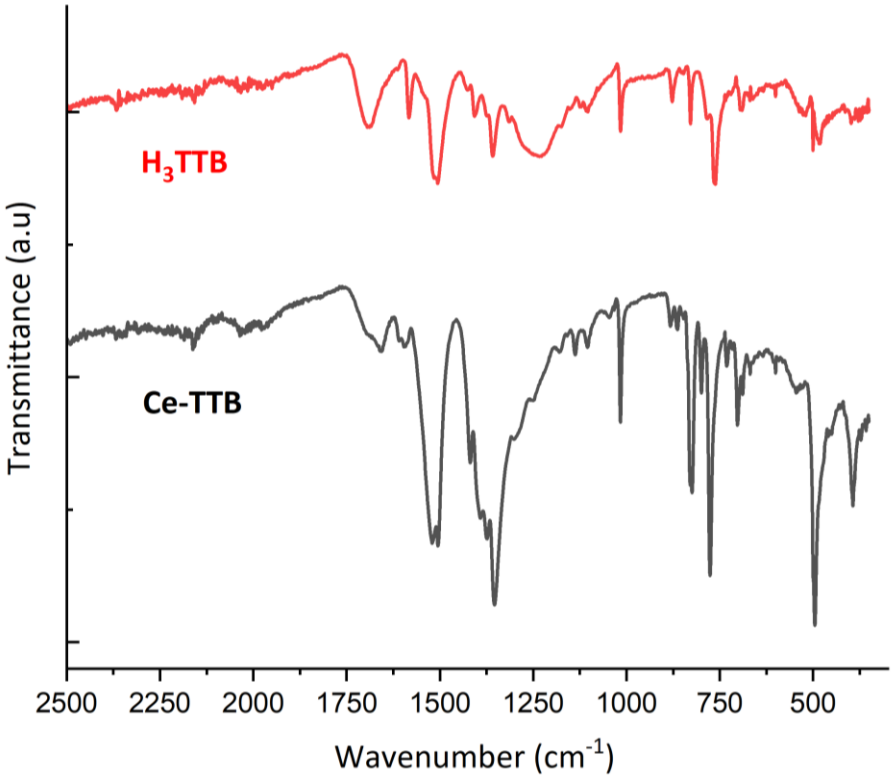

*Figure 2.14: FTIR spectra of **Ce-TTB** (black) and **H_3TTB** (red).*

The thermal stability of **Ce-TTB** was evaluated via thermogravimetric analysis (TGA), conducted under a nitrogen atmosphere (20 mL min^{-1}) at a heating rate of 3 °C min^{-1}. Exhibiting a similar TGA profile to that of **Ce-TTT** and **Ce-BTB**, **Ce-TTB** (Figure 2.15) displays three principal mass-loss events. The first event, accounting for 13% of the initial mass,

occurs below ~120 °C and is attributed to the loss of constitutional solvent molecules located in the MOF pores. A second mass-loss event of approximately 4% is observed between 120 and 300 °C, corresponding to the removal of coordinated dimethylformamide (DMF) molecules from the Ce^{III} centres. Decomposition of the organic linker (**TTB^{3-}**) occurs between 400 and 900 °C, resulting in a cumulative mass loss of ~57%. The remaining 26% of the initial mass is ascribed to the residual inorganic secondary building unit (SBU). .

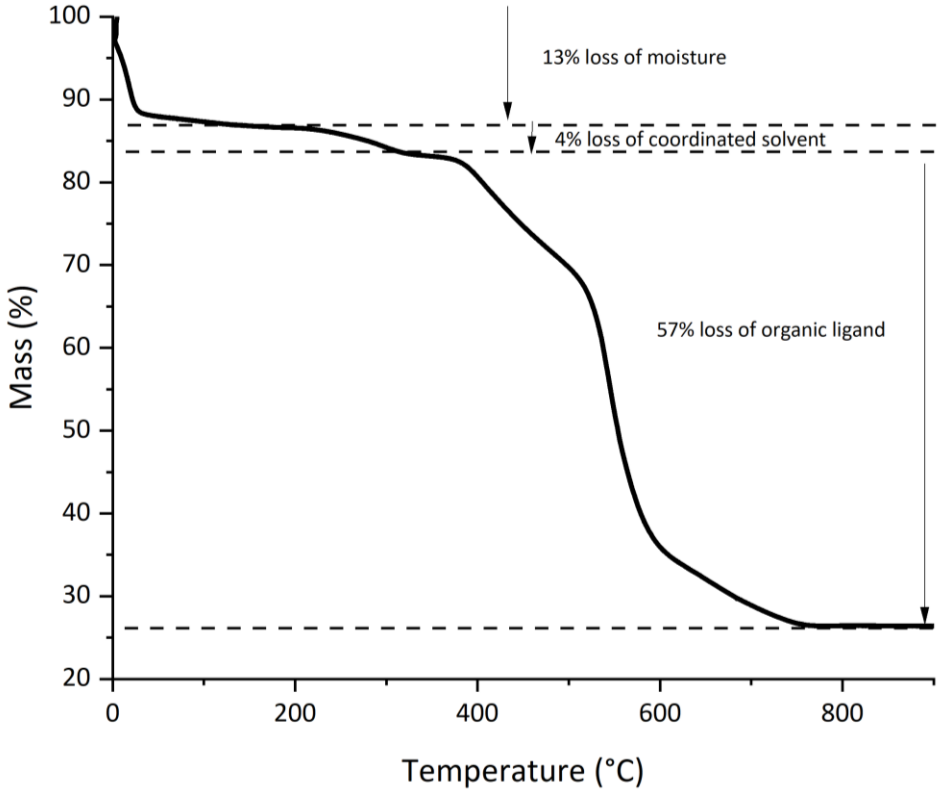

*Figure 2.15: TGA profile of **Ce-TTB** under a nitrogen atmosphere at a flow rate of 20 ml min^{-1} and a heating rate of 3 °C min^{-1}.*

SEM images of **Ce-TTB** crystals on silicon substrate are presented in Figure 2.16. The polycrystalline material exhibit a mostly globular morphology, with a few examples of crystals with straw-bundle-like morphology. Particlesizes were observed to range from 1–30 µm.

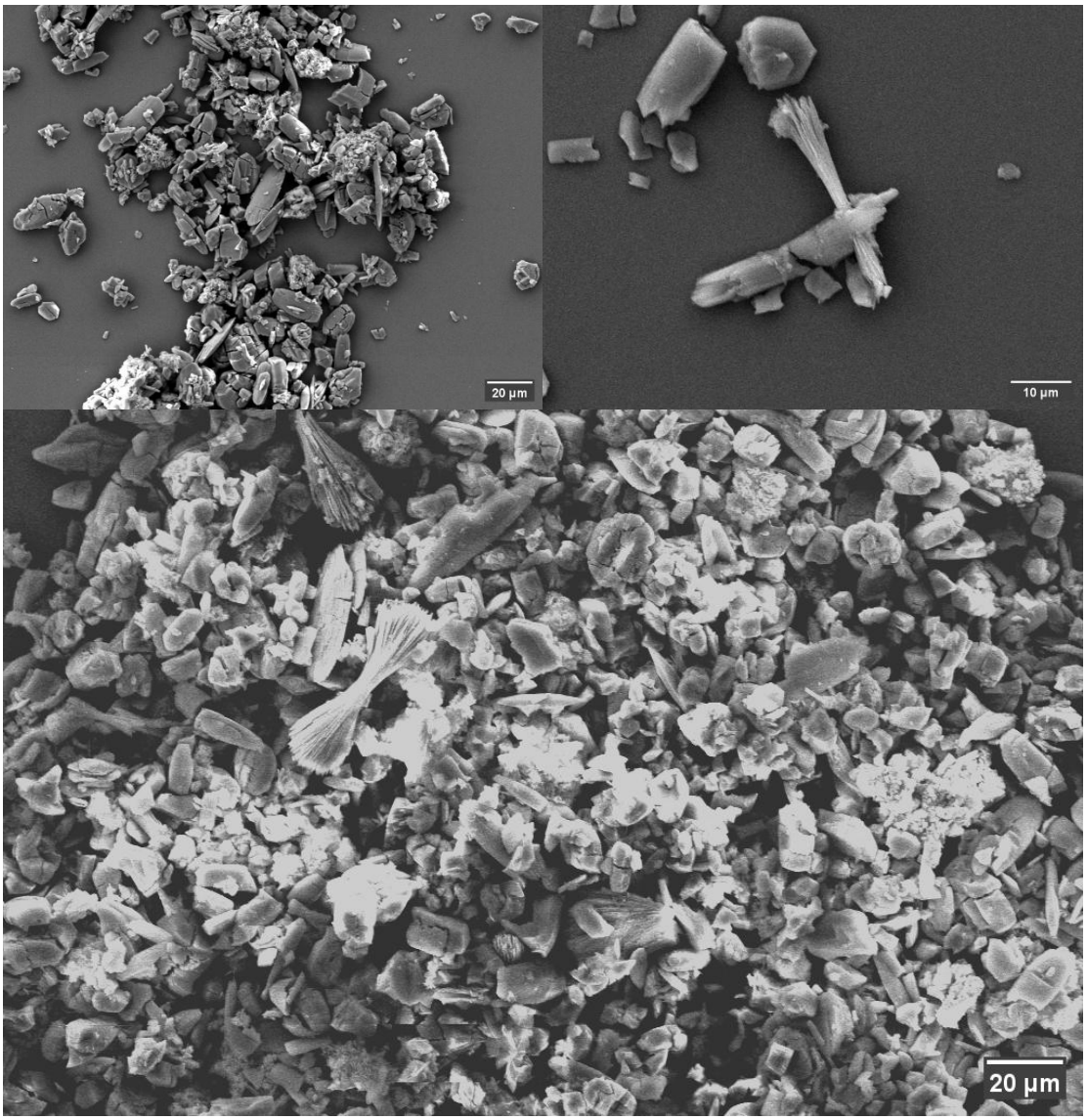

*Figure 2.16: SEM images of **Ce-TTB** crystals. Taken at an accelerating voltage of 15 kV using a secondary electron detector.*

To investigate the elemental composition, EDX spectroscopy was performed on **Ce-TTB** crystals dispersed on a silicon substrate. The observed Ce:O:N ratio of **Ce-TTB** was found to be 1:8:4.5, similar to the Ce:O:N ratio observed for **Ce-TTT** (1:8.5:5.5).

*Table 2.2: Comparison of experimentally observed atomic ratios in **Ce-TTB** and **Ce-TTT**.*

Ce-TTB Observed Ce:O:N ratio	Ce-TTT Observed Ce:O:N ratio
1:8:4.5	1:8.5:5.5

2.5 Electrocatalytic Water Oxidation Studies

2.5.1 OER Activity of Ce(III)-MOFs

To investigate the potential of the Ce(III)-based MOFs as electrocatalysts for the oxygen evolution reaction (OER), heterogeneous electrochemical studies were conducted in 0.5 M aqueous H_2SO_4. This electrolyte was chosen as it is commonly used to simulate the acidic environment present in proton exchange membrane (PEM) electrolysers.[44] As **Ce-TTT**, **Ce-BTB**, and **Ce-TTB** all consist of one-dimensional (1D) Ce(III) chain secondary building units (SBUs), this structural similarity enables investigation of the effect of heteroatom substitution in the tritopic linkers. A commercially available CeO_2 nanopowder (<50 nm) was used as a benchmark catalyst for comparison with the Ce(III) MOFs in the electrocatalytic OER.

The kinetics of the electrocatalytic reaction and the stability of the cerium electrocatalysts under turnover conditions were evaluated using modified carbon paste (**CP**) electrodes as part of rotating disk electrodes in linear sweep voltammetry (RDE-LSV) experiments. Electrocatalyst-modified **CP** electrodes were employed instead of Nafion-based inks due to their superior electronic conductivity, which results in higher current densities. A catalyst loading of 20 wt% was chosen for optimal performance and mechanical stability. Figure 2.17 presents the RDE-LSV plots for each catalyst. For the three Ce(III) MOFs, a characteristic Ce(III) to Ce(IV) oxidation peak is observed at an overpotential (η) of approximately 250 mV (1.48 V vs SHE), in agreement with the literature.[45] This oxidation occurs prior to the onset of water oxidation, which begins above an overpotential of approximately 387 mV. This suggests that Ce(IV) represents the OER-active site and that the Ce(III)-MOFs function as pre-catalysts. The LSV for **CeO_2/CP** lacks the Ce(III) → Ce(IV) oxidation peak, consistent with its initial Ce(IV) oxidation state.

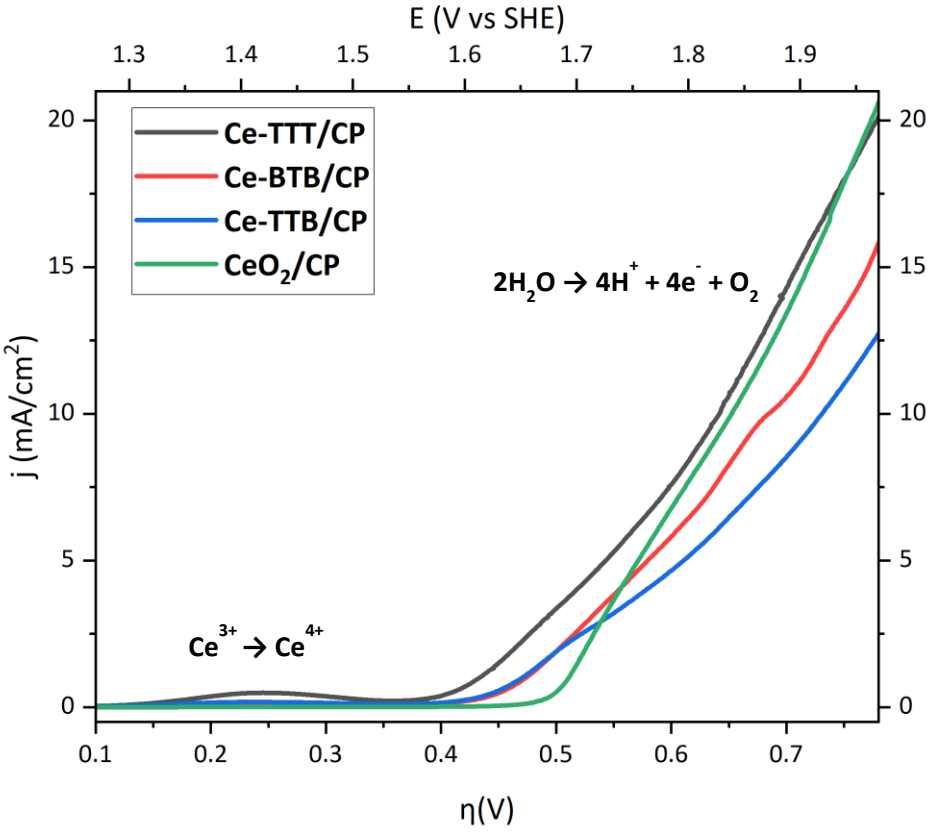

Figure 2.17: RDE-LSV plot of Ce-MOFs and CeO_2 embedded in carbon paste (CP) electrodes. Measurements were performed in 0.5 M H_2SO_4 at a sweep rate of 1 mV s^{-1} with an electrode rotation speed of 1600 rpm.

A comparison of applied overpotentials (η) at various current densities is presented in Table 2.3. The onset overpotential (η), defined as the potential at which OER initiates, was estimated using the Tangent Method (Appendix A: Figure A.5). Among the tested catalysts, **Ce-TTT/CP** exhibits the lowest onset η (387 mV), followed by **Ce-TTB/CP** (404 mV), **Ce-BTB/CP** (410 mV), and **CeO_2/CP** (474 mV). A similar trend is observed at a current density of 1 mA cm^{-2}. At 5 mA cm^{-2}, the overpotential of **CeO_2/CP** (609 mV) begins to intersect those of **Ce-TTB** and **Ce-BTB**. Notably, **Ce-TTT/CP** maintains superior performance across all current densities, being matched only by **CeO_2/CP** at 20 mA cm^{-2}. Given that all three MOFs pre-catalysts are constructed from one-dimensional Ce(III) chain SBUs, these results suggest that the variations in the properties of the tritopic linker can influence the onset characteristics and initial catalytic activity with respect to OER.

Table 2.3: Comparison of applied overpotentials (η) at various current densities for Ce-MOFs and CeO_2 nanoparticles embedded in carbon paste electrodes.

Catalyst	Onset η (mV) (V vs SHE)	η @ 1 mA cm^{-2}	η @ 5 mA cm^{-2}	η @ 10 mA cm^{-2}	η @ 15 mA cm^{-2}	η @ 20 mA cm^{-2}
Ce-TTT/CP	387 (1.59 V)	433 mV	543 mV	644 mV	709 mV	778 mV
Ce-TTB/CP	404 (1.60 V)	470 mV	611 mV	731 mV	—	—
Ce-BTB/CP	410 (1.61 V)	474 mV	581 mV	685 mV	771 mV	—
CeO_2/CP	474 (1.67 V)	511 mV	571 mV	652 mV	719 mV	773 mV

The kinetics of the oxygen evolution reaction (OER) on the various electrodes were studied by Tafel plot analysis using data derived from rotating disk electrode linear sweep voltammetry (RDE-LSV) (Figure 2.18). The Tafel slope indicates the increase in overpotential required to achieve a tenfold increase in current density and is known to depend on the rate-determining step of the electrochemical process. Therefore, a lower Tafel slope—reflecting a more efficient rate-determining step—indicates superior electrocatalytic performance. Each electrode presented in Figure 2.20 exhibits two distinct Tafel regions. For the three Ce-MOFs, these regions are separated by an overpotential of approximately 470 mV. The Tafel slope for **CeO_2/CP** was not measured below 470 mV, as its OER onset is not observed until 474 mV (see Table 2.3).

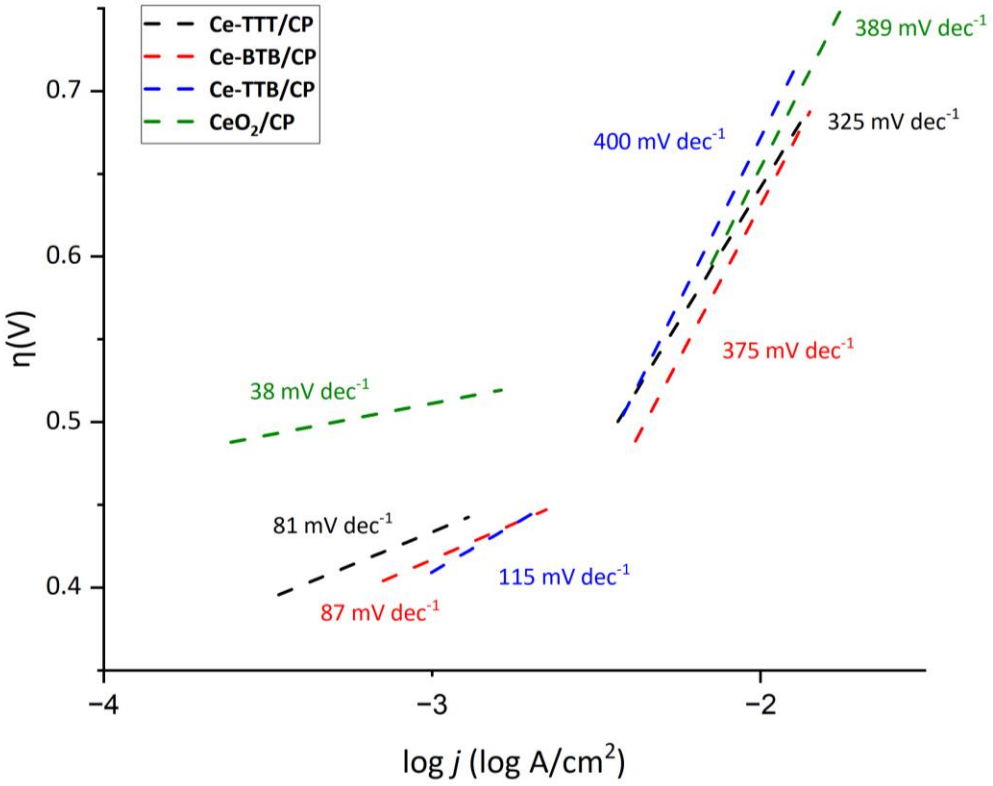

Figure 2.18: Tafel plot obtained from LSV data.

In the lower overpotential region (below 470 mV), **Ce-TTT/CP** exhibits the lowest Tafel slope, at 81 mV dec^{-1}, closely followed by **Ce-BTB/CP** at 87 mV dec^{-1}. **Ce-TTB/CP** exhibits a moderately higher slope in this region, at 115 mV dec^{-1}. These values highlight the promising electrocatalytic behaviour of **Ce-TTT** and **Ce-BTB**, as Tafel slopes below 100 mV dec^{-1} are considered exceptionally good for MOFs that have not been optimised as nanostructures.[46] MOFs synthesised as nano-particulates often demonstrate improved Tafel slopes due to shorter diffusion paths relative to their bulk analogues.[46-48]

As is generally accepted, high Tafel slopes (>120 mV dec^{-1}) indicate that the kinetics of the catalytic OER are limited by mass transport (diffusion-controlled), rather than by the rate of electron transfer.[49] Under diffusion-limited conditions, the rate of O_2 evolution exceeds the rate at which reactants (e.g. H_2O) or products (e.g. O_2) can diffuse to or from the electrode surface. MOF-based electrocatalysts, due to their microporosity, are particularly prone to diffusion limitations, which result in elevated Tafel slopes.

As the applied overpotential increases beyond 470 mV, all three Ce-MOFs transition into a diffusion-limited kinetic regime, contrasting with the electron-transfer-controlled

behaviour observed below this threshold—most notably for **Ce-TTT** and **Ce-BTB**. In the high-overpotential region, **Ce-TTT/CP** again exhibits the lowest Tafel slope, at 325 mV dec^{-1}, followed by **Ce-BTB/CP** at 375 mV dec^{-1} and **Ce-TTB/CP** at 400 mV dec^{-1}.

Initially, in the range of 488–522 mV, **CeO_2/CP** displays more favourable kinetics than the Ce-MOFs, with a Tafel slope of 38 mV dec^{-1}. However, beyond this range, its OER kinetics decline significantly, with the Tafel slope increasing to 389 mV dec^{-1}, placing its performance roughly in line with that of **Ce-BTB/CP** and **Ce-TTB/CP** at similarly high overpotentials.

The turnover frequency (TOF) was calculated from RDE-LSV data using Eq. 2.1.[50] Where *j* is current density at an applied overpotential, N_A is Avogadro's number, *F* is Faraday's constant, *n* is the number of electrons transferred to produce to molecule of product, and Γ represents the number of active sites involved in the reaction, per unit area. The number of active sites was determined using an established method from the literature (see Appendix A for details).[51-53]

$$TOF(\eta) = j \times N_A/(F \times n \times \Gamma) \qquad \textit{Eq. 2.1}$$

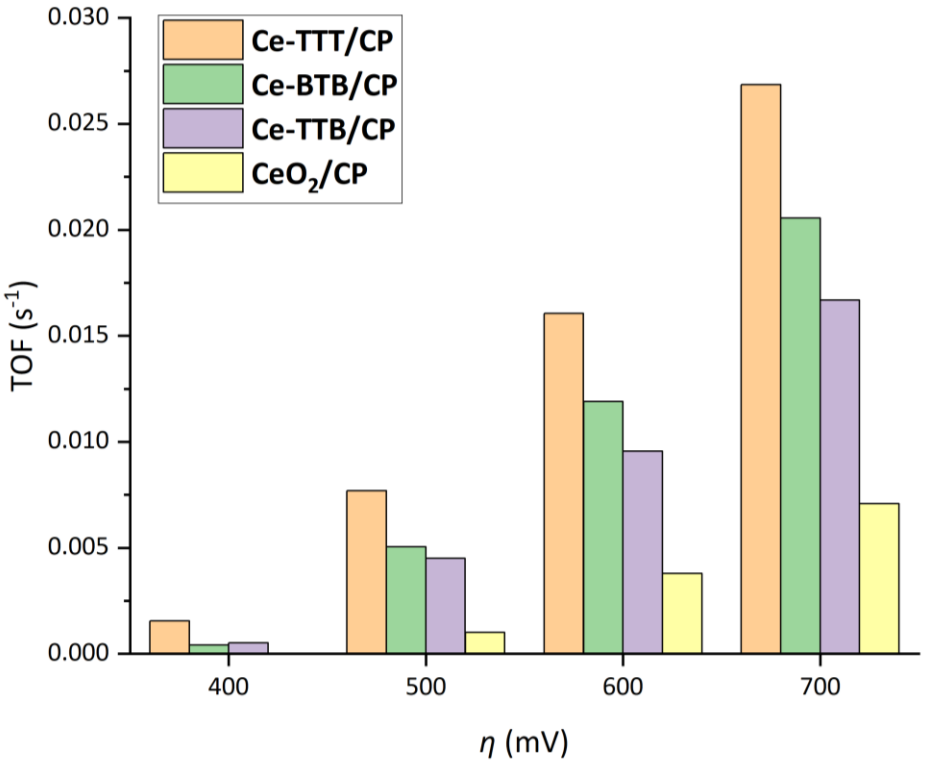

Figure 2.19: Plot of TOF values at various applied overpotentials.

The calculated turnover frequency (TOF) values are plotted in Figure 2.19 as a function of applied overpotential. The Ce-based MOFs clearly outperform commercial CeO_2 nanoparticles, with **Ce-TTT/CP** demonstrating a pronounced enhancement in TOF relative to both **Ce-BTB/CP** and **Ce-TTB/CP**. At an applied overpotential of 500 mV, **Ce-TTT/CP** achieves a TOF of 7.68×10^{-3} s^{-1}, compared to 5.04×10^{-3} s^{-1} and 4.50×10^{-3} s^{-1} for **Ce-BTB/CP** and **Ce-TTB/CP**, respectively. In contrast, **CeO_2/CP** exhibits a considerably lower TOF of 1.00×10^{-3} s^{-1} under the same conditions. These results suggest that the active sites in the Ce-based MOFs facilitate the OER more efficiently than those in commercial CeO_2 nanoparticles.

Using the two-electrode collector–generator method established by Sherman and Meyer *et al.*[54], Faradaic efficiency (FE) measurements were carried out for each catalyst. Faradaic efficiency refers to the percentage of electrons introduced into the system (via an externally applied voltage) that are utilised in product formation.[55]

For this method, the electrocatalyst is drop-cast onto the working electrode (FTO coated glass) designated as the generator. This electrode is termed the generator because it is where the oxygen evolution reaction (OER) occurs, producing molecular oxygen. A second electrode—the collector—is positioned in close proximity to the generator, without making direct electrical contact. During operation, the collector electrode (FTO coated glass) is held at a potential sufficient to drive the oxygen reduction reaction (ORR). Thus, molecular oxygen produced at the generator diffuses the short distance to the collector, where it is reduced, resulting in a current that is directly proportional to the amount of oxygen evolved.

A representative current–time response for this setup is illustrated in Figure 2.20. As both OER and ORR proceed *via* four-electron processes, Faradaic efficiency can be calculated using Eq. 2.2:

$$FE_{O_2} = \left(\frac{Q_{col}}{Q_{gen}}\right)\left(\frac{1}{\eta_{col\,eff}}\right) \qquad \textit{Eq. 2.2}$$

where Q_{col} is the charge passed at the collector associated with ORR, Q_{gen} is the charge passed at the generator associated with OER, and η_{col} is the collection efficiency of the cell.

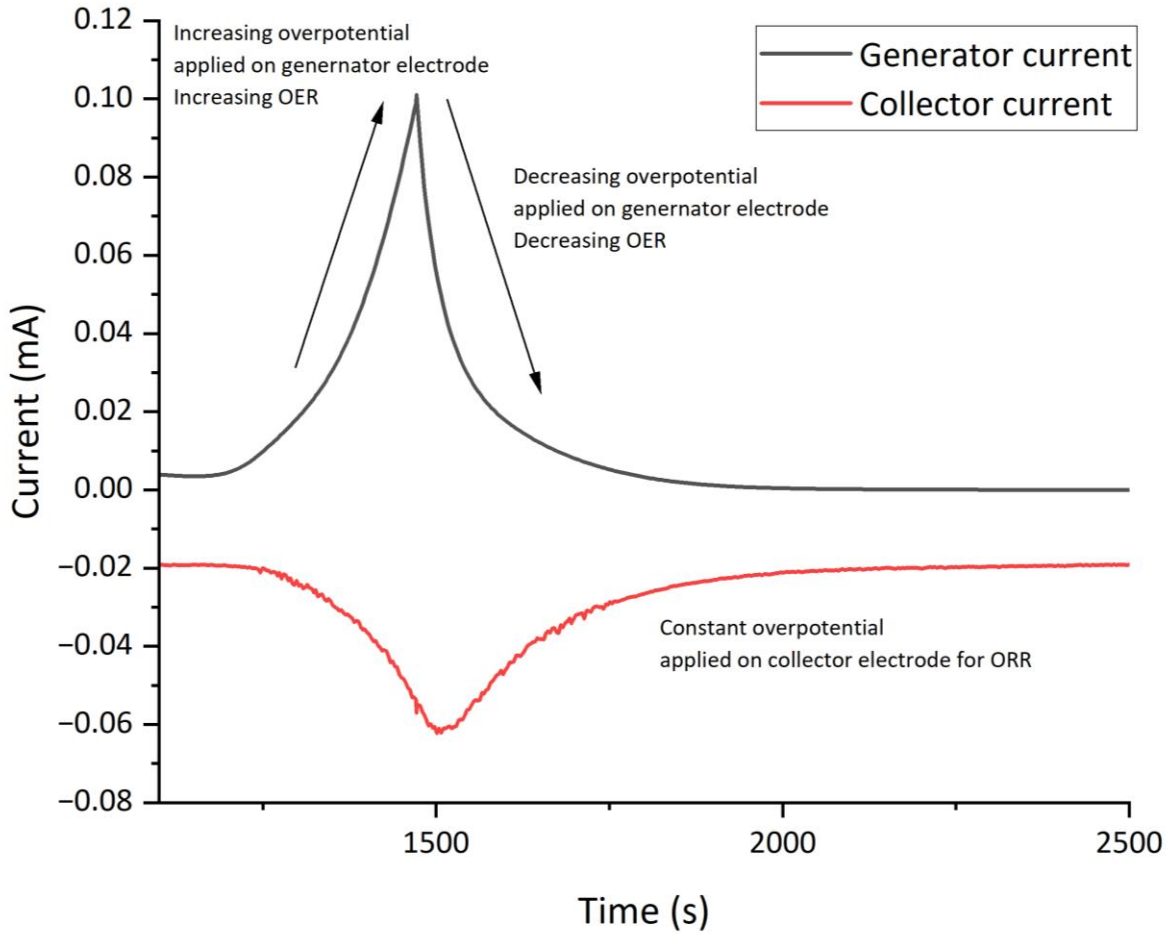

Figure 2.20: Current-time plot with generator electrode (black) and collector electrode (red).

The results of the FE determinations are presented in Figure 2.21. Alls samples exhibit Faradaic efficiencies above 85%; under applied comparative conditions, with the triazine-containing MOFs, **Ce-TTT** and **Ce-TTB**, achieving almost quantitative conversions (98% and 96% respectively). **Ce-BTB** and the commercial CeO_2 nanoparticles achieved Faradaic efficiencies of 88% and 85%, respectively. However, whilst the determined Faradaic efficiencies are reproducible, the experimental uncertainty—approximately ± 9.8% for each catalyst— mean it is not possible to definitively rank the compounds by FE. Nevertheless, it can be concluded that all four catalysts facilitate the oxygen evolution reaction (OER) with high, satisfactory Faradaic efficiency under the conditions tested.

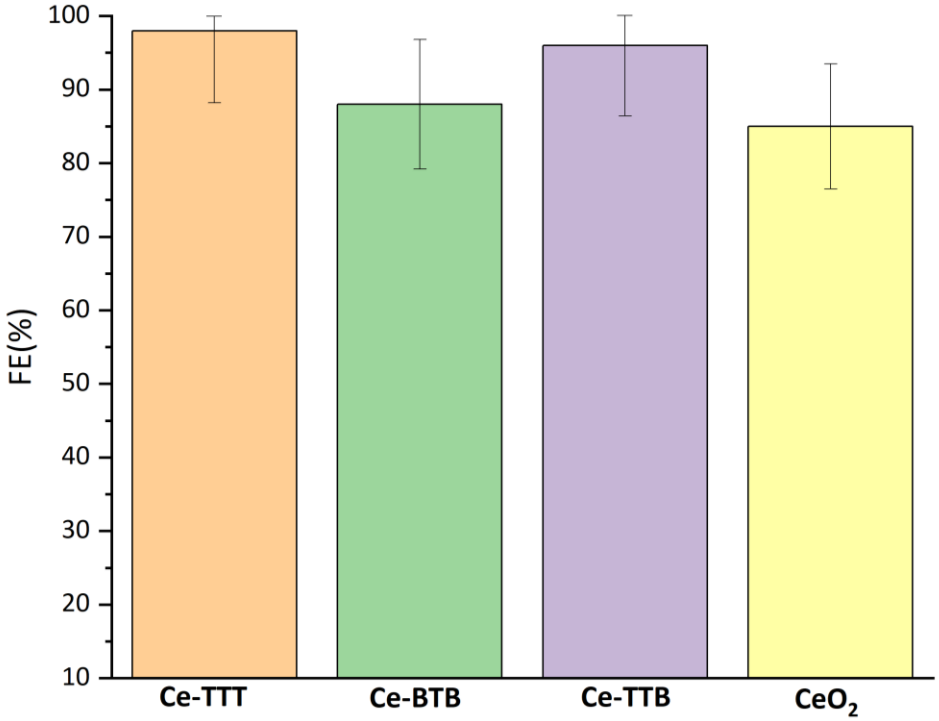

Figure 2.21: Faradaic efficiencies for Ce-MOFs and CeO_2.

2.5.2 Comparison with the State of the Art

Iridium oxide (IrO_2) is considered the state-of-the-art electrocatalyst for PEM electrolyser anodes. With this in mind, a brief comparison is made here in order to assess the OER activity of the Ce-MOFs under acidic conditions versus commercial IrO_2 powder. Figure 2.22 displays RDE-LSVs of the **Ce-TTT**, CeO_2, and IrO_2 embedded in carbon paste (**CP**) working electrodes, using 0.5 M H_2SO_4 as the electrolyte. As expected, **IrO_2/CP** displays a much lower onset overpotential for OER at approximately 265 mV, close to the theoretical limit for an electrocatalyst operating at 25 °C of 250 mV.[56] **IrO_2/CP** continues to outperform the Ce-based electrocatalysts at low overpotentials up until approximately 600 mV and 620 mV, where it intersects with the LSV curves of **Ce-TTT/CP** and **CeO_2/CP**, respectively. After this point, **Ce-TTT/CP** and **CeO_2/CP** display higher current densities than **IrO_2/CP**. For example, at an applied overpotential of 725 mV, both **Ce-TTT/CP** and **CeO_2/CP** achieve a current density of 18 mA cm^{-2}, compared to 15 mA cm^{-2} for **IrO_2/CP**. Importantly, at the benchmark current density of 10 mA cm^{-2} (relevant for practical applications[57]), **Ce-TTT/CP** displays an overpotential of 613 mV, marginally lower than the 619 mV and 623 mV displayed by **IrO_2/CP** and **CeO_2/CP**. When one considers the abundance of cerium in the Earth's crust (66.5 parts per million) versus the abundance of

iridium (1 part per billion),[20] and the subsequent sustainability and economic impacts, the presented results suggest that Ce-based electrocatalysts merit further investigation.

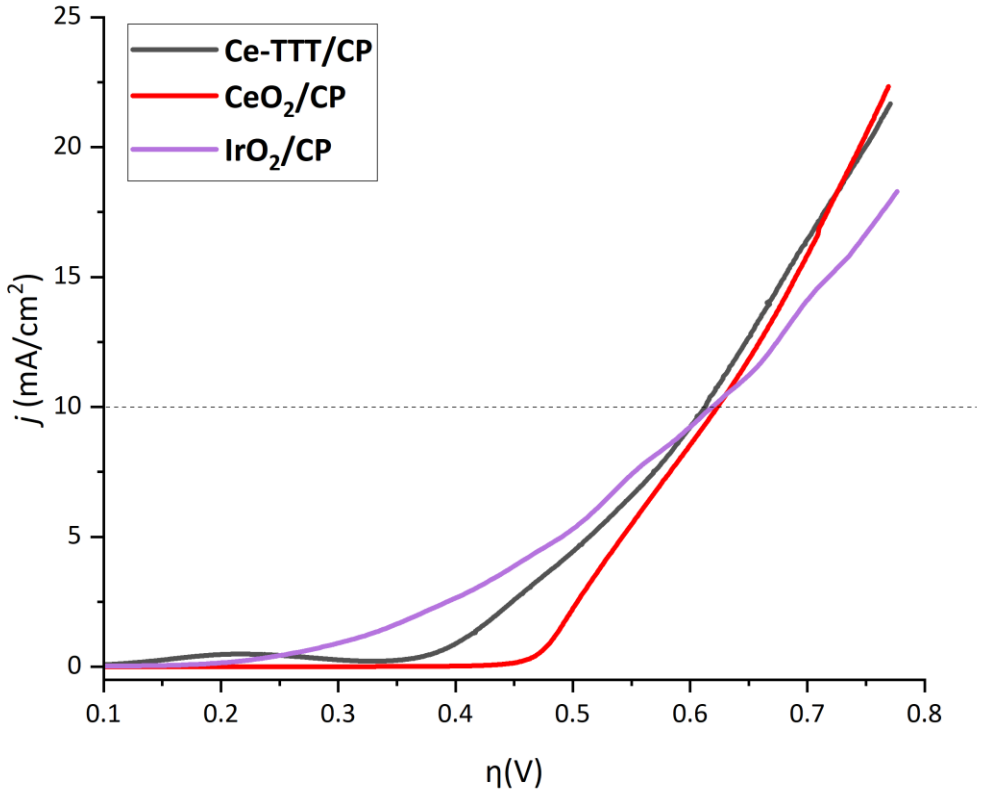

*Figure 2.22: RDE-LSV plot of **Ce-TTT**, CeO_2, and IrO_2 embedded in carbon paste (CP) electrodes. Measurements were performed in 0.5 M H_2SO_4 at a sweep rate of 1 mV s^{-1} with an electrode rotation speed of 1600 rpm.*

2.5.3 Cyclic Voltammetry Stability Study of Ce-MOFs for OER

To assess the stability of the OER activity demonstrated by the Ce-based MOFs, cyclic voltammetry (CV) was employed. Each electrocatalyst was subjected to 1,000 CV cycles at a scan rate of 100 mV s^{-1}, over a potential range of 0.2 V to 2.0 V versus SHE, in 0.5 M H_2SO_4. A linear sweep voltammogram (LSV) was recorded both before and after the CV experiment, at a scan rate of 1 mV s^{-1}. Figure 2.23 shows the evolution of the CV profile over 1,000 cycles for **Ce-TTT/CP**.

Firstly, when examining only the 5th cycle, a number of distinguishable features are

observed. Beginning at 0.9 V and sweeping in the anodic direction, a non-Faradaic region was observed up to approximately 1.4 V, at which point a Faradaic current arises and increases to the upper limit of 2.0 V. This Faradaic current is attributable to the overlapping contributions of Ce(III) → Ce(IV) oxidation and the OER, which could not be clearly distinguished at the relatively fast scan rate applied. In the cathodic sweep direction, a prominent Ce(IV) → Ce(III) reduction peak appears at 1.03 V. A second, distinct reduction feature was observed at 0.75 V. The origin of this second peak may be related to the redox activity of the organic linker, as this feature is also present in the CVs for **Ce-BTB/CP** and **Ce-TTB/CP** (Figures 2.24) but absent in the CV for **CeO_2/CP** (Figure 2.25), suggesting it does not originate from the cerium centre.

It is also notable that in cathodic sweep direction, the two reduction peaks visible in the 5th cycle at 1.03 V and 0.75 V merge into a single peak at approximately 0.9 V by the 500th cycle. As explained for the anodic sweep, this behaviour can be attributed to the increasing capacitive current with cycle number. This interpretation is further supported by the progressive rise in capacitive current within the non-Faradaic region between 0.30 and 0.55 V on the reverse scan.

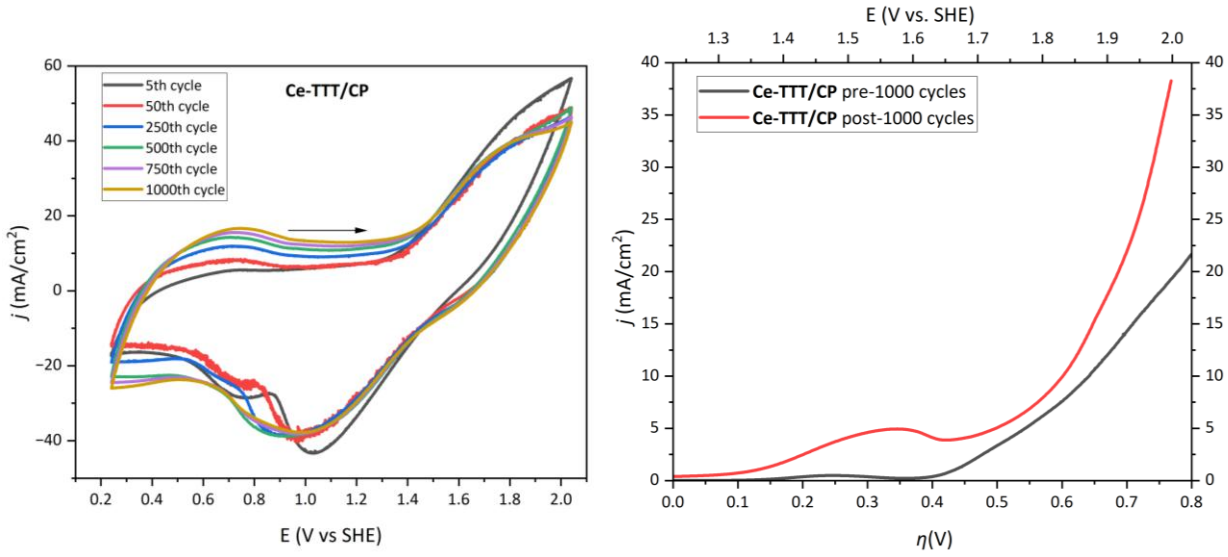

*Figure 2.23: Left, cyclic voltammograms of **Ce-TTT** embedded in a carbon paste (CP) electrode over 1000 cycles. Right, linear sweep voltammograms of **Ce-TTT/CP** before and after 1000 CV cycles.*

Throughout all 1000 cycles, a Faradaic current associated with the OER (between 1.4 V and 2.0 V) is consistently observed. However, a notable decline in current density is evident when comparing the 5th and 50th cycles. At 2.0 V, the current density decreases from 57 mA cm^{-2} for the 5th cycle to 48 mA cm^{-2} for the 50th cycle. Beyond this point,

the decline becomes less pronounced: the 500th cycle maintains a current density of 48 mA cm^{-2}, while the 1000th cycle registers a slight further decrease to 45 mA cm^{-2}.

This decrease in Faradaic current coincides with a progressive increase in capacitive current within the non-Faradaic region as the number of cycles increases. Despite the use of a rotating disk electrode (RDE) operating at 1600 rpm, this growing capacitive current suggests the accumulation of an increasingly prominent electrical double layer at the electrode–electrolyte interface. Given the complex three-dimensional architecture of the working electrode—comprising a porous MOF dispersed in carbon paste—this behaviour is not unexpected.[49] Under fast scan rate conditions, diffusion within the porous matrix does not reach steady state, resulting in capacitive charging with each cycle.

These observations are consistent with the Tafel analysis discussed in the previous section. Specifically, at higher overpotentials, the OER activity of the **Ce-TTT/CP** electrode (as indicated by current density) is limited by mass transport rather than electron transfer. Therefore, the observed decline in current density over successive CV cycles is more plausibly attributed to non-steady-state diffusion limitations than to catalyst deactivation.

This conclusion is further supported by linear sweep voltammograms (LSVs) recorded before and after 1000 CV cycles (Figure 2.24). The slower scan rate (1 mV s^{-1}) used in the LSV measurements minimises capacitive contributions, revealing that **Ce-TTT/CP** actually exhibits enhanced OER activity after prolonged cycling. For example, after 1000 cycles, the electrode achieves a current density of 10 mA cm^{-2} at an applied overpotential of 602 mV, compared to 642 mV prior to cycling.

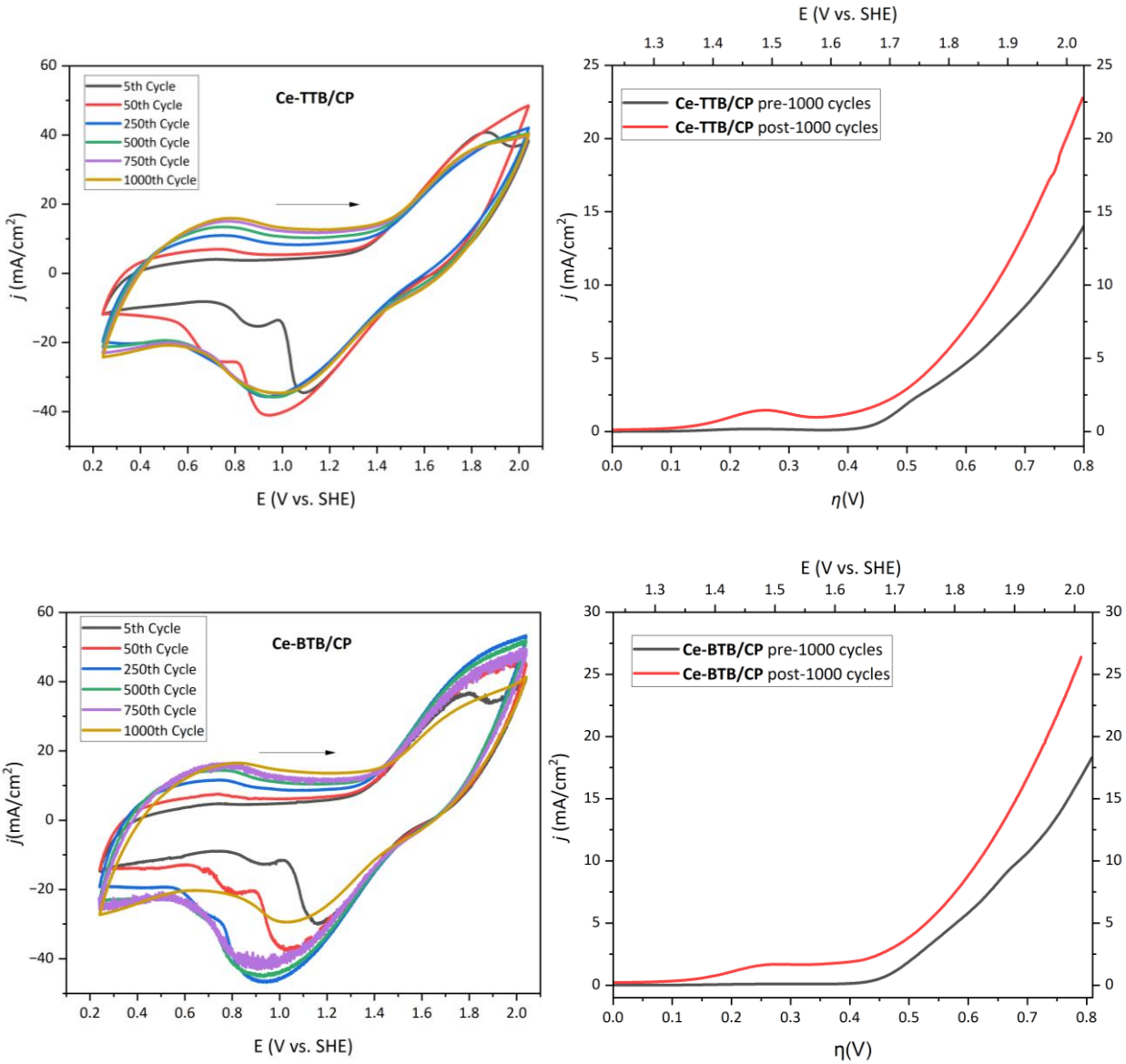

*Figure 2.24: Top left, cyclic voltammograms of **Ce-TTB** embedded in a carbon paste (CP) electrode over 1000 cycles. Top right, linear sweep voltammograms of **Ce-TTB/CP** before and after 1000 CVs. Bottom left, cyclic voltammograms of **Ce-BTB** embedded in a carbon paste (CP) electrode over 1000 cycles. Bottom right, linear sweep voltammograms of **Ce-BTB/CP** before and after 1000 CVs.*

The cyclic voltammetry (CV) profiles of **Ce-BTB/CP** and **Ce-TTB/CP** (Figure 2.24) closely resemble those previously described for **Ce-TTT/CP**. In both cases, a persistent Faradaic current associated with the Ce(III) → Ce(IV) and OER is observed in the potential range of 1.4 V to 2.0 V over the course of 1000 cycles. As with **Ce-TTT/CP**, the capacitive current increases progressively with cycle number, exerting an inverse effect on the OER-related current density due to non-steady-state mass transport limitations, as discussed above.

For the reverse scans, the Ce(IV) → Ce(III) reduction peak undergoes a shift and eventually merges with the minor reduction peak associated with the organic linker. This merging

occurs between the 250th and 500th cycle. These features are likewise observed in the CVs of **CeO_2/CP** (Figure 2.25), with the notable distinction that the latter lacks the reduction peak corresponding to the organic ligands present in the Ce-MOF systems.

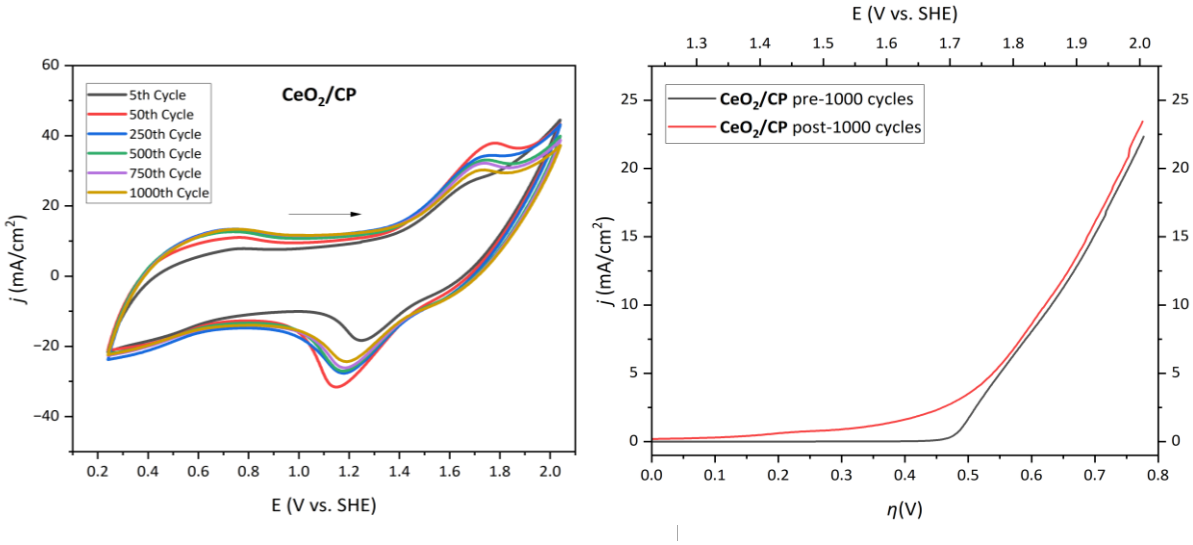

*Figure 2.25:Left, cyclic voltammograms of CeO_2 embedded in a carbon paste (CP) electrode over 1000 cycles. Right, linear sweep voltammograms of **CeO_2/CP** before and after 1000 CVs.*

Comparison of LSVs recorded before and after 1000 CV cycles (Figure 2.25), for both **Ce-BTB/CP** and **Ce-TTB/CP** demonstrate enhanced OER activity after 1000 cycles. For example, Ce-BTB/CP reaches a current density of 10 mA cm^{-2} at an applied overpotential (η) of 685 mV before cycling, which decreases to 617 mV after 1000 CV cycles. Likewise, for **Ce-TTB/CP**, the overpotential required to attain the same current density decreases from 731 mV to 650 mV. In contrast, **CeO_2/CP** (Figure 2.25) displays minimal change in OER performance following 1000 cycles, with only a slight reduction from 652 mV to 642 mV in the overpotential required to reach 10 mA cm^{-2}.

All three **Ce-MOF/CP** electrodes exhibit enhanced OER activity after 1000 CV cycles in 0.5 M H_2SO_4 electrolyte. The magnitude of improvement is comparable across the series: at an applied overpotential of 700 mV, **Ce-TTT/CP** and **Ce-BTB/CP** show increases in current density by 54% and 53%, respectively, while **Ce-TTB/CP** demonstrates a 60% increase. In contrast, **CeO_2/CP** displays no such enhancement in activity following CV cycling but maintains its initial performance. These results support the hypothesis that

Ce(III)-MOFs function as pre-catalysts, undergoing partial transformation during cycling to generate Ce(IV)-based OER active species. The fact that catalytic activity improves for the Ce-MOFs—but not for the CeO_2 nanoparticles—suggests that additional Ce(IV) active sites become accessible as the MOF crystals progressively transform during repeated cycling.

2.5.4 Chronopotentiometry Study

The long-term operational stability of the Ce-MOF based electrocatalysts was further evaluated using 24-hour chronopotentiometry experiments (Figure 2.26). A constant current density of 1 mA cm^{-2} was selected based on the Tafel analysis presented in Section 2.6.1. According to the Tafel plots, at this current density, the Ce-MOF based electrocatalysts operate under steady-state mass transport conditions, meaning that OER kinetics are governed predominantly by electron transfer. Consequently, any observed increase in the applied potential required to maintain 1 mA cm^{-2} can be attributed to electrocatalyst degradation rather than mass transport limitations.

All three Ce-MOF based electrocatalysts appear to be stable over the 24-hour test period. For **Ce-TTT/CP**, the average overpotential between 3 and 24 hours is approximately 460 mV, reaching a maximum of 472 mV at 13 hours, after which the overpotential gradually decreases, reaching 450 mV at 24 hours. This slight decline in overpotential is consistent with the findings from the preceding section, in which prolonged CV cycling led to improved OER activity. As previously discussed, extended electrochemical operation likely induces progressive transformation of the Ce(III)-MOF pre-catalyst into a Ce(IV)-based active species, resulting in a growing number of catalytically active sites and, consequently, improved performance. Similar behaviour is observed for **Ce-BTB/CP** and **Ce-TTB/CP**. With **Ce-BTB/CP** also having an average overpotential of approximately 460 mV, peaking at 477 mV at 13.7 hours before declining to 458 mV at 24 hours. **Ce-TTB/CP** is observed to have a slightly higher average overpotential of 490 mV, reaching a maximum value at 493 mV at 12.1 hours, before gradually declining to 467 mV at the 24-hour mark.

The commercial CeO_2 nanoparticles (**CeO_2/CP**), included here as a benchmark, were also found to be relatively stable over the 24-hour test period, with the overpotential

increasing only slightly from 407 mV at 3 hours to 412 mV at 24 hours.

Overall, the three Ce-MOF-based electrocatalysts displayed comparable behaviour, though the benchmark showed a moderately lower overpotential than the MOFs. This trend is consistent with their Tafel slopes at 1 mA cm^{-2}: **CeO_2/CP** exhibited the lowest slope (38 mV dec^{-1}), followed by **Ce-TTT/CP** (81 mV dec^{-1}) and **Ce-BTB/CP** (87 mV dec^{-1}), and then **Ce-TTB/CP** with its slightly higher overpotential of correlating with its higher Tafel slope (115 mV dec^{-1}). The fact that the Ce-MOF catalysts converge closely with the CeO_2 nanoparticles further reinforces the idea that the Ce(III)-MOF act as a pre-catalyst for a cerium(IV)-oxide active species.

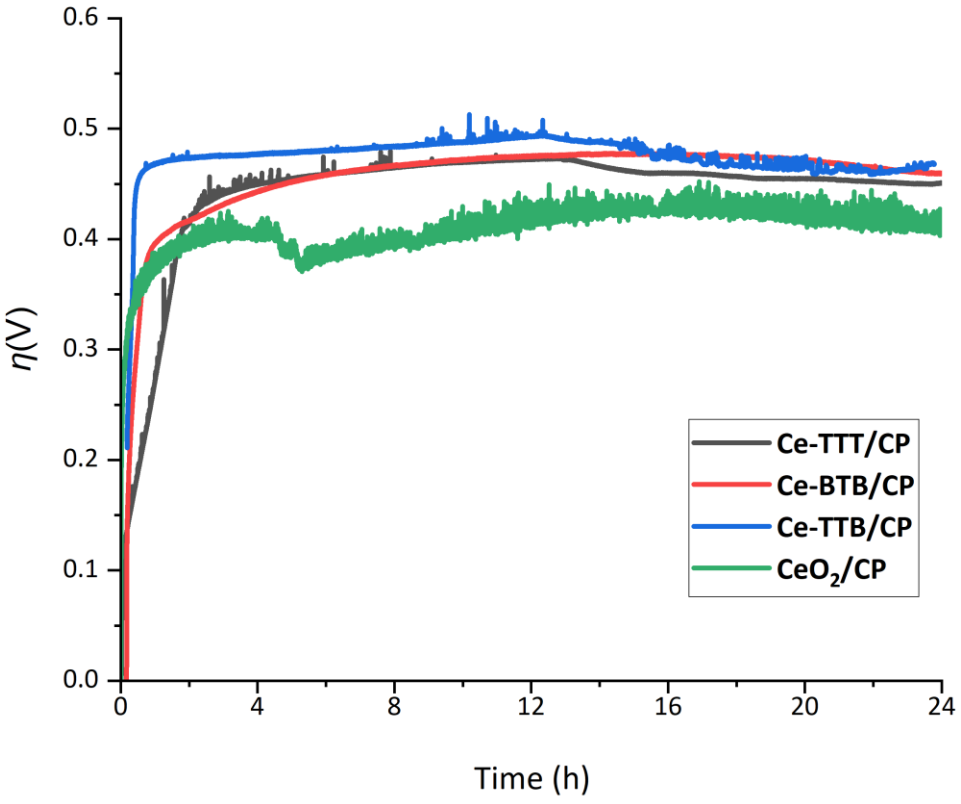

Figure 2.26: Chronopotentiometry data for Ce-MOFs and CeO_2 embedded in carbon paste (CP) working electrodes. Measurements were performed at a constant current density of 1 mA cm^{-2} in 0.5 M H_2SO_4 electrolyte at an electrode rotation speed of 1600 rpm.

2.6 Post-catalysis Characterisation

After bulk electrolysis experiments under acidic conditions, the **Ce-MOF/CP** electrodes were rinsed with deionised water and characterised to evaluate structural stability and, where possible, identify the catalytically active species. Given the strongly oxidising environment, it is expected that cerium oxides phases may form and act as the catalytically active species.

2.7.1 Powder X-ray Diffraction

Powder X-ray diffraction (PXRD) analysis was carried out on **Ce-MOF/CP** electrodes used in the 24-hour chronopotentiometry experiments at 1 mA cm^{-2}. In each case, the MOF–CP composite material was removed from the electrode holder after electrocatalysis and placed on a zero-background PXRD sample holder. PXRD patterns were recorded using a Bruker D8 Advance powder diffractometer with a Cu Kα radiation source (λ = 1.5406 Å). The quality of the PXRD patterns were limited by the small amount of sample (< 40 mg of MOF-CP composite) available.

Figure 2.27 shows the PXRD pattern **of Ce-TTT/CP** after electrocatalysis. Also included are the calculated PXRD patterns for **Ce-TTT**, graphite (a major component of the carbon paste, along with paraffin oil), and CeO_2. It is clear that **Ce-TTT** remains structurally intact in the bulk of the **Ce-TTT/CP** material post-electrocatalysis. However, the bulk of **Ce-TTT/CP** is likely not in contact with the electrolyte and therefore does not participate in electrochemical processes—though some degree of impingement into the carbon paste electrode is expected. Only **Ce-TTT** particles in contact with the electrolyte at the electrochemical interface are involved in electrocatalysis. Supporting this, the PXRD pattern of **Ce-TTT/CP** after electrocatalysis shows a peak at approximately 2θ = 28.5° and a weaker peak at approximately 2θ = 47.5°, indicating the formation of CeO_2, as highlighted in Figure 2.27.

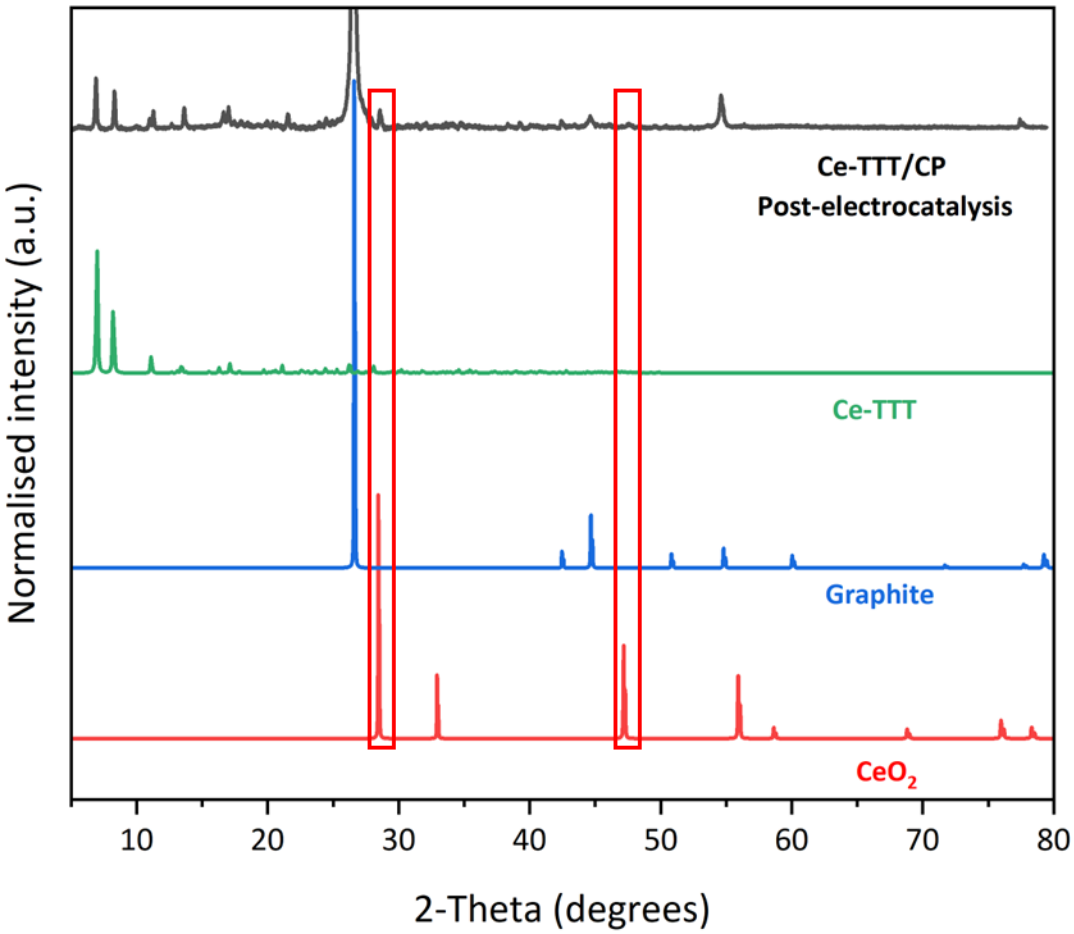

*Figure 2.27: PXRD pattern of **Ce-TTT/CP** post-electrocatalysis (black) compared to calculated PXRD patterns for **Ce-TTT** (green), graphite (blue) and CeO_2 (red). Red boxes highlight shared peaks in patterns of **Ce-TTT/CP** post-electrocatalysis and CeO_2.*

Similarly, the PXRD pattern of **Ce-BTB/CP** after electrocatalysis (Figure 2.28) displays the characteristic reflections of **Ce-BTB** in the bulk of the sample, along with weak, broad peaks at approximately 2θ = 29°, 33°, and 48°, which align with the characteristic reflections of CeO_2.

In the case of **Ce-TTB/CP** (Figure 2.29), the post-electrocatalysis PXRD pattern closely matches that obtained prior to electrolysis, with the addition of CeO_2 reflections again observed at approximately 2θ = 29°, 33°, and 48°.

These PXRD results indicate that the Ce-MOFs remain structurally intact in the bulk of the composite material following electrocatalysis. However, the emergence of CeO_2-derived signals suggests that Ce-MOF particles located at the electrochemical interface undergo oxidation to form CeO_2, which is likely to act as the catalytically active species during the oxygen evolution reaction.

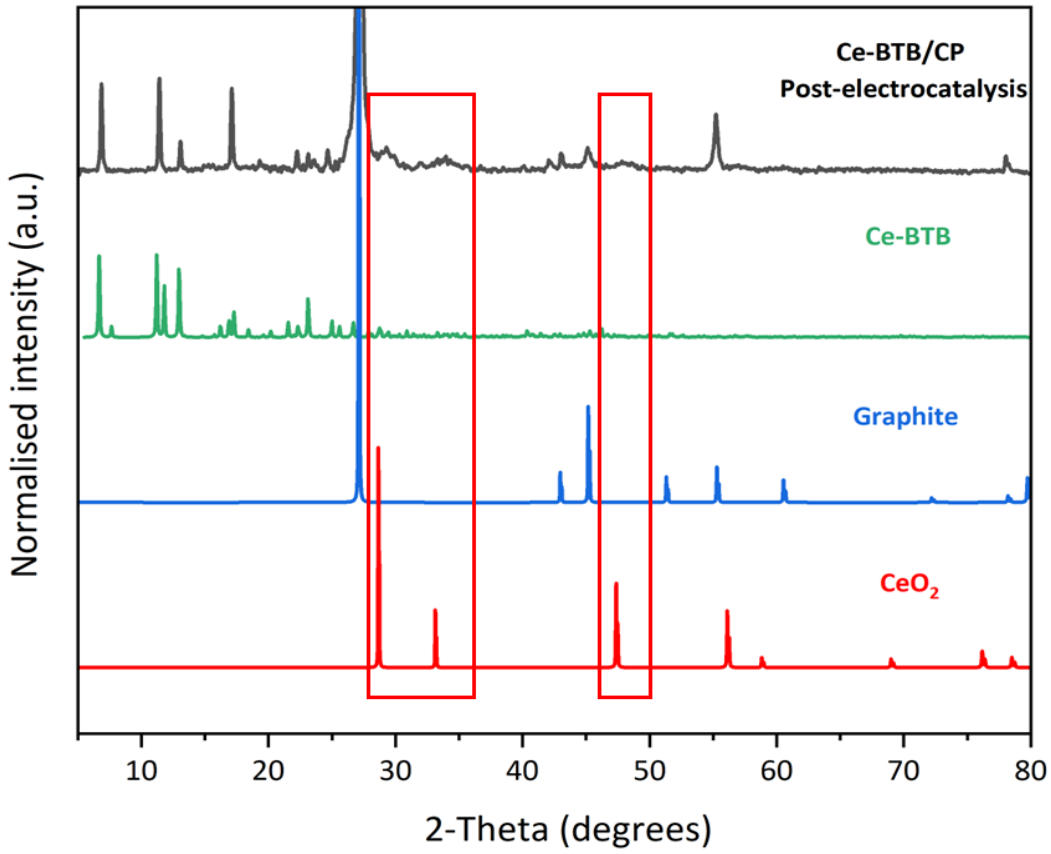

*Figure 2.28: PXRD pattern of **Ce-BTB/CP** post-electrocatalysis (black) compared to calculated PXRD patterns for **Ce-BTB** (green), graphite (blue) and CeO_2 (red). Red boxes highlight shared peaks in patterns of **Ce-BTB/CP** post-electrocatalysis and CeO_2.*

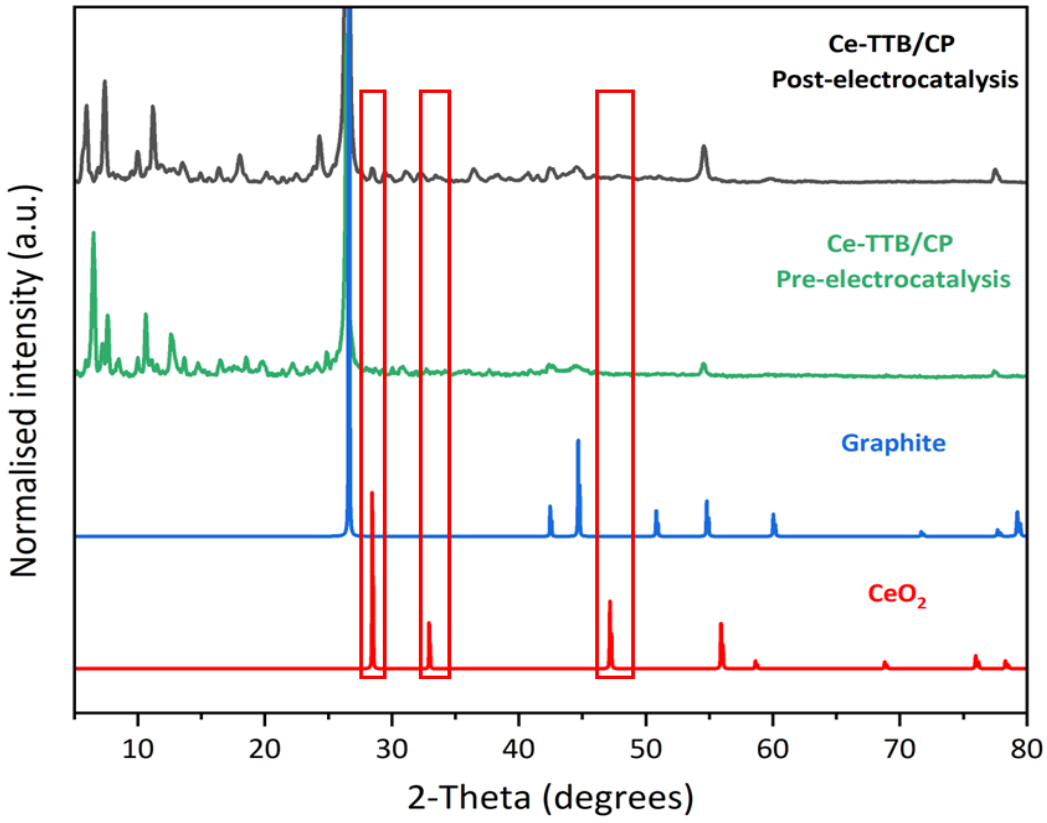

*Figure 2.29: PXRD pattern of **Ce-TTB/CP** post-electrocatalysis (black) compared to calculated PXRD patterns for **Ce-TTB** (green), graphite (blue) and CeO_2 (red). Red boxes highlight shared peaks in patterns of **Ce-TTB/CP** post-electrocatalysis and CeO_2.*

2.7 UV-Vis Spectroscopic Study of Ce Ion Leaching into Electrolyte

To further evaluate the stability of the Ce-MOFs as OER electrocatalysts under operational acidic conditions, UV–Vis spectroscopy was employed to assessing cerium ion leaching into the electrolyte during operation. Electrolyte samples were collected for each Ce-MOF and for CeO_2 following the cyclic voltammetry (CV) stability experiments (1000 cycles; see Section 2.6.3). For quantification, $Ce(NO_3)_3$ stock solution was prepared in 0.5 M H_2SO_4 (to match the electrolyte), followed by serial dilution to obtain five known concentrations ranging from 25 µM to 500 µM. Absorbance values were recorded at the absorption maximum (λ_{max} = 254 nm), and the resulting calibration curve exhibited excellent linearity, with an R^2 value of 0.9991 (Figure 2.30).

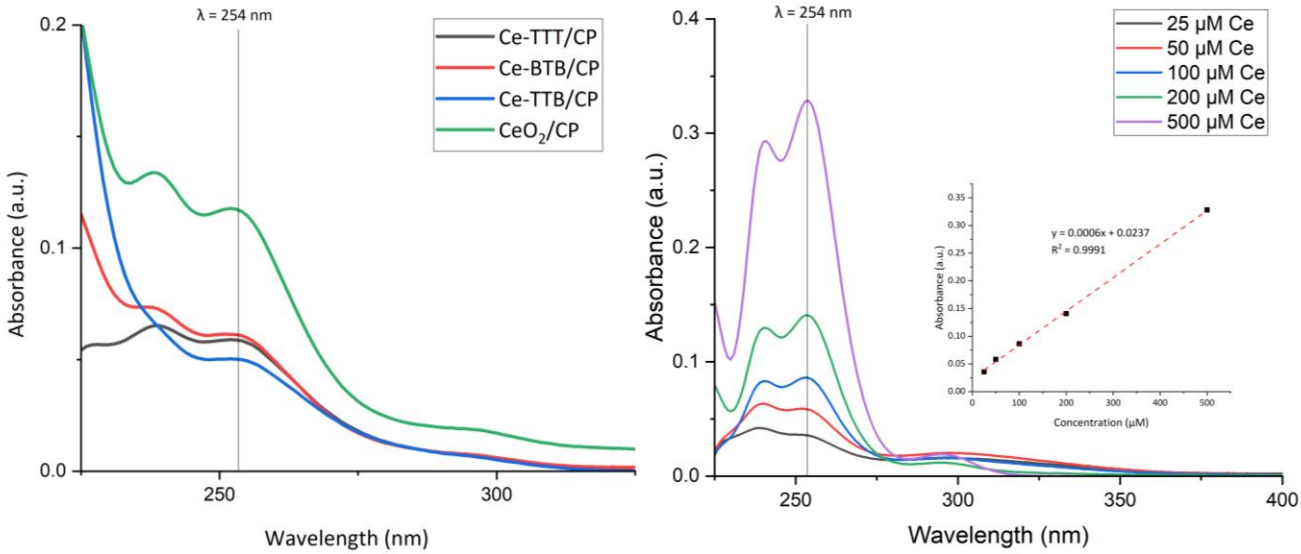

Figure 2.30: UV-Vis absorption data. Left, post-catalysis electrolyte samples. Right, $Ce(NO_3)_3$ standards for known concentration with insert of calibration curve.

UV–Vis absorption measurements of the post-catalysis electrolyte samples (Figure 2.30) confirmed the presence of Ce ions in the solutions in all cases, whereas no Ce was detected in the fresh electrolyte solutions. Using the calibration curve, the Ce concentration was quantified for each sample (Table 2.4). The solid **Ce-TTT/CP** and **Ce-BTB/CP** catalyst blends were found to have lost comparable cerium quantities over the 1000 CV cycles, corresponding to Ce mass losses of 7.11% and 7.60%, respectively. **Ce-TTB/CP** exhibited the lowest Ce leaching, at 5.41%. In contrast, **CeO_2/CP** showed a substantially higher Ce loss of 19.05% over the same period. These results suggest that the Ce-MOFs not only function as more efficient OER catalysts (as demonstrated in

previous sections) but also display greater stability than commercial CeO_2 nanoparticles, under acidic electrolysis conditions.

Table 2.4: Data pertaining to the leaching of Ce ions form Ce-MOFs and CeO_2 electrocatalysts after 1000 CV cycles in 0.5 M H_2SO_4.

	Absorbance @254 nm (a.u.)	**[Ce] (µM)**	**ppm (mg/L)**	**% (mass) Leaching of Ce over 1000 cycles**
Ce-TTT/CP	0.0585	58	8.12	7.11
Ce-BTB/CP	0.0609	62	8.68	7.60
Ce-TTB/CP	0.0502	44	6.18	5.41
CeO_2/CP	0.117	156	21.77	19.05

2.8 Conclusion

Ce(III)-based MOFs with one-dimensional chain SBUs function as pre-catalysts for the oxygen evolution reaction under acidic conditions, undergoing in-situ oxidation to generate catalytically active Ce(IV) species. Of the three linkers investigated, **Ce-TTT/CP** was the most active, becoming competitive with IrO_2 at overpotentials above 600 mV. Given cerium's far greater abundance, this points to a plausible route toward reducing iridium loadings in PEM electrolyser anodes.

All three Ce-MOFs outperformed commercial CeO_2 nanoparticles across turnover frequency, Tafel behaviour, and cycling stability, while maintaining Faradaic efficiencies above 85%. Tafel analysis indicated electron-transfer-limited kinetics below ~470 mV overpotential and diffusion-limited behaviour above this threshold, suggesting that particle size and morphology optimisation (not pursued in this work) could further improve high overpotential performance. The **Ce-MOF/CP** electrodes also sustained stable operation over 24 h of chronopotentiometry at 1 mA cm^{-2}.

Post-catalysis PXRD identified CeO_2 as the likely active species, and UV-Vis measurements

of electrolyte leaching showed that the MOF-derived oxides are markedly more stable than commercial CeO_2 nanoparticles. Together these results indicate that the MOF precursor governs the properties of the resulting cerium oxide phases, yielding a more active and more stable catalyst than the bulk oxide.

Building on these findings, the following chapter explores the use of these Ce-MOFs as sacrificial templates for pyrolytic synthesis of Ce-based electrocatalytic materials.

2.9 References

1. IPCC, Summary for Policymakers, in *Climate Change 2023: Synthesis Report. Contribution of Working Groups I, II and III to the Sixth Assessment Report of the Intergovernmental Panel on Climate Change*, ed. H. Lee and J. Romero, IPCC, Geneva, Switzerland, 2023, pp. 1–34, DOI: 10.59327/IPCC/AR6-9789291691647.001.
2. R. Eisenberg, H. B. Gray and G. W. Crabtree, *Proc. Natl. Acad. Sci. U. S. A.*, 2020, **117**, 12543–12549.
3. M. vd. Spek, W. Goldthorpe, C. Banet, C. Bauer, M. Mazzotti, P. Gabrielli, S. T. Munkejord, N. Shah, N. Sunny, D. Sutter, J. M. Trusler and Matteo Gazzani. *Energy Environ. Sci.*, 2022, **15**, 1034.
4. I. Roger, M. Shipman, & M. Symes, *Nat. Rev. Chem*., 2017 **1**, 0003.
5. J. Yu, S. Giancola, B. Khezri, D. Nieto-Castro, J. Redondo, F. Schiller, S. Barja, M. C. Spadaro, J. Arbiol, F. A. Garcés-Pineda and J. R. Galán-Mascarós, *EES Catal.*, 2023, 1, 765.
6. C. Spöri , J. T. H. Kwan , A. Bonakdarpour , D. P. Wilkinson and P. Strasser , *Angew. Chem., Int. Ed.*, 2017, **56**, 5994 —6021.
7. C. C. L. McCrory, S. Jung, I. M. Ferrer, S. M. Chatman, J. C. Peters, and T. F. Jaramillo, *J. Am. Chem. Soc.* 2015, **137**, 13, 4347–4357.
8. S. R. Batten, N. R. Champness, X.-M. Chen, J. Garcia-Martinez, S. Kitagawa, L. Öhrström, M. O'Keeffe, M. Paik Suh and J. Reedijk, *Pure Appl. Chem.*, 2013, **85**, 1715–1724.

9. A. C. Sudik, A. R. Millward, N. W. Ockwig, A. P. Côté, J. Kim and O. M. Yaghi, *J. Am. Chem. Soc.*, 2005, **127**, 7110–7118.
10. J. L. Wang, C. Wang and W. Lin, *ACS Catal.*, 2012, **2**, 2630–2640.
11. J. Baek, B. Rungtaweevoranit, X. Pei, M. Park, S. C. Fakra, Y. S. Liu, R. Matheu, S. A. Alshmimri, S. Alshehri, C. A. Trickett, G. A. Somorjai and O. M. Yaghi, *J. Am. Chem. Soc.*, 2018, **140**, 18208–18216.
12. Y. Li, H. Xu, S. Ouyang and J. Ye, *Phys. Chem. Chem. Phys.*, 2016, **18**, 7563–7572.
13. D. Sensharma, N. Zhu, S. Tandon, S. Vaesen, G. W. Watson and W. Schmitt, *Inorg. Chem.*, 2019, **58**, 9766–9772.
14. P. Vervoorts, A. Schneemann, I. Hante, J. Pirillo, Y. Hijikata, T. Toyao, K. Kon, K. I. Shimizu, T. Nakamura, S. I. Noro and R. A. Fischer, *ACS Appl. Mater. Interfaces*, 2020, **12**, 9448–9456.
15. B. Chen, C. Liang, J. Yang, D. S. Contreras, Y. L. Clancy, E. B. Lobkovsky, O. M. Yaghi and S. Dai, *Angew. Chemie - Int. Ed.*, 2006, **45**, 1390–1393.
16. J. Wang, J. Wang, Y. Li, M. Jiang, L. Zhang and P. Wu, *New J. Chem.*, 2016, **40**, 8600–8606.
17. M. L. Gao, X. M. Cao, Y. Y. Zhang, M. H. Qi, S. M. Wang, L. Liu and Z. B. Han, *RSC Adv.*, 2017, **7**, 45029–45033.
18. M. H. Zeng, Q. X. Wang, Y. X. Tan, S. Hu, H. X. Zhao, L. S. Long and M. Kurmoo, *J. Am. Chem. Soc.*, 2010, **132**, 2561–2563.
19. H. B. Wu and X. W. Lou, Wu and Lou, *Sci. Adv.*, 2017, **3**, 9252.
20. W. M. Haynes, *CRC Handbook of Chemistry and Physics,* 97th edition (2016–2017), sec. 14, pg 17.
21. X. Wang, J. Wang, Y. Sun, K. Li, T. Shang and Y. Wan. *Front. Chem.*,2022, **10**, 89708.
22. M. Wua , Y. Zhanga , R. Zhanga , J. Maa , N. Alonso-Vante, *Electrochimica Acta,* 2022, **403**, 139630.
23. J. Jacobsen, A. Ienco, R. D'Amato, F. Costantino and N. Stock, *Dalton Trans.*, 2020, 49, 16551.
24. A. F. Kateshali, S. G. Dogaheh, J. Soleimannejad, A. J. Blake, *Coordination Chemistry Reviews*, 2020, **419**, 213392.
25. Y. Cheng, X. Xiao, X. Guo, H. Yao, and H. Pang, *ACS Sustainable Chem. Eng.* 2020, **8**, 8675−8680.

26. H. Zhang, Y. Wang, D. Song, L. Wang, Y. Zhang and Y. Wang, *Nanomaterials,* 2023, 13, 1921.
27. S.Y. Zhong and X.Q. Gong, *Applied Surface Science*, 2019, **496**, 143712.
28. G. Spezzatia , A. D. Benavidezb , A. T. DeLaRivab , Y. Sua , J. P. Hofmanna , S. Asahinac, E. J. Olivierd , J. H. Neethlingd , J. T. Millere , A. K. Datyeb , E. J.M. Hensen, *Applied Catalysis B: Environmental*, 2019, **243**, 36.
29. M. Nolan, S. C. Parker, G. W. Watson, *Surface Science*, 2005, **595**, 223–232.
30. Tana, M. Zhang, J. Li, H. Li, Y. Li, W. Shen, *Catalysis Today*, 2009, **148**, 179–183
31. J. Yu, Z. Wang, J. Wang, W. Zhong, M. Ju, R. Cai, C. Qiu, X. Long and S. Yang, *ChemSusChem,* 2020, **13**, 5.
32. A. Rajapriya, S. Keerthana, A. Rebekah, C. Viswanathan, N. Ponpandian, *International Journal of Hydrogen Energy,* 2021, **46**, 75, 37281-37293.
33. É. Whelan, PhD Thesis, University of Dublin, 2023.
34. H. K. Reimschuessel and N. T. McDevitt, *Journal of the American Chemical Society*, 1960, **82**, 3756-3762.
35. G. B. Deacon and R. J. Phillips, *Coord. Chem. Rev.*, 1980, **33**, 227–250.
36. S. Safat, F. Buazar, Albukhaty, S. Albukhaty and S. Matroodi, *Sci. Rep.*, 2021, **11**, 14734.
37. A. A. Ansari and A. Kaushik, *J. Semicond.*, 2010, **31**, 033001.
38. W. Wattanathana, N. Suetrong, P. Kongsamai, K. Chansaenpak ,N. Chuanopparat, Y. Hanlumyuang, P. Kanjanaboos, and S. Wannapaiboon, *Molecules*, 2021, **26**, 5410.
39. R. Zamiri, H. A. Ahangar, A. Kaushal, A. Zakaria, G. Zamiri, D. Tobaldi, J. M. F. Ferreira, *PLoS ONE*, 2015, **10**, 4, e0122989.
40. Z. Lin, R. Zou, J. Liang, W. Xia, D. Xia, Y. Wang, J. Lin, T. Hu, Q. Chen, X. Wang, Y. Zhao and A. K. Burrell, *Journal of Materials Chemistry*, 2012, **22**, 7813-7818.
41. A. Altomare, C. Cuocci, C. Giacovazzo, A. Moliterni, R. Rizzi, N. Corriero, and A. Falcicchio, *J. Appl. Crystallogr.*, 2013, **46**, 1231–1235.
42. A. Le Bail, *Powder Diffr.*, 2005, **20**, 316–326.
43. W. d. Poel, P. Tinnemans, A. L. L. Duchateau, M. Honing, F. P. J. T. Rutjes, E. Vlieg, and R. d. Gelder, *Chem. Eur. J.*, 2019, **25**, 14999 – 15003.
44. T. Wang, X. Cao, and L. Jiao, *Carbon Neutrality,* 2022, **1**, 21.

45. A. Paulenova, S.E. Creager, J.D. Navratil , Y. Wei, *Journal of Power Sources*, 2002, **109**, 431–438.
46. L. Zhuang, L. Ge, H. Liu, Z. Jiang, Y. Jia, Z. Li, D. Yang, R. K. Hocking, M. Li, L. Zhang, X. Wang, X. Yao, Z. Zhu, *Angew. Chem. Int. Ed.*, 2019, **58**, 13565.
47. X. Hou, J. Zhou, X. Xu, X, Wang, S. Zhang, H. Wang, M. Huang, *Catalysis Communications*, 2022, **165**, 106445.
48. X. Hou, Z. Han, X. Xu, D. Sarker, J. Zhou, M. Wu, Z. Liu, M. Huang, H. Jiang, *Chemical Engineering Journal*, 2021, **418**, 129330.
49. R. L. Doyle and M. E. G. Lyons, *in Photoelectrochemical Solar Fuel Production: From Basic Principles to Advanced Devices*, ed. S. Giménez and J. Bisquert, Springer International Publishing, Cham, 2016, pp. 41–104.
50. A. Sengeni, P. E. Karthik, S. Noda, *Angew. Chem. Int. Ed.* **2021**, *60*, 23051.
51. M. Blasco-Ahicart, J. Soriano-López, J. J. Carbó, J. M. Poblet and J. R. Galán-Mascarós, *Nat. Chem.*, 2018, **10**, 24–30.
52. J. Soriano-Lopez, F. W. Steuber, M. Mulahmetovic, M. Besora, J. M. Clemente-Juan, M. O'Doherty, N. Y. Zhu, C. L. Hill, E. Coronado, J. M. Poblet and Wolfgang Schmitt, *Chem. Sci.*, 2023, **14**, 13722.
53. J. Soriano-López, R. Elliott, A. C. Kathalikkattil, A. M. Ako, M. Mulahmetović, M. Venkatesan, Wolfgang Schmitt, *ACS Sustainable Chem. Eng.*, 2020, **8**, 36, 13648–13659.
54. B. D. Sherman, M. V. Sheridan, C. J. Dares, and T. J. Meyer, *Anal. Chem.* 2016, **88**, 7076−7082.
55. J. Zhao, S. Xue, J. Barber, Y. Zhou, J. Menga and X. Ke, *J. Mater. Chem. A*, 2020, **8**, 4700.
56. P. Trivedi, N. C. Minj, S. Mittal, B. Kamaraj, S. Yadav and A. Sengeni, *J. Mater. Chem. A*, 2025, **13**, 21436.
57. C. C. L. McCrory, S. Jung, J. C. Peters and T.F. Jaramillo, J. Am. Chem. Soc. 2013, 135, 45, 16977–16987.

Chapter 3: Pyrolysed Ce-MOF Derivatives as Water Oxidation Electrocatalysts

3.1 Introduction

The previous chapter established that Ce(III)-based metal–organic frameworks (MOFs) function as effective pre-catalysts for the oxygen evolution reaction (OER) in acidic media, with the in situ formation of catalytically active cerium (IV) oxide phases. While they showed improved activity and stability compared to commercial CeO_2 nanoparticles, the benchmark nanoparticles exhibited better OER kinetics at 1 mA cm^{-2}, attributable to its higher electronic conductivity (due to smaller particle size) and shorter diffusion lengths. Building on these findings, this chapter explores the use of Ce-MOFs as sacrificial templates for the synthesis of cerium-based electrocatalytic materials via controlled pyrolysis. It was anticipated that pyrolysis would generate CeO_2 particles embedded in a conductive carbon matrix with the objective being to improve the OER kinetics on the catalysts while maintaining the activity and stability of their parent MOFs. Furthermore, to assess whether structural features and heteroatom content of the MOF precursors influence the properties and electrocatalytic performance of the resulting pyrolysed materials.

CeO_2 has a fluorite structure with a face-centred cubic unit cell, consisting of Ce^{4+} cations are 8-coordinated by O^{2-} anions occupying the tetrahedral coordination sites. At the surface CeO_2 can expose three stable surfaces, (100), (110), and (111), with the latter being thermodynamically most stable.[1] Unlike in the bulk material, cerium and oxygen atoms have unsaturated coordination for all three aforementioned planes. The polar (100) surface is terminated by sixfold coordinated cerium atoms and twofold coordinated oxygen atoms. Meanwhile the charge neutral (110) and (111) facets have sixfold and sevenfold coordinated cerium atoms, respectively, with both having threefold coordinated oxygen atoms.[1,2,3] The catalytic activity of CeO_2 is highly dependent on which surfaces are exposed, with (110) and (100) having better activity due to lower vacancy formation energy than (111).[4] This was demonstrated by Tana et al. who found that CeO_2 nanowires and nanorods, which predominantly expose (110) and (100) surfaces, had greater oxygen storage capacity and catalytic CO oxidation activity than polyhedral CeO_2

nanoparticles, which predominantly expose the (111) surface.[5] Other methods for increasing oxygen vacancies on CeO_2 are annealing and plasma treatments, as well as doping with heteroatoms, both of which have been using to increase ceria's electrocatalytic OER activity in alkaline media.[6,7] In particular, Rajapriya et al. found that doping CeO_2 with nitrogen and sulfur improved electronic conductivity, increased Ce^{3+} surface concentrations and dramatically improved OER in alkaline conditions.[7]

3.2 Pyrolysis of Ce(III)-MOFs

Samples of the Ce(III)-MOFs studied in the last chapter (**Ce-TTT**, **Ce-BTB** and **Ce-TTB**) were pyrolysed using a tube furnace under an inert nitrogen atmosphere. The heat treatment programme employed is illustrated in Figure 3.1. Prior to sample insertion, the furnace was rapidly heated to 800 °C and held at that temperature for 10 minutes, then quickly cooled to 250 °C. This step was undertaken to remove any oxygen adsorbed within the tube. A crucible containing Ce(III)-MOF powder was then placed at the centre of the tube furnace, which was subsequently heated to 800 °C at a rate of 5 °C per minute. The furnace temperature was maintained at 800 °C for 2 hours, after which the system was allowed to cool rapidly to room temperature. The resulting pyrolysed material, referred to as either **Ce-TTT@800**, **Ce-BTB@800** or **Ce-TTB@800** depending on the MOF precursor used, was recovered from the crucible. The characterisation of **Ce-TTT@800**, **Ce-BTB@800** and **Ce-TTB@800** are presented in section 3.2.

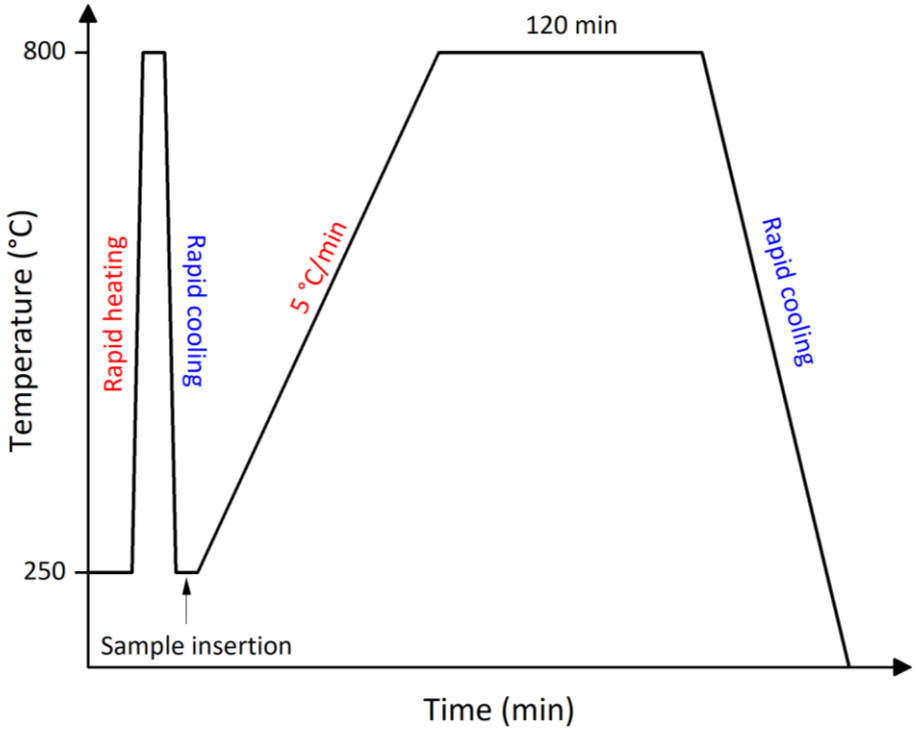

*Figure 3.1: Heat treatment programme used for the pyrolysis of **Ce(III)-MOFs** under an inert nitrogen atmosphere. The tube furnace was first flushed by heating to 800 °C and rapidly cooling to 250 °C prior to sample insertion. Pyrolysis was carried out by heating **Ce(III)-MOFs** to 800 °C at a rate of 5 °C min^{-1}, holding for 2 hours, followed by rapid cooling to room temperature.*

3.3 Characterisation of Pyrolysed Ce(III)-MOFs

3.3.1 Powder X-ray Diffraction

3.3.1.1 Ce-TTT@800

Powder X-ray diffraction (PXRD) analysis of **Ce-TTT@800** reveals that a composite material was formed by the pyrolysis of **Ce-TTT**. The PXRD pattern of **Ce-TTT@800**, presented in Figure 3.2, features two broad reflections centred at 28.6° and 47.4°, which are characteristic of cerium oxide (CeO_2) (111) and (220) planes. Superimposed on these broad peaks are smaller peaks at 25.2°, 32.8°, 39.0°, 47.1°, 49.5°, 54.1°, and 66.7°. Using the DIFFRAC.EVA software package, a database match was made between this pattern of peaks and International Centre for Diffraction Data (ICDD) reference standards for Ce_2S_3 (PDF 00-027-0104) and CeO_2 (PDF 03-65-5923).

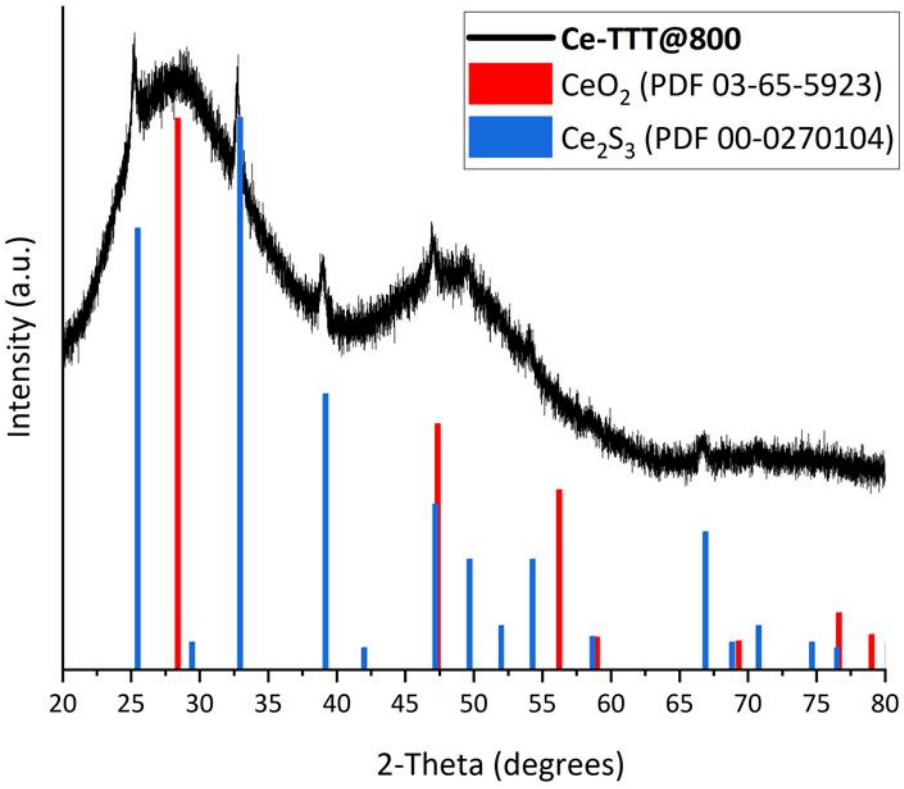

*Figure 3.2: PXRD pattern of **Ce-TTT@800** (black), overlayed with ICDD reference standards for cerium sulfide (PDF 00-027-0104) in blue, and cerium oxide (PDF 03-65-5923) in red.*

The significant disparity in peak broadness between the two cerium phases indicates large difference mean crystallite size. Amorphous contributions from the carbon content in the material may also add to this peak broadness. The Scherrer equation[8] (Eq. 3.1) was employed to estimate the average crystallite size of both the CeO_2 and the Ce_2S_3 phases:

$$T = \frac{K\lambda}{\beta cos\theta} \qquad \text{Eq. 3.1}$$

where *T* is the mean crystallite size, *K* is the shape factor, λ is the X-ray wavelength, β is the full width at half maximum (FWHM) of the diffraction peak (in radians), and θ is the Bragg angle. A shape factor (*K*) of 0.89 was chosen for both the CeO_2 and the Ce_2S_3 phases.

Peak fitting of the **Ce-TTT@800** PXRD pattern using *OriginPro* software required separate Gaussian models for the CeO_2 and Ce_2S_3 phases, as shown in Figure 3.3. Subsequent Scherrer analysis is presented in Table 3.1. The Scherrer equation is generally considered reliable only for crystallite sizes below approximately 200 nm. Accordingly, the calculated mean crystallite size of 251 nm for the Ce_2S_3 phase should be regarded as an

approximation, and it is more accurate to state that the mean crystallite size is >200 nm. In contrast, the mean crystallite size for the CeO_2 phase was determined to be approximately 7 nm, which falls well within the valid range of the Scherrer model.

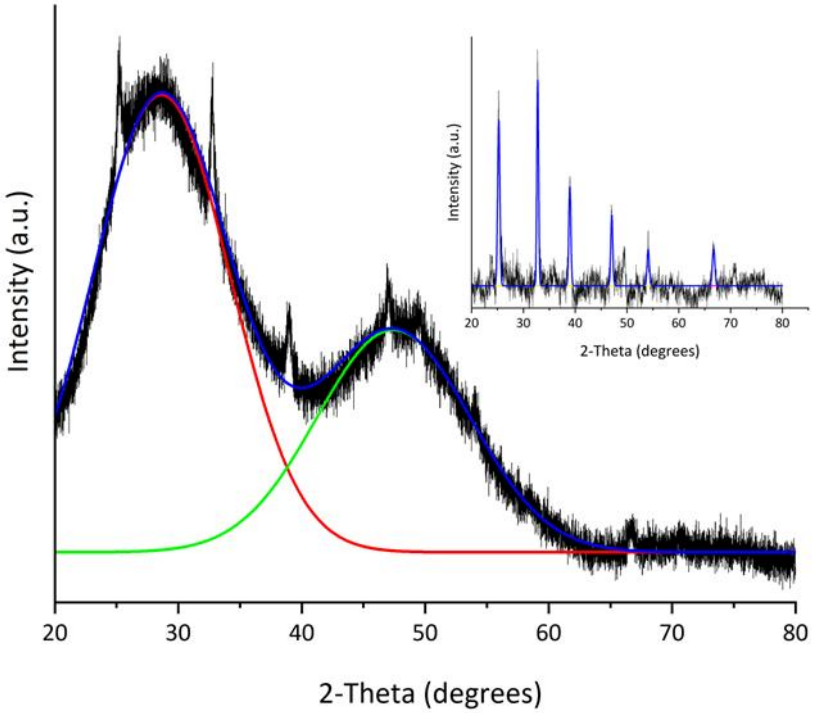

*Figure 3.3: Peak fitting of **Ce-TTT@800** PXRD pattern to a Gaussian model.*

*Table 3.1: Scherrer analysis data for **Ce-TTT@800** PXRD pattern.*

Cerium oxide					
K	**λ**	**2θ**	**FWHM**	***T* (nm)**	**Mean *T* (nm)**
0.89	1.54	28.6	13.06	6.853	
		47.4	14.63	7.938	7.4
Cerium Sulfide					
K	**λ**	**2θ**	**FWHM**	***T* (nm)**	**Mean *T* (nm)**
0.89	1.54	25.3	0.50	173.939	
		32.8	0.39	237.601	
		39.0	0.47	215.709	
		47.1	0.46	249.085	
		54.1	0.49	274.558	
		66.8	0.56	357.480	251.4

The findings of the PXRD analysis suggest that the pyrolytic decomposition of **Ce-TTT** results in the formation of both CeO_2 and Ce_2S_3 phases. The formation of CeO_2 under an inert (oxygen-free) atmosphere can be attributed to the MOF itself acting as an internal

oxygen source, as each Ce(III) centre in **Ce-TTT** is coordinated to nine carboxylate oxygen atoms. It is proposed that, upon thermal decomposition of the inorganic SBU, the Ce(III) centres are oxidised to Ce(IV), leading to the formation of CeO_2 nano-crystallites.

The formation of Ce_2S_3 is similarly attributed to the presence of sulfur within **Ce-TTT**, originating from its thiophene moieties. Under pyrolytic conditions, a sulfurisation reaction appears to occur, in which the decomposed thiophene units of the organic linker act as the sulfur source. To the author's knowledge, this represents the first report of a MOF being used as a precursor for the synthesis of a lanthanide(III) sulfide phase. Hirai et al. previously reported the synthesis of Ce_2S_3 via sulfurisation of CeO_2 powder using carbon disulfide (CS_2) as the sulfur source and argon as the carrier gas at temperatures between 700 and 750 °C.[9] Since CS_2 is a known pyrolysis product of thiophene,[10] it is therefore proposed that **Ce-TTT** undergoes a similar sulfurisation pathway upon thermal decomposition of the thiophene moieties, generating CS_2 *in-situ*.

Furthermore, Hirai et al. found that the addition of carbon black to the sulfurisation reaction accelerated the formation of Ce_2S_3 *via* carbothermic reduction of CeO_2. Given that the pyrolytic decomposition of **Ce-TTT** also yields carbon (see Raman analysis in Section 3.1.3), a similar carbothermic reduction mechanism may also contribute to the formation of Ce_2S_3 in this case.

3.3.1.2 Ce-BTB@800

The PXRD pattern of **Ce-BTB@800**, presented in Figure 3.4, features reflections centred at 28.6°, 33.2°, 47.6°, 56.4°, 59.2°, 69.5°, 76.8°, and 79.2°, which are characteristic of CeO_2 and match the ICDD reference standard PDF 03-65-5923. The observed diffraction peaks were indexed to the (111), (200), (220), (311), (222), (400), (331), and (420) planes. The Scherrer equation (Eq. 3.1) was employed to estimate the average CeO_2 crystallite size in **Ce-BTB@800**. After fitting the PXRD peaks to a Voigt model, the average CeO_2 crystallite size was calculated to be 86.9 nm (see Table 3.5 and Figure 3.2).

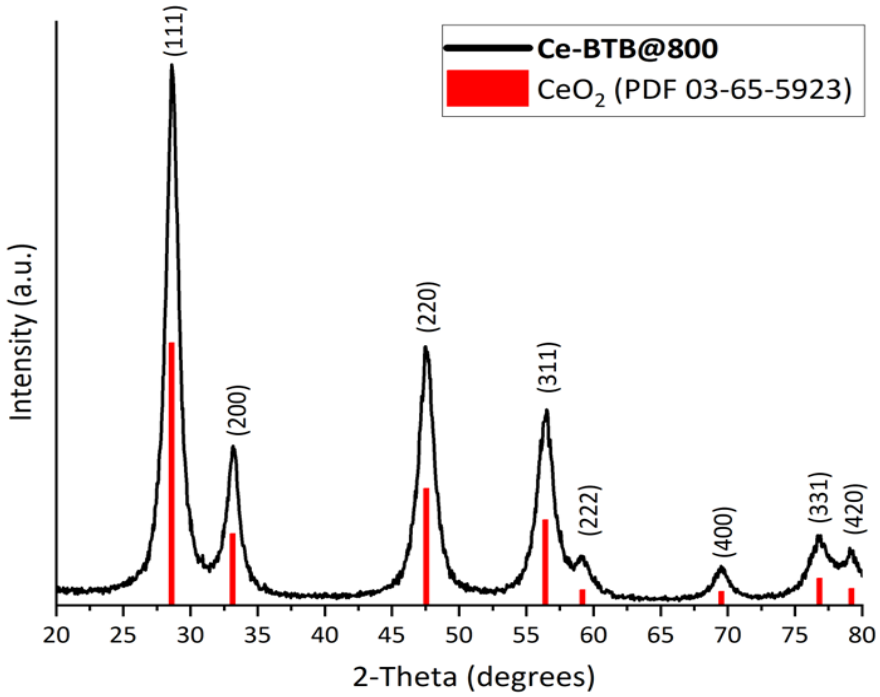

*Figure 3.4: PXRD pattern of **Ce-BTB@800** (black) overlayed with the ICDD reference standard for CeO_2 (PDF 03-65-5923) in red.*

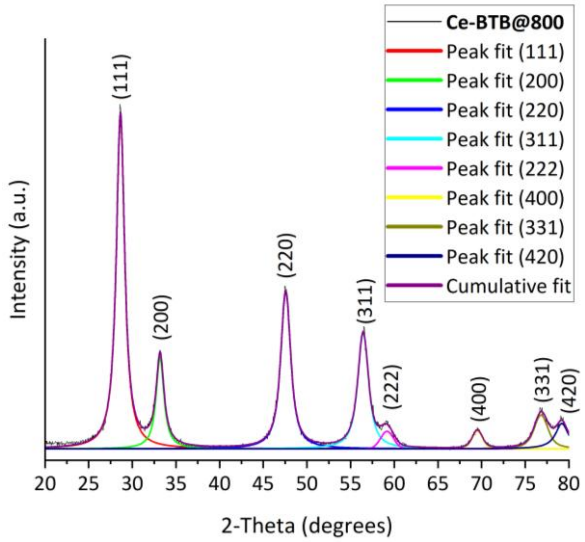

*Figure 3.5: Peak fitting of **Ce-BTB@800** PXRD pattern to a Voigt model.*

*Table 3.2: Scherrer analysis data for **Ce-BTB@800** PXRD pattern*

k	λ	2θ	FWHM	*T* (nm)	Average Crystallite Size (nm)
0.94	1.54	28.640	1.143	78.290	86.89
		33.171	1.071	87.566	
		47.568	1.378	84.491	
		56.437	1.484	95.699	
		59.170	1.734	88.388	

3.3.1.3 Ce-TTB@800

The PXRD pattern of **Ce-TTB@800**, presented in Figure 3.6, is very similar to that of **Ce-BTB@800**, featuring reflections centred at 28.5°, 33.9°, 47.4°, 56.3°, 59.1°, 69.4°, 76.7°, and 79.1°, which are characteristic of CeO_2 and match the ICDD reference standard PDF 03-65-5923. The observed diffraction peaks were indexed to the (111), (200), (220), (311), (222), (400), (331), and (420) planes. The Scherrer equation (Eq. 3.1) was employed to estimate the average CeO_2 crystallite size in **Ce-TTB@800**. After fitting the PXRD peaks to a Voigt model, the average CeO_2 crystallite size was calculated to be 61.8 nm (see Table 3.3 and Figure 3.7).

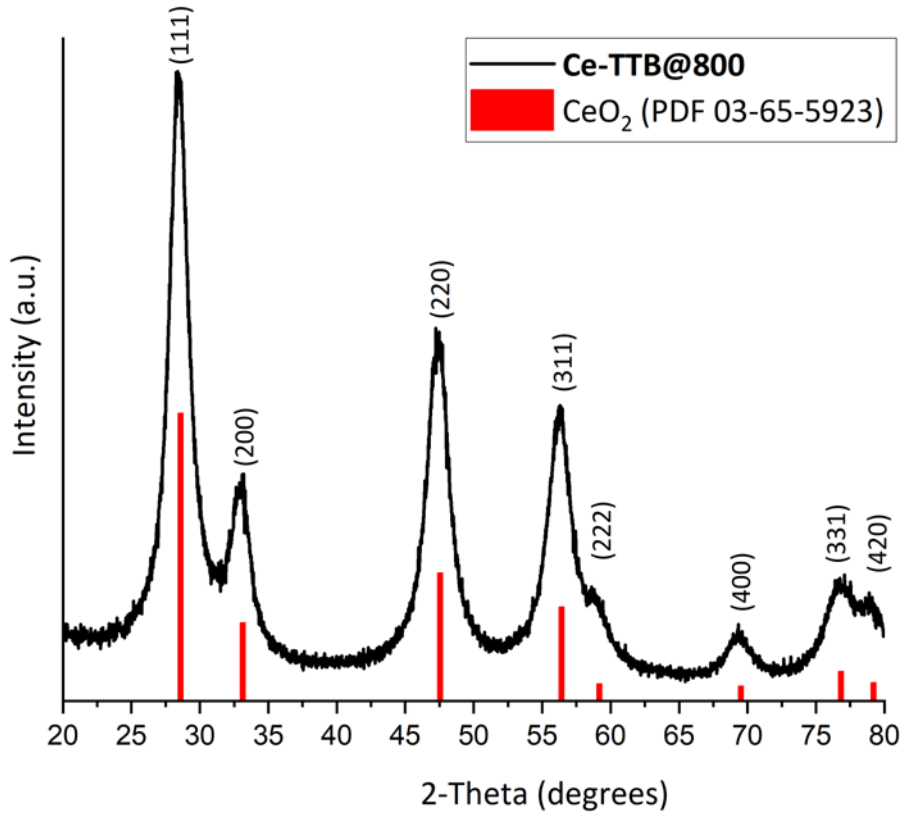

*Figure 3.6: PXRD pattern of **Ce-TTB@800** (black) overlayed with the ICDD reference standard for CeO_2 (PDF 03-65-5923) in red.*

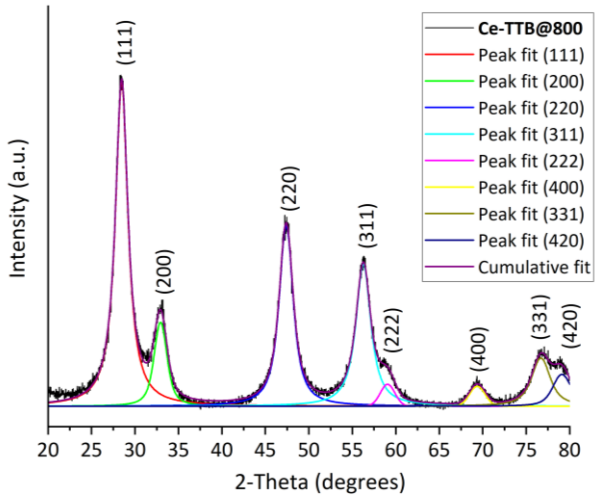

*Figure 3.7: Peak fitting of **Ce-TTB@800** PXRD pattern to a Voigt model.*

*Table 3.3: Scherrer analysis data for **Ce-TTB@800** PXRD pattern.*

k	λ	2θ	FWHM	*T (nm)*	Average Crystalliate Size (nm)
0.94	1.54	28.465	1.750	51.033	61.77
		32.933	1.782	52.518	
		47.391	1.947	59.572	
		56.268	2.079	68.014	
		59.055	1.965	77.703	

3.3.2 Raman Spectroscopy

Raman spectra of the pyrolysed Ce-MOFs were recorded using a Renishaw 1000 micro-Raman spectrometer equipped with a 785 nm excitation laser, a 50× objective lens, and a cooled CCD detector, providing a spectral resolution of 1 cm^{-1}. Each spectrum was acquired with an integration time of 10 s and averaged over 10 accumulations. The instrument was calibrated against the characteristic Si reference band at 520 cm^{-1}.

3.3.2.1 Ce-TTT@800

The Raman spectrum of **Ce-TTT@800**, presented in Figure 3.8, displays two broad peaks at 1312 cm^{-1} and 1570 cm^{-1}, corresponding to the D and G bands of carbon, respectively.[11] The D band arises from the breathing modes of sp^2-hybridised carbon atoms in six-membered aromatic rings and appears in Raman spectra due to a defect-activated double-resonance process; hence, it is absent in defect-free graphite.[11] The G band originates from the stretching modes of sp^2 carbon pairs and is always Raman active.

The intensity ratio of the D and G bands, *I*(D)/ *I*(G), can be used to estimate the relative

proportion of sp^2 to sp^3 hybridised carbon.[12] Deconvolution of the overlapping D and G bands was achieved using Gaussian peak fitting in *OriginPro* (Figure 3.9), yielding an *I*(D)/ *I*(G) ratio of 1.89. Based on the empirical relationship established by Ferrari and Robertson,[12] this ratio corresponds to an estimated composition of 94% sp^2- and 6% sp^3-hybridised carbon in **Ce-TTT@800**.

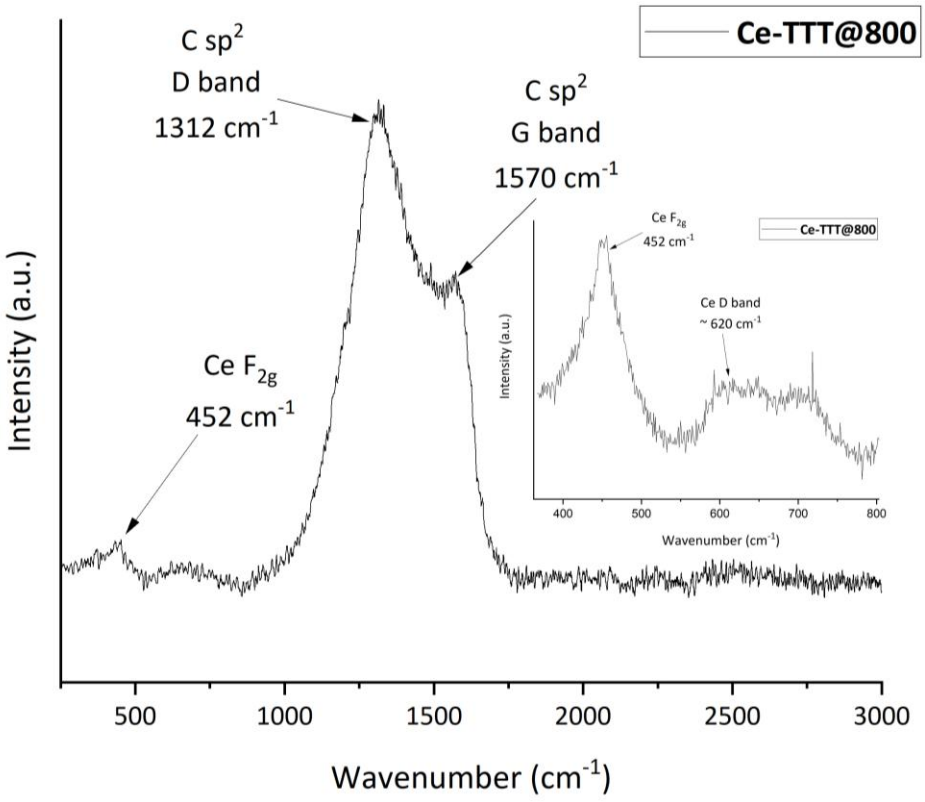

*Figure 3.8: Raman spectrum of **Ce-TTT@800**.*

A peak at 452 cm^{-1}, corresponding to the cerium F_{2g} mode, is observed in Figure 3.8 (magnified in the inset). This vibrational mode arises from the symmetric stretching of Ce–S or Ce-O bonds and is typically reported at ~460 cm^{-1}. The observed red shift to 452 cm^{-1} suggests charge transfer between cerium phases and the pyrolytic carbon substrate, indicating anchoring of the cerium phases to the carbon matrix.[13-16] The predominance of sp^2 hybridisation in the carbon substrate likely facilitates this charge transfer process.

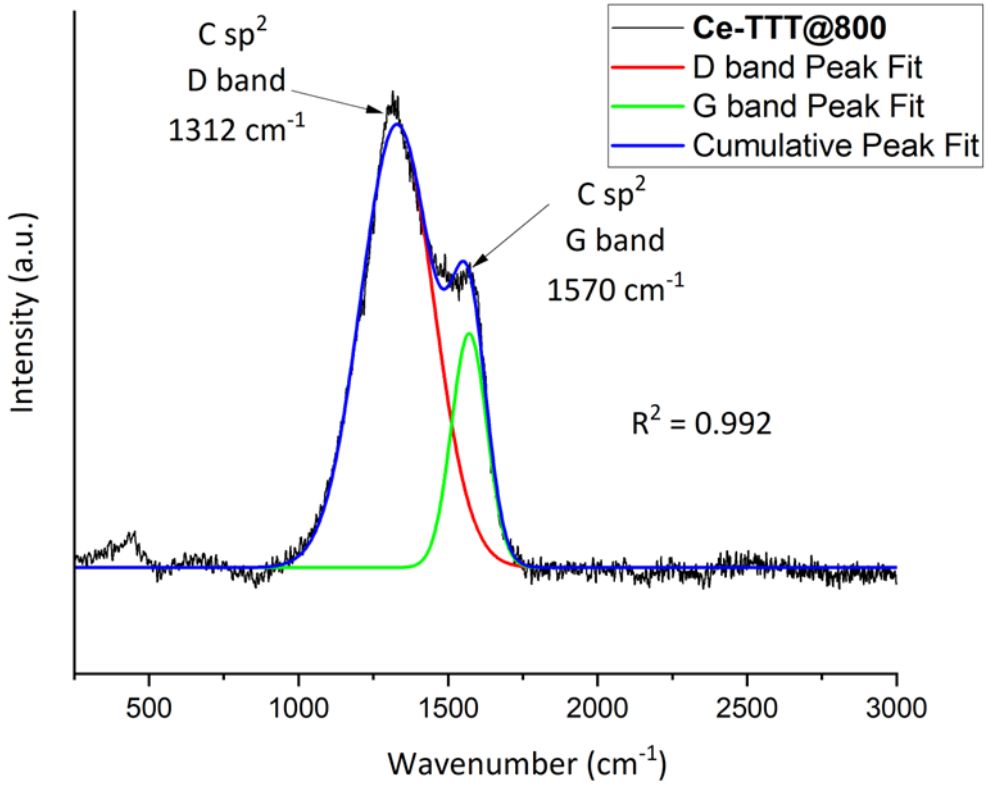

*Figure 3.9: Deconvolution of the overlapping carbon D and G bands in Raman spectrum of **Ce-TTT@800** using a Gaussian peak fitting model.*

3.3.2.2 Ce-BTB@800

The Raman spectrum of **Ce-BTB@800**, presented in Figure 3.10, displays two broad peaks at 1317 cm^{-1} and 1592 cm^{-1}, corresponding to the D and G bands of carbon, respectively. Deconvolution of the overlapping D and G bands using a pseudo-Voigt peak fitting model in OriginPro (Figure 3.10), yielded an *I*(D)/ *I*(G) ratio of 1.35. Utilising the empirical relationship established by Ferrari and Robertson,[12] the carbon composition in **Ce-BTB@800** was estimated to be 68% sp^2- and 32% sp^3-hybridised carbon.

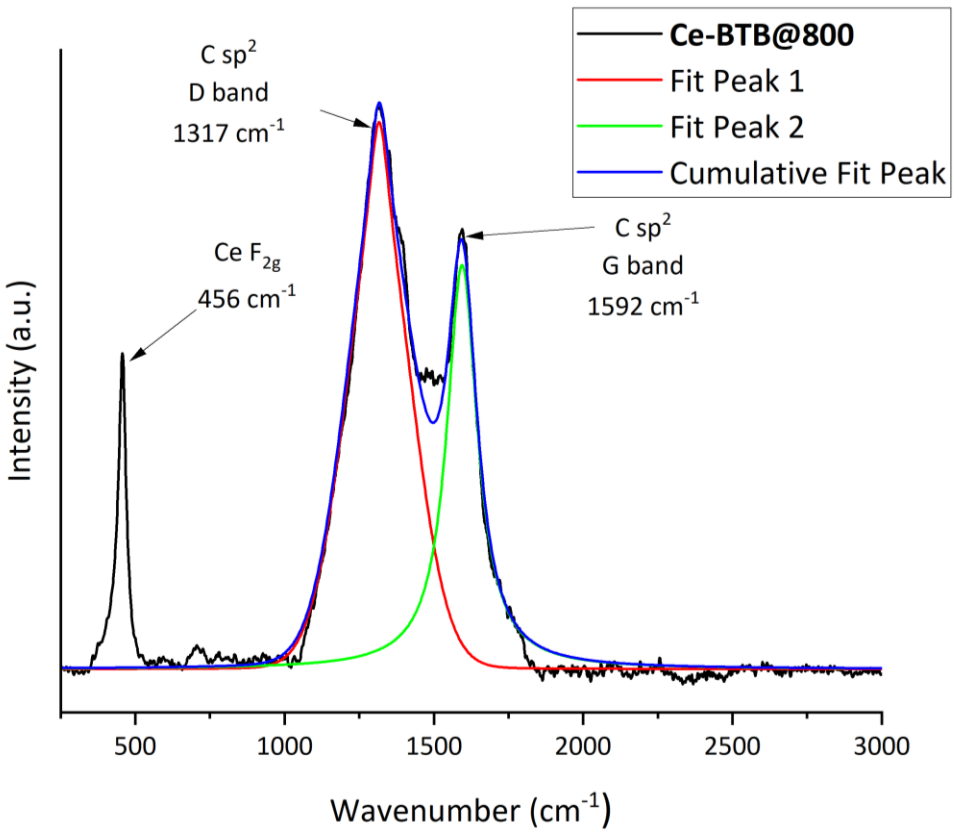

*Figure 3.10: Raman spectrum of **Ce-BTB@800**. Deconvolution of the overlapping carbon D and G bands using pseudo-Voigt peak fitting model (best fit, R^2 = 0.96).*

A peak at 456 cm^{-1}, corresponding to the cerium F_{2g} mode, is observed in Figure 3.10. This vibrational mode arises from the symmetric stretching of Ce-O bonds and is typically reported at 460 cm^{-1}. This is less of an observed red shift than that found for **Ce-TTT@800** (452 cm^{-1}) suggesting less charge transfer between cerium phases and the pyrolytic carbon substrate, indicating weaker anchoring of the cerium phases to the carbon matrix than that exhibited by **Ce-TTT@800**.[13-16]

3.3.2.3 Ce-TTB@800

The Raman spectrum of **Ce-TTB@800**, presented in Figure 3.11, is very similar to that **Ce-BTB@800,** displaying two broad peaks at 1330 cm^{-1} and 1587 cm^{-1}, corresponding to the D and G bands of carbon, respectively. The intensity ratio of the D and G bands, *I*(D)/ *I*(G), were again be used to estimate the relative proportion of sp^2 to sp^3 hybridised carbon.[12] Deconvolution of the overlapping D and G bands was achieved using Gaussian peak fitting in OriginPro (Figure 3.11), yielded an *I*(D)/ *I*(G) ratio of 1.35. This corresponds to 84% sp^2-

and 16% sp^3-hybridised carbon, based on the empirical relationship established by Ferrari and Robertson.[12]

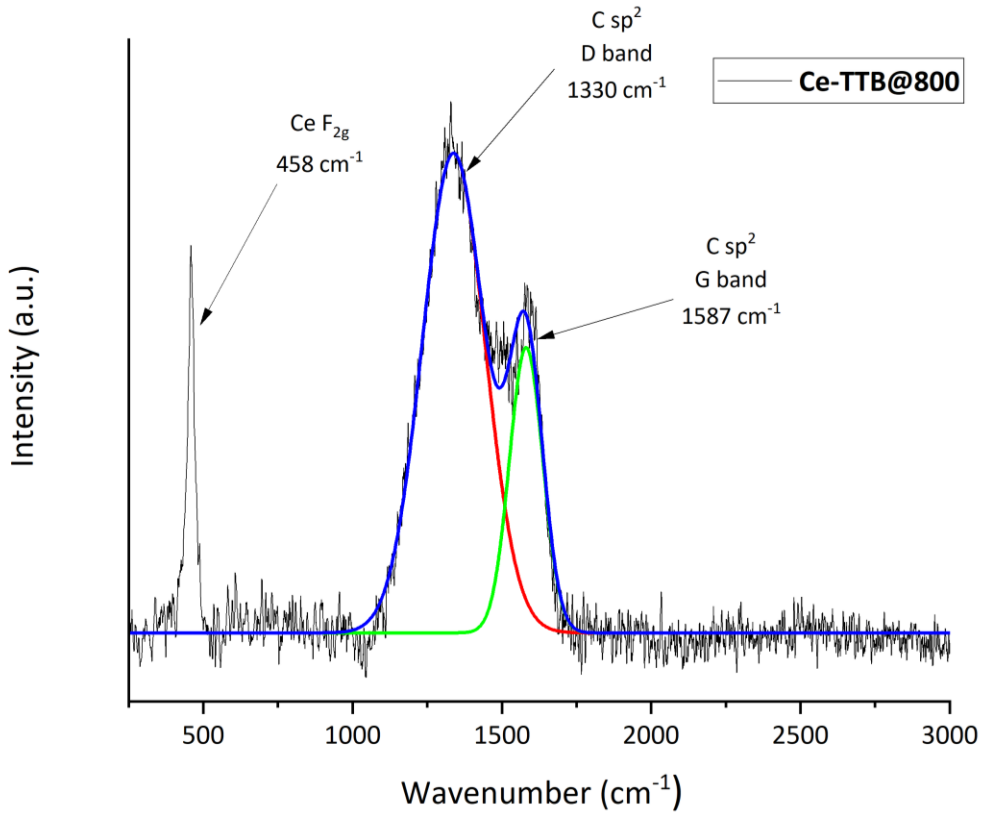

*Figure 3.11:Raman spectrum of **Ce-TTB@800**. Deconvolution of the overlapping carbon D and G bands using Gaussian peak fitting model (best fit, R^2 = 0.93).*

A peak arising from the cerium F_{2g} mode is observed at 458 cm^{-1}, close to the typically reported value of 460 cm^{-1}. As with **Ce-BTB@800**, the lack of red shifting compared to that found for **Ce-TTT@800** (452 cm^{-1}) suggests less charge transfer between cerium phases and the pyrolytic carbon substrate, indicating weaker anchoring of the cerium phases to the carbon matrix than that exhibited by **Ce-TTT@800**.

3.3.3 Scanning Electron Microscopy

Scanning electron microscopy (SEM) was used to study the morphology of the pyrolysed Ce-MOFs. The pyrolysed Ce-MOF powders were dispersed in isopropanol (IPA) and drop-cast onto silicon substrates, followed by sputter-coating with a Au–Pd alloy. Imaging was performed using a Zeiss ULTRA Plus SEM operated at an accelerating voltage of 10–20 kV, under a vacuum of 1×10^{-5} mbar, using a secondary electron detector.

SEM images of **Ce-TTT@800** (Figure 3.12a,b) show that it appears to retain some morphological features of the MOF precursor, **Ce-TTT**, with the high aspect-ratio MOF crystals appearing to be transformed into very fine fibres (100-200 nm diameter) aggregating into larger agglomerates of materials (1–40 µm in length). Similarly, **Ce-BTB@800** (Figure 3.12c) preserves some features of its precursor, with most particles retaining a rod-like morphology of comparable dimensions (1–60 µm in length). **Ce-TTB@800** (Figure 3.12d) also follows this trend, retaining its mixture globular and rod-like morphology of **Ce-TTB**, with agglomerated particles ranging from 10–60 µm in size.

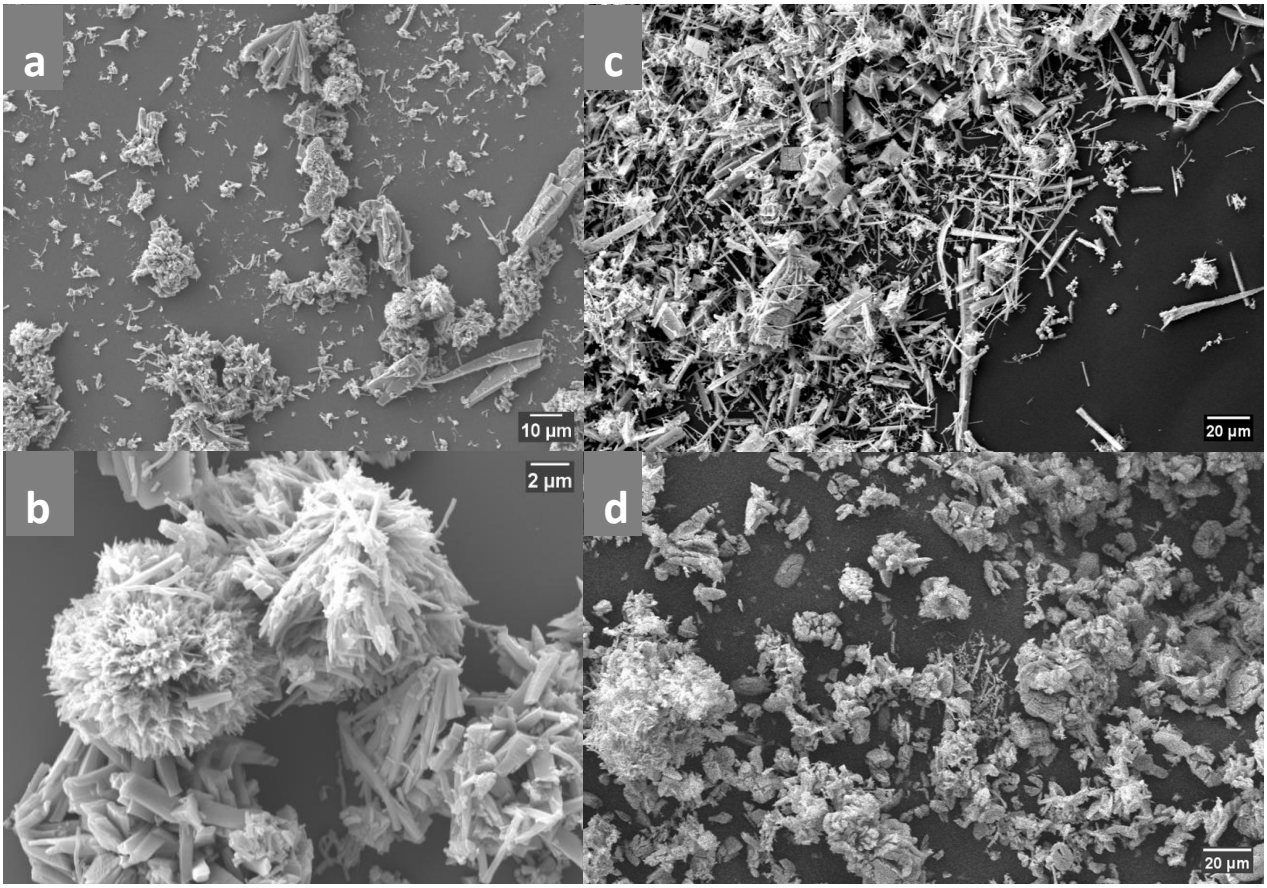

*Figure 3.12: SEM images of pyrolysed Ce-MOFs. a) & b) **Ce-TTT@800**, c) **Ce-BTB@800**, d) **Ce-TTB@800**.*

3.3.4 Transmission Electron Microscopy

High-resolution transmission electron microscopy (HR-TEM) was employed to investigate the local structure of pyrolysed Ce-MOFs. HR-TEM images were acquired using an FEI Titan 80 transmission electron microscope operating at an accelerating voltage of 300 kV, with an informational resolution of 1 Å. The pyrolysed Ce-MOFs powder was sonicated in isopropanol (IPA) and drop-cast onto a lacey carbon-coated copper TEM grid. Image

processing and analysis were carried out using the *DigitalMicrograph-3* software package.

3.3.3.1 Ce-TTT@800

The **Ce-TTT@800** particles were found to be robust under sonication and did not fragment into smaller entities, instead retaining their high aspect-ratio morphology. Representative TEM image of such particles are shown in Figure 3.13. Due to the substantial thickness of the particles, high-resolution imaging of the local structure was restricted to particle edges. However, this limitation is not entirely disadvantageous, as any electrocatalytic reaction will occur at or near the surface of these particles. Therefore, imaging the local structure at the periphery yields the most relevant information for electrocatalytic studies.

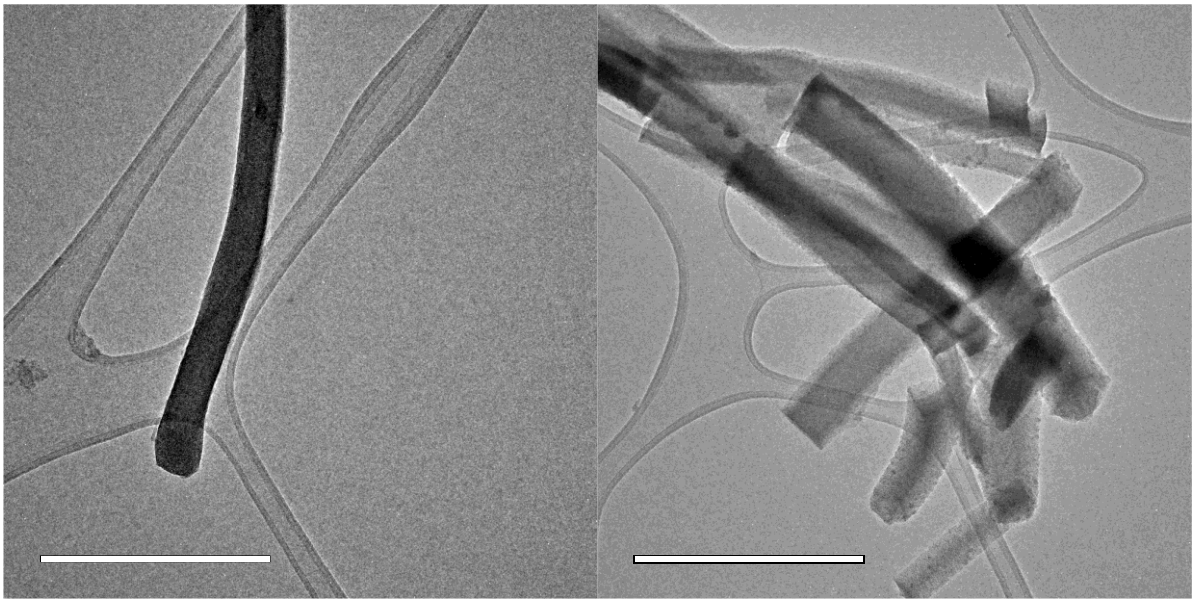

*Figure 3.13: TEM images of **Ce-TTT@800** particles.*

HR-TEM images acquired at the edges of **Ce-TTT@800** particles (Figures 3.14 and 3.15) reveal crystallites measuring 2–3 nm in diameter. Lattice spacings of individual crystallites were determined using the Fast Fourier Transformation (FFT) method (Experimental Section 6.1.10). This analysis revealed the presence of serval phases at or near the particle surfaces.

Figure 3.8 shows a region predominantly composed of CeO_2 crystallites interspersed with amorphous domains. The CeO_2 phase is identified by lattice spacings of 0.31 nm and 0.38 nm, corresponding to the (111) and (110) planes, respectively. In contrast, a separate area on the same particle (Figure 3.9) contains Ce_2S_3 along with either CeO_2 or graphitic carbon crystallites, in addition to amorphous domains. Ce_2S_3 crystallites are identified by a lattice spacing of 0.35 nm, characteristic of the (211) plane. Crystallites with a lattice spacing of 0.33 nm may correspond to the (311) plane of CeO_2. However, since graphitic carbon also exhibits a characteristic lattice spacing of 0.33 nm, arising from the (002) diffraction plane (JCPDS 26–1076),[17-18] this alternative assignment cannot be excluded. Given the peak broadening in the XRD pattern of **Ce-TTT@800** and the presence of sp^2 carbon in the material (as evidenced by Raman spectroscopy in section 3.2.2), the latter interpretation remains plausible.

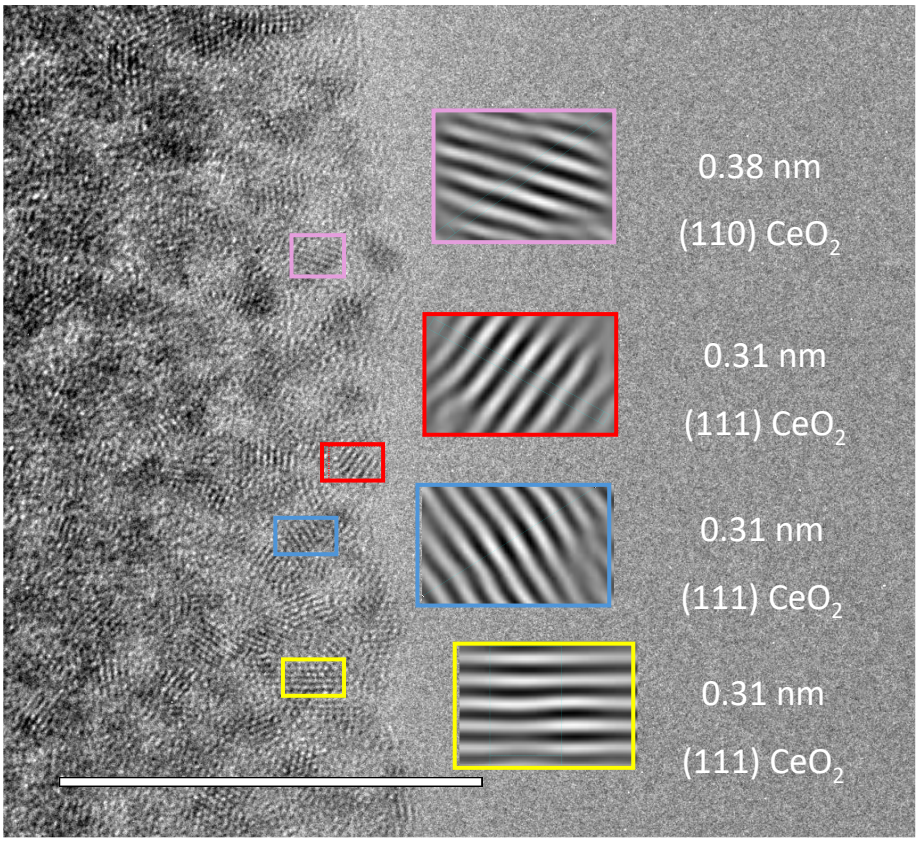

*Figure 3.14: HR-TEM images acquired at the edge of a **Ce-TTT@800** particle dominated by CeO_2 crystallites.*

The HR-TEM findings provide important additional information on the local structural not available from PXRD analysis of the bulk powder and should not be considered contradictory. While PXRD analysis while indicates mean crystallite sizes of 7 nm and >

200 nm for CeO_2 and Ce_2S_3, respectively, HR-TEM shows crystallites of both phases ranging 2-3 nm that the surface of the **Ce-TTT@800** particles. This suggests the interior of these particles contains significantly larger crystallites than those present at that the surface.

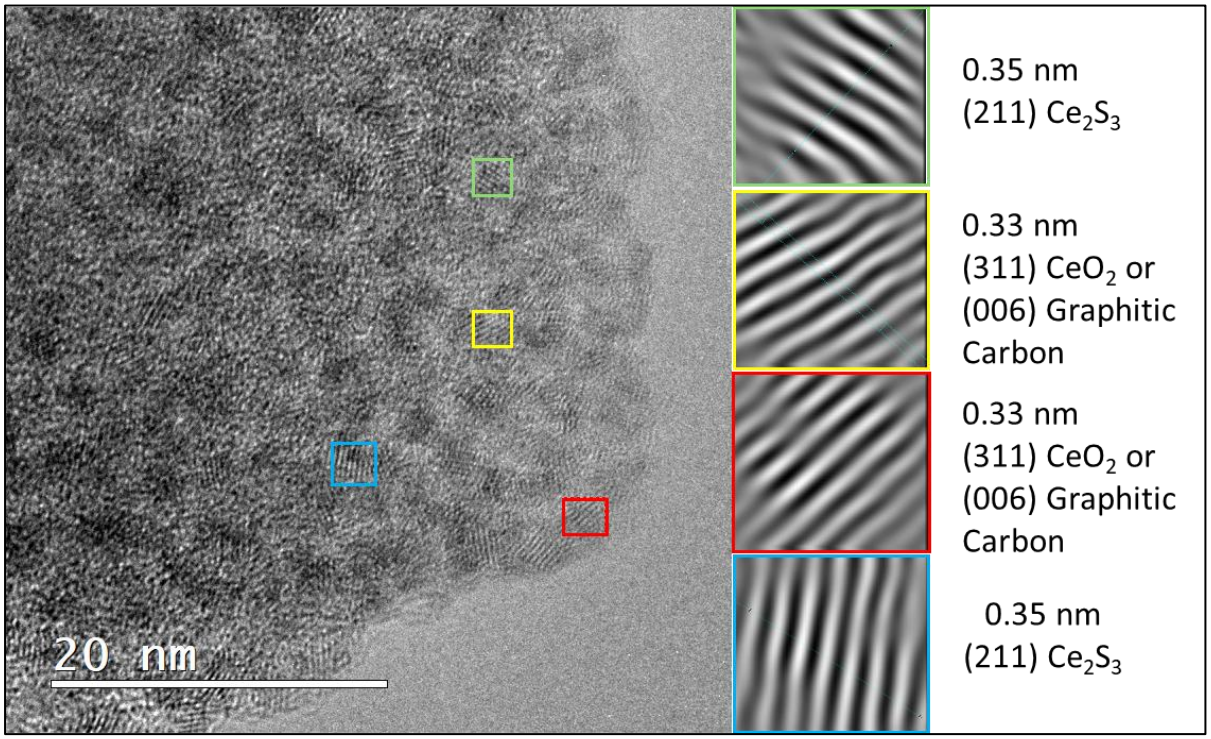

*Figure 3.15: HR-TEM images acquired at the edge of a **Ce-TTT@800** particle dominated by Ce_2S_3 and CeO_2 or graphitic crystallites.*

3.3.3.2 Ce-BTB@800

Representative TEM images of **Ce-BTB@800** particles are shown in Figure 3.16. Unlike the **Ce-TTT@800** particles, the **Ce-BTB@800** particles appear fragmented after sonication. HR-TEM imaging (Figures 3.17 and 3.18) reveals the presence of CeO_2 crystallites at the surface of these particles, typically 2 nm to 6 nm in size. These crystallites appear to be randomly oriented with several CeO_2 lattice planes exposed to the surface, namely the (111), (100) and (222) planes, identified by the lattice spacings of 0.31 nm, 0.28 nm and 0.32 nm respectively.

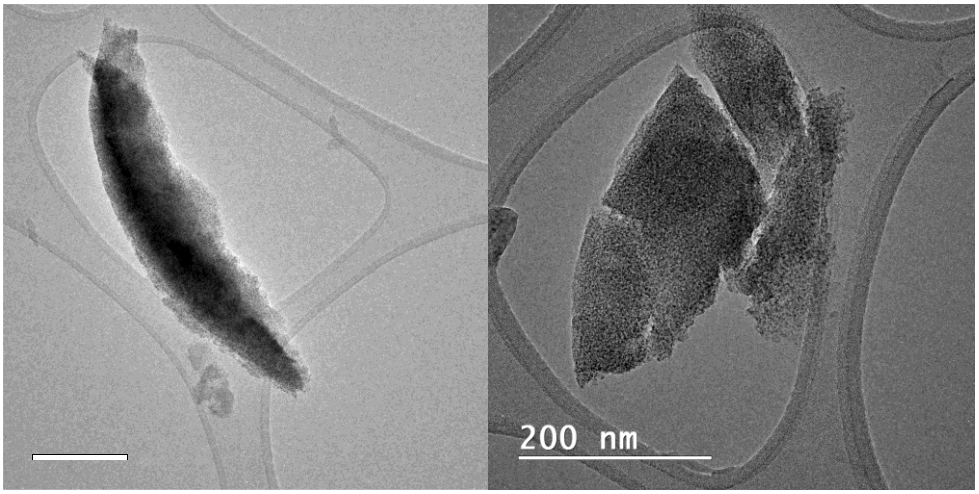

*Figure 3.16: TEM images of **Ce-BTB@800** particles.*

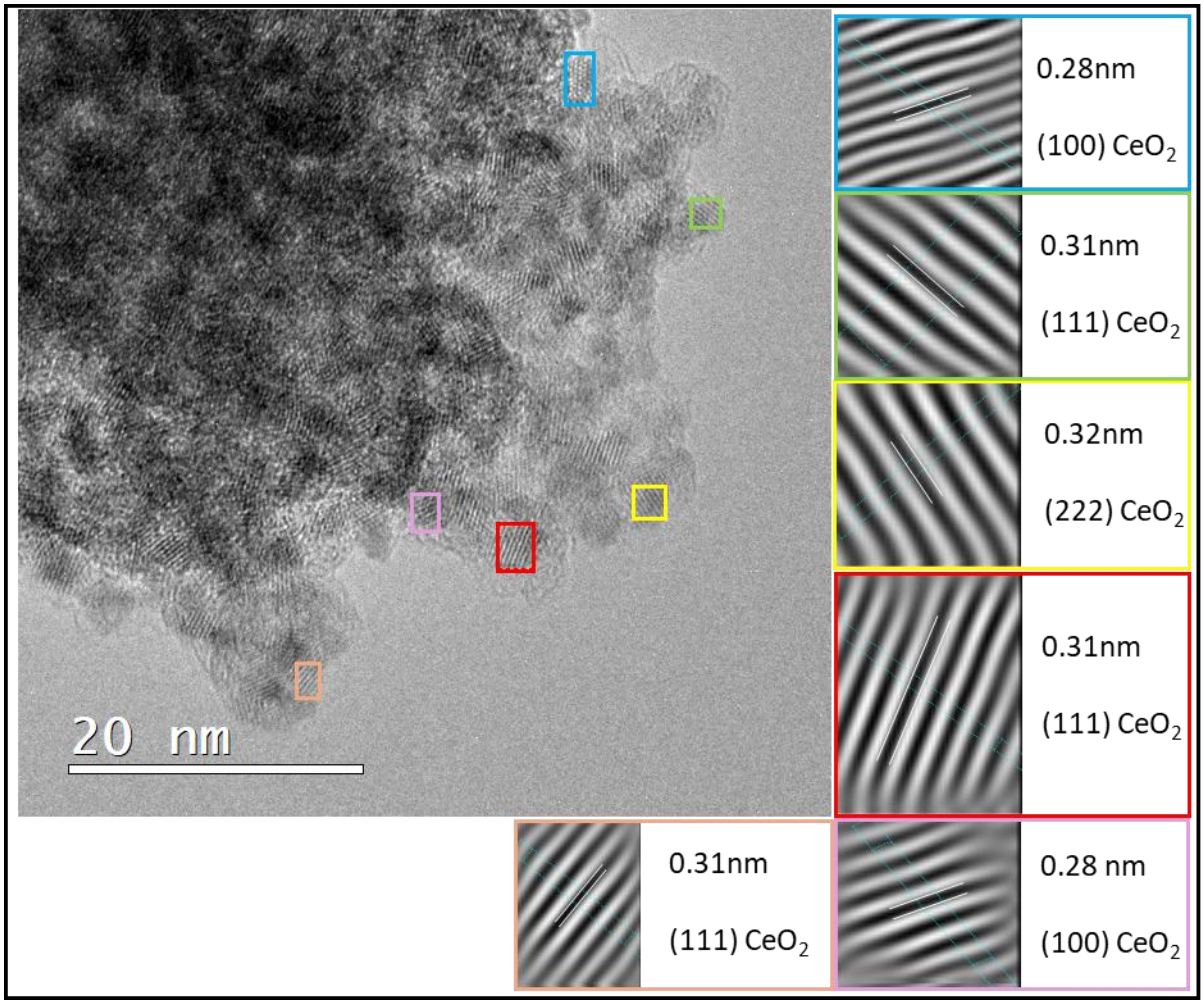

*Figure 3.17: HR-TEM images acquired at the edge of a **Ce-BTB@800** particle.*

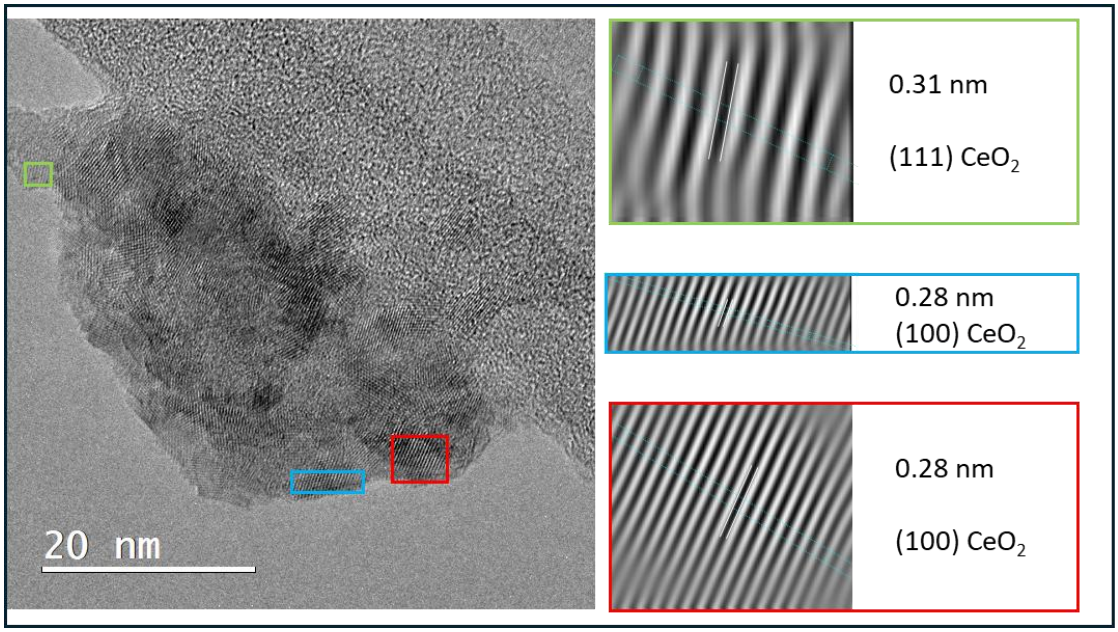

*Figure 3.18: HR-TEM images acquired at the edge of a **Ce-BTB@800** particle.*

3.3.3.3 Ce-TTB@800

Representative TEM images of **Ce-TTB@800** particles are presented in Figure 3.19. HR-TEM imaging (Figures 3.20 and 3.21) reveals the presence of CeO_2 crystallites at the particle surfaces, typically ranging from 4 to 12 nm in size. The exposed lattice planes are predominantly indexed to the (222) and (311) reflections of CeO_2, identified by lattice spacings of 0.32 nm and 0.33 nm, respectively. In this case, it is more reliable to assign the 0.33 nm lattice spacing to the second-order reflection of the CeO_2 (311) plane rather than to the first-order reflection of the (002) plane of graphitic carbon. This interpretation is supported by the PXRD pattern of **Ce-TTB@800** (Figure 3.6), which displays narrower peaks (compared to **Ce-TTT@800**) without a discernible shoulder at 27°, which would be characteristic of graphitic carbon (006) plane.

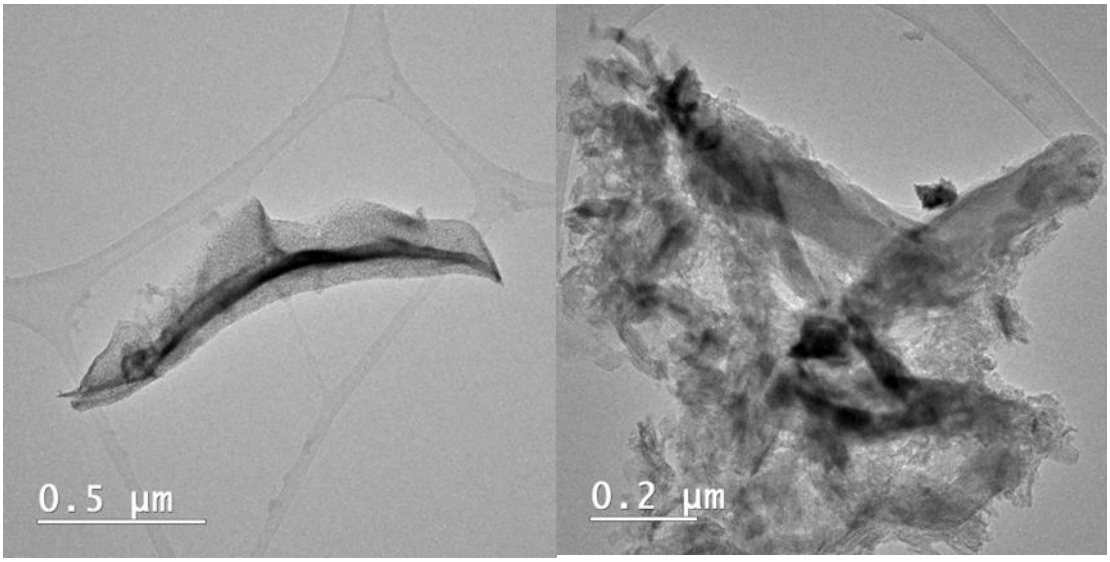

*Figure 3.19:TEM images of **Ce-TTB@800** particles.*

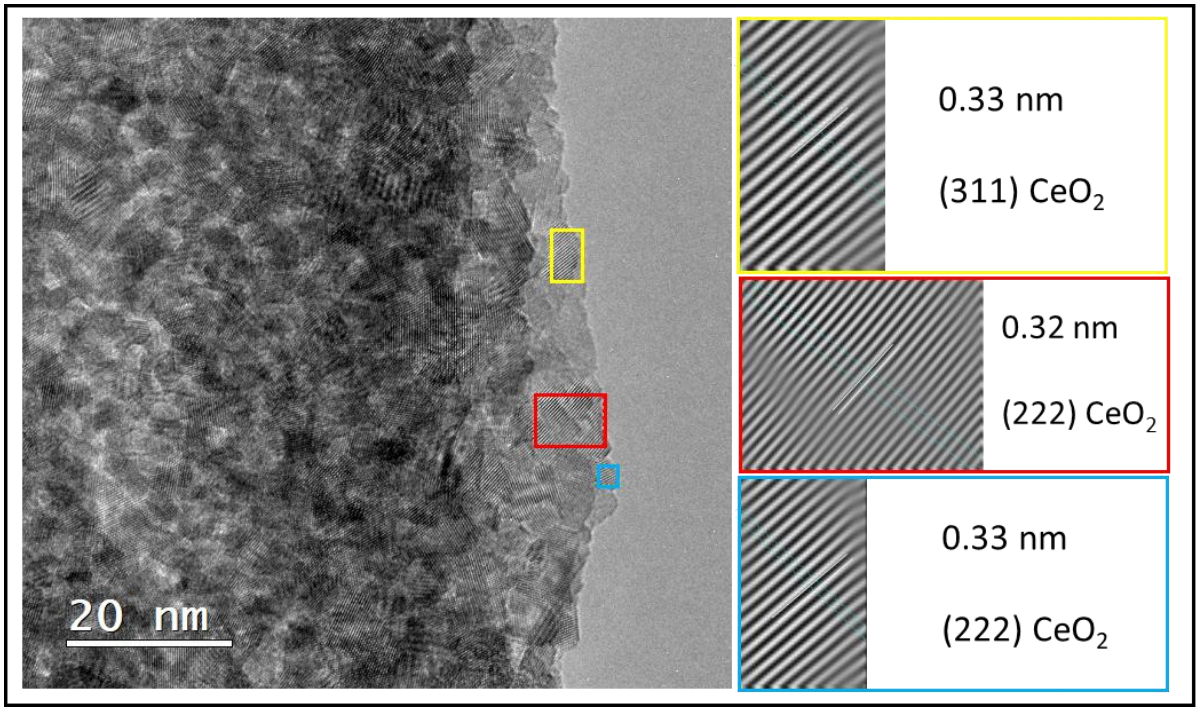

*Figure 3.20:HR-TEM images acquired at the edge of a **Ce-TTB@800** particle.*

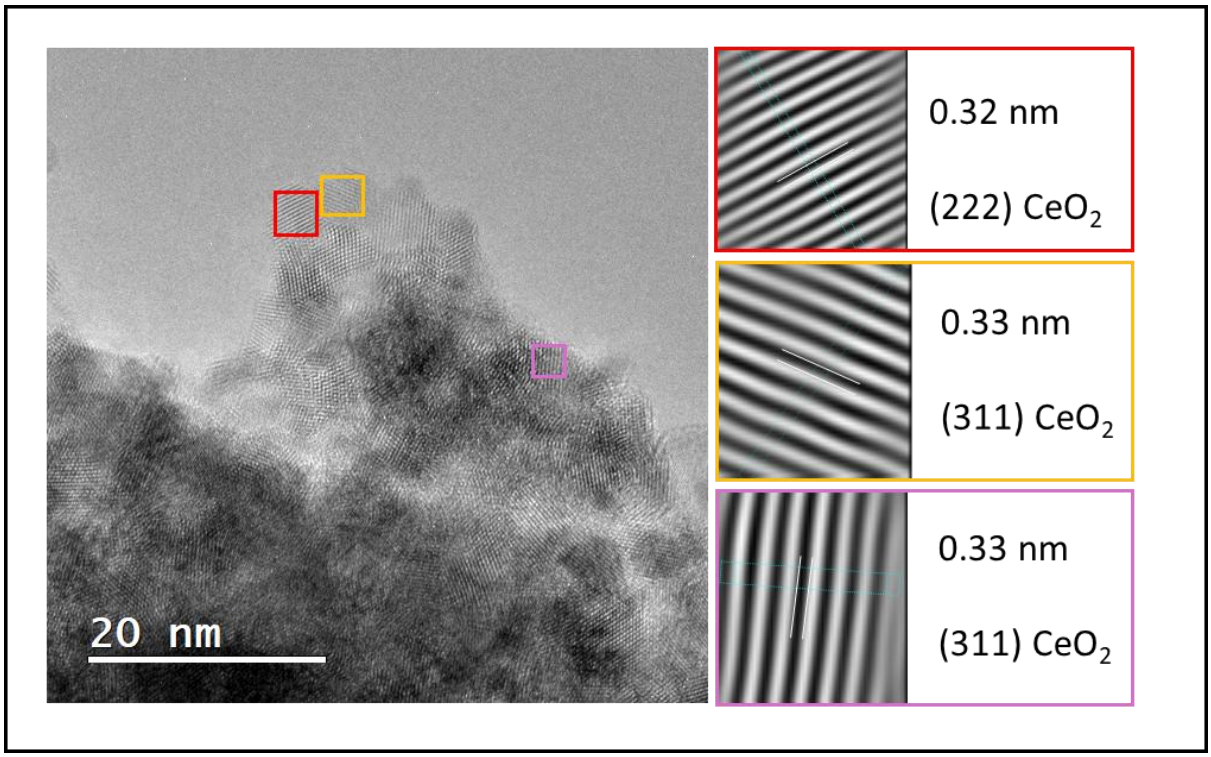

*Figure 3.21: HR-TEM images acquired at the edge of a **Ce-TTB@800** particle.*

3.4 Electrocatalytic Water Oxidation Studies

3.4.1 Activity of Ce-based MOF derivatives for OER

As with the pristine Ce(III)-based MOFs discussed in Chapter 2, the electrocatalytic OER activity of the pyrolysed Ce-MOF derivatives was investigated in 0.5 M aqueous H_2SO_4. The reaction kinetics and electrochemical stability of the cerium-based electrocatalysts under turnover conditions were evaluated using modified carbon paste (CP) electrodes in rotating disk electrode linear sweep voltammetry (RDE-LSV) experiments.

Figure 3.22 presents the RDE-LSV curves for each pyrolysed Ce-based catalyst, along with benchmark commercial CeO_2 and IrO_2. A comparison of the applied overpotentials (η) at various current densities is provided in Table 3.4. The onset overpotential, defined as the potential at which OER initiates, was estimated using the Tangent Method (Appendix B). Among the pyrolysed Ce-based catalysts, **Ce-TTB@800/CP** exhibited the lowest onset overpotential (338 mV), followed by **Ce-TTT@800/CP** (426 mV) and **Ce-BTB@800/CP** (450 mV). In comparison, the benchmark electrocatalyst **CeO_2/CP** displayed an onset overpotential of 472 mV, while **IrO_2/CP**, as expected, demonstrated a significantly lower onset overpotential of 290 mV.

A similar trend is observed at a current density of 1 mA cm^{-2}. Notably, at 5 mA cm^{-2}, **Ce-TTB@800/CP** exhibits slightly better performance than **IrO_2/CP**, with overpotentials of 511 mV and 520 mV, respectively. **Ce-TTT@800/CP** closely follows at 527 mV. At a current density of 10 mA cm^{-2}, all three pyrolysed Ce-MOF catalysts outperform **IrO_2/CP** (648 mV). Specifically, **Ce-TTB@800/CP** and **Ce-TTT@800/CP** display nearly identical overpotentials of 559 mV and 561 mV, respectively, while **Ce-BTB@800/CP** lags slightly behind at 629 mV. This activity trend persists throughout the remainder of the potential sweep.

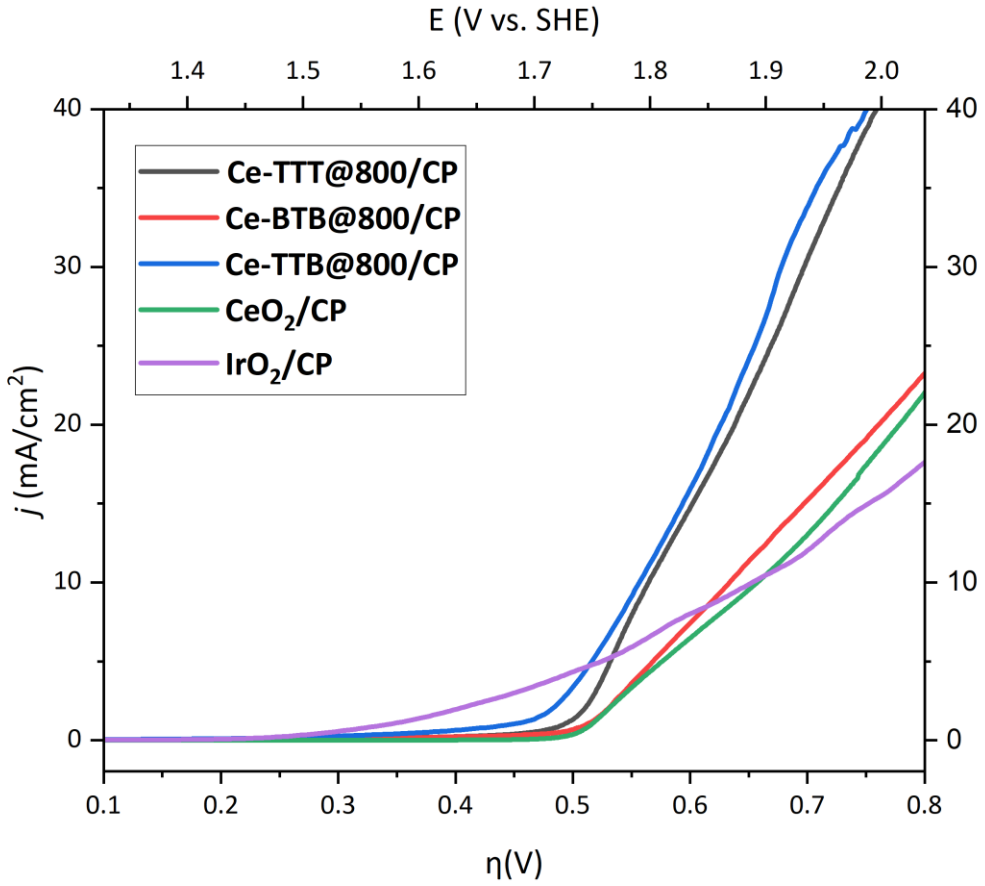

Figure 3.22: RDE-LSV plot of pyrolysed Ce-MOFs, as well as CeO_2 and IrO_2 benchmark electrocatalysts, embedded in carbon paste (CP) electrodes. Measurements were performed in 0.5 M H_2SO_4 at a sweep rate of 1 mV s^{-1} with an electrode rotation speed of 1600 rpm.

Table 3.4 Comparison of applied overpotentials (η) at various current densities for pyrolysed Ce-MOFs, as well as CeO_2 and IrO_2 benchmark electrocatalysts, embedded in carbon paste electrodes.

Electrode	Onset η (V vs. SHE)	η @ 1 mA cm^{-2}	η @ 5 mA cm^{-2}	η @ 10 mA cm^{-2}	η @ 15 mA cm^{-2}	η @ 20 mA cm^{-2}	η @ 30 mA cm^{-2}	η @ 40 mA cm^{-2}
Ce-TTT@800/CP	426 mV (1.655 V)	487 mV	527 mV	560 mV	597 mV	633 mV	692 mV	754 mV
Ce-TTB@800/CP	338 mV (1.567 V)	442 mV	511 mV	552 mV	588 mV	621 mV	673 mV	746 mV
Ce-BTB@800/CP	450 mV (1.679 V)	506 mV	563 mV	629 mV	692 mV	756 mV	—	—
CeO_2/CP	472 mV (1.701 V)	510 mV	538 mV	653 mV	719 mV	774 mV	—	—
IrO_2/CP	290 mV (1.519 V)	337 mV	571 mV	648 mV	747 mV	—	—	—

The kinetics of the oxygen evolution reaction (OER) on the various Ce-based electrodes were studied by Tafel plot analysis using data derived from rotating disk electrode linear sweep voltammetry (RDE-LSV) (Figure 3.23). The Tafel slope indicates the increase in overpotential required to achieve a tenfold increase in current density and is known to depend on the rate-determining step of the electrochemical process. Therefore, a lower Tafel slope—reflecting a more efficient rate-determining step—indicates superior electrocatalytic performance. Each electrode presented in Figure 3.23 exhibits two distinct Tafel regions, above and below an applied overpotential of approximately 550 mV.

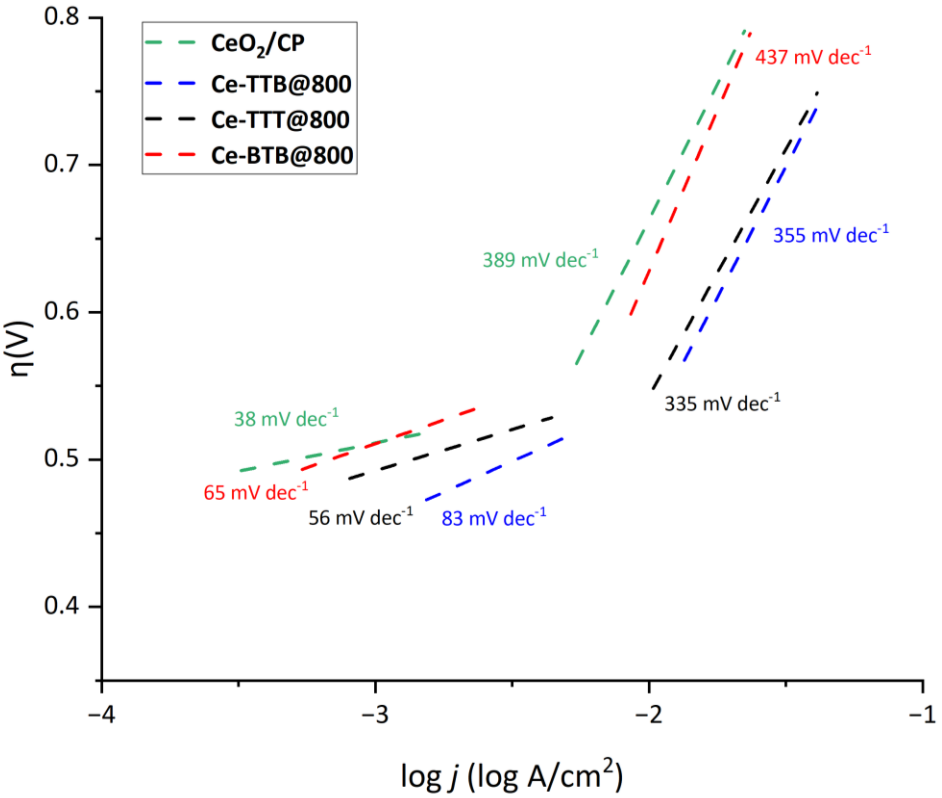

Figure 3.23: Tafel plot obtained from LSV data.

In the lower overpotential region (below approximately 550 mV), **CeO_2/CP** exhibits more favourable OER kinetics than the pyrolysed Ce-MOFs, with a Tafel slope of 38 mV dec^{-1}. Among the pyrolysed materials, **Ce-TTT@800/CP** displays the lowest Tafel slope at 56 mV dec^{-1}, followed by **Ce-BTB@800/CP** at 65 mV dec^{-1}. **Ce-TTB@800/CP** shows a

moderately higher slope of 83 mV dec^{-1} in this region.

These values represent a moderate improvement over the kinetics observed for the pristine Ce-MOF precursors (discussed in the previous chapter), which exhibited Tafel slopes of 81 mV dec^{-1} for **Ce-TTT/CP**, 87 mV dec^{-1} for **Ce-BTB/CP**, and 115 mV dec^{-1} for **Ce-TTB/CP**. Notably, the relative trend in performance is preserved following pyrolysis. This improvement, indicative of enhanced electron transfer, may be attributed to the presence of amorphous and graphitic carbon domains within the pyrolysed Ce-MOFs, which enhance electrical conductivity.

As the applied overpotential increases beyond 550 mV, all four Ce-based catalysts transition into a diffusion-limited kinetic regime, characterised by Tafel slopes greater than 120 mV dec^{-1}.[19] In this higher overpotential region, **Ce-TTT@800/CP** again exhibits the lowest Tafel slope, at 335 mV dec^{-1}, followed by **Ce-TTB@800/CP** at 355 mV dec^{-1}, **CeO_2/CP** at 389 mV dec^{-1}, and **Ce-BTB@800/CP** at 437 mV dec^{-1}.

3.4.2 Chronopotentiometry Study of Ce-based MOF derivatives for OER

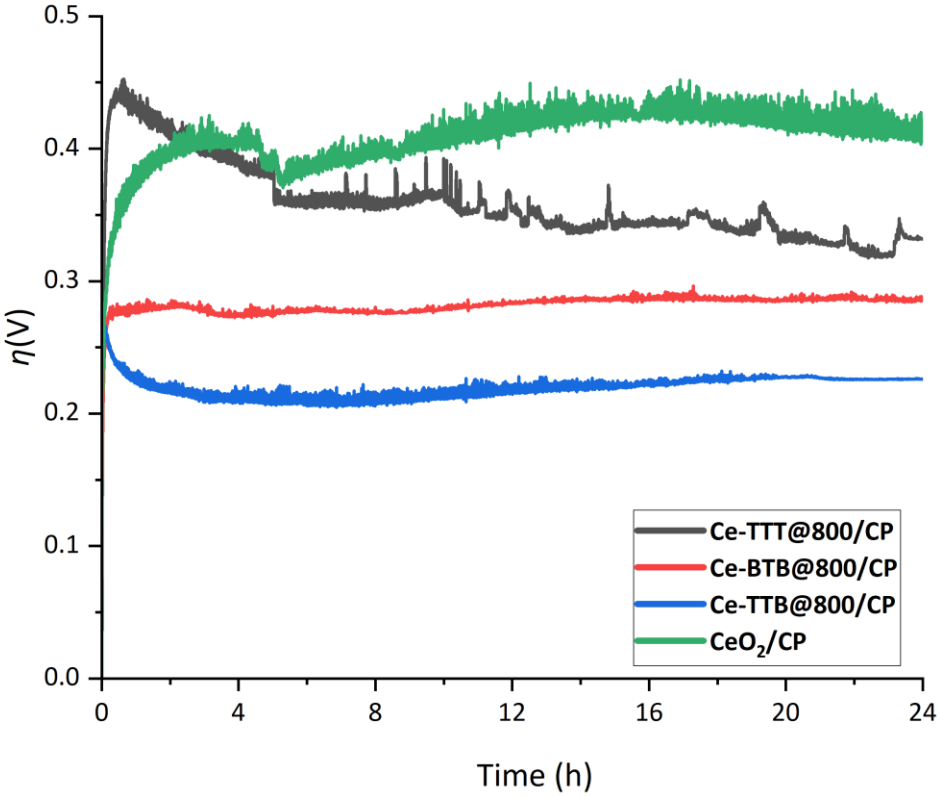

Figure 3.24: Chronopotentiometry data for pyrolysed Ce-MOFs and CeO_2 nanoparticles embedded in carbon paste (CP) working electrodes. Measurements were performed at a constant current density of 1 mA cm^{-2} in 0.5 M H_2SO_4 electrolyte at an electrode rotation speed of 1600 rpm.

As electrolysers generally operate under a fixed current rather than cycling, the long-term operational stability of the pyrolysed Ce-MOF electrocatalysts was further evaluated using 24-hour chronopotentiometry experiments (Figure 3.25). A constant current density of 1 mA cm^{-2} was selected based on the Tafel analysis presented in Figure 3.23. According to the Tafel plots, at this current density, the pyrolysed Ce-MOF electrocatalysts operate under steady-state mass transport conditions, meaning that OER kinetics are governed predominantly by electron transfer. Consequently, any observed increase in the applied potential required to maintain 1 mA cm^{-2} can be attributed to electrocatalyst degradation rather than mass transport limitations.

All three pyrolysed Ce-MOF electrocatalysts appear to be relatively stable over the 24-hour test period. For **Ce-TTT@800/CP**, a gradual decline in the applied overpotential is observed, decreasing from 440 mV at 30 minutes to 326 mV at 24 hours. This

improvement in the overpotential required to maintain 1 mA cm^{-2} likely reflects a progressive transformation—primarily within the first 5 hours—of the **Ce-TTT@800/CP** electrode surface into a more catalytically active state.

Ce-BTB@800/CP and **Ce-TTB@800/CP** also remained highly stable throughout the 24-hour experiment, exhibiting overpotentials of 287 mV and 226 mV at 24 hours, respectively. Their stability and sustained activity under 1 mA cm^{-2} chronopotentiometric conditions contrast with the degradation observed during the CV cycling stability experiments. Taken together, these results suggest that **Ce-BTB@800/CP** and **Ce-TTB@800/CP** exhibit good stability at low overpotentials and current densities up to 1 mA cm^{-2}.

The commercial CeO_2 nanoparticles (**CeO_2/CP**), included here as a benchmark, were also found to be relatively stable over the 24-hour test period, with the overpotential increasing only slightly from 407 mV at 3 hours to 412 mV at 24 hours. Importantly, from 3 to 24 hours, all three pyrolysed Ce-MOFs outperformed the commercial CeO_2 in terms of lower overpotentials. These findings suggest that the pyrolysis of Ce-based MOFs is a promising strategy for enhancing the electrocatalytic performance of CeO_2-based nanomaterials.

3.4.3 Cyclic Voltammetry Stability Study of Ce-based MOF derivatives for OER

Given that the pyrolysed Ce-MOFs displayed excellent stability for 24 hours at 1 mA cm^{-2}, cyclic voltammetry (CV) studies were employed to further test stability under more extreme conditions. Each electrocatalyst was subjected to 1,000 CV cycles at a scan rate of 100 mV s^{-1} over a potential range of 0.2–2.1 V versus the standard hydrogen electrode (SHE), in 0.5 M H_2SO_4. A linear sweep voltammogram (LSV) was recorded both before and after the CV experiment at a scan rate of 1 mV s^{-1}. Figure 3.24a presents the evolution of the CV profile over 1,000 cycles for **Ce-TTT@800/CP**.

Initially, analysis of the 5th cycle reveals several distinguishable features. Beginning at 0.9 V and sweeping anodically, a non-Faradaic region extends up to approximately 1.3 V, beyond which a Faradaic current emerges and increases steadily toward the upper

potential limit of 2.1 V. This Faradaic current arises from overlapping contributions of Ce(III) → Ce(IV) oxidation and the OER. From the 50th to the 1000th cycle, a small peak at approximately 1.65 V becomes distinguishable, corresponding to the Ce(III) → Ce(IV) oxidation.[20]

On the cathodic sweep, a prominent Ce(IV) → Ce(III) reduction peak appears at 1.23 V. A second, distinct reduction peak is observed at 0.86 V, which may also correspond to Ce(IV) → Ce(III) reduction, but attributed to the Ce_2S_3 phase rather than the CeO_2 phase responsible for the 1.23 V peak. This peak is not observed in CV profiles **Ce-BTB@800/CP** or **Ce-TTB@800/CP** as they do not contain Ce_2S_3 phases. The height of this second reduction peak at 0.86 V declines significantly between the 5th and 50th cycle and is no longer observed after the 250th cycle, suggesting degradation of the Ce_2S_3 phase with continued cycling. In addition, the peak at 1.23 V shifts and broadens to 1.14 V, partially overlapping with the original 0.86 V feature.

Between the 5th and 50th cycle, the current density at 2.0 V decreases by 18%, from 39 mA cm^{-2} to 32 mA cm^{-2}. Beyond this point, the decline becomes less pronounced: the 500th cycle retains a current density of 30 mA cm^{-2}, while the 1000th cycle shows a modest further decline to 26 mA cm^{-2}. As observed for the pristine Ce(III)-MOFs in the previous chapter, this decrease in Faradaic current coincides with a progressive increase in capacitive current within the non-Faradaic region over repeated cycles. Despite the use of a rotating disk electrode (RDE) operating at 1600 rpm, the observed increase in capacitive current indicates the growth of an electrical double layer at the electrode–electrolyte interface. Given the complex nature of the electrode architecture—comprising a high surface MOF derivative embedded in carbon paste—this behaviour is not unexpected. At fast scan rates, diffusion within the electrode matrix does not reach steady state, resulting in capacitive charging during each cycle.

These findings are consistent with the Tafel analysis discussed in the previous section. Specifically, at higher overpotentials, the OER activity of the **Ce-TTT@800/CP** electrode (as measured by current density) becomes limited by mass transport rather than electron transfer. Accordingly, the decline in current density observed over successive CV cycles is more plausibly attributed to non-steady-state diffusion limitations than to catalyst degradation.

This explanation is further supported by linear sweep voltammograms (LSVs) recorded before and after 1,000 CV cycles (Figure 3.24b). The slower scan rate (1 mV s^{-1}) employed during LSV acquisition reduces capacitive contributions and shows that **Ce-TTT@800/CP** retains nearly identical OER activity after prolonged cycling. For instance, after 1,000 CV cycles, the electrode reaches a current density of 10 mA cm^{-2} at an applied overpotential of 565 mV, compared to 560 mV prior to cycling.

The CV profile of **Ce-BTB@800/CP** over 1,000 cycles (Figure 3.24c) differs somewhat from that observed for **Ce-TTT@800/CP**. As with the latter, the anodic sweep of **Ce-BTB@800/CP** exhibits a Faradaic current associated with the Ce(III) → Ce(IV) oxidation and OER, observable in the potential range of 1.3–2.1 V throughout the 1,000-cycle experiment. However, on the cathodic sweep, only a single reduction peak at 1.04 V is observed, which is attributable to the Ce(IV) → Ce(III) reduction.

A distinct trend emerges with increasing cycle number: the current density associated with both anodic and cathodic processes increases up to the 500th cycle. At 2.0 V, the anodic current density increases by 77%, from 30 mA cm^{-2} in the 5th cycle to 53 mA cm^{-2} by the 500th cycle. Beyond this point, the current density decreases with increasing cycle number, declining by 19% to 43 mA cm^{-2} by the 1,000th cycle.

Similarly, on the cathodic sweep, the height of the Ce(IV) → Ce(III) reduction peak increases with each cycle and shifts in the cathodic direction. Between the 5th and 500th cycles, the peak height rises from –19 mA cm^{-2} to –52 mA cm^{-2} and shifts by 0.1 V to 0.94 V. After the 500th cycle, the peak intensity declines to –42 mA cm^{-2} by the 1,000th cycle. This behaviour suggests progressive degradation of catalytic performance.

The fact that the peak cathodic Faradaic current (–52 mA cm^{-2} at the 500th cycle) nearly matches the anodic Faradaic current (53 mA cm^{-2} at the 500th cycle) suggests that OER activity has significantly diminished, with the Ce(III)/(IV) redox couple accounting for the majority of the Faradaic current as the number of cycles increases. This is supported by LSV measurements recorded before and after cycling (Figure 3.24d). Prior to cycling, **Ce-BTB@800/CP** reaches a current density of 10 mA cm^{-2} at an applied overpotential of 628 mV. After 1,000 cycles, the same current density requires an overpotential of 704 mV—clear evidence of catalytic degradation.

The CV profile of **Ce-TTB@800/CP** over 1,000 cycles (Figure 3.24e) exhibits a similar decline in OER activity with increasing cycle number, which—like in the case of **Ce-BTB@800/CP**—cannot be attributed to non-steady-state diffusion limitations alone, but rather to catalytic degradation.

In the 5th cycle, the anodic sweep again displays a Faradaic current associated with the Ce(III) → Ce(IV) oxidation and the OER. On the cathodic sweep, a Ce(IV) → Ce(III) reduction peak is observed at 1.14 V (peak height: –33 mA cm^{-2}). This is followed by a second region of Faradaic current between 0.6 V and 0.2 V that is absent in later cycles.

By the 250th cycle, a prominent peak emerges at 1.87 V on the anodic sweep, attributable to Ce(III) → Ce(IV) oxidation, with a peak current density of 67 mA cm^{-2}. On the cathodic sweep, the Ce(IV) → Ce(III) reduction peak shifts cathodically to 1.11 V and increases in intensity to –56 mA cm^{-2}. These observations suggest that by the 250th cycle, the Ce(III)/(IV) redox couple accounts for the majority of the observed Faradaic current.

After the 250th cycle, both anodic and cathodic Faradaic currents progressively decline. Notably, the non-Faradaic current between 0.6 V and 1.2 V in the anodic sweep also decreases with cycling, indicating that non-steady-state diffusion limitations cannot explain the reduction in OER activity.

As with **Ce-BTB@800/CP**, **Ce-TTB@800/CP** appears to undergo catalytic degradation under prolonged cycling. This is further supported by LSV measurements (Figure 3.24.f) recorded before and after cycling. Prior to cycling, **Ce-TTB@800/CP** achieves a current density of 10 mA cm^{-2} at an applied overpotential of 552 mV. After 1,000 cycles, the same current density requires an overpotential of 714 mV—clear evidence of catalytic degradation.

It is notable that **Ce-TTT@800/CP**, which demonstrated robust OER activity throughout the CV experiment, was also the only pyrolysed Ce-MOF to exhibit an increasing non-Faradaic (capacitive) current with cycle number. In contrast, for **Ce-BTB@800/CP** and **Ce-TTB@800/CP**, when capacitive current began to decline with increasing cycle number, so too did OER activity. This reinforces the previously established correlation between mass transport-limited OER activity and increasing capacitive current during CV cycling.

Under mass transport-limited OER conditions, the electrical double layer at the electrode–

electrolyte interface becomes increasingly pronounced. When OER activity diminishes, this electrical double layer also collapses, as reactants and products diffuse away into the bulk and are not replenished at the electrode surface. As observed for **Ce-BTB@800/CP** and **Ce-TTB@800/CP**, the Ce(III)/(IV) redox couple—already located at the electrode surface—then accounts for the majority of the observed Faradaic current.

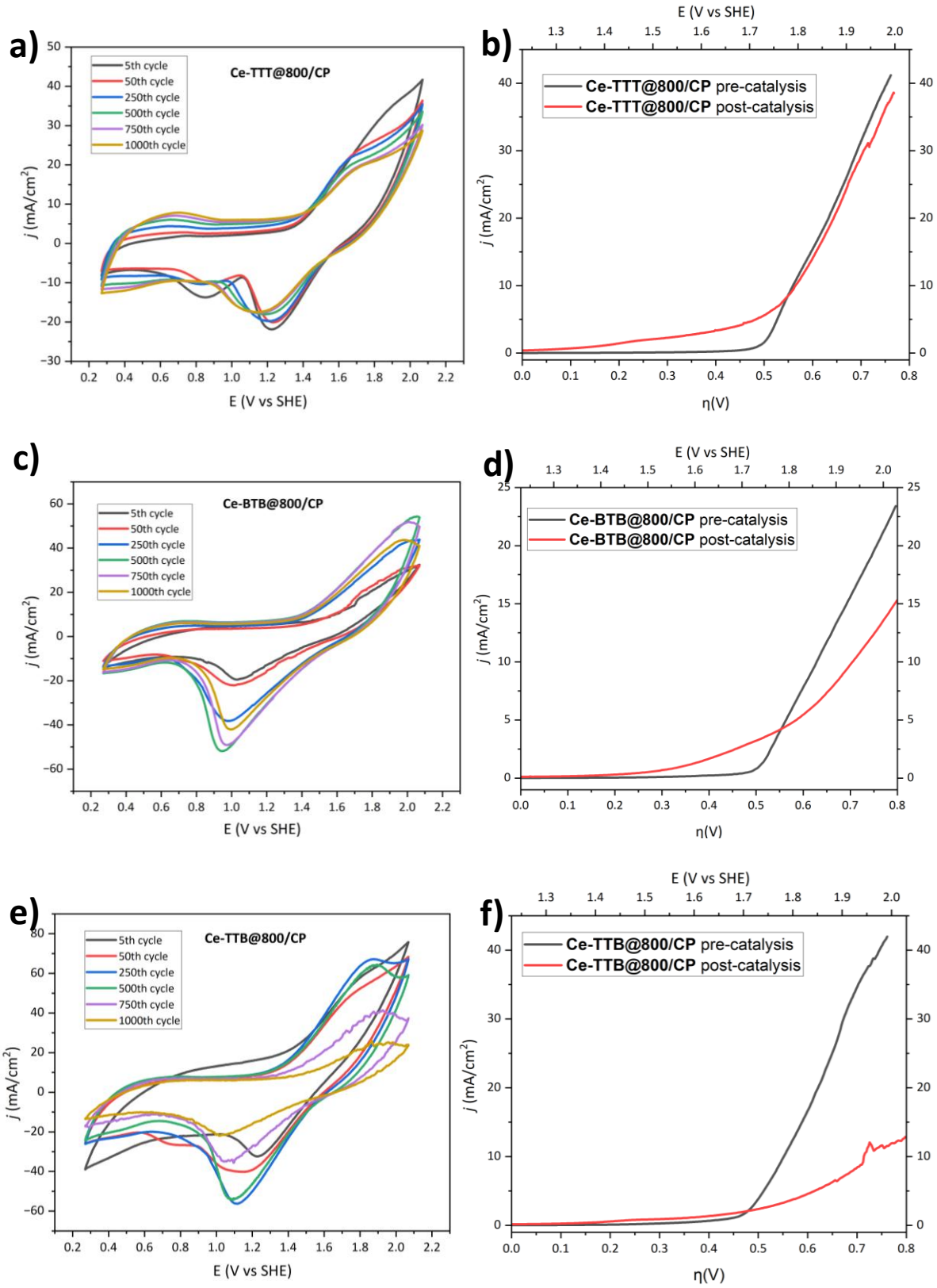

*Figure 3.24: a) CVs of **Ce-TTT@800** embedded in a carbon paste (CP) electrode over 1000 cycles. b) LSVs of **Ce-TTT@800/CP** before and after 1000 CVs. c) CVs of **Ce-BTB@800** embedded in a carbon paste (CP) electrode over 1000 cycles. d) LSVs of **Ce-BTB@800/CP** before and after 1000 CVs. e) CVs of **Ce-TTB@800** embedded in a carbon paste (CP) electrode over 1000 cycles. f) LSVs of **Ce-TTB@800/CP** before and after 1000 CVs.*

3.5 UV-Vis Spectroscopic Study of Ce Ion Leaching into Electrolyte from Ce-based MOF derivatives

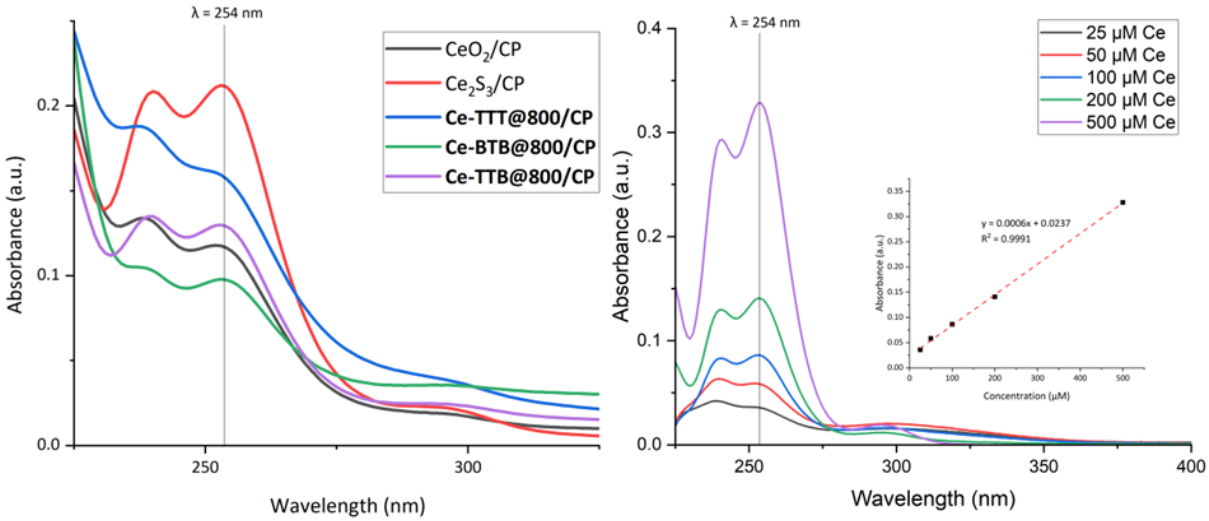

Figure 3.26: UV-Vis absorption data. Left, post-catalysis electrolyte samples. Right, $Ce(NO_3)_3$ standards for known concentration with insert of calibration curve.

As was the case in the previous chapter for the pristine Ce-MOFs, UV–Vis spectroscopy was employed to further evaluate the stability of the pyrolysed Ce-MOFs as OER electrocatalysts under acidic conditions, specifically to assess cerium ion leaching into the electrolyte during operation. Electrolyte samples were collected for each pyrolysed Ce-MOF (as well as for CeO_2 and Ce_2S_3) following the cyclic voltammetry (CV) stability experiments (1,000 cycles; see Section 3.3.2). A $Ce(NO_3)_3$ stock solution was prepared in 0.5 M H_2SO_4 (to match the electrolyte), followed by serial dilution to obtain five known concentrations ranging from 25 µM to 500 µM. Absorbance values were recorded at the absorption maximum (λ_max = 254 nm), and the resulting calibration curve exhibited excellent linearity, with an R^2 value of 0.9991 (Figure 3.26).

UV–Vis absorption measurements of the post-catalysis electrolyte samples (Figure 3.26) confirmed the presence of Ce ions in all cases, whereas no Ce was detected in the fresh electrolyte. Using the calibration curve, the concentration of Ce ions was quantified for each sample and is presented in Table 3.5. Of the three pyrolysed Ce-MOFs, **Ce-TTT@800/CP** was found to have lost the most cerium over the 1,000 CV cycles,

corresponding to a Ce mass loss of 27.36%. Notably, this is close to the midpoint (28.75%) between the Ce mass losses observed for **CeO_2/CP** and **Ce_2S_3/CP** (19.05% and 38.44%, respectively), which is expected given that **Ce-TTT@800/CP** contains both CeO_2 and Ce_2S_3 phases. **Ce-TTB@800/CP** exhibited a Ce mass loss of 21.50% over the 1,000 CV cycles—close to the 19.05% loss observed for the commercial CeO_2 nanoparticles (**CeO_2/CP**). **Ce-BTB@800/CP** was found to have leached 14.95% of its original Ce content into the electrolyte solution.

Table 3.5: Data pertaining to the leaching of Ce ions form pyrolysed Ce-MOFs and CeO_2 electrocatalysts after 1000 CV cycles in 0.5 M H_2SO_4.

	Absorbance @254 nm (a.u.)	Concentration (μM)	ppm	% loss over 1000 cycles
CeO_2/CP	0.117	155.5	21.77	19.05
Ce_2S_3/CP	0.212	313.8	43.94	38.44
Ce-TTT@800/CP	0.1577	223.3	31.27	27.36
Ce-BTB@800/CP	0.0969	122.0	17.08	14.95
Ce-TTB@800/CP	0.129	175.5	24.57	21.50

3.6 Conclusions

Pyrolysis of the Ce(III)-MOFs from the previous chapter at 800 °C yielded CeO_2-carbon composites (**Ce-TTT@800**, **Ce-BTB@800**, **Ce-TTB@800**) with markedly improved OER performance under acidic conditions. **Ce-TTT@800** also contained a Ce_2S_3 phase, representing the first reported lanthanide(III) sulfide derived from a MOF precursor. The Ce_2S_3 phase is likely formed through in-situ generation of CS_2 from the thiophene linker and carbothermic sulfurisation of CeO_2. This serendipitous outcome establishes a facile route to cerium sulfide materials from cerium-thiophene MOFs.

Pyrolysis substantially reduced the overpotential required at 10 mA cm^{-2} (a benchmark relevant for practical applications[21]) relative to the parent MOFs and improved Tafel behaviour in the low-current regime by 25–31%. These gains are consistent with enhanced electronic conductivity from the sp^2-rich carbon matrix revealed by Raman

spectroscopy. Commercial CeO_2 showed superior kinetics at very low current densities but transitioned sharply to diffusion-limited behaviour, whereas the pyrolysed Ce-MOFs sustained electron-transfer-limited kinetics over a wider range. As all three operated under diffusion control kinetics above ~550 mV, future work focusing on particle size and morphology optimisation may offer a plausible route to lower Tafel slopes at device-relevant current densities.[22-24]

Chronopotentiometry over 24 h confirmed stable operation for all three composites with no detectable Ce leaching, and all outperformed commercial CeO_2 at 1 mA cm^{-2}. **Ce-TTT@800** was uniquely stable over 1000 CV cycles despite the greatest Ce leaching, which Raman data attribute to surface Ce_2S_3 domains dissolving in acid while CeO_2 remains strongly anchored to the carbon support, a red shift in the Ce F_2g peak supports this interpretation and points to CeO_2 as the dominant active phase.

Taken together, these results show that CeO_2-based acidic OER electrocatalysts can be meaningfully influenced through the linker choice of pyrolytic MOF precursor, and that anchoring CeO_2 to an sp^2-rich carbon support enhances both activity and stability. This pathway merits further development as a route to lowering Ir loadings in PEM electrolysers, with clear next steps in morphology control and heteroatom doping. Doping with Ir or Ru should be explored under acidic conditions while staying below the 0.1 mg cm^{-2} industry target,[25] and doping with other lanthanides[26-28] or with Ti and/or Zr[28-31] offers further routes to tune band gap, defect density, and morphology.

3.7 References

1. X. Wang, J. Wang, Y. Sun, K. Li, T. Shang and Y. Wan. *Front. Chem.*,2022, **10**, 89708.
2. S.Y. Zhong and X.Q. Gong, *Applied Surface Science*, 2019, **496**, 143712.
3. G. Spezzatia, A. D. Benavidezb, A. T. DeLaRivab, Y. Sua, J. P. Hofmanna, S. Asahinac, E. J. Olivierd, J. H. Neethlingd, J. T. Millere, A. K. Datyeb, E. J.M. Hensen, *Applied Catalysis B: Environmental*, 2019, **243**, 36.
4. M. Nolan, S. C. Parker, G. W. Watson, *Surface Science*, 2005, **595**, 223–232.
5. Tana, M. Zhang, J. Li, H. Li, Y. Li, W. Shen, *Catalysis Today*, 2009, **148**, 179–183.
6. J. Yu, Z. Wang, J. Wang, W. Zhong, M. Ju, R. Cai, C. Qiu, X. Long and S. Yang, *ChemSusChem,* 2020, **13**, 5.

7. A. Rajapriya, S. Keerthana, A. Rebekah, C. Viswanathan, N. Ponpandian, *International Journal of Hydrogen Energy,* 2021, **46**, 75, 37281-37293.
8. P. Scherrer, *Nachrichten von der Gesellschaft der Wissenschaften zu Göttingen, Mathematisch-Physikalische Klasse,* 1918, **1918**, 98-100.
9. S. Hirai, K. Shimakage, Y. Saitou, T. Nishimura, Y. Uemura, M. Mitomo and Leo Brewer, *J. Am. Ceram. Soc.*, 1998, **81**, 1, 145–151.
10. H. Wynberg and Bantjes, *The Journal of Organic Chemistry*, 1959, **24**, 10, 1421-1423.
11. R.Yuan, Y. Guo, I. Gurgan, N. Siddique, Y.-S. Li, S. Jang, G. A. Noh, S. H. Kim, *Carbon*, 2025, **238**, 120214.
12. A. C. Ferrari and J. Robertson, *Phys. Rev. B*, 2000, **61**, 14095.
13. N. Kandhasamy, G. Murugadoss, T. Kannappan, K. Kirubaharan, R. K. Manavalan, and R. Gopal, *Environmental Science and Pollution Research*, 2023, **30**, 29711–29726.
14. D. Joung, V. Singh, S. Park, A. Schulte, S. Seal, S. Khondaker, *J. Phys. Chem. C*, 2011, **115**, 24494.
15. L. Jiang, M. Yao,B. Liu, Q. Li, R. Liu, Z. Yao, S. Lu, W.Cui, X. Hua, B. Zou, T. Cui, *Cryst. Eng. Comm.*, 2013, **15**, 739.
16. M. Srivastava, A.K. Das, P. Khanra, M.E. Uddin, N.H. Kim, J.H. Lee, J. *Mater. Chem. A*, 2013, **1**, 9792.
17. M.K. Kumawat, M. Thakur, R.B. Gurung, R. Srivastava, *Sci.Rep.*, 2017, **7**, 15858.
18. L. Tian, D. Ghosh, W. Chen, S. Pradhan, X. Chang, S. Chen, *Chem. Mater.*, 2009, **21**, 13, 2803–2809.
19. R. L. Doyle and M. E. G. Lyons, in *Photoelectrochemical Solar Fuel Production: From Basic Principles to Advanced Devices*, ed. S. Giménez and J. Bisquert, Springer International Publishing, Cham, 2016, pp. 41–104.
20. A. Paulenova, S.E. Creager, J.D. Navratil, Y. Wei, *Journal of Power Sources*, 2002, **109**, 431–438.
21. C. C. L. McCrory, S. Jung, J. C. Peters and T.F. Jaramillo, *J. Am. Chem. Soc.* 2013, **135**, 45, 16977–16987.
22. L. Zhuang, L. Ge, H. Liu, Z. Jiang, Y. Jia, Z. Li, D. Yang, R. K. Hocking, M. Li, L. Zhang, X. Wang, X. Yao, Z. Zhu, *Angew. Chem. Int. Ed.*, 2019, **58**, 13565.

23. X. Hou, J. Zhou, X. Xu, X, Wang, S. Zhang, H. Wang, M. Huang, *Catalysis Communications*, 2022, **165**, 106445.
24. X. Hou, Z. Han, X. Xu, D. Sarker, J. Zhou, M. Wu, Z. Liu, M. Huang, H. Jiang, *Chemical Engineering Journal*, 2021, **418**, 129330.
25. C. Locci, M. Mertens, S. Höyng, G. Schmid, T. Bagus and P. Lettenmeier, *Chem. Ing. Tech.*, 2024, **96**, 1–2, 22–29.
26. F. J. Trindade, S. Damasceno, L. Otubo, M. R. Felez, D. Z. de Florio, F. C. Fonseca, and A. S. Ferlauto, *ACS Applied Nano Materials,* 2022, **5**, 7, 8859-8867.
27. M. Laqdiem, A. J. Carrillo, G. Dimitrakopoulos, M. Balaguer, J. Garcia-Fayos, A. F. Ghoniem and J. M. Serra, *Solid State Ionics*, 2023, **394**, 116192.
28. S. Chahal, S. Singh, A. Kumar and P. Kumar, *Vacuum*, 2020, **177**, 109395.
29. J. M. Soney and T. Dhannia, *Inorganic Chemistry Communications*, 2024, **165**, 112535.
30. K. Sood, P. Tiwari, S. Dhall and S. Basu, *Journal of Electroanalytical Chemistry*, 2022, **925**, 116902.
31. J. L. Núñez-Rico, M. Rellán-Piñeiro, B. Puértolas, A. Vidal-Ferran, N. López, J. Pérez-Ramírez and S. Wershofen, *Chem. Eur. J.*, 2020, **26**, 16129 – 16137.

Chapter 4: Isostructural Series of Two-Dimensional Ln-MOFs Composed of Photosensitising Ru(II)-Metalloligand and Dinuclear SBUs (Ln = Ce^{III}, Nd^{III}, Sm^{III}, Eu^{III}, Gd^{III}, Tb^{III}, Dy^{III}, and Er^{III})

4.1 Introduction

Photoactive metal–organic frameworks (MOFs) represent an emerging class of materials that have attracted increasing interest over the past decade.[1] This growing attention is driven by their potential in a wide range of applications, including luminescent chemical sensing, electroluminescent devices, photocatalysis, and photoelectrocatalysis.[1] Photoactive MOFs typically incorporate a light-harvesting unit within their structure either as a conjugated aromatic organic linker,[2,3] as light-absorbing guest molecules housed within the pores,[4] or, in some cases, as photoactive metal clusters comprising the MOF's secondary building units (SBUs).[5]

Metalloligands can also serve as light-harvesting components in MOFs. Notably, metalloporphyrin ligands and polypyridyl-based Ru(II) or Ir(III) complexes have been successfully integrated as photosensitising linkers within MOF structures.[1,2,6,7] Ru(II) polypyridyl complexes—such as $[Ru(bpy)_3]^{2+}$ and its derivatives-have been extensively studied owing to their high molar absorptivities in the visible region, long-lived metal-to-ligand charge transfer (MLCT) excited states, and redox potentials that make them ideally suited for driving endergonic photocatalytic reactions, including the water oxidation reaction (WOR) and carbon dioxide reduction reaction (CO_2RR).[8-11] These Ru(II) polypyridyl moieties are known to retain their photophysical properties when integrated into complex molecular and supramolecular systems.[12,13] Pyridyl-carboxylate derivatives of $[Ru(bpy)_3]^{2+}$ have been employed as photoactive linkers in several MOFs.[14-18] The Schmitt Group has previously reported the synthesis of first-row transition-metal MOFs using a tetratopic, acetylene-extended Ru(II) bipyridyl metalloligand, $\mathbf{[H_4L_{Ru}]^{2+}}$.[19] Notably, the incorporation of alkynyl bridges in such systems has been shown to enhance electron transfer kinetics from the Ru-based photosensitiser to the catalytic metal centre.[20]

While numerous reports exist on photoactive transition metal–based MOFs, there remain relatively few examples of photoactive lanthanide-based MOFs, and scarcely any that employ light-harvesting metalloligands. One notable example is reported by Yan et al., who synthesised a europium-based MOF incorporating Ru(II) polypyridyl linkers and demonstrated its efficacy as a robust photocatalyst for CO_2RR.[21]

Building on the successful investigation of cerium-based MOFs as electrocatalysts as described in Chapter 2, and drawing upon prior group experience with light-harvesting Ru(II) polypyridyl metalloligands, the synthesis of novel lanthanide MOFs—specifically cerium and europium analogues—based on the $\mathbf{[H_4L_{Ru}]^{2+}}$ linker was identified as a promising route to photocatalysts for WOR and CO_2RR.

This chapter reports the synthesis of a series of photoactive lanthanide MOFs featuring $\mathbf{L_{Ru}^{2-}}$ as the light-harvesting linker, and describes their structural characterisation, physicochemical properties, and photophysical behaviour.

4.2 Synthesis of MOFs based of Ce^{III}, Nd^{III}, Sm^{III}, Eu^{III}, Gd^{III}, Tb^{III}, Dy^{III}, Ho^{III}, and Er^{III}

The ruthenium metallo-ligand, $\mathbf{[H_4L_{Ru}](ClO_4)_2}$, was successfully synthesised using the procedure reported by Dr. Muhamed Mulahmetović.[19] See Chapter 6 for experimental and characterisation details and Appendix C for schematic of synthetic procedure. Efforts were directed towards the preparation of lanthanide-based metal-organic frameworks (**LnRu-MOFs**) using this metalloligand as a linker. It is well established that a wide range of parameters influence MOF synthesis and the resulting framework structures. These include compositional variables such as the molar ratio of reagents, pH, and solvent system, as well as process variables such as temperature, reaction time, and pressure.[23,24] Therefore, a systematic screening was conducted to identify the conditions that yielded phase-pure MOF crystals of sufficient size and quality for single-crystal X-ray diffraction (SCXRD) analysis. The variables investigated included reaction temperature, time, solvent system, lanthanide-to-ligand molar ratio, and the nature of the metal salt (e.g., nitrate *vs*. chloride).

The screening strategy began with synthetic conditions established for transition-based MOFs that used the same metalloigand,[19] which were subsequently modified in a

stepwise fashion. Initial reactions between Ln^{II} salts and **$[H_4L_{Ru}](ClO_4)_2$** at low metal-to-ligand ratios (1-5 :1) in neat DMF did not yield crystalline materials. Crystallisation only occurred when large excesses of $Ln(NO_3)_3$ salts were employed, and ethanol and water were introduced as co-solvents. Specifically, $Ln(NO_3)_3$ salts were reacted with **$[H_4L_{Ru}](ClO_4)_2$** in a 50:1 metal-to-ligand molar ratio at 85 °C in a mixed DMF:EtOH:H_2O (3:3:2) solvent system. Reaction times of 24-48 hours led to the formation of a series of isostructural MOFs with the formula $[Ln_2(\mathbf{L_{Ru}})(NO_3)_4(DMF)(H_2O)]$, where Ln = Ce (**CeRu-MOF**), Nd (**NdRu-MOF**), Sm (**SmRu-MOF**), Eu (**EuRu-MOF**), Gd (**GdRu-MOF**), Tb (**TbRu-MOF**), Dy (**DyRu-MOF**), and Er (**ErRu-MOF**).

The synthesis was further refined, and a reduced metal-to-ligand molar ratio of 20:1 was also found to afford the same **LnRu-MOF** structures. Crystallisation was observed to occur between 65 °C (after 72 hours) and 85 °C (after 18 hours). Although higher temperatures and longer reaction times improved the overall yield, temperatures of 80 °C and above, when combined with durations exceeding 24 hours, led to the co-crystallisation of Ln^{III} formates. The optimal condition was therefore identified as 80 °C for 24 hours. The addition of trifluoroacetic acid (TFA) as a modulator did not improve the crystal size or yield, and instead promoted the co-crystallisation of undesired Ln^{III}-formates.

The high nitrate content in the resulting MOFs likely explains the necessity of using an excess of $Ln(NO_3)_3$ to drive crystallisation. This requirement could be reduced by the inclusion of sodium nitrate ($NaNO_3$) as an additional nitrate source. Under these modified conditions, a molar ratio of 5:1:15 ($Ln(NO_3)_3$: **$[H_4L_{Ru}](ClO_4)_2$** : $NaNO_3$) was found to be effective.

Small red block-shaped single crystals were formed in the cases of **SmRu-MOF**, **EuRu-MOF**, **GdRu-MOF**, and **DyRu-MOF**. These single crystals were of sufficient size and quality for SCXRD. Attempts to obtain high-quality single crystals of **CeRu-MOF**, **NdRu-MOF**, **TbRu-MOF**, and **ErRu-MOF** were unsuccessful; the crystals were either too small or polycrystalline in nature.

4.3 Structural characterisation of LnRu-MOFs

4.3.1 Single crystal XRD Analysis of LnRu-MOFs

The isostructural MOFs **SmRu-MOF**, **EuRu-MOF**, **GdRu-MOF**, and **DyRu-MOF** were investigated using single crystal x-ray diffraction (SCXRD). The unit cell parameters of each MOF are summarised in Table 4.1. Full crystallographic information for **SmRu-MOF**, **EuRu-MOF**, **GdRu-MOF**, and **DyRu-MOF** are contained in Appendices E, F, G, and H, respectively.

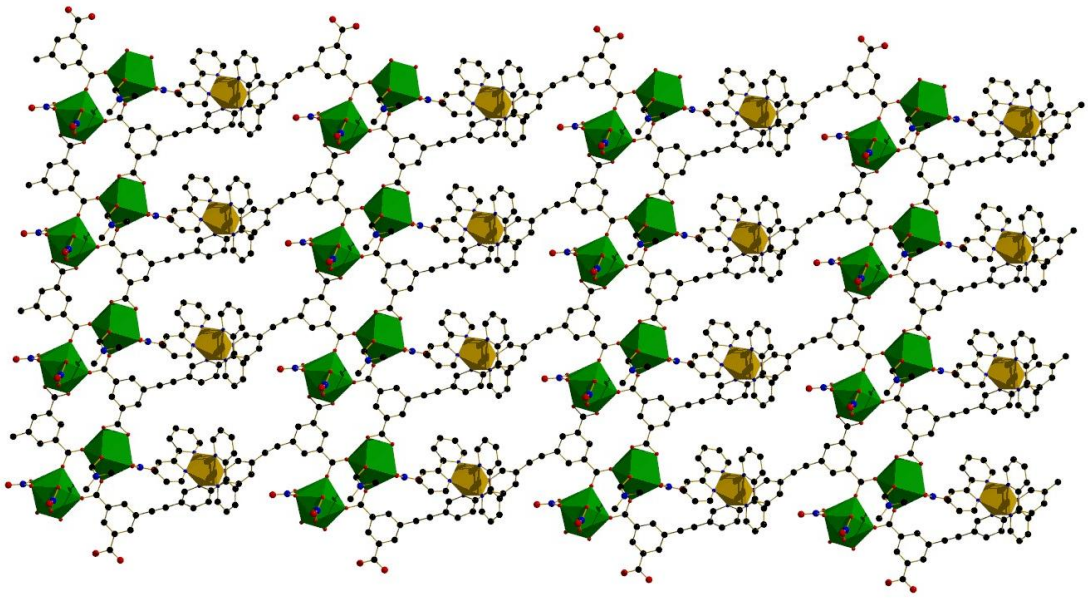

*Figure 4.1: A single 2D layer of **EuRu-MOF** as viewed along the crystallographic c-axis.*

*Table 4.1: unit cell parameters for **LnRu-MOFs** (Ln =Sm, Eu, Gd, or Dy).*

Compound	**SmRu-MOF**	**EuRu-MOF**	**GdRu-MOF**	**DyRu-MOF**
Empirical formula	$[Sm_2(\mathbf{L_{Ru}})(NO_3)_4(DMF)(H_2O)]$	$[Eu_2(\mathbf{L_{Ru}})(NO_3)_4(DMF)(H_2O)]$	$[Gd_2(\mathbf{L_{Ru}})(NO_3)_4(DMF)(H_2O)]$	$[Dy_2(\mathbf{L_{Ru}})(NO_3)_4(DMF)(H_2O)]$
Crystal system	Triclinic	Triclinic	Triclinic	Triclinic
Space group	*P* -1	*P* -1	*P* -1	*P* -1
a (Å)	10.9238(4)	10.9203(7)	10.9309(5)	10.8924(8)
b (Å)	14.1540(7)	14.1292(11)	14.1579(11)	14.1396(17)
c (Å)	18.4473(9)	18.5786(15)	18.4702(15)	18.798(2)
α (°)	86.338(4)	85.999(5)	86.791(6)	84.900(10)
β (°)	89.152(3)	89.191(5)	88.443(5)	89.523(8)
γ (°)	85.177(3)	85.479(5)	85.495(5)	85.812(8)
V ($Å^3$)	2836.21	2850.6	2844.38	2875.99

For a more in-depth structural discussion, **EuRu-MOF** will serve as the representative example for the remainder of this section. Crystal data and refinement parameters for **EuRu-MOF** are provided in Appendix F, Table F1. The structure was solved and refined in the triclinic space group *P*-1, with the asymmetric unit comprising $[Eu_2(\mathbf{L_{Ru}})(NO_3)_4(DMF)(H_2O)]$, as depicted in Figure 4.2. This asymmetric unit contains two Eu^{III} ions and one $\mathbf{L_{Ru}}^{2-}$ metalloligand. Each Eu^{III} ion is coordinated to two nitrate anions (providing charge balance) and one solvent molecule, either DMF or water.

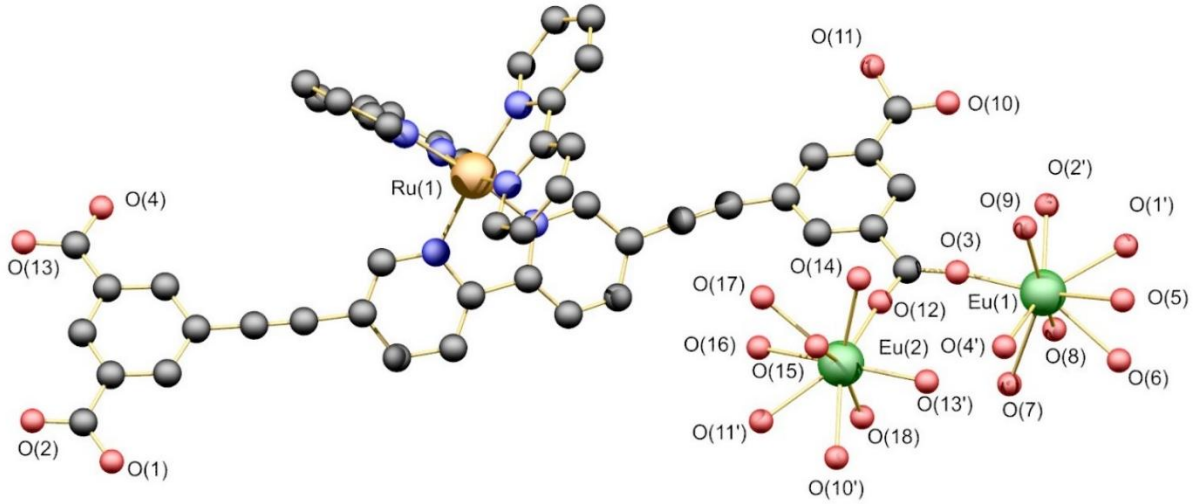

*Figure 4.2: Ball-and-stick representation of the asymmetric unit for **EuRu-MOF**. Atom colour scheme: C, black; N, blue; O, red; Ru, orange; Eu, green. Hydrogens omitted for clarity. Coordinating nitrates and solvent molecules reduced to coordinating O atoms for clarity.*

The inorganic secondary building unit (SBU) of **EuRu-MOF**, shown in Figure 4.6, consists of a dinuclear europium unit in which each Eu^{III} ion adopts a nine-coordinate geometry. These dinuclear units are bridged by $\mathbf{L_{Ru}^{2-}}$ metalloligands to form a two-dimensional coordination network extending within the crystallographic *ab* plane (Figure 4.1). Each dinuclear SBU is connected to four carboxylate groups from four distinct $\mathbf{L_{Ru}^{2-}}$ ligands. Two of these carboxylates coordinate in a bidentate chelating fashion, while the other two adopt syn–syn bidentate bridging modes that link the Eu^{III} centres to form the dinuclear core. The remaining coordination sites of each Eu^{III} ion are occupied by two nitrate anions and either a water or DMF molecule. The presence of these labile, coordinated solvent molecules suggests the potential for open metal sites, which may be exploited in sensing or catalysis applications.[25] Single-crystal X-ray diffraction analysis confirms that the $\mathbf{L_{Ru}^{2-}}$ metalloligand retains its octahedral $\{RuN_6\}$ coordination environment. Each $\mathbf{L_{Ru}^{2-}}$ unit coordinates to six Eu^{III} ions *via* its four carboxylate arms, engaging in either *syn–syn* bidentate bridging or bidentate chelation, as described above.

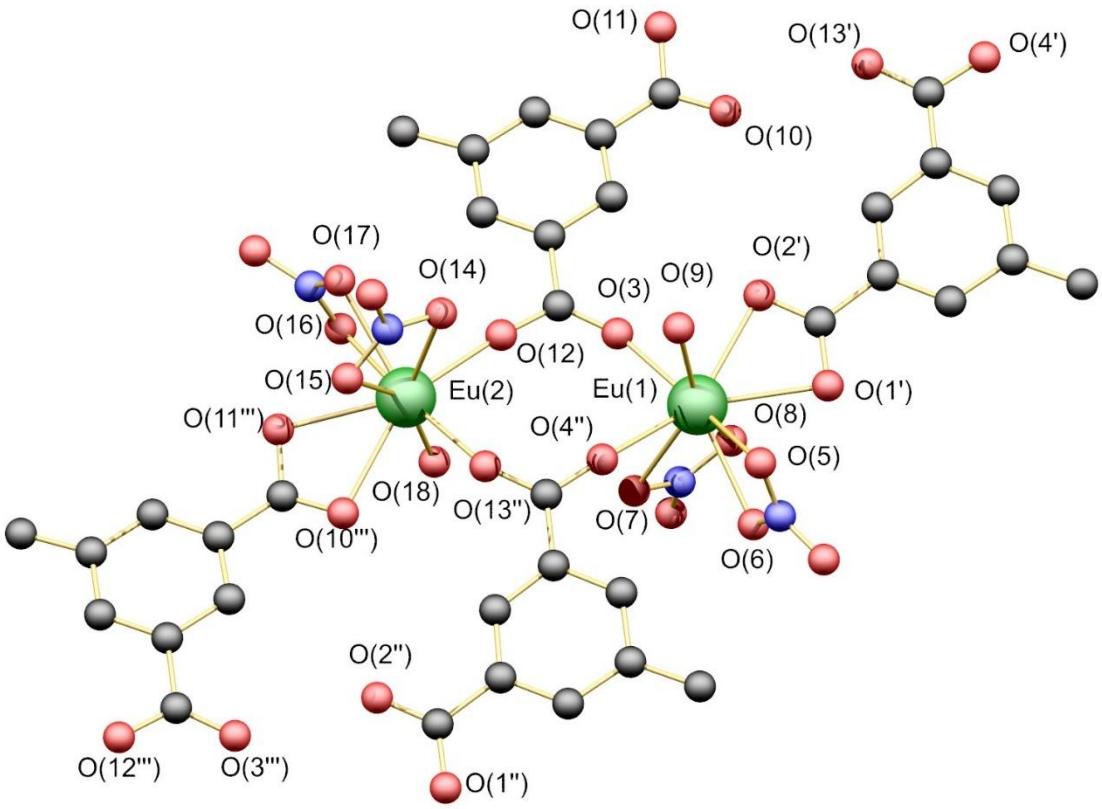

*Figure 4.3: Ball-and-stick representation of the dinuclear Eu^{III} SBU of **EuRu-MOF**. Atom colour scheme: C, black; N, blue; O, red; Eu, green. Hydrogens omitted for clarity. Symmetry codes: (^{I}): 1+X,1+y,-1+z ; (^{II}) : X,1+y,-1+z ; (^{III}) -1+X,y,z.*

*Table 4.2: List Eu^{III}-O bond lengths in the dinuclear Eu^{III} SBU of **EuRu-MOF.***

Eu(1)-O Bonds	Bond Lengths (Å)	Eu(2)-O Bonds	Bond Lengths (Å)
Eu1-O1	2.465(14)	Eu2-O10	2.501(19)
Eu1-O2	2.448(14)	Eu2-O11	2.473(2)
Eu1-O3	2.263(17)	Eu2-O12	2.284(16)
Eu1-O4	2.328(15)	Eu2-O13	2.269(18)
Eu1-O5	2.575(19)	Eu2-O14	2.590(3)
Eu1-O6	2.481(15)	Eu2-O15	2.500(3)
Eu1-O7	2.570(2)	Eu2-O16	2.530(3)
Eu1-O8	2.476(18)	Eu2-O17	2.500(2)
Eu1-O9	2.320(3)	Eu2-O18	2.319(10)

Olex2 software was used to generate Table 4.2, displaying Eu^{III}-O bond lengths, from the CIF of **EuRu-MOF**.[26] Eu^{III}-O bond lengths ranged from 2.473(2) to 2.575(19) Å, which is within the range typically expected for Eu^{III} ions.[27]

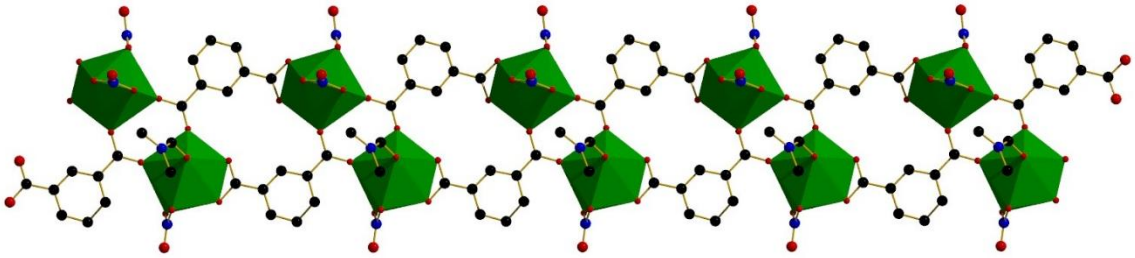

Figure 4.4: Chain of dinuclear Eu^{III} SBUs as viewed from the crystallographic c-axis.

Continuous shape measurement analysis was used to further study the coordination environment of the Eu^{III} ions. Utilising Shape 2.1 software,[28] the coordination geometry of the 9-coordinate Eu^{III} ions was determined to be spherical capped square antiprism. The continuous shape measurement values are presented in Table 4.3. With the lowest value indicating the closest fit between the measured coordination geometry and that of the 13 ideal polyhedral shapes possible for a $\{ML_9\}$ coordination environment. It should be noted that while the spherical capped square antiprism presented the best fit (2.387), the spherical tricapped trigonal prism (2.707) and muffin (2.718) geometries were a close second and third geometrical descriptors, respectively.

*Table 4.3: Continuous shape measurement values for Eu^{III} atoms in **EuRu-MOF**. The lowest value (indicating closest fit) is highlighted in bold.*

Shape	Symmetry	Continuous shape measurement value
Enneagon	D_{9h}	33.821
Octagonal pyramid	C_{8v}	24.708
Heptagonal bipyramid	D_{7h}	17.029
Johnson triangular cupola (J3)	C_{3v}	13.811

Capped cube (J8)	C_{4v}	8.319
Spherical-relaxed capped cube	C_{4v}	7.406
Capped square antiprism (J10)	C_{4v}	3.004
Spherical capped square antiprism	**C_{4v}**	**2.387**
Tricapped trigonal prism (J51)	D_{3h}	3.410
Spherical tricapped trigonal prism	D_{3h}	2.707
Tridiminished icosahedron (J63)	C_{3v}	10.234
Hula-hoop	C_{2v}	10.476
Muffin	C_s	2.718

To confirm the +III oxidation state of the Eu ions bond valance sum (BVS) calculations[29] were carried using Expo 2014 software[30], where R_0 for 9-coordinate Eu-O bonds was set as 2.039 Å.[31]The results of the BVS calculations are shown in Table 4.4 and confirm the +III oxidation state of the Eu ions in **EuRu-MOF.**

Table 4.4: BVS analysis of Eu metal centres in EuRu-MOF.

Metal ion	**R_0(Å)**	**BVS**	**Oxidation state**
Eu1	2.039	3.12	+III
Eu2	2.039	3.35	+III

The two-dimensional metal–organic layers, which extend in the *ab* plane, are stacked along the crystallographic *bc* plane through attractive intermolecular forces. This stacking occurs in two alternating configurations, designated here as *A* and *B* for simplicity. The *A*-

type configuration involves the interdigitation of bipyridine units from two adjacent layers. These bilayer assemblies then stack further through π–π interactions between isophthalate moieties of neighbouring bilayers, forming a three-dimensional crystal lattice. This latter arrangement is referred to as the *B*-type stacking configuration.

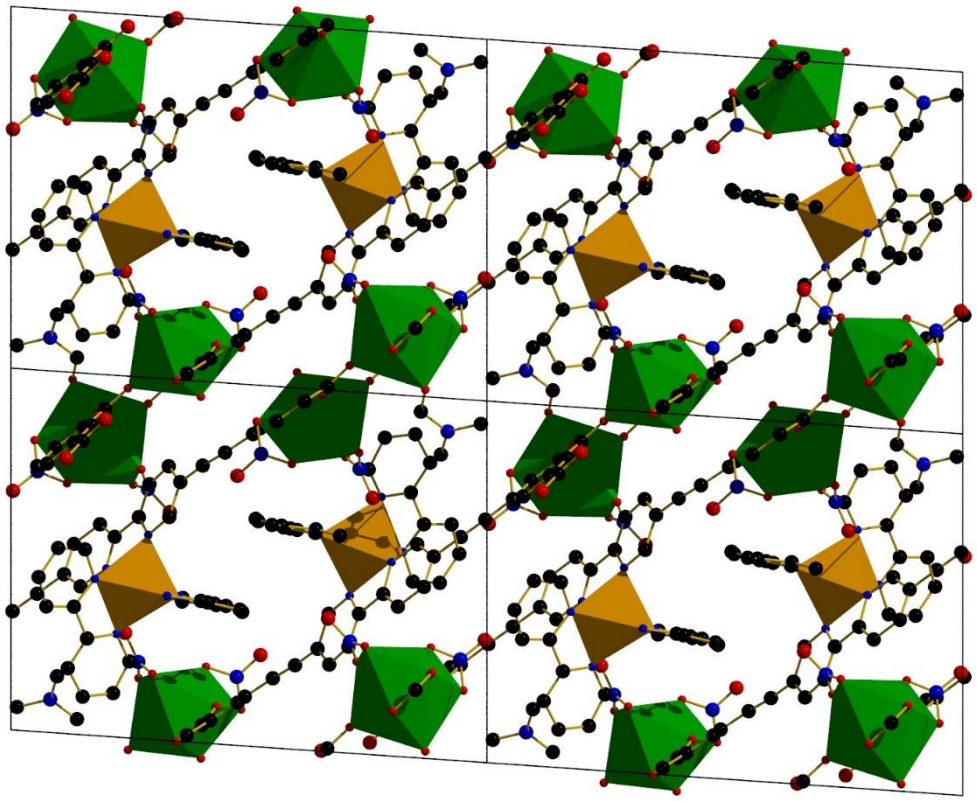

*Figure 4.5: Packing diagram of **EuRu-MOF** as viewed along the crystallographic a-axis. Atom colour scheme: C, black; N, blue; O, red; Ru, orange; Eu, green. Hydrogens omitted for clarity.*

The interdigitation of bipyridine aromatic rings between adjacent layers may, at first glance, resemble staggered (parallel-displaced) π–π stacking. However, the centroid-to-centroid distance between these aromatic rings is 5.543(14) Å, which lies beyond the typical range for π–π interactions as defined by Janiak.[32] Instead, closer inspection reveals the presence of C–H···π interactions between opposing bipyridine units. Due to their inverted symmetry and a lateral offset of 2.047(3) Å, the bipyridine units align such that C(6)–H(6) points toward the centre of the adjacent bipyridine ring. As shown in Figure 4.10, the C–H···π contact has an H···centroid distance of 3.967(13) Å and a C–H···π angle of 122(2)°, both of which fall within the accepted geometric parameters for such interactions.[33] Additional C–H···π interactions are observed between the C(7)–H(7) and C(10)–H(10) atom groups of the bipyridine rings and the nearest acetylene moieties of

adjacent layers, with H···centroid distances of 2.782(5) Å and 3.464(9) Å, and corresponding C–H···π angles of 123(2)° and 138(2)°, respectively (Figure 4.7).

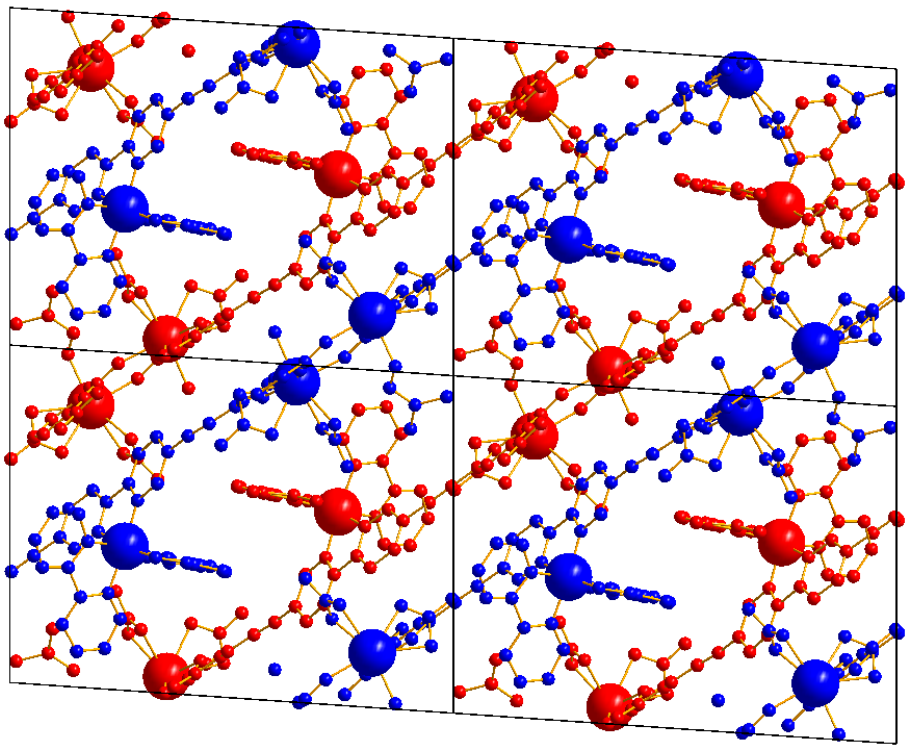

*Figure 4.6: Packing diagram of **EuRu-MOF** with colour differentiation of symmetry operators, as viewed along the crystallographic a-axis. Symmetry codes: blue (x,y,z); red (-x,-y,-z).*

While the *A*-type stacking configuration lacks any true π–π stacking interactions, the *B*-type configuration—i.e. the stacking of bilayers—relies on attractive, parallel-displaced π–π interactions between isophthalate moieties of neighbouring bilayers. Figure 4.8 illustrates this π–π interaction, which exhibits a centroid-to-centroid distance of 3.656(2) Å, a lateral offset of 1.412(4) Å, and a dihedral (displacement) angle of 22.6(9)°. These values meet the criteria established by Janiak[32] for classification as a parallel-displaced π–π stacking interaction.

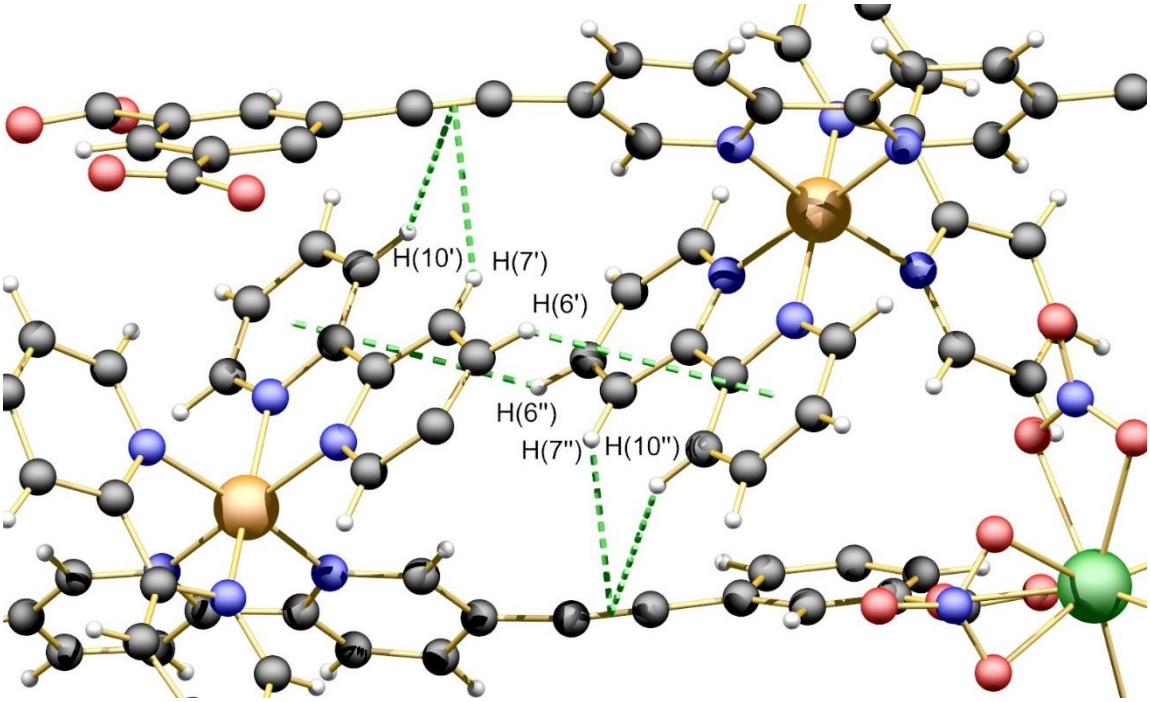

*Figure 4.7: View of the A-type stacking configuration in **EuRu-MOF**, showing the interdigitation of bipyridine units between adjacent two-dimensional layers. C–H···π interactions are observed, with C(6)–H(6) oriented toward the centre of the adjacent bipyridine ring (H···centroid = 3.967 Å; C–H···π angle = 122°; lateral offset = 2.047 Å). Additional C–H···π interactions are also present between C(7)–H(7) and C(10)–H(10) groups of the bipyridine rings and the nearest acetylene moieties of neighbouring layers, with H···centroid distances of 2.782 Å and 3.464 Å, and C–H···π angles of 123° and 138°, respectively.*

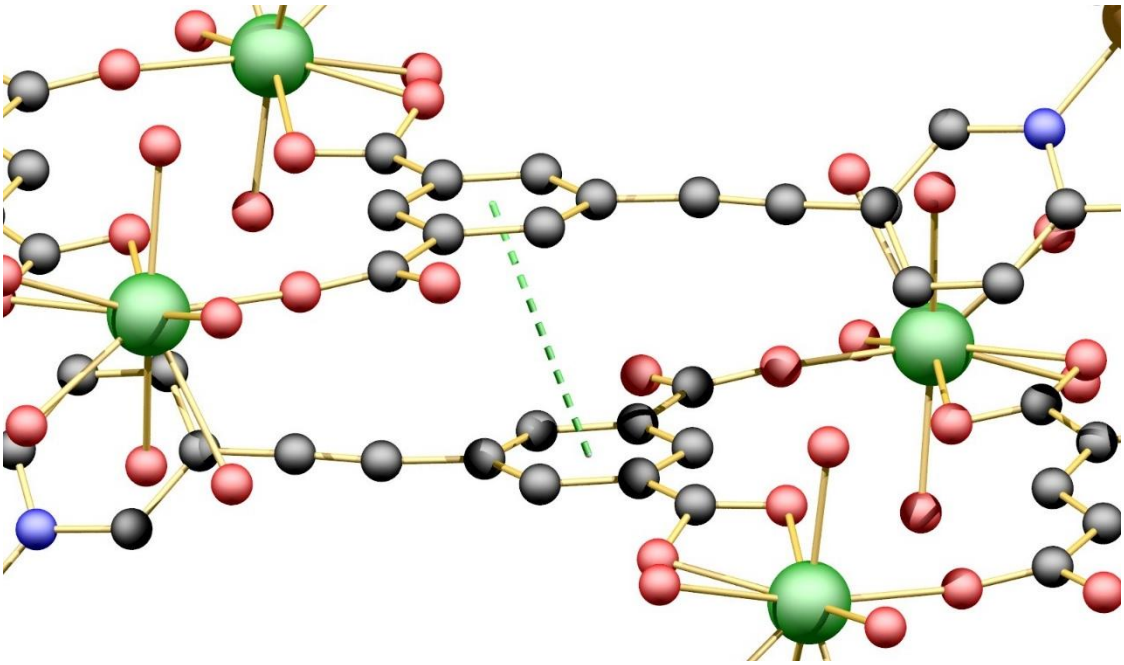

*Figure 4.8: View of the B-type stacking configuration in **EuRu-MOF**, illustrating parallel-displaced π–π stacking interactions between isophthalate moieties of neighbouring bilayers. The centroid-to-centroid distance between aromatic rings is 3.656 Å, with a lateral offset of 1.412 Å and a displacement angle of 22.6°, consistent with established criteria for π–π interactions.[32]*

4.3.2 Powder X-ray Diffraction of LnRu-MOFs

A comparison between the experimental powder X-ray diffraction (PXRD) pattern of bulk **EuRu-MOF** crystals and the simulated pattern calculated from single-crystal X-ray data is shown in Figure 4.9. The close agreement between the two patterns confirms that the **EuRu-MOF** sample was synthesised as a phase-pure crystalline material.

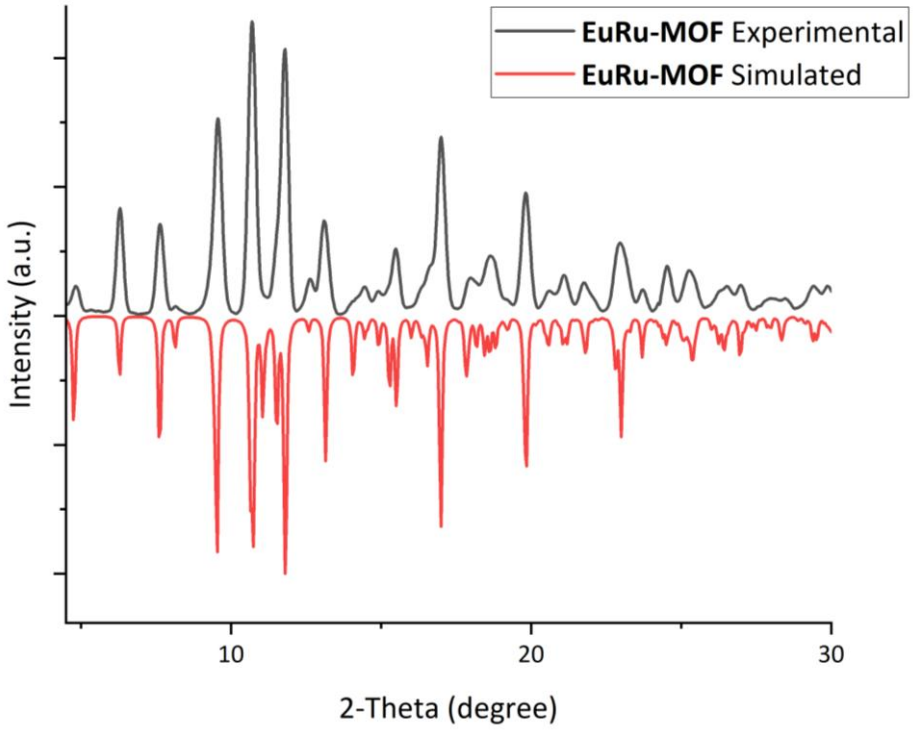

*Figure 4.9: Powder X-ray diffraction patterns for **EuRu-MOF**. Black: Exprimental data. Red: Simulated data, calculated from single crystal XRD data.*

The PXRD patterns of all synthesised **LnRu-MOF** samples are presented in Figure 4.10, alongside the simulated PXRD pattern of **EuRu-MOF**. The experimental patterns are virtually identical, confirming that the **LnRu-MOFs** form an isostructural series and share the same structural features described previously for **EuRu-MOF**.

The PXRD pattern of **NdRu-MOF** exhibits a prominent peak at $2\theta = 21.5°$, which is less apparent in the other experimental patterns. This is most likely an orientation effect.[34] To verify this, the **NdRu-MOF** pattern was fitted to the simulated **EuRu-MOF** pattern using the Le Bail method[35] in EXPO2014 (Appendix C), yielding R_p and R_{wp} values of 1.6 and 2.4, respectively— indicating an excellent fit.

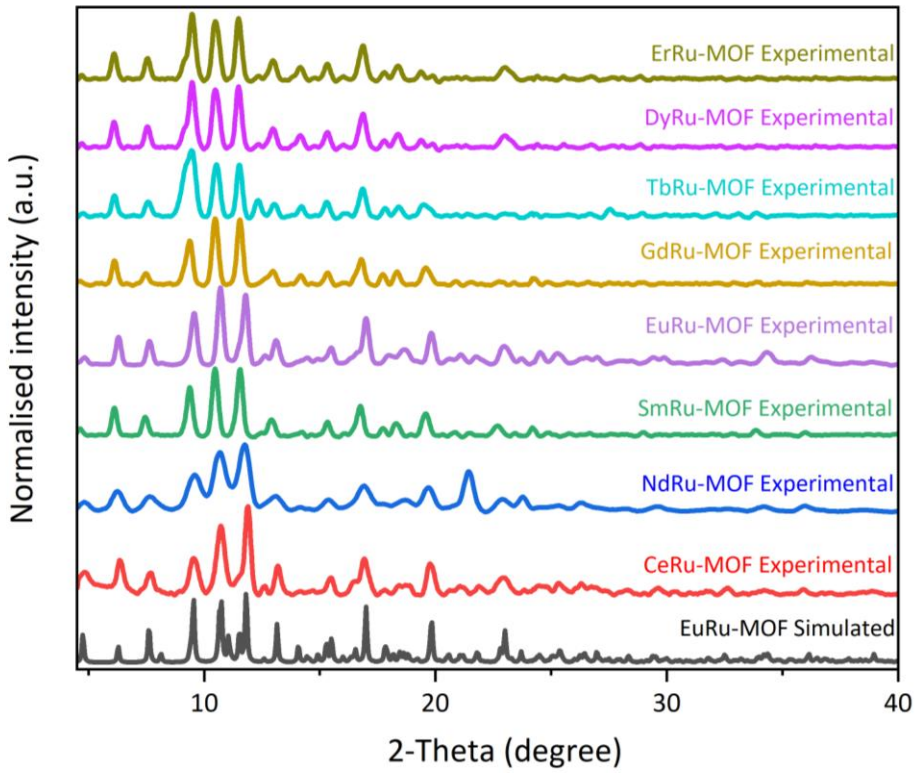

*Figure 4.10: PXRD plot showing experimental **LnRu-MOF** patterns matching the simulated pattern of **EuRu-MOF**.*

The observation that the **LnRu-MOF** series is isostructural from Ce^{III} to Er^{III} is particularly noteworthy, as it represents a rare example in which the so-called *gadolinium break* does not disrupt the structural continuity within a series of lanthanide coordination compounds.[36]

4.4 Physiochemical Characterisation of LnRu-MOFs

4.4.1 FTIR Spectroscopy of LnRu-MOFs

Figure 4.11 presents the Fourier-transform infrared (FTIR) spectra of the **LnRu-MOFs**, which appear virtually identical across the series. A broad band observed between approximately 3700 cm^{-1} and 2500 cm^{-1} arises from ν(O–H) stretching vibrations of coordinated water molecules, and C–H stretching modes. The coordinating carboxylate groups of the $\mathbf{L_{Ru}^{2-}}$ linkers give rise to asymmetric stretching vibrations (ν_{as}(COO)) at approximately 1595 ± 1 cm^{-1} and 1547 ± 5 cm^{-1}, and symmetric stretching vibrations (ν_{s}(COO)) at approximately 1445 ± 2 cm^{-1} and 1423 ± 3 cm^{-1}. These wavenumbers are listed for each **LnRu-MOF** in Table 4.5.

According to the criteria established by Deacon and Phillips,[37] the difference between the asymmetric and symmetric carboxylate stretching frequencies ($\Delta\nu = \nu_{as} - \nu_s$) can be used to infer coordination modes in metal–organic complexes—and in this case metal-organic frameworks. As two distinct asymmetric and symmetric stretching frequencies are observed in each spectrum, two Δν values were calculated per compound, and are presented in Table 4.5. The average Δν values were found to be 150 ± 3 cm^{-1} and 125 ± 6 cm^{-1}. These values are consistent with the presence of two distinct carboxylate coordination modes, as confirmed by single-crystal X-ray diffraction data: a *syn–syn* bridging mode and a bidentate (chelating) mode.

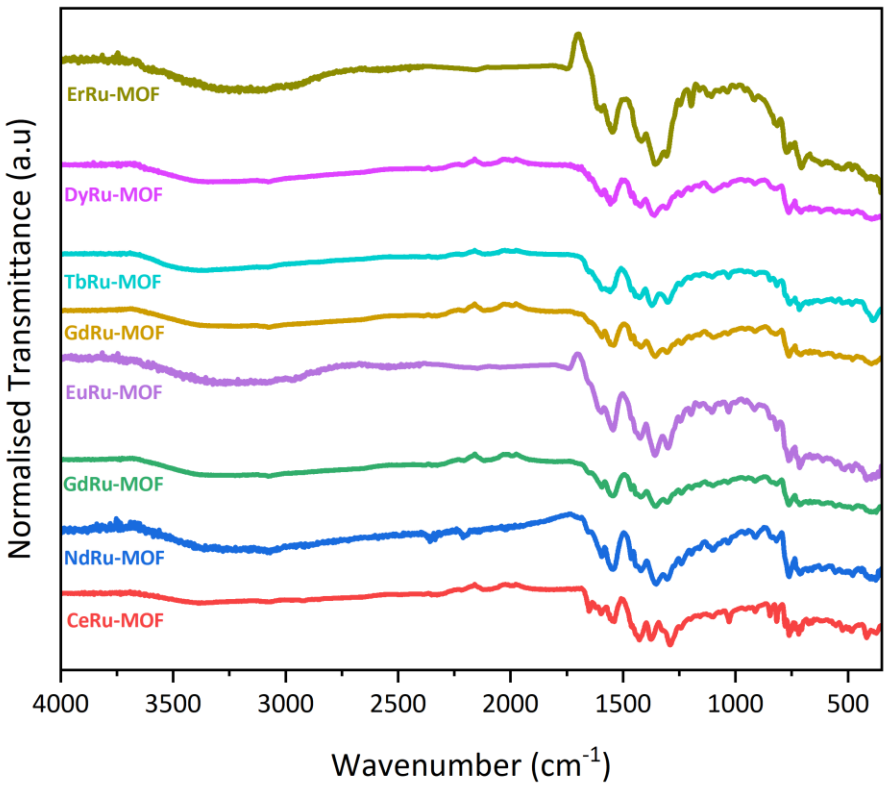

Figure 4.11: FTIR spectra of LnRu-MOFs.

Table 4.5: List of wavenumber values for asymmetric (ν_{as}) and symmetric (ν_s) carboxylate stretching frequencies for each LnRu-MOF compound, as well as the associated shift values ($\Delta\nu$).

Compound	ν_{as} (cm^{-1})	ν_s (cm^{-1})	$\Delta\nu$ (cm^{-1})	ν_{as} (cm^{-1})	ν_s (cm^{-1})	$\Delta\nu$ (cm^{-1})
CeRu-MOF	1597	1443	154	1540	1427	113
NdRu-MOF	1594	1443	151	1545	1420	125
SmRu-MOF	1594	1445	149	1547	1420	127
EuRu-MOF	1596	1444	152	1544	1425	119
GdRu-MOF	1594	1444	150	1546	1422	124
TbRu-MOF	1594	1444	150	1558	1425	133
DyRu-MOF	1596	1444	149	1551	1423	128
ErRu-MOF	1595	1450	145	1547	1419	128
Average ± SD	1595 ± 1	1445 ± 2	150 ± 3	1547 ± 5	1423 ± 3	125 ± 6

4.4.2 Raman Spectroscopy of LnRu-MOFs

As with the FTIR spectra discussed in the previous section, the Raman spectra of the **LnRu-MOFs** (Figure 4.12) are found to be virtually identical across the series. Characteristic vibrational bands are observed at 999 cm^{-1}, 1035 cm^{-1}, 1118 cm^{-1}, and 1151 cm^{-1}, which are attributed to ν(C–H) stretching vibrations associated with aromatic and heteroaromatic moieties. A band at 1200 cm^{-1} corresponds to δ(C–H) bending vibrations, while those at 1277 cm^{-1} and 1320 cm^{-1} can be ascribed to ν(C–C) single bond stretching modes.[38] The symmetric carboxylate stretching vibration, ν_s(COO), is observed as a weak band at 1371 cm^{-1}.[39] Bands at 1492 cm^{-1} and 1591 cm^{-1} are assigned to ν(C=C) stretching vibrations of the aromatic and heteroaromatic systems.[40] Additionally, the band at 2215 cm^{-1} arises from the *ν*(C≡C) triple bond vibrations of the alkyne-moieties.[40]

The Raman spectra of the **LnRu-MOFs** closely match that of the metalloligand **{H_4LRu}**, with only two minor shifts. The δ(C–H) bending vibration shifts from 1200 cm^{-1} in the spectrum of the ligand to 1186 cm^{-1} in the spectra of the MOFs, and one of the ν(C=C) stretching bands is shifted slightly from 1591 cm^{-1} to 1586 cm^{-1}.

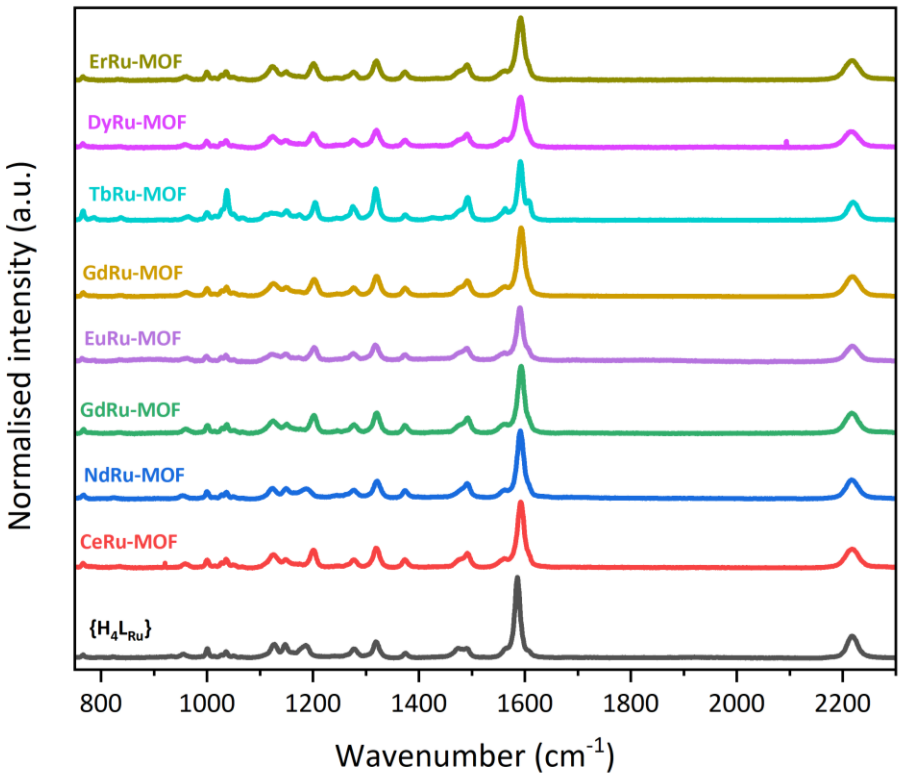

*Figure 4.12: Raman spectra of **LnRu-MOF** compounds and metalloligand **{H_4L_{Ru}}**.*

4.5.3 Scanning Electron Microscopy and Energy Dispersive X-ray Spectroscopy

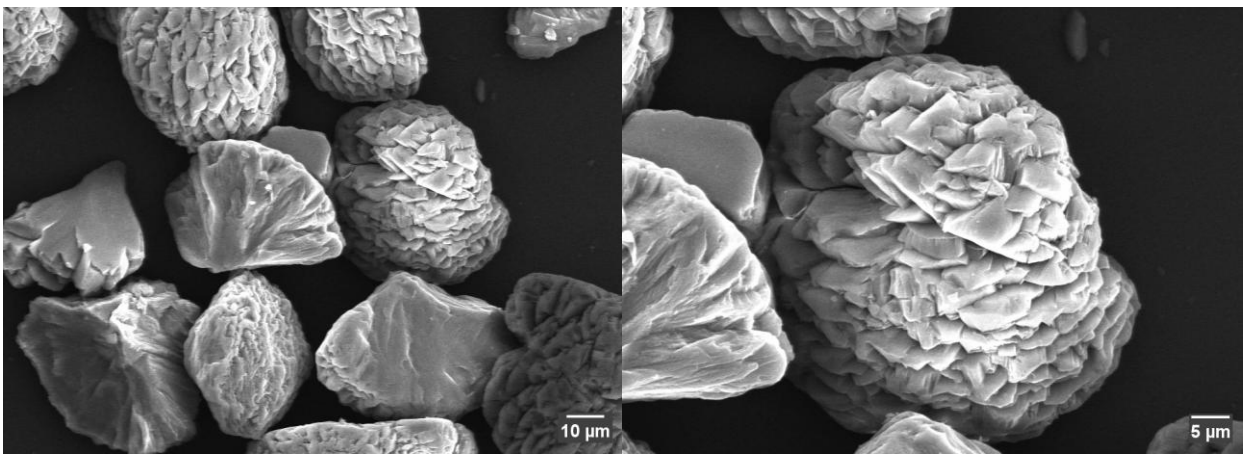

*Figure 4.13: SEM images of **CeRu-MOF** crystals. Taken at an accelerating voltage of 15 kV using a secondary electron detector.*

Scanning electron microscopy (SEM) was employed to examine the morphology of the **LnRu-MOF** crystals. Samples were prepared by drop-casting onto silicon wafers and subsequently sputter-coated with a thin layer of Au/Pd. Imaging was performed using a Zeiss ULTRA Plus SEM operated at an accelerating voltage of 10–20 kV, under a vacuum of 1×10^{-5} mbar, using a secondary electron detector.

Representative SEM images of **CeRu-MOF** crystals are shown in Figure 4.13 and are characteristic of the morphology observed across the **LnRu-MOF** series. The **CeRu-MOF** crystals exhibit a polycrystalline, globular morphology. Closer inspection of individual polycrystals reveals that they are composed of agglomerated, plate-like single crystals.

Energy-dispersive X-ray spectroscopy (EDX) analysis confirmed that all **LnRu-MOF** samples exhibit a lanthanide-to-ruthenium atomic ratio in the range of 1.7:1 to 1.9:1, consistent with the expected stoichiometry of 2:1.

4.5.4 Thermogravimetric Analysis

To access the thermal stability of the **LnRu-MOF** series, TGA measurements were carried out under a nitrogen flow (Figure 4.14). Mass loss below 100 °C can be attributed to the loss of constitutional and coordinated water molecules. Above approximately 250 °C, the organic moieties of the **LnRu-MOFs** undergo thermal degradation. By approximately 460 °C, the organic components are completely degraded, with the remaining materials being remnants of the inorganic SBU, lanthanide and ruthenium oxides, and pyrolytic carbon.

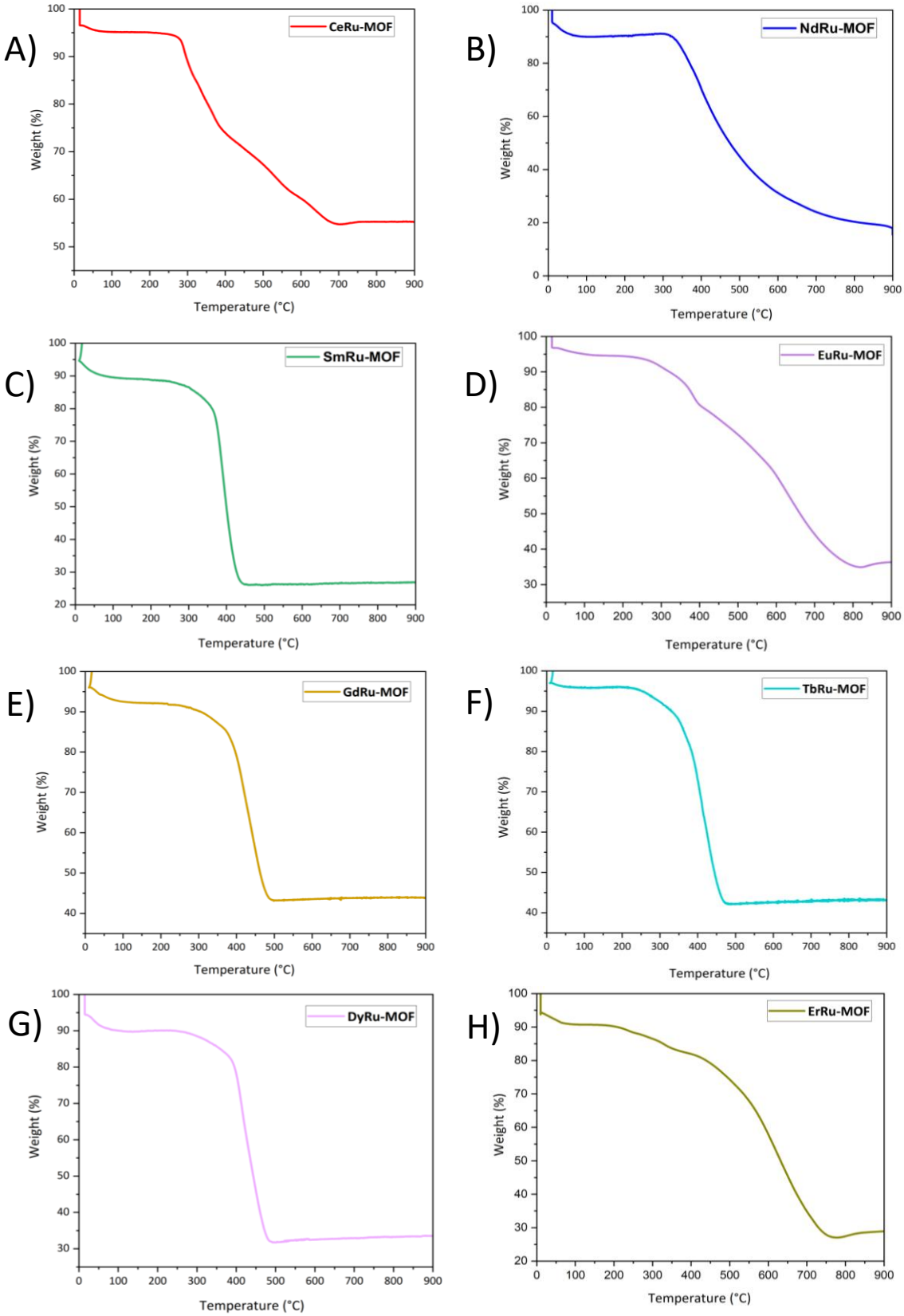

*Figure 4.14: Thermogravimetric analysis of the LnRu-MOF series under nitrogen at a flow rate of 20 ml min^{-1}. A) **CeRu-MOF**; B) **NdRu-MOF**; C) **SmRu-MOF**; D) **EuRu-MOF**; E) **GdRu-MOF**; F) **TbRu-MOF**; G) **DyRu-MOF**; H) **ErRu-MOF**.*

4.6 Photophysical Characterisation

Polypyridyl Ru(II) complexes are well-known photosensitisers and have been extensively studied for a wide range of applications.[9] The photophysical properties of **{H_4L_{Ru}}** have previously been investigated in both solution (**[H_4L_{Ru}]$^{2+}$**) and solid-state forms (**[H_4L_{Ru}](ClO_4)$_2$**).[19] To investigate the effect of immobilising **{L_{Ru}}** within **LnRu-MOFs** on its photophysical behaviour, a series of spectroscopic techniques - absorption, photoluminescence (PL), and time-resolved photoluminescence (TRPL) spectroscopic methods -were employed.

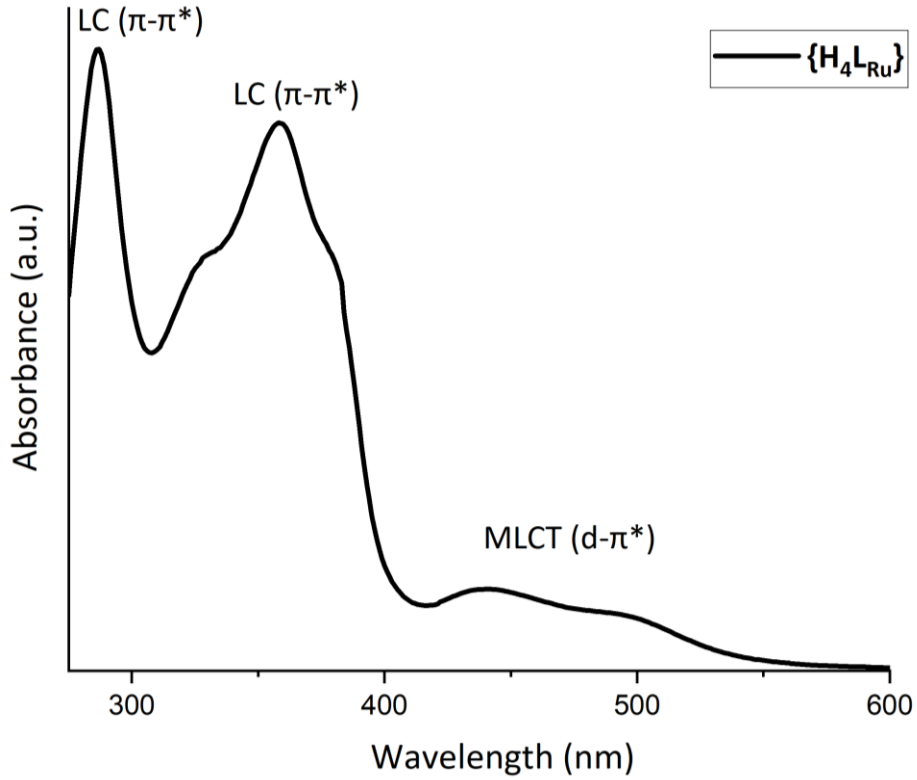

Figure 4.15: UV-vis absorption spectrum of {H_4L_{Ru}}.

The absorption spectrum of **{H_4L_{Ru}}**, shown in Figure 4.15, displays several characteristic features. A strong absorption band centred at 287 nm is assigned to a ligand-centred (LC) π(bpy) → π*(bpy) transition.[9,41] A second prominent absorption band appears at *ca*. 360 nm and is likewise attributed to a LC π → π* transition, in this case originating from the bis-alkynyl-isophthalic acid-functionalised bipyridine ligand.[19,42,43]

A weaker, broad absorption band is observed between 400 and 550 nm, with maxima at approximately 440 and 501 nm. This band arises from metal-to-ligand charge transfer (MLCT) transitions. Its broadness is due to multiple unresolved MLCT transitions, a common feature of polypyridyl Ru(II) complexes when absorption spectra are collected at room temperature.[9,44] The peak at ~440 nm is attributed to a $d\pi^6 \rightarrow d\pi^5\pi^*$ MLCT transition from the t_2g orbital of the Ru(II) metal centre to the π* orbital of a bipyridine.[9] Similarly, the peak at ~501 nm corresponds to a $d\pi^6 \rightarrow d\pi^5\pi^*$ MLCT transition involving the π* orbital of the bis-alkynyl-isophthalic acid-functionalised bipyridine ligand.[42,45]

*Table 4.6: Absorption maxima and associated bathochromic (red) shift of **LnRu-MOFs** in comparison with parent complex, **{H_4L_{Ru}}**.*

Compound	LC (nm)	LC shift (nm)	MLCT (nm)	MLCT shift (nm)
{H_4L_{Ru}}	359	-	501	-
CeRu-MOF	375	16	508	7
NdRu-MOF	407	48	510	9
SmRu-MOF	365	6	502	1
EuRu-MOF	403	44	501	0
GdRu-MOF	378	19	505	4
DyRu-MOF	396	37	515	14
ErRu-MOF	381	22	507	6

Comparisons of the absorption and emission spectra of **{H_4L_{Ru}}** and the **LnRu-MOFs** are presented in Figures 4.16 and 4.17. When comparing the absorption spectra of the **LnRu-MOFs** to that of **{H_4L_{Ru}}**, a general trend emerges: the **LnRu-MOFs** retain the characteristic spectral features of the metalloligand, but exhibit varying degrees of bathochromic (red)

shift in both the ligand-centred (LC) and metal-to-ligand charge transfer (MLCT) bands.

In particular, the LC π → π* transition, associated with the bis-alkynyl-isophthalic acid-functionalised bipyridine moiety (see Table 4.6), undergoes red-shifting to different extents across the series. **NdRu-MOF** and **EuRu-MOF** display the most pronounced shifts, with maxima at 407 nm and 403 nm, corresponding to bathochromic shifts of 48 nm and 44 nm, respectively. In contrast, **SmRu-MOF** exhibits only a modest red shift of 6 nm, with the LC transition observed at 365 nm.

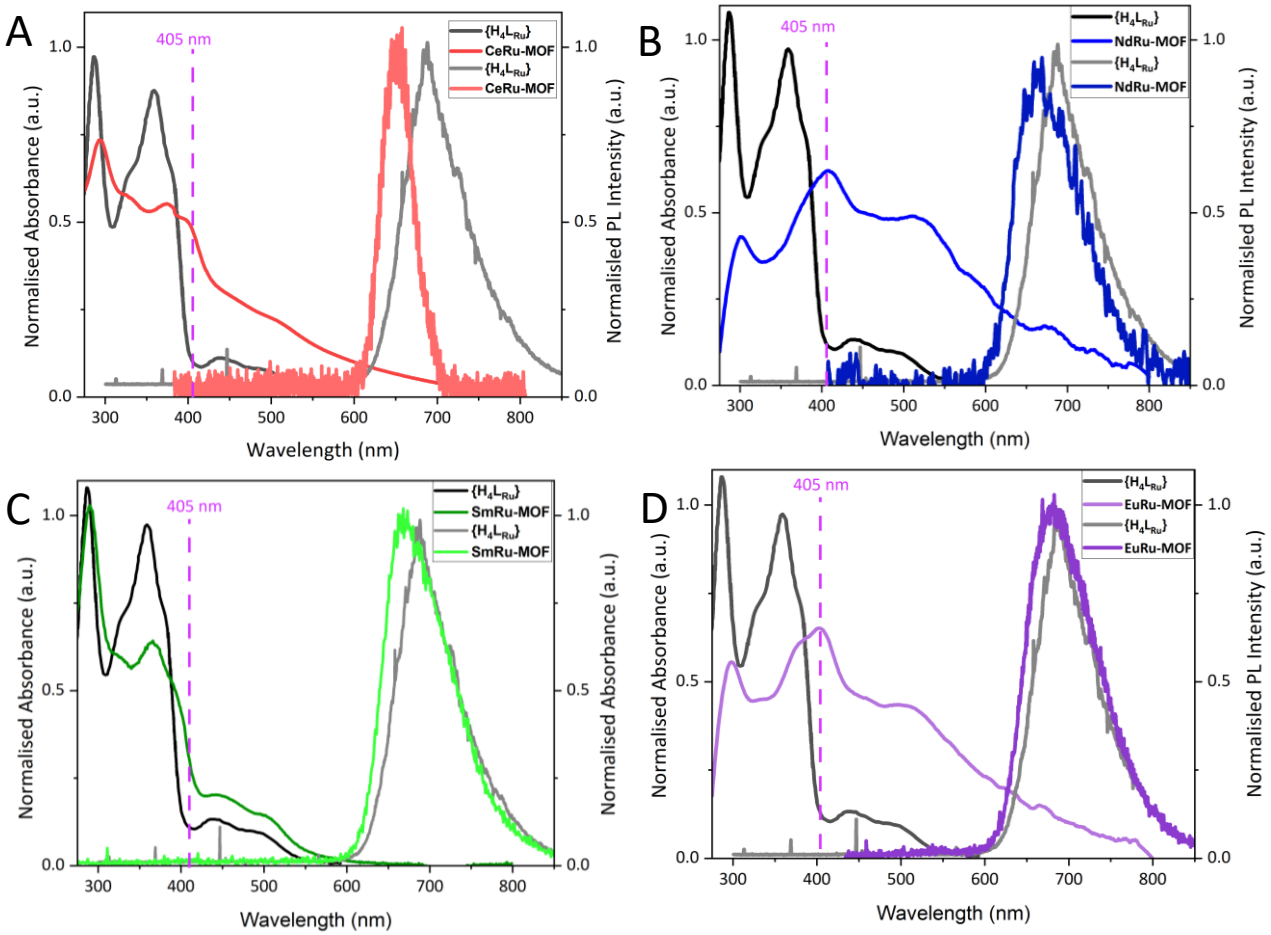

*Figure 4.16: UV-vis absorption (left) and emission (right) spectra of CeRu-MOF (**A**), NdRu-MOF (**B**), SmRu-MOF (**C**), and EuRu-MOF (**D**).*

Solid-state photoluminescence measurements reveal that, when excited at 405 nm, **{H_4L_{Ru}}** exhibits a broad emission spectrum spanning approximately 600–850 nm, with a maximum at 687 nm. All **LnRu-MOFs** display similar emission profiles to **{H_4L_{Ru}}**, with varying degrees of blue shift observed, with the exception of **ErRu-MOF**, which shows a modest red shift relative to **{H_4L_{Ru}}**. Emission maxima and full-width at half-maximum (FWHM) values are summarised in Table 4.7.

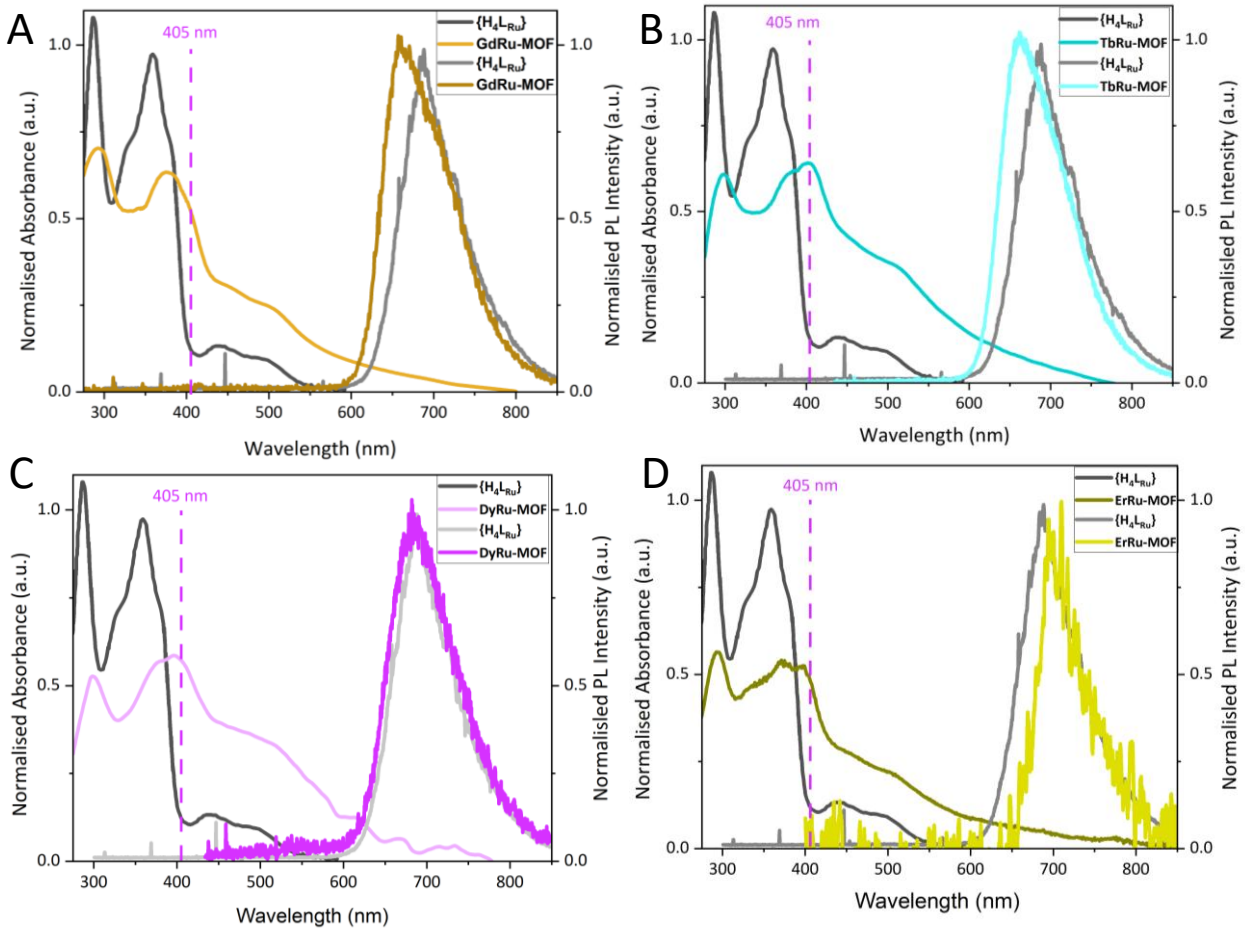

Figure 4.17: UV-Vis absorption (left) and emission (right) spectra of GdRu-MOF (A), TbRu-MOF (B), DyRu-MOF (C), and ErRu-MOF (D).

*Table 4.7: Photoluminescence emission maxima of **LnRu-MOF** series and **{H_4L_{Ru}}** metalloligand.*

Compound	Emission Maxima (nm)	FWHM (nm)
{H_4L_{Ru}}	687	86.7
CeRu-MOF	652	45.9
NdRu-MOF	664	95.2
SmRu-MOF	667	94.0
EuRu-MOF	682	99.1
GdRu-MOF	660	99.1
TbRu-MOF	662	94.3
DyRu-MOF	685	95.0
ErRu-MOF	700	73.4

The most pronounced blue shift (35 nm) is observed for **CeRu-MOF**, which displays an emission maximum at 652 nm and a significantly narrowed emission band ranging from approximately 600 to 700 nm. With a FWHM of 45.9 nm, the **CeRu-MOF** emission is notably sharper than that of **{H_4LRu}** (FWHM = 86.7 nm) or any of the other blue-shifted **LnRu-MOFs** (FWHM = 94–99 nm). **NdRu-MOF**, **SmRu-MOF**, **GdRu-MOF** and **TbRu-MOF** exhibit moderate blue shifts (20 – 27 nm), while **EuRu-MOF** and **DyRu-MOF** show only marginal blue shifts of 5 nm and 2 nm respectively. In contrast, **ErRu-MOF** exhibits a moderately red-shifted (13 nm) emission spectra with a maximum at 700 nm.

When emission band maxima are plotted against Ln(III) ionic radii[46] (see Figure 4.18) a clear trend emerges. As ionic radii decreases from Ce(III) to Eu(III), this coincides with a decrease in the degree of **LnRu-MOF** blue shift (relative to **{H_4L_{Ru}}**) from 35 nm to 5 nm. For Gd(III) there is then a dramatic increase in the degree of blue shift (27 nm), after which the degree of blue shift again decreases with ionic radii from Tb(III) (25 nm) to Dy(III) (2 nm). This is followed by Er(III) with the smallest ionic radius, which appears in the red shifted region of Figure 4.18.

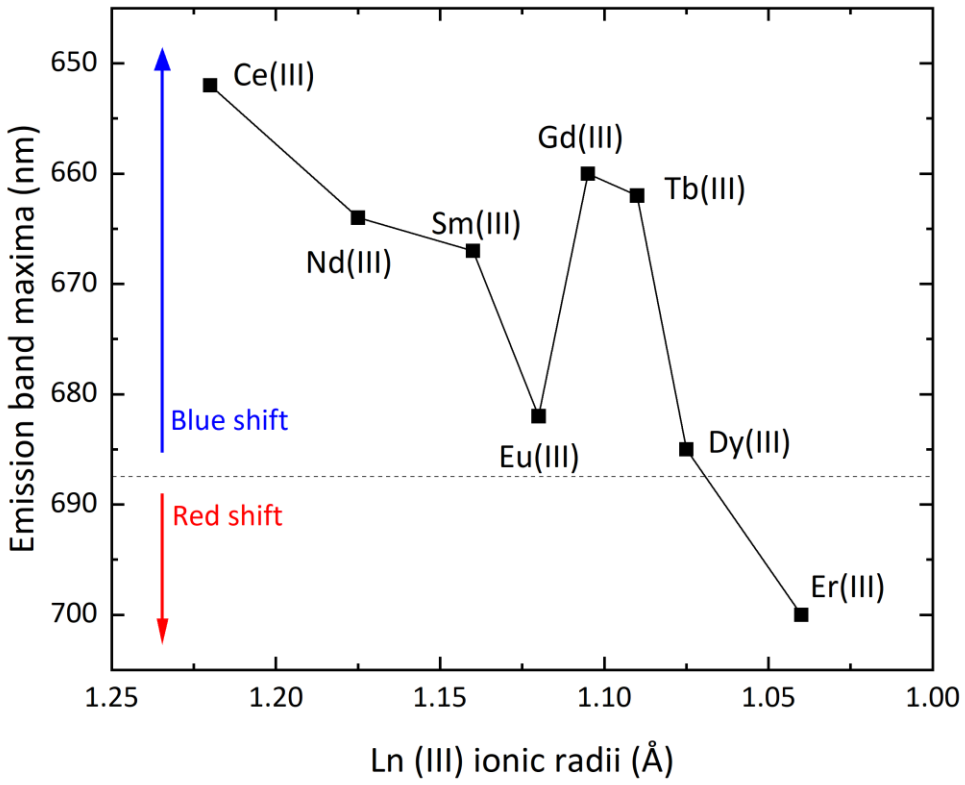

*Figure 4.18: Plot of **LnRu-MOF** emission band maxima versus Ln(III) ionic radii. Dashed line represents emission band maximum of {H_4L_{Ru}}. Ln(III) ionic radii values obtained from D'Angelo et al.*[46]

This trend can be rationalised by considering the *Lewis* acidity of the Ln(III) ions. As the atomic number increases across the lanthanide series, the ionic radii decrease. This is due to the ineffectual atomic shielding provided by the 4*f* electrons, causing the 6*S* electrons to be pulled closer to the nucleus as atomic number increases. This is known as the lanthanide contraction.[46] The *Lewis* acidity, defined as a species' ability to accept an electron pair, increases with the radii contraction due to the increasing positive charge density of the Ln(III) ion. However, there is the well-known *gadolinium break* in the Lewis acidity trend of the lanthanides, where Gd(III) is less *Lewis*-acidic than Eu(III).[47,48] This is explained by Hund's rule, whereby Gd(III) with a half-filled 4*f* sub-shell ($4f^7$) is particularly stable and less willing to accept an electron pair than Eu(III) with its $4f^6$ subshell.[36,49]

Therefore there is a clear relationship between the *Lewis* acidity of the Ln(III) ion in **LnRu-MOF** and its ability to shift the emission wavelength of the **{L_{Ru}}** ligand. It has previously been established that the electron withdrawing nature of the bis-alkynyl moieties and extended π-conjugation of **{H_4L_{Ru}}** influences the LUMO energy of the ligand's π* acceptor

orbital, effectively lowering the energy of its ^{3}MLCT emission band relative to its parent archetype complex, {Ru(bpy)$_3$}, whose emission band centres at 620 nm.[19,42,43] Therefore it would seem plausible that upon coordination of **{L_{Ru}}** to earlier, larger Ln(III) ions with lower *Lewis* acidity , the bis-alkynyl moieties draws electron density from the Ln(III) ions as well as from the Ru(II) metal centre. This effect, results in less electron density being drawn from the Ru(II) metal centre (relative to the uncoordinated metalloligand), increasing the LUMO energy level of the ligands π* acceptor orbital and hence increasing the energy of the ^{3}MLCT emission band. This is observed as a blue shift in the emission band as shown above.

As the ionic radii of Ln(III) ions decrease and their *Lewis* acidity increases, the electron-withdrawing character of the Ln(III) ions also becomes stronger, reducing the bis-alkynyl moieties' ability to withdraw electron density from the Ln(III) ions. As a result, additional electron density is being withdrawn from the Ru(II) metal centre, decreasing the LUMO energy of the ligands π* acceptor orbital and hence decreasing the energy of the ^{3}MLCT emission band. By the time the series reaches Dy(III), its strong *Lewis* acidity leaves very little electron density available for withdrawal by the bis-alkynyl moieties, resulting in only a marginal blueshift of 2 nm. The minimal shift indicates that the LUMO energy of the ligand π* acceptor orbital in **DyRu-MOF** closely matches that of **{H_4L_{Ru}}**.

In the case of **ErRu-MOF**, a red-shift of the emission maximum relative to **{H_4L_{Ru}}** is observed. A logical explanation is that, as a strong Lewis acid, the Er(III) ion has a greater electron-withdrawing ability than the bis-alkynyl moieties. Consequently, more electron density is withdrawn from the Ru(II) centre compared to the uncoordinated **{H_4L_{Ru}}** metalloligand, lowering the energy of the ^{3}MLCT emission band, as reflected in the red-shifted emission band.

*Table 4.8: Average excited state lifetime values, τ_{avg}, calculated (biexponential fit) for each **LnRu-MOF** as well as individual pre-exponential factors and lifetimes*

Material	α_1	τ_1 (ns)	α_2	τ_2 (ns)	τ_{avg} (ns)
{H_4L_{Ru}}	0.0990(9)	7.7(1)	1.396(4)	107.7(7)	107.2(9)
CeRu-MOF	0.183(7)	14(1)	1.49(2)	220(9)	218(10)
NdRu-MOF	0.543(3)	18.2(2)	0.525(3)	85.4(5)	73.2(7)
SmRu-MOF	0.4597(1)	29(2)	0.3038(2)	334(8)	331(10)
EuRu-MOF	0.583(3)	28.9(3)	0.690(3)	313(6)	296(6)
GdRu-MOF	0.0104(2)	20.9(6)	0.03183(7)	235(3)	219(4)
TbRu-MOF	0.403(2)	31.2(4)	1.026(6)	387(6)	376(6)
DyRu-MOF	0.523(3)	20.4(3)	0.590(2)	186(2)	171(2)
ErRu-MOF	0.241(4)	13.8(3)	0.9698(9)	185(1)	182(1)

Time-resolved photoluminescence (TRPL) decay curves of the ^{3}MLCT state for **{H_4L_{Ru}}** and **LnRu-MOFs** are plotted in Figure 4.19. Since the initial decay of the ^{1}MLCT state occurs on the picosecond timescale, it could not be resolved in this experiment due to overlap with the instrument response function (IRF).The measured photoluminescence decay curves were fitted to a bi-exponential model, and average lifetimes (τ_{avg}) were calculated using Eq. 4.1, where α_i and τ_i are the pre-exponential factor and lifetime of the i^{th} component, respectively. Table 4.8 lists τ_{avg} values calculated for the **LnRu-MOF** series as well as the respective pre-exponential factors and lifetimes.

$$\tau_{avg} = \frac{\sum \alpha_i \tau_i^2}{\sum \alpha_i \tau_i} \qquad \textit{Eq. 4.1}$$

The metalloligand **{H_4L_{Ru}}** exhibited a photoluminescence decay with an average lifetime of 107 ns. With the exception of **NdRu-MOF**, all **LnRu-MOFs** exhibited longer average lifetimes than **{H_4L_{Ru}}**, ranging from 171 ns for **DyRu-MOF** to 376 ns for **TbRu-MOF**. This suggests that the coordination of **{L_{Ru}}** to these Ln(III) ions forming a rigid metal-organic frameworks, improves intersystem crossing (ISC) and the stability of the ^{3}MLCT state.

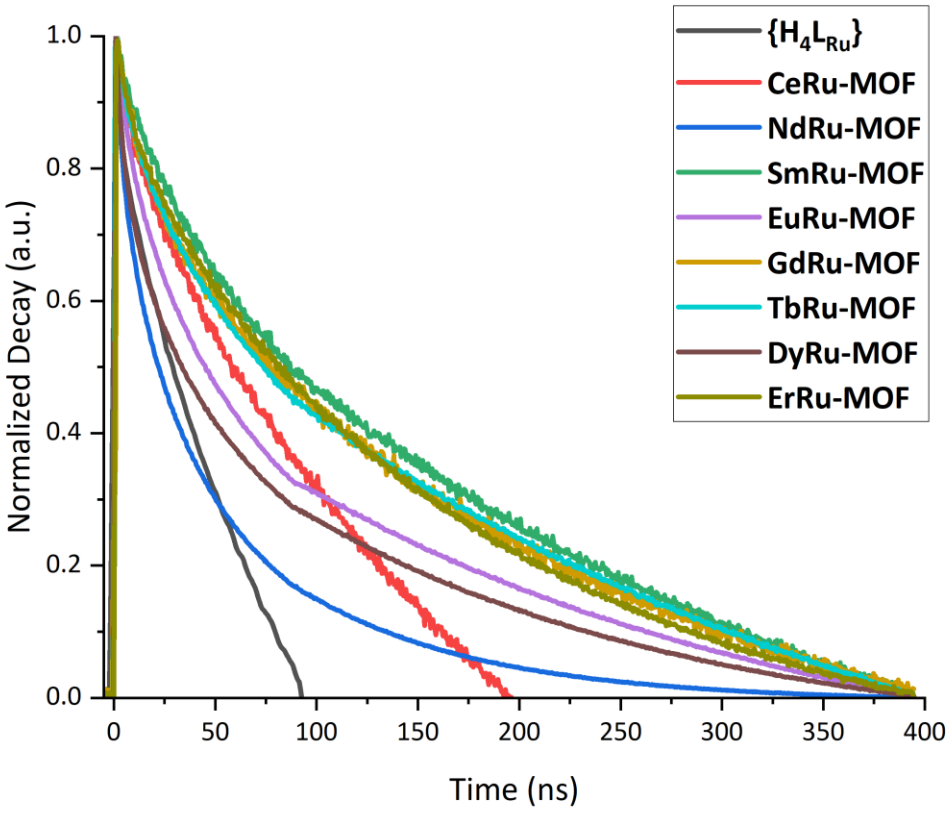

*Figure 4.19: Normalised time-resolved photoluminescence (TRPL) decay curves of the ^{3}MLCT state for **{H_4L_{Ru}}** and **LnRu-MOFs.***

4.7 Conclusion

A novel isostructural series of two-dimensional lanthanide-based metal–organic frameworks (**LnRu-MOF,** Ln = Ce, Nd, Sm, Eu, Gd, Tb, Dy, Er) was synthesised using the Ru(II) polypyridyl metalloligand **{H_4L_{Ru}}** as a photosensitising linker. The series is structurally uninterrupted by the *gadolinium break* in *Lewis* acidity (a rare outcome in lanthanide coordination chemistry) and features dinuclear Ln(III) SBUs with labile binding sites that may enable substrate coordination for catalysis. Phase purity across the series was confirmed by PXRD, supported by FTIR, Raman, TGA, and SEM-EDX characterisation.

The two-dimensional metal–organic layers extend in the *ab* plane and stack along the *bc* plane in two alternating configurations, interdigitating through C–H···π interactions and further associating via π–π interactions between isophthalate moieties to form a three-dimensional lattice.

Photophysical characterisation showed that the archetypal properties of the [$Ru(bpy)_3$] parent complex are preserved within the MOF. Coordination of Ln(III) shifts the emission relative to the free **{H_4L_{Ru}}** metalloligand, with the direction and magnitude of the shift tracking Ln(III) *Lewis* acidity and clearly reflecting the *gadolinium break*. Time-resolved measurements further revealed that incorporation into the rigid 2D framework extends the average Ru(II) ^{3}MLCT excited-state lifetime for all Ln(III) studied except Nd.

This extended excited-state lifetime positions the **LnRu-MOFs** as candidate photosensitisers and photocatalysts, which the following chapter examines.

References

1. É. Whelan, F. W. Steuber, T. Gunnlaugsson, W. Schmitt, *Coord. Chem. Rev.,* 2021, **437**, 213757.
2. J. Hao, X. Xu, H. Fei, L. Li, B. Yan, *Adv. Mater.* 2018, **30**, 1705634.
3. C. J. Setter, M. B. Price, L. Conte, W. Schmitt, S. R. Batten, C. Richardson, M. R. Hill, R. Babarao and L. K. Macreadie, *Chem. Commun.*, 2020, **56**, 13377 —13380.
4. H. A. Schwartz and U. Ruschewitz, *Struct. Bonding*, 2020, **183**, 105.
5. S. Yuan, J.-S. Qin, H.-Q. Xu, J. Su, D. Rossi, Y. Chen, L. Zhang, C. Lollar, Q. Wang, H.-L. Jiang, D. H. Son, H. Xu, Z. Huang, X. Zou and H.-C. Zhou, *ACS Cent. Sci.*, 2017, **4**, 105 —111.
6. L. Martins, L. K. Macreadie, D. Sensharma, S. Vaesen, X. Zhang, J. J. Gough, M. O'Doherty, N.-Y. Zhu, M. Rüther, J. E. O'Brien, A. L. Bradley and W. Schmitt, *Chem. Commun.*, 2019, **55**, 5013.
7. R. Elliott, A. A. Ryan, A. Aggarwal, N. Zhu, F. W. Steuber, M. O. Senge and W. Schmitt, *Molecules*, 2021, **26**, 1 —16.
8. T. J. Meyer, *Acc. Chem. Res.*, 1989, **22**, 163–170.
9. D. W. Thompson, A. Ito, and T. J. Meyer, *Pure Appl. Chem.*, 2013, **85**, 7, 1257–1305.
10. L. Duan, F. Bozoglian, S. Mandal, B. Stewart, T. Privalov, A. Llobet and L. Sun, *Nat. Chem.*, 2012, **4**, 418–423.
11. C. K. Prier, D. A. Rankic and D. W. C. MacMillan, *Chem. Rev.*, 2013, **113**, 5322–5363.
12. T. Zhang and W. Lin, *Chem. Soc. Rev.*, 2014, **43**, 5982–5993.
13. T. Mede, M. Jäger and U. S. Schubert, *Chem. Soc. Rev.*, 2018, **47**, 7577 —7627.
14. A. Santiago-Portillo, H. G. Baldoví, E. Carbonell, S. Navalón, M. Álvaro, H. García and B. Ferrer, *J. Phys. Chem. C*, 2018, **122**, 29190–29199.
15. Y.-X. Tan, S.-X. Lin, C. Liu, Y. Huang, M. Zhou, Q. Kang, D. Yuan and M. Hong, *Appl. Catal. B*, 2018, **227**, 425 —432.
16. W. A. Maza, S. R. Ahrenholtz, C. C. Epley, C. S. Day and A. J. Morris, *J. Phys. Chem. C*, 2014, **118**, 14200–14210.
17. H.-G. Jin, P.-C. Zhao, Y. Qian, J.-D. Xiao, Z.-S. Chao and H.-L. Jiang, Chem. Soc. Rev., 2024, 53, 9378 —9418.

18. Y. Zhao, G. Che, X. Li, T. Lei, Q. Pan, Z. Su, W. Yang, *Separ. Purif. Technol.*, 2025, **356**, 130004.
19. M. Mulahmetović, PhD Thesis, University of Dublin, 2023.
20. L. Zedler, P. Wintergerst, A. K. Mengele, C. Müller, C. Li, B. Dietzek-Ivanšić & S. Rau, *Nat. Commun.*, 2022, **13**, 2538.
21. Z.-H. Yan, M.-H. Du, J. Liu, S. Jin, C. Wang, G.-L. Zhuang, X.-J. Kong, L.-S. Long & L.-S. Zheng, *Nat. Commun.*, 2018, **9**, 3353.
22. D. D'Souza, D. Leigh, M. Papmeyer, and S. Woltering, *Nat. Protoc.*, 2012, **7**, 2022–2028.
23. R. Seetharaj, P.V. Vandana, P. Arya, S. Mathew, *Arab. J. Chem.*, 2019, **12**, 295–315.
24. K. Patra and H. Pal, *RSC Sustainability*, 2025, **3**, 629.
25. Ü. Kökçam-Demir, A. Goldman, L. Esrafili, M. Gharib, A. Morsali, O. Weingart and C. Janiak, *Chem. Soc. Rev.*, 2020, **49**, 2751–2798.
26. O.V. Dolomanov, L.J. Bourhis, R.J. Gildea, J.A.K. Howard, H. Puschmann, *J. Appl. Cryst.*, 2009, **42**, 339-341.
27. F. Morsbach, S. Klenner, R. Pöttgen and W. Frank, *Dalton Trans.*, 2022, **51**, 4814-4828.
28. S. Alvarez, P. Alemany, D. Casanova, J. Cirera, M. Llunell and D. Avnir, *Coord. Chem. Rev.*, 2005, **249**, 1693–1708.
29. I. D. Brown and D. Altermatt, *Acta Crystallogr. Sect. B Struct. Sci.*, 1985, **41**, 244–247.
30. A. Altomare, M. Camalli, C. Cuocci, C. Giacovazzo, A. Moliterni, R. Rizzi, *J. Appl. Cryst.*, 2009, **42**, 1197–1202.
31. A. Trzesowska, R. Kruszynski and T. J. Bartczak, *Acta Crystallogr. Sect. B Struct. Sci.*, 2004, **60**, 174–178.
32. C. Janiak, *J. Chem. Soc., Dalton Trans.*, 2000, **21**, 3885–3896.
33. M. J. Plevin, D. L. Bryce and J. Boisbouvier, *Nature Chem*, 2010, **2**, 466–471.
34. C. F. Holder and R. E. Schaak, *ACS Nano,* 2019, **13**, 7, 7359–7365.
35. A. Le Bail, *Powder Diffr.*, 2005, **20**, 316–326.
36. D. Müller, C. Knoll, A. Herrmann, G. Savasci, J. M. Welch, W. Artner, J. Ofner, B. Lendl, G. Giester, P. Weinberger, and G. Steinhauser, *Eur. J. Inorg. Chem.*, 2018, **19**, 1969–1975.

37. G. B. Deacon and R. J. Phillips, *Coord. Chem. Rev.*, 1980, **33**, 227–250.
38. D. Lin-Vien, N. B. Colthup, W. G. Fateley and J. G. Grasselli, *The Handbook of Infrared and Raman Characteristic Frequencies of Organic Molecules*, Elsevier, 1991, 277–306.
39. K. Nakamoto, *Infrared and Raman Spectra of Inorganic and Coordination Compounds*, Part B, Wiley, 6th Edition, 2008, 64-67.
40. E. Smith and G. Dent, *Modern Raman Spectroscopy: A Practical Approach*, Wiley, New York, 2005.
41. P. Innocenzi, H. Kozuka and T. Yoko, *J. Phys. Chem. B*, 1997, **101**, 2285–2291.
42. M. Shiotsuka, Y. Tsuji, K. Keyaki and K. Nozaki, *Inorg. Chem.*, 2010, **49**, 4186-4193.
43. S. Fraysse, C. Coudret and J.-P. Launay, *J. Am. Chem. Soc.*, 2003, **125**, 5880–5888.
44. S. Xu, J. E. T. Smith and J. M. Weber, *J. Chem. Phys.*, 2016, **145**, 024304.
45. A. Garoufis, A. Koutsodimou, N. Katsaros, C.-A. Mitsopoulou and N. Hadjiliadis, *Polyhedron*, 1998, **18**, 361–369.
46. P. D'Angelo, A. Zitolo, V. Migliorati, G. Chillemi, M. Duvail, P. Vitorge, S. Abadie, and R. Spezia, *Inorg. Chem.*, 2011, **50**, 4572–4579.
47. G. Gibson, A. A. Neverov, and R.S. Brown, *Can. J. Chem*., 2003, **81**, 495–504.
48. H. Tsuruta, K. Yamaguchi and T. Imamoto, *Tetrahedron*, 2003, **59**, 10419–10438.
49. M. Laing*, J. Chem. Educ.* 2009, 86, 2, 188.

Chapter 5: LnRu-MOFs for Photocatalytic and Photoelectrocatalytic Applications (Ln = Ce or Eu).

5.1 Introduction

The previous chapter reported the synthesis and characterisation of an isostructural series of two-dimensional lanthanide-based metal–organic frameworks (**LnRu-MOFs**), composed of dinuclear Ln^{III} secondary building units (SBUs) and Ru(II) polypyridyl metalloligands acting as photosensitising linkers.

This chapter builds on that work by investigating the potential photocatalytic and photoelectrocatalytic applications of **CeRu-MOF** and **EuRu-MOF**. Both cerium and europium possess redox couples (Ce^{3+}/Ce^{4+} and Eu^{3+}/Eu^{2+}, respectively) that are accessible for catalysis. As demonstrated in Chapters 2 and 3, the Ce^{3+}/Ce^{4+} redox couple (1.61 V vs. SHE)[1] is well suited to oxidation reactions, such as the water oxidation reaction (OER). By contrast, the Eu^{3+}/Eu^{2+} redox couple (–0.35 V vs. SHE)[1,2] is suitable for reduction processes, including the hydrogen evolution reaction (HER) and the CO_2 reduction reaction (CO_2RR).[1-6]

Yan et al. synthesised a europium-based MOF incorporating modified $[Ru(phen)_3]^{2+}$ metalloligands as linkers and demonstrated its efficacy as a robust photocatalyst for CO_2 reduction to formate.[6] In that system, photo-excitation of the Ru-based metalloligands initiated electron transfer to the inorganic SBUs, thereby generating Eu(II) centres that served as the active sites for CO_2 reduction.

Inspired by this precedent, this chapter explores the use of **CeRu-MOF** and **EuRu-MOF** as photocatalysts, in which Ru-based metalloligands photosensitise the Ce^{3+}/Ce^{4+} or Eu^{3+}/Eu^{2+} redox couples. Building on this further, the integration of these materials into a photoelectrochemical (PEC) cell will be investigated, with the aim of combining the advantages of both photocatalytic and electrocatalytic pathways.

5.2 Preliminary Photocatalytic Water Splitting Study

Photocatalytic water splitting experiments were carried out using a two-component system comprising a photocatalyst (**CeRu-MOF**, **EuRu-MOF**, or their parent metalloligand, **$[H_4L_{Ru}](ClO_4)_2$**) and either a sacrificial electron acceptor (SEA) or a sacrificial electron donor (SED) in Millipore deionised water. Sodium persulfate was used as the SEA for OER experiments, and methanol was used as the SED for HER experiments.[7,8]The two-component systems were purged with pure Ar gas inside hermetically sealed borosilicate glass vials equipped with rubber septa and magnetic stirring bars. A Clark electrode with a piercing needle tip (UNISENSE, OX NP or H_2 NP) was inserted into the reaction solution *via* the septum. Once a stable baseline was established in the dark, the reaction vessel was illuminated with a 465 nm LED light source (44 mW cm^{-2}), and the dissolved O_2 or H_2 concentrations were measured over time using the Clark electrode, which was connected to a UNISENSE Monometer.

5.2.1 Photocatalytic OER with CeRu-MOF

The development of new photocatalysts for the thermodynamically and kinetically demanding water oxidation half-reaction is crucial for advancing efficient artificial photosynthetic systems.[9] In homogeneous photocatalytic OER systems employing separate photosensitisers and water-oxidation catalysts, electron transfer between these two components is often the rate-limiting step in O_2 production.[10] It was hypothesised that integrating the photosensitiser and water-oxidation catalyst into a single heterogeneous framework could mitigate this kinetic bottleneck by enabling direct electron transfer through the conjugated organic backbone of the MOF. In the case of **CeRu-MOF**, the polypyridyl Ru(II) moiety would act as the photosensitiser, while the dinuclear Ce-based inorganic SBU—bearing labile solvent coordination sites—would serve as the water-oxidation catalyst. Electron transfer between the two metal centres could be facilitated by the conjugated alkynyl-bridged organic backbone of **CeRu-MOF**, a structural motif that has been reported to enhance electron-transfer kinetics between Ru-based photosensitisers and catalytic metal centres.[11] This was evidenced in Chapter 4, where solid-state photophysical characterisation indicated that the alkynyl moieties were capable of withdrawing electron density from the cerium metal centres.

Cyclic voltammetry (CV) of **CeRu-MOF** in an organic electrolyte (0.1 M TBA PF_6 in acetonitrile) revealed that the Ru(II)/Ru(III) and Ce(III)/Ce(IV) redox couples overlap, further suggesting that electron transfer between the two metal centres is possible. Figure 5.1a presents the CV data for **CeRu-MOF**. In the first cycle, a large oxidation peak is observed at 1.18 V; this peak does not appear in subsequent cycles, indicating that the Ce(III)→Ce(IV) oxidation is irreversible under these conditions. From the second cycle onwards, only a smaller oxidation peak at 1.07 V is observed, which can be attributed to the Ru(II)→Ru(III) oxidation. All cycles display a reduction peak at 1.00 V, which could correspond to both the Ce(IV)→Ce(III) and Ru(III)→Ru(II) reductions; however, as the irreversible Ce(III)→Ce(IV) oxidation occurs first, it is likely that only the Ru(III)→Ru(II) reduction contributes to this peak. These assignments were verified by recording CVs of 10 mM $Ce(NO_3)_3$, followed by the addition of $[Ru(bpy)_3]Cl_2$ to the electrolyte and acquisition of additional CVs, which confirmed the overlap of the Ru(II)/Ru(III) and Ce(III)/Ce(IV) redox couples (Figure 5.1b). For **CeRu-MOF**, the $E_{1/2}$ for the Ce(III)/Ce(IV) redox couple was calculated to be 1.09 V, while the $E_{1/2}$ for the Ru(II)/Ru(III) redox couple was calculated to be 1.04 V. This reinforces the plausibility of electron transfer between metal centres. It is also worth noting that the irreversibility of the Ce oxidation is consistent with the Ce(IV) species being consumed by water oxidation in photocatalytic experiment described below, with the catalytic cycle relying on the regeneration of Ce(III) by oxidation of water rather than by an electrochemical reduction step.

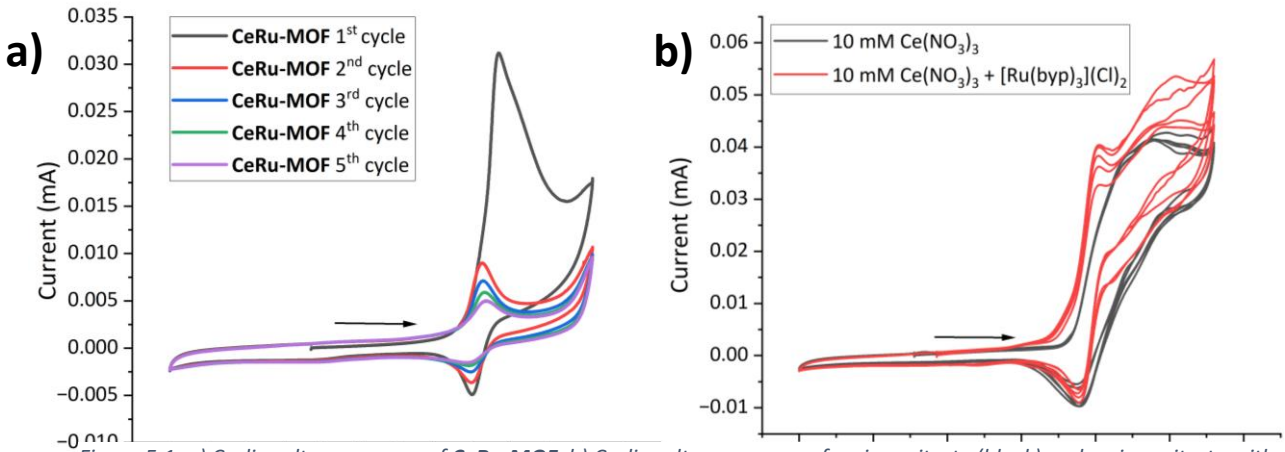

*Figure 5.1: a) Cyclic voltammogram of **CeRu-MOF**. b) Cyclic voltammogram of cerium nitrate (black) and cerium nitrate with the addition of tris(bipyridine)ruthenium(II) chloride. CVs carried out in deaerated 0.1 M TBA PF_6, acetonitrile electrolyte, using a Ag/Ag^+ reference electrode, glassy carbon working electrode and platinum counter electrode, at a scan rate of 100 mV s^{-1}.*

The photocatalytic OER activity of **CeRu-MOF** was assessed according to the procedure described above and detailed in Experimental Section 6.1.14. Control experiments were performed on the individual components of the two-component system (photocatalyst and SEA), with no O_2 evolution observed when only a single component was irradiated (465 nm, 44 mW cm^{-2}). Figure 5.2a illustrates this, with no O_2 detected in the irradiated reaction solution containing **CeRu-MOF** until the SEA (deaerated sodium persulfate solution) was injected into the reaction vessel *via* the septum, at which point O_2 evolution commenced immediately. When an aqueous solution containing **CeRu-MOF** and 10 mM $Na_2S_2O_8$ was deaerated in the dark and then irradiated (Figure 5.2b), O_2 evolution was observed to begin simultaneously with light irradiation and continued steadily for approximately 12 hours, resulting in an O_2 yield of ~145 µmol/$mmol_{cat}$.

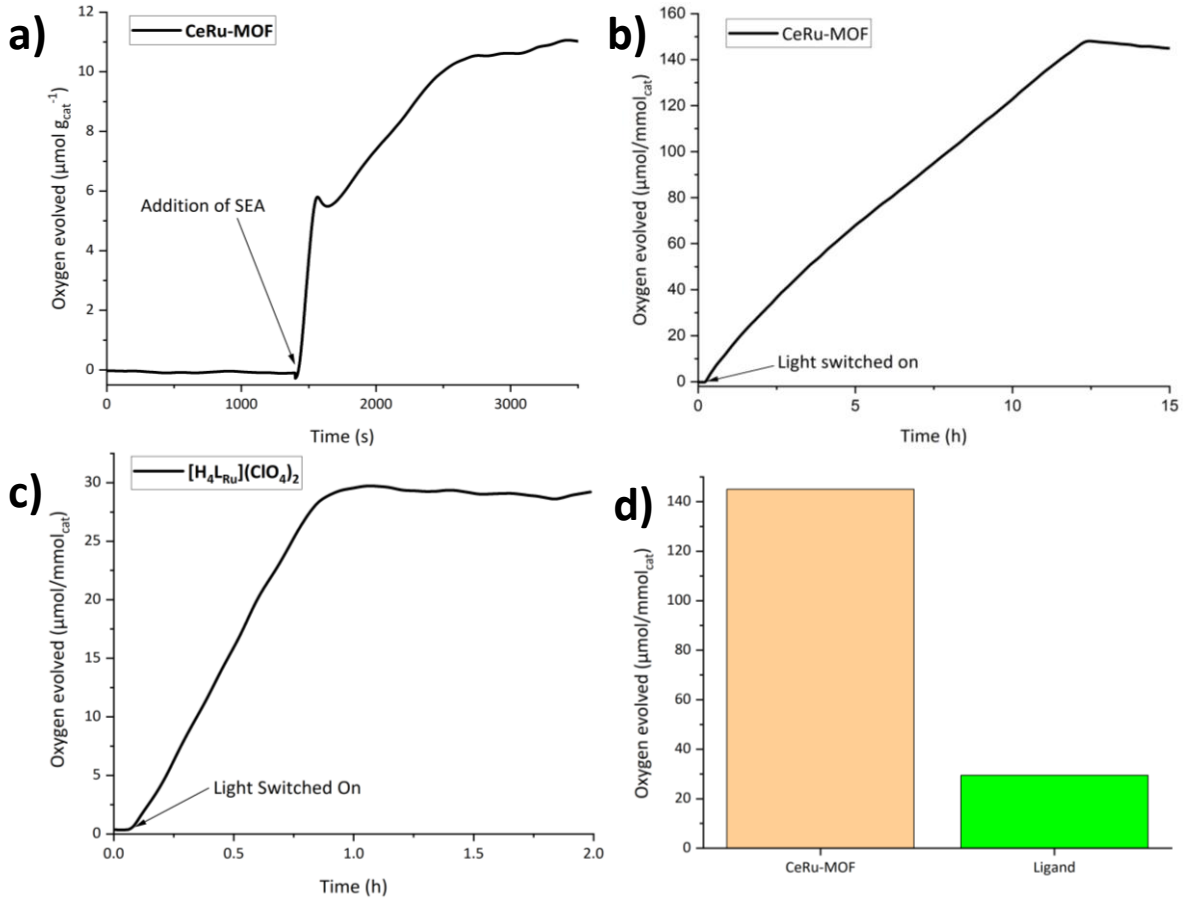

*Figure 5.2: a) Photocatalytic OER activity of **CeRu-MOF** before and after addition the sacrificial electron acceptor (SEA) $Na_2S_2O_8$. b) Photocatalytic OER activity of reaction solution containing **CeRu-MOF** and $Na_2S_2O_8$, O_2 evolution is observed to begin upon light irradiation. c) Photocatalytic OER activity of reaction solution containing **$[H_4L_{Ru}](ClO_4)_2$** and $Na_2S_2O_8$, O_2 evolution is observed to begin upon light irradiation. d) Comparison of OER activity between **CeRu-MOF** and parent metalloligand **$[H_4L_{Ru}](ClO_4)_2$**.*

The same experiment, when repeated using **$[H_4L_{Ru}](ClO_4)_2$** crystals in place of **CeRu-MOF** (Figure 5.2c), also resulted in O_2 evolution upon light irradiation; however, activity persisted for only approximately 1 hour, giving an O_2 yield of ~30 μmol/$mmol_{cat}$ (see Figure 5.2d for yield comparison). The reduced operational lifetime of **$[H_4L_{Ru}](ClO_4)_2$** can be attributed to degradation of the polypyridyl Ru(II) complex. It is well established in the literature that $[Ru(bpy)_3]^{3+}$ is unstable under aqueous conditions, as its bipyridine ligands are susceptible to nucleophilic attack by hydroxyl anions, leading to ligand loss and catalyst degradation.[8,10]

Furthermore, repeating the experiment with **EuRu-MOF** and **GdRu-MOF** did not result in measurable O_2 evolution (Appendix D), further confirming that the dinuclear cerium SBUs serve as the active sites for OER catalysis.

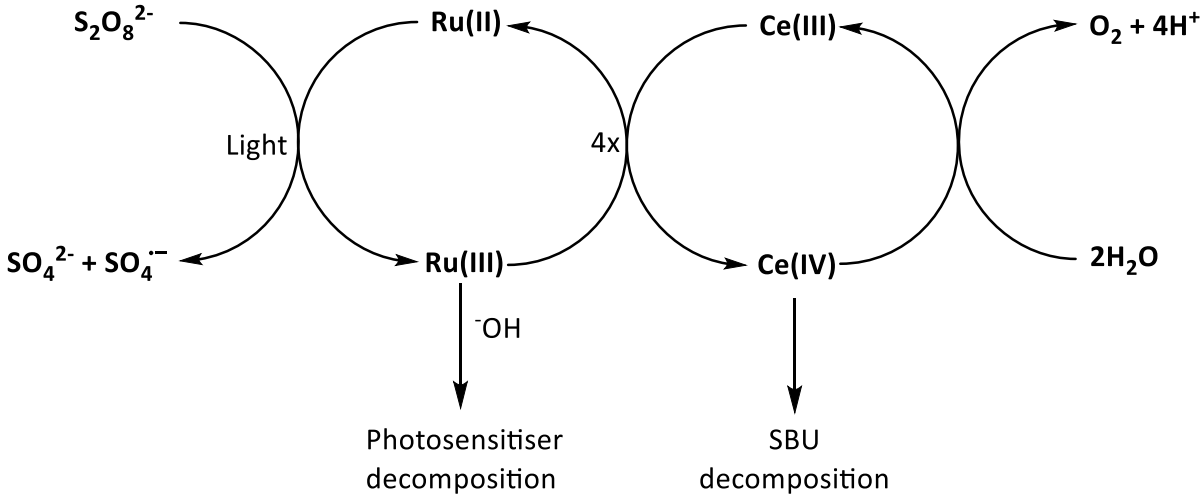

*Figure 5.3: Simplified schematic of the proposed photocatalytic OER mechanism for **CeRu-MOF**.*

Figure 5.3 presents a simplified schematic of the proposed photocatalytic OER mechanism for **CeRu-MOF**. Upon light absorption, the polypyridyl Ru(II) moiety undergoes a metal-to-ligand charge transfer (MLCT) transition, in which an electron from the t_2g orbital of the Ru(II) metal centre is promoted to the π* orbital of a bipyridine ligand. This excited state is quenched by the presence of $S_2O_8^{2-}$, which acts as a sacrificial electron acceptor, resulting in oxidation of the Ru(II) centre to Ru(III). This process has long been established in the literature.[10,12] Taking photophysical (Chapter 4) and cyclic voltammetry experiments (Figure 5.1) into account, it is likely that electron transfer then occurs from an adjacent Ce(III) metal centre to the Ru(III) centre, regenerating Ru(II) and producing Ce(IV), which serves as the active site for water oxidation. The water oxidation reaction,

in turn, regenerates the Ce(III) site, completing the catalytic cycle.

Several decomposition pathways could interrupt this catalytic process. These include the previously mentioned nucleophilic attack on the polypyridyl Ru(III) moiety by hydroxyl anions—although this may be mitigated by rapid electron transfer from Ce(III)—and the generation of sulfate radical anions ($SO_4^{\bullet -}$) via reduction of $S_2O_8^{2-}$. The latter is a powerful oxidising agent and may contribute to photocatalyst degradation.[10]

Table 5.1 compares the O_2 evolution rate of **CeRu-MOF** with values reported in the literature for other MOF-based photocatalysts. Significantly, **CeRu-MOF** appears to outperform favourably relative to other Ce- and Ti-based MOF photocatalysts, exhibiting a rate of 12.1 µmol h^{-1} $mmol_{cat}^{-1}$, compared to 10.2 µmol h^{-1} $mmol_{cat}^{-1}$ for **Ce-UiO-66-NO_2** reported by Dai et al.[13] and 5.5 µmol h^{-1} $mmol_{cat}^{-1}$ for the trimetallic **UiO-66(Zr/Ce/Ti)**. In terms of other MOF benchmarks in the literature, Guo et al.[17] reported the Hg-based MOF **CQNU-1** with a markedly higher O_2 evolution rate of 85.0 µmol h^{-1} $mmol_{cat}^{-1}$. However, any direct comparison between studies should be made with caution, as variations in experimental conditions can significantly influence the reported O_2 evolution rates. For instance, Guo et al. employed a light source with an intensity of ~100 mW cm^{-2} (compared to ~44 mW cm^{-2} in this work), for just 1 hour, using a different catalyst loading, and $AgNO_3$ as SEA rather than $Na_2S_2O_8$. Furthermore, O_2 evolution was quantified from the headspace using inline gas chromatography, whereas in this study dissolved O_2 concentrations in the reaction solution were measured using a Clark electrode. Both approaches are valid, but these methodological differences should be kept in mind when making comparisons.

*Table 5.1: Comparison the O_2 evolution rate of **CeRu-MOF** with values reported in the literature for other Ce- and Ti-based MOF -based photocatalysts.*

MOF Photocatalyst	Rate of O_2 Evolution (µmol h^{-1} $mmol_{cat}^{-1}$)	Reference
CeRu-MOF	12.1	This work
Ce-UiO-66-NO_2	10.2	13
IEF-11	0.82	14
Oxygen-plasma treated MIL-125(Ti)-NH_2	2.1	15

UiO-66(Zr/Ce/Ti)	5.5	16

5.2.2 Photocatalytic HER with EuRu-MOF and CeRu-MOF

The photocatalytic HER activity of **EuRu-MOF**, **CeRu-MOF** and of the parent metalloligand **$[H_4L_{Ru}](ClO_4)_2$** was assessed according to the procedure described above and detailed in Experimental Section 6.1.14. No hydrogen evolution was observed under light irradiation until both components of the two-component systems (photocatalyst and SED) were combined. Figure 5.4.a,b and c illustrates this, with no H_2 detected in the irradiated aqueous solution containing **EuRu-MOF**, **CeRu-MOF** or **$[H_4L_{Ru}](ClO_4)_2$** until the SED (deaerated methanol) was injected into the reaction vessel via the septum, at which point H_2 evolution commenced immediately, reaching 64 μmol $mmol^{-1}$, 47 μmol $mmol^{-1}$ and 24 μmol $mmol^{-1}$ within approximately 150, 180 and 130 seconds, respectively. At this point H_2 evolution is observed to level off instead of increasing with irradiation time. This can be rationalised by considering that in batch reactions an equilibrium is reached between H_2 evolution and H_2 decomposition, as well as the generation of byproducts what may poison or degrade the catalyst.[13] It is also noteworthy that **CeRu-MOF** appears to photocatalyse both OER and HER depending on whether either a SEA or SED is present, respectively. This would make **CeRu-MOF** a bifunctional water splitting photocatalyst according to some definitions[17], however many would reserve the term for a photocatalyst that can perform both half-reactions simultaneously, without the presence of sacrificial electron donors or acceptors. **CeRu-MOF** should therefore be regarded as a single photocatalyst capable of driving either half-reaction under appropriate sacrificial conditions, rather than as an overall water splitting catalyst.

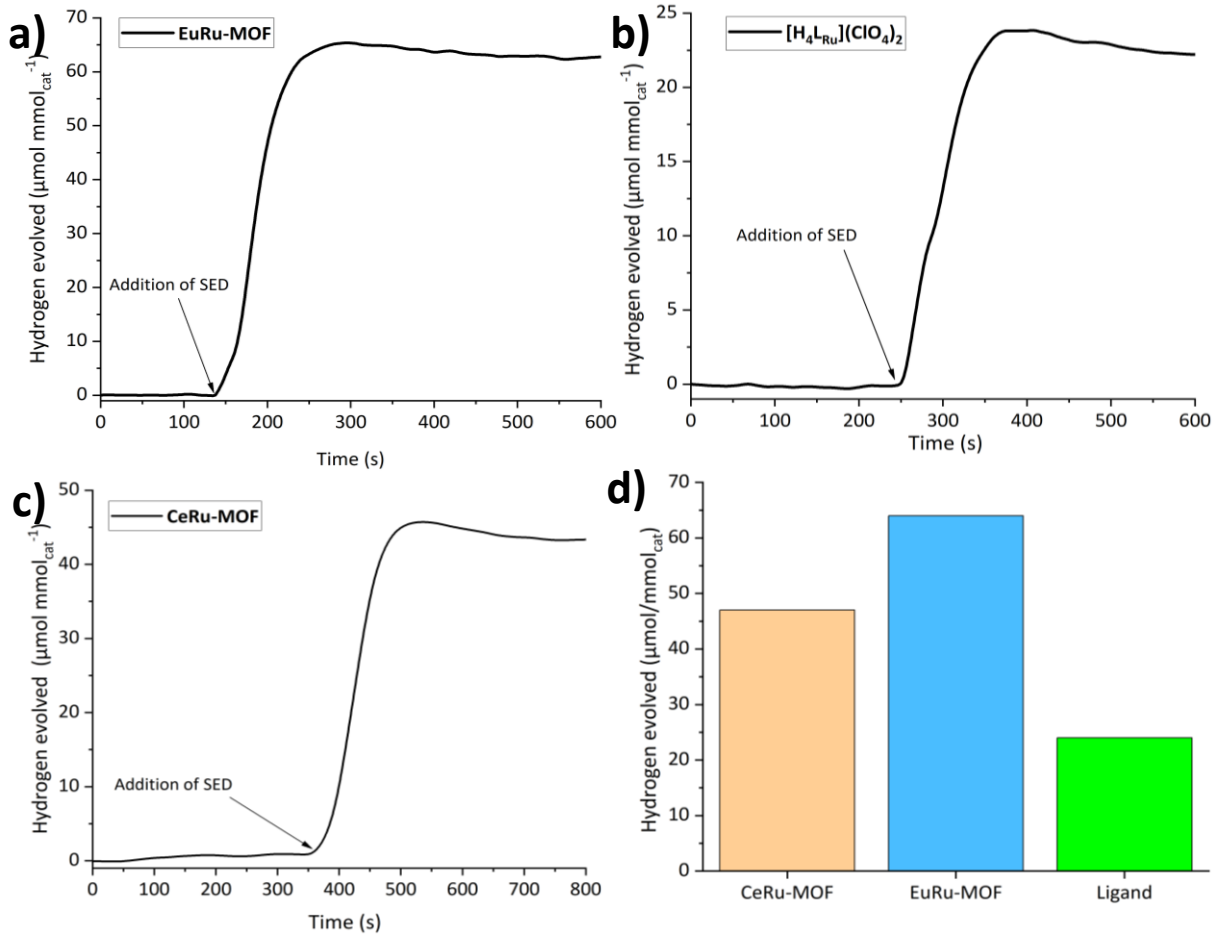

*Figure 5.4: a) Photocatalytic HER activity of **EuRu-MOF** before and after addition the sacrificial electron donor (SED), methanol. b) Photocatalytic HER activity of **[H_4L_{Ru}](ClO$_4$)$_2$** before and after addition the SED, methanol. c) Photocatalytic HER activity of **CeRu-MOF** before and after addition the SED, methanol. d) Comparison of HER activity between **EuRu-MOF**, **CeRu-MOF** and parent metalloligand **[H_4L_{Ru}](ClO$_4$)$_2$**.*

It is well established that $[Ru^{II}(L)_3]^{2+}$-type complexes, where L is 2,2'-bipyridyl, 1,10-phenanthroline, or a derivative thereof, become unstable upon reduction to $[Ru^{II}(L)_2(L^{\bullet-})]^{+}$. The radical ligand ($L^{\bullet-}$) readily undergoes bidentate ligand substitution by solvent molecules or anions present in solution.[18] In the case of **[H_4L_{Ru}](ClO$_4$)$_2$**, which lacks an Eu(III) site to serve as an alternative electron acceptor via Eu(III) → Eu(II) reduction, the H_2O reduction reaction is performed directly through the radicalised bipyridyl ligand ($bpy^{\bullet-}$). However, this increases the likelihood of bidentate ligand loss as described above, thereby accelerating photocatalyst degradation.[18]

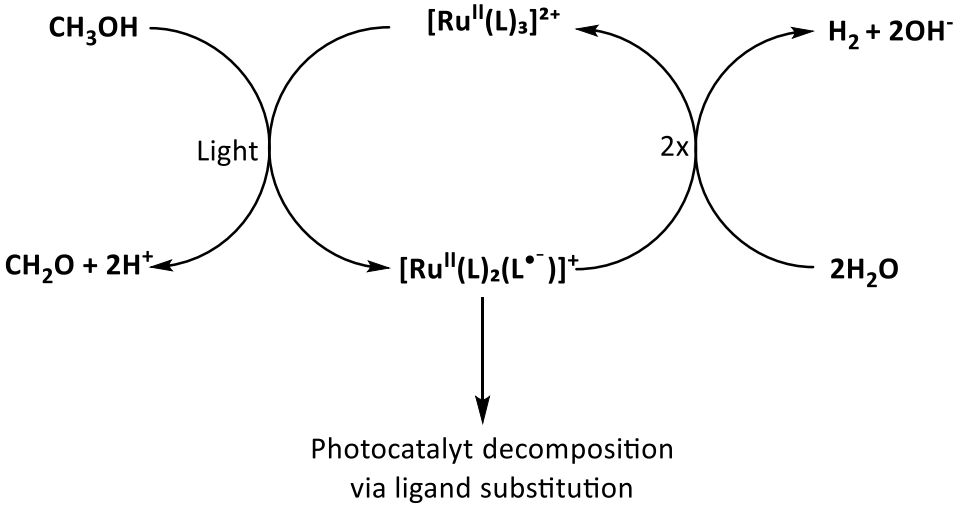

Figure 5.5: Simplified schematic of the proposed photocatalytic HER mechanism for ***[H4LRu](ClO4)2****.*

Figure 5.6 presents a simplified scheme of the proposed mechanism for the photocatalytic reduction of H_2O by **EuRu-MOF**. Upon light absorption, the polypyridyl Ru(II) moiety, $[Ru^{II}(L)_3]^{2+}$, undergoes a MLCT transition, whereby an electron from the t_2g orbital of the Ru(II) centre is promoted to the π* orbital of a bipyridine ligand. The sacrificial electron donor (SED), methanol, donates an electron to fill the hole left in the t_2g orbital of the ruthenium centre, thereby preventing recombination of the excited-state electron in the π* orbital with the metal centre. This process generates a radical bipyridyl ligand ($L^{\bullet-}$) species.[18] Electron transfer from this radical bipyridyl ligand to a neighbouring Eu(III) site occurs *via* the conjugated backbone of **EuRu-MOF**, facilitated by an alkynyl bridge,[11] reducing Eu(III) to Eu(II). Photogeneration of Eu(II) sites by similar $[Ru(phen)_3]^{2+}$-based metalloligands has been previously reported, providing precedent for the modified $[Ru(bpy)_3]^{2+}$ metalloligand employed in this study.[6] The Eu(II) centre serves as the active site for H_2O reduction, with the H_2O molecule coordinating via the labile coordination site (Chapter 4). Reduction of H_2O to H_2 regenerates the Eu(III) site, thus completing the catalytic cycle. Decomposition of **EuRu-MOF** may still proceed through similar or alternative pathways as explained for **$[H_4L_{Ru}](ClO_4)_2$**.

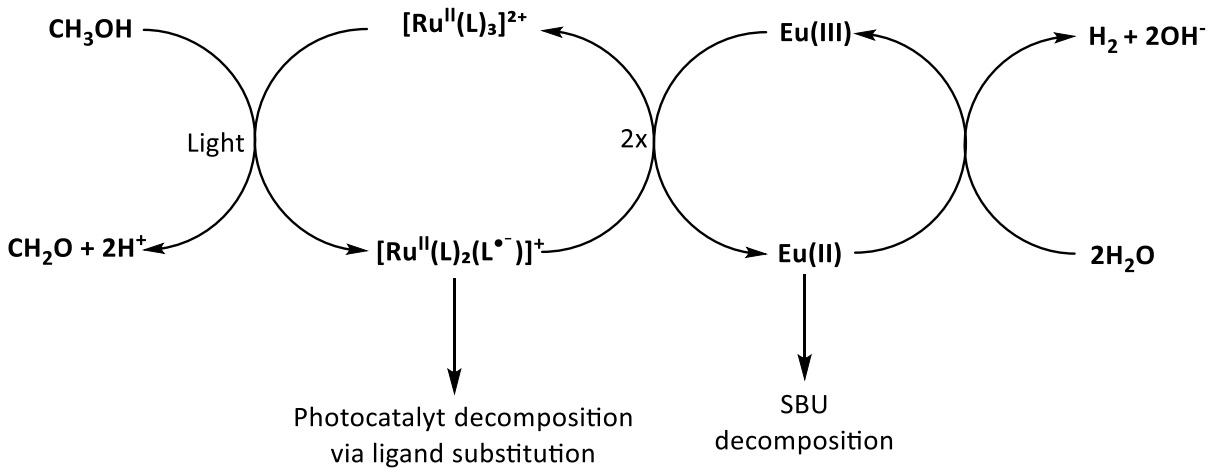

*Figure 5.6: Simplified schematic of the proposed photocatalytic HER mechanism for **EuRu-MOF**.*

The mechanism by which **CeRu-MOF** photocatalyses HER is less straightforward than that for **EuRu-MOF**, as the Ce(III)/Ce(II) reduction is not thermodynamically accessible under these conditions. It is therefore likely that HER proceeds in a similar manner to that described for the parent metalloligand, **$[H_4L_{Ru}](ClO_4)_2$**. The higher HER rate of **CeRu-MOF** compared to the metalloligand may then reflect stabilisation of the radicalised ligand ($L^{\bullet-}$) within the rigid MOF framework, or a kinetic role for the Ce SBU in facilitating water coordination, even if Ce is not directly reduced. Further mechanistic studies (such as transient absorption spectroscopy and electron paramagnetic resonance spectroscopy) would be required to confirm the active site for HER on both **CeRu-MOF** and **EuRu-MOF**.

Table 5.2 compares the H_2 evolution rate of **CeRu-MOF** and **EuRu-MOF** with values reported in the literature for other MOF-based photocatalysts. Both **CeRu-MOF** (1008 µmol h^{-1} $mmol_{cat}^{-1}$) and **EuRu-MOF** (1423 µmol h^{-1} $mmol_{cat}^{-1}$) significantly outperform Ce-based UiO-type MOF photocatalysts such as **Ce-UiO-66-NH_4** (26.1 µmol h^{-1} $mmol_{cat}^{-1}$)[13] and **UiO-66(Zr/Ce/Ti)** (16.6 µmol h^{-1} $mmol_{cat}^{-1}$).[16] Their performance is more comparable to Ce-based porphyrin MOFs reported by Cheng et al. who synthesised **CMF**, an acid modulated MOF consisting of dinuclear Ce SBUs and meso-tetra(4-carboxyphenyl) porphyrin as the organic linker. **CMF** was found to have a HER rate of 760 µmol h^{-1} $mmol_{cat}^{-1}$, which could be improved to 2226 µmol h^{-1} $mmol_{cat}^{-1}$ upon the addition of Zn to the porphyrin ring, **CMF(Zn)**.[19] From the comparison presented here it is clear that incorporation of photoactive metalloligands into Ln-based MOFs can significantly improve photocatalytic HER activity when compared to Ln-based MOFs that rely on organic photosensitising ligands.

*Table 5.2: Comparison of HER rates for **CeRu-MOF** and **EuRu-MOF** with Ce-based MOF photocatalysts in the literature.*

MOF Photocatalyst	Rate of H_2 Evolution (μmol h^{-1} $mmol_{cat}^{-1}$)	Reference
CeRu-MOF	1008	This work
EuRu-MOF	1423	This work
Ce-UiO-66-NH_4	26.1	13
UiO-66(Zr/Ce/Ti)	16.6	16
CMF	760	9
CMF(Zn)	2226	19

5.3 Preliminary Photocatalytic Carbon Dioxide Reduction Study

Photocatalytic CO_2 reduction to value-added chemicals and fuels offers a promising carbon-neutral alternative to the global economy's petrochemical dependence, which is a major driving force behind anthropogenic climate change. While many inorganic semiconductors have been successfully employed as CO_2 reduction photocatalysts, they often suffer from low efficiencies due to large band gaps, a low density of active sites, and rapid electron-hole pair recombination.[20] Yan *et al.* developed a porous, photoactive MOF consisting of dinuclear $Eu(III)_2$ SBUs connected by $Ru(phen)_3$-based metalloligands, which was found to selectively reduce CO_2 to formate under visible-light irradiation.[6] Given the structural similarities between this MOF and EuRu-MOF, the photocatalytic CO_2-reduction properties of **EuRu-MOF** were investigated.

For each experiment, 5 mg of photocatalyst (**EuRu-MOF** or **$[H_4L_{Ru}](ClO_4)_2$**) was added to 5 mL of acetonitrile containing 1.5 mmol (0.3 mol L^{-1}) *N,N*-dimethylaniline (DMA) and hermetically sealed with a butyl-rubber septum. The solutions were purged with CO_2 (or Ar for blank experiments) for 20 minutes before being placed in a Luzchem LZC photoreactor (10 × 8 W Sylvania T5 fluorescent white bulbs, 400 lm each) for a set time under magnetic stirring. Gas-phase products in the vial headspace were analysed using GC-BID (Shimadzu GC-2030), while liquid-phase products were quantified using anion

chromatography (ThermoFisher Dionex Aquion) and HPLC (Varian LC-920).

Gas chromatography and HPLC analyses did not detect any CO_2-reduction products. However, formate was detected by anion chromatography in both **EuRu-MOF** and **$[H_4L_{Ru}](ClO_4)_2$** samples. Figure 5.7 shows formate production for both photocatalysts over a 14-hour period. Samples kept in the dark for two hours (denoted as −2 h on the graph) and those at zero hours reaction time showed no detectable formate. In contrast, irradiation with white light for two hours resulted in formate yields of 153.9 ± 15.5 µmol/mmol$_{cat}$ (99.7% CI) for **EuRu-MOF** and 144.4 ± 11.9 µmol/mmol$_{cat}$ (99.7% CI) for **$[H_4L_{Ru}](ClO_4)_2$**. Given the overlapping measurement uncertainties, it can be concluded that both photocatalysts produced statistically equivalent amounts of formate after two hours of irradiation.

For **$[H_4L_{Ru}](ClO_4)_2$**, formate production appeared to plateau after two hours, with yields at 6 h (150.8 ± 11.9 µmol/mmol$_{cat}$, 99.7% CI) and 12 h (155.6 ± 11.9 µmol/mmol$_{cat}$, 99.7% CI) remaining within error of the 2 h value. By contrast, **EuRu-MOF** continued to produce formate, reaching 205.9 ± 15.5 µmol/mmol$_{cat}$ (99.7% CI) at 6 h and 258.4 ± 15.5 µmol/mmol$_{cat}$ (99.7% CI) at 12 h.

Control experiments (conducted either in the absence of light or with argon purging instead of CO_2) confirmed that formate generation was photocatalytic and that CO_2 was the carbon source, as no formate was detected under these conditions.

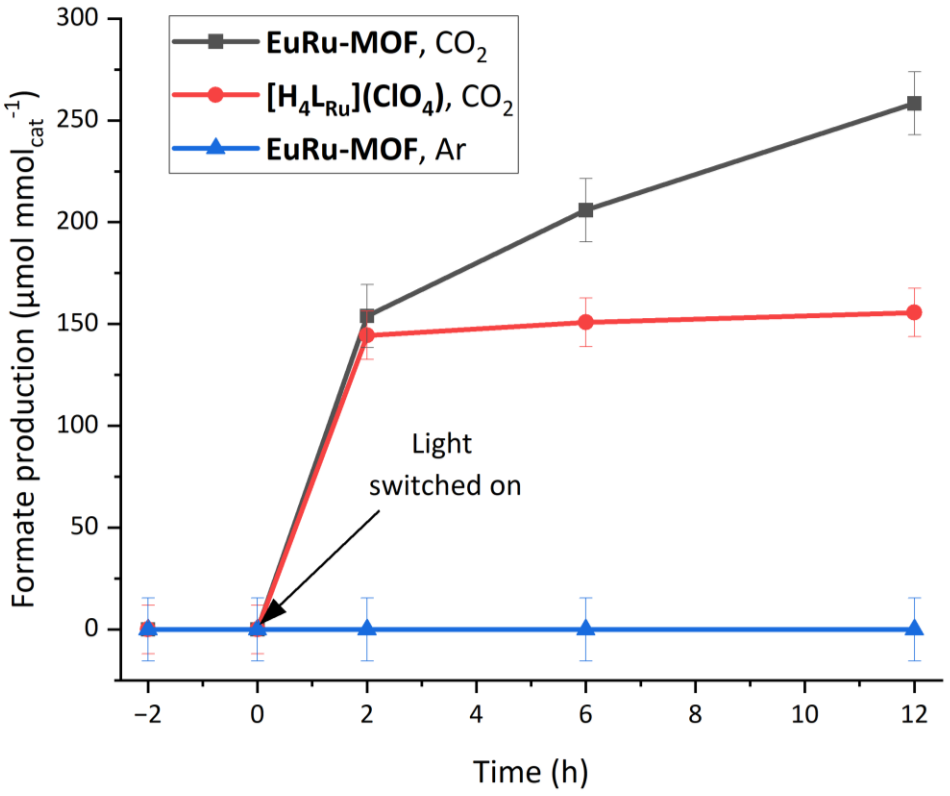

*Figure 5.7: Photocatalytic formate production by **EuRu-MOF** or the parent metalloligand **$[H_4L_{Ru}](ClO_4)_2$**.*

The plateau in formate production observed for **$[H_4L_{Ru}](ClO_4)_2$** after two hours of irradiation may be attributed to photocatalyst degradation. As discussed in the previous section, $[Ru^{II}(L)_3]^{2+}$-type complexes, where L is 2,2′-bipyridyl, 1,10-phenanthroline, or a derivative thereof, become unstable upon reduction to $[Ru^{II}(L)_2(L^{\bullet-})]^{+}$. The radicalised ligand ($L^{\bullet-}$) readily undergoes bidentate substitution by solvent molecules or anions present in solution.[18] In the case of **$[H_4L_{Ru}](ClO_4)_2$**, which lacks an Eu(III) site to act as an alternative electron acceptor via Eu(III) → Eu(II) reduction, CO_2 reduction proceeds directly through the radicalised bipyridyl ligand ($bpy^{\bullet-}$), as illustrated in Figure 5.8. However, this pathway increases the likelihood of ligand loss via substitution, thereby accelerating photocatalyst degradation.

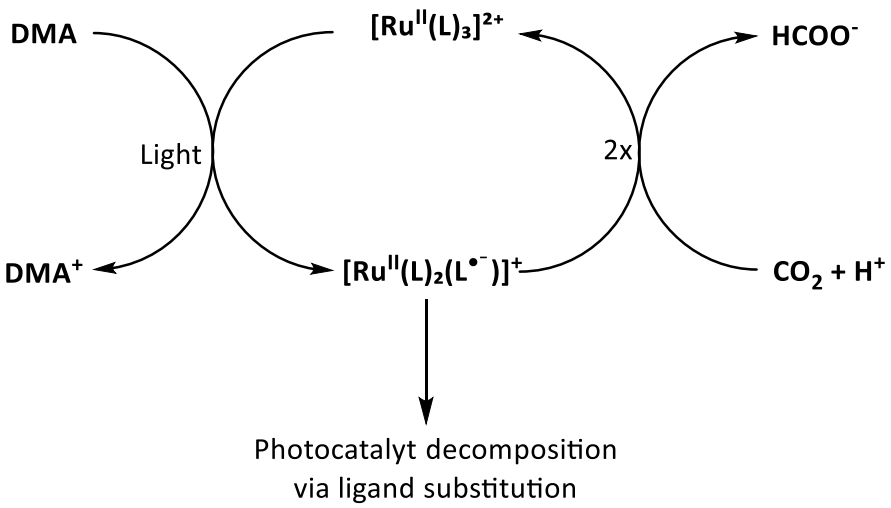

Figure 5.8: Simplified schematic of the proposed mechanism for the photocatalytic reduction of CO_2 by $[H_4L_{Ru}](ClO_4)_2$.

Figure 5.9 presents a simplified scheme of the proposed mechanism for the photocatalytic reduction of CO_2 by **EuRu-MOF**. Similar to the HER pathway, upon light absorption the polypyridyl Ru(II) moiety, $[Ru^{II}(L)_3]^{2+}$, undergoes a metal-to-ligand charge transfer (MLCT) transition, in which an electron from the t_2g orbital of the Ru(II) centre is promoted to the π* orbital of a bipyridine ligand. The sacrificial electron donor (SED), N,N-dimethylaniline, donates an electron to fill the hole left in the t_2g orbital of the Ru centre, thereby preventing recombination of the excited-state electron in the π* orbital with the metal centre. This process generates a radicalised bipyridyl ligand ($L^{\bullet -}$) species. Electron transfer from this radicalised ligand to a neighbouring Eu(III) site occurs via the conjugated backbone of **EuRu-MOF**, facilitated by an alkynyl bridge,[11] reducing Eu(III) to Eu(II). As previously reported by Yan et al., photogeneration of Eu(II) sites can occur in related $[Ru(phen)_3]^{2+}$-based metalloligand systems, providing precedent for the modified $[Ru(bpy)_3]^{2+}$ metalloligand employed here.[6] The Eu(II) centre then serves as the active site for CO_2 reduction, with the CO_2 molecule coordinating at a labile site. Reduction of CO_2 to formate regenerates the Eu(III) centre, thereby completing the catalytic cycle. Decomposition of **EuRu-MOF** may still proceed through similar or alternative pathways as described for $\mathbf{[H_4L_{Ru}](ClO_4)_2}$; however, degradation appears to occur at a slower rate.

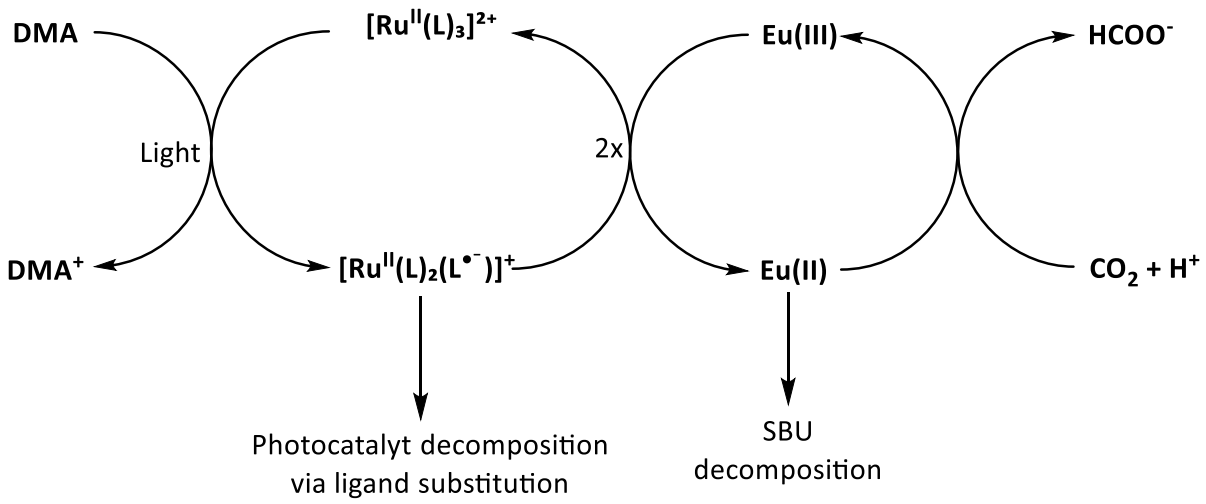

*Figure 5.9: Simplified schematic of the proposed mechanism for the photocatalytic reduction of CO_2 by **EuRu-MOF**.*

Eu-Ru(phen)$_3$-MOF, the similar photoactive MOF reported by Yan et al. had a rate of formate production of 257.3 μmol h^{-1} $mmol_{cat}^{-1}$ (here $mmol_{cat}$ was calculated using the entire MOF unit - inorganic SBU and metallogliand – whereas Yan et al. originally calculated $mmol_{cat}$ using just the inorganic SBU).[6] This would appear to be a order magnitude greater than the 22.7 μmol h^{-1} $mmol_{cat}^{-1}$ rate of formate production by **EuRu-MOF** (averaged over the 12 hour experiment) despite their similarities. However, this discrepancy is largely attributable to the light source employed: Yan et al. used a 300 W Xe lamp, whereas the present work used an 80 W fluorescent lamp. Normalising the rates to light source power gives comparable values of 0.858 μmol h^{-1} $mmol_{cat}^{-1}$ W^{-1} for **Eu-Ru(phen)$_3$-MOF** and 0.284 μmol h^{-1} $mmol_{cat}^{-1}$ W^{-1} for **EuRu-MOF**.

Other experimental factors may also contribute. For instance, Yan et al. employed triethanolamine (TEOA) as the sacrificial electron donor (SED), which is generally regarded in the literature as more effective than N,N-dimethylaniline (DMA), the SED used in this study.[22] However, attempts to use TEOA with **EuRu-MOF** were unsuccessful, as the MOF proved unstable in the basic TEOA solution.

Structural factors are also important; **Eu-Ru(phen)$_3$-MOF** possesses large 1D channels (31 × 16 Å) that provide greater accessibility to Eu(II) active sites,[6] whereas **EuRu-MOF** is nonporous, restricting catalysis to surface-exposed sites and thereby limiting the overall number of accessible Eu(II) centres.

*Table 5.3: Comparison of photocatalytic formate production rate by **EuRu-MOF** with values reported in the literature for other MOF-based photocatalysts. Rate of formate production normalised to power of light source.*

MOF Photocatalyst	Rate of Formate Production ($\mu mol\ h^{-1}\ mmol_{cat}^{-1}\ W^{-1}$)	Reference
EuRu-MOF	0.284	This work
Eu-Ru(phen)$_3$-MOF	0.858	6
PCN-222	0.479	22
NH$_2$-MIL-125(Ti)	0.090	23
NH$_2$-Uio-66(Zr)	0.154	24

5.4 Electrodeposited LnRu-MOF Films for Photoelectrochemical Applications

Photoelectrochemical (PEC) devices represent a promising route toward large-scale production of carbon-neutral solar fuels via artificial photosynthesis, as they combine the advantages of photocatalytic and electrocatalytic approaches.[25] To employ a photoactive material as a photoelectrode in a PEC device, it must be deposited onto a substrate that is both conductive and transparent to visible light—typically glass coated on one side with a conductive film such as indium tin oxide (ITO) or fluorine-doped tin oxide (FTO). Li and Dincă reported the reductive electrosynthesis of MOF-5 on FTO-coated glass by cathodically reducing nitrate to generate hydroxide anions at the electrode surface, producing a local pH increase that deprotonates the ligand and drives MOF crystal growth directly on the cathode.[26] In this section, the reductive electrosynthesis of **LnRu-MOF** films on FTO-coated glass, as well as their properties, is investigated.

5.4.1 Synthesis of LnRu-MOF/FTO Films (Ln = Ce or Eu)

$Ce(NO_3)_3{\cdot}6H_2O$ or $Eu(NO_3)_3{\cdot}5H_2O$ and **$[H_4L_{Ru}](ClO_4)_2$** were dissolved in a 2:1 molar ratio in

a DMF:H_2O (100:1) solvent mixture containing tetrabutylammonium hexafluorophosphate ($TBAPF_6$, 0.1 M) and $NaNO_3$ (50 mM). FTO-coated glass with a surface area of 1 cm^2 was used as the working electrode, Pt wire as the counter electrode, and Ag/Ag(cryptand)$^+$ as the reference electrode. The solution was purged with N_2, and a potential of −1 V vs. Fc/Fc^+ was applied for 5 minutes. The resulting orange-coloured films, **CeRu-MOF/FTO** or **EuRu-MOF/FTO**, were washed with DMF and deionised water and left to dry in air.

5.4.2 Characterisation of LnRu-MOF/FTO Films

The physicochemical properties of the **CeRu-MOF/FTO** and **EuRu-MOF/FTO** films were investigated using FTIR and Raman spectroscopy, as well as **SEM–EDX**. Structural characterisation by PXRD indicate that the films are amorphous, as no diffraction peaks were observed. The photophysical properties were further examined using UV–Vis absorption spectroscopy, steady-state photoluminescence spectroscopy, and time-resolved photoluminescence decay measurements.

5.4.2.1 FTIR Spectroscopy

Figure 5.10 presents the FTIR spectra of the **CeRu-MOF/FTO** and **EuRu-MOF/FTO** films, which appear virtually identical. Most notably, the carboxylate asymmetric and symmetric stretching frequencies (ν_{as}(COO) and ν_s(COO), respectively) are very similar to those observed for the corresponding **LnRu-MOF** crystals discussed in Chapter 4 (Table 5.3), indicating that the electrosynthesised films adopt comparable carboxylate coordination modes to their solvothermally synthesised crystalline analogues. The Δν values derived from the asymmetric and symmetric stretching frequencies are reported in Table 5.3 and compared with those obtained for bulk **CeRu-MOF** and **EuRu-MOF** crystals. While the films exhibit a marginal blue shift in Δν relative to the crystalline samples, this shift falls within the standard deviation observed across the **LnRu-MOF** series in the previous chapter (± 3 cm^{-1} and ± 6 cm^{-1}). This suggests that the same carboxylate coordination modes, syn–syn bridging and bidentate (chelating), are retained in the films.

Table 5.4: List of wavenumber values for asymmetric (ν_{as}) and symmetric (ν_s) carboxylate stretching frequencies for, as well as the associated shift values ($\Delta\nu$).

Compound	ν_{as} (cm^{-1})	ν_s (cm^{-1})	$\Delta\nu$ (cm^{-1})	ν_{as} (cm^{-1})	ν_s (cm^{-1})	$\Delta\nu$ (cm^{-1})
CeRu-MOF Film	1599	1441	158	1547	1422	125
CeRu-MOF Crystals	1597	1443	154	1540	1427	113
EuRu-MOF Film	1601	1446	155	1551	1424	127
EuRu-MOF Crystals	1596	1444	152	1544	1425	119

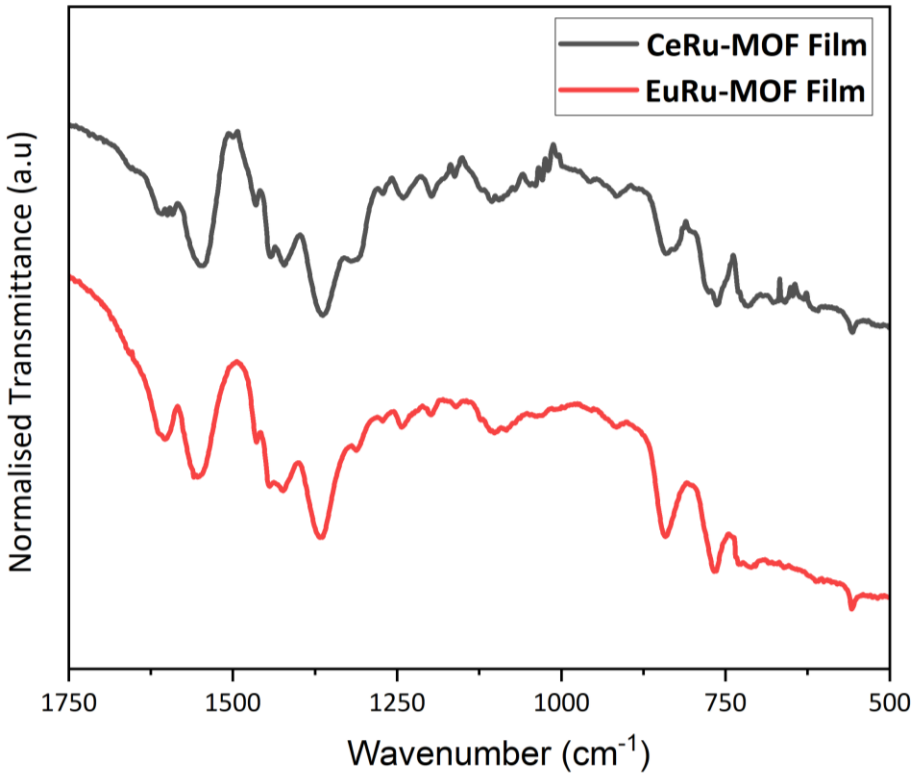

*Figure 5.10: FTIR spectra **CeRu-MOF/FTO** and **EuRu-MOF/FTO** films.*

5.4.2.2 Raman Spectroscopy

The Raman spectra of electrosynthesised **CeRu-MOF** and **EuRu-MOF** films presented in Figure 5.11 match the Raman spectra of **CeRu-MOF** and **EuRu-MOF** bulk crystals, described in Chapter 4.

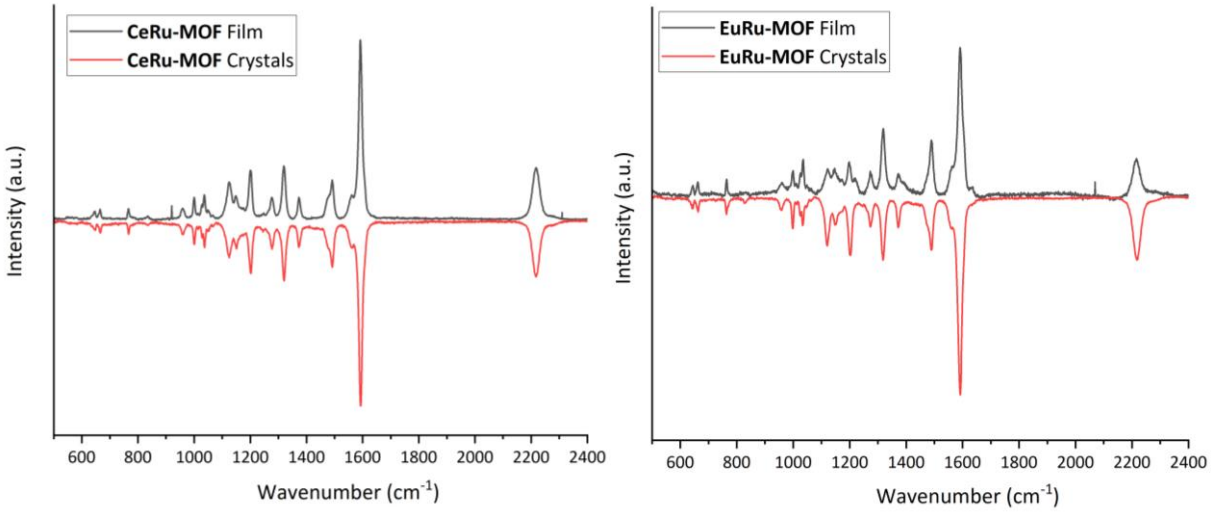

*Figure 5.11: Left, Raman spectra of **CeRu-MOF/FTO** film and **CeRu-MOF** crystals. Right, Raman spectra of **EuRu-MOF/FTO** film and **EuRu-MOF** crystals.*

5.4.2.3 SEM-EDX

The morphology of **CeRu-MOF/FTO** and **EuRu-MOF/FTO** films was characterised by scanning electron microscopy (SEM). Samples were mounted on aluminium stubs, earthed using silver paint, and sputter-coated with a thin Au/Pd layer to minimise charging effects. SEM imaging was conducted on a Zeiss ULTRA Plus instrument, operated at an accelerating voltage of 10–20 kV under high-vacuum conditions (1×10^{-5} mbar), using a secondary electron detector.

Representative SEM micrographs of **CeRu-MOF/FTO** at various magnifications (Figure 5.12) reveal a continuous, homogeneous film surface composed of self-aggregated, sub-micrometre globular particles. These particles assemble into irregular dendritic networks, imparting a textured surface morphology. The morphology of **EuRu-MOF/FTO** films was found to be essentially identical to that of **CeRu-MOF/FTO**. A cross-sectional SEM image of **EuRu-MOF/FTO** (Figure 5.13) shows an amorphous film with an estimated thickness in the range of 3–7 µm.

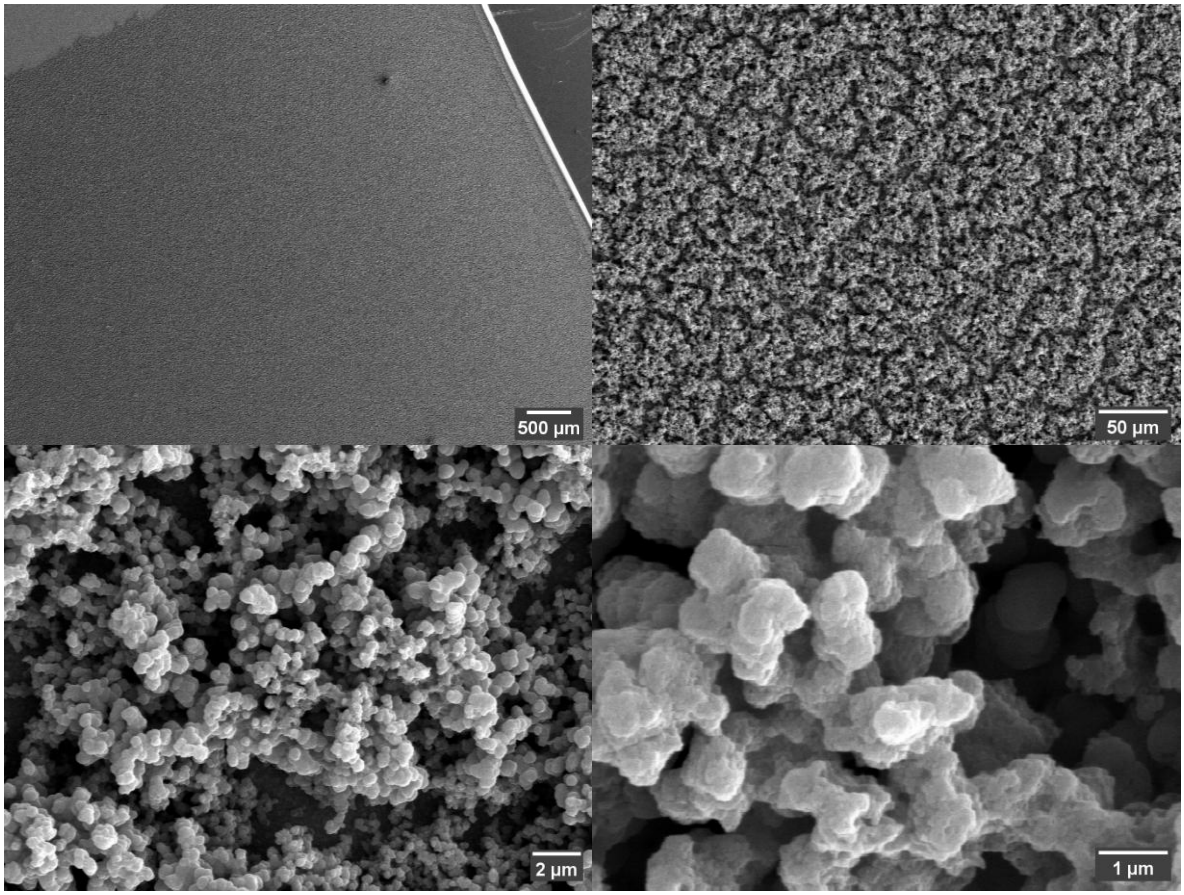

*Figure 5.12: SEM images of a **CeRu-MOF/FTO** film at various magnifications. Taken at an accelerating voltage of 15 kV using a secondary electron detector.*

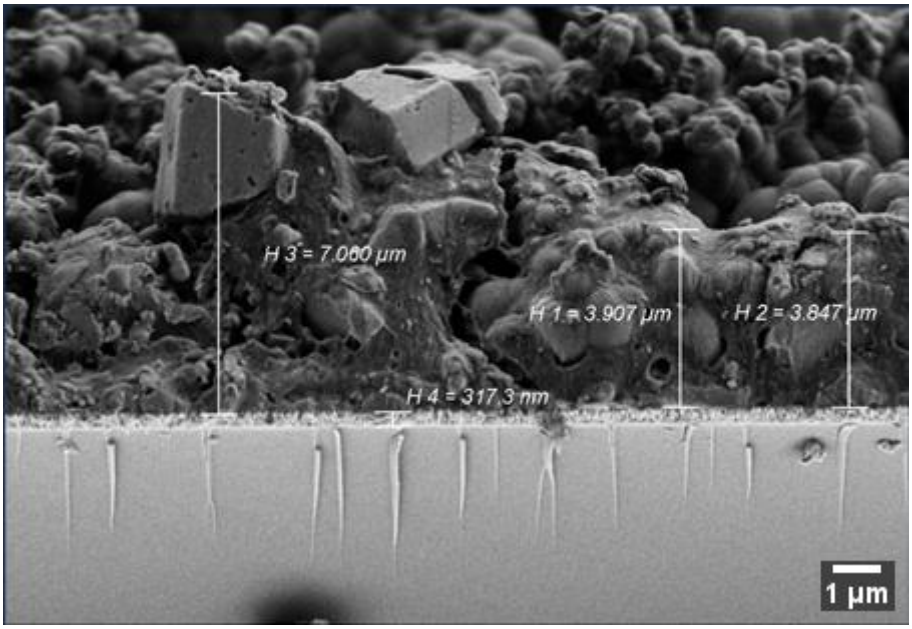

*Figure 5.13: SEM image of a cross section of a **EuRu-MOF/FTO** film. Taken at an accelerating voltage of 15 kV using a secondary electron detector.*

Energy-dispersive X-ray spectroscopy (EDX) analysis revealed that **CeRu-MOF/FTO** films exhibited a Ce-to-Ru atomic ratio of approximately 1.5, while **EuRu-MOF/FTO** films displayed a Eu-to-Ru atomic ratio of approximately 1.3. Elemental mapping by EDX (Figure 5.14) confirmed the homogeneous spatial distribution of Eu and Ru within the films, indicating the absence of phase segregation. In the case of **EuRu-MOF/FTO**, the elemental maps further revealed that the film is composed of discrete "islands" of MOF material, with regions of the underlying FTO substrate remaining exposed. This is evidenced by the inverse spatial correlation between the Sn elemental map (corresponding to the FTO layer) and the Eu/Ru maps.

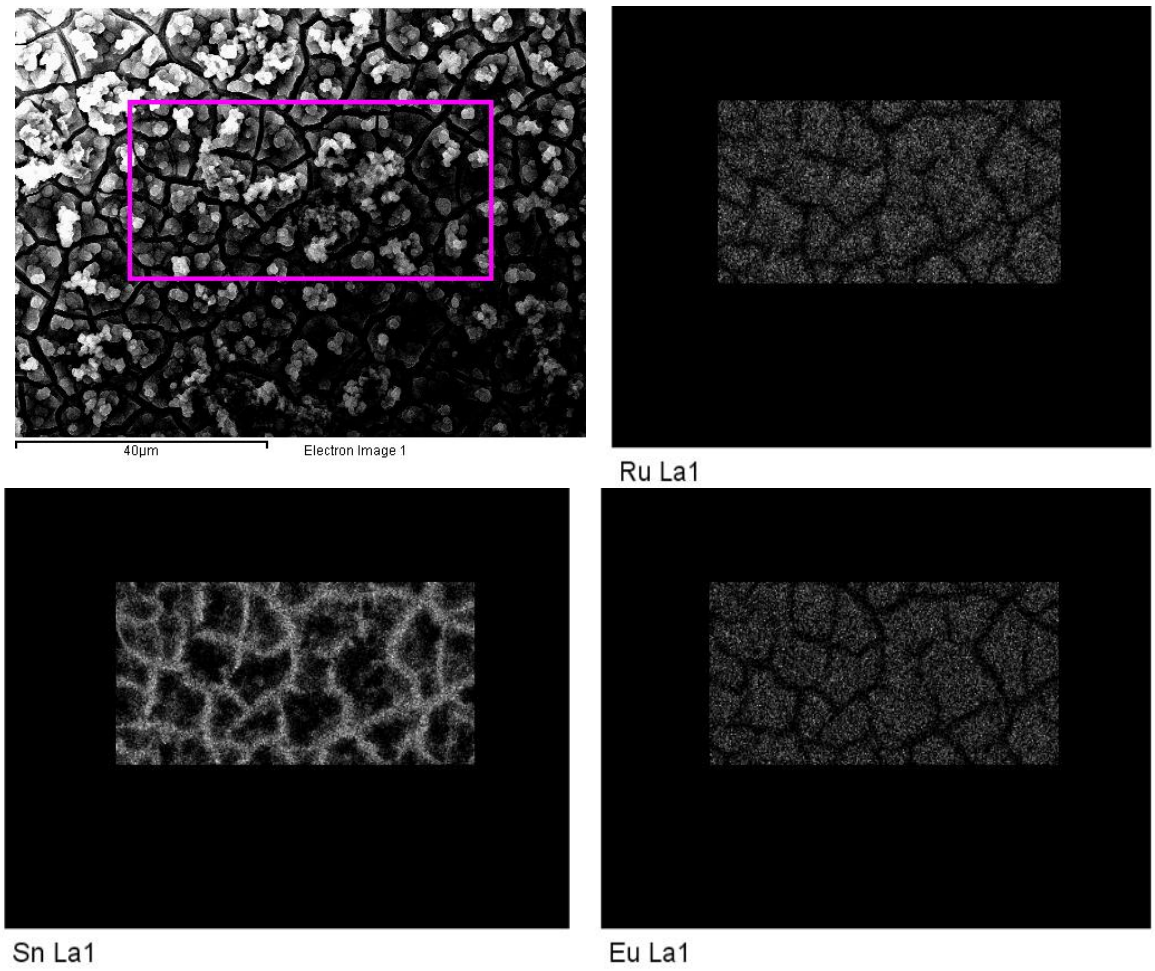

*Figure 5.14: EDX elemental mapping of an **CeRu-MOF/FTO** film confirming the homogeneous spatial distribution of Eu and Ru within the film.*

5.4.2.4 Photophysical Characterisation

The photophysical properties of **CeRu-MOF/FTO** were investigated and compared with

those of bulk **CeRu-MOF** crystals (described in Chapter 4). The UV–Vis absorption spectra of both materials (Figure 5.15a) are very similar, each displaying a strong absorption band centred at approximately 290 nm, assigned to a ligand-centred (LC) π(bpy) → π*(bpy) transition. A second prominent absorption band is observed at approximately 370 nm, likewise attributed to a LC π → π* transition, in this case originating from the bis-alkynyl-isophthalic acid-functionalised bipyridine ligand. In addition, both spectra exhibit a weaker, broad absorption feature between 425 and 550 nm, which arises from metal-to-ligand charge transfer (MLCT) d → π* transitions.

Figure 5.15b presents the photoluminescence spectra of **CeRu-MOF/FTO** films and bulk **CeRu-MOF** crystals under 405 nm laser excitation. Both materials exhibit similar emission profiles; however, the emission maximum of **CeRu-MOF/FTO** is red-shifted by 12 nm compared to the bulk crystals (from 652 nm to 664 nm). In both cases, the emission bands display a full width at half maximum (FWHM) of 46 nm—a notable feature previously discussed in Chapter 4 as distinguishing **CeRu-MOF** from the other LnRu-MOFs and from the parent metalloligand, which exhibited much broader FWHM values of 73–99 nm.

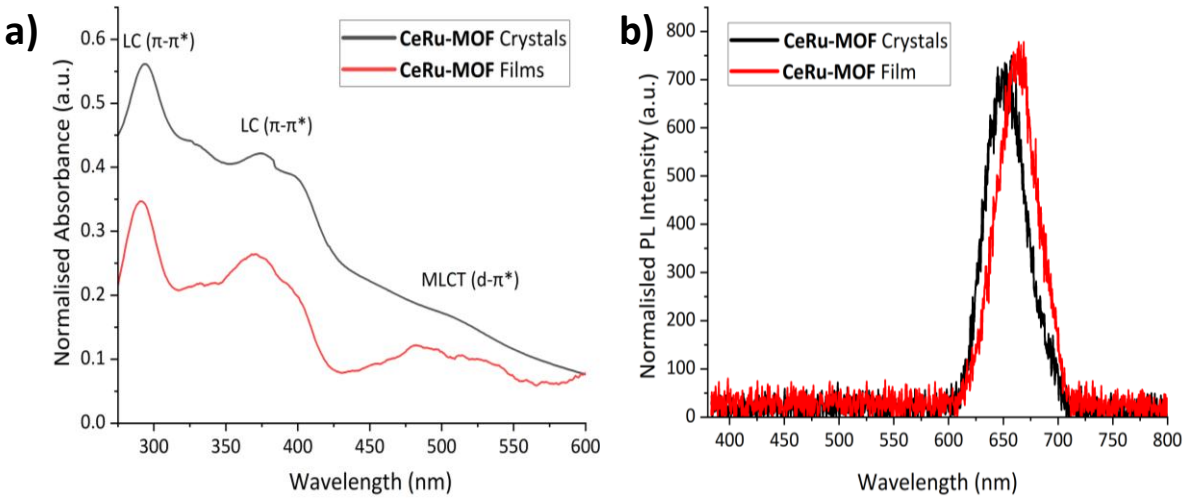

*Figure 5.15: a) UV–Vis absorption spectra of a **CeRu-MOF/FTO film** and **CeRu-MOF** crystals. b) Photoluminescence spectra of a **CeRu-MOF/FTO film** and **CeRu-MOF** crystals.*

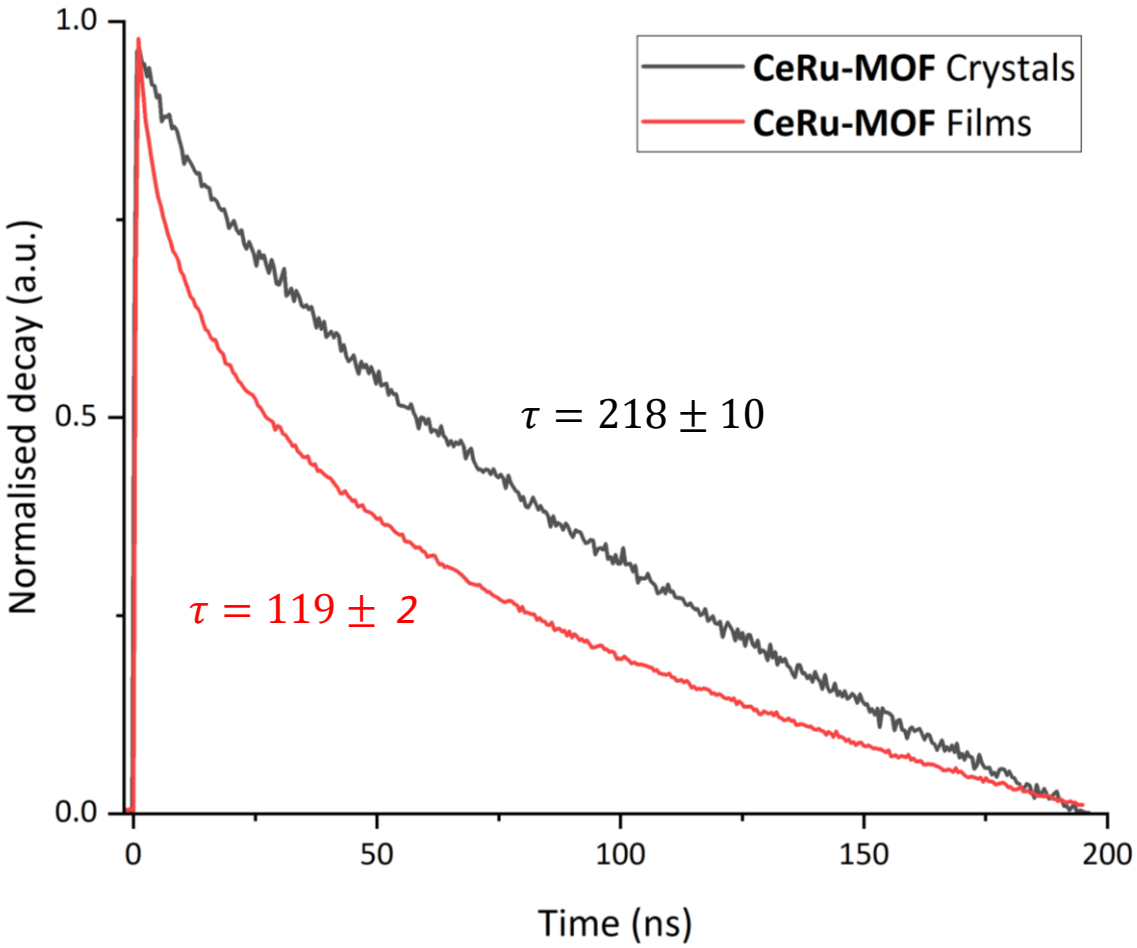

*Figure 5.16: Normalised time-resolved photoluminescence (TRPL) decay curves of the ^{3}MLCT state for a **CeRu-MOF/FTO film (red)** and **CeRu-MOF** crystals (black).*

Time-resolved photoluminescence (TRPL) decay curves of the ^{3}MLCT state for **CeRu-MOF/FTO** films and bulk **CeRu-MOF** crystals are plotted in Figure 5.16. As the initial decays of the ^{1}MLCT state occurs on the picosecond timescale, they could not be measured in this experiment due to overlap with the instrument response function (IRF). The photoluminescence decay curves were fitted to a bi-exponential model, and average lifetimes (τ_{avg}) were calculated using Eq. 5.1, where α_i and τ_i are the pre-exponential factor and lifetime of the *i*th component. Table 5.5 lists τ_{avg} calculated for each **CeRu-MOF/FTO** films and bulk **CeRu-MOF** crystals as well as individual pre-exponential factors and lifetimes.

$$\tau_{avg} = \frac{\sum \alpha_i \tau_i^2}{\sum \alpha_i \tau_i}$$

The **CeRu-MOF/FTO** film exhibited photoluminescence with an average lifetime of 119 ns, substantially shorter than that of the **CeRu-MOF** crystals (218 ns). Photoluminescence

lifetimes typically differ depending on whether the emission event originates within the bulk of the material or at its surface. To capture these contributions, the decay profiles are best described using a bi-exponential model. Bulk-associated lifetimes are generally longer-lived, whereas surface-associated lifetimes are shorter due to the presence of dangling bonds and the increased probability of quenching interactions (non-radiative decay) with the external environment, thereby reducing the average lifetime at the surface. The **CeRu-MOF/FTO** film, as revealed by SEM, possesses a high surface-area-to-volume ratio, which increases the proportion of surface-related decay events and thus accounts for its reduced average lifetime. In contrast, the **CeRu-MOF** crystals consist of micrometre-sized spherical particles (see Chapter 4) and therefore exhibit a much lower surface-area-to-volume ratio, leading to a smaller contribution from surface quenching and correspondingly longer average lifetimes.

*Table 5.5: τ_{avg} calculated (biexponential fit) for a **CeRu-MOF/FTO film** and **CeRu-MOF** crystals as well as individual pre-exponential factors and lifetimes*

Material	**α_1**	**τ_1 (ns)**	**α_2**	**τ_2 (ns)**	**τ_{avg} (ns)**
CeRu-MOF Crystals	0.183(7)	14(1)	1.49(2)	220(9)	218(10)
CeRu-MOF Film	0.32(3)	8.7(2)	0.77(2)	114(1)	73.2(7)

To preliminarly access the abilty of **CeRu-MOF/FTO** act as a photoelectrode, photocurrent measurements were perfomed in a 3-electrode cell with **CeRu-MOF/FTO** used as the working electrode, Pt wire as the counter electrode and an Ag/AgCl (3 M KCl) reference electrode, in 1 M H_2SO_4 as electrolyte. Chronoamperometry was carried out with the potential on the working electrode set to 0 V vs Ag/AgCl, and with an LED light source (465 nm, 44 mW cm^{-2}) intermittantly switched on and off. As shown in Figure 5.17, **CeRu-MOF/FTO** displays a consistent photocurrent of -3.6 µA cm^{-2}.

To preliminarily assess the ability of **CeRu-MOF/FTO** to act as a photoelectrode, photocurrent measurements were performed in a three-electrode cell configuration using

CeRu-MOF/FTO as the working electrode, a Pt wire as the counter electrode, and an Ag/AgCl (3 M KCl) reference electrode, with 1 M H_2SO_4 as the electrolyte. Chronoamperometry was conducted at an applied potential of 0 V vs. Ag/AgCl, with illumination provided by an LED light source (465 nm, 44 mW cm^{-2}) that was intermittently switched on and off. As shown in Figure 5.17, the **CeRu-MOF/FTO** electrode exhibited a stable photocurrent density of –3.6 µA cm^{-2}. This results conifrms that **CeRu-MOF/FTO** undergoes a photoelectric effect that can be used to generate an external current demostrating its ability to as as a photoelectrode. This implies that as a photoelectrode it has potential application as a photodector or similar photoresponsive devices.[27]

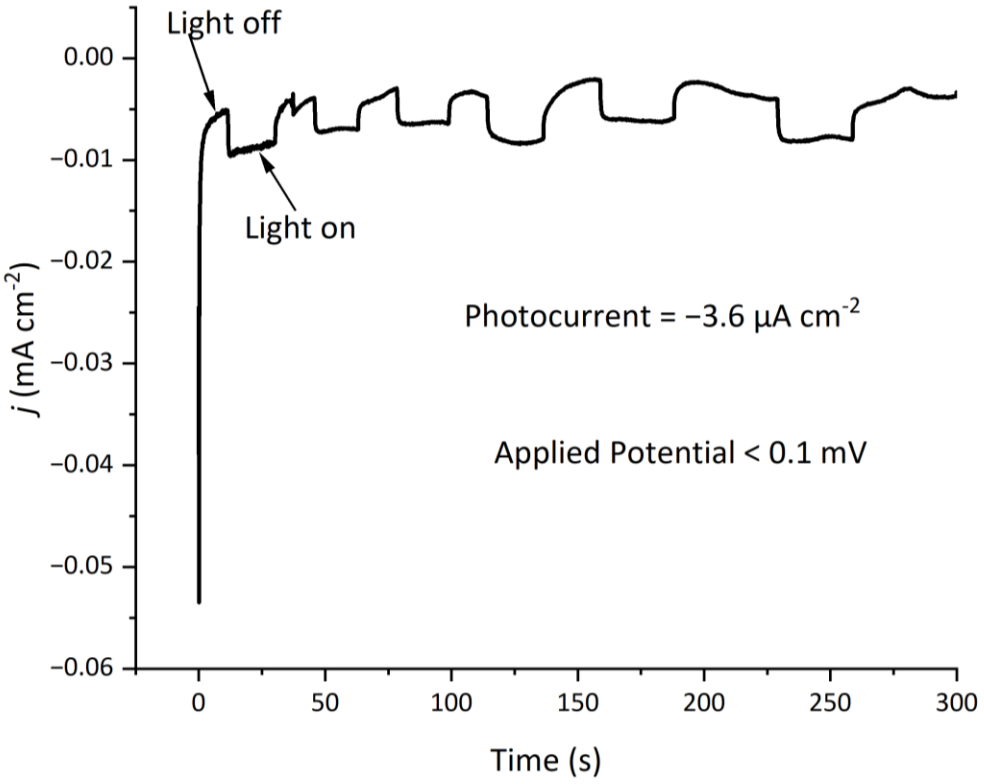

*Figure 5.16: Chronoamperometric measurement of **CeRu-MOF/FTO** with chopped light demonstrating the generation of a photocurrent.*

5.4.3 Preliminary Photoelectrocatalytic Studies

Given the success of **EuRu-MOF** in photocatalytically reducing CO_2 to formate (Section 5.2), **EuRu-MOF/FTO** was investigated as a photocathode for the photoelectrocatalytic reduction of CO_2. The reactions were conducted in a gas-tight three-electrode cell, with **EuRu-MOF/FTO** or bare FTO-coated glass (as a control) serving as the working electrode, a Pt-mesh as the counter electrode, and an Ag/Ag^+ reference electrode (Ag wire, 0.01 M $AgNO_3$, 0.1 M $TBAPF_6$ acetonitrile solution) connected via a Luggin capillary. The electrolyte (0.1 M $TBAPF_6$ in acetonitrile) was purged with pure CO_2 or Ar for control experiments.

Gas-phase products from the cell headspace were analysed using GC-BID (Shimadzu GC-2030), while liquid-phase products were quantified using anion chromatography (ThermoFisher Dionex Aquion) and HPLC (Varian LC-920).

Photoelectrocatalytic CO_2RR experiments were performed at a constant applied potential of –1.5 V vs. Fc/Fc^+ for 24 hours under both illuminated (465 nm LED, 44 mW cm^{-2}) and dark conditions. No CO_2 reduction products were detected by GC or HPLC; however, formate was detected by anion chromatography for **EuRu-MOF/FTO** under both illuminated and dark conditions, as well as for bare FTO. Figure 5.18 compares the formate yields for these three electrodes. Under illumination, **EuRu-MOF/FTO** produced 0.77 ± 0.08 $ppm_{formate}$ (99.7% CI), roughly twice that produced under dark conditions (0.38 ± 0.08 $ppm_{formate}$, 99.7% CI). At first glance this suggests that **EuRu-MOF/FTO** behaves as a photocathode for CO_2RR. However, bare FTO under the same conditions produced significantly more formate (2.13 ± 0.08 $ppm_{formate}$, 99.7% CI).

These results indicate that under the applied conditions, FTO itself acts as the electrocatalyst for CO_2-to-formate reduction, while the **EuRu-MOF** coating acts as a barrier, suppressing catalytic activity. The modest increase in formate yield observed for **EuRu-MOF/FTO** under illumination compared to dark conditions can be rationalised by an increase in the conductivity of the **EuRu-MOF** film under irradiation, allowing greater charge transfer to the catalytically active FTO layer. Overall, **EuRu-MOF/FTO** is concluded to be an ineffective photocathode for CO_2RR due to its poor electronic conductivity.

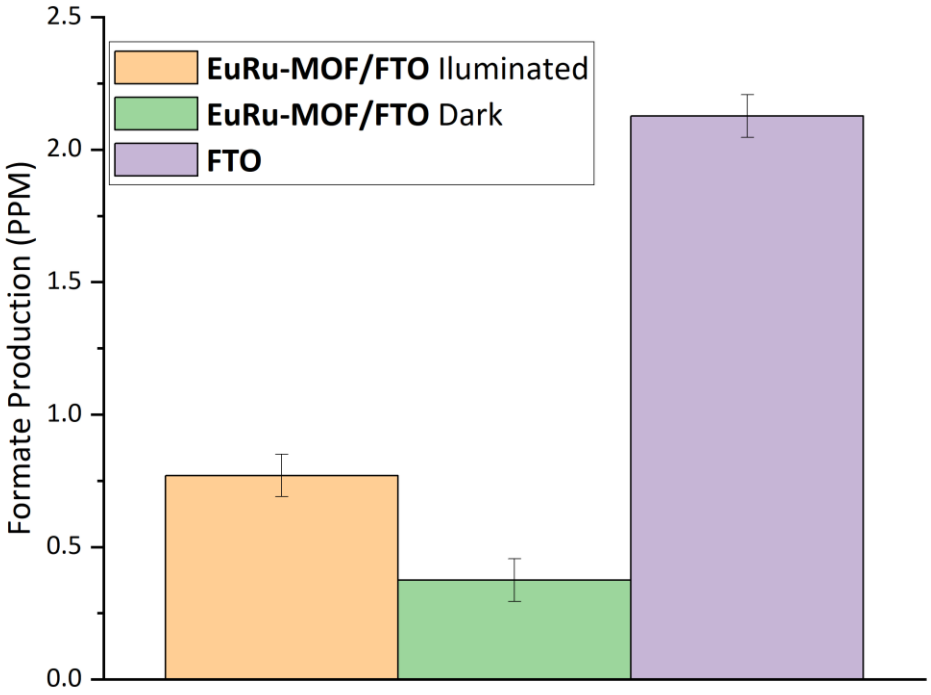

*Figure 5.18: Photoelectrocatalytic formate yields by **EuRu-MOF** in light (orange) and dark (green) conditions as well as bare FTO (purple) as a control.*

5.5 Conclusions

Building on the isostructural **LnRu-MOF** series introduced in the previous chapter, **CeRu-MOF** and **EuRu-MOF** were identified as candidate photocatalysts on the basis of their accessible Ce^{3+}/Ce^{4+} and Eu^{3+}/Eu^{2+} redox couples and subsequently evaluated for both photocatalytic and photoelectrochemical applications.

Under photocatalytic conditions, **CeRu-MOF** oxidised water competitively with other reported Ce- and Ti-based MOF photocatalysts, via oxidative quenching of the Ru metalloligand by $S_2O_8^{2-}$ and subsequent electron transfer from the dinuclear Ce SBU to generate Ce(IV) active sites. The alkynyl bridge of the metalloligand is proposed to facilitate this interfacial electron transfer by delocalising electron density onto the conjugated backbone, in analogy with heterodinuclear molecular photocatalysts.[11] For the hydrogen evolution reaction, both MOFs outperformed the parent metalloligand and matched rates reported for Ce-based porphyrin MOFs, supporting the value of incorporating photoactive Ru(II) metalloligands into Ln-based frameworks. **EuRu-MOF** further catalysed CO_2 reduction to formate over 12 h with sustained activity, whereas the

parent metalloligand deactivated after two hours. Placing **EuRu-MOF** among the more efficient MOF-based CO_2RR photocatalysts, though still below the structurally similar but porous **Eu–Ru(phen)$_3$-MOF** whose superior performance points to active-site accessibility as the key limiting factor here.

In parallel, **CeRu-MOF** and **EuRu-MOF** analogues were electro-synthesised on FTO-coated glass as 3–7 μm films. The films are amorphous and more accurately described as disordered coordination polymer analogues, though FTIR confirmed retention of the carboxylate coordination modes and EDX showed homogeneous Ln and Ru distribution. **CeRu-MOF/FTO** generated a photocurrent under illumination, indicating potential as a photodetector material.[27] **EuRu-MOF/FTO** was investigated as a photocathode for CO_2 reduction but was limited by low electronic conductivity, with the film acting as a barrier to interfacial charge transfer.

Together, these results establish **CeRu-MOF** and **EuRu-MOF** as strong redox photocatalysts for OER, HER, and CO_2RR, and identify clear routes for further development. Structural strategies include synthesis of 2D nanosheets[28-31] to expose more active sites, nitrate replacement to improve alkaline stability, and pillaring to convert the 2D frameworks into porous 3D analogues.[32-35] For PEC applications, optimisation of electrosynthesis to yield thinner, crystalline films[26,37] would address the conductivity barrier and open routes into sensing and photovoltaic devices.[27,38-40] More broadly, the strong Lewis acidity of the lanthanides suggests the wider **LnRu-MOF** series merits investigation for organic photocatalysis (hydrogenations, oxidations, coupling reactions) across an emerging field.[41]

5.6 References

1. Y. Wu, L. Zhou, Y. Xie, Y. Lai, S. Fu, X. Kang, W. Shi, J. Li, X. Zhang, K. Hu, H. Zhang, T. Qi, *Chemical Engineering Journal*, 2024, **500**, 157189.
2. S. Ferro, A. De Battisti, *Journal of Electroanalytical Chemistry*, 2002, **533**, 177-180.

3. M. Ö. Arman, B. Geboes, K. V. Hecke, K. Binnemans, T. Cardinaels, *Electrochimica Acta*, 2024, **484**, 144055.
4. D. L. Douglas and D. M. Yost, *J. Chem. Phys.*, 1949, **17**, 1345–1346.
5. J. Jana, T. S. K. Sharma, M. A. Ghanem, W. M. Choi, C. S. Gopinath, S. H. Hur, *Separation and Purification Technology*, 2025, **372**, 133442.
6. Z.-H. Yan, M.-H. Du, J. Liu, S. Jin, C. Wang, G.-L. Zhuang, X.-J. Kong, L.-S. Long and L.-S. Zheng, *Nat. Commun.*, 2028, **9**, 3353.
7. J. Schneider and D. W. Bahnemann, *J. Phys. Chem. Lett.*, 2013, **4,** 20, 3479–3483.
8. M. Wang, S. Shen, L. Li, Z. Tang and J. Yang, *J. Mater. Sci.*, 2017, **52**, 5155–5164.
9. T. Matsuzaki, K. Kosugi, H. Iwami, T. Kambe, H. Kiuchi, Y. Harada, D. Asakura, T. Uematsu, S. Kuwabata, Y. Saga, M. Kondo & S. Masaoka, *Nat. Commun.*, 2025, **16**, 2145.
10. B. Limburg, E. Bouwman, and S. Bonnet, *ACS Catal.*, 2016, **6**, 5273−5284.
11. L. Zedler, P. Wintergerst, A. K. Mengele, C. Müller, C. Li, B. Dietzek-Ivanšić & S. Rau, *Nat. Commun.*, 2022, **13**, 2538.
12. P. K. Ghosh, B. S. Brunschwig, M. Chou, C. Creutz, and N. Sutin, *Journal of the American Chemical Society*, 1984, **106**, 4772-4783.
13. S. Dai, E. Montero-Lanzuela, A. Tissot, H. G. Baldoví, H. García, S. Navalón and C. Serre*, Chem. Sci.*, 2023, **14**, 3451.
14. P. Salcedo-Abraira, A. A. Babaryk, E. Montero-Lanzuela, O. R. Contreras-Almengor, M. Cabrero-Antonino, E. S. Grape, T. Willhammar, S. Navalón, E. Elkäim and H. García, *Adv. Mater.*, 2021, **33**, 2106627.
15. M. Cabrero-Antonino, J. Albero, C. García-Vallés, M. Álvaro, S. Navalón and H. García, *Chem. Eur. J.*, 2020, **26**, 15682-15689.
16. A. Melillo, M. Cabrero-Antonino, S. Navalón, M. Álvaro, B. Ferrer and H. Garcia, *Appl. Catal. B: Environ.*, 2020, **278**, 119345.
17. W. Guo, S. Shu, T. Zhang, Y.-F. Jian, X. Liu, *ACS Appl. Energy Mater.* 2020, **3**, 2983−2988.
18. F. Camara, J. S. Aguirre-Araque, J. Fortage and M.-N. Collomb, *Sustainable Energy Fuels*, 2024, **8**, 1457.
19. W. Cheng, X. Ren, X. Wang, Z. Huang, Y. Wei, L. Wang, and J. Xu, *Inorg. Chem.*, 2024, **63**, 14050−14061.

20. S. Fang, M. Rahaman, J. Bharti, E. Reisner, M. Robert, G. A. Ozin and Y. H. Hu, *Nat. Rev. Methods* Primers, 2023, **3**, 61.
21. Y. Pellegrin and F. Odobel, *C. R. Chimie*, 2017, **20**, 283-295.
22. H.-Q. Xu, J. Hu, D. Wang, Z. Li, Q. Zhang, Y. Luo, S.-H. Yu, and H.-L. Jiang, *J. Am. Chem. Soc.*, 2015, **137**, 13440−13443.
23. Y. Fu, D. Sun, Y. Chen, R. Huang, Z. Ding, X. Fu, and Z Li, *Angew. Chem.*, 2012, **124**, 3420 –3423.
24. D. Sun, Y. Fu, W. Liu, L. Ye, D. Wang, L. Yang, X. Fu, and Z. Li, *Chem. Eur. J.*, 2013, **19**, 14279 – 14285.
25. C. Jiang, S. J. A. Moniz, A. Wang, T. Zhang and J. Tang, *Chem. Soc. Rev.*, 2017, **46**, 4645.
26. M. Li and M. Dincă, *Journal of the American Chemical Society*, 2011, **133**, 12926-12929.
27. J.-B. Zhang, Y.-B. Tian, Z.-G. Gu, J. Zhang, *Nano-Micro Lett.*, 2024, **16**, 253.
28. P. Wu, S. Geng, X. Wang, X. Zhang, H. Li, L. Zhang, Y. Shen, B. Zha, S. Zhang, F. Huo, W. Zhang, *Angew. Chem. Int. Ed*. 2024, **63**, e202402969.
29. Y. Wang, J. Ma, F. Jin, T. Li, N. Javanmardi, Y. He, G. Zhu, S. Zhang, J. Xu, T. Wang, and Z.-Q. Feng, *Small Sci.*, 2024, **4**, 2400132.
30. M. Zhao, Q. Lu, Q. Ma, H. Zhang, *Small Methods*, 2017, **1**, 1600030.
31. M. Zhao, Y. Huang, Y. Peng, Z. Huang, Q. Ma and H. Zhang, *Chem. Soc. Rev.*, 2018, **47**, 6267-6295.
32. F. Z. Karizi, M. Joharian, and A. Morsali, *J. Mater. Chem. A*, 2018, **6**, 19288-19329.
33. V. Richards, **Commun Chem**, 2022, **5**, 30.
34. R. L. Mander, A. Schmidt, M. Ruf and M. D. Korzyński, *Dalton Trans*., 2024, **53**, 18873-18879.
35. S. Zheng, Y. Sun, H. Xue, P. Braunstein, W. Huang, and H. Pang, *Natl. Sci. Rev.*, 2022, **9**, nwab197.
36. Z. Jia, S. Hao, J. Wen, S. Li, W. Peng, R. Huang, X. Xu, *Microporous and Mesoporous Materials*, 2020, 305, 110322.
37. L.-A. Cao, M.-S. Yao, H.-J. Jiang, S. Kitagawa, X.-L. Ye, W.-H. Lia and G. Xu, *J. Mater. Chem. A*, 2020, **8**, 9085-9090.

38. Y. Liu, M. Mostaghimi, A. Chandresh, S. Jana, W. Wenzel, L. Heinke, *Adv. Funct. Mater.,* 2025, 2423539.
39. M. Sajid, G. Irum, A. Farhan, M. A. Qamar, *Hybrid Advances*, 2024, **5**, 10016.
40. C.-C. Chueh, C.-I. Chen, Y.-A. Su, H. Konnerth, Y.-J. Gu, C.-W. Kung and K. C.-W. Wu*, J. Mater. Chem. A*, 2019, **7**, 17079-17095.
41. Y. Zhang, S. Liu, Z.-S. Zhao, Z. Wang, R. Zhang, L. Liu and Z.-B. Han, *Inorg. Chem. Front.*, 2021, **8**, 590–619.

Chapter 6: Experimental

6.1 Materials and Methods

6.1.1 Reagents

All chemicals were purchased from Sigma-Aldrich, Fluorochem, Fisher Scientific, Acros Organics, VWR, Alfa Aesar, or Sparks Lab Supplies, and were used as received unless otherwise stated. Solvents were of HPLC grade, obtained from the suppliers listed above or supplied internally, and were used without further purification unless otherwise specified. All used water was Millipore deionised water.

6.1.2 NMR Spectroscopy

Samples were dissolved in deuterated solvents, and NMR spectra were recorded at 293 K on a Bruker 400 MHz AVANCE III or Bruker 600 MHz AVANCE II spectrometer by Dr. John O'Brien or Dr. Manuel Rüther. Chemical shifts (δ) are reported in ppm, with residual solvent signals used as internal references. Standard abbreviations are employed: s = singlet; d = doublet; t = triplet; q = quartet; sept = septet; m = multiplet; br = broad; *J* = coupling constant.

6.1.3 Single-Crystal X-Ray Diffraction

Single-crystal X-ray diffraction (SCXRD) data were collected by Dr. Brendan Twamley on a Bruker APEX-II Duo diffractometer equipped with an Incoatec microfocus Cu Kα radiation source (λ = 1.54178 Å) and a Photon 50 CMOS detector. Suitable single crystals were mounted on MiTeGen cryoloops using paraffin oil, and the temperature was controlled at either 100 K or 215 K using an Oxford Cryostream Cobra system. Data reduction and processing were performed with the Bruker *APEX* suite of programs, and absorption corrections were applied using SADABS.[1] Structures were solved by intrinsic phasing with SHELXT[2] and refined against F^2 using full-matrix least-squares methods in SHELXL[3] within the *Olex2* GUI.[4] All non-hydrogen atoms were refined anisotropically, and hydrogen atoms were placed in idealized positions.

6.1.4 Fourier Transform-Infrared Spectroscopy

FTIR spectra were recorded on a PerkinElmer Spectrum 100 spectrometer equipped with

a universal attenuated total reflectance (ATR) accessory. Data were collected and processed using *Spectrum v5.0.1* software. Each spectrum represents an average of eight scans at a spectral resolution of 1 cm^{-1} over the range 4000–350 cm^{-1}. Peak intensities are denoted as: w = weak, m = medium, st = strong, s = shoulder, b = broad.

6.1.5 Raman Spectroscopy

Raman spectra were recorded on a Renishaw 1000 micro-Raman spectrometer equipped with a 785 nm excitation laser, a 50× objective lens, and a cooled CCD detector, providing a spectral resolution of 1 cm^{-1}. Spectra were collected with an integration time of 10 s and averaged over 10 accumulations. The instrument was calibrated against the Si reference band at 520 cm^{-1}. Data acquisition was performed using WiRE 3.2 software, and spectra were processed and analysed with OriginPro 2024.

6.1.6 Thermogravimetric Analysis

Thermogravimetric analysis (TGA) was performed on a Perkin Elmer Pyris-1 thermogravimetric analyser under a nitrogen flow of 20 mL min^{-1}. The instrument was calibrated with nickel and iron standards prior to use. Samples were measured in ceramic crucibles over the temperature range 25–900 °C at heating rates of 3 or 5 °C min^{-1}.

6.1.7 Powder X-Ray Diffraction

Powder X-ray diffraction (PXRD) patterns were recorded on a Bruker D8 ADVANCE diffractometer equipped with a Cu-Kα radiation source (λ = 1.54178 Å) operating at 40 kV and 40 mA. Samples were prepared either on a zero-background holder or in borosilicate glass capillaries (0.5 mm diameter). Data were collected over a 2θ range of 4–80° under ambient conditions and processed using the Bruker DIFFRAC.EVA software package and OriginPro 2024.

6.1.8 Mass Spectrometry

Mass spectrometry (MS) samples were prepared by dissolving approximately 0.5 mg of sample in 1 mL of a suitable HPLC-grade solvent. Electrospray ionisation (ESI) mass spectra were acquired by Dr. Gary Hessman using a Micromass Time-of-Flight LCT mass spectrometer interfaced with a Waters 2690 HPLC.

6.1.9 Scanning Electron Microscopy and Energy Dispersive Spectroscopy

Samples were dispersed in isopropanol (IPA) and drop-cast onto silicon substrates mounted on aluminium stubs using silver paint, followed by sputter-coating with a Au–Pd alloy. Scanning electron microscopy (SEM) imaging was performed on a Zeiss ULTRA Plus SEM operated at an accelerating voltage of 10–20 kV under a vacuum of 1×10^{-5} mbar, using a secondary electron detector. Energy-dispersive X-ray spectroscopy (EDX) spectra were acquired with a 20 mm^2 Oxford Inca detector operated at 15–20 kV, and the resulting data were processed using the *Inca 7.2* software package.

6.1.10 Transmission Electron Microscopy

High-resolution transmission electron microscopy (HR-TEM) images were acquired by Dr. Clive Downing using an FEI Titan 80 transmission electron microscope operated at an accelerating voltage of 300 kV, with an informational resolution of 1 Å. The samples were sonicated in isopropanol (IPA) and drop-cast onto a lacey carbon-coated copper TEM grid. Image processing and analysis were carried out using the *DigitalMicrograph-3* software package.

Lattice spacings of individual crystallites were determined using the Fast Fourier Transformation (FFT) method. As illustrated in Figure 6.1, a diffractogram for a single crystallite was generated via FFT. The diffractogram contains two spots arising from the diffraction of the electron beam (central spot) by a single lattice plane. A mask was placed over the diffractogram so that only the two diffraction spots remained visible, thus removing noise. Inverse FFT processing of the masked diffractogram, reproducing the original crystallite lattice fringes—now denoised—allowed for the accurate measurement of lattice spacing via line profiling.

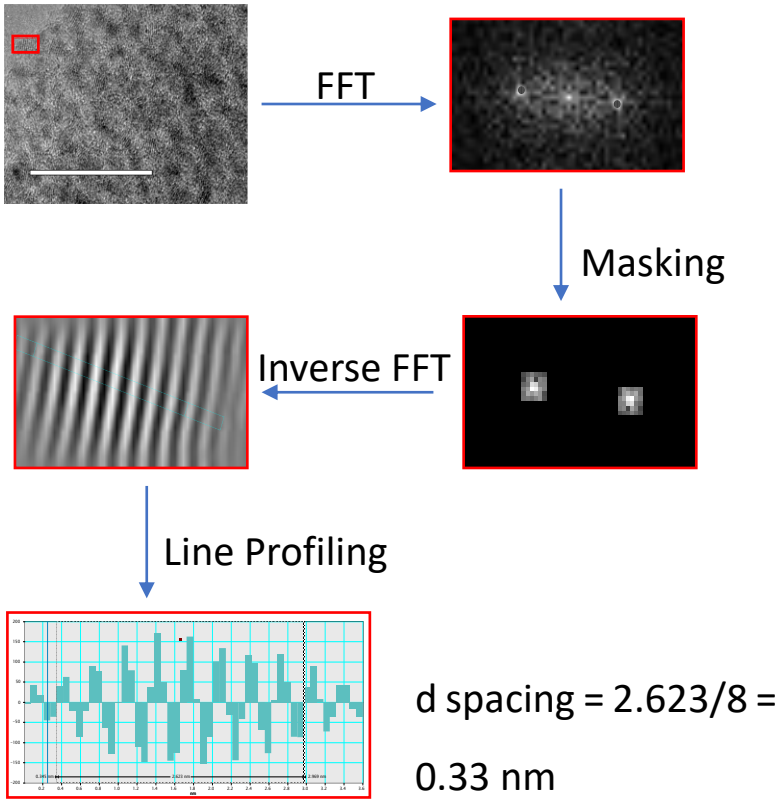

Figure 6.1: Schematic illustration of the FFT method. A diffractogram for a single crystallite is generated via Fast Fourier Transformation (FFT). The diffractogram contains two spots arising from the diffraction of the electron beam (central spot) by a single lattice plane. A mask is place over the diffraction so that only the two diffraction spots remain visible, thus removing noise. Inverse FFT processing of the masked diffractogram reproduced the original crystallite lattice fringes, now denoised, allowing for the accurate measurement of lattice spacing via line profiling.

6.1.11 UV-Vis Absorption Spectroscopy

UV-Vis measurements were performed in an appropriate solvent using matched quartz cuvettes with an optical pathlength of 1 cm. Absorption spectra were measured between the range of 200-800 nm at room temperature using a Perkin Elmer Lambda 35 spectrometer, or by a Cary 50 UV-vis spectrophotometer operated by Kseniia Mamaeva. The obtained spectra were process and analysed in OriginPro 2024.

6.1.12 Photoluminescence and Time-Resolved Photoluminescence Spectroscopy

Solid-state photoluminescence (PL) and time-resolved photoluminescence (TRPL) measurements were carried out by Kseniia Mamaeva using a PicoQuant MicroTime 200 time-resolved confocal microscope. Samples were drop-cast onto glass slides and dried before measurement. Excitation was provided by 90 ps laser pulses at 405 nm with a

repetition rate of 10 MHz, delivered through a 40× objective (NA = 0.65), with a resulting laser spot size of ~430 nm. PL emission was collected in epi-detection mode through the same objective.

All scans were performed over 10 µm × 10 µm areas. For TRPL, the excitation power was set to 0.2 µW, while steady-state PL measurements were performed over the same regions using a higher excitation power of 4 µW. The integration time for TRPL scans was 4 ms per pixel.

6.1.13 Electrochemical Experiments

OER Experiments

Heterogeneous electrocatalytic studies were carried out using an ALS-RRDE-3A rotating disk electrode (RDE) system coupled to a Biologic VSP potentiostat. A standard three-electrode configuration was employed, consisting of a Hg/HgCl (3 M KCl) reference electrode, a Pt wire counter electrode, and a modified carbon paste (CP) working electrode using 0.5 M H_2SO_4 aqueous electrolyte.

The CP electrodes were prepared by thoroughly grinding carbon paste with the desired amount of catalyst in an agate mortar. The resulting CP blend was packed into the electrode cavity (surface area: 0.07 cm^2) and polished with satin weighing paper to ensure a smooth surface. For linear sweep voltammetry (LSV) and cyclic voltammetry (CV) experiments, the catalyst loading was 20 wt%. For chronopotentiometry measurements, a higher loading of 40 wt% was used, and the electrode surface was coated with 10 µL of Nafion® 117 solution and allowed to dry prior to testing.

LnRu-MOF Characterisation

Cyclic voltammetry (CV) experiments were carried using a Bio-logic VSP Potentiostat, with a three-electrode set-up consisting of a glassy carbon working electrode, a Pt-wire as counter electrode, and a Ag/Ag^+ reference electrode (Ag wire, 0.01 M $AgNO_3$, 0.1 M $TBAPF_6$ acetonitrile solution). Ferrocene was used as an external standard for the reference electrode. The electrolyte was 0.1 M tetrabutylammonium hexafluorophosphate ($TBAPF_6$) acetonitrile solution. Extra dry acetonitrile from Acros Organics was used to make the electrolyte, $TBAPF_6$ was recrystallised from hot ethanol:H_2O solution before use. Experiments were conducted under Argon.

Photoelectrocatalytic CO_2 Reduction

Photoelectrocatalytic CO_2 reduction experiments were performed in a gas-tight three-electrode cell, with **EuRu-MOF/FTO** (or bare FTO-coated glass as a control) as the working electrode, a Pt mesh counter electrode, and an Ag/Ag^+ reference electrode (Ag wire in 0.01 M $AgNO_3$, 0.1 M $TBAPF_6$ acetonitrile solution) connected via a Luggin capillary. The electrolyte solution (0.1 M $TBAPF_6$ in acetonitrile) was purged with either CO_2 or Ar (for control experiments) prior to measurements. Photoelectrocatalytic CO_2RR experiments were carried out under a constant applied potential of –1.5 V vs. Fc/Fc^+ for 24 h under both illuminated (465 nm LED, 44 mW cm^{-2}) and dark conditions.

Gas-phase products from the headspace were analysed by gas chromatography with barrier ionisation detection (GC-BID, Shimadzu GC-2030), while liquid-phase products were analysed using anion chromatography (ThermoFisher Dionex Aquion) and high-performance liquid chromatography (HPLC, Varian LC-920).

6.1.14 Photocatalytic Water Splitting Experiments

Photocatalytic water splitting experiments were performed using a two-component system comprising a photocatalyst and either a sacrificial electron acceptor (SEA) or a sacrificial electron donor (SED) in Millipore deionised water. For oxygen evolution reaction (OER) experiments, sodium persulfate (10 mM) was used as the SEA; for hydrogen evolution reaction (HER) experiments, methanol was used as the SED at a MeOH:H_2O ratio of 1:4.

Reactions were carried out in hermetically sealed 5 mL borosilicate glass vials equipped with rubber septa and magnetic stirring bars. The systems were purged with pure Ar prior to illumination. A Clark electrode with a piercing needle tip (UNISENSE, OX NP or H_2 NP) and a ground cable were inserted through the septum into the solution. The reaction mixture was stirred at 500 rpm and maintained at 25 °C in a temperature-controlled water bath. For OER experiments, the photocatalyst and sodium persulfate solution were purged separately in 2.5 mL aliquots before being combined immediately prior to illumination.

After a stable baseline was established in the dark, the samples were irradiated with a 465 nm LED light source (44 mW cm^{-2}), and dissolved O_2 or H_2 concentrations were monitored

using the Clark electrode connected to a UNISENSE Monometer interfaced with a PC operating the Logger application of the SensorTrace Suite software package. Data were recorded at 1 Hz, and the electrode was calibrated before each experiment using a two-point calibration method: (a) a zero-O_2 (or zero-H_2) solution prepared by purging with Ar, and (b) an air-saturated (for O_2) or H_2-saturated (for H_2) water solution at 25 °C.

6.1.15 Photocatalytic CO_2 Reduction Experiments

For each experiment, 5 mg of photocatalyst was suspended in 5 mL of acetonitrile containing 1.5 mmol (0.3 mol L^{-1}) N,N-dimethylaniline (DMA) and sealed in a borosilicate glass vial with a butyl-rubber septum. The solutions were purged with CO_2 for 20 min prior to illumination (Ar purging was used for control experiments). Photocatalytic reactions were conducted in a Luzchem LZC photoreactor (equipped with 10 × 8 W Sylvania T5 fluorescent white bulbs, 400 lm each), under magnetic stirring at 500 rpm for the desired irradiation time.

Gas-phase products in the vial headspace were analysed by gas chromatography with barrier ionisation detection (GC-BID, Shimadzu GC-2030). Liquid-phase products were quantified using anion chromatography (ThermoFisher Dionex Aquion) and high-performance liquid chromatography (HPLC, Varian LC-920).

6.1.16 Gas Chromatography

Gas-phase products were analysed using a Shimadzu GC-2030 equipped with a barrier ionisation detector (BID), following a method adapted from a Shimadzu application note.[5] Helium was used as the carrier gas, and separations were performed on a Restek 2 m × 1 mm micropacked ShinCarbon ST column. Calibration curves were prepared using 5% CO in N_2 (BOC) for CO quantification and a ≥99% methane standard (Sigma-Aldrich) for CH_4.

Samples were introduced by manual injection with a 1:4 split. The injector was maintained at 150 °C, with a carrier gas flow of 7 mL min^{-1} and purge flow of 3 mL min^{-1}. The detector temperature was set at 280 °C, with a helium discharge gas flow of 50 mL min^{-1}. The temperature and pressure programmes applied to the column are shown in Figure 6.2.

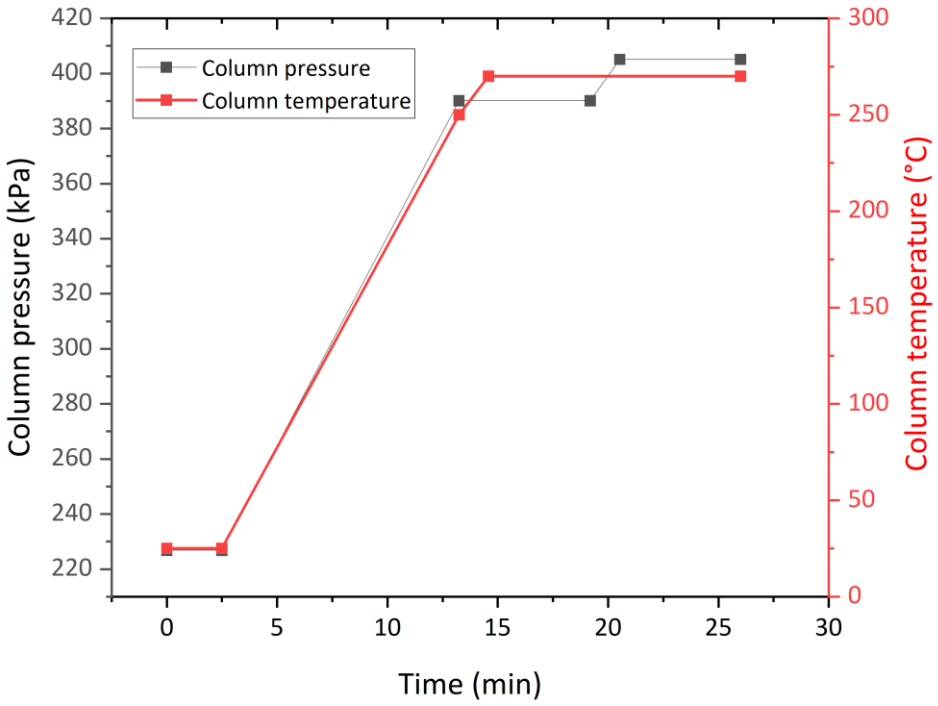

Figure 6.2: Column temperature and pressure programme. Carrier Gas: He, 226.8 kPa (2.5 min) - 15.2 kPa/min - 390.1 kPa (5.95 min) - 11.2 kPa/min - 405.1 kPa (5.42 min) Column Temperature: 35 °C (2.5 min) - 20 °C/min - 250 °C (0 min) - 15 °C/min - 270 °C (11.42 min).

6.1.17 Ion Chromatography

Formate was quantified using ion chromatography on a ThermoFisher Dionex Aquion system operated in anion mode with a conductivity detector. The eluent consisted of 1 mM $NaHCO_3$ and 3.2 mM Na_2CO_3, with the suppressor current set to 5 mA to achieve a stable baseline conductivity signal. The flow rate was maintained at 0.25 mL min^{-1}. Calibration was performed using a sodium formate standard (Sigma-Aldrich), the resulting calibration curve is presented in Figure 6.3.

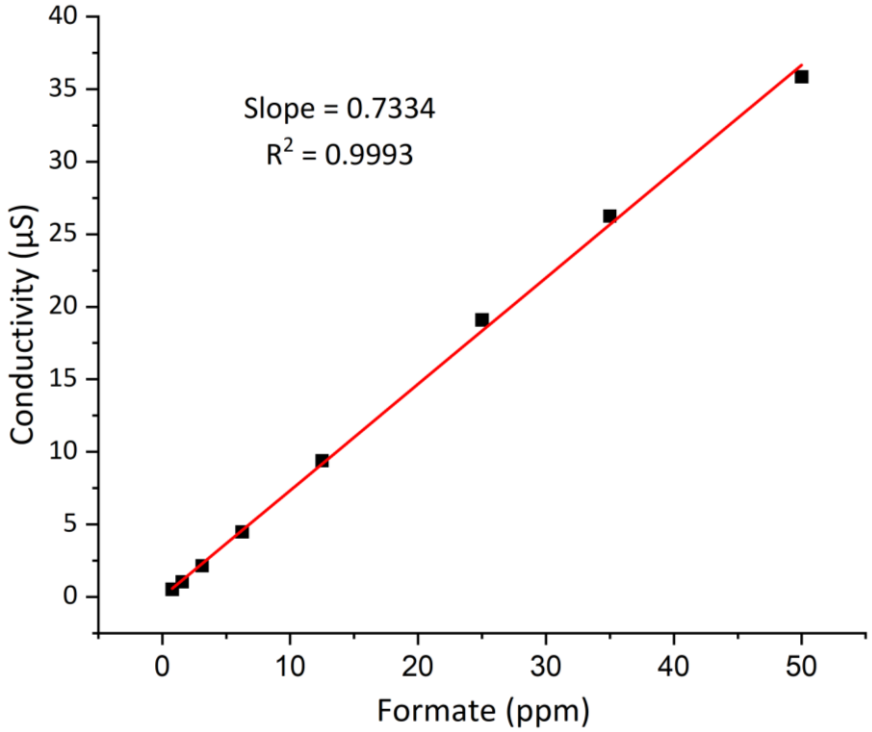

Figure 6.3: Ion chromatography calibration curve for formate.

6.2 Synthesis of MOF Linkers

The two-step synthesis of **H_3TTT** (6.2.1-6.2.2) was carried out according to procedures reported by Trindade and Whelan.[6,7] The synthesis of **$[H_4L_{Ru}](ClO_4)_2$** (6.2.3-6.2.10) was achieved using an 8-step synthetic procedure first reported by Mulahmetović.[8]

6.2.1 Synthesis of 2,4,6-tri(thiophen-2-yl)-1,3,5-triazine (TTT)

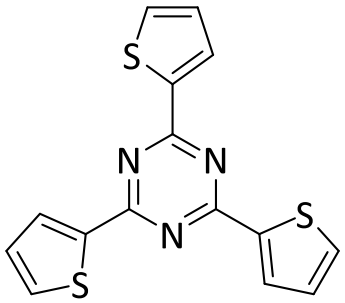

Trifluoromethanesulfonic acid (17.64 mL, 200 mmol) was added dropwise over 1 h to a stirred solution of thiophene-2-carbonitrile (9.30 mL, 100 mmol) in dry chloroform at 0 °C under an argon atmosphere. All glassware was evacuated and refilled with argon three times prior to use. The reaction mixture was stirred at 0 °C for 1 h, then allowed to warm to room temperature and stirred for an additional 16 h, during which the solution gradually turned orange. The reaction was quenched by pouring into dilute aqueous NH_4OH, followed by filtration. The solid was washed sequentially with water (50 mL), acetone (50 mL), and methanol (100 mL), affording 2,4,6-tri(thiophen-2-yl)-1,3,5-triazine as an off-white solid (9.96 g, 30 mmol, 90% yield). **^{1}H NMR** (600 MHz, $CDCl_3$): δ (ppm) = 7.24 (3H,

dd, J = 3.92, 5.05 Hz), 7.64 (3H, dd, J = 1.2, 5.05 Hz), 8.31 (3H, dd, J = 3.92, 1.2 Hz). **^{13}C{^{1}H} NMR** (100 MHz, $CDCl_3$): δ (ppm) = 77.0, 128.5, 131.7, 132.4, 141.4, 167.7. **FTIR** (ATR, $\bar{\nu}_{max}$, cm^{-1}): 486 (m), 574 (m), 630 (m), 707 (s), 773 (m), 815 (s), 860 (m), 1030 (m), 1219 (w), 1372 (s), 1422 (s), 1498 (s). **HRMS** (ESI^+): *m/z* = 328.0083 $[M+H]^+$ ($C_{15}H_9N_3S_3$ requires 327.4507).

6.2.2 Synthesis of 5,5',5''-(1,3,5-triazine-2,4,6-triyl)tris(thiophene-2-carboxylic acid) (H_3TTT)

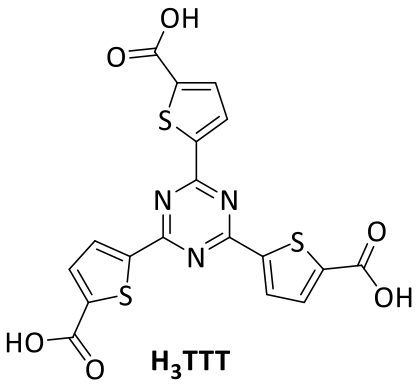

H_3TTT

A solution of lithium diisopropylamide (LDA) was prepared by adding *n*-butyllithium (10 mL, 2.5 M, 25.0 mmol) dropwise to diisopropylamine (3.5 mL, 24.8 mmol) in dry THF (40 mL) at –78 °C under an argon atmosphere. The mixture was stirred for 15 min, after which a solution of 2,4,6-tri(thiophen-2-yl)-1,3,5-triazine (2.00 g, 6.11 mmol) in dry THF (40 mL) was added dropwise. The resulting solution was stirred for 10 min before dry ice pellets were added slowly. The reaction mixture was allowed to warm to room temperature and stirred for 24 h under argon, during which the colour changed from purple to pale yellow. The solvent was removed under reduced pressure, and the resulting residue was dissolved in water. The aqueous solution was acidified to pH 1 with 1 M HCl, affording a pale-yellow precipitate, which was collected by filtration and recrystallised from THF. The product was dried under vacuum for 24 h to yield **H_3TTT** as a beige solid (1.45 g, 3.16 mmol, 52% yield). **^{1}H NMR** (600 MHz, DMSO-d_6): δ(ppm) = 7.84 (3H, d, J = 3.6 Hz), 8.26 (3H, d, J = 3.95 Hz), 13.66 (3H, br, COOH). **^{13}C{^{1}H} NMR** (100 MHz, DMSO-d_6): δ(ppm) = 132.5, 133.9, 140.5, 144.8, 162.4, 166.6. **FTIR** (ATR, $\bar{\nu}_{max}$, cm^{-1}): 218 (m), 574 (w), 750 (s), 784 (s), 999 (w), 1261 (s), 1367–1408 (m), 1505 (s), 1674 (s), 2856 (w), 2982 (w), 3380 (w). **HRMS** (ESI^+): *m/z* = 459.9728 $[M+H]^+$ ($C_{18}H_9N_3S_3O_6$ requires 459.4777).

6.2.3 Synthesis of 2,2'-bipyridine-dihydrobromide

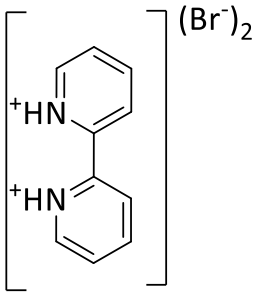

Hydrobromic acid (21.5 mL, 48 wt%, ~190 mmol HBr) was added dropwise to a stirred solution of 2,2'-bipyridine (10.0 g, 64.0 mmol) in methanol (100 mL) at 0 °C. The reaction mixture was stirred for 1 h while warming to room temperature, after which the solvent was removed under reduced pressure. The resulting bright yellow solid was dried under vacuum overnight to afford the product in quantitative yield. **^{1}H NMR** (400 MHz, $CDCl_3$): δ(ppm) = 7.78 (s, 2H), 8.30 (s, 4H), 8.70 (s, 2H).

6.2.4 Synthesis of 5,5'-dibromo-2,2'-bipyridine

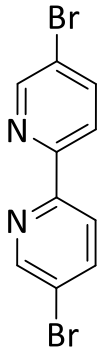

2,2'-Bipyridine-dihydrobromide (12.0 g, 37.7 mmol) was finely ground in a mortar and pestle, and bromine (4.00 mL, 2.40 g, 77.6 mmol) was added dropwise to the powder while continuously grinding until a fine, non-fuming orange powder was obtained. The resulting mixture was transferred to Teflon-lined stainless-steel autoclaves and heated at 185 °C for 72 h. After cooling to room temperature, the reaction mixture was slowly quenched with 1 M aqueous NaOH (200 mL). EDTA-tetrasodium salt (10.0 g), Na_2SO_3 (10.0 g), and dichloromethane (250 mL) were then added sequentially. The suspension was stirred at room temperature for 2 h, during which a white precipitate formed. The solid was collected by filtration, washed sequentially with boiling H_2O (2 × 50 mL) and EtOH (2 × 50 mL), and dried overnight to afford the product as a white solid (8.4g, 26.8 mmol, 71% yield). **^{1}H NMR** (400 MHz, $CDCl_3$): δ(ppm) = 7.96 (dd, J = 8.65, 2.11 Hz, 2H), 8.31 (d, J = 8.43 Hz, 2H), 8.73 (d, J = 1.87 Hz, 2H).

6.2.5 Synthesis of dimethyl 5-(2-(trimethylsilyl)ethynyl)isophthalate

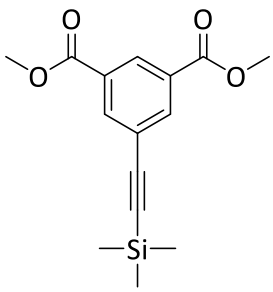

Dimethyl 5-bromoisophthalate (5.00 g, 18.3 mmol), CuI (0.175 g, 0.92 mmol), and $Pd(PPh_3)_2Cl_2$ (0.640 g, 0.92 mmol) were added to a pre-evacuated round-bottom flask under a nitrogen atmosphere. Trimethylsilylacetylene (3.80 mL, 27.5 mmol), THF (100 mL), and triethylamine (10.0 mL, 71.8 mmol) were then added via syringe. The reaction mixture was stirred at room temperature under nitrogen for

24 h and subsequently concentrated under reduced pressure. The residue was redissolved in dichloromethane, washed sequentially with aqueous NH_4Cl (2 × 50 mL), H_2O (2 × 50 mL), and brine (50 mL). The organic phase was dried over $MgSO_4$, filtered, and the solvent removed in vacuo. Purification by column chromatography over silica gel (hexane/DCM, 4:1 v/v) afforded the product as an off-white crystalline solid (4.15 g, 12.4 mmol, 68% yield). **^{1}H NMR** (400 MHz, $CDCl_3$): δ(ppm) = 0.29 (s, 9H), 3.96 (s, 6H), 8.31 (d, J = 1.67 Hz, 2H), 8.63 (t, J = 1.70 Hz, 1H).

6.2.6 Synthesis of dimethyl 5-ethynylisophtalate

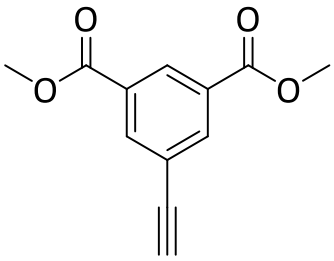

Dimethyl 5-(2-(trimethylsilyl)ethynyl)isophthalate (2.50 g, 9.16 mmol) and K_2CO_3 (2.50 g, 18.1 mmol) were dissolved in dichloromethane (50 mL) and methanol (25 mL) in a pre-evacuated three-neck round-bottom flask under a nitrogen atmosphere. The reaction mixture was stirred at room temperature for 6 h. The solvent was removed under reduced pressure, and the residue was redissolved in dichloromethane, washed sequentially with H_2O (2 × 30 mL) and brine (30 mL), dried over $MgSO_4$, filtered, and concentrated under reduced pressure to give the product in quantitative yield. **^{1}H NMR** (400 MHz, $CDCl_3$): δ(ppm) = 3.18 (s, 1H), 3.97 (s, 6H), 8.33 (d, J = 1.70 Hz, 2H), 8.65 (t, J = 1.69 Hz, 1H).

6.2.7 Synthesis of bis-(2,2'-bipyridine)-ruthenium(II) dichloride

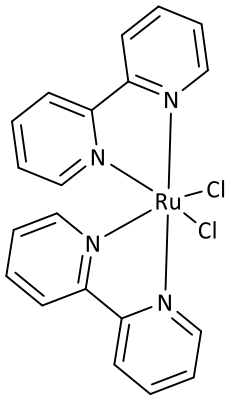

$RuCl_3 \cdot xH_2O$ (2.00 g, 8.40 mmol), LiCl (0.40 g, 9.60 mmol), and 2,2'-bipyridine (2.60 g, 16.65 mmol) were added to a 100 mL three-neck round-bottom flask that had been evacuated and flushed with N_2 three times. Dry DMF (30 mL) was added, and the mixture was refluxed at 160 °C for 18 h under stirring. After cooling to ~50 °C, acetone (30 mL) was added, and the mixture was stirred for 1 h. The resulting dark purple crystalline precipitate was collected by filtration, washed with cold H_2O until the filtrate was colourless, and dried to afford the product in 46% yield (1.87g, 3.86mmol). **^{1}H NMR** (400 MHz, DMSO-d_6,): δ(ppm) = 7.12 (t, J = 6.20 Hz, 2H), 7.48 (m, 2H), 7.67 (t, J = 7.70 Hz, 2H), 7.78 (t, J = 6.20 Hz, 2H), 8.08 (t, J = 7.77 Hz, 2H), 8.50 (d, J = 7.84 Hz, 2H), 8.65 (d, J = 7.89 Hz, 2H), 9.94 (m, 2H). **^{13}C{^{1}H} NMR** (150.9 MHz, DMSO-d_6,): δ(ppm)

= 122.5, 122.9, 125.3, 125.4, 133.3, 134.6, 152.0, 153.2, 158.2, 160.2. **HRMS** (ESI$^+$): *m/z* = 449.0103 $[M]^+$ ($C_{20}H_{16}ClN_4Ru$ requires 449.01).

6.2.8 [Ru(bpy)$_2$(5,5'-dibromo-2,2'-dipyridine)](PF$_6$)$_2$

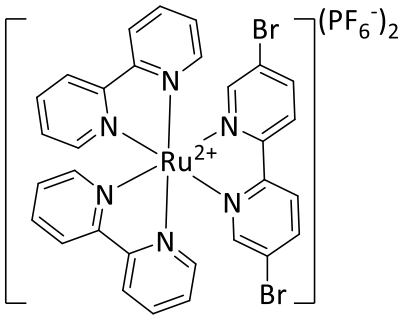

Bis(2,2'-bipyridine)ruthenium(II) dichloride (0.50 g, 1.10 mmol) and 5,5'-dibromo-2,2'-bipyridine (0.35 g, 1.10 mmol) were dissolved in EtOH/H_2O (100 mL, 2:1 v/v) and refluxed at 120 °C overnight under N_2. During the reaction, the solution colour changed from purple to red. After cooling, the solvent was removed under reduced pressure, and the residue was redissolved in deionised water (80 mL) and filtered. Addition of a saturated aqueous solution of NH_4PF_6 afforded a bright orange precipitate, which was collected by filtration, washed with water, and dried under vacuum. Recrystallisation from hot EtOH/H_2O (2:1) yielded the product as an orange crystalline solid (0.64 g, 0.88 mmol, 80% yield). **^{1}H NMR** (400 MHz, DMSO-d_6): δ(ppm) = 7.55 (m, 4H), 7.68 (m, 4H), 7.85 (d, J = 5.23 Hz, 2H), 8.20 (m, 4H), 8.47 (dd, J = 8.75, 2.05 Hz, 2H), 8.80 (m, 6H). **HRMS (ESI$^+$):** *m/z* = 363.9668 $[M]^{2+}$ ($C_{30}H_{21}Br_2N_6Ru^{2+}$ requires 362.97).

6.2.9 Synthesis of [Me$_4$L$_{Ru}$](PF$_6$)$_2$

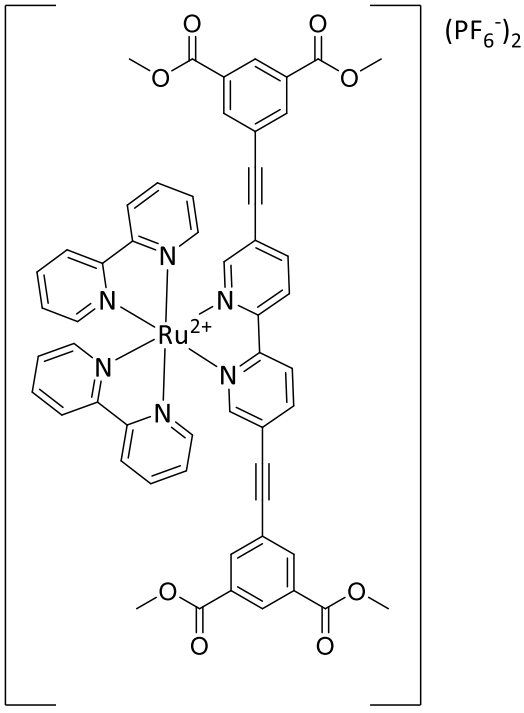

[Ru(bpy)$_2$(5,5'-dibromo-2,2'-dipyridine)](PF$_6$)$_2$ (0.60 g, 0.59 mmol) and dimethyl 5-ethynylisophthalate (1.48 g, 2.5 equiv.) were dissolved in dry THF (25 mL) and dry acetonitrile (9.5 mL) in a three-neck round-bottomed flask under N_2. Diisopropylamine (12 mL), Pd(PPh$_3$)$_2$Cl$_2$ (0.035 g, 0.05 mmol), and CuI (0.010 g, 0.05 mmol) were added, and the reaction mixture was refluxed at 100 °C for 72 h under N_2. The resulting dark orange product was collected by filtration and dried in an oven at 50 °C overnight to afford the desired complex in 76% yield (0.58 g, 0.45 mmol).

^{1}H NMR (400 MHz, DMSO-d_6,): δ(ppm) = 3.92 (s, 12H), 7.57 (m, 4H), 7.70 (m, 2H), 7.88 (m,

2H), 7.93 (m, 2H), 8.20 (m, 4H), 8.27 (m, 4H), 8.48 (m, 4H), 8.85 (m, 4H), 8.99 (m, 2H).**^{13}C{H}-NMR** (DMSO-d_6, 150.9 MHz); δ(ppm) = 52.9, 86.7, 93.9, 122.4, 124.6, , 124.9, 127.9, 130.2, 131.1, 136.0, 138.2, 140.5, 151.2, 151.9, 153.1, 155.8, 156.6, 164.5.b **FTIR** (ATR, $\bar{\nu}_{max}$, cm^{-1}): 2954 (w), 2160 (m), 1977 (m), 1724 (s), 1604 (m), 1442 (m), 1244 (s), 1160 (w), 1104 (w), 992 (m), 828 (s), 754 (s), 747 (s). **HRMS (ESI$^+$):** *m/z* = 501.0983 [M^{2+}] ($C_{54}H_{40}N_6O_8Ru$ requires 501.10).

6.2.10 Synthesis of $[H_4L_{Ru}](ClO_4)_2$

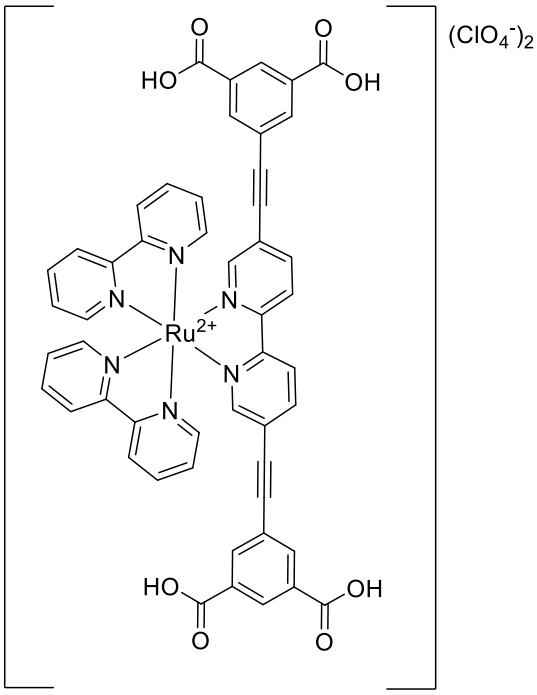

$[Me_4L_{Ru}](PF_6)_2$ (0.450 g, 0.449 mmol) was dissolved in THF (30 mL) and added to an aqueous NaOH solution (15 mL, 1 M). The mixture was stirred overnight at room temperature. THF was removed under reduced pressure, and the resulting basic aqueous solution was acidified by the dropwise addition of $HClO_4$ (25 mL, 70% w/w) over 5 min, followed by stirring for 30 min. An orange precipitate formed, which was collected by filtration, washed with deionised water, and air-dried for two days to afford the product in quantitative yield. *Note:* For the acidification step, the order of addition was found to be important—addition of the basic solution into acid ensured complete protonation, whereas the reverse (acid into base) typically yielded an insoluble, partially protonated, charge-neutral species. **^{1}H NMR** (600 MHz, DMSO-d_6,): δ(ppm) = 7.58 (m, 4H), 7.71 (d, J = 5.25 Hz, 2H), 7.88 (d, J = 5.38 Hz, 2H), 7.91 (d, J = 1.89 Hz, 2H), 8.20 (m, 8H), 8.48 (m, 4H), 8.85 (m, 4H), 8.98 (d, J = 8.50 Hz, 2H), 13.61 (br, 4H). **^{13}C{^{1}H} NMR** (150.9 MHz, DMSO-d_6,): δ(ppm) = 86.2, 94.1, 121.9, 122.4, 124.6, 124.8, 127.9, 130.7, 132.2, 135.8, 138.1, 140.4, 151.2, 151.8, 152.9, 155.7, 156.5, 165.6. **FTIR** (ATR, $\bar{\nu}_{max}$ cm^{-1}): 3286 (br), 2903 (w), 2158 (m), 1974 (m), 1685 (m), 1602 (m), 1465 (m), 1448 (m), 1272 (m), 1231 (w), 1070 (s), 908 (w), 836 (s), 761 (s), 663 (m), 620 (s), 555 (w). **HRMS** (ESI$^+$): *m/z* = 473.0688 [M^{2+}] ($C_{50}H_{32}N_6O_8Ru$ requires 473.07).

6.3 Synthesis of Metal-Organic Frameworks with Lanthanide SBUs

6.3.1 Synthesis of $[Ce(TTT)(DMF)]_n$ (Ce–TTT)

5,5′,5″-(1,3,5-triazine-2,4,6-triyl)tris(thiophene-2-carboxylic acid) (**H_3TTT**, 46.0 mg, 0.10 mmol) and cerium(III) chloride heptahydrate (37.25 mg, 0.10 mmol) were dissolved in DMF (8 mL) in a glass vial and sonicated for 10 min until homogeneous. The mixture was heated at 100 °C for 48 h to afford yellow crystals, which were collected in 77% yield (52 mg, 0.077 mmol). Characterised by PXRD, SEM, TGA and FTIR see section 2.3.

6.3.2 Synthesis of $[Ce(BTB)(DMF)]_n$ (Ce–BTB)

1,3,5-Benzenetrisbenzoic acid (**H_3BTB**, 0.438 g, 1.0 mmol) and cerium(III) chloride heptahydrate (0.373 g, 1.0 mmol) were dissolved in DMF (20 mL) in a Teflon-lined reaction vessel and sonicated for 10 min until homogeneous. A drop of triethylamine was added, and the mixture was further sonicated to homogenise the precipitate. The reaction was then heated at 120 °C for 72 h to yield off-white crystals in 85% yield (650.9 mg, 1.0 mmol). Characterised by PXRD, SEM, TGA and FTIR, see section 2.4.

6.3.3 Synthesis of $[Ce(TTB)(DMF)]_n$ (Ce–TTB)

4,4′,4″-(1,3,5-triazine-2,4,6-triyl)tris(benzoic acid) (**H_3TTB**, 44.0 mg, 0.10 mmol) and cerium(III) chloride heptahydrate (37.25 mg, 0.10 mmol) were dissolved in DMF (8 mL) in a glass vial and sonicated for 10 min until homogeneous. The reaction mixture was heated at 100 °C for 48 h, affording off-white crystals in 80% yield (52 mg, 0.077 mmol). Characterised by PXRD, SEM, TGA and FTIR see section 2.5.

6.3.4 Synthesis of $[Ln_2(L_{Ru})(NO_3)_4(DMF)(H_2O)]_n$ (LnRu-MOF) (Ln = Ce, Nd, Sm, Eu, Gd, Dy, Er)

$[H_4L_{Ru}](ClO_4)_2$ (20 mg, 0.015 mmol), $Ln(NO_3)_3.xH_2O$ (0.075 mmol; Ln = Ce, Nd, Sm, Eu, Gd, Dy or Er; x = 5, 6 or 7) $NaNO_3$ (18 mg, 0.212 mmol) and were dissolved in a solution of DMF:EtOH:H_2O (8 mL, 3:3:2, v/v) in a crimp-top glass vial. This was sonicated for several minutes to ensure a homogeneous solution. The reaction solution was heated to 85℃ in an oven for 24-48 h in the pressurised reaction vessel. Red crystals of **LnRu-MOF** were obtained with a typical yield of 15-20 mg. Characterised by SCXRD, PXRD, SEM, FTIR, Raman, and TGA, see sections 4.4 - 4.5.

6.3.5 Bulk Cathodic Electrochemical Synthesis and Deposition of LnRu-MOF Thin Films (Ln = Ce or Eu)

$[H_4L_{Ru}](ClO_4)_2$ (0.115 g, 0.100 mmol), $Ln(NO_3)_3.xH_2O$ (0.200 mmol; Ln = Ce or Eu; x = 5 or 6), $NaNO_3$ (0.030 g, 0.353 mmol) were combined in 7 mL of electrolyte (0.1 M $TBAPF_6$) in DMF/H_2O (100/1 v/v) and sonicated for several minutes. The electrochemical cell with a fluorine-doped tin oxide (FTO) working electrode, a platinum wire counter electrode, and a Ag/Ag^+ (2,2,2-cryptand) /DMF reference electrode was set up with the reaction mixture. The solution was bubbled with N_2 for several minutes. A potential of -1.5 V vs Ag/Ag^+(222-cryptand) was applied for 300 seconds at ambient temperature under N_2. A homogeneous orange thin film was formed on the surface of the FTO electrode. The FTO electrode was removed from solution and washed with DMF. Characterised by PXRD, SEM, FTIR and Raman spectroscopy, see section 5.3.2.

6.4 References

1. G.M. Sheldrick, SADABS Version 2008/1, Bruker AXS Inc., Germany, 2008.
2. G. M. Sheldrick, *Acta Crystallogr. Sect. A Found. Crystallogr.*, 2015, **A71**, 3-8.
3. G. M. Sheldrick, *Acta Crystallogr. A*, 2008, **64**, 112–122.
4. O. V. Dolomanov, L. J. Bourhis, R. J. Gildea, J. A. K. Howard and H. Puschmann, *J. Appl. Crystallogr.*, 2009, 42, 339–341.
5. Shimadzu Corporation, https://www.shimadzu.com/an/sites/shimadzu.com.an/files/pim/pim_document_file/applications/application_note/13355/jpc117012.pdf (accessed 2022).
6. Z. Wang, J. Liu, Y. Fu, C. Liu, C. Pan, Z. Liu and G. Yu, *Chem. Commun.*, 2017, **53**, 4128–4131.
7. É. Whelan, PhD Thesis, University of Dublin, 2023.
8. M. Mulahmetović, PhD Thesis, University of Dublin, 2023.

Chapter 7: Conclusions & Outlook

This thesis establishes lanthanide-based metal-organic frameworks and their derivatives as a tuneable platform for redox catalysis (utilising the Ce^{3+}/Ce^{4+} and Eu^{3+}/Eu^{2+} redox couples) in solar-to-fuel applications. Novel contributions include the first systematic study of Ce(III)-MOFs as pre-catalysts for acidic OER, a series of CeO_2-carbon composites derived from their controlled pyrolysis (including the first lanthanide(III) sulfide phase synthesised from a MOF precursor) and the first report of a Ru-photosensitised Ln-MOF series that is isostructural from Ce to Er). Together these systems demonstrate the role of linker design in shaping catalytic performance of Ln-MOFs under both electrocatalytic and photocatalytic conditions.

Chapter 2 established that an isoreticular series of Ce(III)-MOFs with 1D rod-type SBUs act as pre-catalysts for OER-active cerium(IV) oxide species under the harsh acidic conditions relevant to PEM electrolysers. The tritopic linker (TTT, BTB, or TTB) governed catalytic performance, with **Ce-TTT** most active by turnover frequency. All three MOFs outperformed commercial CeO_2 nanoparticles in both activity per active site and stability, leaching markedly less Ce into the electrolyte over 1000 CV cycles, though porous-microparticle geometry slowed their intrinsic kinetics relative to nanoparticulate CeO_2. Morphology optimisation, not pursued here, is a plausible route to improve kinetics at higher overpotentials.[1-3]

Chapter 3 built on this by using the same Ce-MOF series as sacrificial templates for controlled pyrolysis at 800 °C, yielding CeO_2–carbon composites with substantially improved acidic OER performance. At 10 mA cm^{-2}, the pyrolysed materials required lower overpotentials than both their parent MOFs and the commercial CeO_2. Tafel analysis and Raman spectroscopy together indicated that the sp^2-rich carbon matrix is responsible for the kinetic improvement, and chronopotentiometry confirmed stable 24 h operation for all three composites. Under the more severe 1000-cycle CV test, only **Ce-TTT@800/CP** retained activity; a red shift of the Ce F_{2g} Raman peak points to stronger anchoring of cerium phases to the carbon matrix in this sample, consistent with its cycling stability. Pyrolysis of **Ce-TTT** also produced a Ce_2S_3 phase formed through in-situ generation of CS_2 from the thiophene linker and carbothermic sulfurisation of CeO_2.[4] This represents the

first report of a lanthanide(III) sulfide derived from a MOF precursor, and establishes a facile route to lanthanide(III) sulfide materials from lanthanide(III)-thiophene MOFs, inviting further study of reaction conditions that control phase formation.

Taken together, Chapters 2 and 3 demonstrate that CeO_2-based acidic OER catalysts can be meaningfully engineered through both linker choice in the Ce-MOF precursor and pyrolytic conditioning, with anchoring of CeO_2 nanocrystallites to an sp^2-rich carbon support emerging as the key design feature for activity and stability in acidic media.

The second half of this work incorporated an acetylene-extended Ru(II) polypyridyl metalloligand, $\mathbf{[H_4L_{Ru}]^{2+}}$, as a photosensitising linker for lanthanide-based MOFs. Chapter 4 reported a novel isostructural series of 2D **LnRu-MOFs** (Ln = Ce, Nd, Sm, Eu, Gd, Tb, Dy, Er), the first such series for a Ru-photosensitised Ln-MOF system, and a rare example of a lanthanide coordination series structurally uninterrupted by the *gadolinium break* in *Lewis* acidity. The Ru(II) metalloligand retains its photosensitising properties within the framework, and photoluminescence measurements revealed systematic emission shifts that track Ln(III) *Lewis* acidity and clearly reflect the *gadolinium break*. Time-resolved measurements showed that incorporation into the rigid 2D framework extends the Ru(II) ^{3}MLCT excited-state lifetime for all Ln studied except Nd, positioning the **LnRu-MOFs** as candidate photosensitisers and photocatalysts.

Chapter 5 realised this potential for **CeRu-MOF** and **EuRu-MOF**. **CeRu-MOF** drove photocatalytic water oxidation competitively with other reported Ce- and Ti-based MOF photocatalysts, via oxidative quenching of the Ru metalloligand and subsequent electron transfer from the dinuclear Ce SBU to generate Ce(IV) active sites. Both **CeRu-MOF** and **EuRu-MOF** catalysed photocatalytic H_2 evolution at rates surpassing the parent metalloligand and matching Ce-based porphyrin MOFs, with **CeRu-MOF** exhibiting bifunctional water-splitting behaviour depending on the sacrificial agent present. **EuRu-MOF** further catalysed CO_2 reduction to formate with 100% product selectivity (a highly sought-after property in CO_2RR catalysts[5]) maintaining activity over 12 h at rates competitive with other MOF-based photocatalysts.

Overall, these results establish Ln-MOFs and their derivatives as a tuneable platform for redox catalysis in solar fuels and point toward several directions for further development. For Ce-MOF-derived OER electrocatalysts, optimisation of particle morphology and

exploration of heteroatom doping are the clearest next steps: Ir or Ru doping below the 0.1 mg cm^{-2} industry target, lanthanide co-doping for band-gap tuning and defect engineering, and Ti/Zr incorporation for enhanced activity and stability.[6-11] For the Ru-photosensitised Ln-MOFs, structural modification offers the most direct route to improved performance: 2D nanosheet synthesis[12-15] to expose more active sites, pillaring strategies to convert the 2D frameworks into porous 3D analogues,[16-19] and mixed-metal variants that could enhance photocatalytic behaviour[10] or enable a bifunctional catalyst for overall water splitting. More broadly, the strong *Lewis* acidity of the lanthanides suggests that the wider **LnRu-MOF** series merits investigation for organic photocatalysis (hydrogenations, oxidations, and coupling reactions) across an emerging field.

Beyond demonstrating the efficacy of redox active Ln-MOF catalysts (utilising Ce^{3+}/Ce^{4+} and Eu^{3+}/Eu^{2+} redox couples), the results of this thesis reinforce the importance of linker choice in the design of Ln-MOF catalysts. The choice of tritopic linker was shown to influence catalytic activity in the Ce-MOF series and could also determine the phases formed upon pyrolysis. The Ru(II) polypyridyl linker was shown to both photosensitise the **LnRu-MOFs** and, through its alkynyl bridge, is proposed to facilitate interfacial electron transfer to the Ln SBUs.

References

1. L. Zhuang, L. Ge, H. Liu, Z. Jiang, Y. Jia, Z. Li, D. Yang, R. K. Hocking, M. Li, L. Zhang, X. Wang, X. Yao, Z. Zhu, *Angew. Chem. Int. Ed.*, 2019, **58**, 13565.
2. X. Hou, J. Zhou, X. Xu, X, Wang, S. Zhang, H. Wang, M. Huang, *Catalysis Communications*, 2022, **165**, 106445.
3. X. Hou, Z. Han, X. Xu, D. Sarker, J. Zhou, M. Wu, Z. Liu, M. Huang, H. Jiang, *Chemical Engineering Journal*, 2021, **418**, 129330.
4. S. Hirai, K. Shimakage, Y. Saitou, T. Nishimura, Y. Uemura, M. Mitomo and Leo Brewer, *J. Am. Ceram. Soc.*, 1998, **81**, 1, 145–151.
5. J. Fu, K. Jiang, X. Qiu, J. Yu, and M. Liu, *Materials Today*, 2020, **32**, 222-242.
6. F. J. Trindade, S. Damasceno, L. Otubo, M. R. Felez, D. Z. de Florio, F. C. Fonseca, and A. S. Ferlauto, *ACS Applied Nano Materials*, 2022, **5**, 7, 8859-8867.

7. M. Laqdiem, A. J. Carrillo, G. Dimitrakopoulos, M. Balaguer, J. Garcia-Fayos, A. F. Ghoniem and J. M. Serra, *Solid State Ionics*, 2023, **394**, 116192.
8. S. Chahal, S. Singh, A. Kumar and P. Kumar, *Vacuum*, 2020, **177**, 109395.
9. J. M. Soney and T. Dhannia, *Inorganic Chemistry Communications*, 2024, **165**, 112535.
10. K. Sood, P. Tiwari, S. Dhall and S. Basu, *Journal of Electroanalytical Chemistry*, 2022, **925**, 116902.
11. J. L. Núñez-Rico, M. Rellán-Piñeiro, B. Puértolas, A. Vidal-Ferran, N. López, J. Pérez-Ramírez and S. Wershofen, *Chem. Eur. J.*, 2020, **26**, 16129 – 16137.
12. P. Wu, S. Geng, X. Wang, X. Zhang, H. Li, L. Zhang, Y. Shen, B. Zha, S. Zhang, F. Huo, W. Zhang, *Angew. Chem. Int. Ed.* 2024, **63**, e202402969.
13. Y. Wang, J. Ma, F. Jin, T. Li, N. Javanmardi, Y. He, G. Zhu, S. Zhang, J. Xu, T. Wang, and Z.-Q. Feng, *Small Sci.*, 2024, **4**, 2400132.
14. M. Zhao, Q. Lu, Q. Ma, H. Zhang, *Small Methods*, 2017, **1**, 1600030.
15. M. Zhao, Y. Huang, Y. Peng, Z. Huang, Q. Ma and H. Zhang, *Chem. Soc. Rev*., 2018, **47**, 6267-6295.
16. F. Z. Karizi, M. Joharian, and A. Morsali, *J. Mater. Chem. A*, 2018, **6**, 19288-19329.
17. V. Richards, *Commun Chem*, 2022, 5, 30.
18. R. L. Mander, A. Schmidt, M. Ruf and M. D. Korzyński, *Dalton Trans.*, 2024, **53**, 18873-18879.
19. S. Zheng, Y. Sun, H. Xue, P. Braunstein, W. Huang, and H. Pang, *Natl. Sci. Rev.*, 2022, **9**, nwab197.

Appendix A

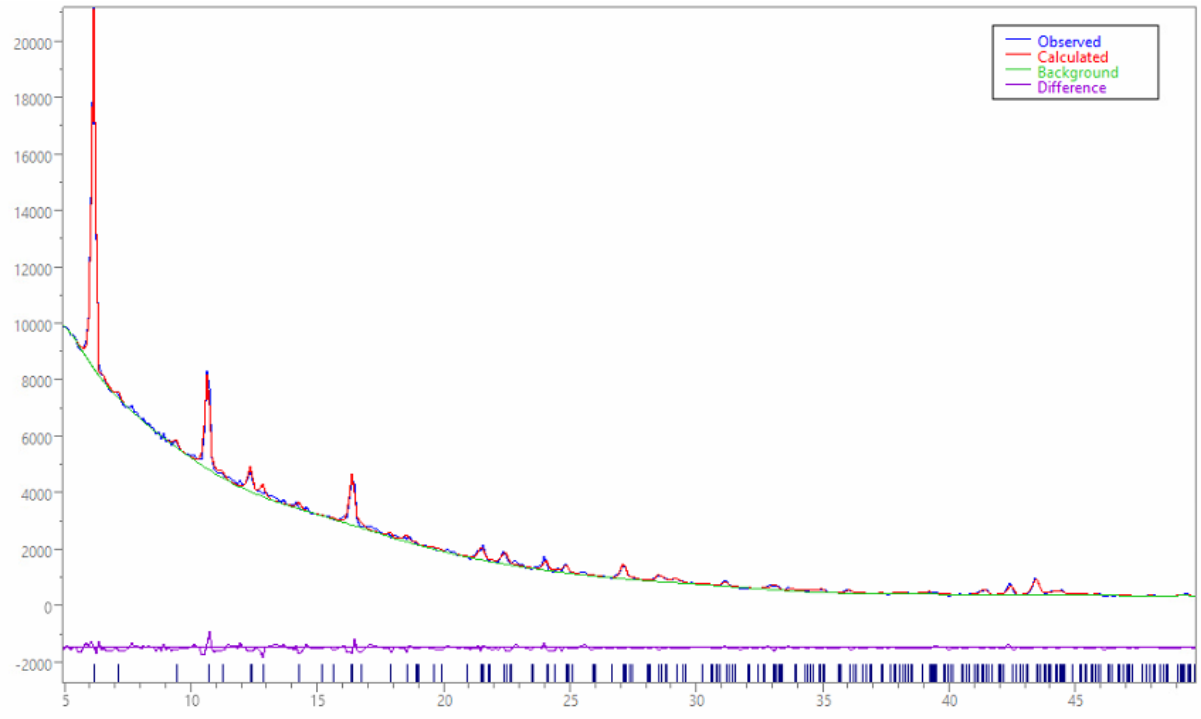

*Figure A.1: Le Bail fitting of experimental **Ce-BTB** PXRD pattern to the calculated PXRD pattern, using EXPO2014 software. R-values of R_p = 2.157 and R_{wp} = 3.083.*

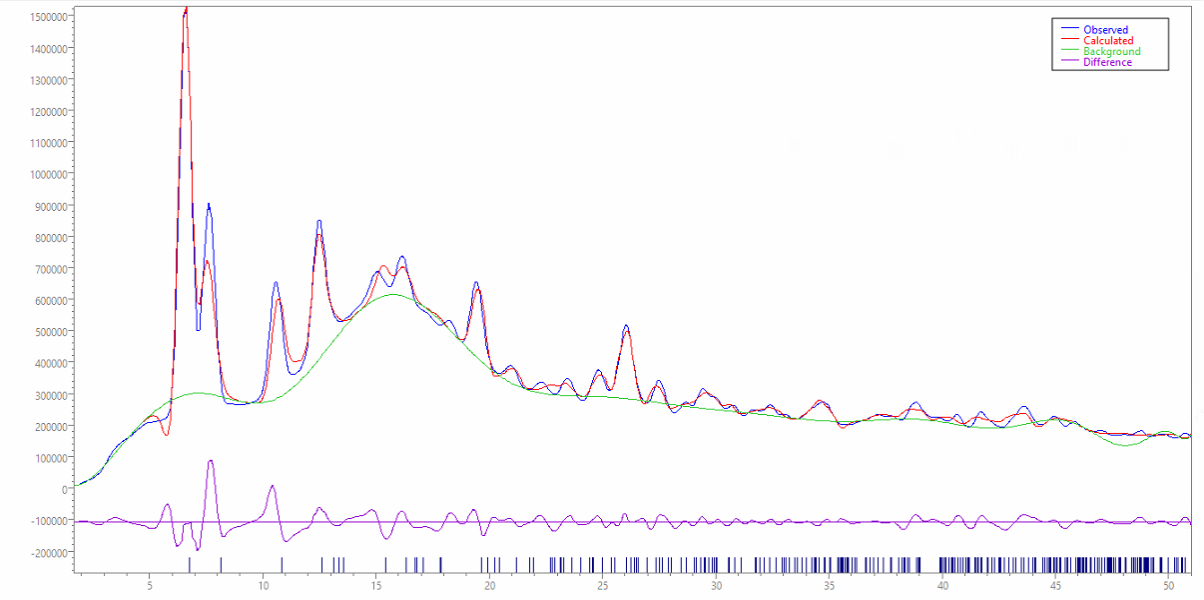

*Figure A.2: Le Bail fitting of experimental **Ce-TTB** PXRD pattern to the calculated PXRD pattern for **Ce-TTT**, using EXPO2014 software. R-values of R_p = 4.640 and R_{wp} = 6.468.*

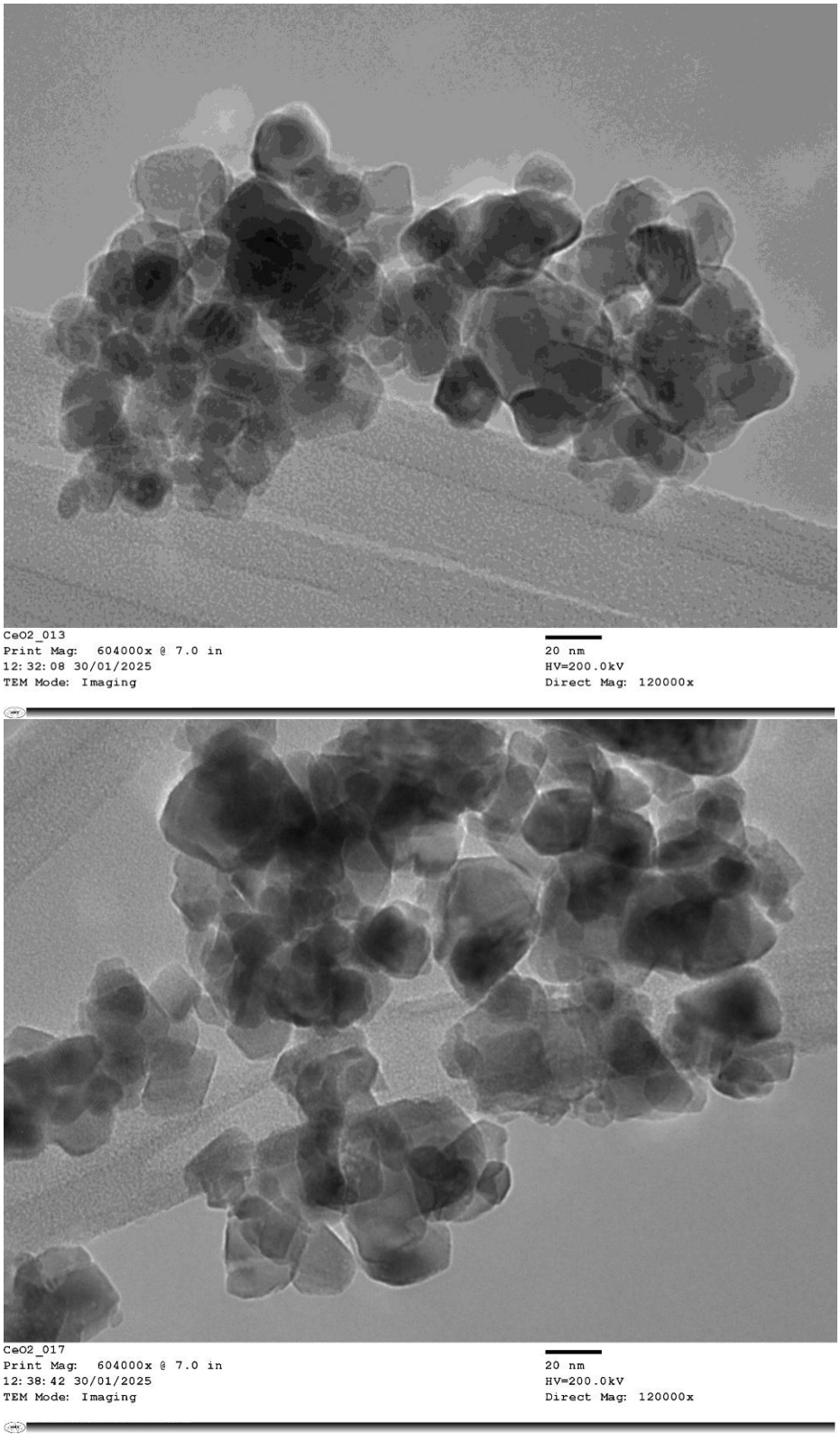

Figure A.3: TEM images of commercial CeO_2 nanoparticles purchased from Sigma-Aldrich.

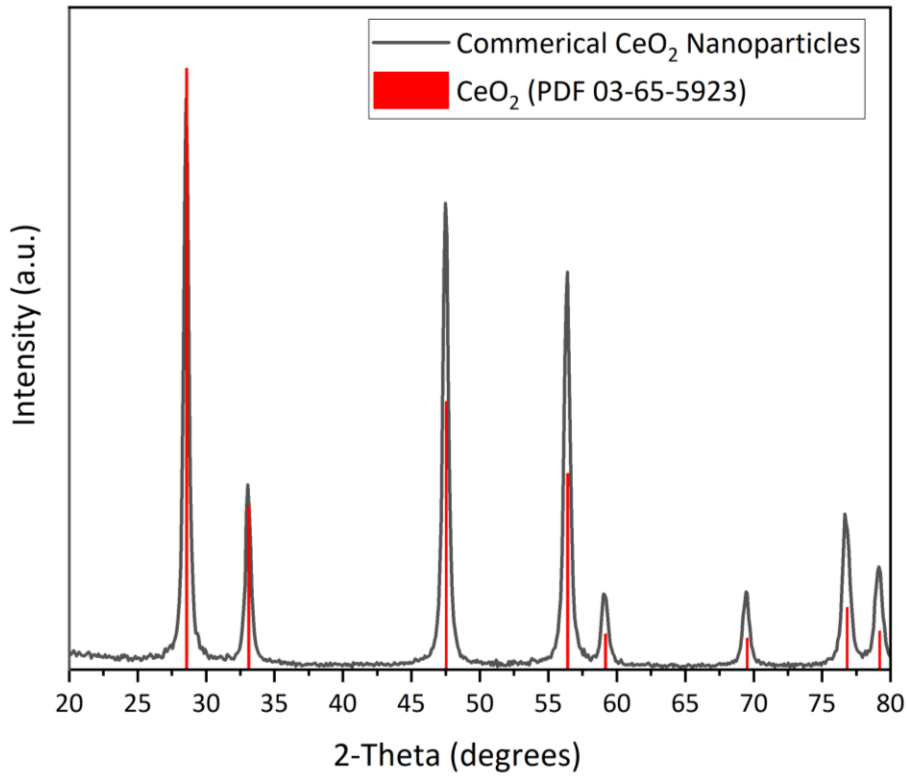

Figure A.4: PXRD pattern of commercial CeO_2 nanoparticles purchased from Sigma-Aldrich (black), overlayed with ICDD reference standard for cerium oxide (PDF 03-65-5923) in red.

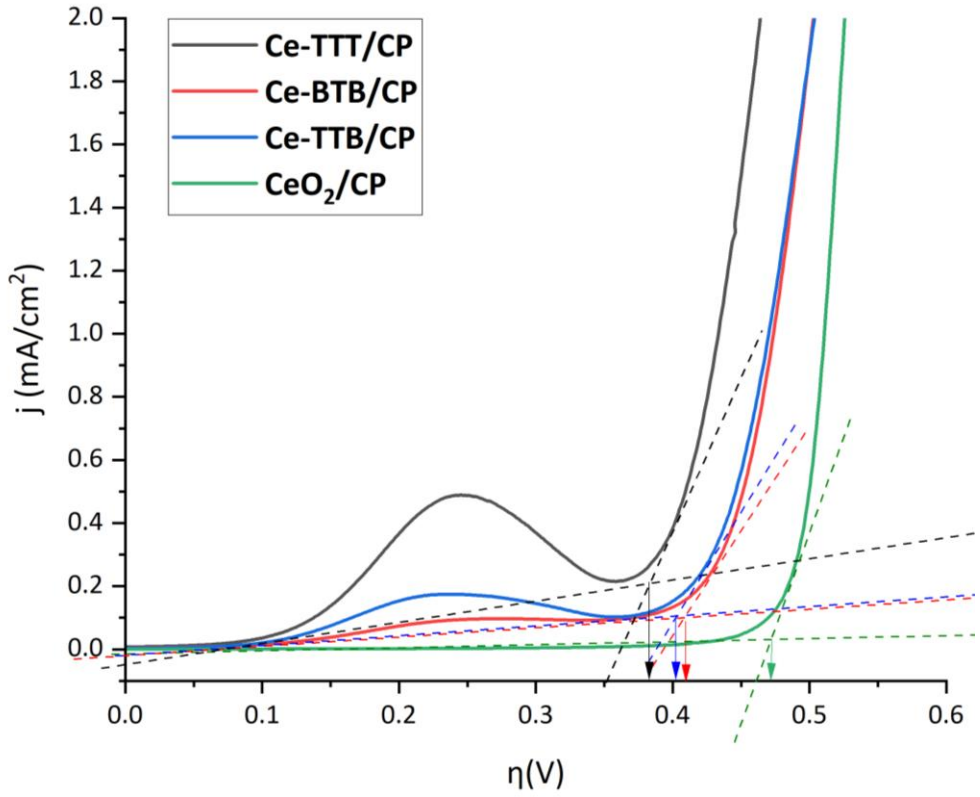

Figure A5: Estimation of onset overpotential using tangent method.

Turnover frequency (TOF) estimation: The electrode pocket had a depth of 4 mm and a surface area of 0.07 cm^2. TOFs were estimated following a published method, which enables the determination of the molar quantity of the active catalyst.[1-3] Following this method, the penetration layer thickness was taken to be 0.5 mm, meaning that only 1/8 of the total electrode pocket volume of the carbon paste (**CP**) blend is in contact with the aqueous electrolyte. To determine the molar quantity of catalyst (Ce-MOF = **Ce-TTT**, **Ce-BTB**, **Ce-TTB**, or the commercial CeO_2 nanoparticle benchmark), electrode masses were recorded before and after loading the 20 wt.% catalyst/**CP** blends. Using the catalyst-to-**CP** ratios and the molecular weights of the respective catalysts, the total moles of catalyst in each blend were calculated. Finally, the effective moles of active catalyst were taken as 1/8 of this total, corresponding to the electrolyte-accessible fraction.

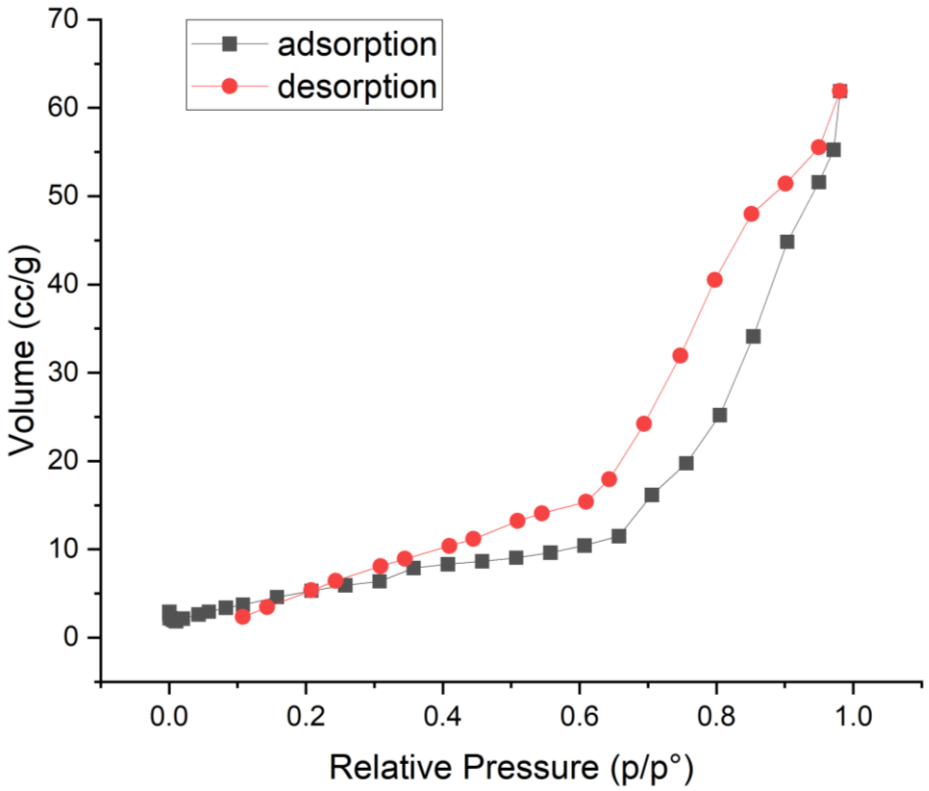

Figure A6: N_2 absorption plot of Ce-TTB at 77 K. The sample was activated at 200 °C, under secondary vacuum.

Ce-TTB BET Summary

Slope =	2.37 g^{-1}
Intercept =	$4.23x10^{-4}$ g^{-1}
R^2 =	0.999992
Constant =	5504.054
Surface area	1496.206 m^2 g^{-1}

Table A1: BET surface areas for Ce-MOFs

Ce-MOF	***BET Surface Area***	***Reference***
Ce-TTT	766 m^2 g^{-1}	4
Ce-BTB	1883 m^2 g^{-1}	5
Ce-TTB	1496 m^2 g^{-1}	This work

References

1. M. Blasco-Ahicart, J. Soriano-López, J. J. Carbó, J. M. Poblet and J. R. Galán-Mascarós, *Nat. Chem.*, 2018, **10**, 24–30.
2. J. Soriano-Lopez, F. W. Steuber, M. Mulahmetovic, M. Besora, J. M. Clemente-Juan, M. O'Doherty, N. Y. Zhu, C. L. Hill, E. Coronado, J. M. Poblet and Wolfgang Schmitt, *Chem. Sci.*, 2023, **14**, 13722.
3. J. Soriano-López, R. Elliott, A. C. Kathalikkattil, A. M. Ako, M. Mulahmetović, M. Venkatesan, Wolfgang Schmitt, *ACS Sustainable Chem. Eng.*, 2020, **8**, 36, 13648–13659.
4. É. Whelan, PhD Thesis, University of Dublin, 2023.
5. Z. Lin, R. Zou, J. Liang, W. Xia, D. Xia, Y. Wang, J. Lin, T. Hu, Q. Chen, X. Wang, Y. Zhao and A. K. Burrell, *Journal of Materials Chemistry*, 2012, **22**, 7813-7818.

Appendix B

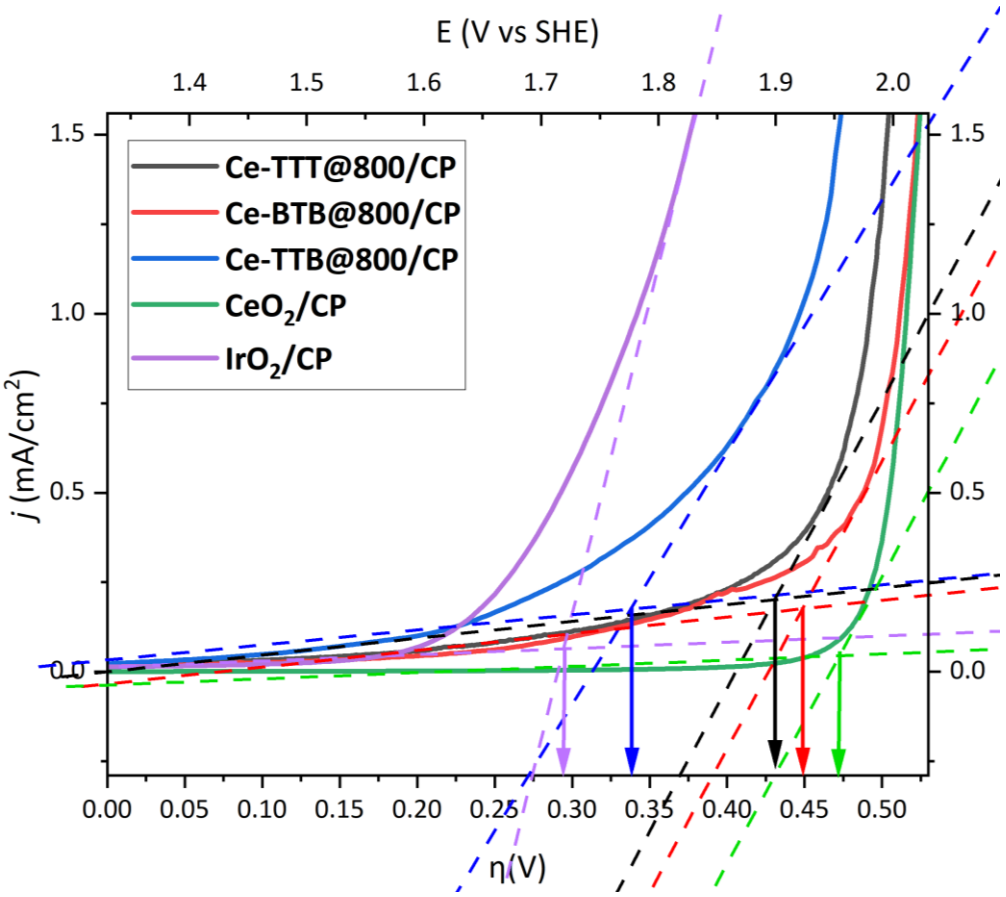

Figure B1: Estimation of onset overpotential using tangent method.

Appendix C

Synthesis of Ruthenium Metallo-ligand, $[H_4L_{Ru}](ClO_4)_2$

The synthesis of the Ru(II) tris-bipyridyl based metallo-ligand **$[H_4L_{Ru}]^{2+}$** was first reported and described by Dr. Muhamed Mulahmetović (PhD Thesis, Trinity College Dublin. 2021). Figure C1 shows a scheme of the procedure used to synthesise the acetylene-extended ruthenium metallo-ligand, **$[H_4L_{Ru}]^{2+}$**. Bromination of 2,2'-bipyrdine at the 5,5' positions was carried out following the procedure reported by Woltering et al.[22] 5,5'-Dibromo-2,2'-bipyridine **(2)** was then reacted with bis-(2,2'-bipyridine)-ruthenium dichloride **(3)**, to give the ruthenium complex, (5,5'-dibromo-2,2'-bipyridine)-bis(2,2'-bipyridine) ruthenium(II) bis(hexafluorophosphate) **(4).** From here, a Sonogashira cross-coupling reaction between **4** and dimethyl 5-ethynylisophtalate (**5**) results (Figure C2) in the synthesis of the methyl ester protected ruthenium complex, **6**, which was subsequently deprotected and protonated to give **$[H_4L_{Ru}](ClO_4)_2$**.

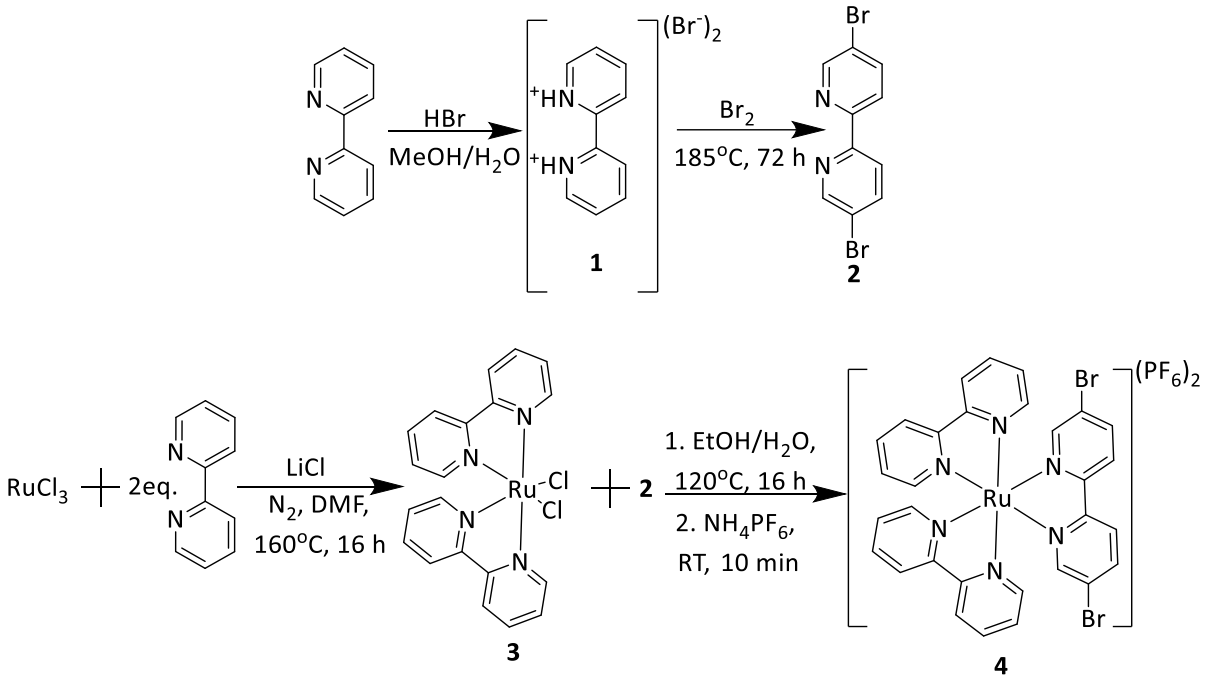

*Figure 4.1: Synthesis of (5,5'-dibromo-2,2'-bipyridine)-bis(2,2'-bipyridine) ruthenium(II) bis(hexafluorophosphate) (**4**).*

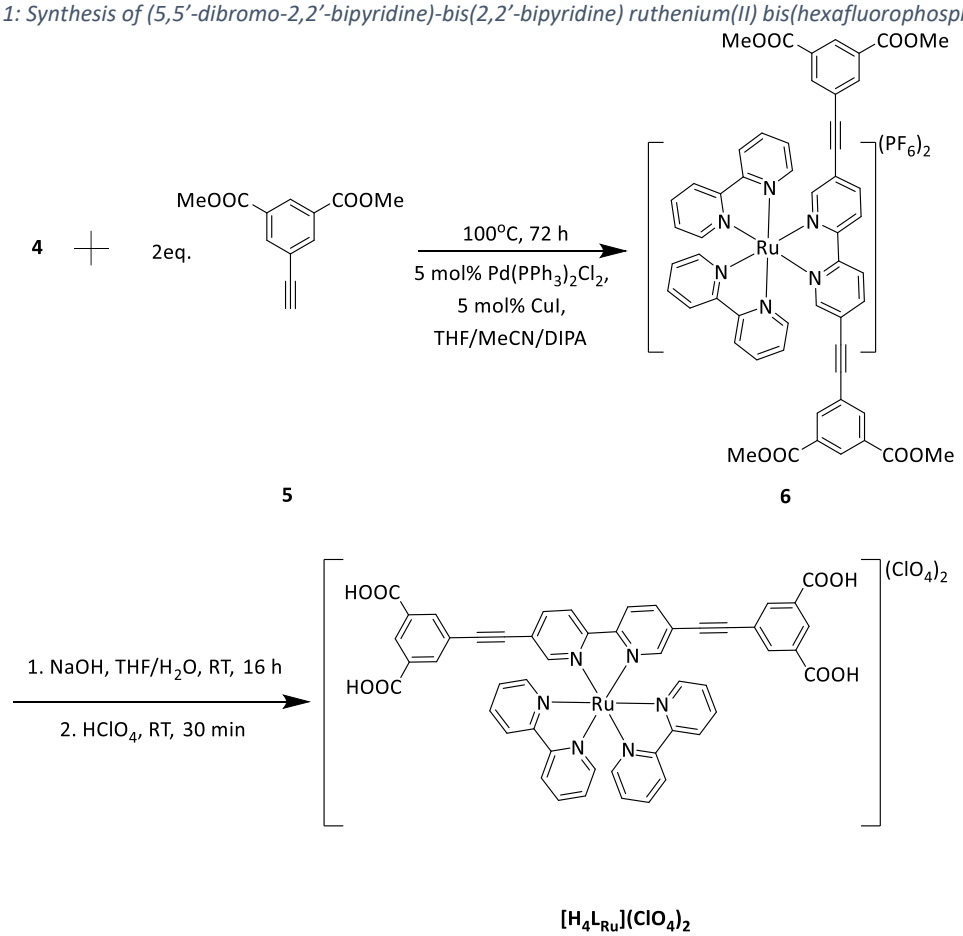

*Figure 4.2: Synthesis of **[H_4L_{Ru}](ClO_4)$_2$**. Sonogashira cross-couplings of **4** and dimethyl 5-ethynylisophtalate (**5**) followed by deprotection and protonation of the methyl ester ruthenium complex, **6**, to give **[H_4L_{Ru}](ClO_4)$_2$**.*

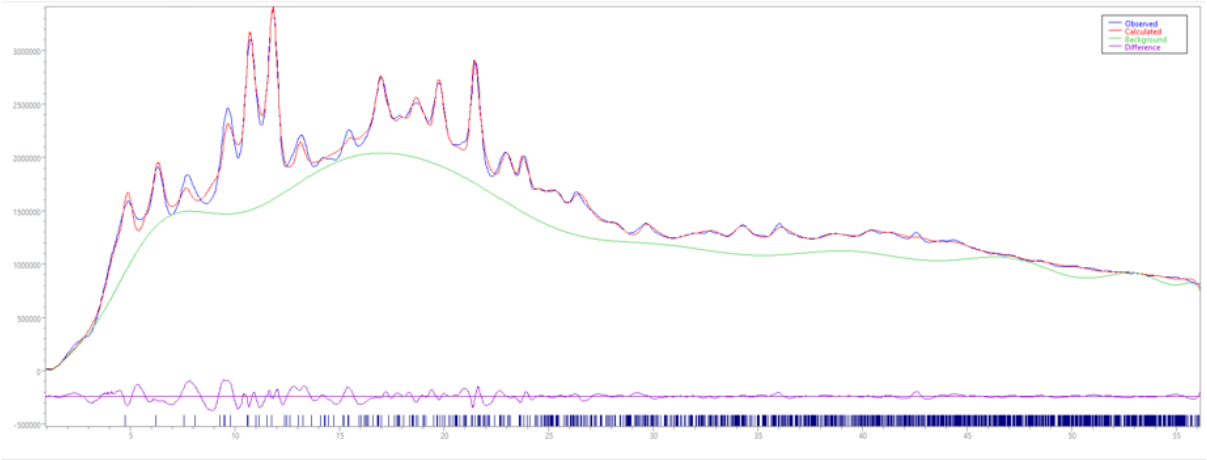

*Figure C3: La Bail fitting of **NdRu-MOF** PXRD pattern to the calculated PXRD pattern of EuRu-MOF, using EXPO2014 software. R_p and R_{wp} values of 1.6 and 2.4, respectively— indicate an excellent fit. The large background (green line) results from micro-loop sample holder.*

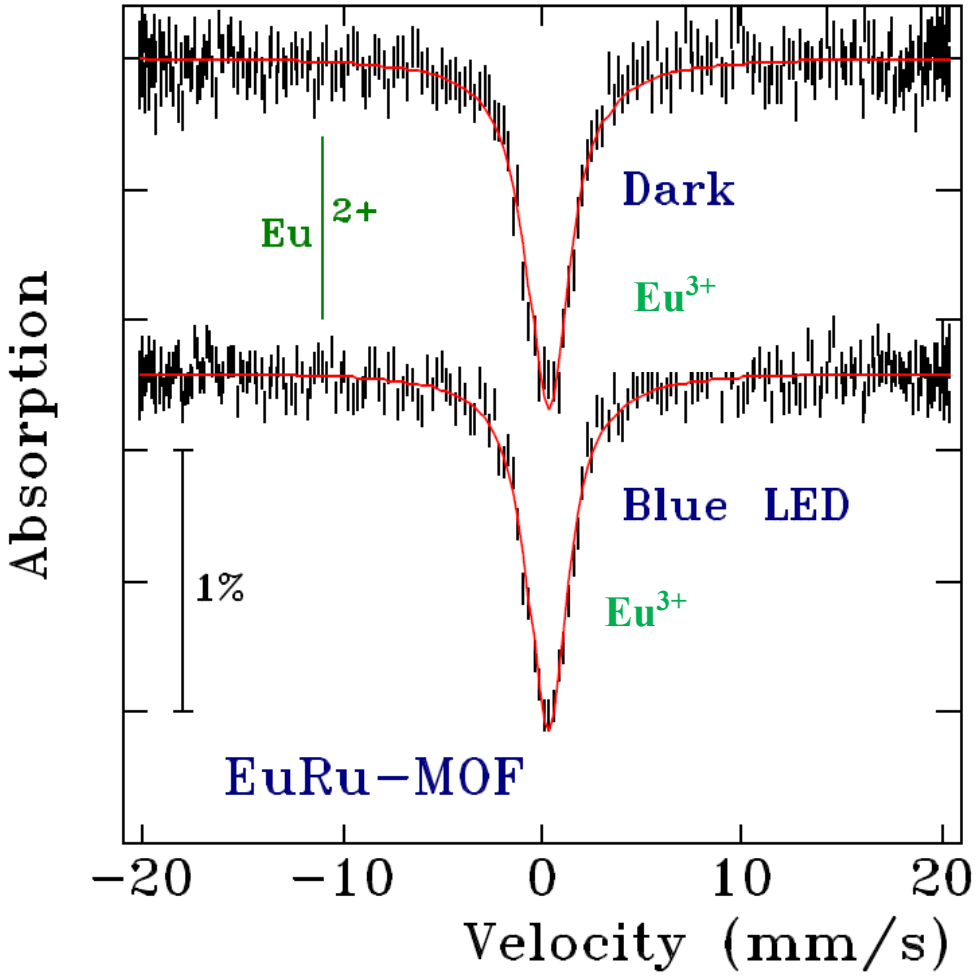

*Figure C4: Eu-151 Mössbauer spectra of **EuRu-MOF**, taken in dark and under illumination.*

Appendix D

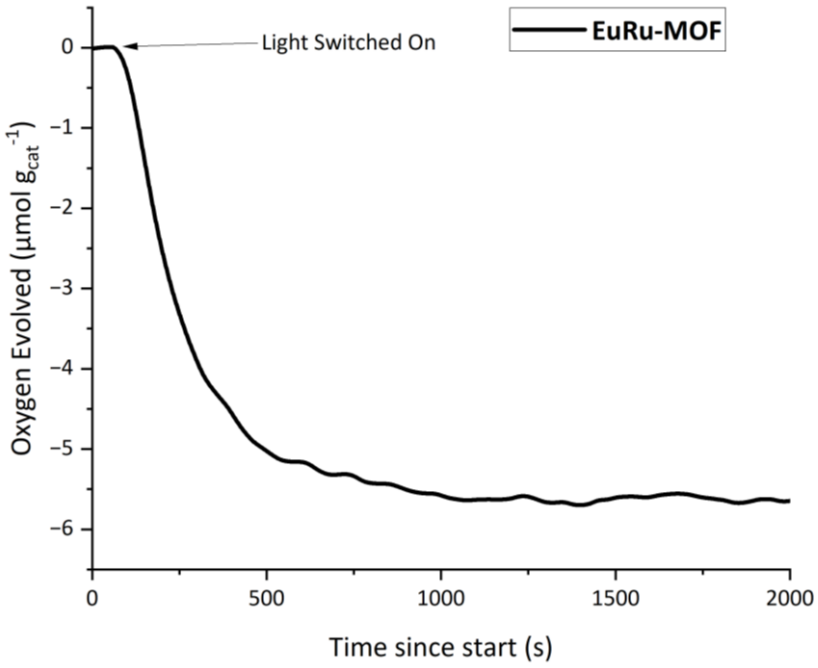

*Figure D1: OER experiment with **EuRu-MOF** as photocatalyst and $Na_2S_2O_8$ as SEA. No oxygen evolved.*

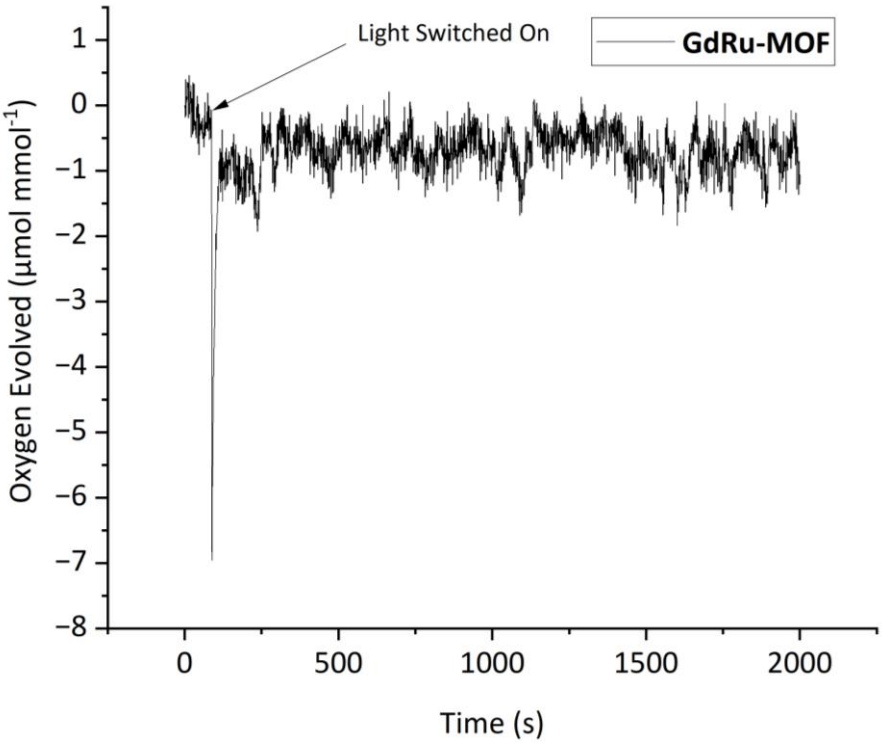

*Figure D2: OER experiment with **GdRu-MOF** as photocatalyst and $Na_2S_2O_8$ as SEA. No oxygen evolved.*

Appendix E: Crystallographic Information for SmRu-MOF

Table E1 Crystal data and structure refinement for SmRu-MOF Final.

Identification code	SmRu-MOF Final
Empirical formula	$C_{26.12}N_{5.38}O_{10.88}Ru_{0.5}Sm$
Formula weight	763.95
Temperature/K	99.98
Crystal system	triclinic
Space group	P-1
a/Å	10.9238(4)
b/Å	14.1540(7)
c/Å	18.4473(9)
α/°	86.338(4)
β/°	89.152(3)
γ/°	85.177(3)
Volume/Å^3	2836.2(2)
Z	4
ρ_{calc}g/cm^3	1.789
μ/mm^{-1}	18.240
F(000)	1462.0
Crystal size/mm^3	0.091 × 0.06 × 0.044
Radiation	CuKα (λ = 1.54178)
2Θ range for data collection/°	4.8 to 122.08
Index ranges	-12 ≤ h ≤ 12, -16 ≤ k ≤ 16, -20 ≤ l ≤ 20
Reflections collected	42577
Independent reflections	8555 [R_{int} = 0.1188, R_{sigma} = 0.1146]
Data/restraints/parameters	8555/776/797
Goodness-of-fit on F^2	1.055
Final R indexes [I>=2σ (I)]	R_1 = 0.1017, wR_2 = 0.2708
Final R indexes [all data]	R_1 = 0.1426, wR_2 = 0.3064
Largest diff. peak/hole / e Å^{-3}	3.11/-1.73

Table E2 Fractional Atomic Coordinates (×10^4) and Equivalent Isotropic Displacement Parameters (Å^2×10^3) for SmRu-MOF Final. U_{eq} is defined as 1/3 of the trace of the orthogonalised U_{IJ} tensor.

Atom	*x*	*y*	*z*	U(eq)
Sm1	6352.4(8)	-1636.9(7)	8146.1(6)	55.3(4)
Sm2	9304.3(12)	10467.1(12)	-3611.3(10)	107.1(7)
Ru1	6759.0(12)	5737.2(10)	2601.3(8)	57.4(4)
O1	7277(14)	223(12)	6589(9)	86(4)
O2	6014(14)	-712(11)	7062(9)	88(4)
O3	1536(18)	-82(14)	6377(12)	130(6)
O4	1062(19)	1000(17)	5614(13)	146(7)
O5	7732(16)	-2529(13)	7214(9)	89(5)
O6	5922(18)	-3036(10)	7396(8)	82(4)
O7	9300(40)	11120(20)	-4887(13)	292(15)
O8	7160(30)	-3690(20)	6584(14)	170(12)
O9	7335(11)	-3099(9)	8810(8)	63(3)
O10	6898(15)	-1957(13)	9514(8)	81(4)

Table E2 Fractional Atomic Coordinates ($\times 10^4$) and Equivalent Isotropic Displacement Parameters ($Å^2 \times 10^3$) for SmRu-MOF Final. U_{eq} is defined as 1/3 of the trace of the orthogonalised U_{IJ} tensor.

Atom	*x*	*y*	*z*	U(eq)
O11	7314(16)	-3362(14)	9984(9)	105(6)
O12	5996(18)	-168(13)	8680(12)	84(5)
O13	8325(11)	8917(10)	-1841(9)	81(4)
O14	9672(13)	9698(16)	-2458(10)	127(9)
O15	14651(10)	7585(10)	-1176(8)	70(4)
O16	14109(10)	8728(10)	-2011(8)	73(4)
O17	9463(8)	9612(6)	-3970(4)	28.3(19)
O18	8390(15)	11704(14)	-2721(11)	115(6)
O19	9370(20)	12875(17)	-2402(14)	166(9)
O20	10288(17)	11783(15)	-3031(14)	153(8)
O21	8910(20)	12634(18)	-5261(10)	167(10)
O22	8460(20)	12055(15)	-4205(10)	139(8)
N1	8298(14)	5371(11)	2001(8)	58(4)
N2	7048(13)	4327(12)	2891(8)	62(4)
N3	5261(14)	5987(13)	3304(8)	86(5)
N4	7675(14)	5992(11)	3554(8)	86(5)
N5	6621(11)	7150(10)	2224(7)	71(4)
N6	5626(16)	5672(10)	1756(9)	81(5)
N7	6970(30)	-3106(19)	7053(14)	104(7)
N8	7165(15)	-2809(13)	9448(10)	65(4)
N9	8920(20)	11956(16)	-4806(10)	192(11)
N10	9356(17)	12122(15)	-2716(12)	140(8)
N11	7150(20)	910(18)	9140(15)	117(7)
C1	4073(16)	6050(20)	3089(11)	114(7)
C2	3143(17)	6170(20)	3618(13)	125(8)
C3	3461(17)	6190(20)	4341(13)	127(8)
C4	4687(18)	6190(20)	4545(10)	112(7)
C5	5580(13)	6086(16)	3996(9)	87(5)
C6	6913(14)	6050(20)	4140(9)	99(6)
C7	7380(19)	6170(20)	4827(9)	119(8)
C8	8620(20)	6280(30)	4888(12)	128(8)
C9	9412(18)	6110(30)	4302(13)	126(8)
C10	8902(16)	5988(16)	3629(11)	111(7)
C11	7159(16)	7876(12)	2498(10)	93(6)
C12	7060(20)	8793(12)	2185(12)	94(6)
C13	6520(20)	8944(13)	1512(12)	102(6)
C14	5960(20)	8222(12)	1222(11)	101(7)
C15	6000(20)	7339(10)	1591(10)	84(5)
C16	5390(20)	6505(11)	1348(13)	106(7)
C17	4670(30)	6522(16)	734(16)	142(10)
C18	3980(30)	5762(17)	630(20)	168(11)
C19	4370(40)	4885(16)	964(19)	154(11)
C20	5190(30)	4881(13)	1532(15)	115(8)
C21	8807(15)	5915(13)	1482(10)	58(5)
C22	9887(16)	5624(13)	1112(9)	57(5)
C23	10505(19)	4746(14)	1303(12)	69(5)
C24	9957(17)	4156(15)	1866(10)	65(5)
C25	8849(16)	4492(12)	2170(9)	52(4)

Table E2 Fractional Atomic Coordinates (×10^4) and Equivalent Isotropic Displacement Parameters (Å^2×10^3) for SmRu-MOF Final. U_{eq} is defined as 1/3 of the trace of the orthogonalised U_{IJ} tensor.

Atom	*x*	*y*	*z*	U(eq)
C26	8168(17)	3921(12)	2686(10)	55(4)
C27	8562(16)	2954(14)	2916(10)	63(5)
C28	7750(20)	2452(15)	3358(11)	73(6)
C29	6615(17)	2852(14)	3529(10)	61(5)
C30	6281(17)	3810(15)	3311(10)	62(5)
C31	5784(18)	2362(14)	4019(10)	62(5)
C32	5225(16)	1933(15)	4461(10)	65(5)
C33	4723(17)	1379(13)	5070(9)	56(4)
C34	3566(17)	1164(15)	5122(13)	78(7)
C35	3226(19)	545(17)	5723(14)	93(6)
C36	4039(17)	184(15)	6221(12)	73(6)
C37	5258(18)	364(14)	6136(10)	62(5)
C38	5586(18)	1022(15)	5571(9)	64(5)
C39	1920(20)	470(14)	5894(11)	127(7)
C40	6260(18)	-93(14)	6635(10)	62(5)
C41	10330(17)	6221(14)	528(11)	62(5)
C42	10639(17)	6737(14)	35(10)	59(5)
C43	10961(17)	7360(13)	-589(10)	59(5)
C44	10067(15)	7927(15)	-962(11)	68(6)
C45	10369(13)	8525(14)	-1550(10)	59(5)
C46	11629(15)	8605(13)	-1726(10)	56(5)
C47	12501(14)	8047(14)	-1357(10)	56(5)
C48	12201(16)	7417(14)	-767(9)	57(5)
C49	9377(16)	9075(15)	-1991(13)	77(7)
C50	13873(14)	8099(14)	-1534(10)	56(4)
C51	8000(40)	1640(30)	9020(30)	139(13)
C52	6670(20)	481(17)	8575(15)	95(7)
C53	6830(50)	560(30)	9874(16)	147(12)

Table E3 Anisotropic Displacement Parameters (Å^2×10^3) for SmRu-MOF Final. The Anisotropic displacement factor exponent takes the form: $-2\pi^2[h^2a^{*2}U_{11}+2hka^*b^*U_{12}+\ldots]$.

Atom	U_{11}	U_{22}	U_{33}	U_{23}	U_{13}	U_{12}
Sm1	28.3(5)	58.4(6)	75.3(7)	27.6(5)	-2.9(4)	-5.5(4)
Sm2	57.0(8)	110.1(12)	141.5(14)	72.6(10)	22.7(8)	2.1(7)
Ru1	46.0(8)	61.6(9)	61.9(8)	18.6(7)	3.4(6)	-6.3(6)
O1	68(7)	99(8)	90(8)	34(7)	-17(6)	-22(6)
O2	75(7)	93(8)	90(8)	41(7)	2(6)	-14(6)
O3	104(9)	117(9)	164(10)	28(7)	36(7)	-20(7)
O4	123(9)	156(10)	155(10)	28(8)	-5(8)	-9(8)
O5	76(11)	102(12)	89(11)	-13(9)	14(9)	-2(9)
O6	112(13)	66(9)	70(9)	7(7)	-30(9)	-17(9)
O7	360(30)	330(20)	129(17)	76(18)	10(20)	240(20)
O8	200(30)	180(20)	127(18)	-83(19)	-47(18)	50(20)
O9	42(7)	56(7)	85(10)	25(7)	-3(6)	11(6)
O10	83(11)	93(12)	67(9)	10(8)	0(7)	-17(9)
O11	93(12)	141(15)	77(10)	55(11)	-15(9)	-41(11)
O12	79(8)	72(8)	101(9)	-9(7)	4(7)	-7(6)
O13	33(7)	86(10)	120(12)	47(8)	-9(7)	-19(6)

Table E3 Anisotropic Displacement Parameters ($Å^2×10^3$) for SmRu-MOF Final. The Anisotropic displacement factor exponent takes the form: $-2π^2[h^2a^{*2}U_{11}+2hka*b*U_{12}+…]$.

Atom	U_{11}	U_{22}	U_{33}	U_{23}	U_{13}	U_{12}
O14	44(8)	200(20)	122(14)	111(14)	-9(8)	-23(10)
O15	32(6)	80(9)	92(9)	48(7)	0(6)	-12(6)
O16	24(6)	90(10)	97(10)	48(8)	-2(6)	-3(6)
O18	80(10)	122(14)	142(16)	13(12)	-9(10)	-18(9)
O19	190(20)	156(18)	160(20)	32(14)	-14(16)	-81(15)
O20	86(11)	129(15)	240(20)	69(14)	-10(13)	-35(11)
O21	127(17)	280(20)	81(12)	69(14)	-21(11)	9(17)
O22	124(15)	157(17)	117(12)	80(12)	24(11)	37(13)
N1	56(9)	64(9)	52(8)	22(7)	-7(7)	-13(7)
N2	42(8)	92(12)	51(8)	14(8)	2(6)	-4(8)
N3	81(9)	73(10)	99(9)	32(9)	8(8)	-10(9)
N4	80(8)	94(12)	85(9)	14(9)	-9(7)	-26(9)
N5	47(8)	73(9)	91(9)	-5(7)	17(6)	1(7)
N6	66(10)	77(8)	96(11)	26(8)	-9(8)	-6(8)
N7	101(19)	116(19)	94(17)	-16(14)	-25(14)	6(16)
N8	55(10)	61(11)	81(13)	17(10)	-5(8)	-22(8)
N9	160(20)	270(20)	105(13)	80(14)	11(13)	122(17)
N10	102(12)	134(16)	180(20)	40(14)	-19(13)	-41(11)
N11	122(11)	115(11)	117(10)	-13(8)	-2(8)	-31(8)
C1	74(10)	126(18)	133(14)	43(14)	12(9)	2(12)
C2	88(13)	120(18)	157(16)	32(17)	33(11)	13(14)
C3	98(11)	118(18)	155(15)	25(17)	40(13)	17(15)
C4	108(11)	101(16)	123(13)	17(13)	42(10)	-6(13)
C5	90(8)	70(12)	96(9)	21(10)	18(7)	-2(10)
C6	96(9)	111(15)	88(10)	18(12)	3(7)	-18(11)
C7	118(13)	150(20)	87(11)	3(14)	-2(10)	-4(16)
C8	127(15)	160(20)	95(13)	-8(16)	-20(11)	-21(17)
C9	93(14)	180(20)	109(14)	-10(17)	-23(9)	-31(16)
C10	83(9)	150(20)	99(12)	-2(15)	-2(9)	-33(13)
C11	83(14)	75(10)	121(14)	-10(9)	16(11)	-13(9)
C12	97(15)	68(9)	118(14)	-15(10)	28(11)	-9(10)
C13	94(15)	88(11)	122(14)	-2(11)	24(11)	-12(11)
C14	112(17)	67(9)	120(15)	15(9)	-2(12)	3(10)
C15	75(12)	67(8)	106(11)	14(8)	-1(9)	7(8)
C16	98(14)	80(9)	136(15)	34(9)	-40(11)	-17(9)
C17	150(20)	99(14)	172(18)	59(14)	-91(16)	-31(14)
C18	180(20)	120(16)	210(20)	48(16)	-125(19)	-44(15)
C19	180(20)	105(14)	180(20)	38(15)	-95(17)	-51(15)
C20	120(18)	81(10)	142(18)	35(12)	-51(14)	-20(11)
C21	37(9)	63(11)	72(12)	13(9)	1(8)	-8(8)
C22	50(10)	68(12)	52(10)	15(9)	-7(8)	-13(9)
C23	68(13)	59(12)	79(13)	17(10)	2(10)	-13(10)
C24	52(11)	80(13)	58(11)	20(10)	17(9)	5(10)
C25	54(10)	55(10)	47(9)	13(8)	7(8)	-10(8)
C26	61(12)	48(10)	56(10)	15(8)	12(8)	-13(8)
C27	43(10)	75(12)	64(11)	36(9)	4(8)	6(9)
C28	70(14)	74(13)	70(13)	32(10)	6(10)	-5(11)
C29	51(11)	74(13)	55(10)	20(9)	4(8)	-5(9)

Table E3 Anisotropic Displacement Parameters ($Å^2×10^3$) for SmRu-MOF Final. The Anisotropic displacement factor exponent takes the form: $-2π^2[h^2a^{*2}U_{11}+2hka*b*U_{12}+…]$.

Atom	U_{11}	U_{22}	U_{33}	U_{23}	U_{13}	U_{12}
C30	56(11)	77(13)	52(10)	16(9)	4(8)	-13(9)
C31	60(12)	66(12)	59(11)	25(9)	-5(9)	-12(9)
C32	35(9)	92(14)	62(11)	29(11)	-6(8)	5(9)
C33	61(12)	53(10)	54(10)	12(8)	-12(8)	-4(9)
C34	37(10)	71(13)	121(18)	45(12)	-1(10)	-19(9)
C35	93(8)	84(10)	97(10)	31(8)	9(8)	-7(8)
C36	43(11)	81(14)	89(14)	30(11)	22(10)	2(10)
C37	66(12)	69(12)	49(10)	10(9)	8(8)	-13(10)
C38	64(12)	85(14)	42(9)	23(9)	4(8)	-20(10)
C39	106(8)	130(10)	141(10)	32(8)	12(7)	-15(7)
C40	58(8)	69(8)	57(8)	17(7)	6(7)	-11(7)
C41	45(10)	73(13)	68(12)	7(10)	16(9)	-14(9)
C42	50(10)	72(12)	55(10)	18(9)	-2(8)	-15(9)
C43	49(11)	58(11)	70(12)	11(9)	15(9)	-19(9)
C44	22(8)	88(14)	89(14)	32(11)	-8(8)	-1(9)
C45	16(7)	86(13)	72(11)	24(10)	1(7)	-12(8)
C46	31(9)	69(11)	69(11)	16(9)	-4(8)	-19(8)
C47	26(8)	73(12)	67(11)	19(9)	-6(7)	-8(8)
C48	41(10)	79(12)	50(10)	16(9)	-2(7)	-16(9)
C49	27(9)	77(13)	123(18)	45(13)	-6(10)	-19(9)
C50	24(8)	70(12)	73(12)	8(10)	-6(8)	-11(8)
C51	148(19)	134(18)	150(20)	-25(14)	-1(15)	-53(15)
C52	89(10)	91(10)	104(10)	-3(8)	7(8)	-16(8)
C53	170(20)	150(20)	120(12)	-2(14)	4(14)	-20(17)

Table E4 Bond Lengths for SmRu-MOF Final.

Atom	Atom	Length/Å	Atom	Atom	Length/Å
Sm1	O2	2.337(14)	N9	O22	1.221(13)
Sm1	O5	2.590(15)	N10	O18	1.253(13)
Sm1	O6	2.567(15)	N10	O19	1.247(13)
Sm1	O9	2.505(11)	N10	O20	1.241(13)
Sm1	O10	2.604(14)	N11	C51	1.452(16)
Sm1	O12	2.357(19)	N11	C53	1.460(16)
Sm1	$O13^1$	2.355(12)	C2	C1	1.404(12)
Sm1	$O15^2$	2.516(11)	C3	C2	1.388(12)
Sm1	$O16^2$	2.479(11)	C4	C3	1.396(12)
Sm1	N8	2.936(17)	C5	C4	1.401(11)
Sm1	$C50^2$	2.814(16)	C6	C5	1.480(15)
Sm2	$O1^3$	2.291(15)	C7	C6	1.399(11)
Sm2	$O3^4$	2.50(2)	C8	C7	1.389(12)
Sm2	$O4^4$	2.51(2)	C9	C8	1.389(12)
Sm2	O7	2.47(2)	C10	C9	1.396(16)
Sm2	O14	2.351(14)	C11	C12	1.383(16)
Sm2	O17	1.413(9)	C12	C13	1.380(12)
Sm2	O18	2.60(2)	C13	C14	1.374(11)
Sm2	O20	2.53(2)	C14	C15	1.382(11)
Sm2	O22	2.545(17)	C15	C16	1.496(15)
Sm2	N9	2.960(17)	C16	C17	1.392(11)

Table E4 Bond Lengths for SmRu-MOF Final.

Atom	Atom	Length/Å	Atom	Atom	Length/Å
Sm2	N10	2.96(2)	C17	C18	1.389(12)
Sm2	C39[4]	2.98(2)	C18	C19	1.388(12)
Ru1	N1	2.048(16)	C19	C20	1.390(12)
Ru1	N2	2.033(17)	C21	C22	1.40(3)
Ru1	N3	2.093(16)	C23	C22	1.39(3)
Ru1	N4	2.101(15)	C23	C24	1.45(3)
Ru1	N5	2.069(14)	C25	C24	1.39(3)
Ru1	N6	2.017(15)	C25	C26	1.45(2)
O1	C40	1.23(2)	C26	C27	1.44(2)
O2	C40	1.18(2)	C27	C28	1.40(3)
O3	C39	1.238(14)	C29	C28	1.36(3)
O4	C39	1.246(14)	C29	C30	1.41(3)
O5	N7	1.26(3)	C29	C31	1.46(2)
O6	N7	1.30(3)	C32	C31	1.18(2)
O9	N8	1.28(2)	C33	C32	1.46(3)
O13	C49	1.21(2)	C33	C34	1.33(3)
O14	C49	1.25(2)	C33	C38	1.37(2)
O15	C50	1.24(2)	C34	C35	1.43(3)
O16	C50	1.25(2)	C36	C35	1.34(3)
N1	C21	1.33(2)	C36	C37	1.38(3)
N1	C25	1.36(2)	C37	C40	1.52(3)
N2	C26	1.37(2)	C38	C37	1.41(2)
N2	C30	1.36(2)	C39	C35	1.470(17)
N3	C1	1.356(12)	C41	C22	1.43(2)
N3	C5	1.347(12)	C42	C41	1.19(2)
N4	C6	1.357(12)	C43	C42	1.46(2)
N4	C10	1.349(12)	C43	C44	1.37(3)
N5	C11	1.354(12)	C45	C44	1.39(2)
N5	C15	1.360(12)	C45	C49	1.50(3)
N6	C16	1.365(12)	C46	C45	1.42(2)
N6	C20	1.344(12)	C46	C47	1.35(2)
N7	O8	1.23(3)	C47	C48	1.41(2)
N8	O10	1.23(2)	C48	C43	1.40(2)
N8	O11	1.23(2)	C50	C47	1.54(2)
N9	O7	1.234(13)	C52	O12	1.232(18)
N9	O21	1.234(13)	C52	N11	1.370(18)

[1]+X,-1+Y,1+Z; [2]-1+X,-1+Y,1+Z; [3]+X,1+Y,-1+Z; [4]1+X,1+Y,-1+Z

Table E5 Bond Angles for SmRu-MOF Final.

Atom	Atom	Atom	Angle/˚	Atom	Atom	Atom	Angle/˚
O2	Sm1	O5	76.5(6)	N8	O10	Sm1	92.9(12)
O2	Sm1	O6	85.0(5)	C52	O12	Sm1	122.8(17)
O2	Sm1	O9	149.6(6)	C49	O13	Sm1[3]	163.4(18)
O2	Sm1	O10	155.7(6)	C49	O14	Sm2	147.3(16)
O2	Sm1	O12	83.6(7)	C50	O15	Sm1[4]	90.4(10)
O2	Sm1	O13[1]	87.6(5)	C50	O16	Sm1[4]	91.9(9)
O2	Sm1	O15[2]	122.2(5)	N10	O18	Sm2	93.4(13)
O2	Sm1	O16[2]	71.3(5)	N10	O20	Sm2	97.4(13)
O2	Sm1	N8	171.5(5)	N9	O22	Sm2	97.3(12)

Table E5 Bond Angles for SmRu-MOF Final.

Atom	Atom	Atom	Angle/˚	Atom	Atom	Atom	Angle/˚
O2	Sm1	C50^{2}	96.8(5)	C21	N1	Ru1	126.5(13)
O5	Sm1	O10	117.4(5)	C21	N1	C25	118.2(16)
O5	Sm1	N8	97.4(6)	C25	N1	Ru1	115.3(11)
O5	Sm1	C50^{2}	126.3(6)	C26	N2	Ru1	114.4(11)
O6	Sm1	O5	49.9(6)	C30	N2	Ru1	125.5(13)
O6	Sm1	O10	119.3(5)	C30	N2	C26	119.8(16)
O6	Sm1	N8	95.6(5)	C1	N3	Ru1	123.7(13)
O6	Sm1	C50^{2}	76.6(6)	C5	N3	Ru1	113.9(11)
O9	Sm1	O5	73.2(5)	C5	N3	C1	122.4(15)
O9	Sm1	O6	73.8(5)	C6	N4	Ru1	112.8(11)
O9	Sm1	O10	49.9(5)	C10	N4	Ru1	125.9(12)
O9	Sm1	O15^{2}	73.6(4)	C10	N4	C6	120.8(14)
O9	Sm1	N8	25.6(5)	C11	N5	Ru1	127.6(11)
O9	Sm1	C50^{2}	99.1(5)	C11	N5	C15	117.3(13)
O10	Sm1	N8	24.7(5)	C15	N5	Ru1	114.8(10)
O10	Sm1	C50^{2}	90.4(5)	C16	N6	Ru1	115.0(11)
O12	Sm1	O5	143.0(6)	C20	N6	Ru1	125.9(11)
O12	Sm1	O6	158.3(6)	C20	N6	C16	118.8(14)
O12	Sm1	O9	123.0(6)	O5	N7	O6	116(2)
O12	Sm1	O10	73.6(7)	O8	N7	O5	124(3)
O12	Sm1	O15^{2}	95.4(6)	O8	N7	O6	120(3)
O12	Sm1	O16^{2}	77.6(6)	O9	N8	Sm1	58.0(8)
O12	Sm1	N8	98.3(7)	O10	N8	Sm1	62.4(10)
O12	Sm1	C50^{2}	86.5(6)	O10	N8	O9	118.6(16)
O13^{1}	Sm1	O5	71.4(6)	O11	N8	Sm1	169.0(13)
O13^{1}	Sm1	O6	120.9(6)	O11	N8	O9	121(2)
O13^{1}	Sm1	O9	85.0(4)	O11	N8	O10	121(2)
O13^{1}	Sm1	O10	79.2(5)	O7	N9	Sm2	55.2(12)
O13^{1}	Sm1	O12	77.0(6)	O7	N9	O21	127.4(19)
O13^{1}	Sm1	O15^{2}	148.6(5)	O21	N9	Sm2	170.0(18)
O13^{1}	Sm1	O16^{2}	148.5(5)	O22	N9	Sm2	58.5(10)
O13^{1}	Sm1	N8	84.8(4)	O22	N9	O7	111.9(17)
O13^{1}	Sm1	C50^{2}	162.3(6)	O22	N9	O21	120.6(18)
O15^{2}	Sm1	O5	121.6(6)	O18	N10	Sm2	61.6(11)
O15^{2}	Sm1	O6	75.3(6)	O19	N10	Sm2	173.7(16)
O15^{2}	Sm1	O10	69.5(5)	O19	N10	O18	119.8(18)
O15^{2}	Sm1	N8	66.0(4)	O20	N10	Sm2	58.0(11)
O15^{2}	Sm1	C50^{2}	26.2(5)	O20	N10	O18	119.3(17)
O16^{2}	Sm1	O5	123.0(6)	O20	N10	O19	120.9(18)
O16^{2}	Sm1	O6	81.3(6)	C51	N11	C53	121(3)
O16^{2}	Sm1	O9	124.9(4)	C52	N11	C51	122(2)
O16^{2}	Sm1	O10	111.0(5)	C52	N11	C53	117(2)
O16^{2}	Sm1	O15^{2}	52.5(4)	N3	C1	C2	118.6(15)
O16^{2}	Sm1	N8	117.2(4)	C3	C2	C1	119.4(15)
O16^{2}	Sm1	C50^{2}	26.4(5)	C2	C3	C4	121.0(14)
C50^{2}	Sm1	N8	91.6(5)	C3	C4	C5	117.2(13)
O1^{3}	Sm2	O3^{4}	152.4(6)	N3	C5	C4	121.1(13)
O1^{3}	Sm2	O4^{4}	152.9(6)	N3	C5	C6	116.2(13)

Table E5 Bond Angles for SmRu-MOF Final.

Atom	Atom	Atom	Angle/˚	Atom	Atom	Atom	Angle/˚
O1[3]	Sm2	O7	102.1(11)	C4	C5	C6	122.7(14)
O1[3]	Sm2	O14	86.6(5)	N4	C6	C5	116.6(13)
O1[3]	Sm2	O18	71.8(6)	N4	C6	C7	120.4(12)
O1[3]	Sm2	O20	121.4(7)	C7	C6	C5	122.7(14)
O1[3]	Sm2	O22	84.2(6)	C8	C7	C6	118.6(13)
O1[3]	Sm2	N9	96.9(6)	C7	C8	C9	119.9(14)
O1[3]	Sm2	N10	96.8(6)	C8	C9	C10	118.6(14)
O1[3]	Sm2	C39[4]	167.6(6)	N4	C10	C9	120.8(14)
O3[4]	Sm2	O4[4]	48.3(5)	N5	C11	C12	123.4(14)
O3[4]	Sm2	O18	121.8(7)	C13	C12	C11	117.7(13)
O3[4]	Sm2	O20	76.8(7)	C14	C13	C12	119.6(13)
O3[4]	Sm2	O22	122.9(6)	C13	C14	C15	119.6(13)
O3[4]	Sm2	N9	106.8(6)	N5	C15	C14	121.7(12)
O3[4]	Sm2	N10	99.9(7)	N5	C15	C16	113.3(12)
O3[4]	Sm2	C39[4]	24.1(3)	C14	C15	C16	124.9(13)
O4[4]	Sm2	O18	114.7(7)	N6	C16	C15	116.0(12)
O4[4]	Sm2	O20	69.8(8)	N6	C16	C17	119.3(12)
O4[4]	Sm2	O22	76.3(6)	C17	C16	C15	124.7(13)
O4[4]	Sm2	N9	58.5(6)	C18	C17	C16	119.6(15)
O4[4]	Sm2	N10	91.5(7)	C19	C18	C17	117.9(15)
O4[4]	Sm2	C39[4]	24.3(3)	C18	C19	C20	116.9(15)
O7	Sm2	O3[4]	94.4(9)	N6	C20	C19	123.4(15)
O7	Sm2	O4[4]	50.8(11)	N1	C21	C22	123.0(17)
O7	Sm2	O18	112.2(7)	C21	C22	C41	119.7(17)
O7	Sm2	O20	98.9(11)	C23	C22	C21	119.8(16)
O7	Sm2	O22	47.8(6)	C23	C22	C41	120.5(18)
O7	Sm2	N9	24.2(4)	C22	C23	C24	117.3(19)
O7	Sm2	N10	105.6(8)	C25	C24	C23	118.2(17)
O7	Sm2	C39[4]	72.7(10)	N1	C25	C24	123.3(15)
O14	Sm2	O3[4]	75.2(6)	N1	C25	C26	114.2(16)
O14	Sm2	O4[4]	120.3(6)	C24	C25	C26	122.5(16)
O14	Sm2	O7	169.2(8)	N2	C26	C25	115.3(15)
O14	Sm2	O18	76.4(8)	N2	C26	C27	121.1(15)
O14	Sm2	O20	81.6(8)	C27	C26	C25	123.3(17)
O14	Sm2	O22	140.9(8)	C28	C27	C26	117.3(17)
O14	Sm2	N9	162.3(8)	C29	C28	C27	120.9(18)
O14	Sm2	N10	79.4(8)	C28	C29	C30	119.8(17)
O14	Sm2	C39[4]	97.5(5)	C28	C29	C31	121.9(17)
O17	Sm2	O1[3]	89.7(6)	C30	C29	C31	117.8(17)
O17	Sm2	O3[4]	71.3(6)	N2	C30	C29	120.9(18)
O17	Sm2	O4[4]	86.2(7)	C32	C31	C29	173(2)
O17	Sm2	O7	80.4(7)	C31	C32	C33	170.6(19)
O17	Sm2	O14	93.4(7)	C34	C33	C32	124.3(17)
O17	Sm2	O18	159.1(5)	C34	C33	C38	121.7(17)
O17	Sm2	O20	147.9(6)	C38	C33	C32	113.7(16)
O17	Sm2	O22	124.4(6)	C33	C34	C35	118.2(19)
O17	Sm2	N9	104.0(6)	C34	C35	C39	119.4(17)
O17	Sm2	N10	170.0(5)	C36	C35	C34	121.8(18)

Table E5 Bond Angles for SmRu-MOF Final.

Atom	Atom	Atom	Angle/˚	Atom	Atom	Atom	Angle/˚
O17	Sm2	C39[4]	78.5(5)	C36	C35	C39	117.4(17)
O18	Sm2	N9	88.1(6)	C35	C36	C37	119.4(17)
O18	Sm2	N10	25.0(3)	C36	C37	C38	118.8(18)
O18	Sm2	C39[4]	120.5(6)	C36	C37	C40	122.8(16)
O20	Sm2	O18	49.5(6)	C38	C37	C40	118.3(17)
O20	Sm2	O22	71.3(8)	C33	C38	C37	119.6(18)
O20	Sm2	N9	81.8(7)	O3	C39	Sm2[2]	55.2(12)
O20	Sm2	N10	24.6(3)	O3	C39	O4	111(2)
O20	Sm2	C39[4]	70.9(6)	O3	C39	C35	124.0(16)
O22	Sm2	O18	64.6(6)	O4	C39	Sm2[2]	56.2(13)
O22	Sm2	N9	24.2(3)	O4	C39	C35	124.5(16)
O22	Sm2	N10	64.1(7)	C35	C39	Sm2[2]	173.1(15)
O22	Sm2	C39[4]	99.6(6)	O1	C40	C37	117.8(16)
N9	Sm2	N10	82.9(6)	O2	C40	O1	123.7(19)
N9	Sm2	C39[4]	82.8(5)	O2	C40	C37	118.5(18)
N10	Sm2	C39[4]	95.5(5)	C42	C41	C22	177(2)
N1	Ru1	N3	173.3(6)	C41	C42	C43	177(2)
N1	Ru1	N4	96.7(6)	C44	C43	C42	120.6(16)
N1	Ru1	N5	94.9(5)	C44	C43	C48	120.6(16)
N2	Ru1	N1	78.8(6)	C48	C43	C42	118.7(17)
N2	Ru1	N3	95.5(6)	C43	C44	C45	120.8(15)
N2	Ru1	N4	87.6(6)	C44	C45	C46	118.9(15)
N2	Ru1	N5	173.7(5)	C44	C45	C49	120.2(14)
N3	Ru1	N4	79.6(6)	C46	C45	C49	120.9(15)
N5	Ru1	N3	90.8(6)	C47	C46	C45	119.7(16)
N5	Ru1	N4	93.9(6)	C46	C47	C48	121.7(15)
N6	Ru1	N1	93.1(7)	C46	C47	C50	121.5(15)
N6	Ru1	N2	99.2(6)	C48	C47	C50	116.7(15)
N6	Ru1	N3	91.1(7)	C43	C48	C47	118.0(16)
N6	Ru1	N4	169.0(7)	O13	C49	O14	124.2(18)
N6	Ru1	N5	80.3(6)	O13	C49	C45	117.0(16)
C40	O1	Sm2[1]	166.2(17)	O14	C49	C45	118.7(15)
C40	O2	Sm1	151.9(15)	O15	C50	Sm1[4]	63.4(8)
C39	O3	Sm2[2]	100.7(14)	O15	C50	O16	125.1(15)
C39	O4	Sm2[2]	99.5(14)	O15	C50	C47	119.8(15)
N7	O5	Sm1	97.1(15)	O16	C50	Sm1[4]	61.7(8)
N7	O6	Sm1	97.1(15)	O16	C50	C47	114.9(15)
N9	O7	Sm2	100.6(14)	C47	C50	Sm1[4]	175.1(14)
N8	O9	Sm1	96.4(10)	O12	C52	N11	122(2)

[1]+X,-1+Y,1+Z; [2]-1+X,-1+Y,1+Z; [3]+X,1+Y,-1+Z; [4]1+X,1+Y,-1+Z

Table E6 Torsion Angles for SmRu-MOF Final.

A	B	C	D	Angle/˚	A	B	C	D	Angle/˚
Sm1	O2	C40	O1	21(5)	C5	N3	C1	C2	-4(4)
Sm1	O2	C40	C37	-156(2)	C5	C4	C3	C2	-4(5)
Sm1	O5	N7	O6	-1(2)	C6	N4	C10	C9	-5(3)
Sm1	O5	N7	O8	176(2)	C6	C5	C4	C3	-179(3)
Sm1	O6	N7	O5	1(2)	C7	C6	C5	N3	178(3)
Sm1	O6	N7	O8	-176(2)	C7	C6	C5	C4	-4(4)

Table E6 Torsion Angles for SmRu-MOF Final.

A	B	C	D	Angle/˚	A	B	C	D	Angle/˚
Sm1	O9	N8	O10	-15.6(17)	C8	C7	C6	N4	3(5)
Sm1	O9	N8	O11	167.2(15)	C8	C7	C6	C5	-169(3)
Sm1[1]	O13	C49	O14	81(5)	C9	C8	C7	C6	-11(6)
Sm1[1]	O13	C49	C45	-103(5)	C10	N4	C6	C5	177.7(16)
Sm1[2]	O15	C50	O16	-1(2)	C10	N4	C6	C7	4(3)
Sm1[2]	O15	C50	C47	-175.8(16)	C10	C9	C8	C7	10(6)
Sm1[2]	O16	C50	O15	1(2)	C11	N5	C15	C14	3(3)
Sm1[2]	O16	C50	C47	176.0(15)	C11	N5	C15	C16	-177.7(18)
Sm2[3]	O1	C40	O2	72(6)	C11	C12	C13	C14	8(4)
Sm2[3]	O1	C40	C37	-110(5)	C12	C13	C14	C15	-3(4)
Sm2[4]	O3	C39	O4	-3(2)	C13	C14	C15	N5	-3(4)
Sm2[4]	O3	C39	C35	171.7(18)	C13	C14	C15	C16	178(3)
Sm2[4]	O4	C39	O3	3(2)	C14	C15	C16	N6	175(3)
Sm2[4]	O4	C39	C35	-171.7(18)	C14	C15	C16	C17	-3(5)
Sm2	O14	C49	O13	-41(6)	C15	N5	C11	C12	3(2)
Sm2	O14	C49	C45	143(2)	C15	C16	C17	C18	-169(4)
Ru1	N1	C21	C22	177.8(13)	C16	N6	C20	C19	-9(5)
Ru1	N1	C25	C24	-174.1(15)	C16	C17	C18	C19	-24(7)
Ru1	N1	C25	C26	7(2)	C17	C18	C19	C20	18(7)
Ru1	N2	C26	C25	-13(2)	C18	C19	C20	N6	-1(7)
Ru1	N2	C26	C27	173.4(15)	C20	N6	C16	C15	-175(3)
Ru1	N2	C30	C29	-174.8(14)	C20	N6	C16	C17	3(4)
Ru1	N3	C1	C2	176(2)	C21	N1	C25	C24	5(3)
Ru1	N3	C5	C4	-175.2(19)	C21	N1	C25	C26	-174.2(16)
Ru1	N3	C5	C6	3(3)	C22	C23	C24	C25	1(3)
Ru1	N4	C6	C5	-10(3)	C24	C23	C22	C21	3(3)
Ru1	N4	C6	C7	177(2)	C24	C23	C22	C41	-176.0(19)
Ru1	N4	C10	C9	-176(2)	C24	C25	C26	N2	-175.0(18)
Ru1	N5	C11	C12	176.7(17)	C24	C25	C26	C27	-1(3)
Ru1	N5	C15	C14	-172(2)	C25	N1	C21	C22	-1(3)
Ru1	N5	C15	C16	8(3)	C25	C26	C27	C28	-173.4(19)
Ru1	N6	C16	C15	-1(3)	C26	N2	C30	C29	-1(3)
Ru1	N6	C16	C17	177(3)	C26	C25	C24	C23	174.1(19)
Ru1	N6	C20	C19	177(3)	C26	C27	C28	C29	3(3)
O3	C39	C35	C34	176(3)	C28	C29	C30	N2	4(3)
O3	C39	C35	C36	-17(3)	C30	N2	C26	C25	172.8(17)
O4	C39	C35	C34	-10(3)	C30	N2	C26	C27	-1(3)
O4	C39	C35	C36	157(3)	C30	C29	C28	C27	-5(3)
O7	N9	O22	Sm2	15(2)	C31	C29	C28	C27	-177(2)
O9	N8	O10	Sm1	14.9(16)	C31	C29	C30	N2	175.9(18)
O11	N8	O10	Sm1	-167.9(15)	C32	C33	C34	C35	175(2)
O12	C52	N11	C51	177(3)	C32	C33	C38	C37	-171.2(19)
O12	C52	N11	C53	0(3)	C33	C34	C35	C36	0(4)
O15	C50	C47	C46	179(2)	C33	C34	C35	C39	166(2)
O15	C50	C47	C48	2(3)	C33	C38	C37	C36	-8(3)
O16	C50	C47	C46	4(3)	C33	C38	C37	C40	173.9(19)
O16	C50	C47	C48	-173.4(19)	C34	C33	C38	C37	4(3)
O18	N10	O20	Sm2	7(2)	C35	C36	C37	C38	8(4)

Table E6 Torsion Angles for SmRu-MOF Final.

A	B	C	D	Angle/˚	A	B	C	D	Angle/˚
O19	N10	O18	Sm2	173.0(19)	C35	C36	C37	C40	-174(2)
O19	N10	O20	Sm2	-172.8(19)	C36	C37	C40	O1	-169(2)
O20	N10	O18	Sm2	-6(2)	C36	C37	C40	O2	9(3)
O21	N9	O7	Sm2	168(2)	C37	C36	C35	C34	-4(4)
O21	N9	O22	Sm2	-168(2)	C37	C36	C35	C39	-170(2)
O22	N9	O7	Sm2	-15(2)	C38	C33	C34	C35	0(4)
N1	C21	C22	C23	-3(3)	C38	C37	C40	O1	10(3)
N1	C21	C22	C41	175.8(18)	C38	C37	C40	O2	-173(2)
N1	C25	C24	C23	-5(3)	C42	C43	C44	C45	180(2)
N1	C25	C26	N2	4(2)	C44	C45	C49	O13	-5(4)
N1	C25	C26	C27	177.4(18)	C44	C45	C49	O14	171(3)
N2	C26	C27	C28	0(3)	C45	C46	C47	C48	-4(3)
N3	C5	C4	C3	-1(4)	C45	C46	C47	C50	179.1(19)
N4	C6	C5	N3	5(3)	C46	C45	C44	C43	-5(3)
N4	C6	C5	C4	-177(2)	C46	C45	C49	O13	175(2)
N4	C10	C9	C8	-3(5)	C46	C45	C49	O14	-9(4)
N5	C11	C12	C13	-8(3)	C46	C47	C48	C43	2(3)
N5	C15	C16	N6	-5(4)	C47	C46	C45	C44	5(3)
N5	C15	C16	C17	178(3)	C47	C46	C45	C49	-175(2)
N6	C16	C17	C18	14(6)	C47	C48	C43	C42	-177.9(18)
N11	C52	O12	Sm1	-128(2)	C47	C48	C43	C44	-2(3)
C1	N3	C5	C4	5(4)	C48	C43	C44	C45	4(3)
C1	N3	C5	C6	-177(2)	C49	C45	C44	C43	175(2)
C3	C2	C1	N3	-1(5)	C50	C47	C48	C43	179.5(18)
C4	C3	C2	C1	5(5)					

[1]+X,1+Y,-1+Z; [2]1+X,1+Y,-1+Z; [3]+X,-1+Y,1+Z; [4]-1+X,-1+Y,1+Z

Table E7 Atomic Occupancy for SmRu-MOF Final.

Atom	*Occupancy*	Atom	*Occupancy*	Atom	*Occupancy*
O12	0.75	N11	0.75	C51	0.75
C52	0.75	C53	0.75		

Table E8 Solvent masks information for SmRu-MOF Final.

Number	X	Y	Z	Volume	Electron count	Content
1	0.000	0.000	0.000	102.1	15.1	?
2	0.120	0.528	0.289	7.2	0.0	?
3	0.160	0.208	0.422	7.2	1.2	?
4	0.431	0.817	0.271	10.5	0.0	?
5	0.569	0.183	0.729	10.5	0.0	?
6	0.840	0.792	0.578	7.2	1.2	?
7	0.880	0.472	0.711	7.2	0.0	?

Experimental

Single crystals of $C_{26.12}N_{5.38}O_{10.88}Ru_{0.5}Sm$ **[SmRu-MOF]** were synthesis (Chapter 4&6). A suitable crystal was selected and measured on a **Bruker APEX-II CCD** diffractometer. The crystal was kept at 99.98 K during data collection. Using Olex2 [1], the structure was solved with the Unknown [2] structure solution program using Unknown and refined with the Unknown [3] refinement package using Unknown minimisation.

1. Dolomanov, O.V., Bourhis, L.J., Gildea, R.J, Howard, J.A.K. & Puschmann, H. (2009), J. Appl. Cryst. 42, 339-341.
2. Sheldrick, G.M. (2015). Acta Cryst. A71, 3-8.
3. Sheldrick, G.M. (2008). Acta Cryst. A64, 112-122

Crystal structure determination of [SmRu-MOF Final]

Crystal Data for $C_{26.125}N_{5.375}O_{10.875}Ru_{0.5}Sm$ (M =763.95 g/mol): triclinic, space group P-1 (no. 2), a = 10.9238(4) Å, b = 14.1540(7) Å, c = 18.4473(9) Å, α = 86.338(4)°, β = 89.152(3)°, γ = 85.177(3)°, V = 2836.2(2) Å^3, Z = 4, T = 99.98 K, μ(CuKα) = 18.240 mm^{-1}, $Dcalc$ = 1.789 g/cm^3, 42577 reflections measured (4.8° ≤ 2Θ ≤ 122.08°), 8555 unique (R_{int} = 0.1188, R_{sigma} = 0.1146) which were used in all calculations. The final R_1 was 0.1017 (I > 2σ(I)) and wR_2 was 0.3064 (all data).

Refinement model description

Number of restraints - 776, number of constraints – unknown.Details:

1. Restrained distances

N10-O18 = N10-O19 1.25 with sigma of 0.02

N10-O20 1.24 with sigma of 0.02

C52-O12 1.22 with sigma of 0.02

C52-N11 1.36 with sigma of 0.02

N11-C51 1.45 with sigma of 0.02

N11-C53 1.46 with sigma of 0.02

O3-C39 = O4-C39 1.26 with sigma of 0.02

C39-C35 1.5 with sigma of 0.02

N5-C11 = N6-C16 = N6-C20 1.34 with sigma of 0.02

N5-C15 1.35 with sigma of 0.02

C11-C12 = C12-C13 = C13-C14 = C14-C15 = C17-C18 = C18-C19 = C19-C20 1.39 with sigma of 0.02

C15-C16 1.48 with sigma of 0.02

C16-C17 1.4 with sigma of 0.02

N4-C10 = N3-C5 = N3-C1 1.34 with sigma of 0.02

N4-C6 1.35 with sigma of 0.02

C10-C9 = C9-C8 = C8-C7 = C7-C6 = C4-C3 = C3-C2 = C2-C1 1.39 with sigma of 0.02

C6-C5 1.48 with sigma of 0.02

C5-C4 1.4 with sigma of 0.02

N9-O7 = N9-O22 1.25 with sigma of 0.02

N9-O21 1.24 with sigma of 0.02

C52-C51 2.46 with sigma of 0.04

C52-C53 2.45 with sigma of 0.04

O3-O4 2.19 with sigma of 0.04

O3-C35 2.38 with sigma of 0.04

O4-C35 2.39 with sigma of 0.04

N5-C12 = N5-C14 = N6-C17 = N6-C19 = C13-C15 = C16-C18 2.4 with sigma of 0.04

N5-C16 = N6-C15 = C11-C13 = C12-C14 = C17-C19 = C18-C20 2.39 with sigma of 0.04

C14-C16 2.52 with sigma of 0.04

C15-C17 2.53 with sigma of 0.04

N4-C9 = N4-C7 = N3-C4 = N3-C2 = C8-C6 = C5-C3 2.4 with sigma of 0.04

N4-C5 = N3-C6 = C10-C8 = C9-C7 = C4-C2 = C3-C1 2.39 with sigma of 0.04

C7-C5 2.52 with sigma of 0.04

C6-C4 2.53 with sigma of 0.04

N10-O18 ≈ N10-O20 ≈ N10-O19 with sigma of 0.02

O18-O20 ≈ O20-O19 ≈ O19-O18 with sigma of 0.04

N11-C51 ≈ N11-C53 with sigma of 0.02

C39-O3 ≈ C39-O4 with sigma of 0.02

O3-C35 ≈ C35-O4 with sigma of 0.04

N5-C11 ≈ N5-C15 ≈ N6-C16 ≈ N6-C20 with sigma of 0.02

C12-C13 ≈ C13-C14 ≈ C14-C15 ≈ C16-C17 ≈ C17-C18 ≈ C18-C19 ≈ C19-C20 with sigma of 0.02

N5-C14 ≈ N5-C12 ≈ N6-C17 ≈ N6-C19 with sigma of 0.04

C11-C15 ≈ C11-C13 ≈ C12-C14 ≈ C13-C15 ≈ C16-C20 ≈ C16-C18 ≈ C17-C19 with sigma of 0.04

N4-C10 ≈ N4-C6 ≈ N3-C5 ≈ N3-C1 with sigma of 0.02

C9-C8 ≈ C8-C7 ≈ C7-C6 ≈ C5-C4 ≈ C4-C3 ≈ C3-C2 ≈ C2-C1 with sigma of 0.02

N4-C7 ≈ N4-C9 ≈ N3-C4 ≈ N3-C2 with sigma of 0.04

C10-C6 ≈ C10-C8 ≈ C9-C7 ≈ C8-C6 ≈ C5-C1 ≈ C5-C3 ≈ C4-C2 with sigma of 0.04

N9-O7 ≈ N9-O21 ≈ N9-O22
with sigma of 0.02
O7-O21 ≈ O21-O22 ≈ O22-O7
with sigma of 0.04
2. Restrained planarity
O18, O19, O20, N10
with sigma of 0.1
O12, N11, C51, C52, C53
with sigma of 0.1
O3, O4, C35, C39
with sigma of 0.1
N5, N6, C11, C12, C13, C14, C15, C16, C17, C18, C19, C20
with sigma of 0.1
N3, N4, C1, C2, C3, C4, C5, C6, C7, C8, C9, C10
with sigma of 0.1
O7, O21, O22, N9
with sigma of 0.1
3. Uiso/Uaniso restraints and constraints
O18 ≈ O19 ≈ O20 ≈ N10: within 2A with sigma of 0.04 and sigma for
terminal atoms of 0.08 within 2A
O12 ≈ N11 ≈ C51 ≈ C52 ≈ C53: within 2A with sigma of 0.04 and
sigma for terminal atoms of 0.08 within 2A
O3 ≈ O4 ≈ C35 ≈ C39: within 2A with sigma of 0.04 and sigma for
terminal atoms of 0.08 within 2A
N5 ≈ N6 ≈ C11 ≈ C12 ≈ C13 ≈ C14 ≈ C15 ≈ C16 ≈
C17 ≈ C18 ≈ C19 ≈ C20: within 2A with sigma of 0.04 and sigma for
terminal atoms of 0.08 within 2A
N3 ≈ N4 ≈ C1 ≈ C2 ≈ C3 ≈ C4 ≈ C5 ≈ C6 ≈ C7
≈ C8 ≈ C9 ≈ C10: within 2A with sigma of 0.04 and sigma for
terminal atoms of 0.08 within 2A
O7 ≈ O21 ≈ O22 ≈ N9: within 2A with sigma of 0.04 and sigma for
terminal atoms of 0.08 within 2A
Uanis(C40) ≈ Ueq, Uanis(O1) ≈ Ueq, Uanis(O2) ≈ Ueq: with sigma of
0.01 and sigma for terminal atoms of 0.02
Uanis(C35) ≈ Ueq, Uanis(C39) ≈ Ueq, Uanis(O3) ≈ Ueq, Uanis(O4)
≈ Ueq, Uanis(C53) ≈ Ueq, Uanis(N11) ≈ Ueq, Uanis(C52) ≈ Ueq,
Uanis(C51) ≈ Ueq, Uanis(O12) ≈ Ueq: with sigma of 0.01 and sigma for
terminal atoms of 0.02
4. Rigid body (RIGU) restrains
O18, O19, O20, N10
with sigma for 1-2 distances of 0.004 and sigma for 1-3 distances of 0.004
O12, N11, C51, C52, C53
with sigma for 1-2 distances of 0.004 and sigma for 1-3 distances of 0.004
O3, O4, C35, C39
with sigma for 1-2 distances of 0.004 and sigma for 1-3 distances of 0.004
N5, N6, C11, C12, C13, C14,

Appendix F: Crystallographic Information for EuRu-MOF

Table F1 Crystal data and structure refinement for EuRu-MOF.

Identification code	EuRu-MOF
Empirical formula	$C_{40}H_{40}N_6O_{10}RuEu$
Formula weight	1017.81
Temperature/K	100.00
Crystal system	triclinic
Space group	P-1
a/Å	10.9203(7)
b/Å	14.1292(11)
c/Å	18.5786(15)
α/°	85.999(5)
β/°	89.191(5)
γ/°	85.479(5)
Volume/Å^3	2850.6(4)
Z	4
ρ_{calc}g/cm^3	2.372
μ/mm^{-1}	20.655
F(000)	2036.0
Crystal size/mm^3	0.106 × 0.048 × 0.016
Radiation	CuKα (λ = 1.54178)
2Θ range for data collection/°	7.628 to 101.34
Index ranges	-10 ≤ h ≤ 10, -13 ≤ k ≤ 14, -18 ≤ l ≤ 18
Reflections collected	27215
Independent reflections	5952 [R_{int} = 0.1455, R_{sigma} = 0.1164]
Data/restraints/parameters	5952/811/806
Goodness-of-fit on F^2	1.061
Final R indexes [I>=2σ (I)]	R_1 = 0.0960, wR_2 = 0.2413
Final R indexes [all data]	R_1 = 0.1528, wR_2 = 0.2847
Largest diff. peak/hole / e Å^{-3}	2.12/-0.87

Table F2 Fractional Atomic Coordinates (×10^4) and Equivalent Isotropic Displacement Parameters (Å^2×10^3) for EuRu-MOF. U_{eq} is defined as 1/3 of the trace of the orthogonalised U_{IJ} tensor.

Atom	*x*	*y*	*z*	U(eq)
Eu01	8644.6(12)	11632.1(14)	1837.2(11)	63.0(6)
Ru01	8246.2(15)	4269.9(13)	7402.5(10)	64.7(7)
N1	7946(15)	5662(12)	7119(9)	58(5)
O1	296(13)	2389(12)	11149(9)	86(5)
C1	10919(19)	9817(18)	3697(14)	82(8)
N2	6682(15)	4641(14)	8004(11)	71(5)
Eu02	5626.5(15)	9504.8(15)	3541.1(11)	106.6(9)
O2	863(13)	1245(12)	11975(9)	79(5)
C2	9680(20)	9643(16)	3841(12)	67(6)
C3	9320(20)	9036(16)	4415(12)	65(6)
N3	9699(16)	4023(14)	6710(10)	90(5)
O3	8939(16)	10730(13)	2887(10)	97(5)
C4	10221(19)	8645(14)	4920(12)	57(6)

Table F2 Fractional Atomic Coordinates (×10^4) and Equivalent Isotropic Displacement Parameters (Å^2×10^3) for EuRu-MOF. U_{eq} is defined as 1/3 of the trace of the orthogonalised U_{IJ} tensor.

Atom	*x*	*y*	*z*	U(eq)
O4	6686(14)	1099(11)	11807(8)	74(4)
N4	7338(16)	4006(11)	6463(9)	84(5)
O5	8100(16)	11942(13)	490(10)	106(5)
N5	8384(16)	2856(12)	7788(10)	86(5)
C5	11432(19)	8807(17)	4759(15)	79(8)
O6	7673(13)	13085(11)	1172(9)	85(5)
N6	9352(14)	4340(12)	8246(9)	94(6)
C6	11750(20)	9358(19)	4177(16)	92(9)
O7	7269(17)	12546(15)	2741(12)	86(6)
N7	8083(17)	13075(15)	2874(11)	94(7)
C7	13040(30)	9490(20)	3988(17)	98(8)
O8	9102(16)	12972(13)	2564(10)	73(5)
N8	7781(14)	12801(12)	551(9)	89(5)
C8	8740(20)	10072(19)	3364(14)	75(7)
O9	8990(20)	10188(18)	1310(16)	63(7)
C9	9768(18)	8080(18)	5507(14)	68(7)
N9	7920(30)	9050(20)	856(18)	158(12)
C10	9190(20)	7680(17)	5981(13)	70(7)
N10	6268(19)	8110(17)	4739(13)	147(9)
O10	13367(18)	9979(15)	3443(12)	110(6)
C11	8410(20)	7167(19)	6440(12)	72(7)
N11	5670(20)	7855(18)	2669(12)	161(9)
O11	13920(20)	8947(16)	4301(12)	125(7)
O12	7637(15)	9841(12)	3452(9)	87(5)
C12	7290(20)	7583(19)	6678(15)	87(8)
C13	6550(20)	7054(17)	7088(13)	68(7)
O13	5318(17)	298(15)	12447(11)	106(6)
O14	6620(20)	8304(19)	2679(13)	158(8)
C14	8710(20)	6196(18)	6680(12)	74(7)
O15	4710(20)	8174(18)	2967(14)	165(9)
C15	6890(20)	6122(18)	7317(12)	66(6)
C16	6150(20)	5552(16)	7830(12)	66(6)
O16	6230(30)	8983(18)	4827(16)	142(9)
O17	6400(20)	7907(16)	4104(13)	146(8)
C17	5070(20)	5850(19)	8129(14)	78(7)
C18	4540(20)	5262(18)	8674(13)	75(7)
O19	5720(20)	7067(19)	2396(15)	178(10)
C19	5150(20)	4403(17)	8881(13)	66(7)
O20	6200(30)	7458(19)	5224(14)	181(10)
C20	6173(18)	4088(15)	8542(12)	56(6)
C21	4700(20)	3810(20)	9449(15)	81(8)
O21	7860(20)	13680(20)	3323(16)	132(9)
C22	4360(20)	3286(18)	9959(15)	71(7)
O22	7593(16)	13387(13)	30(10)	111(6)
C23	4010(18)	2662(16)	10546(11)	59(6)
C24	4907(19)	2103(17)	10928(12)	68(7)
C25	4611(19)	1488(16)	11523(13)	66(6)
C26	3358(18)	1415(17)	11689(12)	65(6)

Table F2 Fractional Atomic Coordinates (×10^4) and Equivalent Isotropic Displacement Parameters (Å^2×10^3) for EuRu-MOF. U_{eq} is defined as 1/3 of the trace of the orthogonalised U_{IJ} tensor.

Atom	*x*	*y*	*z*	U(eq)
C27	2468(19)	1933(17)	11321(12)	65(7)
C28	2770(20)	2566(17)	10750(12)	69(7)
C29	1110(20)	1883(18)	11500(15)	70(7)
C30	6110(18)	4007(16)	6395(12)	118(8)
C32	5570(20)	956(19)	11969(14)	78(7)
C33	8310(30)	9540(20)	1419(19)	125(11)
C34	7020(50)	8350(40)	980(30)	220(20)
C35	8390(60)	9340(40)	140(20)	190(20)
C37	5581(19)	3900(30)	5734(14)	132(9)
C38	6340(20)	3730(30)	5150(13)	135(9)
C39	7600(20)	3780(30)	5205(11)	129(8)
C40	8087(15)	3890(20)	5876(11)	106(6)
C41	9402(14)	3930(19)	6013(11)	94(6)
C42	10310(19)	3850(20)	5480(11)	115(7)
C43	11524(19)	3850(20)	5686(14)	117(8)
C44	11831(18)	3890(20)	6400(14)	119(8)
C45	10892(18)	3983(19)	6907(12)	100(7)
C46	9824(19)	5136(14)	8450(12)	103(7)
C47	10630(30)	5125(15)	9019(16)	134(10)
C48	10870(30)	4289(16)	9443(17)	150(11)
C49	10340(30)	3481(15)	9259(16)	139(10)
C50	9530(30)	3528(12)	8687(13)	110(7)
C51	9050(20)	2674(12)	8404(12)	102(6)
C52	9020(30)	1816(14)	8812(12)	112(8)
C53	8570(30)	1061(14)	8497(14)	117(8)
C54	7950(20)	1210(14)	7853(13)	105(7)
C55	7860(20)	2118(15)	7508(12)	100(6)
O23	5544(12)	10373(10)	3973(7)	24(3)
O24	8650(20)	11194(19)	1554(13)	19(8)
O25	6350(60)	9940(50)	4800(30)	77(18)

Table F3 Anisotropic Displacement Parameters (Å^2×10^3) for EuRu-MOF. The Anisotropic displacement factor exponent takes the form: $-2\pi^2[h^2a^{*2}U_{11}+2hka^*b^*U_{12}+\ldots]$.

Atom	U_{11}	U_{22}	U_{33}	U_{23}	U_{13}	U_{12}
Eu01	36.6(9)	61.5(12)	87.2(13)	25.8(10)	-5.9(7)	-5.5(7)
Ru01	49.3(11)	69.5(13)	71.6(13)	21.4(9)	1.1(8)	-4.5(9)
N1	34(10)	67(12)	66(12)	27(10)	2(9)	-2(9)
O1	35(9)	110(13)	101(13)	58(11)	-14(8)	8(9)
C1	34(14)	97(19)	110(20)	44(16)	8(13)	-1(13)
N2	37(10)	69(13)	99(15)	29(11)	-4(10)	1(10)
Eu02	52.2(11)	121.9(17)	133.0(17)	68.0(13)	8.9(9)	2.0(9)
O2	46(9)	82(11)	103(13)	39(10)	1(8)	-8(8)
C2	66(16)	65(15)	66(16)	25(13)	0(12)	0(12)
C3	51(13)	72(15)	68(15)	41(13)	-3(11)	-18(11)
N3	86(9)	70(12)	110(10)	9(9)	8(7)	2(9)
O3	77(8)	105(9)	105(9)	30(8)	-2(7)	-10(7)
C4	56(15)	44(12)	68(15)	29(11)	10(12)	-9(11)
O4	63(8)	74(8)	83(8)	23(7)	-9(6)	-14(6)

Table F3 Anisotropic Displacement Parameters ($Å^2 \times 10^3$) for EuRu-MOF. The Anisotropic displacement factor exponent takes the form: $-2\pi^2[h^2a^{*2}U_{11}+2hka^*b^*U_{12}+\ldots]$.

Atom	U_{11}	U_{22}	U_{33}	U_{23}	U_{13}	U_{12}
N4	90(9)	68(11)	90(10)	18(9)	-14(7)	4(9)
O5	75(11)	113(10)	126(12)	19(9)	-1(9)	-9(8)
N5	47(10)	90(10)	116(11)	22(8)	13(8)	1(8)
C5	33(13)	70(16)	130(20)	45(16)	-3(13)	-4(11)
O6	36(8)	103(10)	114(10)	26(8)	-17(8)	-12(7)
N6	69(12)	87(9)	117(12)	31(8)	-25(10)	11(8)
C6	53(16)	84(18)	130(20)	61(18)	4(16)	-6(14)
O7	64(11)	87(13)	103(15)	-2(10)	-21(10)	10(9)
N7	73(11)	93(14)	115(15)	-8(11)	-25(10)	2(10)
C7	82(11)	102(12)	104(12)	27(9)	-13(9)	-3(9)
O8	67(10)	56(11)	92(13)	17(9)	-34(9)	3(8)
N8	46(10)	108(11)	109(11)	25(8)	-19(9)	-10(9)
C8	66(10)	82(10)	78(10)	9(9)	11(8)	-19(9)
O9	59(10)	58(10)	72(11)	0(8)	6(8)	-4(8)
C9	27(12)	88(17)	84(18)	22(16)	9(12)	-3(11)
N9	200(20)	160(20)	138(19)	-30(16)	31(17)	-110(20)
C10	72(16)	73(16)	62(16)	18(14)	-15(14)	-14(14)
N10	118(17)	141(15)	174(18)	31(13)	-25(14)	13(14)
O10	93(9)	111(9)	122(10)	29(8)	16(8)	-12(8)
C11	78(19)	87(19)	53(15)	11(14)	6(13)	-30(16)
N11	136(16)	193(19)	152(19)	54(15)	-20(13)	-60(14)
O11	114(10)	127(10)	128(10)	18(8)	-13(8)	4(8)
O12	74(8)	102(9)	80(8)	34(7)	-11(7)	-12(7)
C12	72(18)	75(17)	110(20)	50(16)	17(16)	-3(15)
C13	45(13)	69(16)	86(18)	21(14)	8(12)	4(12)
O13	83(9)	115(9)	114(10)	32(8)	-7(8)	-5(8)
O14	140(15)	200(20)	131(17)	40(15)	-6(13)	-69(14)
C14	78(17)	79(18)	66(16)	28(14)	-12(13)	-35(14)
O15	138(16)	189(19)	162(19)	64(14)	-17(13)	-50(13)
C15	57(16)	77(18)	59(15)	25(13)	-6(12)	-12(14)
C16	77(18)	61(15)	54(15)	16(12)	-1(13)	16(13)
O16	102(18)	143(15)	170(20)	29(14)	-18(16)	11(14)
O17	118(16)	136(15)	174(17)	31(13)	-19(14)	11(13)
C17	38(14)	99(19)	88(18)	24(16)	-2(13)	23(13)
C18	58(15)	81(17)	77(17)	30(14)	25(13)	8(14)
O19	165(18)	198(19)	170(20)	44(15)	-25(15)	-60(14)
C19	46(15)	72(17)	76(17)	34(14)	-6(12)	-11(13)
O20	180(20)	167(17)	184(18)	48(13)	-22(16)	-1(16)
C20	31(12)	56(14)	79(16)	12(12)	7(11)	3(10)
C21	62(16)	100(20)	77(19)	18(18)	-17(14)	29(15)
O21	120(16)	127(17)	152(18)	-42(15)	-20(13)	9(13)
C22	54(15)	80(17)	74(18)	23(16)	-25(13)	1(13)
O22	81(12)	130(12)	119(11)	36(9)	-32(9)	-14(10)
C23	39(13)	73(15)	60(14)	31(12)	-3(11)	-1(11)
C24	39(13)	89(17)	70(16)	23(14)	-2(11)	-4(12)
C25	43(14)	69(15)	86(18)	13(14)	-8(12)	-9(11)
C26	38(14)	86(16)	68(15)	36(13)	3(11)	-23(12)
C27	45(14)	81(16)	66(15)	34(13)	-22(12)	-10(12)

Table F3 Anisotropic Displacement Parameters ($Å^2×10^3$) for EuRu-MOF. The Anisotropic displacement factor exponent takes the form: $-2π^2[h^2a^{*2}U_{11}+2hka*b*U_{12}+…]$.

Atom	U_{11}	U_{22}	U_{33}	U_{23}	U_{13}	U_{12}
C28	50(15)	92(17)	58(15)	37(13)	-7(11)	-6(12)
C29	42(15)	75(16)	93(19)	9(15)	24(13)	-22(13)
C30	94(10)	150(20)	108(13)	-6(13)	-13(8)	-4(10)
C32	62(10)	86(11)	86(11)	16(9)	1(8)	-11(9)
C33	140(20)	114(16)	132(18)	-13(14)	28(15)	-65(16)
C34	280(40)	240(40)	170(30)	-40(30)	50(30)	-190(40)
C35	260(50)	200(40)	140(20)	-31(18)	40(20)	-150(40)
C37	108(12)	180(20)	111(13)	-8(15)	-19(9)	-12(12)
C38	116(12)	170(20)	117(14)	-8(14)	-14(9)	-14(13)
C39	116(12)	160(20)	109(11)	-1(11)	-11(9)	-11(13)
C40	102(8)	109(16)	103(10)	6(10)	-1(7)	-4(8)
C41	95(8)	74(14)	110(10)	9(10)	6(7)	2(8)
C42	110(10)	106(17)	128(12)	1(11)	21(9)	-1(11)
C43	107(11)	98(17)	144(14)	2(13)	19(9)	0(11)
C44	98(11)	108(18)	146(14)	2(14)	18(9)	2(11)
C45	86(10)	83(15)	126(13)	10(11)	5(8)	2(10)
C46	91(15)	87(10)	124(15)	38(9)	-39(12)	3(9)
C47	144(19)	96(12)	157(17)	49(11)	-77(15)	-22(12)
C48	170(20)	101(12)	178(17)	56(11)	-96(17)	-29(12)
C49	146(19)	95(12)	171(16)	51(11)	-76(15)	-21(11)
C50	97(14)	88(9)	138(13)	37(8)	-38(11)	-2(8)
C51	80(13)	86(9)	135(12)	27(8)	-11(10)	-2(8)
C52	110(17)	86(10)	135(14)	26(9)	-15(12)	-8(10)
C53	108(18)	94(11)	148(16)	16(10)	-5(12)	-16(10)
C54	81(15)	96(11)	135(16)	14(9)	10(11)	-13(10)
C55	65(13)	100(11)	132(14)	13(9)	16(10)	-10(10)

Table F4 Bond Lengths for EuRu-MOF.

Atom	Atom	Length/Å	Atom	Atom	Length/Å
Eu01	$O1^1$	2.465(15)	N7	O21	1.239(14)
Eu01	$O2^1$	2.454(14)	C7	O10	1.25(3)
Eu01	O3	2.267(18)	C7	O11	1.30(3)
Eu01	$O4^2$	2.326(15)	N8	O22	1.238(13)
Eu01	O5	2.580(19)	C8	O12	1.28(3)
Eu01	O6	2.491(15)	O9	C33	1.230(19)
Eu01	O7	2.58(2)	O9	O24	1.54(4)
Eu01	N7	2.93(2)	C9	C10	1.21(3)
Eu01	O8	2.487(19)	N9	C33	1.380(19)
Eu01	O9	2.33(3)	N9	C34	1.461(16)
Eu01	$C29^1$	2.80(2)	N9	C35	1.462(16)
Eu01	O24	0.84(3)	C10	C11	1.40(4)
Ru01	N1	2.003(17)	N10	O16	1.254(14)
Ru01	N2	2.080(19)	N10	O17	1.237(14)
Ru01	N3	2.052(18)	N10	O20	1.249(14)
Ru01	N4	2.089(17)	C11	C12	1.39(3)
Ru01	N5	2.069(17)	C11	C14	1.43(3)
Ru01	N6	2.005(17)	N11	O14	1.254(14)
N1	C14	1.39(3)	N11	O15	1.246(14)

Table F4 Bond Lengths for EuRu-MOF.

Atom	Atom	Length/Å	Atom	Atom	Length/Å
N1	C15	1.34(3)	N11	O19	1.253(14)
O1	C29	1.26(3)	C12	C13	1.34(3)
C1	C2	1.41(3)	C13	C15	1.38(3)
C1	C6	1.38(3)	O13	C32	1.28(3)
N2	C16	1.39(3)	C15	C16	1.48(3)
N2	C20	1.36(3)	C16	C17	1.35(3)
Eu02	C7[3]	2.93(3)	O16	O25	1.37(6)
Eu02	N10	2.92(2)	C17	C18	1.41(3)
Eu02	O10[3]	2.51(2)	C18	C19	1.37(3)
Eu02	O11[3]	2.47(2)	C19	C20	1.34(3)
Eu02	O12	2.284(17)	C19	C21	1.41(4)
Eu02	O13[2]	2.268(19)	C21	C22	1.23(3)
Eu02	O14	2.58(3)	C22	C23	1.42(3)
Eu02	O15	2.50(3)	C23	C24	1.38(3)
Eu02	O16	2.53(3)	C23	C28	1.42(3)
Eu02	O17	2.51(2)	C24	C25	1.41(3)
Eu02	O23	1.508(14)	C25	C26	1.41(3)
Eu02	O25	2.60(6)	C25	C32	1.47(3)
O2	C29	1.26(3)	C26	C27	1.34(3)
C2	C3	1.39(3)	C27	C28	1.39(3)
C2	C8	1.43(3)	C27	C29	1.52(3)
C3	C4	1.42(3)	C30	C37	1.386(17)
N3	C41	1.357(12)	C37	C38	1.380(12)
N3	C45	1.354(12)	C38	C39	1.383(12)
O3	C8	1.27(3)	C39	C40	1.388(12)
C4	C5	1.38(3)	C40	C41	1.468(16)
C4	C9	1.41(3)	C41	C42	1.395(12)
O4	C32	1.27(3)	C42	C43	1.385(12)
N4	C30	1.349(13)	C43	C44	1.379(12)
N4	C40	1.366(12)	C44	C45	1.387(12)
O5	N8	1.248(13)	C46	C47	1.383(12)
N5	C51	1.362(12)	C47	C48	1.381(12)
N5	C55	1.363(13)	C48	C49	1.383(12)
C5	C6	1.35(3)	C49	C50	1.387(12)
O6	N8	1.249(13)	C50	C51	1.485(16)
N6	C46	1.352(12)	C51	C52	1.386(12)
N6	C50	1.365(12)	C52	C53	1.379(12)
C6	C7	1.47(4)	C53	C54	1.377(12)
O7	N7	1.245(14)	C54	C55	1.390(16)
N7	O8	1.249(14)			

[1]1+X,1+Y,-1+Z; [2]+X,1+Y,-1+Z; [3]-1+X,+Y,+Z

Table F5 Bond Angles for EuRu-MOF.

Atom	Atom	Atom	Angle/˚	Atom	Atom	Atom	Angle/˚
O1[1]	Eu01	O5	68.5(5)	C29	O2	Eu01[3]	92.3(13)
O1[1]	Eu01	O6	73.2(5)	C1	C2	C8	119(2)
O1[1]	Eu01	O7	121.6(6)	C3	C2	C1	123(2)
O1[1]	Eu01	N7	99.0(6)	C3	C2	C8	118(2)
O1[1]	Eu01	O8	76.1(6)	C2	C3	C4	118.9(19)

Table F5 Bond Angles for EuRu-MOF.

Atom	Atom	Atom	Angle/˚	Atom	Atom	Atom	Angle/˚
O1[1]	Eu01	C29[1]	26.6(6)	C41	N3	Ru01	115.8(12)
O2[1]	Eu01	O1[1]	53.3(5)	C45	N3	Ru01	124.0(14)
O2[1]	Eu01	O5	110.3(6)	C45	N3	C41	120.2(15)
O2[1]	Eu01	O6	125.3(5)	C8	O3	Eu01	156.4(18)
O2[1]	Eu01	O7	124.6(6)	C3	C4	C9	115.1(18)
O2[1]	Eu01	N7	103.4(6)	C5	C4	C3	117.0(18)
O2[1]	Eu01	O8	81.6(6)	C5	C4	C9	128(2)
O2[1]	Eu01	C29[1]	26.7(6)	C32	O4	Eu01[5]	161.7(17)
O3	Eu01	O1[1]	124.0(6)	C30	N4	Ru01	125.3(14)
O3	Eu01	O2[1]	72.3(6)	C30	N4	C40	120.0(15)
O3	Eu01	O4[2]	87.8(6)	C40	N4	Ru01	114.6(12)
O3	Eu01	O5	155.1(7)	N8	O5	Eu01	93.4(12)
O3	Eu01	O6	149.3(7)	C51	N5	Ru01	114.4(12)
O3	Eu01	O7	76.9(7)	C55	N5	Ru01	127.5(13)
O3	Eu01	N7	79.8(7)	C55	N5	C51	118.1(15)
O3	Eu01	O8	84.5(7)	C6	C5	C4	122(2)
O3	Eu01	O9	84.2(9)	N8	O6	Eu01	97.7(11)
O3	Eu01	C29[1]	98.1(7)	C46	N6	Ru01	125.7(12)
O4[2]	Eu01	O1[1]	146.5(5)	C46	N6	C50	118.1(14)
O4[2]	Eu01	O2[1]	148.3(5)	C50	N6	Ru01	115.9(12)
O4[2]	Eu01	O5	78.0(5)	C1	C6	C7	114(2)
O4[2]	Eu01	O6	84.0(5)	C5	C6	C1	123(2)
O4[2]	Eu01	O7	71.8(6)	C5	C6	C7	122(2)
O4[2]	Eu01	N7	96.8(6)	N7	O7	Eu01	93.1(13)
O4[2]	Eu01	O8	121.7(6)	O7	N7	Eu01	61.8(11)
O4[2]	Eu01	C29[1]	161.1(7)	O7	N7	O8	119.2(18)
O5	Eu01	O7	116.6(6)	O8	N7	Eu01	57.4(11)
O5	Eu01	N7	121.7(6)	O21	N7	Eu01	178.8(18)
O5	Eu01	C29[1]	89.8(7)	O21	N7	O7	118.7(19)
O6	Eu01	O5	49.9(5)	O21	N7	O8	122.2(19)
O6	Eu01	O7	72.3(6)	C6	C7	Eu02[6]	172(2)
O6	Eu01	N7	71.9(6)	O10	C7	Eu02[6]	58.4(15)
O6	Eu01	C29[1]	99.1(7)	O10	C7	C6	124(3)
O7	Eu01	N7	25.1(3)	O10	C7	O11	115(3)
O7	Eu01	C29[1]	126.9(7)	O11	C7	Eu02[6]	56.6(16)
O8	Eu01	O5	120.3(6)	O11	C7	C6	120(3)
O8	Eu01	O6	74.9(6)	N7	O8	Eu01	97.6(12)
O8	Eu01	O7	50.2(6)	O5	N8	Eu01	61.4(10)
O8	Eu01	N7	25.0(3)	O5	N8	O6	117.9(16)
O8	Eu01	C29[1]	76.9(7)	O6	N8	Eu01	57.4(9)
O9	Eu01	O1[1]	94.2(8)	O22	N8	Eu01	168.6(13)
O9	Eu01	O2[1]	76.3(8)	O22	N8	O5	123.6(17)
O9	Eu01	O4[2]	77.3(7)	O22	N8	O6	118.5(17)
O9	Eu01	O5	73.0(8)	O3	C8	C2	123(2)
O9	Eu01	O6	122.4(8)	O3	C8	O12	118(2)
O9	Eu01	O7	144.1(8)	O12	C8	C2	119(2)
O9	Eu01	N7	163.1(8)	C33	O9	Eu01	122(2)
O9	Eu01	O8	157.4(8)	C33	O9	O24	122(3)

Table F5 Bond Angles for EuRu-MOF.

Atom	Atom	Atom	Angle/˚	Atom	Atom	Atom	Angle/˚
O9	Eu01	C29[1]	85.4(8)	O24	O9	Eu01	8.9(9)
C29[1]	Eu01	N7	101.9(6)	C10	C9	C4	169(2)
O24	Eu01	O1[1]	92.0(17)	C33	N9	C34	120(3)
O24	Eu01	O2[1]	87.8(16)	C33	N9	C35	116(2)
O24	Eu01	O3	98.9(16)	C34	N9	C35	123(3)
O24	Eu01	O4[2]	70.7(16)	C9	C10	C11	171(3)
O24	Eu01	O5	57.3(16)	O16	N10	Eu02	59.7(14)
O24	Eu01	O6	106.2(16)	O17	N10	Eu02	58.6(13)
O24	Eu01	O7	142.4(16)	O17	N10	O16	114(2)
O24	Eu01	N7	167.6(16)	O17	N10	O20	119(2)
O24	Eu01	O8	167.4(16)	O20	N10	Eu02	161.9(17)
O24	Eu01	O9	16.4(17)	O20	N10	O16	126(2)
O24	Eu01	C29[1]	90.6(16)	C7	O10	Eu02[6]	96.6(18)
N1	Ru01	N2	78.0(7)	C10	C11	C14	122(2)
N1	Ru01	N3	96.2(7)	C12	C11	C10	121(2)
N1	Ru01	N4	87.9(6)	C12	C11	C14	117(2)
N1	Ru01	N5	172.9(7)	O14	N11	Eu02	61.7(14)
N1	Ru01	N6	99.3(7)	O15	N11	Eu02	58.1(13)
N3	Ru01	N2	172.9(7)	O15	N11	O14	119(2)
N3	Ru01	N4	78.7(7)	O15	N11	O19	121(2)
N3	Ru01	N5	90.9(7)	O19	N11	Eu02	170.2(18)
N4	Ru01	N2	96.7(7)	O19	N11	O14	120(2)
N5	Ru01	N2	95.0(7)	C7	O11	Eu02[6]	97.3(18)
N5	Ru01	N4	93.9(6)	C8	O12	Eu02	175.9(16)
N6	Ru01	N2	92.4(7)	C13	C12	C11	119(2)
N6	Ru01	N3	92.6(7)	C12	C13	C15	122(2)
N6	Ru01	N4	169.4(6)	C32	O13	Eu02[5]	151.0(18)
N6	Ru01	N5	80.0(7)	N11	O14	Eu02	93.0(15)
C14	N1	Ru01	125.3(16)	N1	C14	C11	124(2)
C15	N1	Ru01	119.0(14)	N11	O15	Eu02	96.9(15)
C15	N1	C14	115.5(19)	N1	C15	C13	123(2)
C29	O1	Eu01[3]	91.8(12)	N1	C15	C16	114(2)
C6	C1	C2	115(2)	C13	C15	C16	123(2)
C16	N2	Ru01	114.4(15)	N2	C16	C15	114(2)
C20	N2	Ru01	126.3(14)	C17	C16	N2	121(2)
C20	N2	C16	119.2(19)	C17	C16	C15	126(2)
N10	Eu02	C7[4]	89.0(7)	N10	O16	Eu02	95.0(16)
O10[4]	Eu02	C7[4]	25.0(7)	N10	O16	O25	168(4)
O10[4]	Eu02	N10	114.0(6)	O25	O16	Eu02	77(3)
O10[4]	Eu02	O14	118.9(7)	N10	O17	Eu02	96.6(15)
O10[4]	Eu02	O16	111.7(8)	C16	C17	C18	119(2)
O10[4]	Eu02	O25	107.9(15)	C19	C18	C17	119(2)
O11[4]	Eu02	C7[4]	26.1(7)	C18	C19	C21	121(2)
O11[4]	Eu02	N10	62.9(7)	C20	C19	C18	121(2)
O11[4]	Eu02	O10[4]	51.0(7)	C20	C19	C21	118(2)
O11[4]	Eu02	O14	115.9(7)	C19	C20	N2	120.7(19)
O11[4]	Eu02	O15	70.6(8)	C22	C21	C19	177(2)
O11[4]	Eu02	O16	66.0(8)	C21	C22	C23	178(2)

Table F5 Bond Angles for EuRu-MOF.

Atom	Atom	Atom	Angle/˚	Atom	Atom	Atom	Angle/˚
O11[4]	Eu02	O17	74.3(8)	C22	C23	C28	122.8(19)
O11[4]	Eu02	O25	80.2(15)	C24	C23	C22	119.4(19)
O12	Eu02	C7[4]	162.7(8)	C24	C23	C28	117.8(19)
O12	Eu02	N10	89.3(6)	C23	C24	C25	121(2)
O12	Eu02	O10[4]	151.9(6)	C24	C25	C32	121(2)
O12	Eu02	O11[4]	148.4(7)	C26	C25	C24	118(2)
O12	Eu02	O14	75.2(7)	C26	C25	C32	121(2)
O12	Eu02	O15	125.4(7)	C27	C26	C25	122(2)
O12	Eu02	O16	82.4(8)	C26	C27	C28	120(2)
O12	Eu02	O17	86.6(7)	C26	C27	C29	123(2)
O12	Eu02	O25	71.3(15)	C28	C27	C29	117(2)
O13[2]	Eu02	C7[4]	97.5(8)	C27	C28	C23	121.0(19)
O13[2]	Eu02	N10	166.0(7)	O1	C29	Eu01[3]	61.6(11)
O13[2]	Eu02	O10[4]	72.9(7)	O1	C29	C27	122(2)
O13[2]	Eu02	O11[4]	122.5(7)	O2	C29	Eu01[3]	61.0(10)
O13[2]	Eu02	O12	88.1(6)	O2	C29	O1	122.5(19)
O13[2]	Eu02	O14	78.0(8)	O2	C29	C27	115(2)
O13[2]	Eu02	O15	84.2(8)	C27	C29	Eu01[3]	175.4(18)
O13[2]	Eu02	O16	165.8(8)	N4	C30	C37	121.3(16)
O13[2]	Eu02	O17	141.2(8)	O4	C32	O13	121(2)
O13[2]	Eu02	O25	135.4(15)	O4	C32	C25	117(2)
O14	Eu02	C7[4]	121.9(8)	O13	C32	C25	122(2)
O14	Eu02	N10	88.1(7)	O9	C33	Eu01	38.6(16)
O14	Eu02	O25	129.9(15)	O9	C33	N9	121(3)
O15	Eu02	C7[4]	71.7(9)	N9	C33	Eu01	141(2)
O15	Eu02	N10	86.1(7)	C38	C37	C30	118.6(15)
O15	Eu02	O10[4]	74.1(8)	C37	C38	C39	120.4(15)
O15	Eu02	O14	50.2(7)	C38	C39	C40	118.6(14)
O15	Eu02	O16	109.9(8)	N4	C40	C39	120.7(13)
O15	Eu02	O25	140.0(15)	N4	C40	C41	114.9(15)
O16	Eu02	C7[4]	88.8(9)	C39	C40	C41	124.4(15)
O16	Eu02	N10	25.3(4)	N3	C41	C40	115.4(15)
O16	Eu02	O14	109.6(8)	N3	C41	C42	121.0(14)
O16	Eu02	O25	30.8(14)	C42	C41	C40	123.6(15)
O17	Eu02	C7[4]	98.9(8)	C43	C42	C41	118.0(14)
O17	Eu02	N10	24.9(4)	C44	C43	C42	121.1(15)
O17	Eu02	O10[4]	121.2(7)	C43	C44	C45	118.5(16)
O17	Eu02	O14	63.5(8)	N3	C45	C44	121.1(16)
O17	Eu02	O15	68.1(8)	N6	C46	C47	122.6(15)
O17	Eu02	O16	49.1(7)	C48	C47	C46	118.9(15)
O17	Eu02	O25	78.2(15)	C47	C48	C49	118.7(15)
O23	Eu02	C7[4]	81.4(8)	C48	C49	C50	120.4(13)
O23	Eu02	N10	96.9(7)	N6	C50	C49	120.5(13)
O23	Eu02	O10[4]	80.1(7)	N6	C50	C51	114.7(14)
O23	Eu02	O11[4]	86.7(7)	C49	C50	C51	123.2(14)
O23	Eu02	O12	81.7(7)	N5	C51	C50	114.3(14)
O23	Eu02	O13[2]	96.4(7)	N5	C51	C52	121.5(13)
O23	Eu02	O14	156.4(7)	C52	C51	C50	122.6(15)

Table F5 Bond Angles for EuRu-MOF.

Atom	Atom	Atom	Angle/˚	Atom	Atom	Atom	Angle/˚
O23	Eu02	O15	152.9(8)	C53	C52	C51	118.1(14)
O23	Eu02	O16	71.8(8)	C54	C53	C52	120.2(14)
O23	Eu02	O17	120.8(8)	C53	C54	C55	118.6(14)
O23	Eu02	O25	43.0(15)	N5	C55	C54	121.8(15)
O25	Eu02	C7[4]	93.6(15)	Eu01	O24	O9	155(3)
O25	Eu02	N10	55.9(14)	O16	O25	Eu02	72(3)

[1]1+X,1+Y,-1+Z; [2]+X,1+Y,-1+Z; [3]-1+X,-1+Y,1+Z; [4]-1+X,+Y,+Z; [5]+X,-1+Y,1+Z; [6]1+X,+Y,+Z

Table F6 Torsion Angles for EuRu-MOF.

A	B	C	D	Angle/˚	A	B	C	D	Angle/˚
Eu01[1]	O1	C29	O2	3(3)	C12	C13	C15	N1	-4(4)
Eu01[1]	O1	C29	C27	176(2)	C12	C13	C15	C16	173(2)
Eu01[1]	O2	C29	O1	-3(3)	C13	C15	C16	N2	-178(2)
Eu01[1]	O2	C29	C27	-176.7(19)	C13	C15	C16	C17	1(4)
Eu01	O3	C8	C2	153(3)	O14	N11	O15	Eu02	-7(2)
Eu01	O3	C8	O12	-32(6)	C14	N1	C15	C13	2(3)
Eu01[2]	O4	C32	O13	-83(6)	C14	N1	C15	C16	-175.4(19)
Eu01[2]	O4	C32	C25	105(5)	C14	C11	C12	C13	-2(4)
Eu01	O5	N8	O6	-10.4(16)	O15	N11	O14	Eu02	7(2)
Eu01	O5	N8	O22	168.0(15)	C15	N1	C14	C11	-1(3)
Eu01	O6	N8	O5	10.8(17)	C15	C16	C17	C18	-173(2)
Eu01	O6	N8	O22	-167.6(14)	C16	N2	C20	C19	3(3)
Eu01	O7	N7	O8	0(2)	C16	C17	C18	C19	0(4)
Eu01	O7	N7	O21	-179(2)	O16	N10	O17	Eu02	-22(2)
Eu01	O9	C33	N9	134(3)	O17	N10	O16	Eu02	22(2)
Ru01	N1	C14	C11	174.4(17)	O17	N10	O16	O25	-29(18)
Ru01	N1	C15	C13	-173.4(18)	C17	C18	C19	C20	-5(4)
Ru01	N1	C15	C16	9(3)	C17	C18	C19	C21	176(2)
Ru01	N2	C16	C15	-7(2)	C18	C19	C20	N2	4(4)
Ru01	N2	C16	C17	173.5(19)	O19	N11	O14	Eu02	-169(2)
Ru01	N2	C20	C19	-178.7(17)	O19	N11	O15	Eu02	169(2)
Ru01	N3	C41	C40	-8(3)	O20	N10	O16	Eu02	-159(2)
Ru01	N3	C41	C42	174(2)	O20	N10	O16	O25	150(17)
Ru01	N3	C45	C44	-174(2)	O20	N10	O17	Eu02	159(2)
Ru01	N4	C30	C37	174(2)	C20	N2	C16	C15	172(2)
Ru01	N4	C40	C39	-176(3)	C20	N2	C16	C17	-8(3)
Ru01	N4	C40	C41	2(3)	C21	C19	C20	N2	-178(2)
Ru01	N5	C51	C50	1(3)	O21	N7	O8	Eu01	179(2)
Ru01	N5	C51	C52	167(2)	C22	C23	C24	C25	179(2)
Ru01	N5	C55	C54	-174.7(19)	C22	C23	C28	C27	179(2)
Ru01	N6	C46	C47	-177(3)	C23	C24	C25	C26	4(4)
Ru01	N6	C50	C49	176(3)	C23	C24	C25	C32	-175(2)
Ru01	N6	C50	C51	10(3)	C24	C23	C28	C27	0(4)
N1	C15	C16	N2	-1(3)	C24	C25	C26	C27	-3(4)
N1	C15	C16	C17	178(2)	C24	C25	C32	O4	2(4)
O1[3]	Eu01	O24	O9	98(6)	C24	C25	C32	O13	-170(3)
C1	C2	C3	C4	6(4)	C25	C26	C27	C28	0(4)
C1	C2	C8	O3	-12(4)	C25	C26	C27	C29	-179(2)
C1	C2	C8	O12	173(2)	C26	C25	C32	O4	-176(2)

Table F6 Torsion Angles for EuRu-MOF.

A	B	C	D	Angle/°	A	B	C	D	Angle/°
C1	C6	C7	O10	0(5)	C26	C25	C32	O13	11(4)
C1	C6	C7	O11	-165(3)	C26	C27	C28	C23	1(4)
N2	C16	C17	C18	6(4)	C26	C27	C29	O1	179(2)
Eu02	N10	O16	O25	-51(17)	C26	C27	C29	O2	-7(4)
Eu02[2]	O13	C32	O4	45(5)	C28	C23	C24	C25	-3(4)
Eu02[2]	O13	C32	C25	-143(3)	C28	C27	C29	O1	0(4)
O2[3]	Eu01	O24	O9	45(6)	C28	C27	C29	O2	174(2)
C2	C1	C6	C5	-2(5)	C29[3]	Eu01	O24	O9	72(6)
C2	C1	C6	C7	176(3)	C29	C27	C28	C23	180(2)
C2	C3	C4	C5	-7(3)	C30	N4	C40	C39	0(4)
C2	C3	C4	C9	177(2)	C30	N4	C40	C41	178.2(18)
C3	C2	C8	O3	170(3)	C30	C37	C38	C39	-8(6)
C3	C2	C8	O12	-4(4)	C32	C25	C26	C27	176(2)
C3	C4	C5	C6	4(4)	C33	O9	O24	Eu01	95(6)
C3	C4	C9	C10	-21(15)	C34	N9	C33	Eu01	-129(3)
N3	C41	C42	C43	1(4)	C34	N9	C33	O9	-174(3)
O3	Eu01	O24	O9	-27(6)	C35	N9	C33	Eu01	46(4)
C4	C5	C6	C1	1(5)	C35	N9	C33	O9	1(3)
C4	C5	C6	C7	-177(3)	C37	C38	C39	C40	7(6)
O4[4]	Eu01	O24	O9	-111(6)	C38	C39	C40	N4	-3(5)
N4	C30	C37	C38	4(5)	C38	C39	C40	C41	179(3)
N4	C40	C41	N3	4(4)	C39	C40	C41	N3	-178(3)
N4	C40	C41	C42	-178(2)	C39	C40	C41	C42	0(5)
O5	Eu01	O24	O9	161(7)	C40	N4	C30	C37	-1(3)
N5	C51	C52	C53	16(5)	C40	C41	C42	C43	-177(3)
C5	C4	C9	C10	163(13)	C41	N3	C45	C44	3(4)
C5	C6	C7	O10	178(3)	C41	C42	C43	C44	2(5)
C5	C6	C7	O11	13(5)	C42	C43	C44	C45	-3(5)
O6	Eu01	O24	O9	171(5)	C43	C44	C45	N3	0(4)
N6	C46	C47	C48	-7(5)	C45	N3	C41	C40	174(2)
N6	C50	C51	N5	-7(4)	C45	N3	C41	C42	-4(4)
N6	C50	C51	C52	-173(3)	C46	N6	C50	C49	-11(4)
C6	C1	C2	C3	-1(4)	C46	N6	C50	C51	-176.7(19)
C6	C1	C2	C8	-179(3)	C46	C47	C48	C49	3(6)
C6	C7	O10	Eu02[5]	-171(3)	C47	C48	C49	C50	-4(7)
C6	C7	O11	Eu02[5]	172(3)	C48	C49	C50	N6	8(6)
O7	Eu01	O24	O9	-107(6)	C48	C49	C50	C51	173(4)
O7	N7	O8	Eu01	0(2)	C49	C50	C51	N5	-172(3)
N7	Eu01	O24	O9	-110(8)	C49	C50	C51	C52	22(5)
O8	Eu01	O24	O9	78(10)	C50	N6	C46	C47	10(3)
C8	C2	C3	C4	-176(2)	C50	C51	C52	C53	-179(3)
C9	C4	C5	C6	179(3)	C51	N5	C55	C54	3(4)
C10	C11	C12	C13	177(2)	C51	C52	C53	C54	-12(5)
C10	C11	C14	N1	-178(2)	C52	C53	C54	C55	4(5)
N10	O16	O25	Eu02	52(18)	C53	C54	C55	N5	0(4)
O10	C7	O11	Eu02[5]	5(3)	C55	N5	C51	C50	-177(2)
C11	C12	C13	C15	4(4)	C55	N5	C51	C52	-11(4)
O11	C7	O10	Eu02[5]	-5(3)	O24	O9	C33	Eu01	-10.5(12)

Table F6 Torsion Angles for EuRu-MOF.

A	B	C	D	Angle/°	A	B	C	D	Angle/°
C12	C11	C14	N1	1(3)	O24	O9	C33	N9	124(3)

[1]-1+X,-1+Y,1+Z; [2]+X,-1+Y,1+Z; [3]1+X,1+Y,-1+Z; [4]+X,1+Y,-1+Z; [5]1+X,+Y,+Z

Table F7 Hydrogen Atom Coordinates (Å×10^4) and Isotropic Displacement Parameters (Å^2×10^3) for EuRu-MOF.

Atom	*x*	*y*	*z*	U(eq)
H1	11158.63	10222.13	3299.12	98
H3	8493.04	8885.36	4468.73	78
H5	12058.67	8519.98	5070.89	95
H12	7062.07	8235.02	6551.12	105
H13	5764.38	7328.21	7224.91	82
H14	9474.41	5898.44	6530.96	89
H17	4665.28	6448.16	7973.39	94
H18	3783.01	5459.31	8893.94	90
H20	6551.07	3474.1	8676.61	68
H24	5743.12	2135.09	10785.91	81
H26	3139.2	982.96	12075.94	78
H28	2135.06	2939.3	10494.5	83
H30	5597.13	4080.46	6807.98	142
H37	4713.69	3950.62	5683.93	159
H38	6000.63	3582.03	4708.52	162
H39	8114.96	3727.79	4791.26	155
H42	10101.21	3798.98	4990.56	138
H43	12155.36	3819.99	5329.6	141
H44	12666.76	3862.45	6540.59	142
H45	11089.91	4017.37	7400.17	119
H46	9593.44	5725.5	8191.95	124
H47	11011.75	5681.98	9117.33	160
H48	11379.01	4269.8	9853.35	180
H49	10534.25	2891.56	9525.5	167
H52	9309.08	1748.61	9294.01	134
H53	8682.31	437.97	8724.09	140
H54	7582.48	702.31	7649.74	126
H55	7434.12	2225.95	7065.63	120

Table F8 Atomic Occupancy for EuRu-MOF.

Atom	*Occupancy*	Atom	*Occupancy*	Atom	*Occupancy*
O7	0.75	N7	0.75	O8	0.75
O9	0.5	N9	0.75	O16	0.75
O21	0.75	C33	0.75	C34	0.75
C35	0.75	O23	0.75	O24	0.5
O25	0.25				

Experimental

Single crystals of $C_{40}H_{40}N_6O_{10}RuEu$ **[EuRu-MOF]** were synthesised **(Chapter 4&6)**. A suitable crystal was selected and measured on a **Bruker APEX-II CCD** diffractometer. The crystal was kept at 100.00 K during data collection. Using Olex2 [1], the structure was solved with the shelXT [2] structure solution program using Intrinsic Phasing and refined with the XL [3] refinement package using Least Squares minimisation.

Dolomanov, O.V., Bourhis, L.J., Gildea, R.J, Howard, J.A.K. & Puschmann, H. (2009), J. Appl. Cryst. 42, 339-341.
Bourhis, L.J., Dolomanov, O.V., Gildea, R.J., Howard, J.A.K., Puschmann, H. (2015). Acta Cryst. A71, 59-75.
Sheldrick, G.M. (2008). Acta Cryst. A64, 112-122.

Crystal structure determination of [EuRu-MOF]

Crystal Data for $C_{40}H_{40}N_6O_{10}RuEu$ (*M* =1017.81 g/mol): triclinic, space group P-1 (no. 2), *a* = 10.9203(7) Å, *b* = 14.1292(11) Å, *c* = 18.5786(15) Å, *α* = 85.999(5)°, *β* = 89.191(5)°, *γ* = 85.479(5)°, *V* = 2850.6(4) Å^3, *Z* = 4, *T* = 100.00 K, μ(CuKα) = 20.655 mm^{-1}, *Dcalc* = 2.372 g/cm^3, 27215 reflections measured (7.628° ≤ 2Θ ≤ 101.34°), 5952 unique (R_{int} = 0.1455, R_{sigma} = 0.1164) which were used in all calculations. The final R_1 was 0.0960 (I > 2σ(I)) and wR_2 was 0.2847 (all data).

Refinement model description

Number of restraints - 811, number of constraints - unknown.

Details:

1. Fixed Uiso

At 1.2 times of:

All C(H) groups

2. Restrained distances

N4-C30 = N3-C41 = N3-C45

1.34 with sigma of 0.02

N4-C40

1.35 with sigma of 0.02

C30-C37 = C37-C38 = C38-C39 = C39-C40 = C42-C43 = C43-C44 = C44-C45

1.39 with sigma of 0.02

C40-C41

1.48 with sigma of 0.02

C41-C42

1.4 with sigma of 0.02

N5-C55 = N6-C50 = N6-C46

1.34 with sigma of 0.02

N5-C51

1.35 with sigma of 0.02

C55-C54 = C54-C53 = C53-C52 = C52-C51 = C49-C48 = C48-C47 = C47-C46

1.39 with sigma of 0.02

C51-C50

1.48 with sigma of 0.02

C50-C49

1.4 with sigma of 0.02

N11-O19 = N11-O14

1.25 with sigma of 0.02

N11-O15

1.24 with sigma of 0.02

N10-O20 = N10-O17

1.25 with sigma of 0.02

N10-O16

1.24 with sigma of 0.02

N8-O5 = N8-O6

1.25 with sigma of 0.02

N8-O22

1.24 with sigma of 0.02

N7-O8 = N7-O7

1.25 with sigma of 0.02

N7-O21

1.24 with sigma of 0.02

C33-O9

1.22 with sigma of 0.02

C33-N9

1.36 with sigma of 0.02

N9-C35

1.45 with sigma of 0.02

N9-C34

1.46 with sigma of 0.02

N4-C37 = N4-C39 = N3-C42 = N3-C44 = C38-C40 = C41-C43

2.4 with sigma of 0.04

N4-C41 = N3-C40 = C30-C38 = C37-C39 = C42-C44 = C43-C45

2.39 with sigma of 0.04

C39-C41

2.52 with sigma of 0.04

C40-C42

2.53 with sigma of 0.04

N5-C54 = N5-C52 = N6-C49 = N6-C47 = C53-C51 = C50-C48

2.4 with sigma of 0.04

N5-C50 = N6-C51 = C55-C53 = C54-C52 = C49-C47 = C48-C46

2.39 with sigma of 0.04

C52-C50

2.52 with sigma of 0.04

C51-C49

2.53 with sigma of 0.04

C33-C35

2.46 with sigma of 0.04

C33-C34

2.45 with sigma of 0.04

N4-C30 ≈ N4-C40 ≈ N3-C41 ≈ N3-C45

with sigma of 0.02

C37-C38 ≈ C38-C39 ≈ C39-C40 ≈ C41-C42 ≈ C42-C43 ≈ C43-C44

≈ C44-C45

with sigma of 0.02

N4-C39 ≈ N4-C37 ≈ N3-C42 ≈ N3-C44

with sigma of 0.04

C30-C40 ≈ C30-C38 ≈ C37-C39 ≈ C38-C40 ≈ C41-C45 ≈ C41-C43

≈ C42-C44

with sigma of 0.04

N5-C55 ≈ N5-C51 ≈ N6-C50 ≈ N6-C46

with sigma of 0.02

C54-C53 ≈ C53-C52 ≈ C52-C51 ≈ C50-C49 ≈ C49-C48 ≈ C48-C47

≈ C47-C46

with sigma of 0.02

N5-C52 ≈ N5-C54 ≈ N6-C49 ≈ N6-C47

with sigma of 0.04

C55-C51 ≈ C55-C53 ≈ C54-C52 ≈ C53-C51 ≈ C50-C46 ≈ C50-C48

≈ C49-C47

with sigma of 0.04

N11-O19 ≈ N11-O15 ≈ N11-O14

with sigma of 0.02

O19-O15 ≈ O15-O14 ≈ O14-O19

with sigma of 0.04

N10-O20 ≈ N10-O16 ≈ N10-O17

with sigma of 0.02

O20-O16 ≈ O16-O17 ≈ O17-O20

with sigma of 0.04

N8-O5 ≈ N8-O22 ≈ N8-O6

with sigma of 0.02

O5-O22 ≈ O22-O6 ≈ O6-O5

with sigma of 0.04

N7-O8 ≈ N7-O21 ≈ N7-O7

with sigma of 0.02

O8-O21 ≈ O21-O7 ≈ O7-O8

with sigma of 0.04

N9-C35 ≈ N9-C34

with sigma of 0.02

3. Restrained planarity

N3, N4, C30, C37, C38, C39, C40, C41, C42, C43, C44, C45

with sigma of 0.1

N5, N6, C46, C47, C48, C49, C50, C51, C52, C53, C54, C55

with sigma of 0.1

N11, O14, O15, O19

with sigma of 0.1

N10, O16, O17, O20

with sigma of 0.1

O5, O6, N8, O22

with sigma of 0.1

O7, N7, O8, O21

with sigma of 0.1
O9, N9, C33, C34, C35
with sigma of 0.1
4. Uiso/Uaniso restraints and constraints
N3 ≈ N4 ≈ C30 ≈ C37 ≈ C38 ≈ C39 ≈ C40 ≈ C41 ≈ C42 ≈ C43 ≈ C44 ≈ C45: within 2A with sigma of 0.04 and sigma for terminal atoms of 0.08 within 2A
N5 ≈ N6 ≈ C46 ≈ C47 ≈ C48 ≈ C49 ≈ C50 ≈ C51 ≈ C52 ≈ C53 ≈ C54 ≈ C55: within 2A with sigma of 0.04 and sigma for terminal atoms of 0.08 within 2A
N11 ≈ O14 ≈ O15 ≈ O19: within 2A with sigma of 0.04 and sigma for terminal atoms of 0.08 within 2A
N10 ≈ O16 ≈ O17 ≈ O20: within 2A with sigma of 0.04 and sigma for terminal atoms of 0.08 within 2A
O5 ≈ O6 ≈ N8 ≈ O22: within 2A with sigma of 0.04 and sigma for terminal atoms of 0.08 within 2A
O7 ≈ N7 ≈ O8 ≈ O21: within 2A with sigma of 0.04 and sigma for terminal atoms of 0.08 within 2A
O9 ≈ N9 ≈ C33 ≈ C34 ≈ C35: within 2A with sigma of 0.04 and sigma for terminal atoms of 0.08 within 2A
Uanis(O4) ≈ Ueq, Uanis(C32) ≈ Ueq, Uanis(O13) ≈ Ueq, Uanis(C7) ≈ Ueq, Uanis(O10) ≈ Ueq, Uanis(O11) ≈ Ueq: with sigma of 0.01 and sigma for terminal atoms of 0.02
Uanis(O9) ≈ Ueq: with sigma of 0.01 and sigma for terminal atoms of 0.02
Uanis(O3) ≈ Ueq, Uanis(C8) ≈ Ueq, Uanis(O12) ≈ Ueq: with sigma of 0.01 and sigma for terminal atoms of 0.02
5. Rigid body (RIGU) restrains
N3, N4, C30, C37, C38, C39, C40, C41, C42, C43, C44, C45
with sigma for 1-2 distances of 0.004 and sigma for 1-3 distances of 0.004
N5, N6, C46, C47, C48, C49, C50, C51, C52, C53, C54, C55
with sigma for 1-2 distances of 0.004 and sigma for 1-3 distances of 0.004
N11, O14, O15, O19
with sigma for 1-2 distances of 0.004 and sigma for 1-3 distances of 0.004
N10, O16, O17, O20
with sigma for 1-2 distances of 0.004 and sigma for 1-3 distances of 0.004
O5, O6, N8, O22
with sigma for 1-2 distances of 0.004 and sigma for 1-3 distances of 0.004
O7, N7, O8, O21
with sigma for 1-2 distances of 0.004 and sigma for 1-3 distances of 0.004
O9, N9, C33, C34, C35
with sigma for 1-2 distances of 0.004 and sigma for 1-3 distances of 0.004
6. Others
Fixed Sof: O7(0.75) N7(0.75) O8(0.75) O9(0.5) N9(0.75) O16(0.75) O21(0.75) C33(0.75) C34(0.75) C35(0.75) O23(0.75) O24(0.5) O25(0.25)
7.a Aromatic/amide H refined with riding coordinates:
C1(H1), C3(H3), C5(H5), C12(H12), C13(H13), C14(H14), C17(H17), C18(H18), C20(H20), C24(H24), C26(H26), C28(H28), C30(H30), C37(H37), C38(H38), C39(H39), C42(H42), C43(H43), C44(H44), C45(H45), C46(H46), C47(H47), C48(H48), C49(H49), C52(H52), C53(H53), C54(H54), C55(H55)
This report has been created with Olex2, compiled on 2025.07.13 svn.rb7424aed for OlexSys.

Appendix G: Crystallographic Information for GdRu-MOF

Table G1 Crystal data and structure refinement for GdRu-MOF.

Identification code	GdRu-MOF
Empirical formula	$C_{26.12}H_{14}Gd_{0.88}N_{5.12}O_{10.62}Ru_{0.5}$
Formula weight	757.80
Temperature/K	100.00
Crystal system	triclinic
Space group	P-1
a/Å	10.9309(5)
b/Å	14.1579(11)
c/Å	18.4702(15)
α/°	86.791(6)
β/°	88.443(5)
γ/°	85.495(5)
Volume/Å^3	2844.4(3)
Z	4
ρ_{calc}g/cm^3	1.770
μ/mm^{-1}	15.905
F(000)	1478.0
Crystal size/mm^3	0.102 × 0.081 × 0.03
Radiation	CuKα (λ = 1.54178)
2Θ range for data collection/°	4.792 to 116.028
Index ranges	-12 ≤ h ≤ 12, -15 ≤ k ≤ 15, -20 ≤ l ≤ 20
Reflections collected	26129
Independent reflections	7872 [R_{int} = 0.1143, R_{sigma} = 0.1331]
Data/restraints/parameters	7872/967/811
Goodness-of-fit on F^2	1.026
Final R indexes [I>=2σ (I)]	R_1 = 0.1033, wR_2 = 0.2748
Final R indexes [all data]	R_1 = 0.1605, wR_2 = 0.3225
Largest diff. peak/hole / e Å^{-3}	1.81/-0.69

Table G2 Fractional Atomic Coordinates (×10^4) and Equivalent Isotropic Displacement Parameters (Å^2×10^3) for GdRu-MOF Final. U_{eq} is defined as 1/3 of the trace of the orthogonalised U_{IJ} tensor.

Atom	*x*	*y*	*z*	U(eq)
Gd1	8585.9(9)	11621.5(9)	1843.7(7)	77.5(5)
Gd2	5488.9(16)	9494.0(18)	3523.9(14)	93.3(7)
Ru1	8247.8(14)	4269.0(11)	7407.9(9)	76.3(5)
O1	7519(17)	9822(14)	3442(11)	119(5)
O2	8804(15)	10714(12)	2925(9)	107(5)
O3	13273(14)	10026(12)	3440(10)	103(5)
O4	13772(17)	8975(14)	4302(11)	126(6)
O5	9140(15)	12989(13)	2568(10)	116(5)
O6	7295(17)	12584(14)	2746(11)	128(5)
O7	7940(30)	13718(19)	3368(15)	191(10)
O8	7635(16)	13379(12)	48(8)	118(5)
O9	7648(11)	13087(8)	1213(7)	75(3)
O10	8037(14)	11944(10)	496(8)	97(4)

Table G2 Fractional Atomic Coordinates (×10^4) and Equivalent Isotropic Displacement Parameters (Å^2×10^3) for GdRu-MOF Final. U_{eq} is defined as 1/3 of the trace of the orthogonalised U_{IJ} tensor.

Atom	*x*	*y*	*z*	U(eq)
O11	8970(20)	10198(18)	1200(15)	126(7)
O12	6060(30)	9125(18)	4877(15)	142(8)
O13	6260(30)	7953(18)	4149(14)	133(7)
O14	5980(40)	7630(20)	5299(16)	190(11)
O15	5397(7)	10125(9)	3869(5)	23(2)
O16	5362(18)	10631(17)	4060(11)	100(6)
O17	6570(20)	8307(17)	2692(14)	122(7)
O18	4680(20)	8162(18)	2900(15)	135(7)
O19	5770(20)	7036(17)	2394(15)	132(8)
O20	281(11)	2372(10)	11162(7)	79(4)
O21	795(11)	1258(10)	12017(7)	78(3)
O22	5250(15)	315(13)	12404(10)	113(5)
O23	6607(12)	1092(10)	11807(8)	87(4)
N1	7378(15)	4006(15)	6456(9)	110(5)
N2	9719(14)	3999(9)	6692(9)	99(5)
N3	8391(11)	2862(10)	7794(7)	88(4)
N4	9365(17)	4359(10)	8248(10)	102(5)
N5	6692(15)	4602(12)	8032(9)	79(5)
N6	7960(15)	5691(13)	7101(9)	83(5)
N7	6110(20)	8245(17)	4780(13)	149(8)
N8	7774(12)	12802(9)	587(7)	81(4)
N9	8126(17)	13113(14)	2896(10)	135(6)
N10	7730(30)	9120(20)	830(20)	174(10)
N11	5677(19)	7818(15)	2666(12)	123(7)
C1	6157(17)	3970(20)	6407(12)	135(8)
C2	5644(19)	3870(30)	5737(12)	148(9)
C3	6400(20)	3790(30)	5118(12)	153(9)
C4	7660(20)	3800(20)	5186(10)	138(8)
C5	8147(15)	3900(20)	5869(10)	124(6)
C6	9457(15)	3940(20)	5989(10)	120(6)
C7	10380(20)	3850(20)	5457(11)	144(8)
C8	11590(20)	3810(30)	5676(13)	159(10)
C9	11848(17)	3800(30)	6408(14)	152(9)
C10	10891(15)	4008(15)	6908(11)	118(7)
C11	7867(17)	2123(12)	7537(10)	101(6)
C12	7960(20)	1224(12)	7862(11)	101(6)
C13	8550(20)	1092(13)	8514(13)	119(7)
C14	9090(20)	1830(12)	8789(12)	116(7)
C15	9050(20)	2696(10)	8402(10)	96(5)
C16	9600(20)	3546(11)	8656(12)	112(6)
C17	10400(30)	3516(15)	9230(16)	153(10)
C18	10960(30)	4319(16)	9382(19)	168(11)
C19	10650(30)	5159(15)	8998(15)	136(9)
C20	9840(20)	5148(13)	8439(13)	113(7)
C21	8683(19)	6223(14)	6684(11)	78(5)
C22	8406(18)	7170(17)	6443(11)	82(6)
C23	7220(20)	7542(18)	6668(13)	104(8)
C24	6430(20)	6993(17)	7104(12)	92(7)

Table G2 Fractional Atomic Coordinates (×10^4) and Equivalent Isotropic Displacement Parameters (Å^2×10^3) for GdRu-MOF Final. U_{eq} is defined as 1/3 of the trace of the orthogonalised U_{IJ} tensor.

Atom	*x*	*y*	*z*	U(eq)
C25	6860(20)	6078(14)	7333(11)	76(5)
C26	6130(20)	5506(15)	7856(10)	79(6)
C27	4997(19)	5800(15)	8152(13)	87(6)
C28	4477(19)	5217(15)	8691(12)	88(7)
C29	5105(16)	4373(15)	8898(11)	75(6)
C30	6179(17)	4073(16)	8540(11)	80(6)
C31	4644(17)	3805(15)	9490(12)	82(6)
C32	4307(18)	3262(16)	9974(12)	80(6)
C33	3959(15)	2641(13)	10582(11)	68(5)
C34	2750(18)	2565(15)	10760(11)	79(6)
C35	2404(15)	1937(15)	11331(10)	74(5)
C36	3325(16)	1406(15)	11716(12)	79(6)
C37	4546(15)	1480(15)	11539(12)	77(6)
C38	4832(16)	2100(15)	10967(12)	78(6)
C39	1069(16)	1867(13)	11523(10)	68(5)
C40	5487(17)	933(14)	11948(11)	76(5)
C41	9138(18)	7658(15)	5949(11)	80(6)
C42	9635(19)	8050(17)	5527(14)	91(7)
C43	10096(18)	8640(13)	4890(11)	75(5)
C44	9233(19)	9087(15)	4432(13)	88(6)
C45	9517(19)	9666(16)	3836(12)	91(7)
C46	10747(16)	9795(15)	3697(11)	77(6)
C47	11674(16)	9366(14)	4123(11)	76(5)
C48	11345(18)	8798(15)	4729(13)	89(7)
C49	12970(20)	9443(17)	3930(13)	92(6)
C50	8559(19)	10102(16)	3366(12)	82(6)
C51	6870(40)	8400(30)	930(30)	193(16)
C52	7900(60)	9530(40)	100(20)	196(15)
C53	8310(30)	9540(20)	1370(20)	155(10)

Table G3 Anisotropic Displacement Parameters (Å^2×10^3) for GdRu-MOF Final. The Anisotropic displacement factor exponent takes the form: $-2\pi^2[h^2a^{*2}U_{11}+2hka^*b^*U_{12}+\ldots]$.

Atom	U_{11}	U_{22}	U_{33}	U_{23}	U_{13}	U_{12}
Gd1	43.2(6)	86.6(8)	98.3(9)	40.8(7)	-2.4(5)	-9.0(5)
Gd2	53.8(10)	101.2(15)	120.1(17)	55.0(14)	-9.1(10)	-15.5(10)
Ru1	62.6(9)	82.9(10)	80.7(11)	25.5(8)	3.5(7)	-11.9(7)
O1	99(8)	130(9)	128(9)	32(8)	-14(7)	-22(7)
O2	86(8)	117(8)	113(8)	42(7)	-6(7)	-14(7)
O3	81(7)	110(8)	115(8)	31(7)	0(7)	-18(7)
O4	104(9)	136(9)	132(9)	42(8)	-3(8)	-8(8)
O5	109(7)	119(9)	123(9)	-1(7)	-24(6)	-17(7)
O6	116(8)	138(9)	127(9)	-6(7)	17(7)	-5(7)
O7	213(17)	182(15)	181(15)	-58(12)	-8(13)	5(13)
O8	114(11)	137(10)	100(9)	45(8)	-16(8)	-18(9)
O9	59(6)	72(6)	92(6)	23(5)	-5(5)	-7(5)
O10	91(7)	101(6)	98(8)	-1(6)	-1(6)	-14(6)
O11	114(10)	114(10)	146(11)	-4(8)	0(8)	4(7)
O12	130(11)	153(9)	144(11)	1(8)	-17(9)	-18(8)

Table G3 Anisotropic Displacement Parameters ($Å^2 \times 10^3$) for GdRu-MOF Final. The Anisotropic displacement factor exponent takes the form: $-2\pi^2[h^2a^{*2}U_{11}+2hka^*b^*U_{12}+\ldots]$.

Atom	U_{11}	U_{22}	U_{33}	U_{23}	U_{13}	U_{12}
O13	124(11)	127(10)	145(9)	9(8)	1(8)	-6(8)
O14	210(20)	198(16)	164(14)	32(13)	-15(14)	-26(15)
O15	10(4)	32(6)	21(5)	16(5)	10(3)	19(4)
O16	87(9)	131(10)	84(9)	13(8)	-7(7)	-19(8)
O17	119(9)	126(10)	122(10)	3(8)	-14(8)	-15(7)
O18	127(9)	135(11)	142(11)	-5(9)	-3(8)	-12(8)
O19	123(14)	130(11)	147(16)	-7(11)	-5(12)	-22(10)
O20	58(6)	90(7)	86(7)	35(6)	5(5)	-13(5)
O21	55(6)	92(7)	83(7)	28(6)	-4(5)	-7(5)
O22	88(8)	127(9)	118(9)	35(8)	-5(7)	-9(7)
O23	59(6)	97(7)	104(8)	26(6)	-8(6)	-25(6)
N1	108(10)	113(13)	109(11)	21(11)	-20(8)	-25(11)
N2	85(8)	91(11)	117(10)	21(10)	12(8)	-15(9)
N3	71(10)	91(9)	101(11)	4(8)	6(7)	-6(8)
N4	95(12)	96(9)	114(13)	34(9)	-13(9)	-22(8)
N5	71(10)	78(10)	83(11)	34(9)	-7(8)	-9(8)
N6	70(11)	96(12)	78(11)	41(9)	-10(8)	-5(9)
N7	144(12)	153(10)	151(10)	-1(7)	-8(9)	-13(9)
N8	60(7)	90(6)	90(6)	16(5)	-7(6)	-8(6)
N9	135(9)	136(10)	134(10)	-14(8)	-6(7)	-4(7)
N10	174(13)	173(13)	177(13)	-13(9)	-9(9)	-27(9)
N11	120(9)	127(10)	123(11)	-1(8)	-5(8)	-17(7)
C1	110(11)	180(20)	117(14)	26(16)	-11(11)	-37(15)
C2	106(15)	220(20)	124(14)	32(18)	-24(10)	-38(17)
C3	147(15)	190(20)	119(15)	12(18)	-20(12)	-15(19)
C4	143(14)	160(20)	112(12)	13(16)	-5(11)	-17(17)
C5	132(10)	127(16)	111(11)	23(14)	-5(8)	-18(13)
C6	121(10)	122(16)	112(11)	23(13)	13(8)	-14(13)
C7	150(14)	141(19)	136(15)	6(16)	36(12)	-9(17)
C8	136(13)	170(20)	163(16)	0(20)	45(15)	18(19)
C9	110(13)	170(20)	163(17)	10(20)	46(12)	9(16)
C10	77(10)	135(18)	138(14)	23(15)	21(9)	-16(12)
C11	91(13)	98(10)	114(14)	-10(9)	16(10)	-13(10)
C12	89(14)	89(10)	123(14)	-14(11)	30(10)	-9(10)
C13	111(16)	101(12)	142(16)	9(12)	9(12)	-6(11)
C14	115(16)	92(10)	137(16)	29(10)	-24(13)	1(10)
C15	81(12)	85(8)	120(13)	17(9)	-10(9)	3(8)
C16	99(14)	97(9)	139(15)	39(9)	-32(11)	-26(9)
C17	150(20)	129(15)	181(19)	68(15)	-80(15)	-45(14)
C18	180(20)	131(15)	200(20)	41(15)	-103(18)	-33(14)
C19	136(19)	114(14)	159(19)	26(14)	-58(15)	-29(14)
C20	104(15)	100(11)	135(17)	38(12)	-30(12)	-29(11)
C21	75(13)	71(12)	86(14)	21(11)	7(10)	-10(10)
C22	58(12)	113(17)	74(13)	32(12)	-10(9)	-27(11)
C23	108(19)	103(16)	101(17)	53(14)	-28(14)	-43(15)
C24	77(13)	103(16)	91(15)	34(13)	29(11)	-8(12)
C25	88(15)	64(12)	72(12)	10(10)	-10(10)	3(10)
C26	89(14)	85(14)	62(12)	19(10)	12(10)	-20(11)

Table G3 Anisotropic Displacement Parameters ($Å^2×10^3$) for GdRu-MOF Final. The Anisotropic displacement factor exponent takes the form: $-2\pi^2[h^2a^{*2}U_{11}+2hka^*b^*U_{12}+\ldots]$.

Atom	U_{11}	U_{22}	U_{33}	U_{23}	U_{13}	U_{12}
C27	71(13)	81(14)	106(17)	13(12)	14(12)	5(11)
C28	64(12)	93(14)	100(15)	48(13)	8(10)	-2(11)
C29	45(10)	100(14)	79(12)	41(11)	-7(9)	-18(10)
C30	52(11)	98(14)	88(14)	38(12)	-20(10)	-16(10)
C31	56(11)	90(14)	95(15)	38(13)	3(10)	-9(10)
C32	60(11)	93(14)	86(14)	6(13)	-5(10)	-13(10)
C33	45(10)	77(12)	82(13)	19(10)	13(9)	-16(8)
C34	65(12)	83(13)	85(14)	26(11)	5(10)	-2(10)
C35	43(9)	99(14)	77(12)	40(11)	5(8)	-15(9)
C36	47(10)	94(14)	94(14)	36(11)	-3(9)	-24(9)
C37	39(9)	90(13)	100(15)	33(11)	0(9)	-10(9)
C38	40(9)	93(14)	99(15)	26(12)	-4(9)	-21(9)
C39	55(8)	73(8)	74(8)	22(7)	-1(7)	-14(7)
C40	58(8)	81(9)	88(9)	18(8)	7(7)	-22(7)
C41	67(12)	87(13)	80(13)	50(12)	7(10)	-20(10)
C42	61(12)	104(16)	104(17)	40(14)	6(11)	-13(11)
C43	71(12)	71(12)	79(13)	28(10)	-10(10)	-9(10)
C44	65(12)	90(14)	107(16)	23(13)	7(11)	-12(11)
C45	72(13)	102(15)	94(15)	55(13)	-1(11)	-24(11)
C46	49(10)	95(14)	84(13)	25(11)	11(9)	-14(10)
C47	44(10)	81(12)	96(14)	30(11)	-1(9)	4(9)
C48	61(12)	84(14)	119(18)	33(13)	-17(11)	-2(10)
C49	82(9)	96(10)	94(10)	24(8)	-4(8)	-4(8)
C50	66(8)	93(9)	88(9)	18(8)	8(7)	-23(8)
C51	190(20)	190(20)	200(20)	-14(16)	-14(17)	-45(16)
C52	220(20)	190(20)	175(15)	-13(15)	-1(15)	-22(18)
C53	153(13)	151(12)	162(12)	-5(9)	6(9)	-21(9)

Table G4 Bond Lengths for GdRu-MOF Final.

Atom	Atom	Length/Å	Atom	Atom	Length/Å
Gd1	O2	2.321(15)	N9	O6	1.267(13)
Gd1	O5	2.535(17)	N9	O7	1.258(13)
Gd1	O6	2.540(18)	N10	C51	1.440(16)
Gd1	O9	2.484(11)	N10	C52	1.451(16)
Gd1	O10	2.585(15)	N11	O17	1.249(13)
Gd1	O11	2.40(3)	N11	O18	1.237(14)
Gd1	$O20^1$	2.486(12)	N11	O19	1.237(13)
Gd1	$O21^1$	2.455(12)	C2	C1	1.395(12)
Gd1	$O23^2$	2.348(12)	C3	C2	1.394(12)
Gd1	N8	2.901(12)	C4	C3	1.394(12)
Gd1	N9	2.954(19)	C5	C4	1.399(11)
Gd1	$C39^1$	2.807(18)	C6	C5	1.461(15)
Gd2	O1	2.302(18)	C7	C6	1.392(11)
Gd2	$O3^3$	2.486(16)	C8	C7	1.385(12)
Gd2	$O4^3$	2.465(19)	C9	C8	1.387(12)
Gd2	O12	2.61(3)	C10	C9	1.402(16)
Gd2	O13	2.51(3)	C11	C12	1.375(16)
Gd2	O15	1.122(12)	C12	C13	1.377(12)

Table G4 Bond Lengths for GdRu-MOF Final.

Atom	Atom	Length/Å	Atom	Atom	Length/Å
Gd2	O16	1.93(2)	C13	C14	1.368(12)
Gd2	O17	2.54(2)	C14	C15	1.382(11)
Gd2	O18	2.50(3)	C15	C16	1.489(15)
Gd2	O22[2]	2.326(17)	C16	C17	1.386(11)
Gd2	N7	2.90(2)	C17	C18	1.380(12)
Gd2	C49[3]	2.84(2)	C18	C19	1.373(12)
Ru1	N1	2.087(17)	C19	C20	1.380(12)
Ru1	N2	2.080(16)	C22	C21	1.40(3)
Ru1	N3	2.073(15)	C22	C23	1.42(4)
Ru1	N4	2.016(16)	C22	C41	1.39(3)
Ru1	N5	2.067(17)	C24	C23	1.41(3)
Ru1	N6	2.063(17)	C25	C24	1.39(3)
O1	C50	1.23(2)	C25	C26	1.48(3)
O2	C50	1.20(2)	C26	C27	1.38(3)
O3	C49	1.25(3)	C28	C27	1.39(3)
O4	C49	1.25(3)	C28	C29	1.37(3)
O15	O16	0.814(19)	C30	C29	1.38(3)
O20	C39	1.26(2)	C31	C29	1.42(3)
O21	C39	1.27(2)	C31	C32	1.21(3)
O22	C40	1.22(2)	C33	C32	1.45(3)
O23	C40	1.28(2)	C34	C33	1.36(3)
N1	C1	1.344(12)	C34	C35	1.40(3)
N1	C5	1.362(12)	C36	C35	1.39(3)
N2	C6	1.347(12)	C36	C37	1.38(2)
N2	C10	1.353(12)	C37	C40	1.44(3)
N3	C11	1.347(12)	C38	C33	1.37(3)
N3	C15	1.352(12)	C38	C37	1.38(3)
N4	C16	1.352(12)	C39	C35	1.50(2)
N4	C20	1.337(12)	C41	C42	1.09(3)
N5	C26	1.40(3)	C42	C43	1.50(3)
N5	C30	1.31(2)	C43	C44	1.38(3)
N6	C21	1.33(2)	C43	C48	1.42(3)
N6	C25	1.35(3)	C45	C44	1.38(3)
N7	O12	1.266(14)	C46	C45	1.39(3)
N7	O13	1.260(14)	C46	C47	1.38(3)
N7	O14	1.269(14)	C47	C48	1.40(3)
N8	O8	1.256(11)	C47	C49	1.47(3)
N8	O9	1.248(11)	C50	C45	1.45(3)
N8	O10	1.246(11)	C53	O11	1.246(19)
N9	O5	1.253(13)	C53	N10	1.380(19)

[1]1+X,1+Y,-1+Z; [2]+X,1+Y,-1+Z; [3]-1+X,+Y,+Z

Table G5 Bond Angles for GdRu-MOF Final.

Atom	Atom	Atom	Angle/˚	Atom	Atom	Atom	Angle/˚
O2	Gd1	O5	85.4(6)	N9	O6	Gd1	96.0(11)
O2	Gd1	O6	76.5(7)	N8	O9	Gd1	96.4(8)
O2	Gd1	O9	147.1(6)	N8	O10	Gd1	91.6(9)
O2	Gd1	O10	155.4(6)	C53	O11	Gd1	117(2)
O2	Gd1	O11	88.9(8)	N7	O12	Gd2	90.1(15)

Table G5 Bond Angles for GdRu-MOF Final.

Atom	Atom	Atom	Angle/˚	Atom	Atom	Atom	Angle/˚
O2	Gd1	O20[1]	124.9(5)	N7	O13	Gd2	94.8(15)
O2	Gd1	O21[1]	72.9(5)	O16	O15	Gd2	170.8(19)
O2	Gd1	O23[2]	86.6(5)	O15	O16	Gd2	5.3(11)
O2	Gd1	N8	167.9(5)	N11	O17	Gd2	94.4(14)
O2	Gd1	N9	79.7(6)	N11	O18	Gd2	97.0(15)
O2	Gd1	C39[1]	99.1(5)	C39	O20	Gd1[5]	91.1(10)
O5	Gd1	O6	50.2(5)	C39	O21	Gd1[5]	92.3(10)
O5	Gd1	O10	119.0(5)	C40	O22	Gd2[6]	153.4(17)
O5	Gd1	N8	95.1(5)	C40	O23	Gd1[6]	164.0(15)
O5	Gd1	N9	24.9(3)	C1	N1	Ru1	123.7(14)
O5	Gd1	C39[1]	73.6(6)	C1	N1	C5	121.8(15)
O6	Gd1	O10	116.0(6)	C5	N1	Ru1	114.4(12)
O6	Gd1	N8	94.6(5)	C6	N2	Ru1	117.1(11)
O6	Gd1	N9	25.2(3)	C6	N2	C10	121.2(15)
O6	Gd1	C39[1]	123.7(6)	C10	N2	Ru1	121.1(12)
O9	Gd1	O5	73.8(5)	C11	N3	Ru1	128.3(11)
O9	Gd1	O6	70.6(6)	C11	N3	C15	117.4(14)
O9	Gd1	O10	50.4(4)	C15	N3	Ru1	114.3(10)
O9	Gd1	O20[1]	73.6(4)	C16	N4	Ru1	115.4(11)
O9	Gd1	N8	25.3(3)	C20	N4	Ru1	125.7(11)
O9	Gd1	N9	70.7(5)	C20	N4	C16	118.9(14)
O9	Gd1	C39[1]	99.2(5)	C26	N5	Ru1	113.5(12)
O10	Gd1	N8	25.4(3)	C30	N5	Ru1	128.3(14)
O10	Gd1	N9	121.0(5)	C30	N5	C26	118.1(18)
O10	Gd1	C39[1]	91.2(5)	C21	N6	Ru1	128.0(15)
O11	Gd1	O5	156.0(7)	C21	N6	C25	119.0(18)
O11	Gd1	O6	149.8(8)	C25	N6	Ru1	112.9(13)
O11	Gd1	O9	120.0(7)	O12	N7	Gd2	64.1(14)
O11	Gd1	O10	69.8(7)	O12	N7	O14	122(2)
O11	Gd1	O20[1]	91.2(7)	O13	N7	Gd2	59.5(13)
O11	Gd1	O21[1]	78.3(7)	O13	N7	O12	120.0(19)
O11	Gd1	N8	95.2(7)	O13	N7	O14	117.9(19)
O11	Gd1	N9	168.6(8)	O14	N7	Gd2	159(2)
O11	Gd1	C39[1]	84.2(8)	O8	N8	Gd1	168.2(11)
O20[1]	Gd1	O5	73.2(5)	O9	N8	Gd1	58.3(7)
O20[1]	Gd1	O6	118.9(6)	O9	N8	O8	120.1(13)
O20[1]	Gd1	O10	69.6(5)	O10	N8	Gd1	62.9(8)
O20[1]	Gd1	N8	66.4(4)	O10	N8	O8	120.0(14)
O20[1]	Gd1	N9	96.1(5)	O10	N8	O9	119.9(13)
O20[1]	Gd1	C39[1]	26.6(5)	O5	N9	Gd1	58.5(10)
O21[1]	Gd1	O5	77.7(5)	O5	N9	O6	117.2(16)
O21[1]	Gd1	O6	120.7(6)	O5	N9	O7	121.9(18)
O21[1]	Gd1	O9	125.0(4)	O6	N9	Gd1	58.8(10)
O21[1]	Gd1	O10	112.8(5)	O7	N9	Gd1	177.3(17)
O21[1]	Gd1	O20[1]	53.4(4)	O7	N9	O6	120.8(18)
O21[1]	Gd1	N8	119.0(4)	C51	N10	C52	117(4)
O21[1]	Gd1	N9	99.1(5)	C53	N10	C51	126(3)
O21[1]	Gd1	C39[1]	26.8(5)	C53	N10	C52	116(3)

Table G5 Bond Angles for GdRu-MOF Final.

Atom	Atom	Atom	Angle/˚	Atom	Atom	Atom	Angle/˚
O23^{2}	Gd1	O5	124.4(6)	O17	N11	Gd2	60.4(13)
O23^{2}	Gd1	O6	74.4(6)	O18	N11	Gd2	58.1(13)
O23^{2}	Gd1	O9	84.5(4)	O18	N11	O17	117.2(18)
O23^{2}	Gd1	O10	77.3(5)	O19	N11	Gd2	171.1(18)
O23^{2}	Gd1	O11	78.5(7)	O19	N11	O17	121.5(19)
O23^{2}	Gd1	O20^{1}	146.9(5)	O19	N11	O18	121.2(19)
O23^{2}	Gd1	O21^{1}	149.1(5)	N1	C1	C2	119.9(16)
O23^{2}	Gd1	N8	83.1(4)	C3	C2	C1	120.0(15)
O23^{2}	Gd1	N9	99.6(5)	C4	C3	C2	119.0(15)
O23^{2}	Gd1	C39^{1}	161.7(6)	C3	C4	C5	119.4(13)
N8	Gd1	N9	95.7(5)	N1	C5	C4	119.9(13)
C39^{1}	Gd1	N8	92.7(5)	N1	C5	C6	116.9(14)
C39^{1}	Gd1	N9	98.5(6)	C4	C5	C6	123.2(15)
O1	Gd2	O3^{3}	150.3(6)	N2	C6	C5	113.1(14)
O1	Gd2	O4^{3}	147.4(7)	N2	C6	C7	121.5(13)
O1	Gd2	O12	81.2(8)	C7	C6	C5	125.2(15)
O1	Gd2	O13	85.5(8)	C8	C7	C6	117.8(13)
O1	Gd2	O17	73.0(7)	C7	C8	C9	120.2(14)
O1	Gd2	O18	122.8(7)	C8	C9	C10	119.0(14)
O1	Gd2	O22^{2}	87.0(6)	N2	C10	C9	118.7(15)
O1	Gd2	N7	87.7(7)	N3	C11	C12	123.6(14)
O1	Gd2	C49^{3}	164.3(8)	C11	C12	C13	117.8(13)
O3^{3}	Gd2	O12	110.0(8)	C14	C13	C12	119.8(13)
O3^{3}	Gd2	O13	123.2(7)	C13	C14	C15	119.3(13)
O3^{3}	Gd2	O17	123.2(7)	N3	C15	C14	121.7(12)
O3^{3}	Gd2	O18	78.3(7)	N3	C15	C16	114.4(12)
O3^{3}	Gd2	N7	114.6(6)	C14	C15	C16	123.6(13)
O3^{3}	Gd2	C49^{3}	26.0(6)	N4	C16	C15	115.7(13)
O4^{3}	Gd2	O3^{3}	51.9(5)	N4	C16	C17	120.4(12)
O4^{3}	Gd2	O12	66.2(8)	C17	C16	C15	123.7(13)
O4^{3}	Gd2	O13	74.0(8)	C18	C17	C16	119.8(13)
O4^{3}	Gd2	O17	118.3(7)	C19	C18	C17	119.6(14)
O4^{3}	Gd2	O18	74.5(8)	C18	C19	C20	117.9(14)
O4^{3}	Gd2	N7	63.0(6)	N4	C20	C19	123.2(15)
O4^{3}	Gd2	C49^{3}	26.1(6)	N6	C21	C22	126(2)
O12	Gd2	N7	25.9(4)	C21	C22	C23	113.4(18)
O12	Gd2	C49^{3}	89.3(8)	C41	C22	C21	123(2)
O13	Gd2	O12	50.6(7)	C41	C22	C23	123(2)
O13	Gd2	O17	65.3(8)	C24	C23	C22	122(2)
O13	Gd2	N7	25.7(4)	C25	C24	C23	118(2)
O13	Gd2	C49^{3}	98.0(8)	N6	C25	C24	121.3(19)
O15	Gd2	O1	83.4(7)	N6	C25	C26	118.1(17)
O15	Gd2	O3^{3}	77.2(6)	C24	C25	C26	121(2)
O15	Gd2	O4^{3}	83.2(7)	N5	C26	C25	113.2(18)
O15	Gd2	O12	65.4(7)	C27	C26	N5	121.4(17)
O15	Gd2	O13	116.0(7)	C27	C26	C25	125.4(19)
O15	Gd2	O16	3.8(8)	C26	C27	C28	118.6(19)
O15	Gd2	O17	156.3(7)	C29	C28	C27	118.5(19)

Table G5 Bond Angles for GdRu-MOF Final.

Atom	Atom	Atom	Angle/˚	Atom	Atom	Atom	Angle/˚
O15	Gd2	O18	153.8(7)	C28	C29	C30	120.6(17)
O15	Gd2	O22[2]	97.5(6)	C28	C29	C31	119.5(19)
O15	Gd2	N7	90.9(6)	C30	C29	C31	120.0(18)
O15	Gd2	C49[3]	81.3(7)	N5	C30	C29	122.3(19)
O16	Gd2	O1	81.7(8)	C32	C31	C29	175(2)
O16	Gd2	O3[3]	77.4(7)	C31	C32	C33	176(2)
O16	Gd2	O4[3]	86.3(8)	C34	C33	C32	120.2(17)
O16	Gd2	O12	68.6(8)	C34	C33	C38	119.2(16)
O16	Gd2	O13	119.1(8)	C38	C33	C32	120.5(16)
O16	Gd2	O17	154.1(8)	C33	C34	C35	120.5(18)
O16	Gd2	O18	155.2(8)	C34	C35	C39	119.8(16)
O16	Gd2	O22[2]	93.9(8)	C36	C35	C34	118.4(16)
O16	Gd2	N7	94.3(7)	C36	C35	C39	121.7(15)
O16	Gd2	C49[3]	83.2(8)	C37	C36	C35	121.3(17)
O17	Gd2	O12	112.0(8)	C36	C37	C38	117.8(17)
O17	Gd2	N7	90.5(7)	C36	C37	C40	120.5(17)
O17	Gd2	C49[3]	122.4(7)	C38	C37	C40	121.7(16)
O18	Gd2	O12	115.7(9)	C33	C38	C37	122.8(16)
O18	Gd2	O13	71.1(9)	O20	C39	Gd1[5]	62.3(9)
O18	Gd2	O17	49.8(6)	O20	C39	O21	123.3(16)
O18	Gd2	N7	91.0(8)	O20	C39	C35	118.9(15)
O18	Gd2	C49[3]	72.6(7)	O21	C39	Gd1[5]	60.9(9)
O22[2]	Gd2	O3[3]	73.6(6)	O21	C39	C35	117.8(15)
O22[2]	Gd2	O4[3]	124.1(6)	C35	C39	Gd1[5]	176.4(15)
O22[2]	Gd2	O12	160.1(8)	O22	C40	O23	119.6(19)
O22[2]	Gd2	O13	144.5(8)	O22	C40	C37	122.3(18)
O22[2]	Gd2	O17	79.3(8)	O23	C40	C37	118.1(17)
O22[2]	Gd2	O18	84.2(8)	C42	C41	C22	174(2)
O22[2]	Gd2	N7	169.5(7)	C41	C42	C43	170(2)
O22[2]	Gd2	C49[3]	98.4(6)	C44	C43	C42	117.3(18)
C49[3]	Gd2	N7	89.1(7)	C44	C43	C48	117.0(17)
N2	Ru1	N1	77.5(7)	C48	C43	C42	125.7(17)
N3	Ru1	N1	94.8(7)	C45	C44	C43	124(2)
N3	Ru1	N2	90.4(5)	C44	C45	C46	117.2(19)
N4	Ru1	N1	168.7(8)	C44	C45	C50	120.9(19)
N4	Ru1	N2	92.4(7)	C46	C45	C50	121.9(17)
N4	Ru1	N3	80.1(6)	C47	C46	C45	122.8(17)
N4	Ru1	N5	92.5(8)	C46	C47	C48	118.1(17)
N4	Ru1	N6	99.4(6)	C46	C47	C49	121.9(17)
N5	Ru1	N1	97.8(7)	C48	C47	C49	119.8(17)
N5	Ru1	N2	174.3(6)	C47	C48	C43	121.0(17)
N5	Ru1	N3	93.3(5)	O3	C49	Gd2[4]	61.1(12)
N6	Ru1	N1	86.7(8)	O3	C49	O4	121(2)
N6	Ru1	N2	95.5(6)	O3	C49	C47	120(2)
N6	Ru1	N3	174.1(6)	O4	C49	Gd2[4]	60.2(13)
N6	Ru1	N5	80.8(7)	O4	C49	C47	119(2)
C50	O1	Gd2	172.6(17)	C47	C49	Gd2[4]	176.9(18)
C50	O2	Gd1	155.2(17)	O1	C50	C45	118.2(19)

Table G5 Bond Angles for GdRu-MOF Final.

Atom	Atom	Atom	Angle/˚	Atom	Atom	Atom	Angle/˚
C49	O3	Gd2[4]	92.9(14)	O2	C50	O1	123(2)
C49	O4	Gd2[4]	93.7(15)	O2	C50	C45	119.2(19)
N9	O5	Gd1	96.6(11)	O11	C53	N10	119(3)

[1]1+X,1+Y,-1+Z; [2]+X,1+Y,-1+Z; [3]-1+X,+Y,+Z; [4]1+X,+Y,+Z; [5]-1+X,-1+Y,1+Z; [6]+X,-1+Y,1+Z

Table G6 Torsion Angles for GdRu-MOF Final.

A	B	C	D	Angle/˚	A	B	C	D	Angle/˚
Gd1	O2	C50	O1	-28(6)	C6	N2	C10	C9	-10(2)
Gd1	O2	C50	C45	152(3)	C6	C5	C4	C3	-178(3)
Gd1[1]	O20	C39	O21	0(2)	C7	C6	C5	N1	-180(3)
Gd1[1]	O20	C39	C35	176.1(17)	C7	C6	C5	C4	-2(5)
Gd1[1]	O21	C39	O20	0(2)	C8	C7	C6	N2	1(5)
Gd1[1]	O21	C39	C35	-176.2(17)	C8	C7	C6	C5	-174(3)
Gd1[2]	O23	C40	O22	-80(5)	C9	C8	C7	C6	4(6)
Gd1[2]	O23	C40	C37	101(5)	C10	N2	C6	C5	177.7(18)
Gd2[3]	O3	C49	O4	9(3)	C10	N2	C6	C7	2(3)
Gd2[3]	O3	C49	C47	-177(2)	C10	C9	C8	C7	-12(6)
Gd2[3]	O4	C49	O3	-9(3)	C11	N3	C15	C14	-7(3)
Gd2[3]	O4	C49	C47	177(2)	C11	N3	C15	C16	-179.8(17)
Gd2[2]	O22	C40	O23	44(5)	C11	C12	C13	C14	-5(4)
Gd2[2]	O22	C40	C37	-138(3)	C12	C13	C14	C15	-1(4)
Ru1	N1	C1	C2	175(3)	C13	C14	C15	N3	7(4)
Ru1	N1	C5	C4	-175(2)	C13	C14	C15	C16	179(3)
Ru1	N1	C5	C6	3(3)	C14	C15	C16	N4	-173(3)
Ru1	N2	C6	C5	-11(3)	C14	C15	C16	C17	13(5)
Ru1	N2	C6	C7	174(2)	C15	N3	C11	C12	1(2)
Ru1	N2	C10	C9	178(2)	C15	C16	C17	C18	173(4)
Ru1	N3	C11	C12	-175.9(17)	C16	N4	C20	C19	6(5)
Ru1	N3	C15	C14	170(2)	C16	C17	C18	C19	5(7)
Ru1	N3	C15	C16	-3(3)	C17	C18	C19	C20	-4(6)
Ru1	N4	C16	C15	3(3)	C18	C19	C20	N4	-1(6)
Ru1	N4	C16	C17	177(3)	C20	N4	C16	C15	-179(2)
Ru1	N4	C20	C19	-177(3)	C20	N4	C16	C17	-5(4)
Ru1	N5	C26	C25	-8(2)	C21	N6	C25	C24	5(3)
Ru1	N5	C26	C27	171.8(18)	C21	N6	C25	C26	-174(2)
Ru1	N5	C30	C29	-177.3(15)	C21	C22	C23	C24	1(3)
Ru1	N6	C21	C22	174.7(16)	C23	C22	C21	N6	-2(3)
Ru1	N6	C25	C24	-171.7(18)	C24	C25	C26	N5	-180(2)
Ru1	N6	C25	C26	10(2)	C24	C25	C26	C27	0(4)
O1	C50	C45	C44	-12(4)	C25	N6	C21	C22	-1(3)
O1	C50	C45	C46	167(2)	C25	C24	C23	C22	2(4)
O2	C50	C45	C44	168(2)	C25	C26	C27	C28	-174(2)
O2	C50	C45	C46	-13(4)	C26	N5	C30	C29	1(3)
O5	N9	O6	Gd1	1.4(19)	C26	C25	C24	C23	173(2)
O6	N9	O5	Gd1	-1.4(19)	C27	C28	C29	C30	-5(4)
O7	N9	O5	Gd1	177(2)	C27	C28	C29	C31	175(2)
O7	N9	O6	Gd1	-176.9(19)	C29	C28	C27	C26	-1(4)
O8	N8	O9	Gd1	-166.4(13)	C30	N5	C26	C25	173.6(19)
O8	N8	O10	Gd1	167.0(13)	C30	N5	C26	C27	-7(3)

Table G6 Torsion Angles for GdRu-MOF Final.

A	B	C	D	Angle/˚	A	B	C	D	Angle/˚
O9	N8	O10	Gd1	-13.1(14)	C33	C34	C35	C36	1(4)
O10	N8	O9	Gd1	13.7(15)	C33	C34	C35	C39	180(2)
O11	C53	N10	C51	-175(3)	C33	C38	C37	C36	1(4)
O11	C53	N10	C52	-3(3)	C33	C38	C37	C40	-178(2)
O12	N7	O13	Gd2	-22(2)	C35	C34	C33	C32	178(2)
O13	N7	O12	Gd2	21(2)	C35	C34	C33	C38	0(3)
O14	N7	O12	Gd2	-157(2)	C35	C36	C37	C38	0(4)
O14	N7	O13	Gd2	156(2)	C35	C36	C37	C40	179(2)
O17	N11	O18	Gd2	-13(2)	C36	C37	C40	O22	9(4)
O18	N11	O17	Gd2	13(2)	C36	C37	C40	O23	-173(2)
O19	N11	O17	Gd2	-170(2)	C37	C36	C35	C34	-1(4)
O19	N11	O18	Gd2	170(2)	C37	C36	C35	C39	-180(2)
O20	C39	C35	C34	0(3)	C37	C38	C33	C32	-178(2)
O20	C39	C35	C36	179(2)	C37	C38	C33	C34	-1(4)
O21	C39	C35	C34	177(2)	C38	C37	C40	O22	-172(2)
O21	C39	C35	C36	-5(3)	C38	C37	C40	O23	6(3)
N1	C5	C4	C3	0(5)	C41	C22	C21	N6	-173(2)
N2	C6	C5	N1	5(4)	C41	C22	C23	C24	173(2)
N2	C6	C5	C4	-177(3)	C41	C42	C43	C44	2(17)
N2	C10	C9	C8	15(4)	C41	C42	C43	C48	180(100)
N3	C11	C12	C13	5(3)	C42	C43	C44	C45	179(2)
N3	C15	C16	N4	0(3)	C42	C43	C48	C47	-180(2)
N3	C15	C16	C17	-174(3)	C44	C43	C48	C47	-1(3)
N4	C16	C17	C18	-1(6)	C45	C46	C47	C48	-2(4)
N5	C26	C27	C28	6(4)	C45	C46	C47	C49	174(2)
N5	C30	C29	C28	5(3)	C46	C45	C44	C43	0(4)
N5	C30	C29	C31	-174(2)	C46	C47	C48	C43	2(4)
N6	C25	C24	C23	-5(4)	C46	C47	C49	O3	12(4)
N6	C25	C26	N5	-1(3)	C46	C47	C49	O4	-174(2)
N6	C25	C26	C27	179(2)	C47	C46	C45	C44	1(4)
N10	C53	O11	Gd1	129(3)	C47	C46	C45	C50	-178(2)
C1	N1	C5	C4	3(4)	C48	C43	C44	C45	0(4)
C1	N1	C5	C6	-179(3)	C48	C47	C49	O3	-172(2)
C3	C2	C1	N1	0(6)	C48	C47	C49	O4	2(4)
C4	C3	C2	C1	3(6)	C49	C47	C48	C43	-174(2)
C5	N1	C1	C2	-2(5)	C50	C45	C44	C43	179(2)
C5	C4	C3	C2	-2(6)					

[1]-1+X,-1+Y,1+Z; [2]+X,-1+Y,1+Z; [3]1+X,+Y,+Z

Table G7 Hydrogen Atom Coordinates (Å×10^4) and Isotropic Displacement Parameters (Å^2×10^3) for GdRu-MOF Final.

Atom	*x*	*y*	*z*	U(eq)
H13	5644.39	4027.52	6829.26	162
H12	4781.68	3839.62	5702.07	178
H11	6051.79	3745.64	4656.02	184
H10	8194.42	3725.66	4773.61	165
H7	10189.74	3815.26	4961.22	173
H6	12236.57	3786.23	5324.28	191
H5	12662.72	3649.62	6566.95	182

Table G7 Hydrogen Atom Coordinates (Å×10^4) and Isotropic Displacement Parameters (Å^2×10^3) for GdRu-MOF Final.

Atom	*x*	*y*	*z*	U(eq)
H4	11062.52	4153.66	7388.77	141
H14	7405.7	2228.88	7107.33	121
H15	7633.95	709.64	7644.43	121
H16	8584.96	491.05	8770.81	143
H8	9489.7	1748.76	9242.08	139
H17	10553.15	2944.29	9518.53	184
H18	11554.87	4290.42	9748.72	202
H19	10985.27	5729.95	9114.7	163
H20	9612.87	5728.01	8176.54	136
H013	9457.28	5933.14	6538.32	94
H21	6949.61	8176	6521.26	124
H014	5631.58	7242.42	7237.03	111
H9	4583.12	6387	7993.31	105
H015	3705.28	5401.22	8910.42	106
H00O	6560.21	3462.61	8667.63	96
H34	2136.97	2938.78	10494.5	95
H36	3105.28	985.59	12108.6	95
H38	5670.83	2152.08	10835.34	93
H2	8393.14	8991.26	4532.17	106
H1	10962.38	10196.49	3291.88	92
H3	11966.41	8513.94	5039.16	107

Table G8 Atomic Occupancy for GdRu-MOF Final.

Atom	*Occupancy*	Atom	*Occupancy*	Atom	*Occupancy*
Gd2	0.75	O11	0.75	O12	0.75
O13	0.75	O14	0.75	O17	0.75
O18	0.75	O19	0.75	N7	0.75
N10	0.75	N11	0.75	C51	0.75
C52	0.75	C53	0.75		

Table G9 Solvent masks information for GdRu-MOF Final.

Number	X	Y	Z	Volume	Electron count	Content
1	0.073	0.180	0.727	10.9	0.0	?
2	-0.073	0.820	0.273	10.9	0.6	?
3	0.500	1.000	0.000	86.4	16.9	?
4	0.460	0.578	0.654	7.4	1.6	?
5	0.540	0.422	0.346	7.4	1.7	?

Experimental

Single crystals of $C_{26.12}H_{14}Gd_{0.88}N_{5.12}O_{10.62}Ru_{0.5}$ **[GdRu-MOF]** were synthesised (Chapters 4&6). A suitable crystal was selected and measured on a **Bruker APEX-II CCD** diffractometer. The crystal was kept at 100.00 K during data collection. Using Olex2 [1], the structure was solved with the SHELXT [2] structure solution program using Intrinsic Phasing and refined with the XL [3] refinement package using Least Squares minimisation.

1. Dolomanov, O.V., Bourhis, L.J., Gildea, R.J, Howard, J.A.K. & Puschmann, H. (2009), J. Appl. Cryst. 42, 339-341.
2. Sheldrick, G.M. (2015). Acta Cryst. A71, 3-8.
3. Sheldrick, G.M. (2008). Acta Cryst. A64, 112-122.

Crystal structure determination of [GdRu-MOF Final]

Crystal Data for $C_{26.125}H_{14}Gd_{0.875}N_{5.125}O_{10.625}Ru_{0.5}$ (*M* =757.80 g/mol): triclinic, space group P-1 (no. 2), *a* = 10.9309(5) Å, *b* = 14.1579(11) Å, *c* = 18.4702(15) Å, *α* = 86.791(6)°, *β* = 88.443(5)°, *γ* = 85.495(5)°, *V* = 2844.4(3) Å^3, *Z* = 4, *T* = 100.00 K, μ(CuKα) = 15.905 mm^{-1}, *Dcalc* = 1.770 g/cm^3, 26129 reflections measured (4.792° ≤ 2Θ ≤ 116.028°), 7872 unique (R_{int} = 0.1143, R_{sigma} = 0.1331) which were used in all calculations. The final R_1 was 0.1033 (I > 2σ(I)) and wR_2 was 0.3225 (all data).

Refinement model description

Number of restraints - 967, number of constraints - unknown.

Details:

1. Restrained distances

N11-O18 = N11-O17
1.25 with sigma of 0.02
N11-O19
1.24 with sigma of 0.02
N7-O14 = N7-O12
1.25 with sigma of 0.02
N7-O13
1.24 with sigma of 0.02
N8-O10 = N8-O9
1.25 with sigma of 0.02
N8-O8
1.24 with sigma of 0.02
N9-O6 = N9-O7
1.25 with sigma of 0.02
N9-O5
1.24 with sigma of 0.02
C53-O11
1.22 with sigma of 0.02
C53-N10
1.36 with sigma of 0.02
N10-C51
1.45 with sigma of 0.02
N10-C52
1.46 with sigma of 0.02
N2-C10 = N1-C5 = N1-C1
1.34 with sigma of 0.02
N2-C6
1.35 with sigma of 0.02
C10-C9 = C9-C8 = C8-C7 = C7-C6 = C4-C3 = C3-C2 = C2-C1
1.39 with sigma of 0.02
C6-C5
1.48 with sigma of 0.02
C5-C4
1.4 with sigma of 0.02
N3-C11 = N4-C16 = N4-C20
1.34 with sigma of 0.02
N3-C15
1.35 with sigma of 0.02
C11-C12 = C12-C13 = C13-C14 = C14-C15 = C17-C18 = C18-C19 = C19-C20
1.39 with sigma of 0.02
C15-C16
1.48 with sigma of 0.02
C16-C17
1.4 with sigma of 0.02
C53-C51
2.46 with sigma of 0.04
C53-C52
2.45 with sigma of 0.04
N2-C9 = N2-C7 = N1-C4 = N1-C2 = C8-C6 = C5-C3
2.4 with sigma of 0.04
N2-C5 = N1-C6 = C10-C8 = C9-C7 = C4-C2 = C3-C1
2.39 with sigma of 0.04
C7-C5
2.52 with sigma of 0.04
C6-C4
2.53 with sigma of 0.04
N3-C12 = N3-C14 = N4-C17 = N4-C19 = C13-C15 = C16-C18
2.4 with sigma of 0.04
N3-C16 = N4-C15 = C11-C13 = C12-C14 = C17-C19 = C18-C20
2.39 with sigma of 0.04
C14-C16
2.52 with sigma of 0.04
C15-C17
2.53 with sigma of 0.04
N11-O18 ≈ N11-O19 ≈ N11-O17
with sigma of 0.02
O18-O19 ≈ O19-O17 ≈ O17-O18
with sigma of 0.04
N7-O14 ≈ N7-O13 ≈ N7-O12
with sigma of 0.02
O14-O13 ≈ O13-O12 ≈ O12-O14
with sigma of 0.04
N8-O10 ≈ N8-O8 ≈ N8-O9
with sigma of 0.02
O10-O8 ≈ O8-O9 ≈ O9-O10
with sigma of 0.04
N9-O6 ≈ N9-O5 ≈ N9-O7
with sigma of 0.02
O6-O5 ≈ O5-O7 ≈ O7-O6
with sigma of 0.04
N10-C51 ≈ N10-C52
with sigma of 0.02
N2-C10 ≈ N2-C6 ≈ N1-C5 ≈ N1-C1
with sigma of 0.02
C9-C8 ≈ C8-C7 ≈ C7-C6 ≈ C5-C4 ≈ C4-C3 ≈ C3-C2 ≈ C2-C1
with sigma of 0.02
N2-C7 ≈ N2-C9 ≈ N1-C4 ≈ N1-C2
with sigma of 0.04
C10-C6 ≈ C10-C8 ≈ C9-C7 ≈ C8-C6 ≈ C5-C1 ≈ C5-C3 ≈ C4-C2
with sigma of 0.04
N3-C11 ≈ N3-C15 ≈ N4-C16 ≈ N4-C20
with sigma of 0.02
C12-C13 ≈ C13-C14 ≈ C14-C15 ≈ C16-C17 ≈ C17-C18 ≈ C18-C19
≈ C19-C20
with sigma of 0.02
N3-C14 ≈ N3-C12 ≈ N4-C17 ≈ N4-C19
with sigma of 0.04
C11-C15 ≈ C11-C13 ≈ C12-C14 ≈ C13-C15 ≈ C16-C20 ≈ C16-C18
≈ C17-C19
with sigma of 0.04

2. Restrained planarity

O17, O18, O19, N11
with sigma of 0.1
O12, O13, O14, N7
with sigma of 0.1
O8, O9, O10, N8
with sigma of 0.1
O5, O6, O7, N9
with sigma of 0.1
O11, N10, C51, C52, C53
with sigma of 0.1
N1, N2, C1, C2, C3, C4, C5, C6, C7, C8, C9, C10
with sigma of 0.1
N3, N4, C11, C12, C13, C14, C15, C16, C17, C18, C19, C20
with sigma of 0.1

3. Uiso/Uaniso restraints and constraints

O17 ≈ O18 ≈ O19 ≈ N11: within 2A with sigma of 0.04 and sigma for
terminal atoms of 0.08 within 2A
O12 ≈ O13 ≈ O14 ≈ N7: within

2A with sigma of 0.04 and sigma for
terminal atoms of 0.08 within 2A
O8 ≈ O9 ≈ O10 ≈ N8: within 2A with sigma of 0.04 and sigma for
terminal atoms of 0.08 within 2A
O5 ≈ O6 ≈ O7 ≈ N9: within 2A with sigma of 0.04 and sigma for
terminal atoms of 0.08 within 2A
O11 ≈ N10 ≈ C51 ≈ C52 ≈ C53: within 2A with sigma of 0.04 and
sigma for terminal atoms of 0.08 within 2A
N1 ≈ N2 ≈ C1 ≈ C2 ≈ C3 ≈ C4 ≈ C5 ≈ C6 ≈ C7
≈ C8 ≈ C9 ≈ C10: within 2A with sigma of 0.04 and sigma for
terminal atoms of 0.08 within 2A
N3 ≈ N4 ≈ C11 ≈ C12 ≈ C13 ≈ C14 ≈ C15 ≈ C16 ≈
C17 ≈ C18 ≈ C19 ≈ C20: within 2A with sigma of 0.04 and sigma for
terminal atoms of 0.08 within 2A
Uanis(N7) ≈ Ueq, Uanis(O13) ≈ Ueq, Uanis(O14) ≈ Ueq, Uanis(O12)
≈ Ueq, Uanis(O17) ≈ Ueq, Uanis(N11) ≈ Ueq, Uanis(O19) ≈ Ueq,
Uanis(O18) ≈ Ueq, Uanis(O11) ≈ Ueq, Uanis(C53) ≈ Ueq, Uanis(N10)
≈ Ueq, Uanis(C52) ≈ Ueq, Uanis(C51) ≈ Ueq, Uanis(O10) ≈ Ueq,
Uanis(N8) ≈ Ueq, Uanis(O8) ≈ Ueq, Uanis(O9) ≈ Ueq, Uanis(O6) ≈
Ueq, Uanis(O5) ≈ Ueq, Uanis(N9) ≈ Ueq, Uanis(O7) ≈ Ueq, Uanis(Gd1)
≈ Ueq, Uanis(Gd2) ≈ Ueq, Uanis(O1) ≈ Ueq, Uanis(O2) ≈ Ueq,
Uanis(C50) ≈ Ueq, Uanis(O4) ≈ Ueq, Uanis(C49) ≈ Ueq, Uanis(O3)
≈ Ueq: with sigma of 0.01 and sigma for terminal atoms of 0.02
Uanis(C40) ≈ Ueq, Uanis(O23) ≈ Ueq, Uanis(O22) ≈ Ueq, Uanis(C39)
≈ Ueq, Uanis(O20) ≈ Ueq, Uanis(O21) ≈ Ueq: with sigma of 0.01 and
sigma for terminal atoms of 0.02
Uanis(O16) ≈ Ueq: with sigma of 0.01 and sigma for terminal atoms of 0.02

4. Rigid body (RIGU) restrains

O17, O18, O19, N11
with sigma for 1-2 distances of 0.004 and sigma for 1-3 distances of 0.004
O12, O13, O14, N7
with sigma for 1-2 distances of 0.004 and sigma for 1-3 distances of 0.004
O8, O9, O10, N8
with sigma for 1-2 distances of 0.004 and sigma for 1-3 distances of 0.004
O5, O6, O7, N9
with sigma for 1-2 distances of 0.004 and sigma for 1-3 distances of 0.004
O11, N10, C51, C52, C53
with sigma for 1-2 distances of 0.004 and sigma for 1-3 distances of 0.004
N1, N2, C1, C2, C3, C4, C5, C6, C7, C8, C9, C10
with sigma for 1-2 distances of 0.004 and sigma for 1-3 distances of 0.004
N3, N4, C11, C12, C13, C14, C15, C16, C17, C18, C19, C20
with sigma for 1-2 distances of 0.004 and sigma for 1-3 distances of 0.004

5. Others

Fixed Sof: Gd2(0.75) N11(0.75) O18(0.75) O19(0.75) O17(0.75) N7(0.75)
O14(0.75) O13(0.75) O12(0.75) C53(0.75) O11(0.75) N10(0.75) C51(0.75) C52(0.75)

6.a Aromatic/amide H refined with riding coordinates:

C34(H34), C38(H38), C30(H00O), C46(H1), C36(H36), C21(H013), C24(H014), C28(H015), C48(H3), C27(H9), C44(H2), C10(H4), C9(H5), C8(H6), C7(H7), C4(H10), C3(H11), C2(H12), C1(H13), C11(H14), C12(H15), C13(H16), C14(H8), C17(H17), C18(H18), C19(H19), C20(H20), C23(H21)

This report has been created with Olex2, compiled on 2025.07.13 svn.rb7424aed for OlexSys

Appendix H: Crystallographic Information for DyRu-MOF

Table H1 Crystal data and structure refinement for DyRu-MOF.

Identification code	DyRu-MOF
Empirical formula	$C_{52.25}H_{28}Dy_2N_{10.75}O_{21.75}Ru$
Formula weight	1580.42
Temperature/K	100.00
Crystal system	triclinic
Space group	P-1
a/Å	10.8924(8)
b/Å	14.1396(17)
c/Å	18.798(2)
α/°	84.900(10)
β/°	89.523(8)
γ/°	85.812(8)
Volume/Å^3	2876.0(5)
Z	2
ρ_{calc}g/cm^3	1.825
μ/mm^{-1}	16.557
F(000)	1534.0
Crystal size/mm^3	0.124 × 0.069 × 0.034
Radiation	CuKα (λ = 1.54178)
2Θ range for data collection/°	4.72 to 115.634
Index ranges	-11 ≤ h ≤ 11, -15 ≤ k ≤ 15, -20 ≤ l ≤ 20
Reflections collected	30514
Independent reflections	7765 [R_{int} = 0.1797, R_{sigma} = 0.1506]
Data/restraints/parameters	7765/1012/802
Goodness-of-fit on F^2	1.039
Final R indexes [I>=2σ (I)]	R_1 = 0.1082, wR_2 = 0.2708
Final R indexes [all data]	R_1 = 0.1907, wR_2 = 0.3249
Largest diff. peak/hole / e Å^{-3}	2.09/-1.35

Table H2 Fractional Atomic Coordinates (×10^4) and Equivalent Isotropic Displacement Parameters (Å^2×10^3) for DyRu-MOF. U_{eq} is defined as 1/3 of the trace of the orthogonalised U_{IJ} tensor.

Atom	*x*	*y*	*z*	U(eq)
Dy01	8676.5(10)	11603.8(11)	1790.5(8)	71.9(6)
Dy02	5605.6(12)	9547.8(15)	3512.0(9)	93.3(8)
Ru1	8232.2(15)	4288.3(14)	7402.2(11)	70.6(7)
O1	8909(13)	10695(15)	2843(11)	103(7)
O2	7621(14)	9907(15)	3455(10)	101(7)
O3	13928(13)	9010(16)	4323(11)	117(9)
O4	13416(12)	9992(12)	3402(9)	79(5)
O5	5469(16)	10681(19)	4025(11)	123(7)
O6	5700(30)	7120(20)	2358(18)	183(12)
O7	4697(16)	8224(16)	2898(12)	123(7)
O8	7711(15)	13052(11)	1156(9)	79(5)
O9	8097(16)	11937(13)	459(10)	94(5)
O10	7623(18)	13381(15)	12(10)	122(8)

Table H2 Fractional Atomic Coordinates (×10^4) and Equivalent Isotropic Displacement Parameters (Å^2×10^3) for DyRu-MOF. U_{eq} is defined as 1/3 of the trace of the orthogonalised U_{IJ} tensor.

Atom	*x*	*y*	*z*	U(eq)
O11	7353(18)	12523(16)	2655(14)	132(8)
O12	9223(19)	12914(15)	2480(12)	124(7)
O13	8030(30)	13670(20)	3213(18)	207(14)
O14	6360(20)	7495(16)	5197(12)	142(9)
O15	6335(19)	9041(14)	4814(11)	117(7)
O16	6333(17)	7934(15)	4059(11)	113(6)
O17	6580(17)	8359(17)	2649(15)	141(8)
O18	9042(18)	10250(20)	1286(17)	120(9)
O19	338(12)	2376(13)	11121(9)	84(6)
O20	888(13)	1231(13)	11963(10)	93(7)
O21	6715(12)	1117(12)	11772(9)	73(5)
O22	5378(14)	430(20)	12430(11)	150(12)
N1	7312(15)	4009(17)	6465(10)	103(7)
N2	9699(14)	3998(10)	6712(9)	82(5)
N3	8341(16)	2887(12)	7817(9)	78(5)
N4	9319(15)	4356(13)	8258(10)	104(7)
N5	6689(12)	4662(11)	7981(9)	70(5)
N6	7995(11)	5729(11)	7113(7)	77(5)
N7	8010(30)	9090(30)	810(20)	162(13)
N8	6366(16)	8161(14)	4699(11)	108(7)
N9	5655(17)	7886(16)	2628(12)	136(9)
N10	7832(14)	12791(12)	539(8)	76(5)
N11	8199(19)	13042(16)	2784(12)	139(9)
C1	6092(17)	4020(30)	6380(13)	121(9)
C2	5560(20)	3800(30)	5753(14)	131(10)
C3	6300(20)	3730(30)	5157(13)	135(10)
C4	7560(20)	3770(30)	5226(11)	132(9)
C5	8055(15)	3900(20)	5889(11)	115(8)
C6	9389(14)	3910(20)	6031(11)	97(7)
C7	10290(20)	3810(20)	5513(11)	116(8)
C8	11513(19)	3780(20)	5725(14)	119(9)
C9	11821(17)	3820(20)	6434(15)	121(9)
C10	10869(17)	4007(15)	6923(12)	107(8)
C11	9790(20)	5142(15)	8451(13)	118(9)
C12	10630(40)	5133(18)	9011(18)	154(11)
C13	10830(40)	4295(18)	9444(18)	157(11)
C14	10260(30)	3497(17)	9291(15)	139(10)
C15	9620(20)	3517(12)	8654(13)	102(7)
C16	8930(20)	2711(12)	8451(12)	93(6)
C17	9040(30)	1806(13)	8808(13)	108(8)
C18	8520(30)	1068(14)	8522(14)	104(8)
C19	7930(20)	1225(14)	7872(13)	96(7)
C20	7840(20)	2146(15)	7552(13)	98(7)
C21	8758(14)	6216(13)	6657(9)	69(6)
C22	8494(16)	7175(13)	6435(11)	70(6)
C23	7390(17)	7624(13)	6639(12)	83(7)
C24	6600(15)	7121(12)	7081(12)	86(7)
C25	6895(14)	6172(12)	7299(12)	78(6)

Table H2 Fractional Atomic Coordinates (×10^4) and Equivalent Isotropic Displacement Parameters (Å^2×10^3) for DyRu-MOF. U_{eq} is defined as 1/3 of the trace of the orthogonalised U_{IJ} tensor.

Atom	*x*	*y*	*z*	U(eq)
C26	6164(15)	5558(12)	7800(11)	77(6)
C27	5061(16)	5881(14)	8099(11)	81(7)
C28	4555(17)	5326(14)	8659(12)	85(7)
C29	5107(15)	4429(13)	8860(11)	68(6)
C30	6167(16)	4105(14)	8508(10)	70(6)
C31	4610(20)	3840(20)	9446(12)	77(8)
C32	4316(19)	3240(20)	9907(13)	78(8)
C33	4014(18)	2673(15)	10515(12)	58(6)
C34	4917(17)	2150(20)	10916(12)	85(10)
C35	4626(16)	1544(16)	11508(12)	56(6)
C36	3399(17)	1377(15)	11668(11)	50(6)
C37	2479(16)	1934(18)	11325(12)	66(7)
C38	2797(17)	2575(15)	10717(12)	63(7)
C39	1137(16)	1868(18)	11480(13)	67(7)
C40	5644(17)	990(20)	11945(13)	77(9)
C41	9240(20)	7649(17)	5944(13)	68(7)
C42	9800(20)	8100(20)	5506(15)	87(9)
C43	10302(18)	8697(16)	4896(11)	57(6)
C44	11473(16)	8791(16)	4727(13)	68(8)
C45	11783(16)	9370(18)	4135(12)	67(7)
C46	10910(18)	9820(20)	3636(13)	84(9)
C47	9650(16)	9673(17)	3807(13)	65(7)
C48	9341(18)	9116(16)	4430(12)	67(7)
C49	13149(16)	9498(19)	3937(13)	78(9)
C50	8647(16)	10090(17)	3328(13)	66(7)
C51	8400(30)	9580(20)	1360(20)	128(12)
C52	7130(60)	8360(40)	940(40)	220(30)
C53	8450(60)	9450(40)	110(20)	170(20)

Table H3 Anisotropic Displacement Parameters (Å^2×10^3) for DyRu-MOF. The Anisotropic displacement factor exponent takes the form: $-2\pi^2[h^2a^{*2}U_{11}+2hka^*b^*U_{12}+\ldots]$.

Atom	U_{11}	U_{22}	U_{33}	U_{23}	U_{13}	U_{12}
Dy01	29.9(7)	81.4(11)	95.9(12)	49.9(9)	-10.5(6)	-16.3(6)
Dy02	36.3(8)	138.5(17)	93.2(13)	60.5(12)	-2.5(7)	-11.3(8)
Ru1	42.2(9)	76.9(14)	86.0(14)	37.5(11)	-1.5(8)	-12.6(8)
O1	39(8)	132(17)	126(15)	73(14)	-8(9)	-28(9)
O2	53(10)	140(17)	92(13)	75(12)	-4(8)	-3(10)
O3	27(8)	170(20)	132(16)	92(15)	10(9)	-13(10)
O4	36(7)	82(12)	108(13)	55(10)	7(8)	-11(7)
O5	65(10)	185(17)	107(13)	73(12)	-23(9)	-21(11)
O6	170(20)	170(20)	220(30)	-20(20)	20(20)	-68(18)
O7	70(10)	146(17)	149(18)	36(14)	-22(11)	-25(11)
O8	70(10)	72(10)	92(9)	29(9)	-14(9)	-17(8)
O9	78(11)	103(11)	99(13)	9(10)	8(9)	-17(10)
O10	101(14)	151(16)	107(12)	66(12)	-42(11)	-38(12)
O11	103(13)	124(18)	170(20)	-8(14)	-49(14)	8(12)
O12	112(13)	93(15)	162(19)	18(13)	-53(13)	-9(12)
O13	190(30)	200(30)	240(30)	-90(20)	-70(20)	20(20)

Table H3 Anisotropic Displacement Parameters ($Å^2×10^3$) for DyRu-MOF. The Anisotropic displacement factor exponent takes the form: $-2π^2[h^2a^{*2}U_{11}+2hka*b*U_{12}+…]$.

Atom	U_{11}	U_{22}	U_{33}	U_{23}	U_{13}	U_{12}
O14	150(20)	135(16)	137(16)	37(14)	-32(15)	-26(15)
O15	91(13)	120(13)	136(16)	20(12)	-6(12)	-30(13)
O16	70(11)	127(15)	134(14)	18(12)	-3(12)	16(11)
O17	80(11)	131(18)	210(20)	17(16)	3(14)	-33(11)
O18	22(11)	150(20)	180(20)	23(18)	-13(13)	-2(11)
O19	34(8)	106(14)	103(13)	52(11)	3(8)	-24(8)
O20	35(8)	114(15)	118(14)	70(12)	-15(8)	-11(8)
O21	32(8)	89(12)	90(12)	36(9)	-8(7)	-5(7)
O22	37(9)	280(30)	112(16)	130(19)	-4(9)	-25(13)
N1	70(9)	108(16)	124(14)	36(13)	-11(9)	-17(11)
N2	67(9)	60(12)	110(12)	52(11)	13(8)	-18(9)
N3	49(10)	75(12)	104(13)	14(10)	-1(8)	-1(8)
N4	68(12)	84(11)	151(17)	43(12)	-16(11)	-3(9)
N5	22(7)	90(11)	88(12)	48(9)	-8(7)	-13(6)
N6	35(7)	104(12)	82(12)	43(10)	-11(7)	-14(7)
N7	150(30)	170(30)	160(30)	-10(20)	10(20)	-50(20)
N8	68(12)	117(13)	134(14)	21(11)	-2(13)	-11(13)
N9	79(11)	149(19)	180(20)	7(16)	-7(14)	-37(12)
N10	51(10)	88(11)	85(10)	31(9)	-8(9)	-21(9)
N11	112(14)	140(20)	170(20)	-21(14)	-58(15)	7(13)
C1	74(10)	170(20)	111(16)	25(18)	-20(11)	-17(14)
C2	119(17)	160(20)	115(17)	23(19)	-25(11)	-49(18)
C3	140(17)	140(20)	121(17)	24(18)	-16(13)	-47(19)
C4	136(16)	140(20)	120(15)	37(17)	-10(12)	-43(18)
C5	92(10)	129(19)	113(14)	46(15)	-7(8)	-3(13)
C6	84(9)	84(16)	114(13)	32(14)	12(8)	0(12)
C7	111(12)	96(19)	136(16)	11(16)	32(12)	2(15)
C8	100(12)	83(18)	166(18)	13(19)	41(14)	12(15)
C9	83(13)	99(19)	176(19)	0(20)	26(12)	8(15)
C10	68(10)	100(19)	149(17)	12(16)	7(10)	-2(12)
C11	106(18)	99(13)	140(20)	64(15)	-30(14)	-34(13)
C12	160(20)	120(18)	180(20)	70(16)	-72(17)	-63(17)
C13	160(20)	120(18)	190(20)	63(15)	-103(18)	-54(16)
C14	130(20)	114(17)	163(19)	48(15)	-69(15)	-41(15)
C15	71(13)	87(11)	140(16)	39(11)	-36(11)	-9(10)
C16	74(13)	78(10)	119(14)	33(11)	-20(10)	-2(10)
C17	99(17)	69(12)	147(19)	24(12)	-19(14)	9(11)
C18	79(16)	80(13)	149(19)	15(14)	-1(13)	0(12)
C19	79(15)	77(12)	129(18)	-7(13)	15(12)	-1(12)
C20	73(14)	90(14)	129(17)	5(11)	-6(12)	-15(11)
C21	54(10)	82(12)	65(13)	29(11)	-4(8)	-16(9)
C22	64(10)	80(12)	63(13)	21(11)	-7(9)	-11(9)
C23	75(11)	88(14)	77(15)	45(12)	7(10)	-3(9)
C24	46(10)	107(13)	93(15)	63(12)	-3(9)	-6(9)
C25	44(8)	87(12)	96(14)	38(11)	0(8)	-19(8)
C26	43(9)	89(12)	89(14)	47(10)	0(8)	-6(8)
C27	51(10)	98(15)	85(15)	46(12)	6(9)	2(9)
C28	46(11)	100(14)	98(15)	46(12)	9(9)	-3(9)

Table H3 Anisotropic Displacement Parameters ($Å^2×10^3$) for DyRu-MOF. The Anisotropic displacement factor exponent takes the form: $-2π^2[h^2a^{*2}U_{11}+2hka*b*U_{12}+…]$.

Atom	U_{11}	U_{22}	U_{33}	U_{23}	U_{13}	U_{12}
C29	36(9)	83(13)	79(14)	31(11)	-3(8)	-20(8)
C30	52(10)	84(13)	68(13)	35(10)	0(8)	-9(9)
C31	62(14)	110(20)	50(14)	49(15)	-9(11)	-28(14)
C32	36(11)	120(20)	74(17)	35(17)	4(11)	-15(12)
C33	46(12)	45(14)	79(16)	24(12)	-3(10)	-18(10)
C34	20(9)	170(30)	59(14)	60(16)	-14(9)	-41(12)
C35	28(10)	64(15)	73(15)	21(12)	-1(9)	-13(9)
C36	39(11)	48(13)	59(14)	18(11)	6(9)	-15(9)
C37	23(10)	101(19)	64(15)	41(14)	-7(9)	0(10)
C38	32(10)	54(14)	91(17)	46(13)	-5(10)	8(9)
C39	11(9)	94(19)	89(17)	27(15)	-9(10)	-6(10)
C40	25(11)	130(20)	70(16)	47(16)	4(10)	-12(12)
C41	86(17)	54(15)	57(15)	34(13)	-6(13)	-9(13)
C42	39(12)	110(20)	100(20)	39(19)	-30(13)	-7(13)
C43	48(12)	61(15)	56(14)	23(12)	5(10)	-4(10)
C44	22(10)	69(16)	104(19)	48(14)	1(10)	-13(9)
C45	19(9)	96(19)	74(16)	44(14)	7(9)	3(10)
C46	30(11)	130(20)	83(17)	65(17)	7(10)	-5(12)
C47	21(9)	74(16)	91(17)	42(14)	2(9)	-11(9)
C48	41(11)	72(16)	82(17)	45(14)	2(10)	-23(11)
C49	10(9)	120(20)	94(17)	71(17)	1(9)	-16(10)
C50	14(10)	72(16)	108(19)	35(15)	8(10)	-26(9)
C51	70(20)	160(30)	160(30)	-10(20)	20(20)	-22(15)
C52	260(50)	210(50)	200(50)	-40(40)	30(40)	-130(40)
C53	240(50)	110(40)	150(30)	-30(30)	30(30)	-40(40)

Table H4 Bond Lengths for DyRu-MOF.

Atom	Atom	Length/Å	Atom	Atom	Length/Å
Dy01	O1	2.266(16)	N10	O8	1.250(12)
Dy01	O8	2.448(15)	N10	O9	1.244(12)
Dy01	O9	2.581(18)	N10	O10	1.249(13)
Dy01	O11	2.54(2)	N11	O11	1.256(14)
Dy01	O12	2.46(2)	N11	O12	1.257(14)
Dy01	O18	2.22(3)	N11	O13	1.258(14)
Dy01	$O19^1$	2.461(13)	C2	C1	1.387(12)
Dy01	$O20^1$	2.446(14)	C3	C2	1.381(12)
Dy01	$O21^2$	2.294(14)	C4	C3	1.385(12)
Dy01	N10	2.882(14)	C5	C4	1.395(12)
Dy01	N11	2.90(2)	C6	C5	1.481(16)
Dy01	$C39^1$	2.783(18)	C7	C6	1.388(12)
Dy02	O2	2.288(17)	C8	C7	1.385(12)
Dy02	$O3^3$	2.489(14)	C9	C8	1.384(12)
Dy02	$O4^3$	2.427(13)	C10	C9	1.406(17)
Dy02	O5	1.94(3)	C11	C12	1.396(17)
Dy02	O7	2.55(2)	C12	C13	1.382(12)
Dy02	O15	2.60(2)	C13	C14	1.384(12)
Dy02	O16	2.495(19)	C14	C15	1.385(12)
Dy02	O17	2.60(3)	C15	C16	1.485(15)

Table H4 Bond Lengths for DyRu-MOF.

Atom	Atom	Length/Å	Atom	Atom	Length/Å
Dy02	O22[2]	2.293(16)	C16	C17	1.388(11)
Dy02	N8	2.919(18)	C17	C18	1.377(12)
Dy02	C49[3]	2.790(17)	C18	C19	1.375(12)
Ru1	N1	2.116(19)	C19	C20	1.383(12)
Ru1	N2	2.090(17)	C21	C22	1.393(16)
Ru1	N3	2.060(17)	C22	C23	1.385(12)
Ru1	N4	2.018(19)	C23	C24	1.381(11)
Ru1	N5	2.057(14)	C24	C25	1.383(11)
Ru1	N6	2.060(15)	C25	C26	1.489(14)
O1	C50	1.24(2)	C26	C27	1.387(11)
O2	C50	1.18(2)	C27	C28	1.390(11)
O3	C49	1.25(2)	C28	C29	1.386(11)
O4	C49	1.22(2)	C29	C30	1.395(12)
O19	C39	1.25(2)	C31	C29	1.45(2)
O20	C39	1.26(3)	C31	C32	1.21(3)
O21	C40	1.23(2)	C33	C32	1.39(3)
O22	C40	1.20(3)	C33	C34	1.38(3)
N1	C1	1.340(12)	C33	C38	1.39(3)
N1	C5	1.358(12)	C34	C35	1.39(3)
N2	C6	1.347(12)	C35	C40	1.52(3)
N2	C10	1.339(12)	C36	C35	1.40(3)
N3	C16	1.355(12)	C36	C37	1.36(3)
N3	C20	1.350(12)	C37	C39	1.50(3)
N4	C11	1.338(13)	C38	C37	1.45(3)
N4	C15	1.364(12)	C41	C22	1.39(3)
N5	C26	1.367(12)	C42	C41	1.18(3)
N5	C30	1.358(12)	C42	C43	1.49(3)
N6	C21	1.365(12)	C43	C44	1.33(3)
N6	C25	1.369(12)	C45	C44	1.38(3)
N7	C52	1.460(16)	C45	C46	1.42(3)
N7	C53	1.466(16)	C47	C46	1.43(3)
N8	O14	1.268(13)	C47	C48	1.40(3)
N8	O15	1.279(13)	C47	C50	1.48(3)
N8	O16	1.273(13)	C48	C43	1.43(3)
N9	O6	1.239(13)	C49	C45	1.55(2)
N9	O7	1.239(13)	C51	O18	1.224(19)
N9	O17	1.252(14)	C51	N7	1.385(19)

[1]1+X,1+Y,-1+Z; [2]+X,1+Y,-1+Z; [3]-1+X,+Y,+Z

Table H5 Bond Angles for DyRu-MOF.

Atom	Atom	Atom	Angle/˚	Atom	Atom	Atom	Angle/˚
O1	Dy01	O8	146.8(7)	N11	O12	Dy01	96.9(14)
O1	Dy01	O9	154.9(7)	N8	O15	Dy02	91.0(13)
O1	Dy01	O11	76.3(8)	N8	O16	Dy02	96.1(13)
O1	Dy01	O12	84.8(8)	N9	O17	Dy02	95.4(14)
O1	Dy01	O19[1]	125.3(5)	C51	O18	Dy01	125(2)
O1	Dy01	O20[1]	73.2(5)	C39	O19	Dy01[5]	91.2(12)
O1	Dy01	O21[2]	86.6(5)	C39	O20	Dy01[5]	91.6(10)
O1	Dy01	N10	167.7(5)	C40	O21	Dy01[6]	161.1(19)

Table H5 Bond Angles for DyRu-MOF.

Atom	Atom	Atom	Angle/˚
O1	Dy01	N11	79.7(8)
O1	Dy01	C39[1]	99.4(6)
O8	Dy01	O9	50.7(5)
O8	Dy01	O11	70.5(7)
O8	Dy01	O12	74.7(6)
O8	Dy01	O19[1]	73.9(5)
O8	Dy01	N10	25.5(3)
O8	Dy01	N11	70.6(6)
O8	Dy01	C39[1]	99.7(6)
O9	Dy01	N10	25.6(3)
O9	Dy01	N11	121.2(6)
O9	Dy01	C39[1]	91.1(6)
O11	Dy01	O9	115.8(6)
O11	Dy01	N10	94.6(6)
O11	Dy01	N11	25.7(4)
O11	Dy01	C39[1]	125.2(7)
O12	Dy01	O9	120.1(6)
O12	Dy01	O11	51.2(6)
O12	Dy01	N10	96.1(6)
O12	Dy01	N11	25.5(4)
O12	Dy01	C39[1]	74.1(8)
O18	Dy01	O1	85.6(10)
O18	Dy01	O8	123.1(8)
O18	Dy01	O9	72.6(8)
O18	Dy01	O11	147.0(8)
O18	Dy01	O12	154.8(7)
O18	Dy01	O19[1]	93.1(8)
O18	Dy01	O20[1]	76.4(7)
O18	Dy01	O21[2]	80.3(7)
O18	Dy01	N10	98.2(8)
O18	Dy01	N11	165.2(9)
O18	Dy01	C39[1]	84.5(8)
O19[1]	Dy01	O9	69.7(6)
O19[1]	Dy01	O11	119.9(7)
O19[1]	Dy01	O12	73.8(7)
O19[1]	Dy01	N10	66.4(5)
O19[1]	Dy01	N11	96.9(7)
O19[1]	Dy01	C39[1]	26.7(6)
O20[1]	Dy01	O8	125.9(5)
O20[1]	Dy01	O9	112.3(6)
O20[1]	Dy01	O11	122.6(7)
O20[1]	Dy01	O12	78.5(7)
O20[1]	Dy01	O19[1]	53.7(5)
O20[1]	Dy01	N10	119.1(5)
O20[1]	Dy01	N11	100.8(7)
O20[1]	Dy01	C39[1]	27.0(5)
O21[2]	Dy01	O8	82.8(5)
O21[2]	Dy01	O9	77.6(6)

Atom	Atom	Atom	Angle/˚
C40	O22	Dy02[6]	156.7(18)
C1	N1	Ru1	126.1(15)
C1	N1	C5	118.8(16)
C5	N1	Ru1	114.8(12)
C6	N2	Ru1	115.6(11)
C10	N2	Ru1	121.4(14)
C10	N2	C6	122.6(15)
C16	N3	Ru1	115.1(12)
C20	N3	Ru1	127.7(12)
C20	N3	C16	117.1(15)
C11	N4	Ru1	125.6(12)
C11	N4	C15	118.1(15)
C15	N4	Ru1	116.3(13)
C26	N5	Ru1	115.1(9)
C30	N5	Ru1	126.0(11)
C30	N5	C26	118.9(13)
C21	N6	Ru1	124.1(11)
C21	N6	C25	118.8(13)
C25	N6	Ru1	116.2(9)
C51	N7	C52	120(3)
C51	N7	C53	114(3)
C52	N7	C53	125(4)
O14	N8	Dy02	162.7(15)
O14	N8	O15	123.0(18)
O14	N8	O16	117.5(18)
O15	N8	Dy02	63.0(11)
O16	N8	Dy02	58.2(11)
O16	N8	O15	119.4(17)
O6	N9	O17	121.9(19)
O7	N9	O6	121.6(19)
O7	N9	O17	116.5(18)
O8	N10	Dy01	57.5(9)
O9	N10	Dy01	63.6(10)
O9	N10	O8	119.5(15)
O9	N10	O10	120.7(17)
O10	N10	Dy01	170.3(13)
O10	N10	O8	119.7(16)
O11	N11	Dy01	61.3(13)
O11	N11	O13	121(2)
O12	N11	Dy01	57.6(12)
O12	N11	O11	118.8(19)
O12	N11	O13	120(2)
O13	N11	Dy01	178.0(17)
N1	C1	C2	122.5(17)
C3	C2	C1	118.3(16)
C2	C3	C4	119.2(15)
C3	C4	C5	119.4(14)
N1	C5	C4	120.9(14)

Table H5 Bond Angles for DyRu-MOF.

Atom	Atom	Atom	Angle/˚	Atom	Atom	Atom	Angle/˚
O21[2]	Dy01	O11	71.4(7)	N1	C5	C6	115.1(15)
O21[2]	Dy01	O12	122.3(7)	C4	C5	C6	124.0(16)
O21[2]	Dy01	O19[1]	147.1(5)	N2	C6	C5	115.8(14)
O21[2]	Dy01	O20[1]	150.0(6)	N2	C6	C7	120.4(13)
O21[2]	Dy01	N10	82.6(5)	C7	C6	C5	123.9(15)
O21[2]	Dy01	N11	96.9(6)	C8	C7	C6	118.0(13)
O21[2]	Dy01	C39[1]	163.2(7)	C9	C8	C7	121.1(14)
N10	Dy01	N11	95.8(6)	C8	C9	C10	118.2(14)
C39[1]	Dy01	N10	92.7(5)	N2	C10	C9	119.0(15)
C39[1]	Dy01	N11	99.6(7)	N4	C11	C12	123.1(15)
O2	Dy02	O3[3]	144.7(6)	C13	C12	C11	117.7(14)
O2	Dy02	O4[3]	151.9(6)	C12	C13	C14	119.4(14)
O2	Dy02	O7	125.6(7)	C13	C14	C15	119.2(14)
O2	Dy02	O15	78.4(6)	N4	C15	C14	120.9(14)
O2	Dy02	O16	87.8(6)	N4	C15	C16	113.9(14)
O2	Dy02	O17	77.1(7)	C14	C15	C16	123.3(14)
O2	Dy02	O22[2]	86.1(6)	N3	C16	C15	113.9(13)
O2	Dy02	N8	86.1(5)	N3	C16	C17	121.5(13)
O2	Dy02	C49[3]	161.4(9)	C17	C16	C15	123.8(14)
O3[3]	Dy02	O7	75.3(8)	C18	C17	C16	119.7(13)
O3[3]	Dy02	O15	66.5(6)	C19	C18	C17	119.8(15)
O3[3]	Dy02	O16	73.8(6)	C18	C19	C20	117.4(15)
O3[3]	Dy02	O17	118.1(8)	N3	C20	C19	124.3(16)
O3[3]	Dy02	N8	64.3(5)	N6	C21	C22	121.4(13)
O3[3]	Dy02	C49[3]	26.6(5)	C23	C22	C21	119.1(12)
O4[3]	Dy02	O3[3]	52.4(5)	C23	C22	C41	119.6(16)
O4[3]	Dy02	O7	74.1(6)	C41	C22	C21	120.8(16)
O4[3]	Dy02	O15	114.2(6)	C24	C23	C22	119.4(12)
O4[3]	Dy02	O16	120.0(6)	C23	C24	C25	120.1(12)
O4[3]	Dy02	O17	117.7(7)	N6	C25	C24	120.9(11)
O4[3]	Dy02	N8	116.6(5)	N6	C25	C26	112.9(11)
O4[3]	Dy02	C49[3]	25.8(5)	C24	C25	C26	125.9(12)
O5	Dy02	O2	81.2(8)	N5	C26	C25	115.3(11)
O5	Dy02	O3[3]	84.6(8)	N5	C26	C27	121.7(11)
O5	Dy02	O4[3]	79.2(7)	C27	C26	C25	122.9(12)
O5	Dy02	O7	152.8(7)	C26	C27	C28	119.0(12)
O5	Dy02	O15	72.9(7)	C29	C28	C27	119.1(13)
O5	Dy02	O16	124.0(7)	C28	C29	C30	119.7(13)
O5	Dy02	O17	156.8(7)	C28	C29	C31	120.6(16)
O5	Dy02	O22[2]	92.1(10)	C30	C29	C31	119.7(16)
O5	Dy02	N8	98.5(6)	N5	C30	C29	121.2(14)
O5	Dy02	C49[3]	81.2(9)	C32	C31	C29	171(3)
O7	Dy02	O15	113.9(6)	C31	C32	C33	171(3)
O7	Dy02	O17	48.6(6)	C34	C33	C32	120.6(18)
O7	Dy02	N8	89.2(6)	C34	C33	C38	117.8(17)
O7	Dy02	C49[3]	72.6(8)	C38	C33	C32	121.5(18)
O15	Dy02	O17	110.1(7)	C33	C34	C35	121.3(17)
O15	Dy02	N8	26.0(3)	C34	C35	C36	120.6(17)

Table H5 Bond Angles for DyRu-MOF.

Atom	Atom	Atom	Angle/˚	Atom	Atom	Atom	Angle/˚
O15	Dy02	C49[3]	90.8(6)	C34	C35	C40	120.0(16)
O16	Dy02	O7	67.8(7)	C36	C35	C40	119.1(17)
O16	Dy02	O15	51.2(6)	C37	C36	C35	119.6(18)
O16	Dy02	O17	63.4(8)	C36	C37	C38	118.3(17)
O16	Dy02	N8	25.7(4)	C36	C37	C39	124.8(18)
O16	Dy02	C49[3]	97.3(7)	C38	C37	C39	116.7(16)
O17	Dy02	N8	88.1(7)	C33	C38	C37	121.5(16)
O17	Dy02	C49[3]	121.2(8)	O19	C39	Dy01[5]	62.1(9)
O22[2]	Dy02	O3[3]	126.7(5)	O19	C39	O20	123.6(17)
O22[2]	Dy02	O4[3]	74.7(5)	O19	C39	C37	121.3(19)
O22[2]	Dy02	O7	85.6(9)	O20	C39	Dy01[5]	61.4(9)
O22[2]	Dy02	O15	159.8(8)	O20	C39	C37	115.0(17)
O22[2]	Dy02	O16	141.9(9)	C37	C39	Dy01[5]	175.8(18)
O22[2]	Dy02	O17	78.5(10)	O21	C40	C35	117.7(18)
O22[2]	Dy02	N8	165.7(8)	O22	C40	O21	123(2)
O22[2]	Dy02	C49[3]	100.3(6)	O22	C40	C35	119.3(17)
C49[3]	Dy02	N8	90.8(5)	C42	C41	C22	174(2)
N2	Ru1	N1	77.9(7)	C41	C42	C43	171(2)
N3	Ru1	N1	93.9(8)	C44	C43	C42	127.9(18)
N3	Ru1	N2	90.5(7)	C44	C43	C48	120.7(18)
N3	Ru1	N6	172.2(7)	C48	C43	C42	111.2(17)
N4	Ru1	N1	169.7(8)	C43	C44	C45	120.4(18)
N4	Ru1	N2	94.3(7)	C44	C45	C46	123.4(17)
N4	Ru1	N3	79.4(7)	C44	C45	C49	121.0(16)
N4	Ru1	N5	91.2(7)	C46	C45	C49	115.4(17)
N4	Ru1	N6	97.4(6)	C45	C46	C47	115.5(18)
N5	Ru1	N1	97.1(7)	C46	C47	C50	121.0(17)
N5	Ru1	N2	173.3(6)	C48	C47	C46	120.6(18)
N5	Ru1	N3	94.3(6)	C48	C47	C50	118.4(16)
N5	Ru1	N6	78.6(5)	C47	C48	C43	119.2(17)
N6	Ru1	N1	90.3(7)	O3	C49	Dy02[4]	63.1(10)
N6	Ru1	N2	96.9(5)	O3	C49	C45	115.8(17)
C50	O1	Dy01	156.9(15)	O4	C49	Dy02[4]	60.2(9)
C50	O2	Dy02	171.1(19)	O4	C49	O3	123.3(17)
C49	O3	Dy02[4]	90.3(12)	O4	C49	C45	120.6(17)
C49	O4	Dy02[4]	94.0(11)	C45	C49	Dy02[4]	174(2)
N9	O7	Dy02	98.5(13)	O1	C50	C47	117.6(15)
N10	O8	Dy01	97.0(11)	O2	C50	O1	122(2)
N10	O9	Dy01	90.8(11)	O2	C50	C47	119.7(19)
N11	O11	Dy01	93.1(14)	O18	C51	N7	124(3)

[1]1+X,1+Y,-1+Z; [2]+X,1+Y,-1+Z; [3]-1+X,+Y,+Z; [4]1+X,+Y,+Z; [5]-1+X,-1+Y,1+Z; [6]+X,-1+Y,1+Z

Table H6 Torsion Angles for DyRu-MOF.

A	B	C	D	Angle/˚	A	B	C	D	Angle/˚
Dy01	O1	C50	O2	-28(7)	C8	C7	C6	N2	2(5)
Dy01	O1	C50	C47	159(4)	C8	C7	C6	C5	-177(3)
Dy01[1]	O19	C39	O20	1(3)	C9	C8	C7	C6	2(5)
Dy01[1]	O19	C39	C37	177(2)	C10	N2	C6	C5	179.4(19)
Dy01[1]	O20	C39	O19	-1(3)	C10	N2	C6	C7	1(3)

Table H6 Torsion Angles for DyRu-MOF.

A	B	C	D	Angle/˚	A	B	C	D	Angle/˚
Dy01[1]	O20	C39	C37	-177(2)	C10	C9	C8	C7	-8(5)
Dy01[2]	O21	C40	O22	-73(7)	C11	N4	C15	C14	8(4)
Dy01[2]	O21	C40	C35	109(4)	C11	N4	C15	C16	173.0(19)
Dy02[3]	O3	C49	O4	-1(3)	C11	C12	C13	C14	3(7)
Dy02[3]	O3	C49	C45	173(2)	C12	C13	C14	C15	9(7)
Dy02[3]	O4	C49	O3	1(3)	C13	C14	C15	N4	-15(6)
Dy02[3]	O4	C49	C45	-173(3)	C13	C14	C15	C16	-178(4)
Dy02[2]	O22	C40	O21	31(9)	C14	C15	C16	N3	178(3)
Dy02[2]	O22	C40	C35	-150(5)	C14	C15	C16	C17	-12(5)
Ru1	N1	C1	C2	-178(3)	C15	N4	C11	C12	4(3)
Ru1	N1	C5	C4	-176(3)	C15	C16	C17	C18	-170(3)
Ru1	N1	C5	C6	5(3)	C16	N3	C20	C19	-2(4)
Ru1	N2	C6	C5	-8(3)	C16	C17	C18	C19	3(5)
Ru1	N2	C6	C7	174(2)	C17	C18	C19	C20	-4(5)
Ru1	N2	C10	C9	-179(2)	C18	C19	C20	N3	4(5)
Ru1	N3	C16	C15	-12(3)	C20	N3	C16	C15	171(3)
Ru1	N3	C16	C17	178(2)	C20	N3	C16	C17	1(4)
Ru1	N3	C20	C19	-178(2)	C21	N6	C25	C24	-5(3)
Ru1	N4	C11	C12	-174(3)	C21	N6	C25	C26	-179.7(16)
Ru1	N4	C15	C14	-173(3)	C21	C22	C23	C24	2(4)
Ru1	N4	C15	C16	-9(3)	C22	C23	C24	C25	-2(4)
Ru1	N5	C26	C25	-9(3)	C23	C24	C25	N6	3(4)
Ru1	N5	C26	C27	174(2)	C23	C24	C25	C26	177(3)
Ru1	N5	C30	C29	-179.2(17)	C24	C25	C26	N5	-175(2)
Ru1	N6	C21	C22	174.6(17)	C24	C25	C26	C27	1(4)
Ru1	N6	C25	C24	-174.7(19)	C25	N6	C21	C22	6(2)
Ru1	N6	C25	C26	11(3)	C25	C26	C27	C28	-168(3)
O3	C49	C45	C44	4(4)	C26	N5	C30	C29	1(3)
O3	C49	C45	C46	-171(3)	C26	C27	C28	C29	-6(4)
O4	C49	C45	C44	178(3)	C27	C28	C29	C30	1(4)
O4	C49	C45	C46	3(4)	C27	C28	C29	C31	179(2)
O6	N9	O7	Dy02	169(2)	C28	C29	C30	N5	2(4)
O6	N9	O17	Dy02	-169(2)	C30	N5	C26	C25	171(2)
O7	N9	O17	Dy02	10(2)	C30	N5	C26	C27	-5(4)
O8	N10	O9	Dy01	-13.7(16)	C31	C29	C30	N5	-177(2)
O9	N10	O8	Dy01	14.6(17)	C32	C33	C34	C35	-177(3)
O10	N10	O8	Dy01	-169.2(14)	C32	C33	C38	C37	176(3)
O10	N10	O9	Dy01	170.1(15)	C33	C34	C35	C36	7(4)
O11	N11	O12	Dy01	0(2)	C33	C34	C35	C40	-179(3)
O12	N11	O11	Dy01	0(2)	C33	C38	C37	C36	-4(4)
O13	N11	O11	Dy01	-180(2)	C33	C38	C37	C39	-178(2)
O13	N11	O12	Dy01	180(2)	C34	C33	C38	C37	-1(4)
O14	N8	O15	Dy02	-161.2(18)	C34	C35	C40	O21	3(4)
O14	N8	O16	Dy02	160.7(17)	C34	C35	C40	O22	-176(3)
O15	N8	O16	Dy02	-15.8(19)	C35	C36	C37	C38	11(4)
O16	N8	O15	Dy02	15.0(18)	C35	C36	C37	C39	-176(3)
O17	N9	O7	Dy02	-11(2)	C36	C35	C40	O21	177(3)
O18	C51	N7	C52	-173(3)	C36	C35	C40	O22	-2(4)

Table H6 Torsion Angles for DyRu-MOF.

A	B	C	D	Angle/˚	A	B	C	D	Angle/˚
O18	C51	N7	C53	0(3)	C36	C37	C39	O19	-177(3)
N1	C5	C4	C3	-1(5)	C36	C37	C39	O20	-1(4)
N2	C6	C5	N1	1(4)	C37	C36	C35	C34	-12(4)
N2	C6	C5	C4	-177(3)	C37	C36	C35	C40	174(2)
N2	C10	C9	C8	10(4)	C38	C33	C34	C35	-1(4)
N3	C16	C17	C18	-1(5)	C38	C37	C39	O19	-3(4)
N4	C11	C12	C13	-9(6)	C38	C37	C39	O20	173(3)
N4	C15	C16	N3	14(4)	C41	C22	C23	C24	175(3)
N4	C15	C16	C17	-176(3)	C42	C43	C44	C45	179(3)
N5	C26	C27	C28	8(4)	C44	C45	C46	C47	4(4)
N6	C21	C22	C23	-5(3)	C46	C45	C44	C43	-7(5)
N6	C21	C22	C41	-176.7(18)	C46	C47	C48	C43	0(4)
N6	C25	C26	N5	-1(3)	C46	C47	C50	O1	-12(4)
N6	C25	C26	C27	175(2)	C46	C47	C50	O2	175(3)
N7	C51	O18	Dy01	133(3)	C47	C48	C43	C42	-177(3)
C1	N1	C5	C4	-2(5)	C47	C48	C43	C44	-3(4)
C1	N1	C5	C6	180(3)	C48	C43	C44	C45	6(4)
C3	C2	C1	N1	-12(6)	C48	C47	C46	C45	-1(4)
C4	C3	C2	C1	8(6)	C48	C47	C50	O1	169(3)
C5	N1	C1	C2	9(5)	C48	C47	C50	O2	-4(4)
C5	C4	C3	C2	-2(6)	C49	C45	C44	C43	179(3)
C6	N2	C10	C9	-7(3)	C49	C45	C46	C47	178(3)
C6	C5	C4	C3	177(3)	C50	C47	C46	C45	-179(3)
C7	C6	C5	N1	-180(3)	C50	C47	C48	C43	179(2)
C7	C6	C5	C4	2(5)					

[1]-1+X,-1+Y,1+Z; [2]+X,-1+Y,1+Z; [3]1+X,+Y,+Z

Table H7 Hydrogen Atom Coordinates (Å×10^4) and Isotropic Displacement Parameters (Å^2×10^3) for DyRu-MOF.

Atom	*x*	*y*	*z*	U(eq)
H6	5568.65	4181.16	6763.68	145
H8	4711.49	3692.93	5733.57	157
H9	5953.71	3655.29	4705.7	162
H10	8089.28	3700.93	4824.63	158
H7	10084.76	3762.66	5028.94	139
H3	12147.13	3736.17	5376.98	143
H1	12652.57	3714.2	6586.99	145
H4	11054.15	4140.12	7395.27	129
H11	9545.63	5734.31	8194.85	141
H12	11036.96	5682.95	9092.01	185
H13	11367.18	4266.52	9843.97	188
H14	10295.53	2943.49	9617.69	166
H17	9474.09	1695.95	9247.28	129
H18	8558.63	452.75	8772.19	125
H19	7604.8	719.21	7650.96	115
H1N	7395.51	2266.51	7116.7	117
H5	9483.76	5894.43	6488.77	82
H16	7179.49	8270.31	6477.46	100
H2	5852.16	7428.12	7235.41	104

Table H7 Hydrogen Atom Coordinates (Å×10^4) and Isotropic Displacement Parameters (Å^2×10^3) for DyRu-MOF.

Atom	*x*	*y*	*z*	U(eq)
H27	4656.52	6473.72	7924.86	98
H28	3840.59	5558.35	8900.15	102
H30	6531.13	3483.34	8639.42	85
H34	5755.72	2197.39	10785.83	102
H36	3210.45	878.02	12014.78	60
H38	2158.74	2935.02	10450.55	75
H44	12102.55	8456.57	5016.09	81
H46	11144.07	10183.99	3216.52	101
H48	8504.2	9019.33	4540.47	81

Table H8 Atomic Occupancy for DyRu-MOF.

Atom	*Occupancy*	Atom	*Occupancy*	Atom	*Occupancy*
O18	0.75	N7	0.75	C51	0.75
C52	0.75	C53	0.75		

Table H9 Solvent masks information for DyRu-MOF.

Number	X	Y	Z	Volume	Electron count	Content
1	0.068	0.183	0.727	12.8	0.0	?
2	-0.068	0.817	0.273	12.8	0.0	?
3	0.500	1.000	0.000	110.6	19.6	?
4	0.444	0.653	0.641	16.4	3.9	?
5	0.556	0.347	0.359	16.4	3.8	?

Experimental

Single crystals of $C_{26.12}H_{14}Gd_{0.88}N_{5.12}O_{10.62}Ru_{0.5}$ **[GdRu-MOF]** were synthesised (Chapters 4&6). A suitable crystal was selected and measured on a **Bruker APEX-II CCD** diffractometer. The crystal was kept at 100.00 K during data collection. Using Olex2 [1], the structure was solved with the SHELXT [2] structure solution program using Intrinsic Phasing and refined with the XL [3] refinement package using Least Squares minimisation.

1. Dolomanov, O.V., Bourhis, L.J., Gildea, R.J, Howard, J.A.K. & Puschmann, H. (2009), J. Appl. Cryst. 42, 339-341.
2. Sheldrick, G.M. (2015). Acta Cryst. A71, 3-8.
3. Sheldrick, G.M. (2008). Acta Cryst. A64, 112-122.

Crystal structure determination of [DyRu-MOF]

Crystal Data for $C_{52.25}H_{28}Dy_2N_{10.75}O_{21.75}Ru$ (*M* =1580.42 g/mol): triclinic, space group P-1 (no. 2), a = 10.8924(8) Å, b = 14.1396(17) Å, c = 18.798(2) Å, α = 84.900(10)°, β = 89.523(8)°, γ = 85.812(8)°, V = 2876.0(5) Å^3, Z = 2, T = 100.00 K, μ(CuKα) = 16.557 mm^{-1}, *Dcalc* = 1.825 g/cm^3, 30514 reflections measured (4.72° ≤ 2Θ ≤ 115.634°), 7765 unique (R_{int} = 0.1797, R_{sigma} = 0.1506) which were used in all calculations. The final R_1 was 0.1082 (I > 2σ(I)) and wR_2 was 0.3249 (all data).

Refinement model description

Number of restraints - 1012, number of constraints - unknown.

Details:

1. Restrained distances	1.45 with sigma of 0.02	1.35 with sigma of 0.02
C51-O18	N7-C53	C10-C9 = C9-C8 = C8-C7 =
1.22 with sigma of 0.02	1.46 with sigma of 0.02	C7-C6 = C4-C3 = C3-C2 = C2-
C51-N7	N2-C10 = N1-C5 = N1-C1	C1
1.36 with sigma of 0.02	1.34 with sigma of 0.02	1.39 with sigma of 0.02
N7-C52	N2-C6	C6-C5

1.48 with sigma of 0.02
C5-C4
1.4 with sigma of 0.02
N4-C11 = N3-C16 = N3-C20
1.34 with sigma of 0.02
N4-C15
1.35 with sigma of 0.02
C11-C12 = C12-C13 = C13-C14 = C14-C15 = C17-C18 = C18-C19 = C19-C20
1.39 with sigma of 0.02
C15-C16
1.48 with sigma of 0.02
C16-C17
1.4 with sigma of 0.02
N6-C21 = N5-C26 = N5-C30
1.34 with sigma of 0.02
N6-C25
1.35 with sigma of 0.02
C21-C22 = C22-C23 = C23-C24 = C24-C25 = C27-C28 = C28-C29 = C29-C30
1.39 with sigma of 0.02
C25-C26
1.48 with sigma of 0.02
C26-C27
1.4 with sigma of 0.02
N8-O15 = N8-O14
1.25 with sigma of 0.02
N8-O16
1.24 with sigma of 0.02
N9-O17 = N9-O7
1.25 with sigma of 0.02
N9-O6
1.24 with sigma of 0.02
N10-O8 = N10-O10
1.25 with sigma of 0.02
N10-O9
1.24 with sigma of 0.02
N11-O11 = N11-O13
1.25 with sigma of 0.02
N11-O12
1.24 with sigma of 0.02
C51-C52
2.46 with sigma of 0.04
C51-C53
2.45 with sigma of 0.04
N2-C9 = N2-C7 = N1-C4 = N1-C2 = C8-C6 = C5-C3
2.4 with sigma of 0.04
N2-C5 = N1-C6 = C10-C8 = C9-C7 = C4-C2 = C3-C1
2.39 with sigma of 0.04
C7-C5
2.52 with sigma of 0.04
C6-C4
2.53 with sigma of 0.04
N4-C12 = N4-C14 = N3-C17 = N3-C19 = C13-C15 = C16-C18
2.4 with sigma of 0.04
N4-C16 = N3-C15 = C11-C13 = C12-C14 = C17-C19 = C18-C20
2.39 with sigma of 0.04
C14-C16
2.52 with sigma of 0.04
C15-C17
2.53 with sigma of 0.04
N6-C22 = N6-C24 = N5-C27 = N5-C29 = C23-C25 = C26-C28
2.4 with sigma of 0.04
N6-C26 = N5-C25 = C21-C23 = C22-C24 = C27-C29 = C28-C30
2.39 with sigma of 0.04
C24-C26
2.52 with sigma of 0.04
C25-C27
2.53 with sigma of 0.04
N7-C52 ≈ N7-C53
with sigma of 0.02
N2-C10 ≈ N2-C6 ≈ N1-C5 ≈ N1-C1
with sigma of 0.02
C9-C8 ≈ C8-C7 ≈ C7-C6 ≈ C5-C4 ≈ C4-C3 ≈ C3-C2 ≈ C2-C1
with sigma of 0.02
N2-C7 ≈ N2-C9 ≈ N1-C4 ≈ N1-C2
with sigma of 0.04
C10-C6 ≈ C10-C8 ≈ C9-C7 ≈ C8-C6 ≈ C5-C1 ≈ C5-C3 ≈ C4-C2
with sigma of 0.04
N4-C11 ≈ N4-C15 ≈ N3-C16 ≈ N3-C20
with sigma of 0.02
C12-C13 ≈ C13-C14 ≈ C14-C15 ≈ C16-C17 ≈ C17-C18 ≈ C18-C19
≈ C19-C20
with sigma of 0.02
N4-C14 ≈ N4-C12 ≈ N3-C17 ≈ N3-C19
with sigma of 0.04
C11-C15 ≈ C11-C13 ≈ C12-C14 ≈ C13-C15 ≈ C16-C20 ≈ C16-C18
≈ C17-C19
with sigma of 0.04
N6-C21 ≈ N6-C25 ≈ N5-C26 ≈ N5-C30
with sigma of 0.02
C22-C23 ≈ C23-C24 ≈ C24-C25 ≈ C26-C27 ≈ C27-C28 ≈ C28-C29
≈ C29-C30
with sigma of 0.02
N6-C24 ≈ N6-C22 ≈ N5-C27 ≈ N5-C29
with sigma of 0.04
C21-C25 ≈ C21-C23 ≈ C22-C24 ≈ C23-C25 ≈ C26-C30 ≈ C26-C28
≈ C27-C29
with sigma of 0.04
N8-O15 ≈ N8-O16 ≈ N8-O14
with sigma of 0.02
O15-O16 ≈ O16-O14 ≈ O14-O15
with sigma of 0.04
N9-O17 ≈ N9-O6 ≈ N9-O7
with sigma of 0.02
O17-O6 ≈ O6-O7 ≈ O7-O17
with sigma of 0.04
N10-O8 ≈ N10-O9 ≈ N10-O10
with sigma of 0.02
O8-O9 ≈ O9-O10 ≈ O10-O8
with sigma of 0.04
N11-O11 ≈ N11-O12 ≈ N11-O13
with sigma of 0.02
O11-O12 ≈ O12-O13 ≈ O13-O11
with sigma of 0.04

2. Restrained planarity

O18, N7, C51, C52, C53
with sigma of 0.1
N1, N2, C1, C2, C3, C4, C5, C6, C7, C8, C9, C10
with sigma of 0.1
N3, N4, C11, C12, C13, C14, C15, C16, C17, C18, C19, C20
with sigma of 0.1
N5, N6, C21, C22, C23, C24, C25, C26, C27, C28, C29, C30
with sigma of 0.1
O14, O15, O16, N8
with sigma of 0.1
O6, O7, O17, N9
with sigma of 0.1
O8, O9, O10, N10
with sigma of 0.1
O11, O12, O13, N11
with sigma of 0.1

3. Uiso/Uaniso restraints and constraints

O18 ≈ N7 ≈ C51 ≈ C52 ≈ C53: within 2A with sigma of 0.04 and
sigma for terminal atoms of

0.08 within 2A
N1 ≈ N2 ≈ C1 ≈ C2 ≈ C3 ≈ C4 ≈ C5 ≈ C6 ≈ C7
≈ C8 ≈ C9 ≈ C10: within 2A with sigma of 0.04 and sigma for
terminal atoms of 0.08 within 2A
N3 ≈ N4 ≈ C11 ≈ C12 ≈ C13 ≈ C14 ≈ C15 ≈ C16 ≈
C17 ≈ C18 ≈ C19 ≈ C20: within 2A with sigma of 0.04 and sigma for
terminal atoms of 0.08 within 2A
N5 ≈ N6 ≈ C21 ≈ C22 ≈ C23 ≈ C24 ≈ C25 ≈ C26 ≈
C27 ≈ C28 ≈ C29 ≈ C30: within 2A with sigma of 0.04 and sigma for
terminal atoms of 0.08 within 2A
O14 ≈ O15 ≈ O16 ≈ N8: within 2A with sigma of 0.04 and sigma for
terminal atoms of 0.08 within 2A
O6 ≈ O7 ≈ O17 ≈ N9: within 2A with sigma of 0.04 and sigma for
terminal atoms of 0.08 within 2A
O8 ≈ O9 ≈ O10 ≈ N10: within 2A with sigma of 0.04 and sigma for
terminal atoms of 0.08 within 2A
O11 ≈ O12 ≈ O13 ≈ N11: within 2A with sigma of 0.04 and sigma for
terminal atoms of 0.08 within 2A
Uanis(O5) ≈ Ueq: with sigma of 0.01 and sigma for terminal atoms of 0.02

4. Rigid body (RIGU) restrains

O18, N7, C51, C52, C53
with sigma for 1-2 distances of 0.004 and sigma for 1-3 distances of 0.004
N1, N2, C1, C2, C3, C4, C5, C6, C7, C8, C9, C10
with sigma for 1-2 distances of 0.004 and sigma for 1-3 distances of 0.004
N3, N4, C11, C12, C13, C14, C15, C16, C17, C18, C19, C20
with sigma for 1-2 distances of 0.004 and sigma for 1-3 distances of 0.004
N5, N6, C21, C22, C23, C24, C25, C26, C27, C28, C29, C30
with sigma for 1-2 distances of 0.004 and sigma for 1-3 distances of 0.004
O14, O15, O16, N8
with sigma for 1-2 distances of 0.004 and sigma for 1-3 distances of 0.004
O6, O7, O17, N9
with sigma for 1-2 distances of 0.004 and sigma for 1-3 distances of 0.004
O8, O9, O10, N10
with sigma for 1-2 distances of 0.004 and sigma for 1-3 distances of 0.004
O11, O12, O13, N11
with sigma for 1-2 distances of 0.004 and sigma for 1-3 distances of 0.004

5. Others

Fixed Sof: C51(0.75) O18(0.75) N7(0.75) C52(0.75) C53(0.75)

6.a Aromatic/amide H refined with riding coordinates:

C36(H36), C34(H34), C38(H38), C48(H48), C46(H46), C44(H44), C10(H4), C9(H1),
C8(H3), C7(H7), C4(H10), C3(H9), C2(H8), C1(H6), C11(H11), C12(H12), C13(H13),
C14(H14), C17(H17), C18(H18), C19(H19), C20(H1N), C21(H5), C23(H16), C24(H2),
C27(H27), C28(H28), C30(H30)

This report has been created with Olex2, compiled on 2025.07.13 svn.rb7424aed for OlexSys.